NASA-CR-195706

IN-02-CR
906
189 P

NONEQUILIBRIUM RADIATION AND CHEMISTRY MODELS FOR AEROCAPTURE VEHICLE FLOWFIELDS

AEROSPACE ENGINEERING DEPARTMENT

Final Report

TEXAS A&M UNIVERSITY

TAMRF Report No. 6382-94-01
March 1994

NASA Grant No. NAG-1-1003

Leland A. Carlson
Professor of Aerospace Engineering
Texas A&M University
College Station, TX 77843-3141

TEXAS ENGINEERING EXPERIMENT STATION

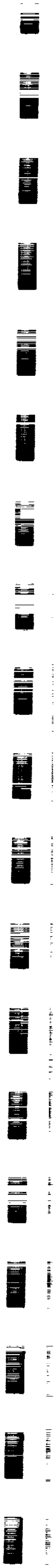

NONEQUILIBRIUM RADIATION AND CHEMISTRY MODELS FOR AEROCAPTURE VEHICLE FLOWFIELDS

Final Report

TAMRF Report No. 6382-94-01
March 1994

NASA Grant No. NAG-1-1003

Leland A. Carlson
Professor of Aerospace Engineering
Texas A&M University
College Station, TX 77843-3141

NONEQUILIBRIUM RADIATION AND CHEMISTRY MODELS FOR AEROCAPTURE VEHICLE FLOWFIELDS

I. Introduction

This report will attempt to concisely summarize the activities and accomplishments associated with NASA Grant NAG-1-1003. The project started on June 7, 1989 and officially terminated on December 31, 1993. Total funding for the project was $209,909, and all grant funds were essentially expended by August 31, 1993. The project also received financial support from the Aerospace Engineering Department in the form of Graduate Assistantship funds and faculty salary support. Also, an integral member of the research team, Dr. Thomas Gally, was supported most of the time by a Graduate Student Researchers Fellowship from the NASA Johnson Space Center. Finally, significant moral and technical support was provided by many individuals at NASA Langley Research Center. As a result of all of these contributions, significant accomplishments were achieved by the project; and these are summarized below.

II. Personnel

The individuals who have been associated with the project are as follows:

Leland A. Carlson, Professor of Aerospace Engineering -- Dr. Carlson served as the principal investigator for the project. At various times, Dr. Carlson was partially supported by the project.

Thomas A. Gally, Graduate Research Assistant and Visiting Assistant Professor -- Dr. Gally joined the project at its inception and was associated with it throughout. During the project, he earned his Ph.D. degree using research associated with the project for his dissertation. Dr. Gally was the primary researcher on the project and developed, among other items, the three temperature radiatively coupled nonequilibrium viscous shock layer (VSL) code, the nonequilibrium molecular and radiation models, and the full multi-component diffusion model. Dr. Gally was supported by a Graduate Student Researchers' Fellowship from the NASA Johnson Space Center and by the Department of Aerospace Engineering.

Derek Green, Graduate Research Assistant -- Mr. Green was on the project during his masters' thesis research. His research primarily concerned the development of the MCVD vibrational dissociation coupling model for the VSL code. Mr. Green was funded by the project during his masters' studies.

Scott A. Stanley, Graduate Research Assistant -- Mr. Stanley was on the project during his masters' thesis research. His research primarily concerned the development of a precursor model and a study of the effects of the pre-shock precursor on the shock structure. Mr. Stanley was funded by the project during his masters' studies.

Rajeev Koteshwar, Graduate Research Assistant -- Mr. Koteshwar used the codes and models developed by the project to study the effects of different vibrational relaxation and chemical reaction models on the flow about a vehicle entering the Martian atmosphere and used the results for his masters' research. Mr. Koteshwar was funded by the Department of Aerospace Engineering.

David Mott, Graduate Research Assistant -- Mr. Mott developed as part of his masters' research a viscous normal shock version of the radiatively coupled nonequilibrium VSL code. He also developed methods for determining the radiative emission normal to the flow axis in the region behind the shock wave including the effects of absorption and compared his predictions with shock tube data. Thus, his work served to validate the present VSL codes. Mr. Mott was funded by an American Society for Engineering Education -- Office of Naval Research Graduate Fellowship.

David McGough, Graduate Research Assistant -- Mr. McGough developed as part of his masters' research a preferential vibration dissociation coupling model and incorporated it into the nonequilibrium radiation coupled VSL code. He also developed a version which included and computed separate vibrational temperatures for the various diatomic species. Mr. McGough was funded by the project during his masters' studies.

III. Accomplishments

The primary accomplishments of the project were as follows:

1. From an overall standpoint, the primary accomplishment of this research was the development of a complete gasdynamic-radiatively coupled nonequilibrium viscous shock layer solution method for axisymmetric blunt bodies. This method can be used for rapid engineering modeling of nonequilibrium re-entry flowfields over a wide range of conditions. The model includes thermal nonequilibrium thru the inclusion of separate translational-rotational, vibrational, and electron-electronic energy models and temperatures, chemical nonequilibrium in a multi-temperature environment, multi-component multi-temperature diffusion, coupled nonequilibrium radiation that includes in detail emission and absorption phenomena and local thermodynamic nonequilibrium (LTNE) effects, shock slip, viscous and conduction effects, and partially catalytic walls. The overall model constitutes a significant advancement in the engineering modeling of nonequilibrium re-entry flowfields.

2. Another significant accomplishment was the development of an air radiation model that included LTNE phenomena. While this model was based upon a reliable radiation model for equilibrium flows, it was modified to include chemical

nonequilibrium, multi-temperature effects, and local thermodynamic nonequilibrium. For atomic LTNE phenomena, first and second order models were developed; and new excitation and ionization rates for the electron impact ionization of nitrogen and oxygen atoms were derived. These two atomic LTNE models are significant because atomic radiative phenomena is dominant during earth re-entry from Lunar-Mars missions. LTNE effects were also included for molecular radiation by incorporating appropriate excitation effects into the molecular model. Studies with these models demonstrated that on a blunt body LTNE effects are significant in the nonequilibrium zone immediately behind the shock front and are also important in the viscous-conduction layer near the wall. They also showed that excited levels in the immediate post-shock zone are usually depleted, which tends to reduce wall radiative heating and reduce radiative cooling phenomena, while those in the region near the wall are often over populated. The studies also indicated that with currently accepted excitation rates, the $N_2^+(1-)$ radiation is theoretically relatively unaffected by LTNE. The second order atomic LTNE model consistently showed a higher level of atomic line radiation, indicating that the first order assumption of full equilibrium between the excited states and the ions and electrons is approximate. However, the usage of the excitation rates developed for the second order model in the first order model yielded acceptable engineering results.

3. As part of this research, three electron-electronic energy models were developed. The first was a quasi-equilibrium electron (QEE) model which determined an effective free electron temperature and assumed that the electronic states were in equilibrium with the free electrons. The second was a quasi-equilibrium electron-electronic (QEEE) model which computed an effective electron-electronic temperature. These two models are algebraic models and served to delineate the importance of electron-electronic energy in both the chemical and radiative nonequilibrium phenomena; and their "simplicity" may be useful in some cases. The third model was a full electron-electronic (FEE) differential equation model which included convective, collisional, viscous, conductive, vibrational coupling, and chemical effects on electron-electronic energy. This complete model is recommended for general usage and is the one used in most of the results reported by this project.

4. Since vibration-dissociation coupling phenomena as well as vibrational thermal nonequilibrium phenomena are important in the nonequilibrium zone behind a shock front, a vibrational energy and vibration-dissociation coupling model was developed and included in the flowfield model. This model was a modified coupled vibrational dissociation vibrational (MCVDV) model and also included electron-vibrational coupling. The "usual" version of this model uses a single vibrational temperature and is nonpreferential in that it assumes that dissociation will occur with an equal probability from all vibrational energy levels, given a sufficiently energetic collision. This model determines the effective dissociation rate based upon local multi-temperature phenomena and chemical composition from a consistent theoretical derivation. Since there has always been a belief that given a

sufficient energetic collision, dissociation should occur with a higher probability from higher energy levels, a preferential model was also developed. In addition, a multi-vibrational temperature model allowing separate vibrational temperatures and vibrational energy models for each diatomic species was developed and studied. As will be discussed below, surprisingly, the MCVDV nonpreferential model with a single vibrational temperature yielded the best agreement with flight experiments.

5. Another accomplishment of the project was the usage of the developed models to investigate radiative heating. Radiative heating and radiative coupling phenomena over a wide range of conditions were investigated, and the regions where such phenomena is important were determined. These studies identified for various entry conditions the spectral origin of the radiative phenomena as a function of vehicle size, flight velocity, and altitude. The studies also examined the effects of partially catalytic, non-catalytic, and fully catalytic wall phenomena and the absorption effects associated with the cool wall thermal layer. Details are presented in the various publications associated with the project.

6. A multi-component diffusion model which properly models the multi-component nature of diffusion in complex gas mixtures such as air, was developed and incorporated into the blunt body model. Interestingly, comparison of results calculated for both nitrogen and air freestreams using both this new model and a simple multicomponent binary gas model showed that the differences were not significant for the conditions considered. Since the calculations with the new model are more complicated and intense, it was concluded that the simpler model was adequate and should be used for most engineering analyses.

7. A model was developed to predict the magnitude and characteristics of the shock wave precursor ahead of vehicles entering the Earth's atmosphere. This model included chemical and thermal nonequilibrium, utilized detailed mass production rates for the photodissociation and photoionization reactions, and accounted for the effects of radiative absorption and emission on the individual internal energy modes of both atomic and diatomic species. Comparison of results with shock tube data indicated that the model was reasonably accurate. Studies indicated that there is a significant production of atoms, ions, and electrons ahead of the shock front due to radiative absorption and that the precursor is characterized by an enhanced electron-electronic temperature and molecular ionization. However, the studies also showed that the precursor has a negligible effect on the shock layer flowfield.

8. Since considerable data exists for radiating nonequilibrium flow behind normal shock waves, a normal shock wave version of the blunt body code was developed. This one-dimensional model included chemical, thermal, and local thermodynamic nonequilibrium as well as viscous and thermal conduction phenomena. It also included axial radiative cooling, and methods were developed for predicting the total and spectral variation of radiation which would be measured

normal to the flow direction. These methods included appropriate filter functions. Predicted spectral radiation intensity, spectrally integrated intensity traces, time to peak radiation, and ionization time data for shocks in air between 9.6 km/sec and 12.6 km/sec agreed reasonably well with available experimental data. Reproduction of the experimental data was best achieved when integrated values over broad frequency bands were considered and when the details concerning the experimental measurements, particularly the filters used, were known. The characteristics of the experimental radiation measurements were reproduced without adding iron contamination to the radiation model.

9. By comparing predictions from the models and codes with available normal shock data and the flight data of Fire II, it is believed that the developed flowfield and nonequilibrium radiation models have been essentially validated for engineering applications. Based upon these studies, it appears that the usage of reduced absorption coefficients for $N_2^+(1-)$ and $N_2(1+,2+)$ bands is warranted and that little if any vibrational preferential phenomena exist. While some uncertainties still exist in the radiative phenomena associated with some molecular species and the modeling of excited atomic states could possibly benefit from either multiple electron temperatures or additional grouping of excited states, the present model appears to be adequate for many engineering calculations.

IV. Progress in the Last Six Months

During the last six months, the primary research effort was in finishing the normal shock studies and the vibrational modeling and dissociation studies. While these two efforts are detailed in the masters' theses of David Mott and David McGough, they will be summarized briefly here. Copies of the theses of Mr. Mott and Mr. McGough will be sent under separate cover.

Normal Shock Studies

During this reporting period, the normal shock version of the code was completed and results obtained with it were compared with available shock tube data. Figs. 1-9 compare calculated intensity traces with those measured by Wilson in his shock tube experiments. Wilson used spectral filters in his measurements, and these were included in the calculated data. However, since the source of observed radiation originates from different spectral regions during the equilibrium zone than during the nonequilibrium post-shock region, the scale associated with the experimental data is different for the two zones. Hence, the comparisons are shown in two forms for the 5000 A° data. The first is plotted to match the nonequilibrium peak while the second is plotted to match the equilibrium intensity level. In the 5000 A cases, the time to peak and the behavior of the immediate post shock calculated traces agree well with the experimental results. In addition, the changing character and shape of the traces with shock velocity is well reproduced by the theoretical results. The IR results also show reasonably good agreement.

Notice that the theoretical results also predict in most cases the measured increases and decreases observed in the "equilibrium" zones. These variations have in the past been attributed to shock attenuation in the experiment. However, in most cases, no such significant shock attenuation was ever detected in the experiments. Since the present theoretical results do not include any shock attenuation and since the agreement is good, it is concluded that these downstream intensity variations are a radiative-gasdynamic phenomena and not due to variations in shock speed.

Some previous computations have attempted to obtain good correlation with Wilson's data by assuming that Wilson's aluminum shock tube was contaminated with iron. In the present case, by basing a frequency weighting function on the spectral response curves of the filters used in the experiment, the 5000 A intensities exhibit the secondary effects without including iron as a radiator. It should be noted that all data used in the comparisons is, based upon the experimental traces, obviously before the arrival of the driver gas and diaphragm contamination. Thus, it appears that the variations in the experimental traces could be due to the filters used in the experiment rather than flowfield contamination.

Figures 10 and 11 compare the present predictions with experimental data for time to peak radiation and ionization distances for various shock speeds and conditions. As can be seen, the present radiation model predicts the trends and the magnitudes of these quantities quite well.

Figures 12-16 compare the spectral variation of the predicted flows and those measured experimentally by Avco and by Sharma. For the Avco data, Figs. 12-14, while the overall agreement and trends is good, the present model does appear to overpredict the radiative intensity in the 2.5-4 eV regime. This overprediction for this regime is consistent with previous comparison of the blunt body model results with the FIRE II flight data and lends support to the need to reduce the absorption coefficients of the dominant radiators in that region, primarily $N_2^+(1-)$. The Sharma nonequilibrium data, Fig. 15, also indicates that perhaps the present model slightly overpredicts the radiation in this region. It also indicates some radiation from the 2 eV to 2.5eV region that is not predicted by the present model.

On the other hand, the Sharma equilibrium data, Fig. 16, and the calculated profiles exhibit similar behavior, including the effect of atomic lines, although the Sharma data may predict slightly higher intensities. In this case, while the calculated detailed profiles are below the experimental points in the 1.75-2.25 eV , the grouped intensities show good agreement with the experimental values. Nevertheless, it appears that the region between 1.75 eV and 2. eV may require further study and that the radiation model could benefit from some improvements in this region. It also appears that the radiation originating in the 2 - 4 eV range could be refined in the model.

However, in spite of these two minor points, the overall agreement between the normal shock predictions based upon the present flowfield and radiation model is quite good; and it indicates that the present models should be adequate for engineering computations.

Vibration-Dissociation Studies

In the last progress report, it was shown that there was little evidence, based upon comparison with the Fire II flight data, that vibrational preferentiality existed. Further, since the above normal shock computations reproduced times to peak and relaxation distances, which are very sensitivity to preferentiality, and since those computations did not use the preferential vibrational model, it is believed that the nonpreferential MCVDV model is probably adequate for engineering studies. It was also demonstrated in the last report that slightly better agreement could be obtained with the Fire II data using reduced absorption coefficients for $N_2^+(1-)$ and $N_2(1+,2+)$ radiation. Thus, during this reporting period, the effort concentrated on examining the effect of using multiple vibrational temperatures instead of a single vibrational temperature to represent vibrational energy. Results were obtained for the nonpreferential MCVDV single vibrational temperature model for Fire II conditions from 1634 to 1640.5 seconds while multiple vibrational temperatures were obtained from 1634 to 1639 seconds.

Typical multiple vibrational temperature results are shown on Figures 17 and 18. While these results include vibrational-dissociation coupling and electron-vibration coupling as appropriate, they do not include vibration-vibration coupling. Since V-V coupling would tend to equilibrate the vibrational temperatures among themselves, the present results should exhibit the greatest possible effects due to multiple vibrational temperatures and energies. As shown on the figures, the vibrational temperatures for N_2^+, NO, NO^+, and O_2^+ rapidly equilibrate with the translational rotational temperature. Since these species are formed by atom-atom collisions and by particle exchange rather than ionization of the diatomic molecules, this result is not surprising. Also, as known from experimental data, the O_2 vibrational energy equilibrates faster than N_2. Further, due to electron-vibrational coupling the N_2 vibrational temperature is almost always very close to the electron temperature.

Examination of the radiative heat transfer reveals that the multiple vibrational temperature reults predict radiative heating loads for the nonequilibrium portion of the Fire II profile in the 2-4 eV and 0 - 6.2 eV range above those obtained with single vibrational temperature results. Since the values predicted by the single vibrational temperature model are slightly above the Fire II data, these comparisons indicate the single vibrational temperature model should be adequate for engineering purposes, particularly considering the extra computational work required to compute and handle multiple vibrational temperatures.

Figures 19-20 summarize the comparisons of the present models with the Fire II flight data. In general, the overall agreement and trends are reasonably good. In particular, it appears that the present model using reduced absorption coefficients and a single vibrational temperature with the MCVDV model reasonably predicts the radiation in the 2- 4 eV range. Also, since the total heating is predicted quite well, it is believed that the atomic radiation model, which primarily influences the region above 6.2 eV is also reasonably accurate. However, there is some disagreement for the predictions in the 0 - 6.2 eV range, with the calculated values being slightly low at the higher times. This trend in theoretical results has also been observed by other investigators. Since the higher times are for essentially equilibrium flowfields and since the equilibrium portion of the present radiation model was extensively verified in the past against incident and reflected shock tube data by its developers, the present discrepancy at the higher times may be due to some other explanation. Since Fire II is a single experiment, this difference probably will not be explained until further flight experiments are conducted.

Based upon these results and upon the normal shock results, it is believed that the present nonequilibrium radiation and chemistry model is reasonably accurate and suitable for engineering use. As further experimental data becomes available, the present model could, of course, be refined and improved.

V. Publications and Degrees

The following degrees were earned at Texas A&M University by individuals associated with this research project:

Stanley, Scott A., Master of Science (Aerospace Engineering), December 1990.

Green, Derek S., Master of Science (Aerospace Engineering), May 1991.

Koteshwar, Rajeev, Master of Science (Aerospace Engineering), May 1992.

Gally, Thomas A., Doctor of Philosophy (Aerospace Engineering), May 1992.

McGough, David E., Master of Science (Aerospace Engineering), December 1993.

Mott, David R., Master of Science (Aerospace Engineering), December 1993.

The following publications resulted from research associated with this project:

Carlson, L. A. and Gally, T. A., "The Effect of Electron Temperature and Impact Ionization on Martian Return AOTV Flowfields," AIAA Paper 89-1729, June 1989.

Stanley, S. A., "The Effects of Shock Wave Precursors Ahead of Hypersonic Entry Vehicles," Master of Science Thesis, Aerospace Engineering Department, Texas A&M University, College Station, Texas, December 1990.

Carlson, L. A. and Gally, T. A., "Effect of Electron Temperature and Impact Ionization on Martian Return AOTV Flowfields," ***Journal of Thermophysics and Heat Transfer***, Vol. 5, No. 1, January 1991, pp. 9-20.

Carlson, L. A. and Gally, T. A., "Nonequilibrium Chemical and Radiation Coupling Phenomena in AOTV Flowfields," AIAA Paper 91-0569, January 1991.

Green, D. S., "A Comparative Study of Vibrational Relaxation Models for the Aeroassisted Orbital Transfer Vehicle Flight Regime," Master of Science Thesis, Aerospace Engineering Department, Texas A&M University, College Station, Texas, May 1991.

Gally, T. A., Carlson, L. A., and Green, D., "A Flowfield Coupled Excitation and Radiation Model for Nonequilibrium Reacting Flows," AIAA Paper 91-1463, June 1991.

Stanley, S. A. and Carlson, L. A., "The Effects of Shock Wave Precursors Ahead of Hypersonic Entry Vehicles," AIAA Paper 91-1465, June 1991.

Stanley, S. A. and Carlson, L. A., "Effects of Shock Wave Precursors Ahead of Hypersonic Entry Vehicles," ***Journal of Spacecraft and Rockets***, Vol. 29, No. 2, March-April 1992, pp. 190-197.

Koteshwar, R., "A Comparative Study of Vibrational Relaxation and Chemical Reaction Models for the Martian Entry Vehicle," Master of Science Thesis, Aerospace Engineering Department, Texas A&M University, College Station, Texas, May 1992.

Gally, T. A., "Development of Engineering Methods for Nonequilibrium Radiative Phenomena about Aeroassisted Entry Vehicles," Doctor of Philosophy Dissertation, Aerospace Engineering Department, Texas A&M University, College Station, Texas, May 1992.

Gally, T. A. and Carlson, L. A., "An Approximate Local Thermodynamic Nonequilibrium Radiation Model for Air," AIAA Paper 92-2972, July 1992.

Carlson, L. A. and Gally, T. A., "Nonequilibrium Chemical and Radiation Coupling, Part I: Theory and Models," ***Journal of Thermophysics and Heat Transfer***, Vol. 6, No. 3, July-September 1992, pp. 385-391.

Gally, T. A. and Carlson, L. A., "Nonequilibrium Chemical and Radiation Coupling, Part II: Results for AOTV Vehicles," ***Journal of Thermophysics and Heat Transfer***, Vol. 6, No. 3, July-September 1992, pp. 391-399.

Gally, T. A., Carlson, L. A., and Green, D., "Flowfield Coupled Excitation and Radiation Model for Nonequilibrium Reacting Flows," ***Journal of Thermophysics and Heat Transfer***, Vol. 7, No. 2, April-June 1993, pp. 285-293.

Gally, T. A. and Carlson, L. A., "Survey of Nonequilibrium Re-Entry Heating for Entry Flight Conditions," AIAA Paper 93-3230, July 1993.

McGough, D. E., Carlson, L. A., and Gally, T. A., "A Preferential Vibration Dissociation Coupling Model for Nonequilibrium Flowfields," AIAA Paper 93-3197, July 1993.

McGough, D. E., "A Preferential Vibration Dissociation Coupling Model for Nonequilibrium Hypersonic Flowfields," Master of Science Thesis, Aerospace Engineering Department, Texas A&M University, College Station, Texas, December 1993.

Mott, D. R., "Normal Shock Solutions to the Viscous Shock Layer Equations Including Thermal, Chemical, Thermodynamic, and Radiative Nonequilibrium," Master of Science Thesis, Aerospace Engineering Department, Texas A&M University, College Station, Texas, December 1993.

Mott, D. R., Gally, T. A., and Carlson, L. A., "Viscous Normal Shock Solutions Including Thermal, Chemical, and Radiative Nonequilibrium," AIAA Paper 94-2415, June 1994.

Stanley, S. A. and Carlson, L. A., "Complete Radiative Terms for the Electron-Electronic Energy Equation," ***Journal of Spacecraft and Rockets***, (to be published), 1994.

VI. Acknowledgments

The NASA technical monitor for this grant has been Dr. Lin C. Hartung, Aerothermodynamics Branch, Space Systems Division, NASA Langley Research Center, Hampton, Virginia. The participants in the project express their thanks and appreciation to Lin Hartung, Ken Sutton, Peter Gnoffo, Rick Thompson, and the entire Aerothermodynamics Branch for their assistance, helpful suggestions, and technical support. The Principal Investigator also wishes to thank Dr. Tom Gally for his dedicated efforts, hard work, and unique insight during all the phases of this project.

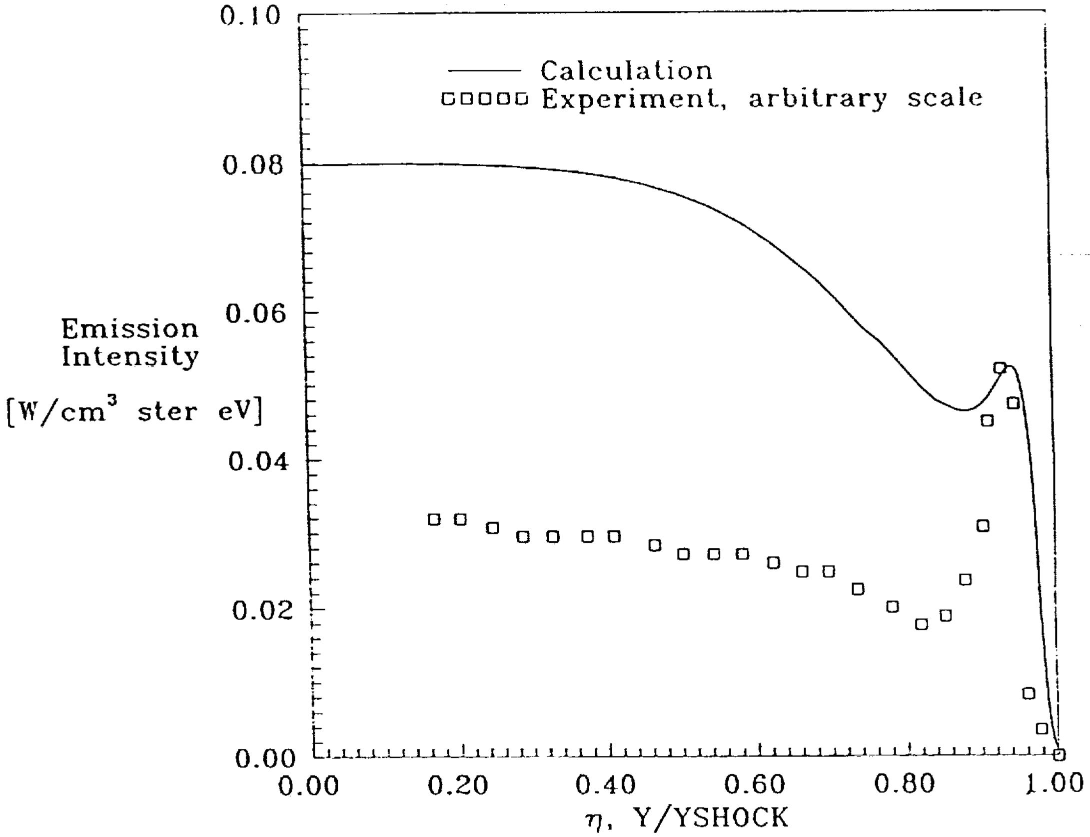

Fig. 1 -- 5000 A Intensity Traces for the Wilson 9.5 km/sec Case, Experimental Data Scaled to Match Initial Peak; $P_{initial}$ = 0.2 mm Hg.

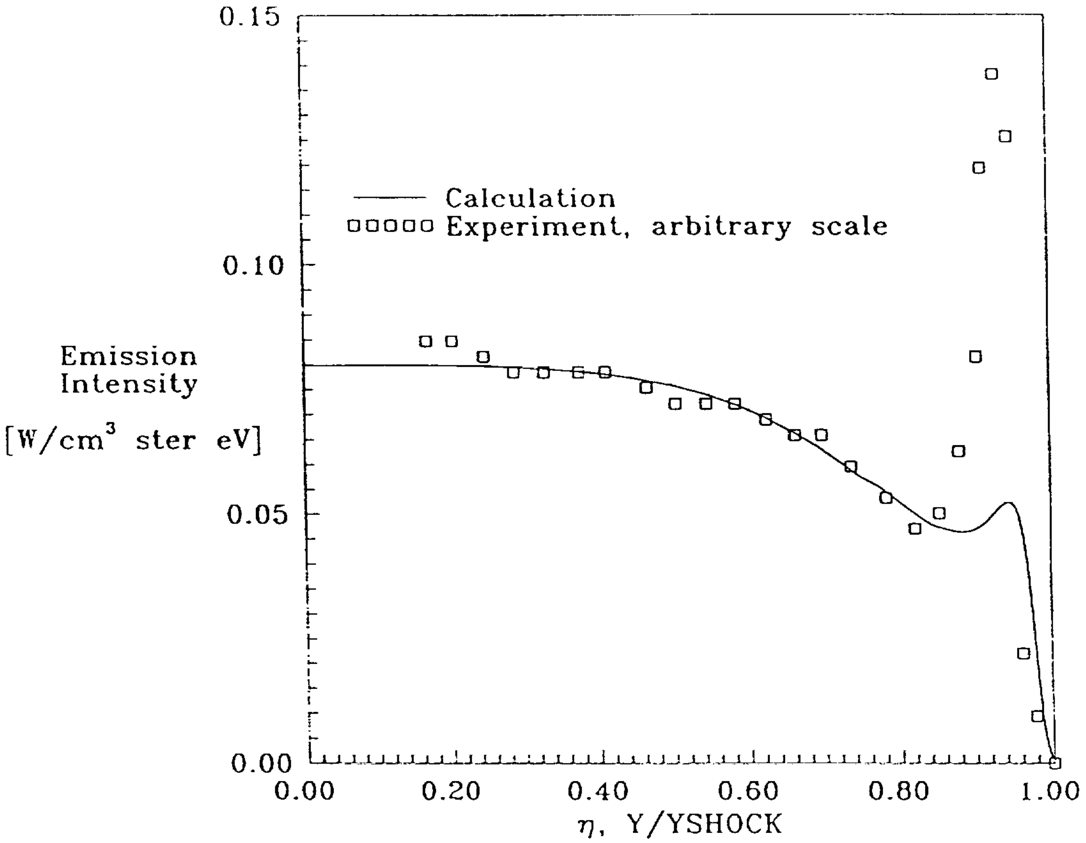

Fig. 2 -- 5000 A Intensity Traces for the Wilson 9.5 km/sec Case, Experimental Data Scaled to Match Secondary Rise; $P_{initial}$ = 0.2 mm Hg.

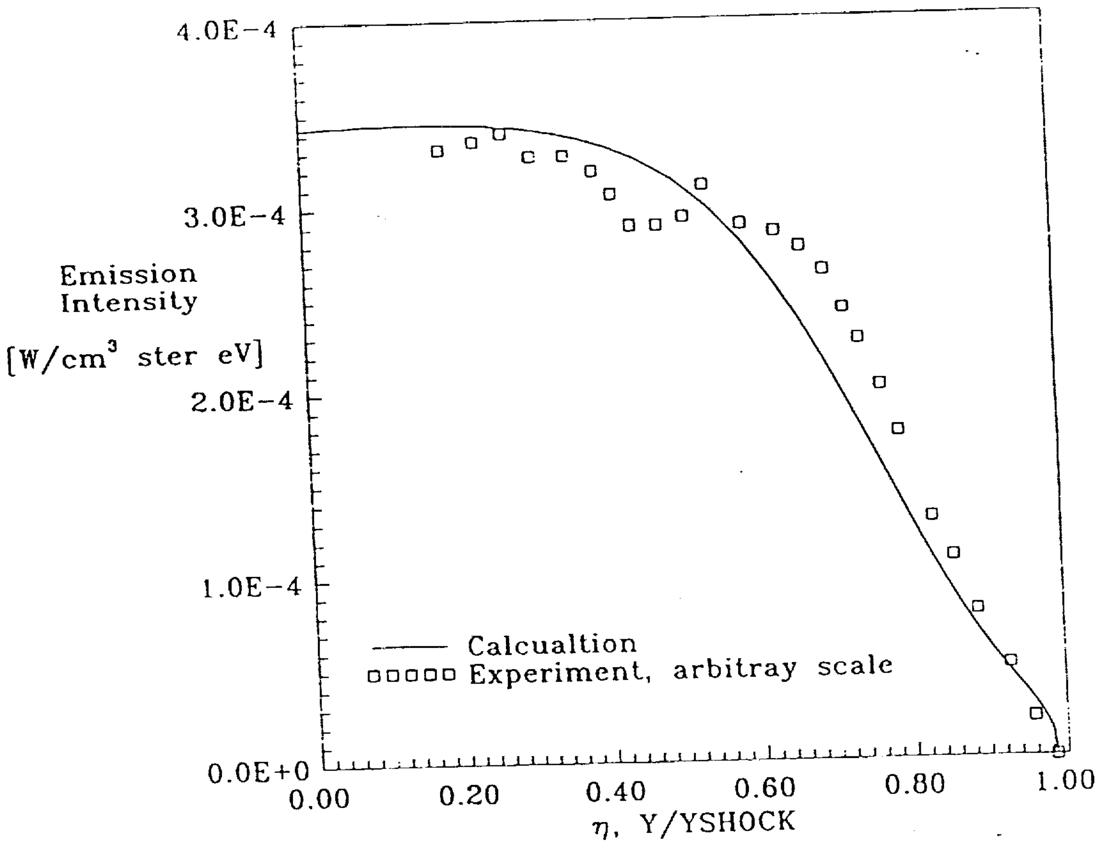

Fig. 3 -- IR Intensity Traces for the Wilson 9.5 km/sec Case, $P_{initial}$ = 0.2 mm Hg.

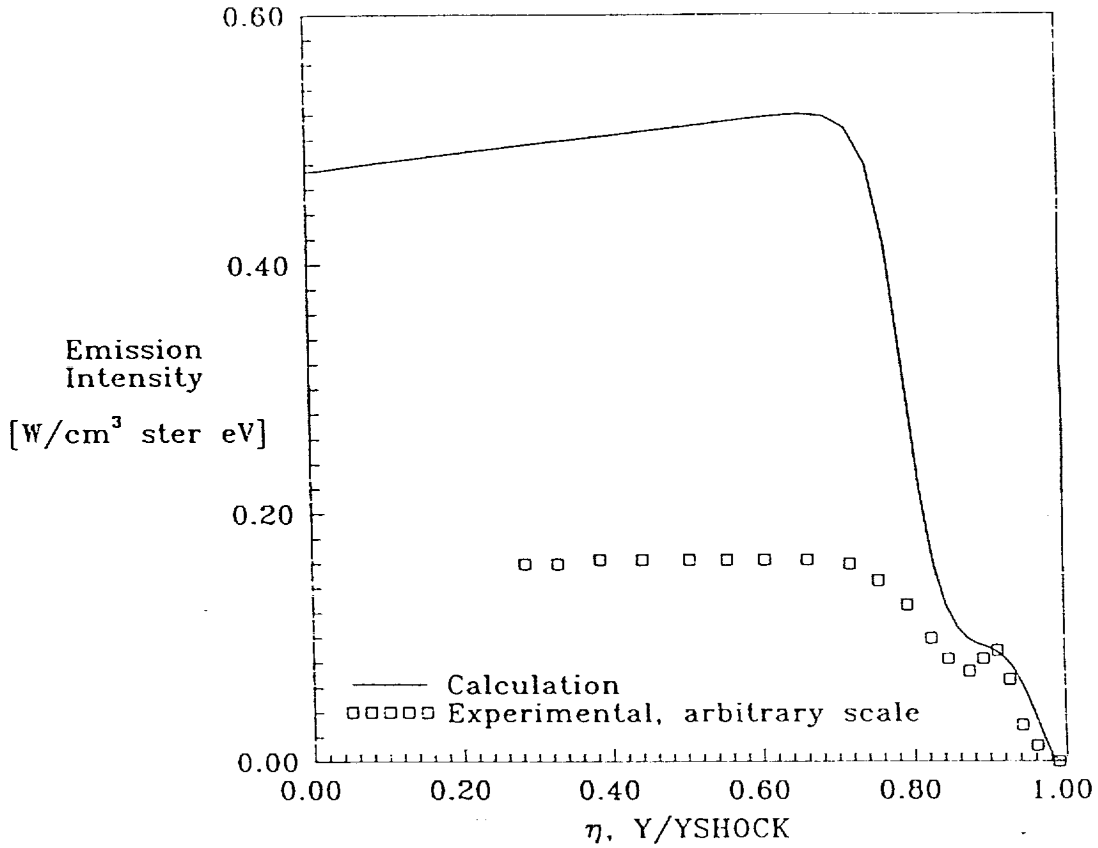

Fig. 4 -- 5000 A Intensity Traces for the Wilson 10.9 km/sec Case, Experimental Data Scaled to Match Initial Peak; $P_{initial}$ = 0.1 mm Hg.

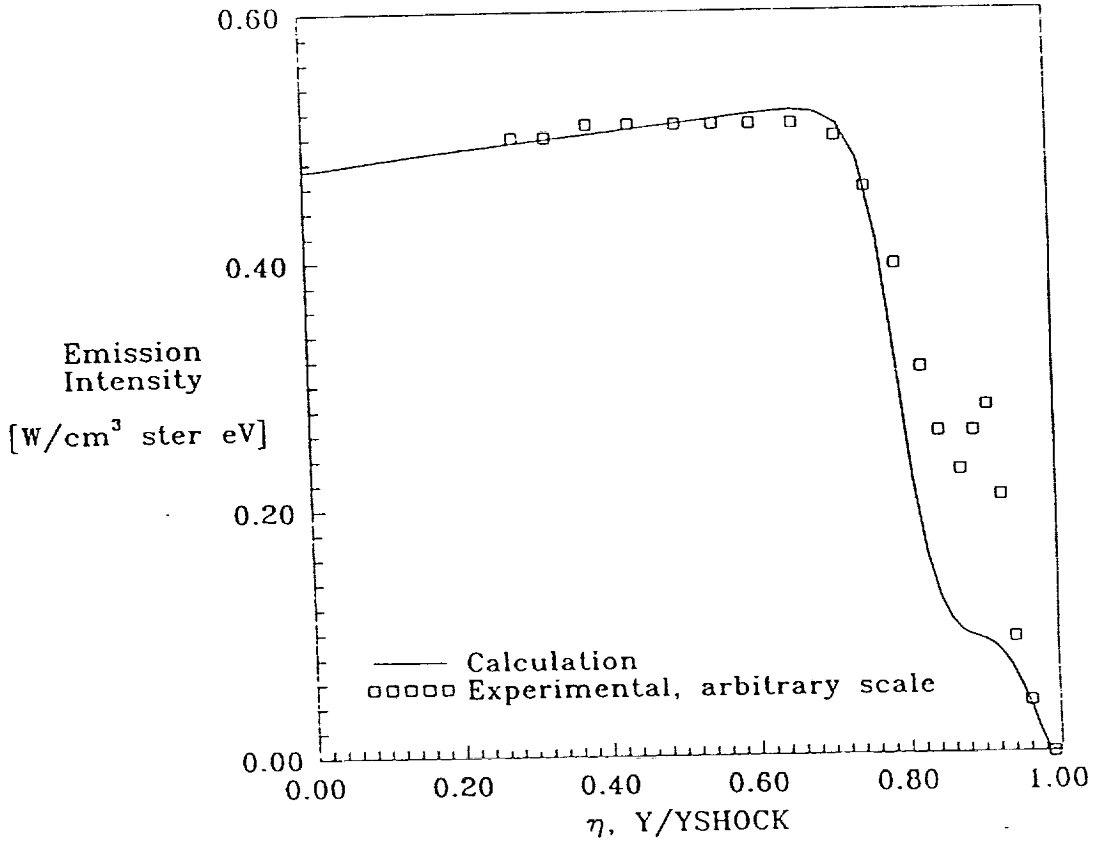

Fig. 5 -- 5000 A Intensity Traces for the Wilson 10.9 km/sec Case, Experimental Data Scaled to Match Secondary Rise; $P_{initial}$ = 0.1 mm Hg.

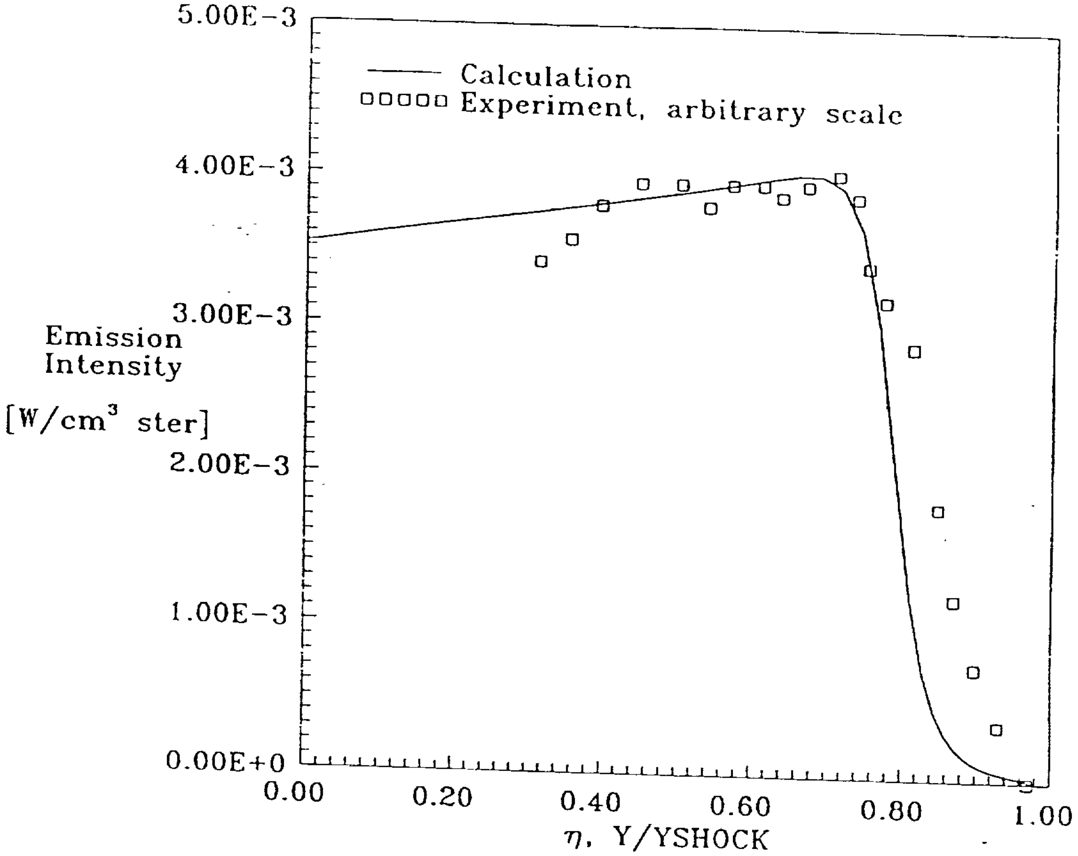

Fig. 6 -- IR Intensity Traces for the Wilson 10.9 km/sec Case, $P_{initial}$ = 0.1 mm Hg.

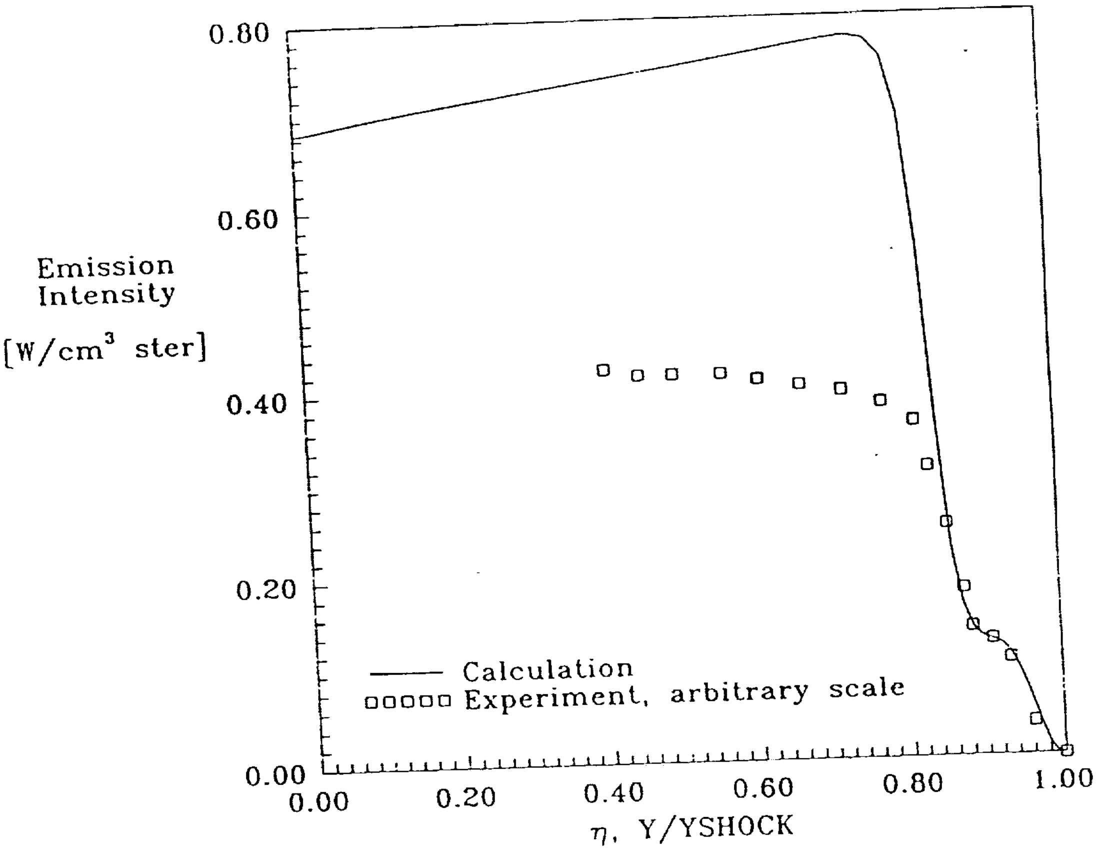

Fig. 7 -- 5000 A Intensity Traces for the Wilson 11.3 km/sec Case, Experimental Data Scaled to Match Initial Peak; $P_{initial}$ = 0.1 mm Hg.

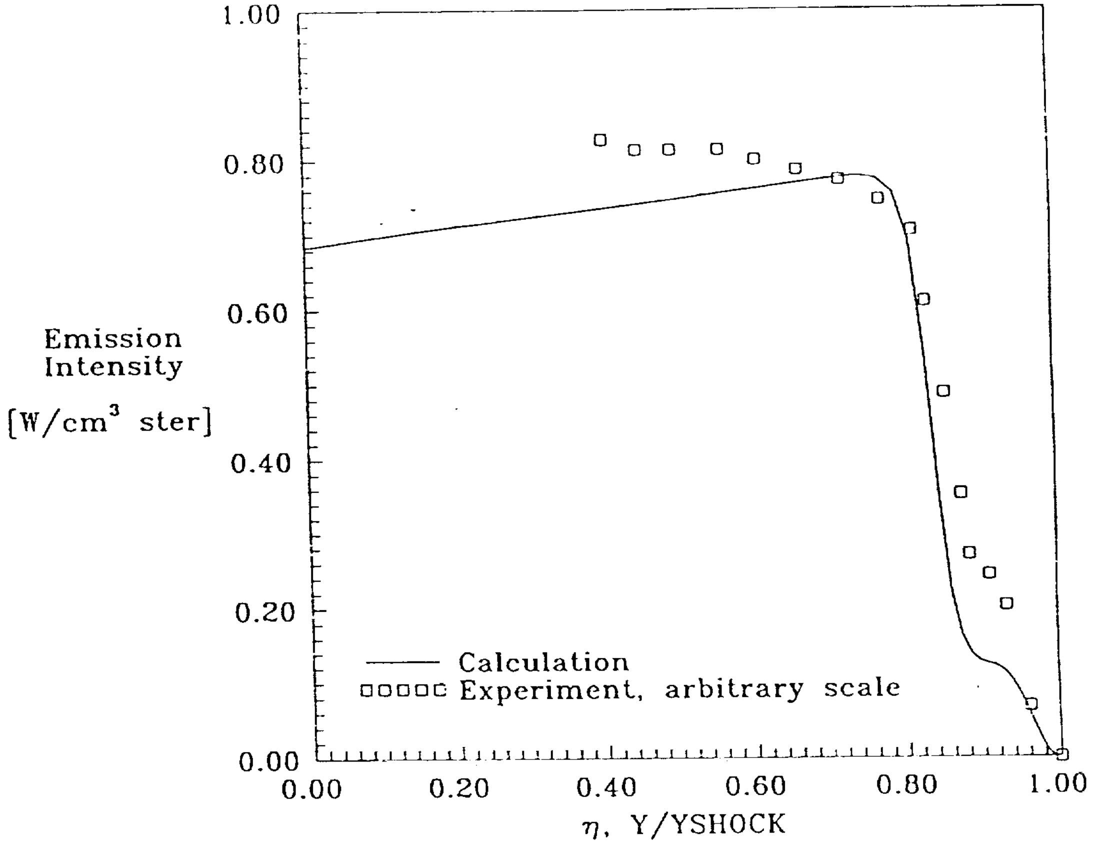

Fig. 8 -- 5000 A Intensity Traces for the Wilson 11.3 km/sec Case, Experimental Data Scaled to Match Secondary Rise; $P_{initial}$ = 0.1 mm Hg.

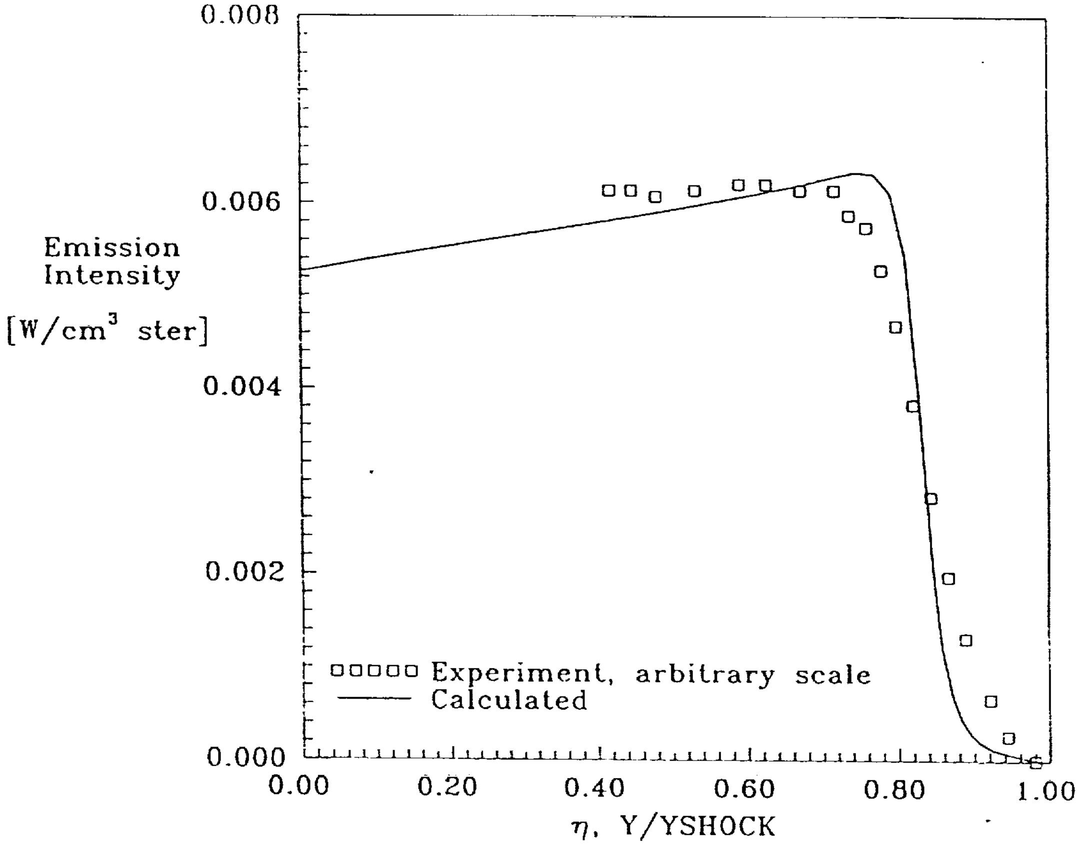

Fig. 9 -- IR Intensity Traces for the Wilson 11.3 km/sec Case, $P_{initial}$ = 0.1 mm Hg.

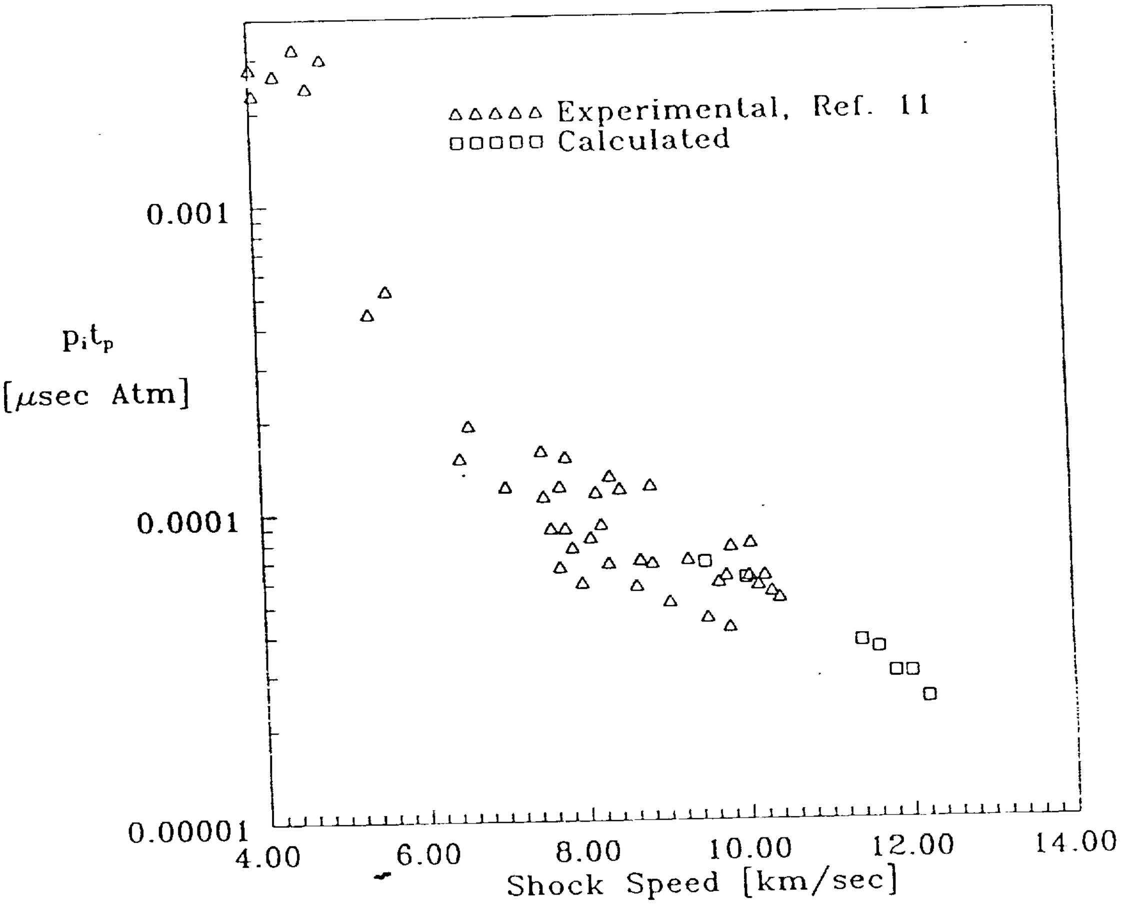

Fig. 10 -- Time to Peak Radiation for Various Shock Speeds

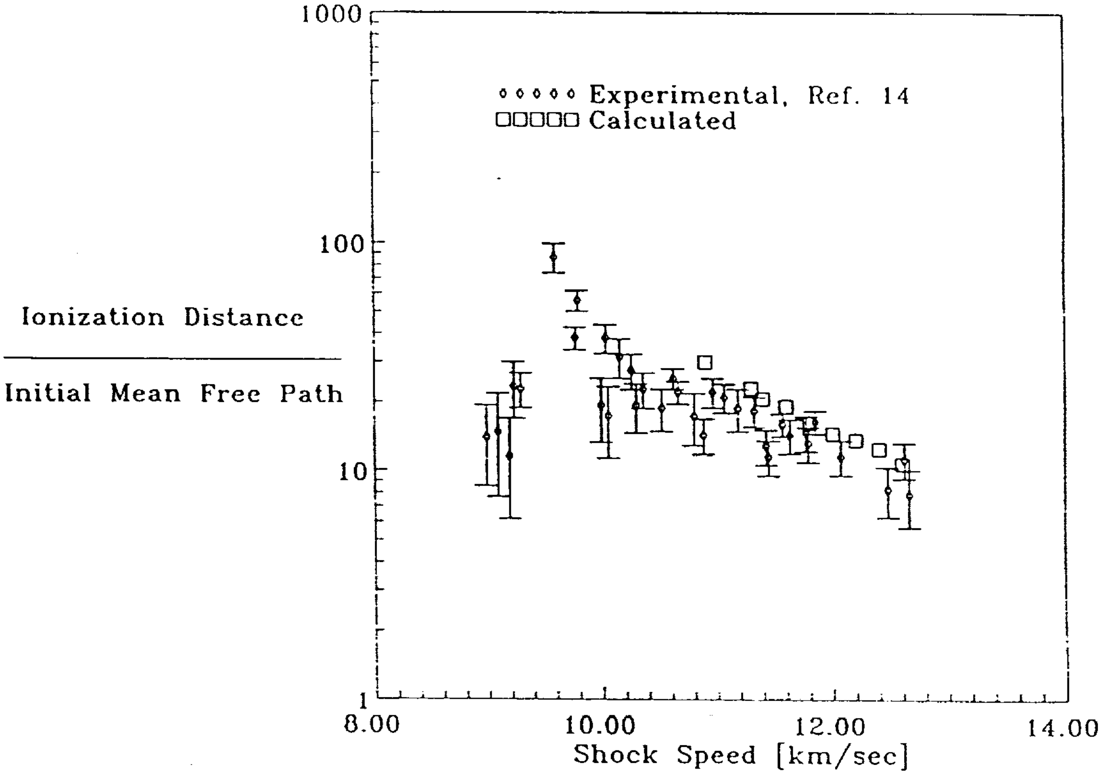

Fig. 11 -- Ionization Distance for Various Shock Speeds

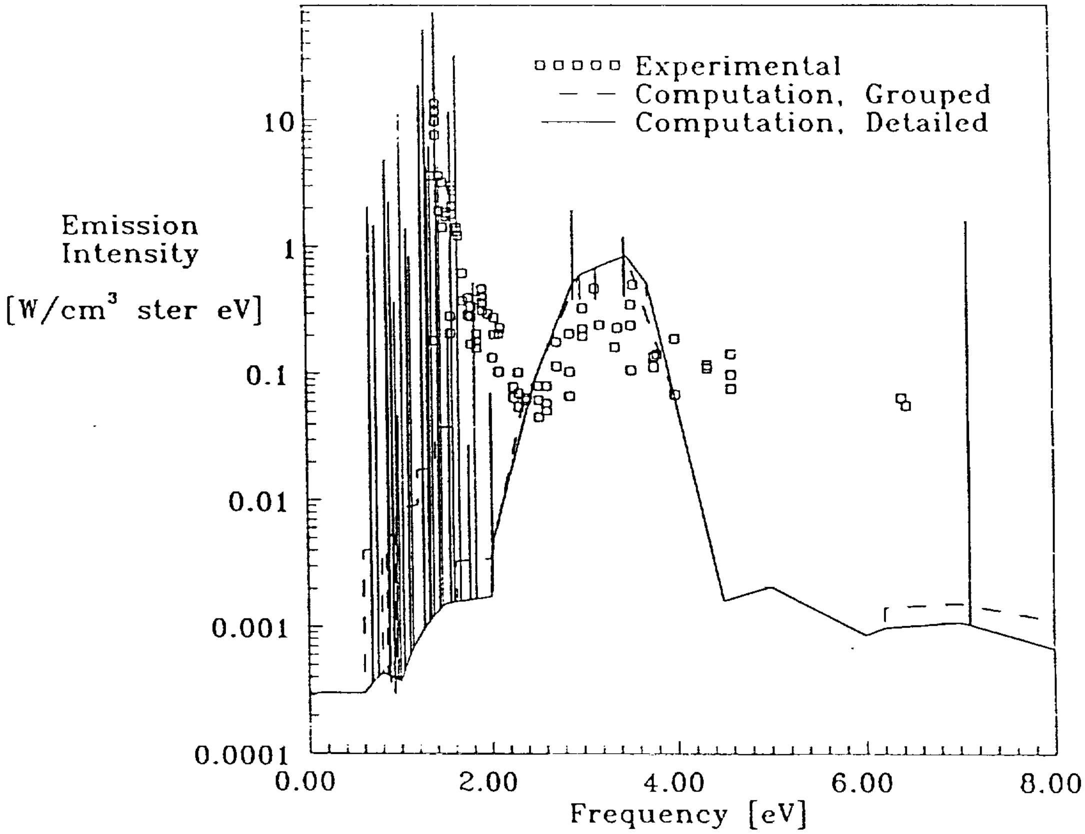

Fig. 12 -- Peak Radiation Spectra for the Avco Case; Shock Speed = 10 km/sec, $P_{initial}$ = 0.1 mm Hg.

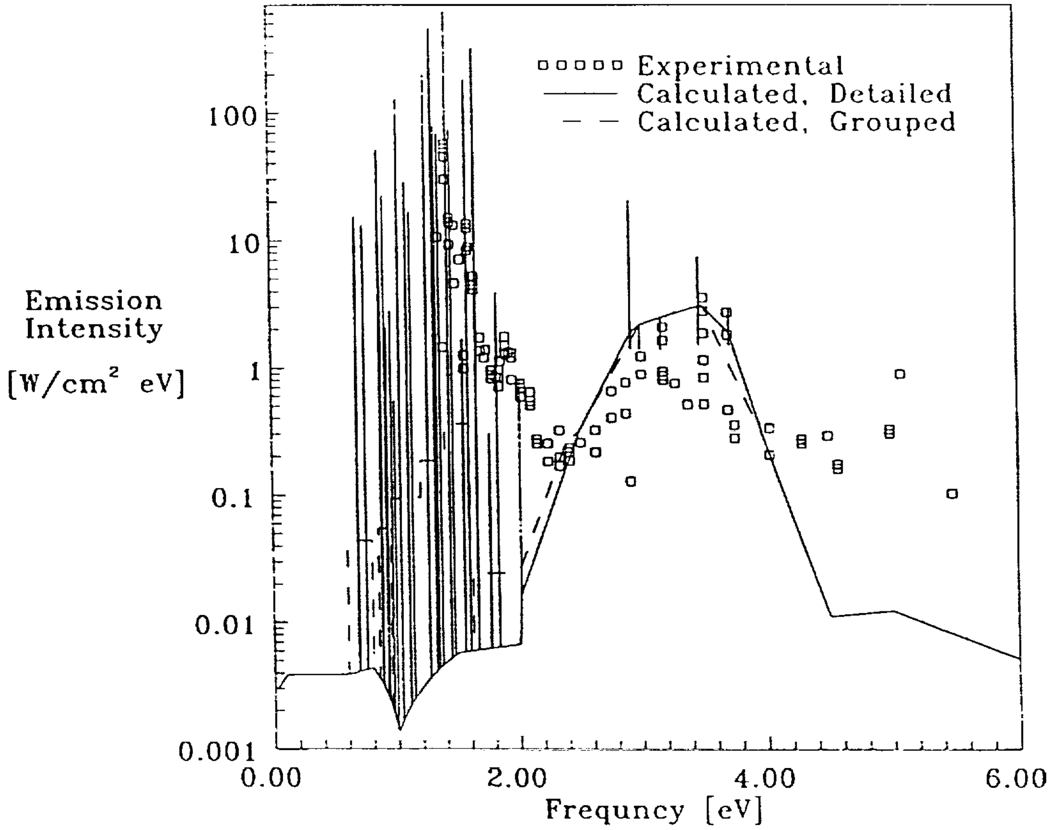

Fig. 13 -- Spatially Integrated Nonequilibrium Radiation Spectra for the Avco Case; Shock Speed = 10 km/sec, $P_{initial}$ = 0.1 mm Hg.

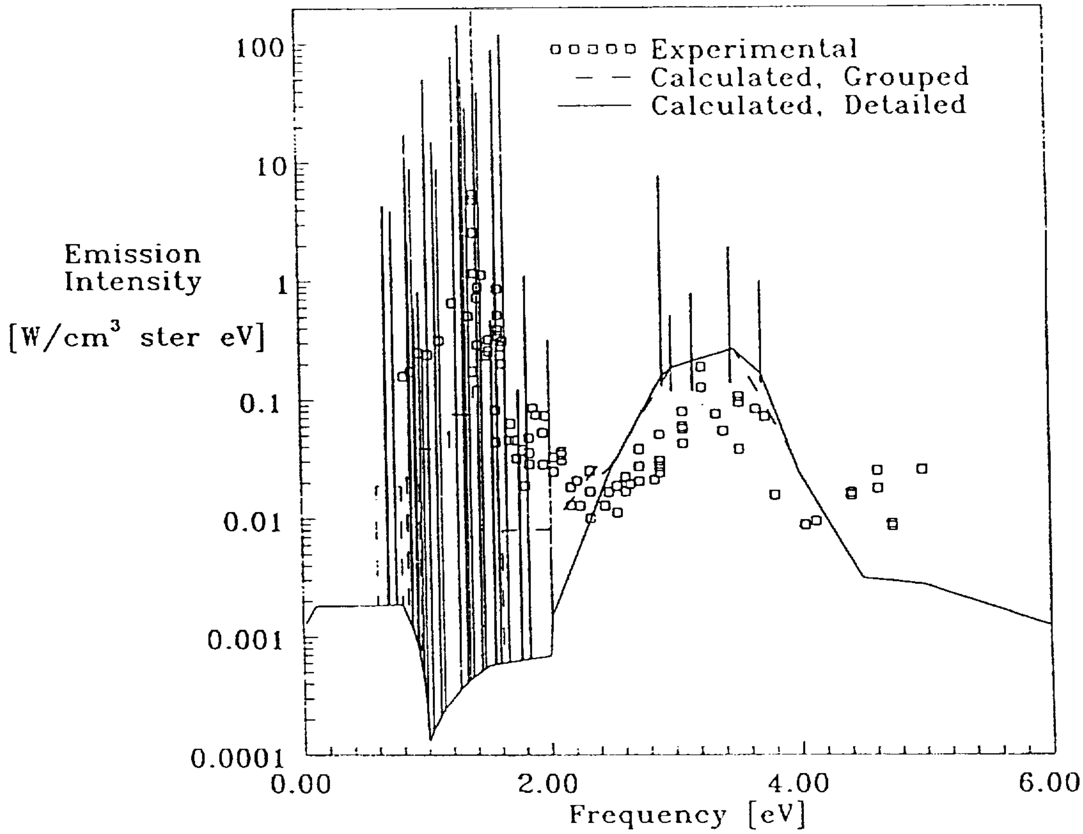

Fig. 14 -- Equilibrium Radiation Spectra for the Avco Case; Shock Speed = 10 km/sec, $P_{initial}$ = 0.1 mm Hg.

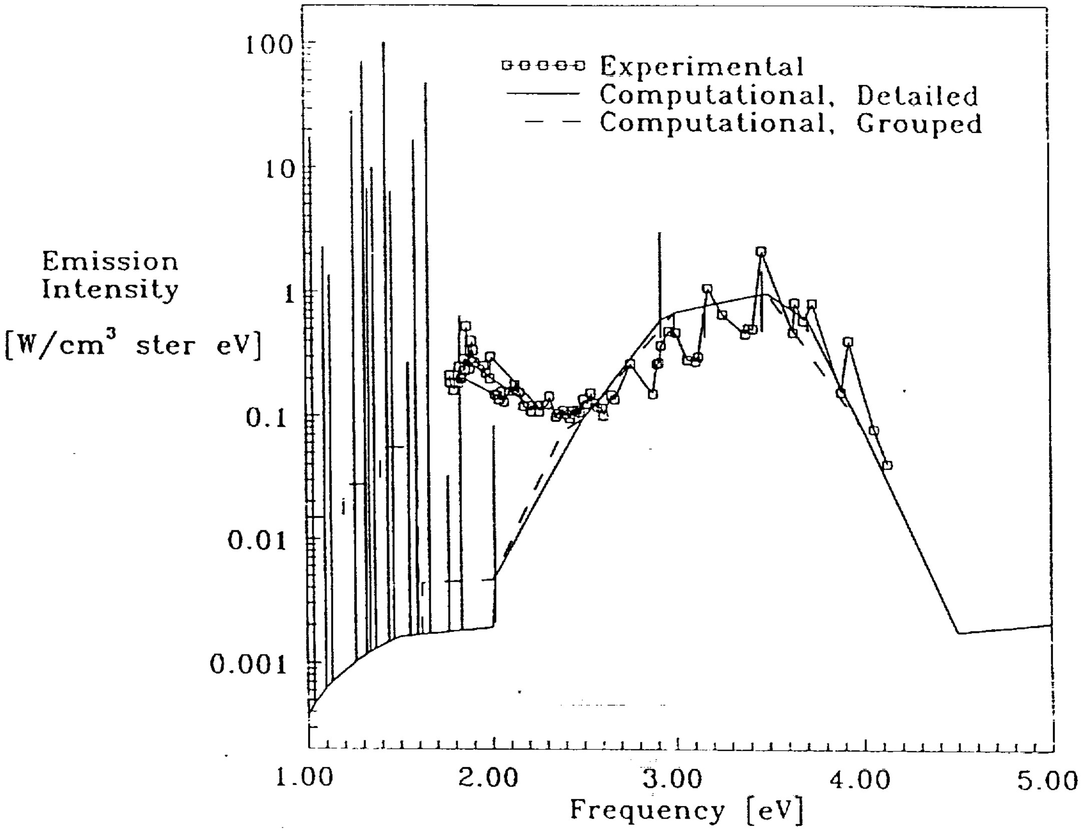

Fig. 15 -- Nonequilibrium Radiation Spectra for the Sharma Case: Shock Speed = 10.2 km/sec, $P_{initial}$ = 0.1 mm Hg.

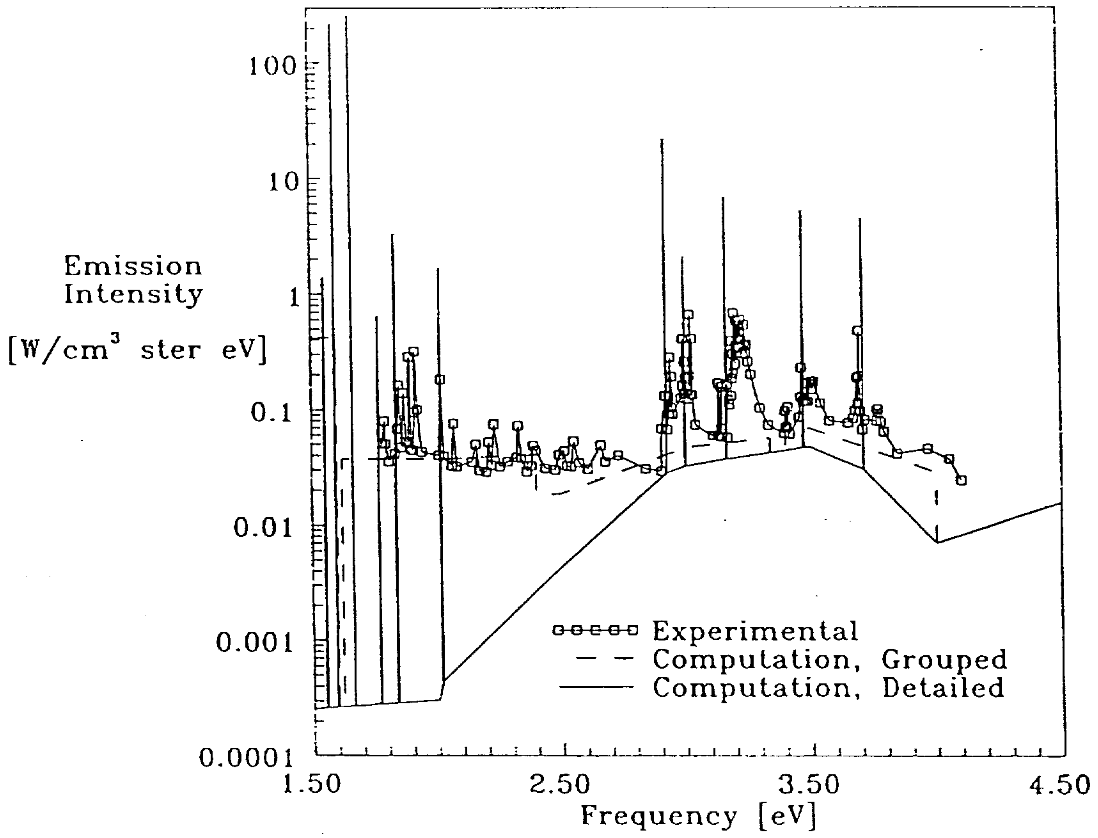

Fig. 16 -- Equilibrium Radiation Spectra for the Sharma Case: Shock Speed = 10.2 km/sec, $P_{initial}$ = 0.1 mm Hg.

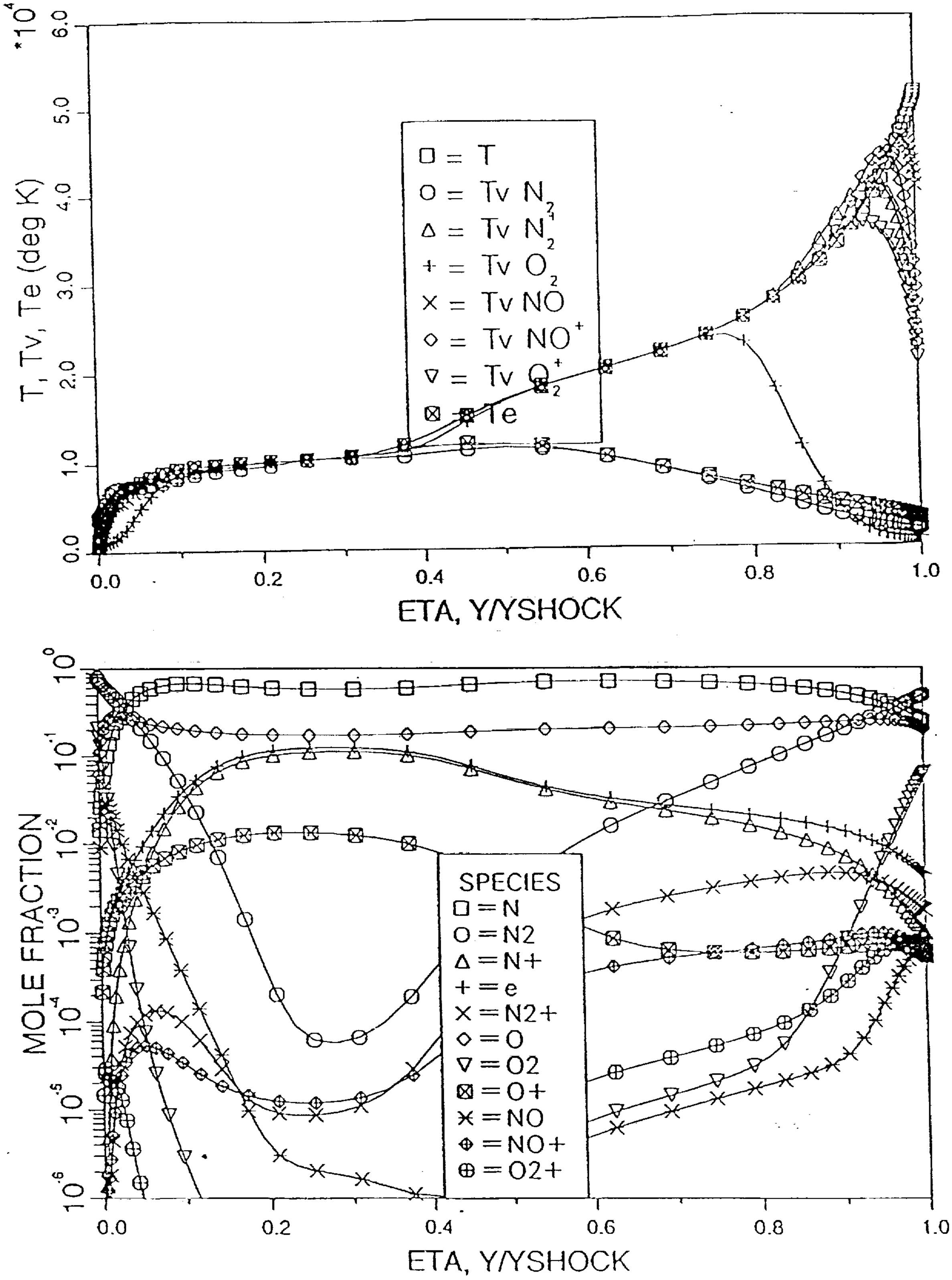

Fig. 17 -- Case 1634 -- Air Results with Nonpreferential Model and Multiple Vibrational Temperatures, Temperature and Mole Fractions

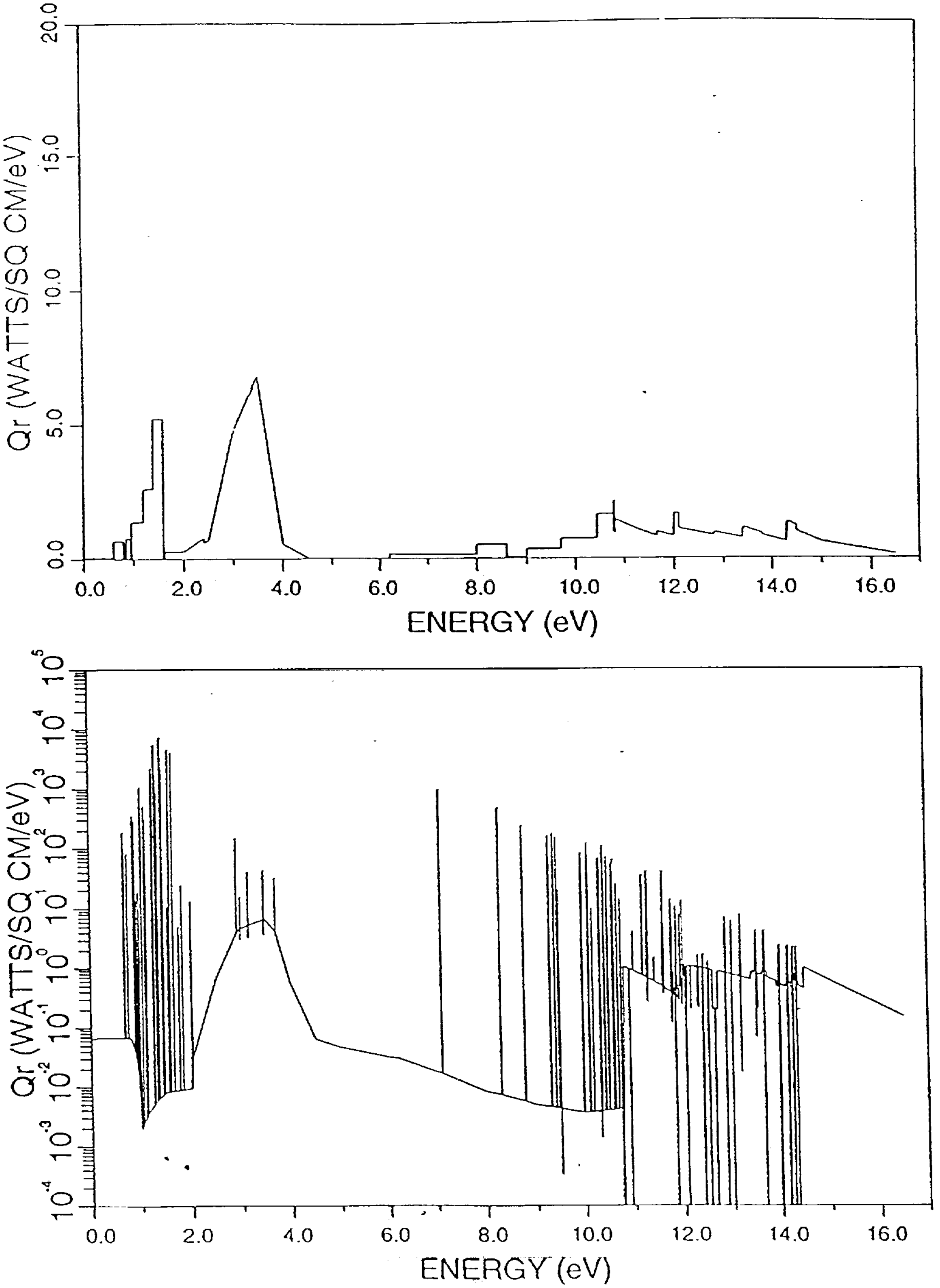

Fig. 18 -- Case 1634 -- Air Results with Nonpreferential Model and Multiple Vibrational Temperatures, Grouped and Detailed Radiation Spectra

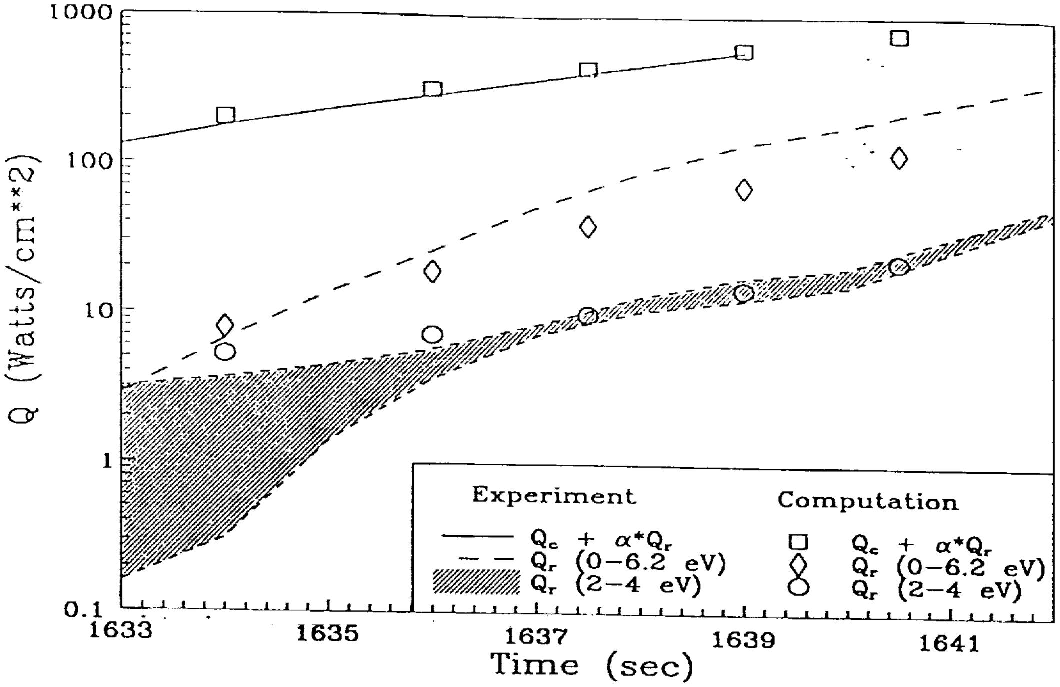

Fig. 19 -- Comparison of Nonpreferential Model with Fire II Flight Data

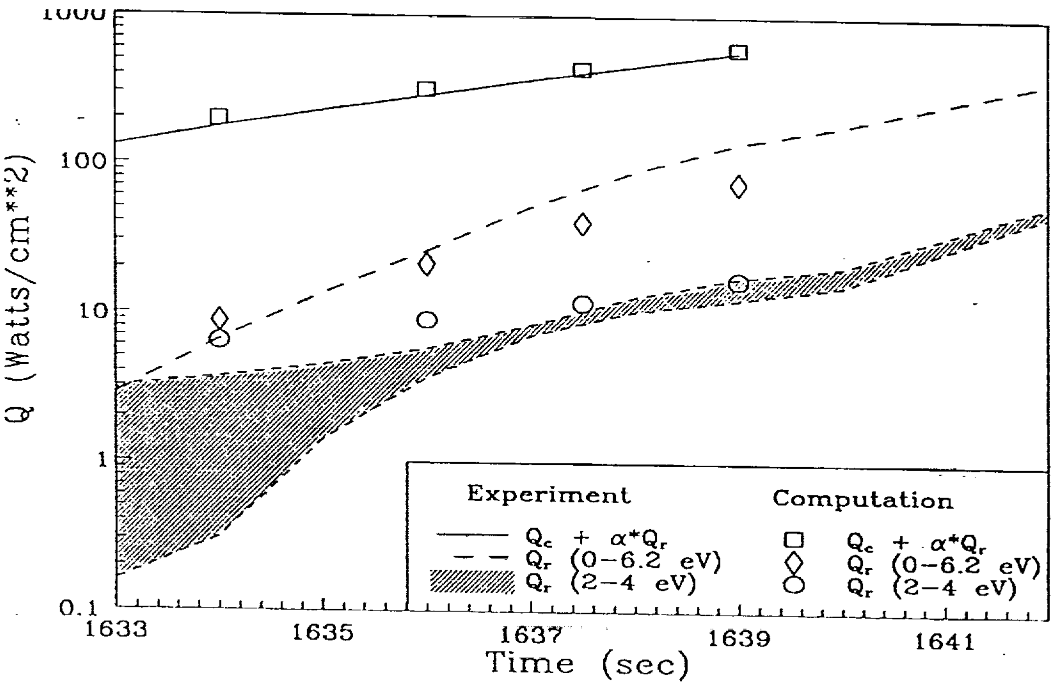

Fig. 20 -- Comparison of Multiple Vibrational Temperature Model with Fire II Flight Data

APPENDIX

Relevant Publications

from the Project

AIAA-89-1729

The Effect of Electron Temperature and Impact Ionization on Martian Return AOTV Flowfields

L. A. Carlson and T. A. Gally
Texas A&M University
College Station, TX

AIAA 24th Thermophysics Conference
Buffalo, New York / June 12-14, 1989

The Effect of Electron Temperature and Impact Ionization on Martian Return AOTV Flowfields

Leland A. Carlson*
and
Thomas A. Gally**
Texas A&M University
College Station, Texas

Abstract

Various electron impact ionization models in conjunction with a quasi-equilibrium electron temperature model have been investigated and applied to the stagnation region of a hypothetical 2.3 m nose radius Martian return AOTV. For the conditions considered, $U = 12$ km/sec at 80 km, both multi-temperature inviscid and viscous results indicate that a two-step ionization impact model predicts ionization distances in agreement with experimental data, that nonequilibrium chemistry and radiation effects are important throughout the stagnation zone, and that the quasi-equilibrium electron temperature model is reasonable. Also, using a non-grey emission-absorption radiation step model, it is shown that nonequilibrium causes a reduction in radiative heating from that predicted for equilibrium conditions and that compared to an adiabatic wall a cool wall (1650°K) results in a 28 to 45% reduction in radiative heating due to absorption near the wall.

Introduction

In the future, various space programs will be conducted which will require the efficient return of large payloads to low earth orbit (LEO) from missions to the moon or planets like Mars. To accomplish this task, the return vehicles will utilize aerocapture techniques that will involve reentry and deceleration at high altitudes; and in order to design these vehicles, a thorough understanding of the physical phenomena will be required. Because of the high altitudes associated with aerocapture, the vehicle flowfields will be dominated by chemical, thermal, and radiative nonequilibrium phenomena which in many cases have not been extensively studied since the Apollo era[1]. Recently, as a result of the Aeroassisted Flight Experiment (AFE) program, results have been presented for aerocapture flowfields in the 7.5 - 10 km/sec range[2-7]; and these have demonstrated the importance of nonequilibrium phenomena in this flight regime.

However, for a Martian return vehicle, the minimum nominal earth entry velocity is approximately 12 km/sec; and the vehicle might be required under certain conditions to be able to operate and survive at earth entry speeds up to 16 km/sec[8]. At these higher velocities, the nonequilibrium phenomena will be different that those associated with the AFE vehicle. In the stagnation region, for example, nonequilibrium should be dominated by electron impact ionization processes instead of dissociation reactions, extensive thermal nonequilibrium invovling at least three temperatures (heavy particle, vibrational, and electron) will exist, and the radiative heat transfer may be significantly affected by local thermodynamic nonequilibrium (LTNE) or nonequilibrium radiation effects. In addition, the electron temperature and nonequilibrium chemistry will be strongly coupled; and this coupling will influence the radiative heat transfer to the vehicle. Further, at the higher end of the velocity range (14-16 km/sec), the radiative transfer and the flowfield gasdynamics will be coupled due to the significant energy losses associated with radiation cooling.

Currently, several different engineering models and reaction rates have been postulated for electron impact ionization chemistry, all of which depend upon the accurate prediction of electron temperature. The purpose of the present effort is to examine these different electron impact ionization models using flowfield results obtained from both invisicid and viscous nonequilibrium chemistry multi-temperature computational models. By comparing the results with each other, the consequences of using a specific model can be determined. Further, by comparing with experimental data, a suitable ionization model for the stagnation region can be determined.

Problem Formulation

Flowfield Models

In this study, both inviscid and viscous flowfield representations have been utilized. For the inviscid calculations, an improved version of a previously developed[6] nonequilibrium chemistry axisymmetric inverse method based upon the work of Grosse[9] has been utilized as the basic Euler equation flow solver. This method permits arbitrary chemistry, includes options for a variety of vibration-dissociation coupling models, and, in the computation of radiative transfer, accounts for non-gray gas spectral and local thermodynamic nonequilibrium phenomena. For the present effort, it has been further modified to include an electron temperature model and both single and two-step atomic ionization models.

Since at the high altitudes and low densities of interest in aerocapture, viscous phenomena and wall thermal boundary layer effects will be important, calculations have also been obtained using a modified version of the NASA Langley nonequilibrium chemistry viscous shock layer code VSL3DNQ, which is an axisymmetric version of the SHTNEQ code described in Ref. 10. Like the inviscid code, this VSL method has also been modified to include an electron temperature model and both single and two-step atomic ionization formulations. In addition, it has been combined with a non-gray emission-absorption radiation model to permit the computation of radiative heat transfer. However, the effects of radiation gasdynamic coupling due to radiation cooling have not yet been included in the VSL formulation.

---

* Professor Aerospace Engineering, Associate Fellow AIAA

** Research Assistant, Student Member AIAA

Electron Impact Ionization

At conditions of interest for earth return from Mars, the nonequilibrium chemistry region behind the bow shock will be dominated by ionization chemistry. Initially, ions will be produced via reactions involving NO^+ and N_2^+ and precursor photoionization; but once significant dissociation has occured and reasonable amounts of atomic nitrogen and oxygen are present, the atoms will directly ionize in collisional reactions. Of these the most important are the electron impact reactions

$$\begin{aligned} N + e^- &= N^+ + e^- + e^- \\ O + e^- &= O^+ + e^- + e^- \end{aligned} \tag{1}$$

since they can induce electron avalanche, and, thus, strongly affect the length and character of the nonequilibrium zone.

The classical model for these reactions uses standard forms for the species production terms, reactions rates, and equilibrium constant. This approach essentially assumes that the ionization mechanism proceeds via a one step process, and a widely used set of reaction rates for these reactions is:
For $N + e^- = N^+ + e^- + e^-$

$$k_f = 1.1 \times 10^{32} T_e^{-3.14} \, exp\left(\frac{-169000}{T_e}\right) \tag{2}$$

$$k_b = 2.2 \times 10^{40} T_e^{-4.5} \tag{3}$$

where k_f and k_b are the forward and reverse rate coefficients based upon the local electron temperature, T_e. For $O + e^- = O^+ + e^- + e^-$

$$k_f = 3.6 \times 10^{31} T_e^{-2.91} \, exp\left(\frac{-158000}{T_e}\right) \tag{4}$$

$$k_b = 2.2 \times 10^{40} T_e^{-4.5} \tag{5}$$

Following normal practice, it is assumed that in these reactions that the governing temperatures are the electron temperature. These rates were presented by Kang et al[11] as part of an extensive reaction chemistry set, and results using this set yielded good agreement with electron probe measurements on the flank region of the RAM-C flight vehicle experiment. Both recombination coefficients, Eqs. (3) and (5), have the form resulting from elementary[12] and variational theory three-body collision theory[13] and the coefficient is near the upper bound determined by Makin and Keck[13]. In fact, several figures in Ref. 11 are labeled "Results are for upper-bound reaction rate coefficients for deionization reactions."

Similar recombination rates were also used in reflected shock tunnel nozzle flow investigations of C^+ recombination and O_2^+ and N_2^+ dissociative recombination in which good results were obtained[14-16]. However, as noted by the investigators, these experiments may not have been sensitive to these reactions since in one case the leading coefficient in Eq. (3) was varied by plus and minus two orders of magnitude with no effect on the data[16]. Also, these laboratory and flight experiments were for flows dominated by recombination and at lower electron densities and temperatures (2500 - 8000°K) than of interest in the current investigation. Thus, while not establishing the validity of these rates for the present conditions, these experiments do not indicate that they are incorrect.

However, Park[17-18] measured the nitrogen ionic recombination rate at a nominal temperature of 10,000°K using an arc plasma wind tunnel and obtained values which corresponded to a recombination rate of

$$k_b = 5.02 \times 10^{42} T_e^{-5.27} \tag{6}$$

which is in reasonable agreement with the value of Kang et al. He also suggested that the forward rate be obtained from the equilibrium constant, K_{eq}, via

$$K_{eq} = \frac{k_f}{k_b} \tag{7}$$

Both the Park forward rate corresponding to Eq. (6) and the Kang et al forward rate given in Equation (2) are plotted on Figure 1. As can be seen the agreement between the two rates over the range of electron temperatures of interest in the present study is good.

Now it should be recognized that for the high temperatures of interest in the present effort that three body deionization recombination will include significant electron capture into low lying levels and that collisonal deexcitation should be rapid[12]. In addition, while the atomic electronic excited state populations may during recombination be in a Boltzman distribution (i.e. local thermodynamic equilibrium, LTE), at T_e, experimental evidence[19] indicates that many of the excited state population densities may not be in equilibrium with the number density of free electrons. As will be discussed below, this nonequilbrium with the free electrons during recombination is in contrast with the behavior which can be assumed to occur behind a shock wave during ionization.

Recently, Park[4], used a two-temperature ionizing air model and obtained good agreement with shock tube, shock tunnel, and flight measurements of phenomena immediately behind a shock front and/or in the stagnation zone and forward face region of blunt bodies. For these studies, several of the reaction rates were adjusted so as to yield good comparisons with experimental data; and the forward rates for the reactions in Eq. (1) are considerably different than those given by Eqs. (2-7). These rates are
For $N + e^- = N^+ + e^- + e^-$

$$k_f = 2.5 \times 10^{33} T_e^{-3.82} \, exp\left(\frac{-168600}{T_e}\right) \tag{8}$$

For $O + e^- = O^+ + e^- + e^-$

$$k_f = 3.9 \times 10^{33} T_e^{-3.78} \, exp\left(\frac{-158500}{T_e}\right) \tag{9}$$

and the forward rate for atomic nitrogen electron impact ionization is plotted on Fig. 1. Note that it is almost two orders of magnitude smaller than the rates based upon recombination.

The second model for atomic ionization is an engineering approximation based upon various theories involving the ionization of argon[20-24] and the application of these theories to nitrogen and oxygen[25-26]. This approach assumes that atomic ionization is not a single step process but proceeds via a two step chain involving excitation to an excited state followed by rapid ionization controlled by the local charged particle concentrations and the electron temperature. This concept applies not only to electron impact ionization but also to heavy particle ionization involving atom-atom and atom-ion collisions.

Unfortunately, because of the two step process, the usual mass production rate formulation is not completely adequate. For example, assume that the atom-atom ionization process proceeds as follows:

$$N_g + N = N^* + N; \tag{10}$$

$$N^* = N^+ + e^-; \tag{11}$$

where N^* refers to atomic nitrogen in an excited state. By assuming that the first step is rate determining, that dN^*/dt is approximately zero, and that the ground state concentration approximately equals the atom concentration, kinetics yields the rate of species mass production per unit volume, $\dot{w}_s$, to be

$$\begin{aligned} &\dot{w}_{N^*,total} = \\ &\mathcal{M}_N \left\{k_f\,[N_g]\,[N] - k_b\,[N^*]\,[N]\right\} + \dot{w}_{N^*,11} \end{aligned} \tag{12}$$

where k_f and k_r are for Eq. (10), brackets denote concentration, and $\mathcal{M}_s$ is the molecular weight of species s. However, by assumption

$$\dot{w}_{N^*,total} = 0$$

so that

$$\begin{aligned} &\dot{w}_{N^*,11} = \\ &-\mathcal{M}_N \left\{k_f\,[N_g]\,[N] - k_b\,[N^*]\,[N]\right\} \end{aligned} \tag{13}$$

But k_f and k_r are related by the equilibrium constant for Eq. (10)

$$K_{eq} = \frac{g^*\,exp(-E^*/kT)}{g_g} = \frac{k_f}{k_b}$$

where g is the degeneracy of the indicated energy level, E, and k is Boltzmann's constant. Thus, Eq. (13) becomes

$$\begin{aligned} \dot{w}_{N^*,11} = &-\mathcal{M}_N k_f\,[N_g]\,[N] \\ &\left\{1 - \frac{g_g\,exp(E^*/kT)\,[N^*]}{g^*\,[N_g]}\right\} \end{aligned} \tag{14}$$

At this point, a rate expression relating the excited state to the ions and free electrons could be introduced instead. However, based upon experimental evidence for monoatomic gases[19,24], it can be assumed as an approximation that the excited states of nitrogen are in equilibrium with the free electrons and ions at the electron temperature. Thus,

$$\frac{N_e N_{N^+}}{N_{N^*}} = \frac{Q^{el}_{N^+} Q_{e^-}\,exp(-X/kT_e)}{g^*} \tag{15}$$

where X is the ionization potential from the excited state, Q^{el}_s is the electonic partition function of species s, and Q_{e^-} is the partition function for the electrons defined by

$$Q_{e^-} = 2\left(\frac{2\pi m_e kT_e}{h^2}\right)^{3/2}$$

where h is Plank's constant, m_e is the electron particle mass. Substitution of Eq. (15) into (14) then yields

$$\begin{aligned} \dot{w}_{e,NN} = &\mathcal{M}_e k_f [N]^2 \\ &\left[1 - \frac{g_g\,exp\left(\frac{E^*}{kT} + \frac{X}{kT_e}\right) AV[e^-][N^+]}{Q_{e^-} Q^{el}_{N^+}[N]}\right] \end{aligned} \tag{16}$$

where AV is Avogadro's constant.

A similar analysis for $N^+ - N$ ionization yields

$$\begin{aligned} \dot{w}_{e,NN^+} = &\mathcal{M}_e k_f [N][N^+] \\ &\left[1 - \frac{Q^{el}_N\,exp\left(\frac{E^*}{kT} + \frac{X}{kT_e}\right) AV[e^-][N^+]}{Q_{e^-} Q^{el}_{N^+}[N]}\right] \end{aligned} \tag{17}$$

while for electron-atom ionization impact the result is

$$\begin{aligned} \dot{w}_{e,eN} = &\mathcal{M}_e k_f [N][e^-] \\ &\left[1 - \frac{g_g\,exp\left(\frac{I}{kT_e}\right) AV[e^-][N^+]}{Q_{e^-} Q^{el}_{N^+}[N]}\right] \end{aligned} \tag{18}$$

Similar expressions could be obtained for atomic oxygen ionization.

Notice that the production rates involving heavy particles (atoms or ions) are governed by both the electron and the heavy particle temperature, while the production rate for the atom-electron reactions involves only the electron temperature but has the classical form. Further, the forward rate coefficient is for the limiting step and only uses the energy of the assumed excited state and not the ionization energy. Wilson[25], based upon the work of Petschek and Byron[27], assumed that the rate limiting step in the ionization process was excitation of the atoms to the level involving the largest energy jump, i.e. to the 3s^{4}P for nitrogen and to the 3s^{5}S state for oxygen, and proposed a form for the excitation rate. It should be noted that for oxygen and nitrogen this rate limiting step is for the temperatures of interest here different than that used in Ref. 13, which was only 2.5kT below the ionization level.

Using this theory, Wilson obtained good agreement with shock tube data for ionization distances behind shock waves in air. Susbsequently, these forms were used to deduce rates which were used to study nonequilibrium radiating phenomena behind reflected shock waves[26] and the AFE stagnation region[8].

Thus, based upon the theory and results presented in Ref. 24-26, reaction rates consistent with the two step approximate model given by Eqs. (10-18) are:

For $N + e^- = N^+ + e^- + e^-$

$$k_f = 4.16 \times 10^{13} T_e^{0.5}\, exp\left(\frac{-120000}{T_e}\right) \qquad (19)$$

For $O + e^- = O^+ + e^- + e^-$

$$k_f = 5.49 \times 10^{13} T_e^{0.5}\, exp\left(\frac{-104500}{T_e}\right) \qquad (20)$$

For $N + N = N^+ + e^- + N$ and $N + N^+ = N^+ + e^- + N^+$

$$k_f = 2.34 \times 10^{11} T^{0.5}\, exp\left(\frac{-120000}{T}\right) \qquad (21)$$

The forward rate given by Eq. (19) is also shown on Fig. 1, and it is in reasonable agreement with the ionization rate of Park[4]. As can be seen, both of the rates associated with ionization processes are considerably slower than those deduced from recombination experiments and theory. However, the difference might be due to fundamental differences in the processes involved. In the shock tube case, the process is dominated by forward ionization; and in the rate derivation it was assumed that the excited states were in equilibrium with the free electrons and ions. In the shock and arc tunnel experiments, the chemistry is dominated by recombination and, as mentioned above, there is experimental evidence[19] that during recombination the excited states may not be in equilibrium with the free electrons.

Electron Temperature Model

Besides chemical nonequilibrium, it is possible for a partially ionized gas to have regions of thermal nonequilibrium between electrons and the other heavier species. Such thermal nonequilibrium occurs because the rate of energy exchange between electrons and heavy particles is very slow due to the large mass differences in the species, and it is characterized by different free electron and heavy particle temperatures. Since atomic ionization and radiative transfer are dependent upon and strongly coupled to the electron temperature, accurate models for computing it are essential.

Over the years, a variety of models for determining the electron temperature have been presented[4-6,20-23,26,28-33], which differ in detail, level of complexity, and ease of solution. All of these start from the equation representing conservation of electron energy which can be written as

$$\frac{D(\rho_e h_e)}{Dt} + \rho_e \vec{U}_e \cdot \frac{D(\vec{u})}{Dt} + \frac{\partial}{\partial \vec{r}} \cdot \vec{q}_e + \rho_e h_e \left(\frac{\partial}{\partial \vec{r}} \cdot \vec{u}\right) - \frac{D(p_e)}{Dt} + [\tau_e] : [\frac{\partial}{\partial \vec{r}}; \vec{u}] - N_e \vec{X}_e \cdot \vec{U}_e; - \dot{w}_e \frac{u^2}{2} = \sum_{j=1}^{S} \left(\xi_{ej} + \vec{U}_e \cdot \vec{P}_{ej}\right) + Q_e \qquad (22)$$

If Bremmstrahlung and viscous stress effects are ignored, this equation becomes, showing only one dimension for simplicity,

$$\rho_e u_e \frac{\partial h_e}{\partial x} - u \frac{\partial p_e}{\partial x} + \frac{\partial}{\partial x}\left(-\lambda_e \frac{\partial T_e}{\partial x}\right) + \frac{\partial}{\partial x}(\rho_e U_e h_e) + \dot{w}_e h_e - h_e \frac{\partial}{\partial x}(\rho_e U_e) - \dot{w}_e \frac{u^2}{2} = U_e \frac{\partial p_e}{\partial x} + \sum_{j=1}^{S}\left(\xi_{ej} + \vec{U}_e \vec{P}_{ej}\right) + Q_e \qquad (23)$$

The first term on the right hand side represents the effect of external forces and is obtained from the electron momentum equation, the second accounts for the rate of energy gain by electrons due to elastic encounters because of thermal motion of the particles, the third represents the energy gain resulting from elastic encounters because of the relative fluid motion of the electrons, and the last term represents energy change due to inelastic encounters. The velocity, U_e, is the electron diffusion velocity.

In the past, several investigators[20-23,26] using the full electron energy equation have obtained results which indicate that when significant ionization is present in the post-shock nonequilibirum zone that the electron temperature is essentially constant at a value 10-15% above the theoretical equilibrium temperature until the heavy particle temperature falls to that value. After that, the two temperatures are essentially the same. Obviously, the use of such a constant temperature would simplify the electron temperature calculations; and this approach has been used in approximate flowfield solutions[31,34] and was considered for the present study. However, preliminary calculations demonstrated the difficulty of selecting a priori an appropriate effective constant electron temperature; and this approach was abandoned.

Another approach successfullly used in the past for AFE flowfields[4,6] is to assume that the nitrogen vibrational temperature and the electron temperature are equal and to combine the electron and vibrational energy equations. This method is based upon experimental data[35] and theoretical calculations[4-5] that show that near 7000°K vibrational processes strongly influence the electron temperature. However, for the conditions of the present study, temperatures are normally above 10,000°K, dissociation occurs rapidly behind the shock front, and the concentration of N_2 is very low over most of the nonequilbrium zone. Thus, vibration electronic coupling should not be significant; and this approach was not utilized in the present study.

Another model which has been used in the past[32-33] is the "quasi-equilibrium approximation" in which all derivative terms are neglected in the electron energy equation. If it is further assumed that the charge exchange cross section between atoms and ions is sufficient to insure that they have the same diffusion velocity and due to rapid dissociation that the concentration of diatomic molecues is low over most of the shock layer, then diffusion terms can also be neglected. Thus, Eq. (23) becomes

$$\dot{w}_e h_e - \dot{w}_e \frac{u^2}{2} = \sum_{j=1}^{S} \xi_{ej} + Q_e \qquad (24)$$

Since vibration electronic coupling has been neglected, the inelastic term, Q_e, is composed of effects due to chemical reactions involving electrons. When an electron is created by an electron-atom reaction, the electron which casued the ionization will lose energy equivalent to the ionization potential, E_I, plus the energy of the created electron, which on the average is say e_{av}. The original electrons will rapidly equilibrate by elastic collisions and will have collectively lost energy $E_I + e_{av}$. The equilibration between the original electrons and the newly created one will not affect the energy per unit volume since it only involves a transfer of energy from one particle to another. Thus, the net energy loss from an electron atom ionization process is E_I and the total is $\dot{w}_{e,eA} E_I / m_e$.

Similarly, every time an atom-atom ionization occurs an electron of average energy e_{AA} is created and the total energy gain for these processes is $\dot{w}_{e,AA} e_{AA} / m_e$. Similarly for atom-ion ionization. Thus,

$$Q_e = -\frac{\dot{w}_{e,eA} E_I}{m_e} + \frac{\dot{w}_{e,AA} e_{AA}}{m_e} + \frac{\dot{w}_{e,AI} e_{AI}}{m_e} \qquad (25)$$

For the present conditions, however, the electron-atom process should be the dominant ionization mechanism and the last two terms should be negligible[21,26]. For those parts of the flowfield where the other reactions are important, the concentration of electrons should be low enough that any error resulting from neglecting them in Eq. (25) should be small. Thus, only the first term of Eq. (25) need be retained.

General forms for the elastic interaction terms have been derived using collision integral theory in Ref. 36. Since diffusion effects are ignored in the quasi-equilibrium model, these interaction terms can be reduced to

$$\xi_{ej} = \frac{(m_e T_e)^{\frac{1}{2}}}{m_j} S_{ej} N_e N_j (1.03478 \times 10^{-23})(T - T_e) \qquad (26)$$

where cgs units are assumed, terms involving m_e have been dropped relative to heavy particle masses, and S_{ej} is the collision cross section between electrons and species j.

By substituting Eqs. (25-26) into (24), dropping the small term involving u^2, and rearranging, an approximate equation for the free electron temperature is

$$T_e = T - \frac{1.23357 \times 10^{-10}}{T_e^{\frac{1}{2}} SX [e^-] m_e} \left[\dot{w}_{e,eN} E_{I_N} + \dot{w}_{e,eO} E_{I_O} + \dot{w}_e \frac{5}{2} k T_e \right] \qquad (27)$$

where

$$SX = N_N S_{eN} + N_O S_{eO} + N_{N+} S_{eN+} + N_{eO+} S_{eO+} + \frac{1}{2}(N_{N_2} + N_{O_2}) S_{eM}$$

Note that this equation is nonlinear since the cross sections are functions of translational and electron temperature as well as concentrations and that the various production rates also depend upon both temperatures. In the present study, an iterative method for solving this equation has been developed and included in both the inviscid and viscous flowfield solvers.

Chemistry Models

Since the primary objective of the present effort is to use multi-temperature flowfield models to investigate the effect of different impact ionization models, the reaction chemistry schemes have been kept as simple as possible. For air, the ten species eleven reaction model shown in Table I has been used. While this scheme is not as complete as some others (Ref. 11 for example), it should be adequate for the present study. In addition, numerical experiments were conducted using for the nitrogen dissociation reaction a series of reaction rates which varied by several orders of magnitude. For the conditions investigated, no significant effects on the ionization processes were observed.

However, since the air model did not contain all possibilities, particularly with respect to dissociation and oxygen ionization, results have also been obtained assuming a pure nitrogen freestream. At the conditions of interest, nitrogen is a reasonable representation of nonequilibrium radiating air, and more details can be included using a smaller number of species and reactions. The nitrogen reaction chemistry set consisting of five species and eight reactions is shown in Table II. Notice that charge exchange is included.

In general, with the exception of the atomic ionization reactions, the rates shown in Tables I and II are similar to those used by other investigators[3,6,26,33,35] and are in the form

$$k_{f,b} = A T^B \, exp \frac{-E}{T}.$$

As noted on the tables, computations involving the one step ionization models and the rates in Eqs. (2-5) will be termed Case I and those using the two-step ionizaiton model and the rates in Eqs. (19-20) Case II.

Vibration Dissociation Coupling

It is well established that in general vibration dissociation coupling strongly influences the dissociation of diatomic molecules[4-6]. However, at the temperatures and velocities associated with the present study, dissociation occurs rapidly; and the influence of vibration dissociation coupling on the ionization processes is small. To confirm this, numerical experiments were conducted with the inviscid flowfield model using vibrational equilibrium, CVDV coupling, and MCVDV coupling; and no significant differences between the results as to the ionization processes were observed. Consequently, in the inviscid flow solver the MCVDV model developed in Ref. 6 has been used. This coupling model includes corrections to the Landau-Teller relaxation time correlation to prevent unrealistically short relaxation times at high temperatures and accounts for the diffusive nature of vibrational relaxation at high temperatures[4].

In its original form the viscous shock layer code, VSL3DNQ, did not contain any vibration dissociation coupling model. Since the inviscid studies indicated that for conditions associated with earth entry return from Mars that vibrational coupling effects were small, the VSL code has not been modified; and all viscous calculations have assumed vibrational equilibrium.

Radiation Model

At the lower velocities associated with the earth return from

Reaction	A	B	E	Direction
$O_2+M = 2O + M$	1.19×10^{21}	-1.5	59380	Forward
$NO + M = N + O + M$	5.18×10^{21}	-1.5	75490	Forward
$N_2+M = 2N + M$	2.27×10^{21}	-1.5	0	Backward
$N + O_2 = NO + O$	1.00×10^{12}	0.5	3120	Forward
$N_2+O = NO + N$	7.00×10^{13}	0.0	38016	Forward
$N + O = NO^+ + e^-$	1.80×10^{21}	-1.5	0	Backward
$N + N = N_2^+ + e^-$	1.40×10^{13}	0.0	67800	Forward
$N + N = N + N^+ + e^-$	2.34×10^{11}	0.5	120000	Forward
$N + N^+ = 2N^+ + e^-$	2.34×10^{11}	0.5	120000	Forward
$N + e^- = N^+ + 2e^-$	Eq.(2,3) for Case I or Eq.(19) for Case II			
$O + e^- = O^+ + 2e^-$	Eq.(4.5) for Case I or Eq.(20) for Case II			

TABLE I. Air Reaction System

Reaction	A	B	E	Direction
$N_2+N_2 = 2N + N_2$	4.70×10^{17}	-0.5	113000	Forward
$N_2+N = 2N + N$	4.085×10^{22}	-1.5	113000	Forward
$N_2+M = 2N + M$	1.90×10^{17}	-0.5	113000	Forward
$N_2+N^+ = N_2^+ + N$	2.02×10^{11}	0.8	13000	Forward
$N + N = N_2^+ + e^-$	1.40×10^{13}	0.0	67800	Forward
$N + N = N + N^+ + e^-$	2.34×10^{11}	0.5	120000	Forward
$N + N^+ = 2N^+ + e^-$	2.34×10^{11}	0.5	120000	Forward
$N + e^- = N^+ + 2e^-$	Eq.(2,3) for Case I or Eq.(19) for Case II			

TABLE II. Nitrogen Reaction System

Mars of an AOTV, i.e. 12 km/sec, radiative heat transfer and associated self-aborption effects should be important; but the total radiative losses from the flowfield should be sufficiently small so that there is not any significant radiative gasdynamic coupling. Thus, once a flowfield solution has been obtained for a given reaction chemistry system, the flowfield solution can be used to compute the body radiative heat transfer. In the present study, the tangent slab approximation has been used, the wall surface is assumed to be non-emitting and nonablating, and percursor effects are assumed negligible. Also, an eight step non-gray absorption coefficient model based upon the work of Olstad[37] and similar to that used in Ref. 6 has been used. However, it has been modified to yield, under equilibrium conditions, results with respect to both magnitude and spectral distribution which in general agree with the RADICAL detailed radiation model[38]. Based upon a series of calculations, these modifications consisted of a reduction in the effective absorption cross sections in the frequency range 6.89 - 10.98 ev, which is composed not only of continuum radiation but also several important lines. This step model has yielded reasonable engineering results for AFE flowfields[6] and in conjunction with an approximate flow solver has correlated well with the Fire 2 flight experiment[34].

A spectral comparison between stagnation point radiative heating predictions obtained obtained using the present eight step model and RADICAL is shown on Figure 2. These results were obtained using the viscous flow solver with 99 points between the shock and the wall, Case I rates, and assuming an adiabatic wall; and almost the entire shock layer for this case was in chemical and thermal equilibrium. The presence of line contributions is evident in the RADICAL results by the tall narrow peaks on top of the continuum curves in the infrared (0 - 3.1 ev) and ultra-violet (8-12 ev). Since the radiative heating to the wall is the area under these curves, it can be seen that in general the two models agree quite well, and in fact the results are within fifteen percent overall. (Note: The vacuum ultra-violet band in the eight step model which starts at 14.56 ev actually extends to 31 ev.) However, the eight-step model does appear to still overpredict slightly the heating in the 6.89 - 10.98 ev range; and further improvements probably can still be made. Nevertheless, particularly when computational efficiency is considered, the modified eight step absorption coefficient model should be adequate for engineering and comparison studies.

In addition, the present radiation model contains a method for computing approximate correction factors which account for the effects of local thermodynamic nonequilibrium (LTNE). Such LTNE can exist in the chemical nonequilibrium region immediately behind the shock front where, due to ionization via excited states, the populations of the electronic states may not be that predicted by an LTE assumption using the ground state. The rationale behind these factors and their derivation has been presented in Ref. 6 and 34, and similar factors have been used for monoatomic gases[20-23]. The inclusion of radiation nonequilibrium effects is essential for accurately predicting radiative heat transfer at high altitude conditions[4-6,34].

Originally, these LTNE factors were expressed in terms of the degree of dissociation and ionization[6,34] which often were difficult to compute accurately. However, Greendyke[39] has pointed out that they can be more simply expressed in terms of the partition functions. Thus, the atomic nitrogen LTNE correction factor can be written as

$$\frac{N_{N+} N_e Q_N^{el}\, exp(169000/T_e)}{N_N Q_{N+}^{el} Q_{e-}} \tag{28}$$

For radiation processes involving the ground state this factor is multiplied by the black-body function for that region to yield the effective source function and the absorption coefficient is unchanged. On the other hand, for processes involving excited states, the factor is multiplied by the absorption cross section to yield the effective absorption coefficient, and the source function for that spectral region is unchanged. Additional details are presented in Ref. 6, and similar forms can be obtained for molecular radiation.

For those cases where the reaction chemistry set is such that an opposite rate is obtained from a forward or reverse rate in conjunction with an equilibrium coefficient computed from partition functions, the correction factor form given in Eq.(28) is appropriate. This situation is the case with the two-step ionization model, whose rates have been designated Case II. In other words, in that case the factor predicted by Eq. (28) will go to one as the flow approaches ionization equilibrium.

However, when the one step Kang et al ionization rates are used, Case I, the ionization equilibrium coefficient is determined by the ratio of the forward to reverse rates (Eqs. 2-5) and not by partition functions. In that case, the atomic nitrogen LTNE correction factor should be computed using

$$\frac{N_{N+} N_e}{N_N AV K_{eq}} \tag{29}$$

and the equilibrium coefficient is given by

$$K_{eq} = \frac{k_f}{k_b} = 5 \times 10^{-9} T_e^{1.36}\, exp\left(\frac{-169000}{T_e}\right) \tag{30}$$

If this approach is not taken, the factors will not approach one as chemical equilibrium is approached; and ridiculous answers may result.

For viscous cases in which a cool wall is considered, recombination processes will dominate in the wall thermal layer; and as mentioned previously, there is evidence that during recombination that the excited states may not be in equilibrium with the free electrons and ions and that the electronic states may all be populated according to a Boltzman distribution, i.e. in LTE with the ground state. Consequently, in the wall thermal layer, the radiation should be computed using the local electron temperature and nonequilibrium species concentrations; and the LTNE factors should not be used (or set to unity).

Discussion of Results

Inviscid and viscous results have been obtained for the stagnation region of a 2.3 m nose radius axisymmetric blunt body for a freestream velocity of 12 km/sec at an altitude of 80 km. This condition was selected because it is within the range of possible Martian return trajectories; and yet the velocity is low enough that radiation losses should be minor, at the most a few percent, compared to the total flow energy. Thus, radiation cooling and gasdynamic coupling effects should be small. Each inviscid solution covers the region between the shock and the body and from the centerline up to 10 cm above the axis and is typically composed of over ten thousand computational points. Invsicid solutions using both air and nitrogen freestreams have been obtained. Viscous solutions have been obtained along the stagnation streamline for nitrogen freestreams for adiabatic and cool wall situations. In both cases the wall was assumed to be nonemitting and noncatalytic; and in the cool wall case the wall temperature was assumed to be 1650°K, which is representative of nonablating heat shield materials.

Inviscid Results

While flowfield properties along twenty-one different streamlines in the stagnation region were actually computed, details will only be presented for Streamline C which crossed the shock front 1.5 cm above the axis. This streamline is shown on Figure 3 as a solid line, along with several other streamlines, the shock front, and the body. Depending upon the reaction chemistry system, Streamline C was typically composed of 700 to 2000 spatial grid points.

Figure 4 shows air results obtained using the one step ionization model with Case I rates, the quasi-equilibrium electron temperature model, and MCVDV vibration dissociation coupling. While individual vibrational temperatures were computed for N_2, O_2, NO, NO^+, and N_2^+, for clarity they are not included on the plots. Immediately behind the shock front the heavy particle temperature, T, is almost 70,000°K; while the electron temperature, T_e, is at the freestream value, 180.65°K. Initially, T_e rapidly rises to about 10,000°K while the heavy particle temperature falls sharply due to the rapid dissociation of N_2 and O_2. Subsequently, the electron temperature gradually increases until it equilibrates with the heavy particle temperature.

As can be seen on the concentration profiles, in the region immediately behind the shock front the concentration of atomic nitrogen and oxygen rises extremely rapidly, indicating that dissociation essentially occurs in the shock "front" as has been assumed in some approximate solutions[25,34]. Also, N_2^+, NO, and NO^+ peak rapidly and essentially "disappear", and from a practical standpoint the entire nonequilibrium portion of the flowfield is dominated by atomic ionization. Interestingly, at the end of the equilibrium zone, the concentrations of N^+ and O^+ are similar. Further, the heavy particle temperature and $[e^-]$ profiles exhibit a change in curvature around 2.5 cm, which is associated with the onset of electron avalanche from the electron impact ionization reactions.

The magnitude of this phenomena is shown on Figure 5, which portrays the total electron production rate in gm/(cu cm -sec) for this case. While the plot is somewhat lacking in detail since only approximately every twentieth point is plotted, it can be seen that avalanche starts at about one cm along the streamline. Apparently, by this point other ionization reactions have produced sufficient electrons and the electron temperature has risen sufficiently to permit electron impact ionization to dominate. Both Figures 4 and 5 indicate that for the Case I rates that the flow equilibrates in about 4.5 cm. It should be noted that the high electron production rate associated with the Case I impact ionization rates prevents the free electron temperature from peaking and instead leads to its gradual rise until equilibrium is attained.

Similar results are shown on Figure 6 for nitrogen, where the reaction chemistry set of Table II and Case I ionization rates have been used. As for air, $[N]$ rises rapidly behind the shock front; but in this case the N_2 dissociation is somewhat slower, probably due to the absence of the $N_2 + O = N + NO$ exchange reaction that is very efficient at dissociating nitrogen in air. However, the $[N_2^+]$ profile is similar to the air case even though the atomic ionization is somewhat faster with equilibrium occuring at about 4 cm. Interestingly, neither the heavy particle or $[e^-]$ profiles exhibit the reverse curvature that was evident in the air results. In any event, both the air and nitrogen results shown on Figs. 4-6 indicate that for Case I electron impact ionization rates that most of the shock layer in the stagnation region is in equilibrium.

Inviscid results obtained using the two-step approximate ionization model with Case II rates are shown for air on Figures 7 and 8. The $[N]$ and $[O]$ profiles indicate rapid dissociation and are similar to those with the one step model shown on Figure 4. Likewise, the peak values for $[N_2^+]$ and $[NO^+]$ are similar but occur slightly later. The electron temperature initially rises to about 14,000°K, after which it remains relatively constant until it equilibrates with the heavy particle temperature. As can be seen by comparing the values on Figures 8 and 5, the electron production rate for this case is significantly lower than for the Case I situation; and as a result the electron temperature is higher over most of the nonequilibrium region.

The biggest difference, however, between the Case I and Case II air results is in the behavior and length of the atomic ionization region. After the initial dissociation, the decrease in heavy particle temperature and increase in electron concentration is, by comparison, slow; and equilibrium is not achieved until 11 cm along the streamline. In addition, the $[N^+]$ concentration is significantly higher than the $[O^+]$ value. This latter difference is due to the fact that in this case the equilibrium composition is determined from the equilibrium coefficient computed by partition functions, while for the one step Case I rates it is specified by the ratio of the forward and reverse rates in Eqs. (2-5). At the present equilibrium temperatures, these two approaches yield equilibrium constants which differ by an order of magnitude, with resultant differences in final composition and temperatures.

In addition, Figure 8 shows that the electron production rate for the two-step ionization model is different than that for the one-step case. Initially, electrons are created due to NO^+, N_2^+, atom-atom, and atom-ion reactions; and the production from these reactions rapidly peaks and then decreases. However, once $[e^-]$ becomes sufficiently high, electron atom processes become important, the electron production rate increases, and electron avalance occurs. However, since the two step electron atom ionization rate is less, the process is slower than in the one step model and the time and distance to equilibrium is longer.

Equivalent results for a nitrogen freestream for the Case II rates are shown on Figure 9. While there are some differences from the air results in that the electron temperature peaks earlier and that the later stages of N_2 dissociation are slower, the overall ionization relaxation behavior is similar; and the relaxation distance for Streamline C is again 11 - 12 cm. Thus, both the air and the nitrogen results indicate that for the two step ionization model with Case II rates that almost two-thirds of the stagnation region shock layer is in chemical nonequilibrium.

It is believed that these inviscid results demonstrate that predictions of ionization relaxation are strongly dependent upon the atomic ionization model and the electron impact ionization rate. In addition, they show that results obtained using a reaction chemistry set only involving nitrogen (i.e. Table II) can for the present conditions of interest reasonably simulate the nonequilibrium ionization processes in air.

Viscous Results

Using the nitrogen reaction chemistry set given in Table II, viscous results have been obtained for the stagnation streamline with the modified VSL3DNQ code. In all cases, ninety-nine points have been used between the shock front and the wall, and binary diffusion between molecular and atomic species has been included. Unlike the inviscid solver, which primarily used the partition function approach, the thermodynamic properties in the viscous solutions were computed using the curve fits presented by Gnoffo et al[40].

Figure 10 shows temperature and concentration profiles for the cool wall case (T_w = 1650°K) for the Case I electron impact ionization rate. Notice that computational points have been clustered in the region immediately behind the shock front where nonequilibrium effects should be important and in the region near the wall where thermal and concentration gradients could be large. In the outer portion of the shock layer, these results are almost identical to the equivalent invsicid case in that dissociation is rapid behind the shock front, the electron temperature "peaks" and then gradually rises to equilibrate with the heavy particle temperature, and about two-thirds of the shock layer is in chemical equilibriuum. In addition, they show that the cool wall thermal layer affects about twenty percent of the shock layer and that in this region ion and molecular recombination processes are dominant. For this case, the shock standoff distance was 11.8 cm and the computed convective heating rate to the non-catalytic wall was 46.7 watts/sq cm.

Stagnation profiles for the two-step ionization model and the Case II electron impact ionization are presented on Figure 11. For the nonequilibrium zone behind the shock front, these are virtually the same as those presented on Fig. 9 for the equivalent inviscid case in that while dissociation is rapid and N_2^+ rapidly peaks and disappears, two-thirds or more of the shock layer is affected by ionization nonequilibrium relaxation. In addition, the relaxing temperature profile never reaches a constant plateau but smoothly merges into the wall thermal layer. For this case, the shock detachment length was 12.0 cm and the convective heating was 44.4 watts/sq cm.

The electron production rate for this cool wall case is presented on Figure 12. While there are some differences between this profile and the inviscid curve shown on Figure 8 due to differences in velocity along and location of the streamlines, the overall pattern is similar. Initially, electron production is high due to N_2^+ ionization, atom-atom, and atom-ion reactions; and then it decreases. Subsequently, electron-atom ionization becomes important, as evidenced by the plateau around y/yshock of 0.8, followed by an approach towards equilibrium. Unlike Figure 8, no second peak appears in the viscous profile possibly due to diffusion effects and to the influence of the charge exchange reaction. Also, the electron production rate indicates that an equilibrium region is never achieved along the stagnation streamline; but that the flow simply transitions from an ionizing flow to one involving recombination (negative production rates) in the wall thermal layer.

Obviously, the different species concentration and temperature profiles between the Case I and Case II models and rates will greatly influence the predicted radiative heat transfer to the vehicle surface, since radiative heating depends upon both electron temperature and species concentrations. However, it also depends upon the extent of radiative nonequilibrium or the degree to which the excited state populations are depleted due to ionization. This nonequilibrium has previously been referred to as local thermodynamic nonequilibrium (LTNE) in the discussion concerning the radiation model, and it can be approximately accounted for via LTNE correction factors such as those in Eqs. (28) and (29).

Values for the correction factors for atomic nitrogen radiation are shown on Figure 13 for both the Case I and Case II rates and models. For the one-step Case I model, the correction factor is small in the chemical nonequilibrium zone; but then it rises rapidly and is essentially unity through the rest of the stagnation layer. Thus, for the one step impact ionization model, most of the shock layer is in local thermodynamic equilibrium radiatively. Similarly, the two-step Case II factors are also very small in the chemical nonequilibrium zone; but they subsequently only increase slowly and only very near the body in the wall thermal layer do they become one. Hence, for the Case II flowfield, radiative nonequilibrium or LTNE effects are very important. Interestingly, when the approximate technique of Ref. 34 is applied to this case, it also predicts that most of the stagnation region is in LTNE.

In examining these results, it should be realized that the two-step ionization chemistry and LTNE radiation models are approximate and the most optimistic from the standpoint of reducing radiation and the rate of ionization since they assume that the excited states are in equilibrium with the ions and free electrons. In actuality the rate of ionization from the excited state, Eq. (11), may be finite, and the extent of LTNE indicated by the Case II results on Figure 13 may be less. Thus, the two sets of results on Fig. 13 could be viewed as bracketing the problem.

Stagnation Point Radiative Heat Transfer

The viscous stagnation streamline nonequilibrium flowfields have been used to compute the radiative heat transfer to the wall. In all cases the wall has been assumed to be nonemitting and nonablating, and results have been obtained for both an adiabatic and the cool wall case. Considering the many factors invoved in the current models, these radiative heating results should not be construed as definitive and should primarily be used for comparison purposes and model development until they have been verified by more detailed models and/or experiments. Nevertheless, these results do include both the ultra-violet and the visible-IR spectrum, emission and absorption phenomena, the variation of absorption coefficients with wavelength, chemical and thermal nonequilibrium, and radiative nonequilibrium. Thus, the present results include many effects not accounted for in other studies[8] which assumed the gas cap to be in equilibrium and transparent and only included emission in the visible and IR spectrum.

Figures 14 and 15 present stagnation point radiative heat transfer for the present cases as a function of energy, and several significant points are evident. First, there is an order of magnitude difference in heat transfer both totally and in the individual spectral regions between the one-step Case I flowfield and the two-step Case II results. This difference is due to the larger chemical nonequilrium region predicted by the Case II rates and the subsequent greater extent of the radiative nonequilibrium zone. Second, for both ionization models, most of the radiation reaching the wall for the region below 6.89 ev (above 1800 Angstroms), which is often referred to as the visible region since it is optically visible through quartz and sapphire windows, is in the region below 3.1 ev and due to infrared continuum and lines.

Third, the absorption effects of the cool wall thermal layer may not be as great as previously hoped[5,8,33]. With the present data, the effect of the wall thermal layer can be determined by comparing the cool wall results with the adiabatic wall values. For the Case I situation on Figure 14, lowering the wall temperature to 1650°K reduces the overall radiative heating 28%; and in the separate spectral bands the reduction is 22 to 25% except for the vacuum ultraviolet band from 14.56 ev to 31 ev. For that band the reduction is 61%, indicating that the far vacuum ultraviolet is extensively absorbed in the cool wall layer. Likewise, for the Case II rates, Figure 15 shows a reduction due to wall cooling of 46% in the total radiative heating. In this case, since the total input is considerably less than for the one step model, the thermal boundary layer has more of an effect. In the individual bands the reduction ranges from 39 to 44%, but again in the 14.56 - 31 ev VUV band the reduction is large, 72%. Obviously, for both cases, while a cool wall significantly attenuates the far VUV and reduces somewhat the heating from other regions of the spectrum, significant radiative heat transfer still reaches the wall. This trend is consistent with previous approximate calculations at similar conditions[34].

Fourth, there is significant radiative heat input to the wall from the spectral region above 6.89 ev (below 1801 Angstroms). In fact, for both ionization models approximately seventy-five percent of the total radiative heating is from this region. This result is consistent with what has been observed and predicted for the Fire 2 experiment[1,33,41], and it is also consistent with the shock tube experiments of Wood et al[42]. The latter conducted measurements with and without a quartz window and determined that fifty to seventy-five percent of the total radiant intensity was from the ultraviolet region of the spectrum. Interestingly, they also concluded from their experiments that a cool boundary layer would not absorb appreciably.

Comparison with Experimental Data

Based upon the temperature, species, and radiative heat transfer profiles discussed above, it is apparent that the choice of ionization model and electron impact ionization rate greatly affects the resultant predictions; and it would be desirable to determine which model is more appropriate for blunt body calculations. While there is almost no radiation experimental data at the present velocity and pressure conditions, Wilson[25] did make measurements of the ionization rate of air behind shock waves having velocities between 9 and 12.5 km/sec. By making infrared measurements around 6.1 microns, he was able to determine variations in electron density and thus the ionization relaxation distances.

Consequently, the concentration and temperature profiles for the present inviscid air data along Streamline C have been used to compute theoretical infrared emission profiles similar to those measured by Wilson for both the Case I and Case II models. These profiles are shown on Figure 16, and they have the same general shape as the signals measured by Wilson. Following his procedure, the intercept with the equilibrium value of a line drawn through the maximum slope of the rising signal has been used to determine an ionization distance, denoted by the vertical dashed line on the figure, for each ionization model. Then, the shock tube data of Wilson has been used, accounting for differences in freestream pressure and for particle velocity differences behind a normal shock and along Streamline C, to determine an experimental ionization distance for the present case. These distances are shown by the square symbols on Figure 16. The center symbol is the nominal value, while the end points correspond to the data scatter and error band limits indicated in Ref. 25.

As can be seen, the agreement between the shock tube data and the prediction obtained using the two step ionization model and the Case II electron impact ionization rates is very good. Thus, based upon the results presented, it appears that a two step ionization model in conjunction with ionization reaction rates based upon forward processes should be used for the computation of nonequilibrium blunt body flowfields associated with earth aerocapture from Mars.

However, this conclusion does not mean that the ion recombination rates used by Kang et al[11] or measured by Park[17] are in error. Unfortunately, there are many possible explanations for the observed differences. First, there could be an error in the experimental data[25] or its interpretation to the present problem. Second, at the current electron densities and temperatures, the results of Hinnov and Hirschberg[19] and of Bates et al[43] indicate that the effective recombination rate is not strictly a function of electron temperature and that radiative recombination is still significant. Thus, the flow may not be totally collision dominated. In such a situation, if a measured or effective reverse rate were used via an equilibrium constant to determine a forward rate, the resulting forward rate would be too large. As pointed out by Park[18,44–45] the effective forward and reverse rates are only related via the equilibrium constant if the flow is collision dominated. Third, there is the possibility[18] that in the region immediately behind the shock front that due to the time scales involved the forward and reverse rates are not related by the equilibrium constant and that reasonable chemistry can only be predicted using a proper forward rate. Fourth, there exists the possibility that the electronic temperatures are not in reality the same as the free electron temperature and that this fact requires the use of a different set of rates. A discussion of this situation and also the details of atomic ionization is presented in Ref. 45 and 46. Finally, as mentioned previously, there exists the possibility that ionic recombination in a nozle or arc tunnel is not the direct inverse of atomic ionization behind a shock wave. If anything, the present results indicate the difficulty of creating engineering models for these problems and the need for further analytical and experimental investigation.

Future Efforts

In the near future, it is planned to continue these studies by developing a nonequilibrium radiation model based upon RADICAL. This new model will be incorporated into the VSL code along with radiation gasdynamic coupling. In addition, there exists a need to improve the ionization chemistry model and the LTNE correction factors by taking into account finite rate processes between excited state atoms and ions. Also, there is a definite need for additional experimental data at velocities and pressures appropriate for a Mars return AOTV. This data should be for an ionizing, as opposed to a recombining flow, and probably could be obtained in a shock tube, although flight data would be desirable. Finally, the inclusion of pre-shock precursor, photoionization and recombination, and shock and wall slip effects would be desirable.

Conclusion

Based upon the results presented, it appears that an approximate two step ionization model in conjunction with a quasi-equilibrium electron temperature model is suitable for the computation of nonequilibrium blunt body flowfields associated with earth aeroacapture from Mars. Also, nonequilibrium chemical and radiation effects are important at these conditions throughout the entire stagnation zone; and, when compared to equilibrium predictions, these nonequilibrium phenomena can lead to a reduction in radiative heating. Further, compared to an adiabatic wall, a cool wall results in a significant reduction in radiative heating due to absorption near the wall. However, the present results also indicate a need for further analytical and experimental investigations.

Acknowledgements

The authors gratefully acknowledge the assistance of the Associate Provost for Computing for providing a portion of the computational resources used in this effort. This work was initiated under a subportion of NASA Grant No. NAG 9-192 from the NASA Johnson Space Center. The authors would like to thank the technical monitor, Dr. Carl Scott, Aerosciences Branch, JSC,. for his suggestions and Dr. Ken Sutton, Aerothermodynamics Branch, NASA Langley Research Center, for his comments and assist ance in providing the RADICAL and VSL3DNQ programs. Mr. Gally is partially supported by a NASA Graduate Student Researchers Fellowship thru the NASA Johnson Space Center.

REFERENCES

[1] Sutton, K.,"Air Radiation Revisted," in ***Thermal Design of Aeroassisted Orbital Transfer Vehicles***, Progress in Astronautics and Aeronautics, Vol. 96 , Ed. H. F. Nelson, AIAA, 1985, pp. 419-441.

[2] Moss, J. N, Bird, G. A., and Dogra, V. K., "Nonequilibrium Thermal Radiation for an Aeroassist Flight Experiment Vehicle," AIAA Paper No. 88-0081, January 1988.

[3] Gnoffo, P. A. and Green, F. A., "A Computational Study of the Flowfield Surrounding the Aeroassist Flight Experiment Vehicle," AIAA Paper No. 87-1575, June 1987.

[4] Park, C., "Assessment of Two Temperature Kinetic Model for Ionizing Air," AIAA Paper No. 87-1574, June 1987.

[5] Candler, G. and Park, C., "The Computation of Radiation from Nonequilibrium Hypersonic Flows," AIAA Paper No. 88-2678, June 1988.

[6] Carlson, L. A., Bobskill, G. J., and Greendyke, R. B., "Comparison of Vibration Dissociation Coupling and Radiative Heat Transfer Models for AOTV/AFE Flowfields," AIAA Paper No. 88-2673, June 1988.

[7] Li, C. P. and Wey, T. C., "Numerical Simulation of Hypersonic Flow Over an Aeroassist Flight Experiment Vehicle," AIAA Paper No. 88-2675, June 1988.

[8] Park, C. and Davies, C. B., "Aerothermodynamics of Manned Mars Mission," AIAA Paper No. 89-0313, January 1989..

[9] Grosse, W. L., "A Thin Shock Layer Solution for Nonequilibrium, Inviscid Flows in Earth, Martian, and Venusian Atmospheres," NASA TN D-6529, December 1971.

[10] Thompson, R. A., "Comparison of Nonequilibrium Viscous Shock Layer Solutions with Windward Surface Shuttle Heating Data," AIAA Paper 87-1473, June 1987.

[11] Kang, S. W., Jones, W. L., and Dunn, M. G., "Theoretical and Measured Electron Density Distributions at High Altitudes," *AIAA Journal*, vol. 11, No. 2, February 1973, pp. 141-149.

[12] Zeldovich, Y. B. and Raizer, Y. P.,*Physics of Shock Waves and High Temperature Hydrodynamic Phenomena*,Academic Press,New York,1966,pp. 407-413.

[13] Makin, B. and Keck, J. C., "Variational Theory of Three-Body Electron Ion Recombination Rates," *Physical Review Letters*, vol. 11, Nol. 6, 15 September 1963, pp. 281-283.

[14] Dunn, M. G., "Measurement of $C^+ + e^- + e^-$ and $CO^+ + e^-$ Recombination in Carbon Monoxide Flows," *AIAA Journal*, vol. 9, No. 11, November 1971, pp. 2184-2191.

[15] Dunn, M. G. and Lordi, J. A., "Measurement of $O_2^+ + e^-$ Dissociative Recombination in Expanding Oxygen Flows," *AIAA Journal*, vol. 8, No. 4, April 1970, pp. 614-618.

[16] Dunn, M. G. and Lordi, J. A., "Measurement of $N_2^+ + e^-$ Dissociative Recombination in Expanding Nitrogen Flows," *AIAA Journal*, vol. 8, No. 2, February 1970, pp. 339-345.

[17] Park, C., "Measurement of Ionic Recombination Rate of Nitrogen," *AIAA Journal*, vol. 6, No. 11, November 1968, pp. 2090-2094.

[18] Park, C., "Collisional Ionization and Recombination Rates of Atomic Nitrogen," *AIAA Journal*, vol. 7, No. 8, August 1969, pp. 1653-1654.

[19] Hinnov, E. and Hirschberg, J. G., "Electron-Ion Recombination in Dense Plasmas," *Physical Review*, vol. 125, No. 3, February 1962, pp. 795-801.

[20] Nelson, H. F. and Goulard, R., "Structure of Shock Waves with Nonequilibrium Radiation and Ionization," *Physics of Fluids*, vol. 12, No. 8, Aug. 1969, pp. 1605-1617.

[21] Chapin, C. E., "Nonequilibrium Radiation and Ionization in Shock Waves," AA&ES Report, June 1967, Purdue Univ., Lafayette, Ind.

[22] Foley, W. H. and Clarke, J. H., "Shock Waves Structured by Nonequilibrium Ionizing and Thermal Phenomena," *Physics of Fluids*, vol. 16, No. 3, March 1973, pp. 373-383.

[23] Vinolo, A. R. and Clarke, J. H., "Interrelated Structures of the Transport Shock and Collision Relaxation Layer in a Multitemperature, Multilevel Ionized Gas," *Physics of Fluids*, vol. 16, No. 10, October 1973., pp. 1612-1620.

[24] Zeldovich, Y. B. and Raizer, Y. P.,*Physics of Shock Waves and High Temperature Hydrodynamic Phenomena*, Academic Press, New York, 1966, pp. 382-396, 505-515.

[25] Wilson, J., "Ionization Rate of Air Behind High Speed Shock Waves," *Physics of Fluids*, vol. 9, NO. 10, October 1966, pp. 1913-1921.

[26] Carlson, L. A., "Radiative Gasdynamic Coupling and Nonequilibrium Effects behind Reflected Shock Waves," *AIAA Journal*, vol. 9, No. 5, May 1971, pp. 858-865.

[27] Petschek, H. and Byron, S., "Approach to Equilibrium Ionization Behind Strong Shock Waves in Argon," *Anals of Physics*, vol. 1, 1957, pp. 270-315.

[28] Dix, D. M., "Energy Transfer Processes in a Partially Ionized Two Temperature Gas," *AIAA Journal*, vol. 2, No. 12, December 1964, pp. 2081-2090.

[29] Dix, D. M., "The Governing Macroscopic Equations of Partially Ionizaed Gases," Aerospace Corporation Report, TDR-69-2330-04 TN-2, July 1962.

[30] Lee, J. H., "Basic Governing Equations for the Flight Regimes of Aeroassisted Orbital Transfer Vehicles," *Thermal Design of Aeroassisted Orbital Transfer Vehicles*, ED. H. F. Nelson, Progress in Astronautics and Aeronautics, Vol. 96, AIAA, New York, NY, 1985, pp. 3-53.

[31] Carlson, L. A., "Radiative Cooling and Nonequilibrium Chemistry Coupling Behind Normal Shock Waves," *AIAA Journal*, vol. 10, No. 2, February 1972, pp. 230-232.

[32] Tiwari, S. N. and Szema, K. Y., "Effects of Precursor Heating on Radiative and Chemically Reacting Viscous Flow Around a Jovian Entry Body," NASA CR 3186, October 1979.

[33] Gupta, R. N., "Navier Stokes and Viscous Shock Layer Solutions for Radiating Hypersonic Flows," AIAA Paper No. 87-1576, June 1987.

[34] Carlson, L. A., "Approximations for Hypervelocity Nonequilibrium Radiating, Reacting, and Conducting Stagnation Regions," AIAA Paper No. 88-2672, June 1988.

[35] Carlson, L. A., and Rieper, R. G., "Electron Temperature and Relaxation Phenomena behind Shock Waves," *J. of Chemical Physics*, vol. 57, No. 2, July 1972, pp. 760-766.

[36] Carlson, L. A., "Expressions for the Exchange of Energy and Momentum between Gases at Different Temperatures and Velocities," *Physics of Fluids*, vol. 13, No. 7, July 1970, pp. pp. 1869-1870.

[37] Olstad, W. B., "Nongray Radiating Flow about Smooth Symmetric Bodies," *AIAA Journal*, vol. 9, No. 1, January 1971, pp. 122-130.

[38] Nicolet, W., "User's Manual for the Gneralized Radiation Transfer Code (RAD/EQUIL or RADICAL)," NASA CR 116353, October 1969.

[39] Greendyke, R. B., private communications, Analytical Methods and Services Corporation, Hampton, Va., 1989.

[40] Gnoffo, P. A., Gupta, R. N., and Shinn, J., "Governing Equations and Physical Models for Hypersonic Air Flows in Thermal and Chemical Nonequilibrium," NASA TP 2867, 1989.

[41] Bird, G. A., "Nonequilibrium Radiation During Reentry at 10 km/sec," AIAA Paper No. 87-1543, June 1987.

[42] Wood, A. D., Hoshizaki, H., Andrews, J. C., and Wilson, K. H., "Measurements of the Total Radiant Intensity of Air," *AIAA Journal*, vol. 7, No. 1, January 1969, pp. 130-139.

[43] Bates, D. R., Kingston, A. E., and McWhirter, R. W. P., "Recombination Between Electrons and Atomic Ions I. Optically Thin Plasmas," *Proceedings of the Royal Society, London, Series A.*, vol. 267, No. 1330, May 1962, pp. 297-312.

[44] Park, C., "Spectral Line Intensities in a Nonequilibrium Nitrogen Plasma," *J. Quantatative Spectroscopy and Radiative Transfer*, vol. 8, 1968, pp. 1633-1653.

[45] Park, C., "Comparison of Electron and Electronic Temperatures in Recombining Nozzle Flow of Ionized Nitrogen-Hydrogen Mixture. Part 1. Theory," *Journal of Plasma Physics*, vol. 9, Part 2, 1973, pp. 187-215.

[46] Kunc, J. A. and Soon, W. H., "Nonequilibrium of High Temperature Nitrogen and Oxygen," AIAA Paper No. 88-2779, June 1988.

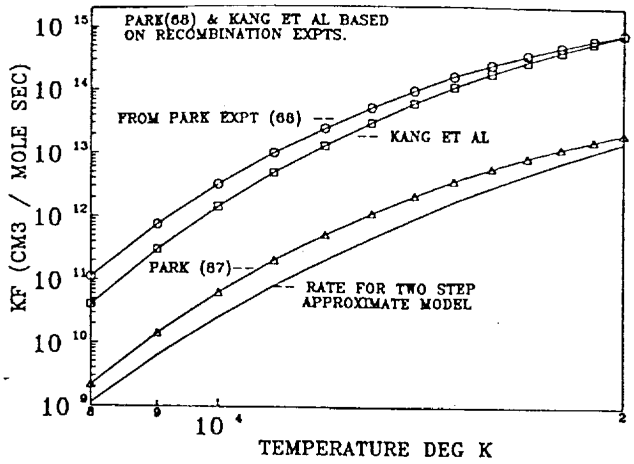

Fig. 1 Comparison of Forward Rate Constants for $N + e^- = N^+ + e^- + e^-$.

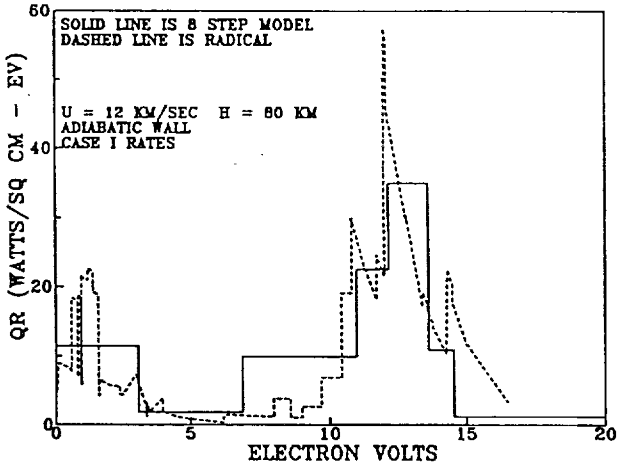

Fig. 2 Stagnation Point Radiative Heat Transfer from RADICAL and 8-Step Model.

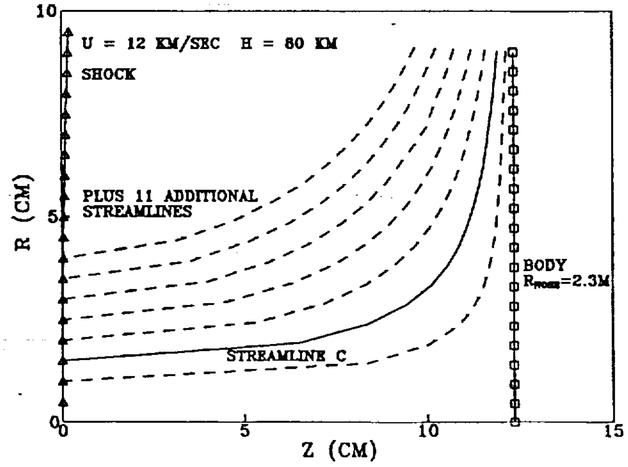

Fig. 3 Solution Region for Inviscid Cases Showing Streamline C.

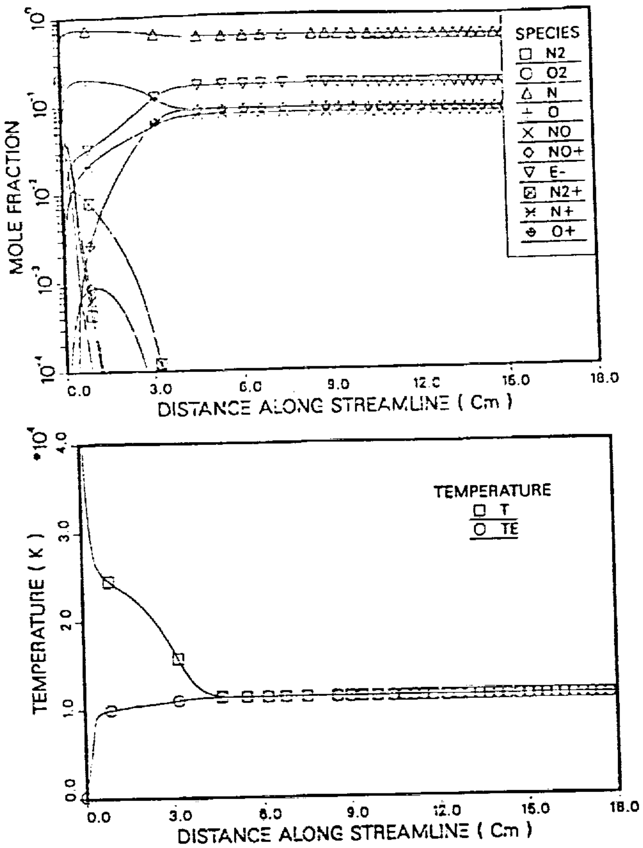

Fig. 4 Species and Temperature Profiles for Air Along Streamline C, Inviscid Flow, Case I.

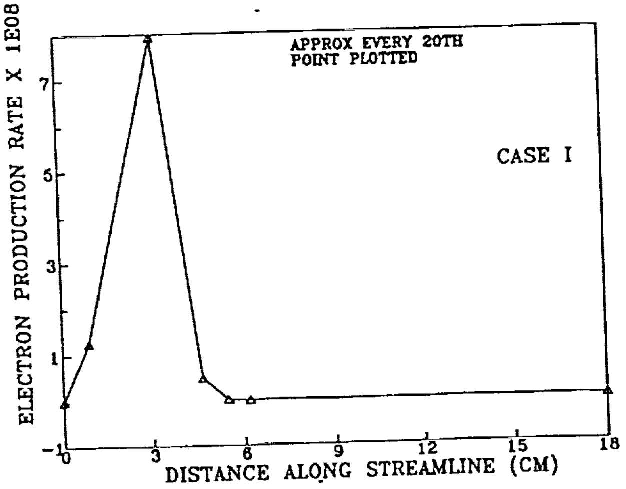

Fig. 5 Electron Mass Production Rate Along Streamline C, Inviscid Case I.

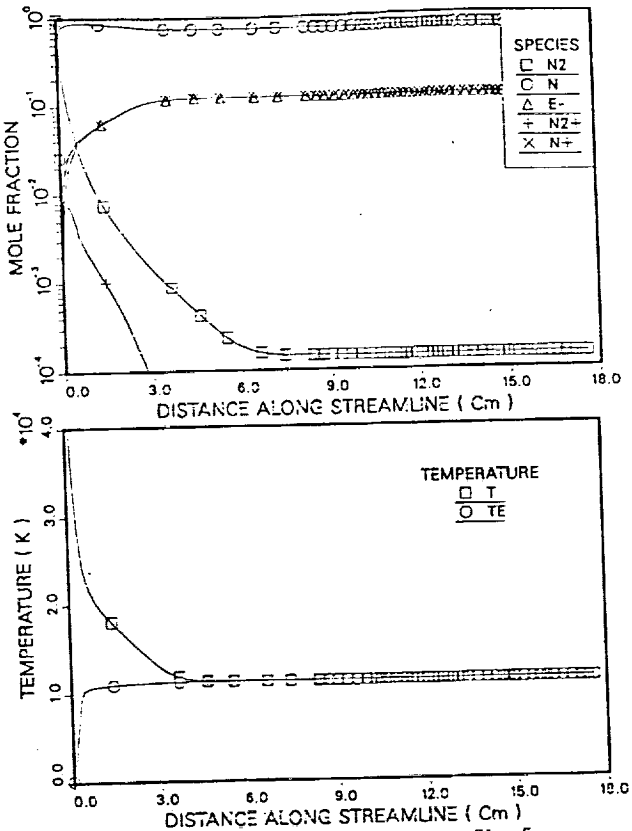

Fig. 6 Species and Temperature Profiles for Nitrogen, Streamline C, Inviscid Case I.

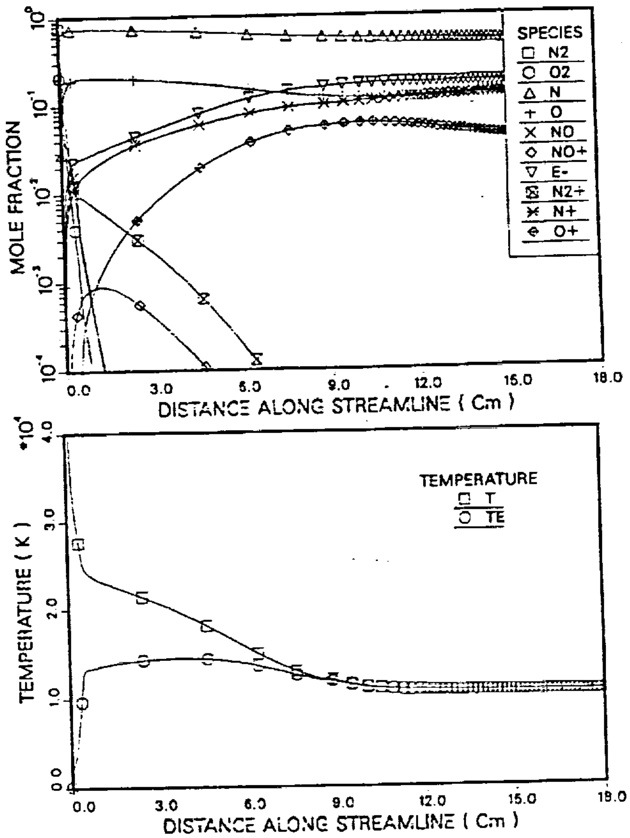

Fig. 7 Species and Temperature Profiles for Air Along Streamline C, Inviscid Flow, Case II

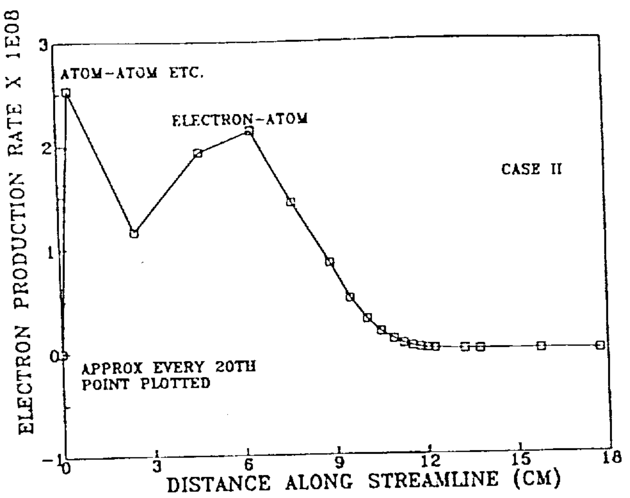

Fig. 8 Electron Mass Production Rate Along Streamline C, Inviscid Case II.

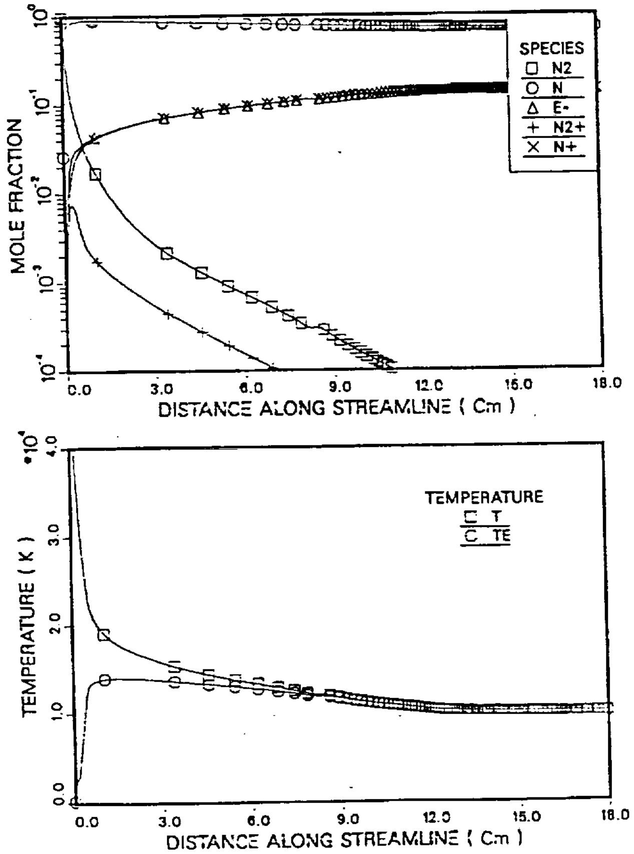

Fig. 9 Species and Temperature Profiles for Nitrogen, Streamline C, Inviscid Case II.

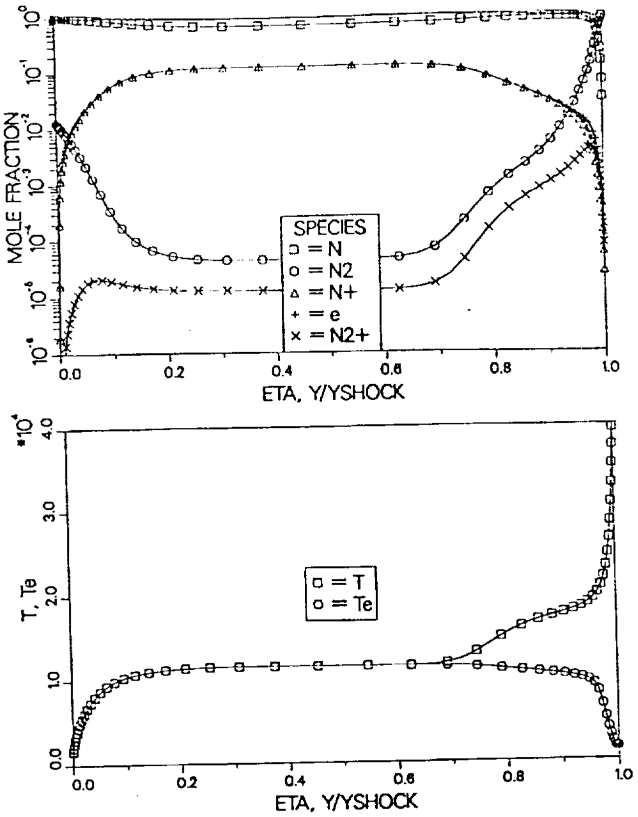

Fig. 10 Stagnation Streamline Species and Temperature Profiles, Viscous Case I.

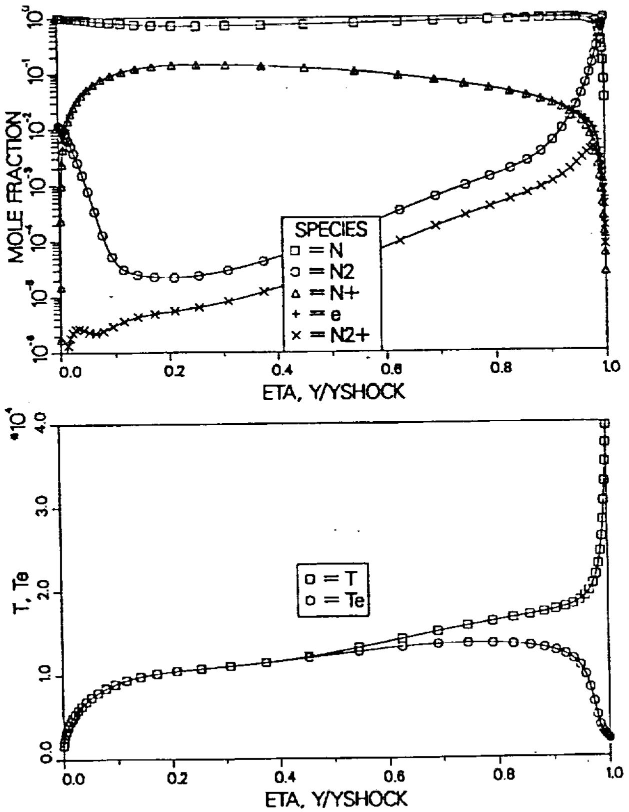

Fig. 11 Stagnation Streamline Species and Temperature Profiles, Viscous Case II.

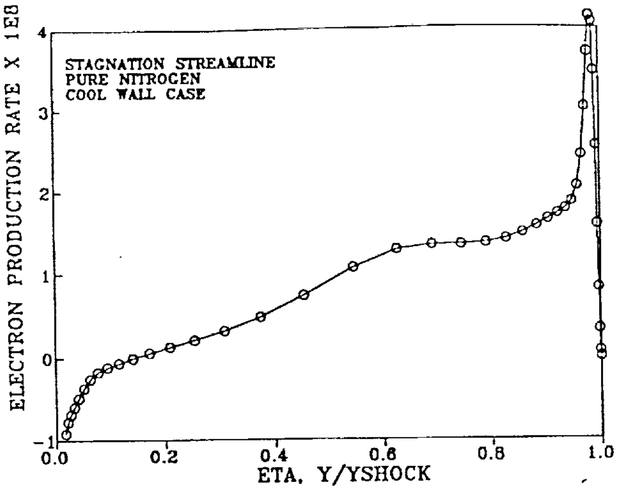

Fig. 12 Stagnation Streamline Electron Mass Production Rate, Viscous Flow, Case II.

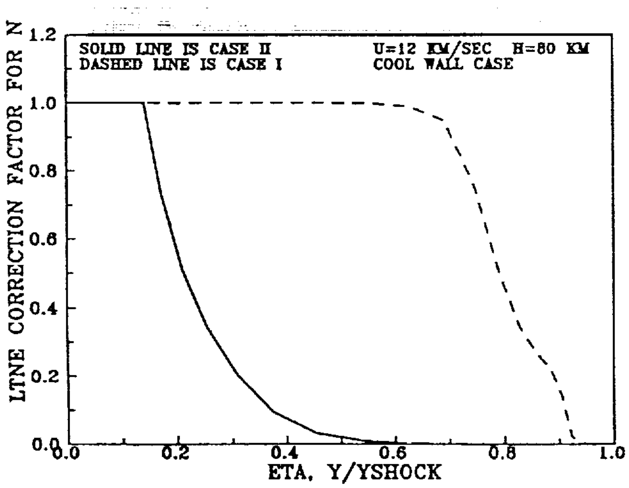

Fig. 13 Nonequilibrium Radiation Correction Factors Along Stagnation Streamline.

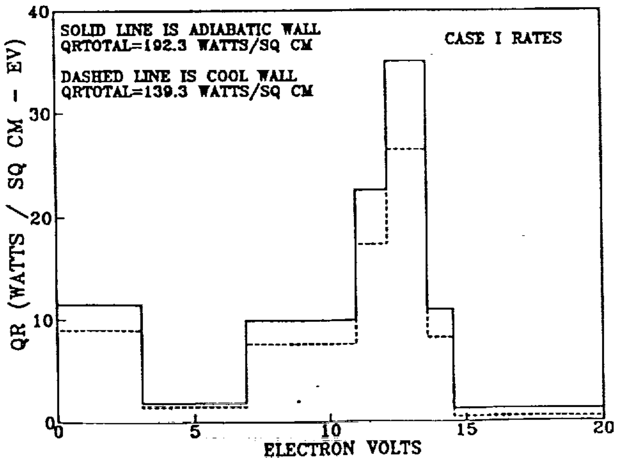

Fig. 14 Stagnation Point Radiative Heat Transfer for Case I.

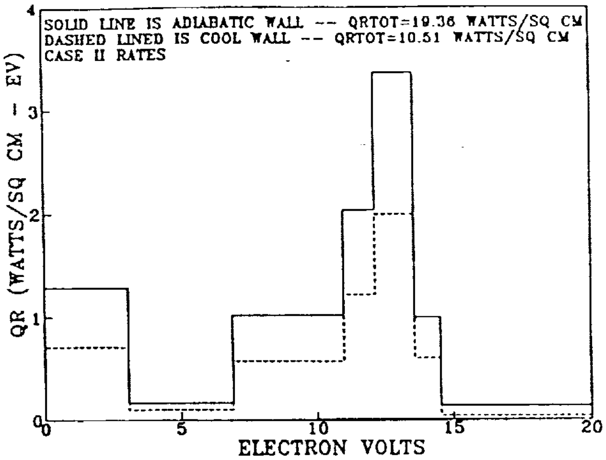

Fig. 15 Stagnation Point Radiative Heat Transfer for Case II.

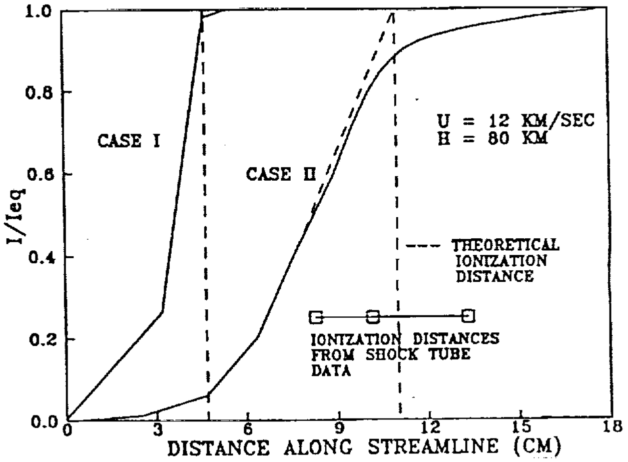

Fig. 16 Theoretical Emission Profiles and Ionization Distances for Streamline C.

AIAA 91-0569

Nonequilibrium Chemical and Radiation Coupling Phenomena in AOTV Flowfields

L. A. Carlson and T. A. Gally
Texas A&M University
College Station, TX

29th Aerospace Sciences Meeting

January 7-10, 1991/Reno, Nevada

For permission to copy or republish, contact the American Institute of Aeronautics and Astronautics
370 L'Enfant Promenade, S.W., Washington, D.C. 20024

Nonequilibrium Chemical and Radiation Coupling Phenomena in AOTV Flowfields

Leland A. Carlson*
and
Thomas A. Gally**
Texas A&M University
College Station, Texas

Abstract

A flowfield model for the nonequilibrium stagnation region of high altitude entry vehicles which includes nonequilibrium chemistry, multi-temperature, viscous, conduction, and diffusion effects is presented. It contains coupled nongray nonequilbrium radiative transfer for atoms and molecules and local thermodynamic nonequilibrium phenomena. Comparison with Fire 2 flight data verifies that the model is reasonably accurate; and it has been applied to two AFE trajectory points, a high speed return from Mars, a series of points at 80 km for 12 to 16 km/sec, and three altitudes at 16 km/sec. Based on these results shock slip is significant, radiation cooling/coupling is minor at AFE conditions but important by 14 km/sec and dominant at 16 km/sec, radiation for the AFE is small but important and primarily molecular, above 12 km/sec atomic radiation is a significant or dominant portion of the total heating, and local thermodynamic nonequilibrium is important and should be included in all models.

Nomenclature

c_e = mean thermal velocity of electrons
c_p = specific heat at constant pressure
E = ionization potential
h = enthalpy
k = Boltzmann constant
m = mass
N = number density
n, s, ϕ = coordinate axis
p = pressure
Q = rate of inelastic energy exchange
T = Temperature
u, v, w = mass averaged velocity components
U = diffusional velocity
y_s = shock standoff distance
$\mathcal{D}$ = binary diffusion coefficient
ϵ = Reynolds number parameter
e = magnitude of electron charge
η = heat conduction coefficient
ξ_e = rate of elastic electron energy exchage
ρ = density
Φ = wall sheath electric potential

subscripts
e = electron
eI = electron impact reaction
r = species
s = value behind shock
superscripts
e = electronic
$n, n+1$ = iteration step
tr = translational

Introduction

In the future, various space programs will be conducted which will require the efficient return of large payloads from missions to the moon or to planets such as Mars. To accomplish this task, the return vehicles will either utilize direct entry at very high velocities or aerocapture techniques. In either case, a significant portion of the entry will involve high velocities at high altitudes; and, during this part of the trajectory, the vehicle flowfields will be dominated by chemical, thermal, and radiative nonequilibrium phenomena. To design and operate such vehicles, it is essential to develop engineering flowfield models which appropriately and accurately describe these chemical, thermal, and radiative nonequilibrium processes and the coupling between them.

Previously[1], the importance of properly predicting electron temperature and modeling electron impact ionization was investigated and a quasi-equilibrium free electron energy model and a two step ionization model formulated. In addition, an approximate method of handling nonequilibrium atomic radiation, which assumed that the excited states of atoms are in equilibrium with the local free electrons and ions, was developed[1-3] and applied to an eight step nongray emission-absorption radiation model. While the results obtained with these models were informative, the lack of detail in the radiation model, particularly with respect to atomic lines and the bands associated with molecular ions, and the highly approximate nature of the nonequilibrium molecular radiation portion of the model, which for some molecular bands appeared to underestimate the actual radiation, indicated a need for improvement. Further, while the quasi-equilibrium free electron energy model and its associated assumption that the electronic temperature was determined solely by the free electron temperature should be a good approximation for many conditions of interest in aerocapture and entry, it was felt that additional models should be developed in an effort to improve the modeling of electron energy, and hence temperature, due to its importance in determining nonequilbirum ionization chemistry and radiative transfer.

---

* Professor Aerospace Engineering, Associate Fellow AIAA

** NASA Graduate Student Researcher, Student Memeber AIAA

Thus, the objective of this paper is to present an improved engineering flowfield model for high altitude AOTV flowfields having extensive chemical, thermal, and radiative nonequilibrium and to use this model over a wide range of conditions to investigate the magnitude and extent of nonequilibrium chemical and radiation coupling phenomena in high altitude entry vehicle flowfields.

Problem Formulation

Flowfield Model

The flowfield model used in this investigation is a viscous shock layer analysis which includes the effects of chemical nonequilibrium, multi-temperature thermal nonequilibrium (heavy particle and electron or electron-electronic temperature), viscosity, heat conduction, diffusion, and radiative gasdynamic coupling. The basic method, which is a significantly modified version of the NASA Langley code VSL3DNQ[4] is similar to the version used in Ref. 1; but a number of additional modifications have been incorporated since the earlier study. First, the VSL code has been coupled with modified versions of the radiation routines of the NASA Langley program, RADICAL[5], which is described below, giving the ability to calculate flowfield solutions with the effects of radiative cooling present. Second, the chemical reaction rate input data has been changed to allow the use of a single reaction rate, k_f or k_b, and the equilibrium constant, K_{eq}, rather than using both forward and backward rates. With this modification, species concentrations in the equilibrium regions of a flowfield are now in agreement with results from equilibrium analysis. Third, the effects of multi-temperatures on the shock jump conditions and thermodynamic state variables have been improved from those at the time of Ref. 1.

One of the advantages of a VSL method is the ability to distribute many flowfield points in regions of large gradients, such as in the region immediately behind the shock front and in the highly nonequilibrium thermal layer near the wall. However, this approach requires proper shock front jump conditions since diffusion and thermal conduction phenomena can be significant in the region immediately behind the shock front. Thus, the present method includes multi-temperature shock slip boundary conditions, and the importance of including and utilizing these conditions will be shown later. In addition, the present method permits various wall catalycity properties and includes appropriate spectral variations in the treatment of the wall boundary conditions.

Radiative Transfer Model

The radiation analysis in RADICAL is a detailed method which includes atomic continuum radiation, molecular band radiation, and atomic line radiation for the standard CHON (carbon, hydrogen, oxygen, nitrogen) gas system. While the original method used individual species number densities and assumed a Boltzmann distribution to calculate the excited state number densities for each species, and, from this data, the individual radiative absorption coefficients associated with each radiative process, such an approach is not suitable for nonequilibrium conditions. Thus, the original model has been extensively expanded and modified to include nonequilibrium chemical and thermal effects and to account for excited state population distributions different from those predicted by a Boltzmann distribution. Consequently, in the present engineering approach, nonequilibrium radiation is computed using the modified RADICAL radiative analysis code and absorption coefficient model with actual species concentrations, the appropriate electron-electronic temperature, and with correction factors on the effective source function and absorption coefficients. This correction factor approach accounts for the existence of non-Boltzmann distribution state populations (i.e. local thermodynamic nonequilibrium, LTNE) and effectively determines the correct state populations.

Nonequilibrium Molecular Radiation Model

Previously, approximate correction factors for molecular radiation had been developed[3]; but it is now believed that these factors overcorrect and for some molecular bands underestimate the actual radiation. This belief is reenforced by experimental measurements made in molecular radiation dominated shock flows which exhibit a radiation intensity peak behind the shock front in conjunction with the predicted electron temperature peak. Thus, significant depletion of all of the excited molecular states, as predicted by the theory of Ref. 3, is not expected. Consequently, new improved molecular correction factors for molecular nonequilibrium radiation have been developed.

After examining various approaches, a quasi-steady approach similar to that of Ref. 6 has been developed which computes the electronic state populations associated with the radiating molecular bands. Specifically, for N_2, the populations of the X, A, B, a, and C states are computed; while for N_2^+ the X, A, B, and D are included. This approach has been incorporated into the flowfield and radiative transport code; and there is no assumption concerning the existence of equilibrium between excited molecular states and atoms as there was in Ref. 3. Thus, in this new molecular model, both source functions and absorption coefficients associated with molecular band radiation are modified for nonequilibrium effects. However, in this quasi-steady approach there is the inherent assumption that the rates used to determine the state populations are compatible with the overall rate chemistry. For the molecules, it is believed that the various rates are reasonably well known and that this inherent assumption is satisfied.

In general, results indicate that for the N_2 Birge-Hopfield band the correction factor for the absorption coefficient is frequently near unity but that for the corresponding source function it is quite small in the nonequilibrium portion of the shock layer immediately behind the shock front. Since the absorption coefficient depends upon the number density of the absorbing state and the effective source fuction is proportional to the ratio of the populations of the emitting and the absorbing states, this behavior is what would "normally" be expected. For the N_2(BH) band, emission is from high excited states, which should be depleted by nonequilibrium effects, and absorption is to the ground electronic state, whose population density sould be closely predicted by a Boltzmann distribution. Likewise $N_2(1+)$ typically displays only a slight correction (from unity) for the source function but a significant decrease from that predicted using Boltmann distributions in the absorption coefficient. This trend is also "expected" since $N_2(1+)$ involves two excited states, B and A. On the other hand, while the absorption coefficient factor for $N_2(2+)$ is similar to that for $N_2(1+)$, the source function for $N_2(2+)$ is typically significantly reduced in the chemical and thermal nonequilibrium region behind the shock front, indicating that pre-dissociation is significantly depleting the population of the C electronic state.

The most interesting result, however, is that the $N_2^+(1-)$ radiation is usually only slightly affected by nonequilibrium phenomena. This result is in agreement with experiments which, at least at lower velocities, have indicated a strong $N_2^+(1-)$ contribution. However, since the number density of N_2^+ is often only significant in the region immediately behind the shock front, any $N_2^+(1-)$ radiation should originate from that region. This feature will be discussed further in the results section.

Another interesting phenomena associated with the molecular nonequilibrium radiation is that often in the thermal boundary layer near the wall, several of the factors accounting for LTNE exceed unity and become large. This behavior indicates an overpopulation of excited states above values which would be predicted by a Boltzmann distribution when intuitively an equilibrium distribution might be expected due to the increased density near the wall. However, the thermal boundary layer is often in significant nonequilibrium since the chemical reaction rates are finite and cannot keep up with the true local equilibrium, which leads to atom and sometimes ion concentrations above local equilibrium. In addition, diffusion tends to perturb the species population densities and leads to atom and ion densities above equilibrium values, which in turn creates enhanced molecular excited state populations. This enhancement, however, does not lead to increased radiative emission near the wall; and in fact, probably due to the lower electron-electronic temperature in that region, it does not, for the cases examined, appear to affect the radiative heat transfer. Thus, in the present studies limitations on the molecular nonequilibrium correction factors have not been imposed.

Nonequilibrium Atomic Radiation Model

Local thermodynamic nonequilibrium effects (LTNE) on atomic radiation are also computed by applying correction factors which account for the deviations in state populations from Boltzmann distributions to the absorption coefficient and source function values utilized in the radiative analysis. Such atomic LTNE definitely exists in the chemical nonequilibrium region immediately behind the shock front[1-3,6,7] where, due to ionization via excited states, the populations of the electronic states will be lower than predicted by an LTE assumption using the ground state. Likewise, in regions of recombination the reverse processes can lead to state populations above those obtained using LTE.

The current model, which should probably be termed a first order approximation, has been presented previously in Ref. 1-3 and similar models have been used for monatomic gases[8-11]. Briefly, this model assumes that atomic ionization proceeds by excitation from the three low ground states (for nitrogen) to the high excited states followed by rapid ionization. Consequently, the model assumes that excitation from the ground states to the higher states is a rate limiting step for the ionization process and that the excited states, because of their energy proximity to the ionized state, are in equilibrium with the free electrons and ions. With this approach, for example[1-3], the atomic nitrogen LTNE correction factor, which represents the ratio of the actual population in an excited state to that which would exist for a Boltzmann distribution, can be written as

$$\frac{N_{N+} N_e Q_N^e exp(169000/T_e)}{N_N Q_{N+}^e Q_e} \qquad (1)$$

This factor is usually less than one in ionization regions and can be greater than one in zones involving extensive deionization. For the results presented later, it was usually applied with no restrictions.

In contrast, Park[12] and Kunc et al[13] handle atomic LTNE by using a quasi-steady analysis in which, while rate processes between all the bound states and between the bound states and the ionized state are assumed finite, they are assumed to be fast relative to changes induced by the flowfield. Thus, at any point in a flowfield an equilibrium between the states will exist which is perturbed from a Boltzmann distribution due to radiative effects. Kunc et al have performed calculations in which they specify the electron temperature and the total number of charged particles (defined as two times the number of atoms plus the number of ions plus the number of electrons), leaving the actual number of ions and free electrons to be determined as part of the unknown populations.

Park, on the other hand, in the application of his method[6] assumes the number of ions and electrons to be given by a flowfield solution. Under this approach, a non-Boltzmann distribution can be achieved even in the absence of radiation, if the number of ions and electrons differs from equilibrium. To be totally correct, however, the excitation and ionization rates associated with each level must overall be consistent with the ionization rates used in the flowfield solution.

Obviously, the present first order approach and those of Park and Kunc et al represent the extremes of modeling LTNE atomic phenomena. While the present first order approach is simplified in its assumption that the rates between the excited states and the free ions and electrons are infinitely fast (i.e. local equilibrium), it does directly couple the predicted excited state populations to the flowfield and, unlike the detailed quasi-steady approaches, it is not computationally intensive. In addition, the latter are sensitive to the choice of the individual rates; and it is difficult to know which rate to adjust when comparing with experimental results and attempting to improve the correlation. Finally, the present model when coupled with a compatible electron impact ionization rate has been shown to yield good agreement with experimental ionization distances[1].

Electron-Electronic Energy Models

For the present studies, three different electron-electronic energy models have been used and investigated. The first, termed the quasi-equilibrium electron energy model (QEE), is essentially a free electron energy model in which all derivative terms in the electron energy equation are neglected; and it can be expressed as

$$\dot{w}_e h_e^{tr} - \dot{w}_e \frac{u^2}{2} = \sum_r \xi_{er} + Q_e \tag{2}$$

where the ξ_{er} terms account for elastic collisional effects and Q_e represents inelastic effects due to chemical reactions involving electrons. It should be noted that the term $\dot{w}_e u^2/2$ is usually very small and can be neglected. This model was previously presented in Ref. 1, which contains additional details. The second is termed the quasi-equilibrium electron-electronic energy model (QEEE) and is similar to the first model in that it computes the electron temperature assuming quasi-equilibrium. However, it explicity accounts for the effect of elastic and inelastic collisions on the energy contained in electronic states of each species as well as the free electron energy; and, thus, the resulting temperature is truly representative of electron-electronic energy. The resulting equation is

$$\dot{w}_e h_e^{tr} + \sum_r \dot{w}_r h_r^e - \dot{w}_e \frac{u^2}{2} = \sum_r \xi_{er} + Q_e \tag{3}$$

where the term $\sum_r \dot{w}_r h_r^e$ accounts for the production and depletion of electronic energy due to chemical reactions.

The third model utilizes a combined electron-electronic energy differential equation which includes the effects of convection, conduction, and diffusion, in addition to the production and loss of electron energy through elastic and inelastic collisions. The current full electron-electronic energy equation for the stagnation line is

$$\begin{aligned} \rho u c_p^e \frac{\partial T_e}{\partial n} - \frac{\partial}{\partial n}\left(\eta_e \frac{\partial T_e}{\partial n}\right) - \left(\sum_r \rho \mathcal{D}_r c_{p_r}^e \frac{\partial}{\partial n}\frac{\rho_r}{\rho}\right)\frac{\partial T_e}{\partial n} & \\ - u\frac{\partial p_e}{\partial n} + \dot{w}_e h_e^{tr} + \sum_r \dot{w}_r h_r^e & \qquad (4) \\ = \sum_r \xi_{er} + Q_e & \end{aligned}$$

where

$$c_p^e = c_{p_e}^{tr}\frac{\rho_e}{\rho} + \sum_r c_{p_r}^e \frac{\rho_r}{\rho} \tag{5}$$

In this equation, the viscous work terms have not been included due to the fact that they are of lower order. In addition, radiation effects on electron-electronic energy have been neglected as have diffusion effects on the form of the collisional energy exchange, ξ_{er}. The latter are expected to be small in most cases due to the rapid dissociation of molecules and the existence of ambipolar diffusion. However, it might be important at some of the lower AFE velocities. It should be noted that Eqs. (4) is equivalent to that presented by Ref. 14 and 15. However, it differs slightly from that presented in Ref. 1 and 16 in that the latter contain the additional terms

$$\dot{w}_e \frac{u^2}{2} + U_e \frac{\partial p_e}{\partial n}$$

which arise as a result of the differences in the derivation of the species energy and momentum equations. It is believed that these additional terms occur as a result of using the more detailed approach of Chapman and Cowling[17]. In any event, these two terms are expected to be small, and their neglect in the present studies should not affect the results.

When Eqs. (4-5) are expressed in three dimensions and transformed into the viscous shock layer coordinate system they become

$$A_0 \frac{\partial^2 T_e}{\partial n^2} + A_1 \frac{\partial T_e}{\partial n} + A_2 T_e + A_3 + A_4 \frac{\partial T_e}{\partial s} + A_5 \frac{\partial T_e}{\partial \phi} = 0 \tag{6}$$

$$\begin{aligned} A_0 =& -\epsilon^2 \frac{\eta_e \eta_s}{y_s{}^2} \\ A_1 =& -\epsilon^2 \frac{\eta_s}{y_s{}^2}\left[\frac{\partial \eta_e}{\partial n} + \frac{\eta_e}{h_3}\frac{\partial h_3}{\partial n} + \frac{\eta_e}{h_1}\frac{\partial h_1}{\partial n}\right] \\ & + \frac{c_p^e \rho_s}{y_s}\left[\rho v - \frac{\rho u_s u n}{h_1}\frac{\partial y_s}{\partial s} - \frac{\rho w n}{h_3}\frac{\partial y_s}{\partial \phi}\right] \\ & - \frac{\epsilon^2}{y_s^2} C_{sum}^e \\ A_2 =& \rho_s \rho \frac{\partial}{\partial T_e}(\dot{w}h)^e - \frac{\partial}{\partial T_e}\sum_r \xi_{er} \qquad (7) \\ A_3 =& -\frac{u_s u p_e}{h_1}\frac{\partial p_s}{\partial s} + \frac{p_s u_s u n}{h_1 y_s}\frac{\partial y_s}{\partial s}\frac{\partial p_e}{\partial n} - \frac{p_s v}{y_s}\frac{\partial p_e}{\partial n} \\ & + \frac{p_s w n}{h_3 y_s}\frac{\partial y_s}{\partial \phi}\frac{\partial p_e}{\partial n} + \rho_s \rho (\dot{w}h)^e - \rho_s \rho T_e \frac{\partial}{\partial T_e}(\dot{w}h)^e \\ & - \sum_r \xi_{er} + T_e \frac{\partial}{\partial T_e}\sum_r \xi_{er} \\ A_4 =& \frac{\rho_s u_s \rho u c_p^e}{h_1} \\ A_5 =& \frac{\rho_s \rho w c_p^e}{h_3} \end{aligned}$$

where:

$$\begin{aligned} C_{sum}^e =& C_{p_e}^{tr} \mathcal{D}_e \frac{\partial}{\partial n}\frac{\rho_e}{\rho} + \sum_r C_{p_r}^e \mathcal{D}_r \frac{\partial}{\partial n}\frac{\rho_r}{\rho} \\ (\dot{w}h)^e =& \dot{w}_e h_e^{tr} + \sum_r \dot{w}_r h_r^e + \dot{w}_{eI} E_{eI} \qquad (8) \end{aligned}$$

and h_1 and h_3 are geometric factors for the axisymetric coordinate system.

This full electron energy equation is integrated into the VSL code by setting up the terms in the same form as those for the global energy equation and then solving the equations using the existing routine for solving the global energy equation. In the cascade order of solving the governing conservation equations typical of VSL methods, the electron energy equation is included folowing the global energy equation, which is where the QEE or QEEE equation is normally included. Initially, the electron energy equation was not well behaved when solved in this manner primarily due to the large order of magnitude of the elastic and inelastic exchange terms, which, since they are nonlinear, were originally included explicitly in the calculations. Consequently, to provide iterative stability, these terms have been linearized as follows:

$$[(\dot{w}h)^e]^{n+1} = [(\dot{w}h)^e]^n + (T_e^{n+1} - T_e^n)\left(\frac{\partial}{\partial T_e}(\dot{w}h)^e\right)^n \tag{9}$$

$$\xi_{er}^{n+1} = \xi_{er}^n + (T_e^{n+1} - T_e^n)\left(\frac{\partial \xi_{er}}{\partial T_e}\right)^n \tag{10}$$

Another item which needs to be considered in modeling electron-electronic energy is the proper boundary condition on electron temperature at the wall. In most past analyses[1,12], it has been assumed that at the wall the electron temperature is equal to the wall temperature. Since the heavy particle temperature is also assumed equal to the wall temperature at the wall, this approach effectively assumes that the electron temperature is equal to the heavy particle temperature. At first, this approach seems reasonable and follows the philosophy that in the thermal boundary layer near the wall the flow should be near equilibrium and collision dominated. However, in the thermal boundary layer the chemical rection rates are finite and often cannot keep up with local equilibirum. This lag combined with diffusion leads to atom, ion, and electron densities above equilibrium values and in turn enhanced excited state populations. In addition, as can be seen in the electron-electronic energy equation, ionic recombination yields an increase in electron energy and tends to force the electron temperature above the heavy particle temperature.

Further, since almost all walls are catalytic to ions and electrons, there exists a thin plasma sheath adjacent to the wall across which a potential develops in order to maintain zero charge flux at the sheath edge. Since the thickness of the plasma sheath is negligible in comparison to that of the wall thermal layer, the edge of the sheath can be construed as being physically at the wall. Thus, the proper wall boundary conditions on the continuum equations should be obtained by matching the particle description in the plasma sheath to the corresponding continuum description at the wall. Examination of appropriate sheath models shows that continuity of electron energy flux requires

$$\left(\eta_e \frac{\partial T_e}{\partial n} - \rho_e U_e h_e\right)_{n=0} = [2kT_e + |e\Phi|]\,\frac{N_e c_e}{4}\, exp\left(\frac{-|e\Phi|}{kT_e}\right) \tag{11}$$

where the sheath potential is determined by enforcing charge neutrality at the sheath edge. Further analysis indicates that the heavy particle species, being in good contact with the wall, should be at the wall temperature. An approximation of this type of electron boundary condition has been incorporated as an option into the present full electron-electronic equation model.

Since the present flowfield formulation does not include vibrational nonequilibrium, the above electron-electronic energy models do not include vibrational-electronic coupling. While this phenomena should not be important at higher entry velocities due to the rapid dissociation of diatomic species in and near the shock front, it could be important at lower velocities. Thus, efforts are in progress to include vibrational nonequilibrium and vibrational electronic coupling; and these will be reported in a later paper.

Discussion of Results

Several sets of results obtained using the above methods and models are presented in this section. In all cases, results are for the stagnation streamline, utilize ninety-nine points between the shock front and the wall, and, for simplicity, assume a nitrogen freestream. The nonequilibrium chemistry model is similar to the Case II set of Ref. 1 and is shown in Table I; and it should be representative of high temperature radiating air. For diffusion, the approximate multi-component model of Ref. 18 has been used with a Lewis number of 1.4. Since in a high temperature ionized diatomic gas, charge exchange and ambipolar effects cause atoms, ions, and electrons to all have to a first approximation similar diffusion velocities, such a gas should be dominated by only two diffusion velocities, that of the molecules and that of the atoms, ions, and electrons. Thus, the present model should adequately represent the diffusion phenomena present, including multi-component effects. In addition, except for the Fire 2 cases, the wall has been assumed to be radiatively black, noncatalytic to atomic recombination, fully catalytic to ionic recombination, and at 1650°K. This value, which corresponds approximately to the maximum possible for a nonablating surface, has been used for convenience and to illuminate cool wall phenomena. However, it is recognized that for many cases of interest the heat transfer load will be more than adequate to induce ablation and to raise the wall temperature to significantly higher values. Finally, in all cases, unless stated otherwise, shock slip is assumed, coupled nongray radiative transfer has been included, and local thermodynamic nonequilibrium effects have been accounted for using the molecular and first order atomic models described above.

Fire 2 Cases

In order to ensure that the present method and models are reasonably correct and appropriate, results have been obtained for five trajectory points along the Fire 2 entry profile covering the time period from 1634 through 1637.5 sec. These points were selected because they encompass a period of the flight involving extensive chemical and thermal nonequilibrium and changing radiative behavior. These results have been computed assuming a fully catalytic wall at the wall temperature measured in flight, and the full electron-electronic energy model has been used in conjunction with an approximate wall sheath boundary condition on the electron temperature. Slip conditions have been enforced at the shock; and the correct wall absorptivity and reflection properties of the wall, as described in Ref. 19 and 20, have been included.

Figures 1 and 2 show temperature and concentration profiles for two of these trajectory points. At 1634 seconds (Fig. 1), as evidenced by comparing the "coupled" and "uncoupled" profiles, radiation cooling/coupling is insignificant; and, as can be seen on the temperature and species profiles, the flow never approaches a chemical equilibrium situation. Further, extensive thermal nonequilibrium exists in the region behind the shock front and also in the thermal boundary layer. The latter results from the sheath boundary condition on electron temperature and three body ion recombination which adds energy to both the free electrons and the excited electronic states. Interestingly, results obtained by forcing T_e to equal T_w at the wall yielded only slight differences in heating and the flowfield structure, with the exception of the electron temperature profile near the wall.

By 1637.5 seconds (Fig. 2), the temperature profile seems to indicate that the post shock nonequilibrium region only comprises about twenty percent of the layer and that much of the flowfield is in equilibrium. However, while thermal equilibrium is achieved near y/yshock of 0.75, careful examination reveals that ionization equilibrium is not reached until about y/yshock of 0.55. Further, as indicated by the temperature decrease and changes in species concentrations, radiation coupling/cooling is evident throughout much of the shock layer. These phenomena can be seen more easily on Fig. 3 which portrays the enthalpy behavior along the stagnation streamline. The profiles show that radiation cooling is significant for 0.2 < y/yshock < 0.6. While not shown, the degree of ionization in this region also decreases due to the loss of energy by radiation.

In Fig. 4, the present predictions for various heating rates are compared to the flight data. In flight, a total calorimeter measured the sum of the convective heating plus that portion of the radiative heating absorbed by the gage, which is indicated by the QC + ALPHA*QR line on the figure. The present predictions, indicated by the open squares, are in reasonable agreeement with the flight data; and, while not shown, the present predictions for convective heating are in excellent agreement with corresponding predictions of Ref. 21-23. The high value at 1634 seconds is typical of theoretical predictions; and, since this conditions is dominated by convective heating, the difference may indicate that at this point the wall (or gage) was not fully catalytic. This possibility is suggested by the results of Ref. 24, which obtained good correlation with Fire 2 data by not assuming fully catalytic walls.

Also shown on Fig. 4 are comparisons for radiative heating to the wall for two wavelength regions, .02 - 6.2 eV which is in the visible and infrared, and 2 - 4 eV which primarily should be due to $N_2^+(1-)$ emission. For the latter case, the flight data (Ref. 19-20) exhibited extensive scatter, and this is indicated on the figure by the cross-hatching. The present predictions in the 2-4 eV range are within the data scatter at early times and slightly low at the later times, while the predictions for the visible and infrared regions are low throughout the times considered. However, the data do appear to have the correct trends.

At first glance the radiation predictions appearing on Fig. 4 are distrubing due to their underprediction. However, the Fire 2 data is a single experiment, and thus must be viewed with care; and the present results are for a nitrogen freesteam and not air. While it is generally true that equilibrium nitrogen and equilibrium air will yield almost identical wall radiative heating rates if they are at the same temperature and pressure, identical freestream conditions will yield for the Fire 2 cases cooler equilibrium temperatures for nitrogen than for air. For example, for the 1637.5 sec case, the equilibrium temperature for a nitrogen freestream would be 10555°K while for an air freestream it would be 11021°K. This small 4.5% difference, however, leads to a radiative heating rate for air 60% higher than that for nitrogen. Since the present results were obtained matching freestream conditions on velocity, temperature, and pressure and not post shock conditions, the present radiative heating predictions should be below the flight values, particularly at the later times where the flow is approaching equilibrium. As can be seen on Fig. 4, this situation is indeed the case.

To further test this conjecture, a case was run using a slightly different freestream velocity and pressure that were designed to match the 1637.5 case in air. While this test was not completely successful in that the resultant temperature was still slightly low, the radiative heating results from this case, shown as solid symbols on Fig. 4, are higher and closer to the flight data.

To further identify the characteristics of the radiative heating of Fire 2, the stagnation point radiative flux is presented on Figure 5 as a function of energy (frequency) for two trajectory points. On this plot, the line and continuum contributions are plotted jointly. Also, for convenience, the line radiation is presented for lines that are close together as an average value over an appropriate width. It should be noted, however, that in the actual calculations the lines are treated individually using appropriate line shapes.

As can be seen, at 1634 seconds most of the radiative flux is in continuum radiation between 2 and 4 eV and in infrared lines, with about 20% of the total being from lines. In fact, for this condition seventy percent of the predicted stagnation point radiation is below 6.2 eV. In contrast, by 1637.5 sec there is extensive line and VUV flux; and the character of the radiation has changed so that 53% is from lines and only 43% of the total is below 6.2eV. However, at all trajectory points there is extensive radiation in the 2-4eV range.

Based upon these comparisons with the Fire 2 flight data, it is believed that the present method and models are reasonable and appropriate. Thus, they should be useful in studying a wide variety of entry vehicle flowfield situations.

AFE CFD Point 2

This condition corresponds to what is often referred to as the "max Q" computational point for one of the initial AFE trajectories at which the freestream velocity, pressure, and temperature are 8.915 km/sec, 15.715 dyne/sq cm, and 197.101°K respectively. For this case the nose radius has been assumed to be 2.3 meters, and the electron temperature was required to equal the heavy particle temperature at the wall.

The results, presented on Figs. 6(a) and 6(b), were obtained using the quasi-equilibrium free electron energy model without the electron impact molecular dissociation reaction, and profiles obtained with both fixed and slip shock jump conditions using a Lewis number of 1.4 are portrayed. As shown, the electron temperature rapidly rises behind the shock front and equilibrates with the heavy particle temperature. However, as evidenced by the continual decrease in temperature and the variations in composition across the shock layer, the stagnation flow for this case is always in chemical nonequilibrium. Also, the wall thermal layer comprises approximately twenty percent of the 12.2 cm thick shock layer. For this case, the convective heating was 13.55 watts/sq cm, the total radiative heat flux to the wall was 1.56 watts/sq cm, and radiative cooling effects were insignificant.

With respect to temperature, the effects of slip versus fixed shock jump conditions seem to be confined to a small region immediately behind the shock front. However, the impact on concentration and particularly on total enthalpy are significant. In fact, the total enthalpy profiles clearly show that the fixed shock boundary condition results in an incorrect value for enthalpy in the interior of the shock layer, leading to incorrect species concentration values. Interestingly, when a Lewis number of one is used with the fixed shock boundary conditions the enthalpy profile appears to be correct and when a value less than unity is used, the enthalpy is high in the flow interior. However, for the shock slip condition, the enthalpy profiles are unaffected by Lewis number. Since a Lewis number of 1.4 is more appropriate for describing atom molecule diffusion, which is the dominant diffusion mechanism in this flow, and since the enthalpy ratio in the flow interior in the absence of significant radiative cooling should be unity, these results demonstrate the importance of using slip shock boundary conditions at these conditions.

Since at these conditions, vibrational nonequilibrium should also be important, it is planned in a future paper to present results which include vibrational nonequilibrium. Also, it should be noted that since the results shown on Fig. 6 are for a nitrogen freestream, the radiative heating values in air, based upon the Fire 2 data, will probably be slightly higher.

AFE CFD Point 4

This condition corresponds to a "max Q" point for a heavier AFE vehicle at which the freestream conditions are 9.326 km/sec, 26.4 dynes/ sq cm, and 200°K. Stagnation line temperature and concentration profiles are presented on Fig. 7, which compares results obtained using the quasi-equilibrium electron-electronic model (QEEE) including the electron impact dissociation reaction with those using the quasi-equilibrium electron (QEE) energy model only. The primary effect of using the QEEE model is more extensive thermal nonequilibrium and a lower electron temperature through much of the shock layer. Also, the combined effect of electron impact dissociation and the QEEE model leads to a more dissociated flow having slightly different N_2 and N_2^+ profiles.

However, the most significant difference in the two models is the radiative heat transfer. For the QEEE case, the lower electron temperature yields a total radiative flux of 1.18 watts/sq cm, a shock standoff distance of 11.96 cm, and a convective heating of 25.8 watts/sq cm. For the QEE model it is 2.91 watts/sq cm., 11.89 cm, and 25.7 watts/sq cm respectively.

Fig. 8(a) shows the stagnation point continuum and line radiation distributions predicted with the QEEE model. In the actual radiative transfer analysis, lines are considered and integrated individually, but they are presented on Fig. 8(a) as average values for various line groups for convenience. While there are many infrared line groups and some in the ultra-violet, the line contributions are negligible compared to the continuum. Also, most of the continuum radiation (about 90%) is in the visible and infrared below 6.2 eV; and most of that is between 2 and 4 eV. At these conditions, this radiation is due to the $N_2^+(1-)$ band. In addition, there is some continuum contribution in the ultra-violet, probably due to nitrogen free-bound processes and N_2(BH) bands.

Fig. 8(b) shows the same information as Fig. 8(a) except each line is shown individually. Many of the VUV lines above 10 eV are absorbing in their line centers, but the IR lines are essentially transparent and appear to be strongly emitting. However, line radiation at this condition is insignificant compared to the continuum contribution.

As part of this study computations were also conducted using the QEE model without including molecular LTNE effects; and the resulting radiative heat transfer result was 8.90 watts/sq cm. Obviously, molecular LTNE is important at AFE conditions and leads to lower radiative heating. Examination of the results indicate that the LTNE induced by chemical and thermal nonequilibirum drastically reduces radiation from the $N_2(1+)$ and $N_2(2+)$ bands and significantly decreases that due to N_2(BH). However, $N_2^+(1-)$ is virtually unaffected by chemical and thermal nonequilibrium phenomena. Thus, on Fig. 8, the primary stagnation point radiation is in the continuum between 2 and 4 eV and is from the $N_2^+(1-)$ band.

At shock speeds below 10 km/sec, shock tube radiative intensity photomultiplier mesurements indicate a sharp rise to a peak immediately behind the shock front followed by a decrease until equilibrium is achieved[25]. Similar results have been obtained computationally for nonequilibrium flows for the visible region of the spectrum assuming the gas to be transparent[7]. Fig. 9 shows for the present QEEE model the variation along the stagnation line of radiative flux towards the stagnation point, QR+, and its negative derivative, -D(QR+)/DY. The latter is essentially what Candler[7] and others have termed radiation intensity. As can be seen, -D(QR+)/DY is similar to observed photomultiplier traces in having a peak near the shock front followed by a steady decrease towards the wall. For this case, no equilibrium plateau is achieved since the flow never reaches chemical equilibrium prior to the wall thermal boundary layer. (The oscillations near the wall are an artifact due to significant digit error resulting from providing the plot routine formatted data. The actual curve is smooth.) Comparison with the temperature plots indicates that the "intensity" peak corresponds to the maximum value in electron temperature; and near the wall the "intensity" is negative, indicating absorption. However, as shown by only the slight decrease in QR(+), the amount of absorption near the wall is negligible at these conditions.

High Speed Mars Return Case

In a recent paper[26], results have been presented for the stagnation line of a one meter nose radius body at a trajectory point of 14.5 km/sec at 65 km, which is representative of a high speed earth entry return from Mars. These results include chemical nonequilibrium, thermal nonequilibrium assuming that the vibrational, electronic, and electron temperatures can be represented by a single temperature, and uncoupled nonequilibrium radiation. The investigators obtained for this trajectory point an uncoupled radiative heating rate of 1700 watts/cm^2, a shock standoff distance of 5.7 cm, and a post-shock chemical nonequilibrium zone 1.1 cm thick in which the electron-electronic vibrational temperature never significantly exceeded the equlibrium temperature. They also stated that most of the radiative heating was from the ultra-violet below 2000 A, that it originated from the nonequilibrium region behind the shock wave, and that very little was absorbed in the wall thermal layer. The latter is different from previous beliefs by some researchers[6] but is in agreement with approximate studies[2]. In addition, separate results were obtained for the same case with an equilibrium viscous shock layer method[27] that used a coupled radiation model similar to RADICAL; and these predicted a standoff distance of 3.5 cm and a radiative heating rate of 970 watts/cm^2.

As a result of these differences, the present model using the full electron-electronic energy model with LTNE effects and a partially catayltic wall has been applied to this case; and temperature and ionization profiles are presented on Fig. 10. Here, the predicted shock standoff distances are 3.92 cm and 3.67 cm for the radiatively uncoupled and coupled cases respectively; and most of the shock layer is in chemical equilibrium. The difference in the standoff lengths between the present results and the nonequilibrium result of Ref. 26 is believed to be primarily due to the electron temperature profile and its subsequent effect on chemistry. In Ref. 26 T_e is low in the region behind the shock front, possibly due to the combining of electron-electronic with vibrational phenomena. However, the present results show significant dissociation at the shock front with diatomic species being insignificant over most of the shock layer and ionization dominating the chemistry. Thus, in the present case the full electronic-electron energy model is strongly influenced by collisional and ionization phenomena; and T_e significantly exceeds the equilibrium temperature in the nonequilibrium zone. Since the dominant ionization mechanism behind the shock front is electron impact[1] which is governed by free electron temperature, this enhancement of T_e accelerates ionization, shortens the chemical nonequilibrium zone to about 0.3 cm, and decreases the overall shock layer thickness. However, as expected, the present thickness prediction is greater than that for the equilibrium case discussed above. It should also be noted that the difference between the present results and those of Ref. 26 show the strong sensitivity of solutions to electron temperature models at such trajectory points.

Results obtained with the present model predict the stagnation point radiative heat transfer for the case without any radiation gasdynamic coupling to be 2831 watts/cm^2, which is higher than that of Ref. 26. Comparison of the spectral variation of the stagnation point radiative flux indicates that the present results have significant radiation above 11 eV, primarily due to free-bound continuum processes, while those of Ref. 26 have little or no flux in this region. Since both methods treat lines in detail and since both have previously been shown to be in reasonable agreement in the visible and infrared, it appears that the differences are primarily due to the treatment of atomic continuum radiation in the vacuum ultraviolet. It should be noted that the present radiation model has for equilibrium conditions shown good agreement with experimental data over the total spectrum[23]. Further, the present results indicate that most of the radiation originates from the high temperature equilibrium portion of the shock layer in the range $0.4 < y/yshock < 0.9$ and not from the post-shock nonequilibrium zone. In the latter, chemical nonequilibrium induces extensive local thermodynamic nonequilibrium and depopulates the excited states rapidly via ionization with the result that very little radiation originates in the nonequilibrium region.

Moreover, the radiation coupled results for this case indicate significant radiation cooling, as evidenced by the decrease in radiative heating to 1347 watts/cm^2 and by the steady decrease in temperature and ionization throughout the equiilbrium zone[10]. Further, while the equilibrium coupled prediction for this case was only 970 watts/cm^2, it is probable that the difference between it and the present prediction is due to the influence of reaction chemistry, differences in assumed wall catalycity, and the amount of absorption in the wall thermal layer. Basically, equilibrium chemistry should predict more molecules and hence more absorption. This possibility is supported by the equilibrium results which indicate that the wall thermal layer absorbs about 32% of the wall directed flux while in the present model only about 20% is absorbed. Thus, while most of the shock layer is in chemical equilibrium, nonequilibrium effects may still be important and affect the radiative heating; and, obviously, radiation cooling is important for this case and needs to be included in an analysis model.

Velocity Effects at 80 km

Results have also been obtained for a 2.3 meter nose radius vehicle for three different velocities, 12, 14, and 16 km/sec, at an altitude of 80 km. These velocities are, depending upon the trajectory chosen, within the possible range of entry speeds associated with certain Martian and Lunar return vehicles.

The temperature and composition profiles for the 12 km/sec case are shown on Fig. 11; and, as shown by the continually decreasing temperature and the variation in the N^+ concentration, the entire shock layer at this flight condition is in chemical nonequilibrium. Immediately behind the shock front, which is 11.5 cm from the wall, the electron-electronic temperature slowly rises to a peak value and then gradually equilibrates with the heavy particle temperature. In the wall thermal layer, which comprises about 20% of the shock layer, deionization and recombination processes are important. For this case, when radiative coupling and LTNE effects are included, the radiative heat transfer is 24.3 watts/cm^2 and the convective rate is 33 watts/cm^2.

The temperature and composition profiles for the 14 km/sec case are shown on Fig. 12. Since the freestream velocity is higher, the post-shock nonequilibrium zone is shorter than at 12 km/sec, occupying only the outer 30-40% of the 9.1 cm shock layer. The electron-electronic temperature rises rapidly and peaks at a value several thousand degrees above the equilibrium temperature, and the wall sheath representation only affects the electron temperature in a small zone near the wall. For this case the convective heating is 56.4 watts/cm^2 and the radiative flux is 110.7 watts/cm^2. Interestingly, especially when compared to the AFE cases, only about ten percent of this radiative heating is due to molecular processes.

As part of this study, several cases were also conducted at this condition using the quasi-equilibirum electron-electronic and quasi-equilibrium electron energy models; and the only difference between the models was that the peak in electron temperature was slightly higher and slightly further from the shock front with the exact model than with the quasi-equilibrium models. This behavior has been observed at freestream velocities of 12 km/sec and higher and is in sharp contrast to the trends displayed at the AFE velocities. At the higher velocities there are more electrons and the flow is dominated by ionization processes. Consequently, the electron-electronic energy is dominated by the free electrons. At the lower AFE speeds, there is very little ionization and the electronic energy portion dominates the combination. Thus, the shape and character of the electron temperature profiles appears to be significantly different at the higher velocities than at AFE speeds.

The spectral variation in radiative heat flux to the wall at 14 km/sec is shown on Fig. 13(a), where the contributions due to line and continuum processes have been combined and the convenient representation of lines as group averages has been utilized. Here, the heating due to continuum and lines is similar in magnitude with extensive infrared and UV lines as well as significant VUV bound-free processes. In fact, only about twenty-eight percent of the wall flux is from the visible and infrared below 6.2 eV. Notice that a measureable portion of the visible radiation is between 2 and 4 eV and is due to $N_2^+(1-)$ molecular radiation. Nevertheless, while this type of presentation is informative and useful, especially for continuum radiation, the characteristics and number of lines is not evident on this type of plot.

As mentioned previously, the actual radiative transfer analysis treats lines individually, and Fig. 13(b) displays the same information but with each line shown separately. From this representation, it is evident that in the visible and infrared the line radiation is primarily transparent. However, in the VUV, many of the line centers are highly absorbing with most of the line emission reaching the wall originating from the line wings.

In contrast to results below 10 km/sec, shock tube photomultiplier results at higher speeds show that the radiative intensity peak behind a shock front changes from a single peak to a double hump peak system[25]. Experimental spectral data indicates that the first is due to molecular radiation near the shock front while the second is atomic radiation coupled to the ionization process. Figure 14 shows for the 14 km/sec condition theoretical predictions of the radiative flux towards the wall, QR+, and the negative of its derivative, -DQR(+),DY. As discussed previously, the latter is closely related to radiative intensity.

The present profile clearly exhibits this double hump behavior. The first peak corresponds to the maximum value of the electron temperature, while the second occurs at the onset of thermal equilibrium and the establishment of near Boltzmann distributions in the excited states. Subsequently, radiative cooling occurs and the "intensity" rapidly decreases. During this period, examination of the species concentrations and of LTNE phenomena indicates nonequilibrium recombination is induced with resultant overpopulation, compared to a Boltzmann distribution, of the excited states. Around y/yshock of 0.3 the flow begins to absorb more than it emits and QR+ begins to decrease. However, as shown by the QR+ profile, which only decreases slightly between 0.3 and the wall, the absorption in the wall thermal layer only results in a mild decrease in QR+ at this condition.

The temperature and composition profiles at 16 km/sec are shown on Fig. 15, and the corresponding predicted radiative and convective heating rates are 272.6 and 87.3 watts/cm^2 respectively. Here, the electron temperature rises very rapidly and peaks near 20,000°K, confirming the trend that as speed increases, the peak electron-electronic temperature increases in magnitude and occurs nearer to the shock front. Likewise, again due to the increase in velocity, the nonequilibrium zone is shorter at about 20-25% of the 7.5 cm shock layer. Finally, on Fig. 15 notice that radiation cooling effects induce both atomic and ionic recombination starting near the end of the post-shock nonequilibrium zone and continuing all the way to the wall.

The effect on the temperature and ionization profiles of including radiative gasdynamic coupling in the flowfield and local thermodynamic nonequilibrium effects in the radiation is shown for the 16 km/sec case on Fig. 16. The curves denoted uncoupled do not include either radiation cooling or LTNE phenomena and indicate for this case that nominally the nonequilibrium post-shock zone and the wall thermal layer each affect about 20% of the shock layer. For this case, the shock standoff distance is 8.16 cm. However, when radiation coupling is included but LTNE is excluded, the shock layer thickness is reduced to 7.15 cm due to the lower temperature and increased density. The resultant profiles, designated as uncorrected, show that without LTNE effects significant cooling occurs in the nonequilibrium region with corresponding decreases in the electron and heavy particle temperatures and in the apparent length of the relaxation zone. Further, radiative losses through the shock front from the high temperature nonequilibrium zone reduce the total enthalpy forty percent, which leads to a cooler equilibrium zone having less than half the ionization of the uncoupled case.

Fortunately, when both radiation coupling and LTNE effects are included, the radiative losses are much less. As shown on the curves denoted as corrected, the corresponding temperature and ionization variations in the nonequilibrium post-shock region are only slightly affected since in that region the radiative losses are low due to LTNE effects. However, once equilibrium is nearly established around 0.8, radiative cooling becomes the dominant feature, the temperature steadily decreases, and the degree of ionization rapidly decreases. Obviously, at these conditions both LTNE phenomena and radiation coupling are important and need to be included.

A graphical summary of the 80 km radiative heating results is presented as Fig. 17, and several interesting features are evident. First, the inclusion of LTNE significantly affects the predicted radiative heat transfer at all three flight velocities, independent of whether or not radiative coupling is included. Second, the amount of radiative cooling is lower in the LTNE corrected predictions as compared to the LTE uncorrected flows; and, third, when both phenomena are properly included, radiative cooling ranges from relatively minor at 12 km/sec to significant at 16 km/sec.

Finally, for all three flight velocities, the predicted radiative heating is significant compared to the convective heating; and, in the 16 km/sec case, the radiative heating is about three times the convective value. Since it is anticipated that advanced heat shield materials can withstand 70 watts/cm^2 without ablating, these results indicate that at 80 km non-ablative heat shields possibly could be used up to about 12.5 km/sec.

Altitude Effects at 16 km/sec

In order to investigate altitude effects and to use the model under a situation on a vehicle where most of the shock layer is in equilibrium, results have been obtained for the 2.3 meter body at 16 km/sec at 75 and 72 km as well as at 80 km. Since the resultant profiles do not exhibit any new phenomena, they are not shown. However, as the pressure increases with decreasing altitude, the post-shock nonequilibrium chemical relaxation zone decreases significantly so that by 72 km it only encompasses about five percent of the shock layer. At that condition, the present model predicts a shock layer thickness of 7.05 cm, and radiative and convective heating rates of 1064 and 209 watts/cm^2. Also, since the extent of nonequilibrium decreases with altitude, LTNE phenomena decrease and have a minor affect on the coupled radiative heat transfer predictions by 72 km. However, as shown on Fig. 18, radiative coupling/cooling is important at all three altitudes and increases as altitude decreases. Interestingly, the coupled results at 72 and 75 km, which have nearly equilibrium shock layers, are in excellent agreement with the equilibrium radiative heating predictions of Ref. 28. However, the present nonequilibrium radiative predictions at 80 km are higher than those of Ref. 28 at both 14 and 16 km/sec.

Conclusions

In this paper an engineering flowfield model suitable for analyzing the stagnation region of high altitude entry vehicles having extensive nonequilibrium has been presented. This model includes nonequilibrium chemistry, multi-temperature, viscous, conduction, and diffusion effects. It also includes coupled nongray radiative transfer in a form that contains the effect of local thermodynamic nonequilibrium phenomena resulting from chemical and thermal nonequilibrium on the emission and absorption characteristics of atoms and molecules. The boundary conditions include multi-temperature shock slip and a partially catalytic wall having frequency dependent radiative properties. After comparing with Fire 2 flight data, which verified that the model has the correct behavior and is reasonably accurate, it has been applied to a variety of cases including two AFE trajectory points, a condition representative of the high speed return from Mars of a small vehicle, a series of points at 80 km for velocities 12 to 16 km/sec, and a study of the effects of altitude at 16 km/sec. Based on these results the following conclusions can be stated:

(1) Shock slip phenomena is important at all conditions investigated
(2) Radiation cooling/coupling is important for many cases. Specifically,
    (a) It is measureable even in the early portions of the Fire 2 trajectory.
    (b) It is a minor effect for the AFE conditions investigated.
    (c) At 80 km, it is small at 12 km/sec, important by 14 km/sec, and the dominant phenomena at 16 km/sec at all altitudes.
    (d) It is very important for the high speed Mars return case.
(3) Radiation heat transfer should be included and varies as to source. Specifically,
    (a) In the early stages of the Fire 2 entry, the radiative transfer is primarily molecular and infrared lines. Later, atomic VUV continuum and line radiation becomes very important.
    (b) For the AFE radiation, while small, is important and primarily molecular, ($N_2^+(1-)$).
    (c) At 12 km/sec and above radiation is a significant portion of the total heating and is primarily due to atomic processes. By 14 km/sec it is dominant.
(4) Local thermodynamic nonequilibrium is important and should be included in all models. In addition,
    (a) LTNE depopulates the excited states of atoms and N_2 molecules in the post-shock nonequilibrium region.
    (b) LTNE can lead to an overpopulation of excited states in regions of radiative cooling and in the wall thermal layer.
    (c) $N_2^+(1-)$ is relatively unaffected by LTNE.
    (d) Its importance is independent of radiative coupling.
    (e) The inclusion of LTNE reduces the magnitude of radiation cooling effects.

Acknowledgement

This work was primarily supported by NASA Grant NAG-1-1003 from the Langley Research Center, with Lin C. Hartung as technical monitor. Mr. Gally is partially supported by a NASA Graduate Student Researchers Fellowship through the NASA Johnson Space Center.

REFERENCES

[1] Carlson, L. A. and Gally, T. A., "The Effect of Electron Temperature and Impact Ionization on Martian Return AOTV Flowfields," AIAA Paper 89-1729, June 1989.

[2] Carlson, L. A., "Approximations for Hypervelocity Nonequilibrium Radiating, Reacting, and Conducting Stagnation

Regions," *J. of Thermophysics and Heat Transfer*, vol. 3, No. 4, October 1989, pp. 380-388.

[3] Carlson, L. A., Bobskill, G. J., and Greendyke, R. B., "Comparison of Vibration Dissociation and Radiative Transfer Models for AOTV/AFE Flowfields," *J. of Thermophysics and Heat Transfer*, vol. 4, No. 1, January 1990, pp. 16-26.

[4] Thompson, R. A., "Comparison of Nonequilibrium Viscous Shock Layer Solutions with Windward Surface Shuttle Heating Data," AIAA Paper 87-1473, June 1987.

[5] Nicolet, W. E., "User's Manual for the Generalized Radiation Transfer Code (RAD/EQUIL or RADICAL)," NASA CR 116353, October 1969.

[6] Park, C., "Assessment of Two Temperature Kinetic Model for Ionizing Air," AIAA Paper No. 87-1574, June 1987.

[7] Candler, G. and Park, C., "The Computation of Radiation from Nonequilibrium Hypersonic Flows," AIAA 88-2678, June 1988.

[8] Foley, W. H. and Clarke, J. H., "Shock Waves Structered by Nonequilibrium Ionizing and Thermal Phenomena," *Physics of Fluids*, vol. 16, No. 3, March 1973, pp. 1612-1620.

[9] Nelson, H. F., "Nonequilibrium Structure of Argon Shock Waves," *Physics of Fluids*, vol. 16, No. 12, December 1973, pp. 2132-2142.

[10] Nelson, H. F. and Goulard, R., "Structure of Shock Waves with Nonequilibrium Radiation and Ionization," *Physics of Fluids*, vol. 12, No. 8, August 1969, pp. 1605-1617.

[11] Chapin, C. E., "Nonquilibrium Radiation and Ionization in Shock Waves," AA&ES Report, June 1967, Purdue, Univ., Lafayette, Ind.

[12] Park, C., "Calculation of Nonequilibrium Radiation in the Flight Regimes of Aeroassisted Orbital Transfer Vehicles," in ***Thermal Design of Aeroassisted Orbital Transfer Vehicles***, Progress in Astronautics and Aeronautics, Vol. 96, Ed. H. F. Nelson, AIAA, 1985, pp. 395-418.

[13] Kunc, J. A. and Soon, W. H., "Collisional Radiative Nonequilibrium in Partially Ionized Atomic Nitrogen," *Physical Review A*, vol. 40, No. 10, November 15, 1989, pp. 5822 ff.

[14] Gnoffo, P. A., Gupta, R. N., and Shinn, J. L.,, "Conservation Equations and Physical Models for Hypersonic Air Flows in THermal and Chemical Nonequilibrium," NASA TP 2867, February 1987.

[15] Lee, J. H., "Basic Governing Equations for the Flight Regimes of Aeroassisted Orbital Transfer Vehicles," in ***Thermal Design of Aeroassisted Orbital Transfer Vehicles***, Progress in Astronautics and Aeronautics, Vol. 96, Ed. H. F. Nelson, AIAA, 1985, pp. 3-53.

[16] Carlson, L. A., "Radiative Gasdynamic Coupling and Nonequilibrium Effects Behind Reflected Shock Waves," *AIAA Journal*, vol. 9, No. 5, May 1971, pp. 858-865.

[17] Chapman, S. and Cowling, T. G., ***The Mathematical Theory of Non-Uniform Gases***, Cambridge, 1964.

[18] Miner, E. W. and Lewis, C. H., "Hypersonic Ionizing Air Viscous Shock Layer FLows over Nonanalytic Blunt Bodies," NASA CR-2550, May 1975.

[19] Cauchon, D. L., "Radiative Heating Results from the Fire II Flight Experiments at a Reentry Velocity of 11.4 Kilometers Per Second," NASA TM X-1402, 1966.

[20] Cauchon, D. L., McKee, C. W., and Cornette, E. S., "Spectral Measurements of Gas-Cap Radiation During Project Fire Flight Experiments at Reentry Velocities Near 11.4 Kilometers per Second," NASA TM X-1389, October 1967.

[21] Gupta, R. N., "Navier Stokes and Viscous Shock Layer Solutions for Radiating Hypersonic Flows," AIAA Paper No. 87-1576, June 1987.

[22] Balakrishnan, A., C. Park, and Green, J. M., "Radiative Viscous Shock Layer Analysis of Fire, Apollo, and PAET Flight Data," in ***Thermophysical Aspects of Re-Entry Flows***, Progress in Astronauticss and Aeronautics, Vol. 103, Ed. J. N. Moss and C. D. Scott, AIAA, 1986, pp.514-540.

[23] Sutton, K., "Air Radiation Revisited," in ***Thermal Design of Aeroassisted Orbital Transfer Vehicles***, Progress in Astronautics and Aeronautics, Vol. 96, AIAA, 1985, pp. 419-442

[24] Bird, G. A., "Nonequilibrim Radiation During Re-Entry at 10 km/sec," AIAA Paper No. 87-1543, June 1987.

[25] Wilson, J., "Ionization Rate of Air Behind High Speed Shock Waves," ***The Physics of Fluids***, vol. 9, No. 10, October 1966, pp. 1913-1921.

[26] Park, C. and Milos, F. S., "Computational Equations for Radiating and Ablating Shock Layers," AIAA Paper 90-0356, January 1990.

[27] Nicolet, W. E., Waterland, L. R., and Kendall, R. M., "Methods for Predicting Radiation Coupled Flowfields about Planetary Entry Probes," in ***Aerodynamic Heating and Thermal Protections Systems***, Progress in Astronautics and Aeronautics, Vol. 59, Ed. L. S. Fletcher, AIAA, 1978, pp. 120-136.

[28] Sutton, K. and Hartung, L. C., "Equilibrium Radiative Heating Tables for Earth Entry," NASA TM 102652, May 1990.

Reaction	A	B	E
$N_2+N = 2N + N$	4.085×10^{22}	-1.5	113000
$N_2+N_2 = 2N + N_2$	4.70×10^{17}	-0.5	113000
$N_2+N^+ = N_2^+ + N$	2.02×10^{11}	0.8	13000
$N + N = N_2^+ + e^-$	1.40×10^{13}	0.0	67800
$N + e^- = N^+ + 2e^-$	4.160×10^{13}	0.5	120000
$N + N = N + N^+ + e^-$	2.34×10^{11}	0.5	120000
$N + N^+ = 2N^+ + e^-$	2.34×10^{11}	0.5	120000
$N_2 + e^- = 2N^+ + e^-$	3.00×10^{24}	-1.6	113100

Rates in the form $k_f = A\,T^B \exp(-E/T)$.
$T = T_e$ in electron impact reactions.

Table 1. Reaction Rate System

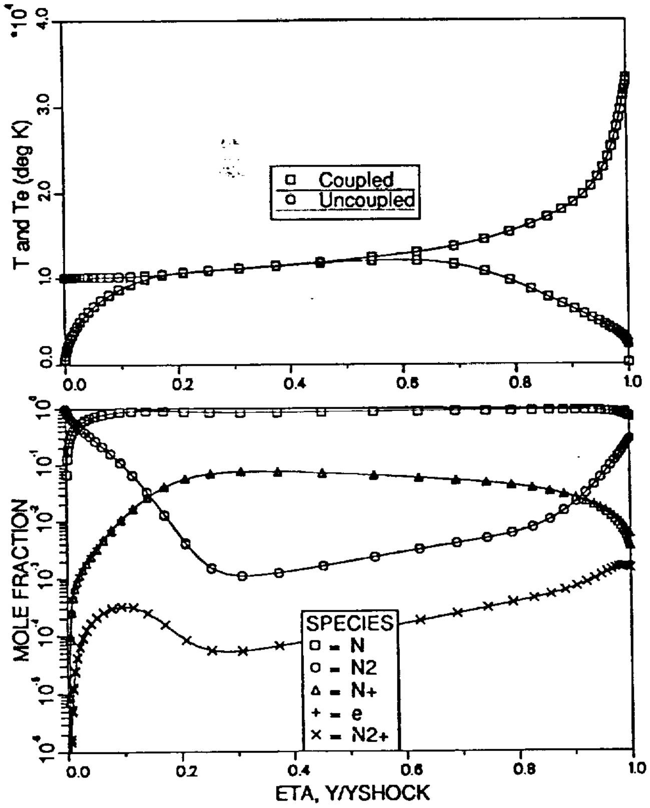

Fig. 1 – Stagnation Profiles for Fire 2 at 1634 seconds, YSHOCK = 4.12 cm

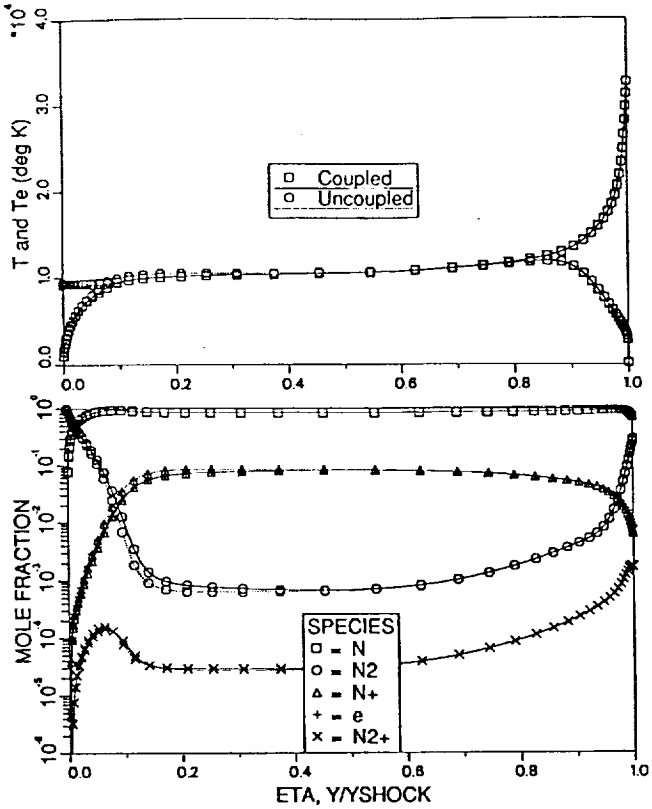

Fig. 2 – Stagnation Profiles for Fire 2 at 1637.5 seconds, YSHOCK = 3.72 cm

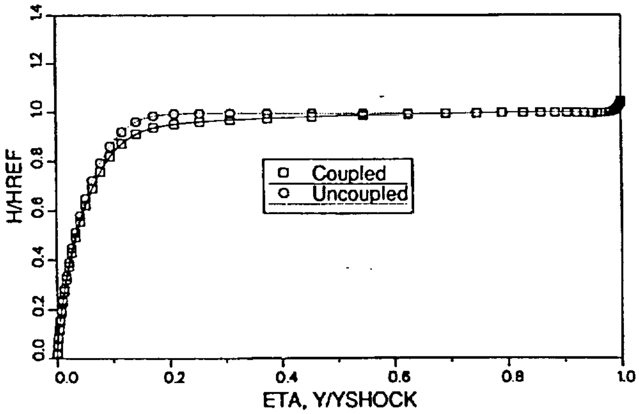

Fig. 3 – Enthalpy Profiles for Fire 2 at 1637.5 seconds

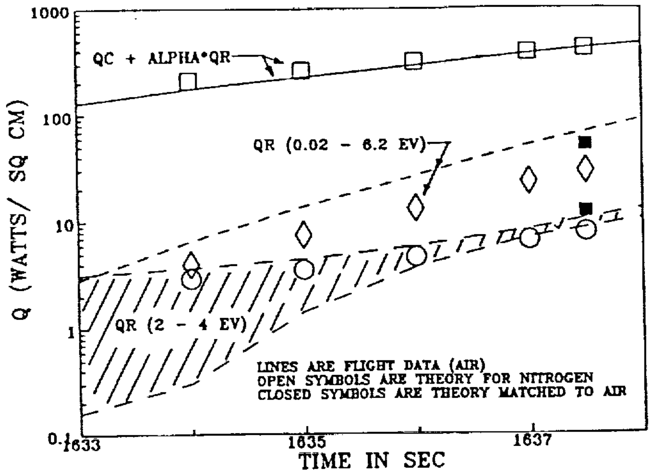

Fig. 4 – Comparison of Present Fire 2 Predictions (Nitrogen) with Flight Data (Air)

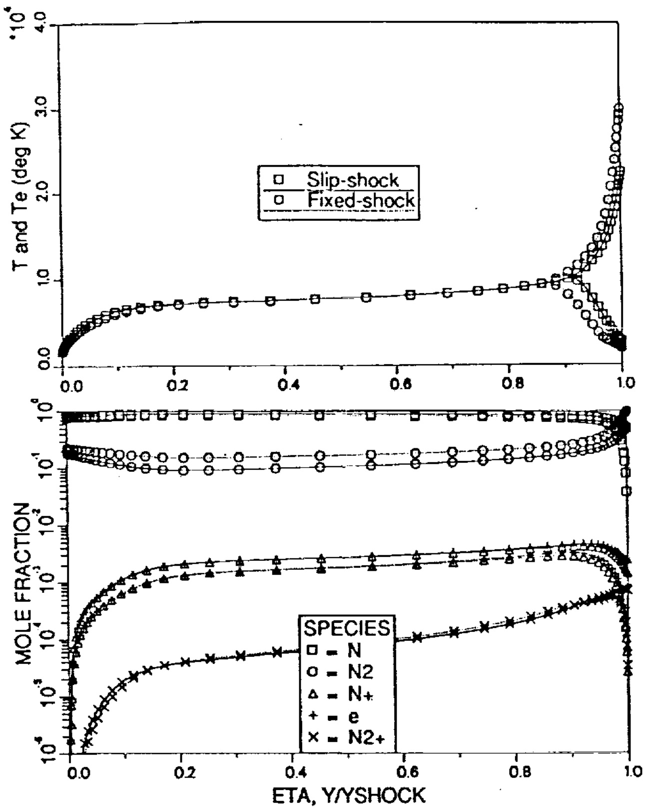

Fig. 6(a) – Stagnation Profiles for AFE CFD Point 2 Using QEE Model, U = 8.915 km/sec, H = 77.9 km, QR = 1.56 watts/cm^2, QC = 13.6 watts/cm^2, YSHOCK = 12.2 cm

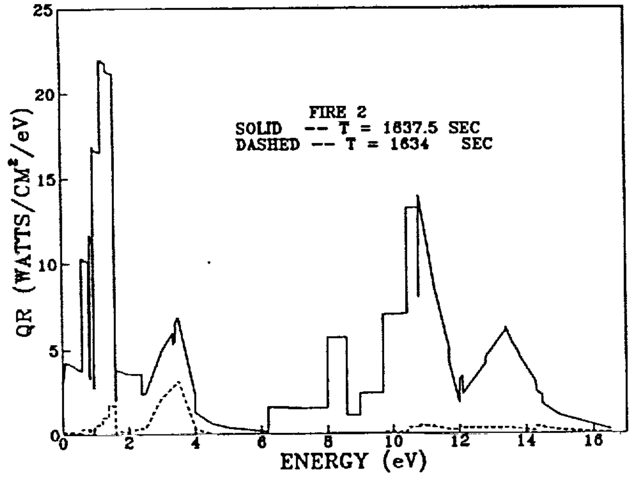

Fig. 5 – Spectral Variation of Stagnation Point Radiative Heat Transfer for Fire 2

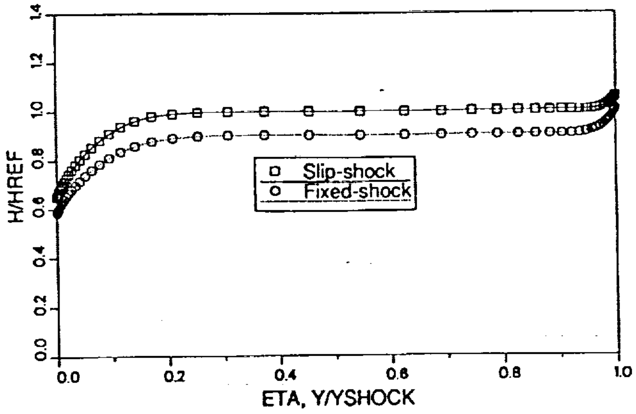

Fig. 6(b) – Enthalpy Profiles for AFE CFD Point 2 Using QEE Model

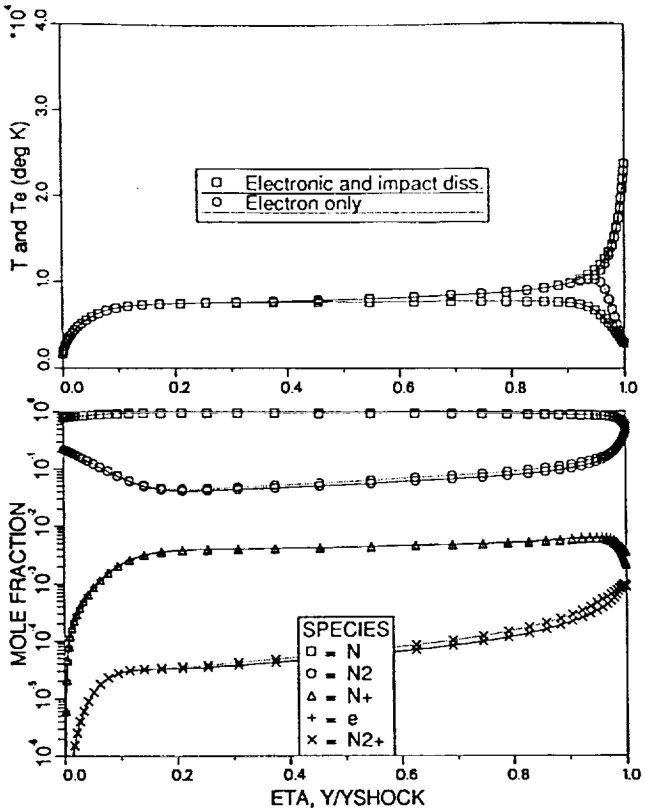

Fig. 7 – Stagnation Profiles for AFE CFD Point 4
U = 9.326 km/sec, H = 75.2 km
For QEEE Case: QR = 1.18 watts/cm^2, QC = 25.8 watts/cm^2, YSHOCK = 12.0 cm
For QEE Case: QR = 2.91 watts/cm^2, QC = 25.7 watts/cm^2, YSHOCK = 11.9 cm

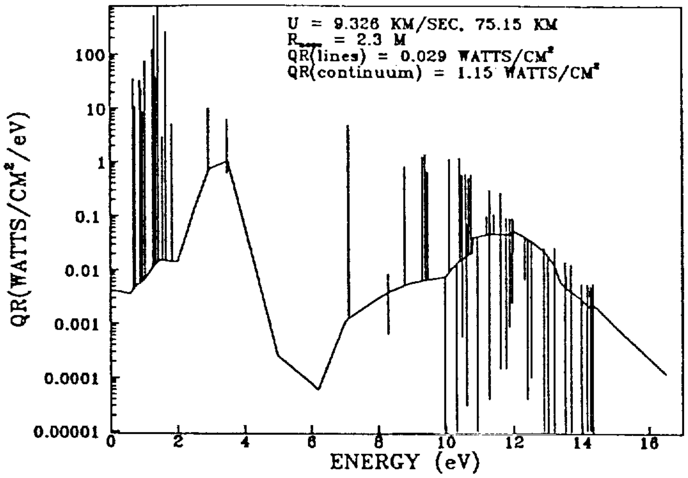

Fig. 8(b) – Detailed Spectral Variation of Stagnation Radiative Heat Transfer AFE CFD Point 4, QEEE Model

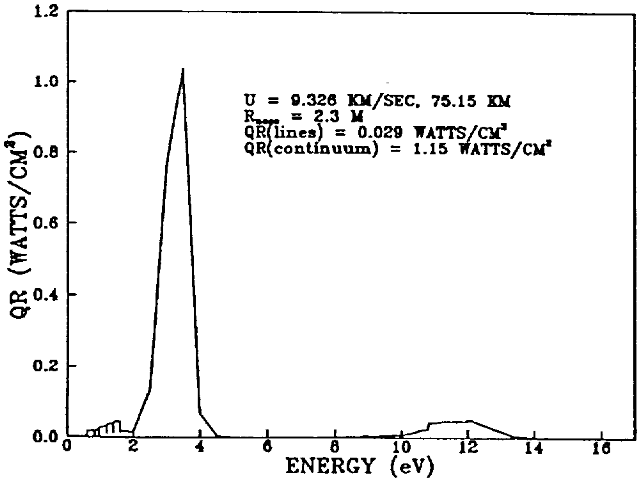

Fig. 8(a) – Usual Presentation of Spectral Variation of Stagnation Radiative Heat Transfer AFE CFD Point 4, QEEE Model

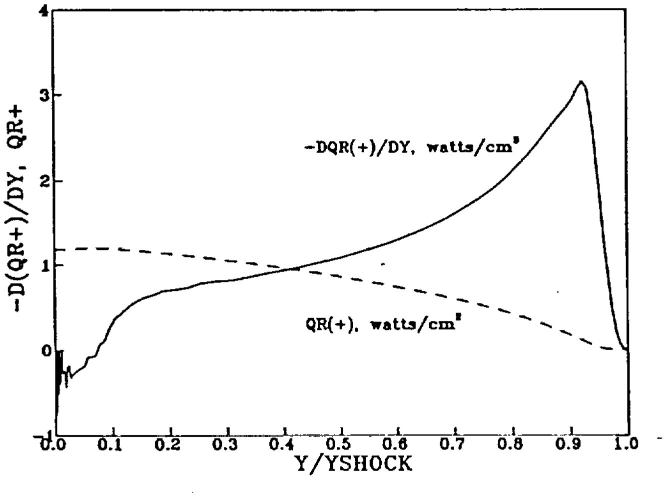

Fig. 9 – Intensity and Radiative Flux Towards Stagnation Point, AFE CFD Point 4, QEEE Model

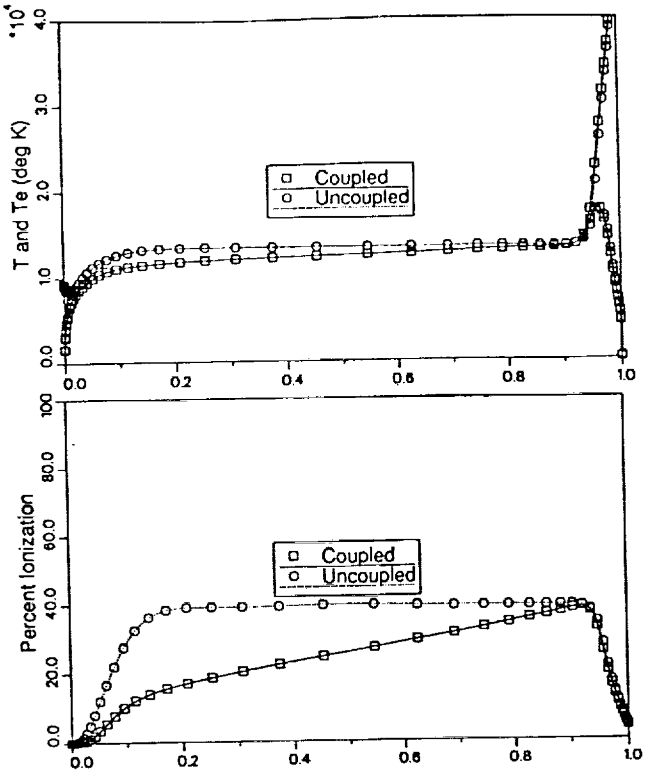

Fig. 10 – Stagnation Profiles at 14.5 km/sec, 65 km, Rnose = 1 m
Uncoupled: QR = 2831 watts/cm^2, QC = 426 watts/cm^2, YSHOCK = 3.92 cm
Coupled: QR = 1347 watts/cm^2, QC = 430 watts/cm^2, YSHOCK = 3.67 cm

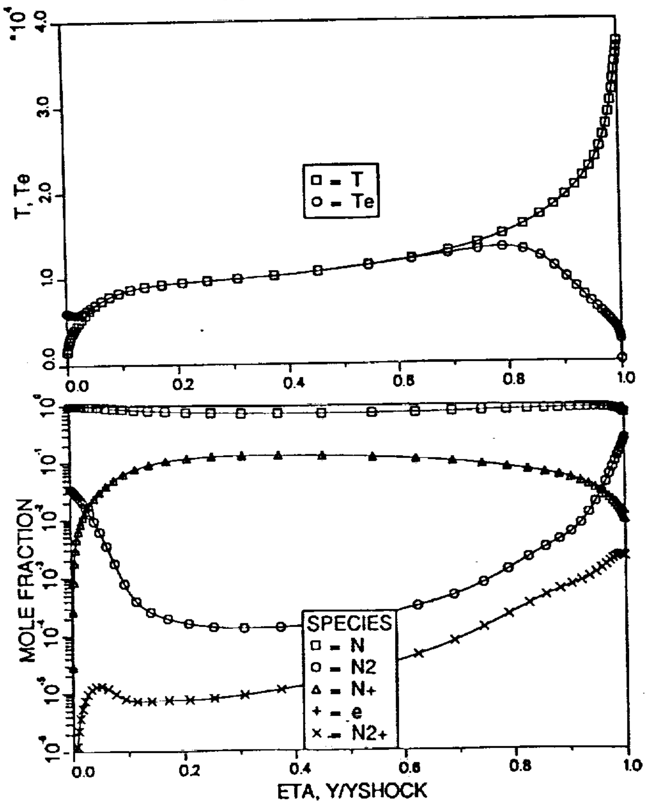

Fig. 11 – Coupled Stagnation Profiles at 12 km/sec, 80 km, Rnose = 2.3 m, QR = 24.3 watts/cm^2, QC = 33 watts/cm^2, YSHOCK = 11.5 cm

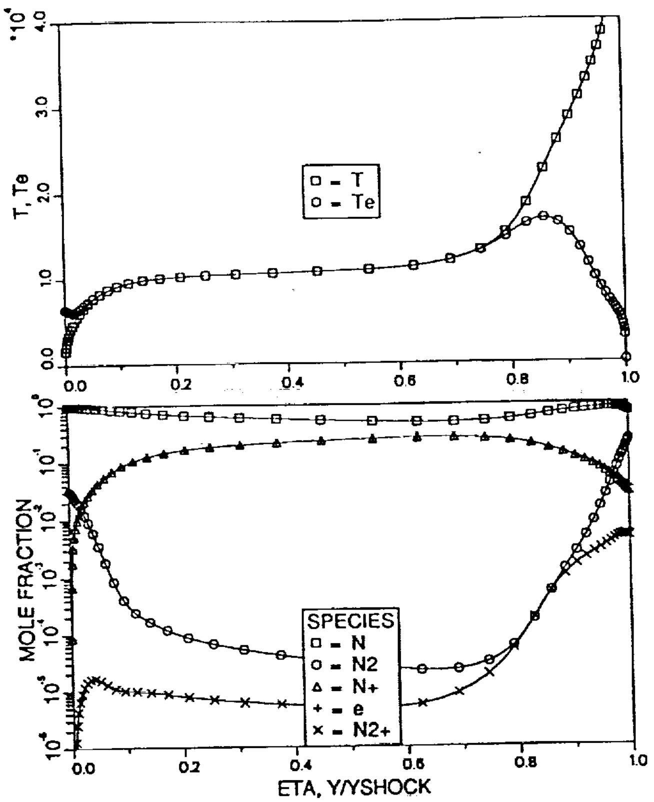

Fig. 12 – Coupled Stagnation Profiles at 14 km/sec, 80 km, Rnose = 2.3 m, QR = 111 watts/cm^2, QC = 56.4 watts/cm^2, YSHOCK = 9.1 cm

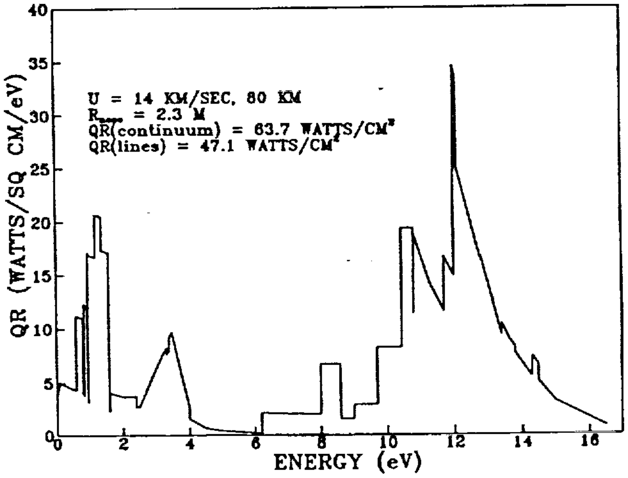

Fig. 13(a) – Usual Presentation of Spectral Variation of Stagnation Radiative Heat Transfer

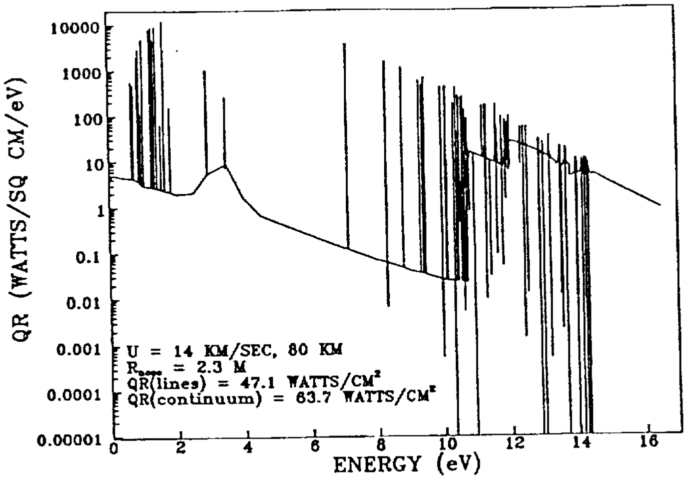

Fig. 13(b) – Detailed Spectral Variation of Stagnation Radiative Heat Transfer

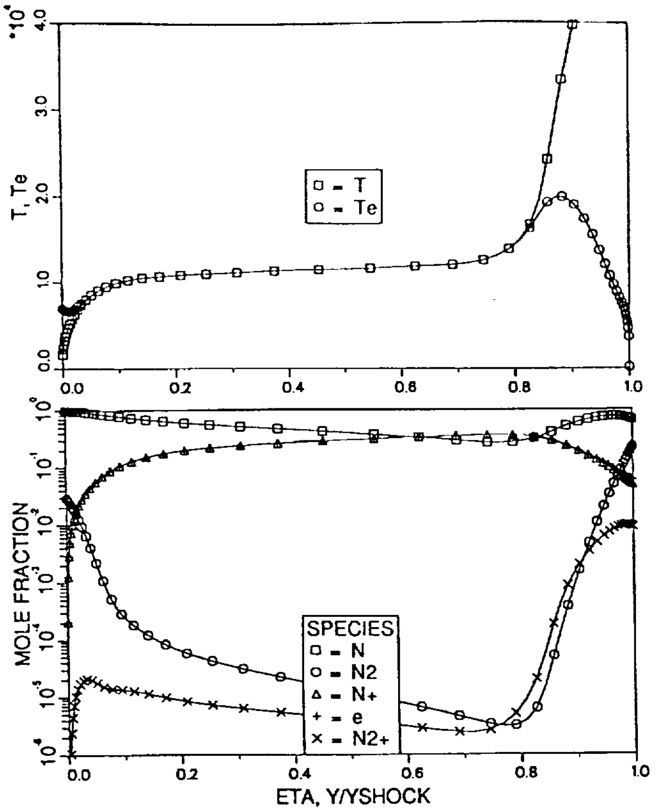

Fig. 15 – Coupled Stagnation Profiles at 16 km/sec, 80 km, Rnose = 2.3 m, QR = 273 watts/cm^2, QC = 87.3 watts/cm^2, YSHOCK = 7.5 cm

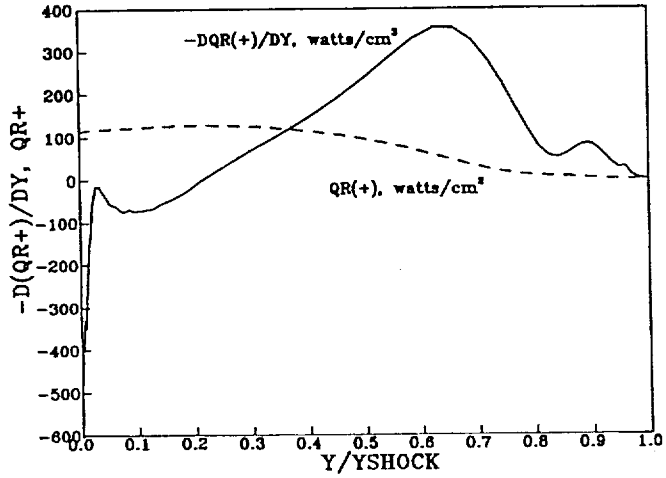

Fig. 14 – Intensity and Radiative Flux Towards Stagnation Point, 14 km/sec, 80 km

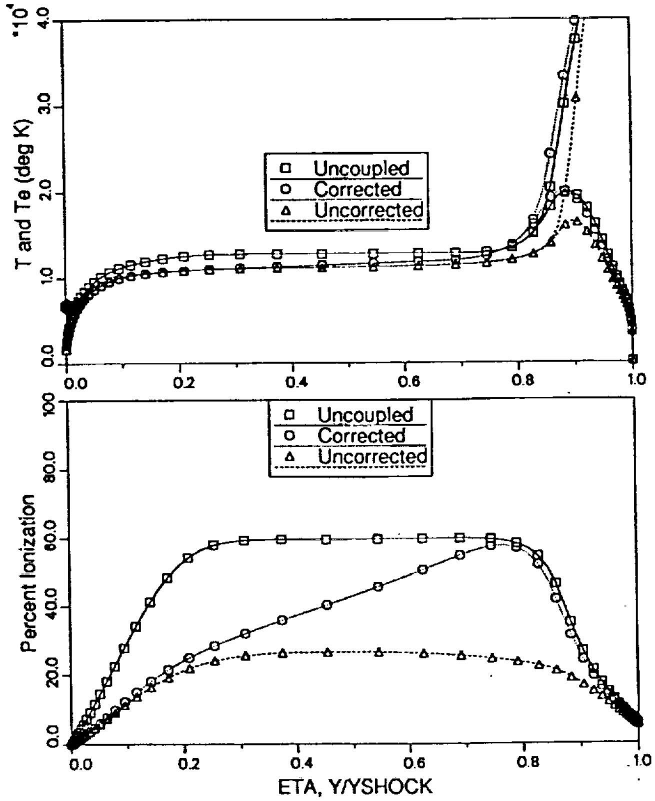

Fig. 16 – LTNE and Coupling Effects at 16 km/sec and 80 km

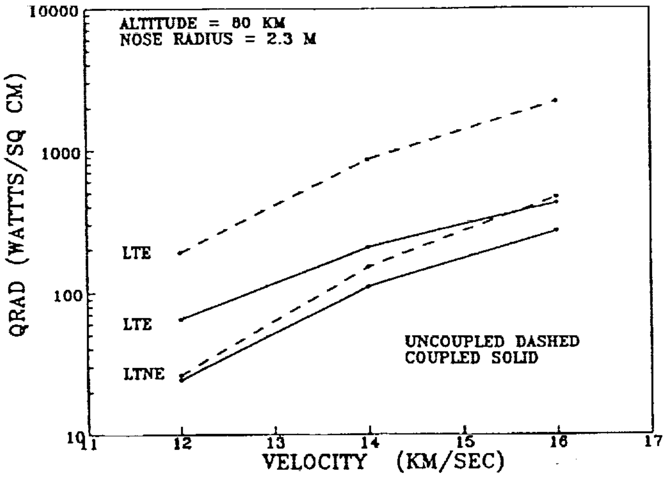

Fig. 17 – LTNE and Coupling Effects on Radiative Heat Transfer

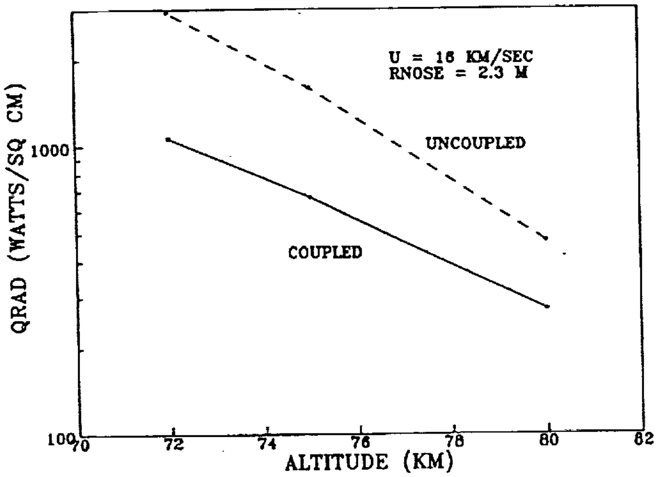

Fig. 18 – Radiative Gasdynamic Coupling Effects on Radiative Heat Transfer

Effect of Electron Temperature and Impact Ionization on Martian Return AOTV Flowfields

L. A. Carlson and T. A. Gally

Reprinted from

Journal of Thermophysics and Heat Transfer

Volume 5, Number 1, January 1991, Pages 9–20

AIAA

A publication of the
American Institute of Aeronautics and Astronautics, Inc.
The Aerospace Center, 370 L'Enfant Promenade, SW
Washington, DC 20024-2518

VOL. 5, NO. 1, JANUARY 1991 J. THERMOPHYSICS 9

Effect of Electron Temperature and Impact Ionization on Martian Return AOTV Flowfields

Leland A. Carlson* and Thomas A. Gally†
Texas A&M University, College Station, Texas 77843

Various electron impact ionization models in conjunction with a quasiequilibrium electron temperature model have been investigated and applied to the stagnation region of a hypothetical 2.3-m nose radius Martian return aeroassisted orbital transfer vehicle (AOTV). For the conditions considered, $U = 12$ km/s at 80 km, both multitemperature inviscid and viscous results indicate that a two-step ionization impact model predicts ionization distances in agreement with experimental data, that nonequilibrium chemistry and radiation effects are important throughout the stagnation zone, and that the quasiequilibrium electron temperature model is reasonable. Also, using a nongray emission-absorption radiation step model, it is shown that nonequilibrium causes a reduction in radiative heating from that predicted for equilibrium conditions and that, compared to an adiabatic wall, a cool wall (1650 K) results in a 28–45% reduction in radiative heating due to absorption near the wall.

Introduction

IN the future, various space programs will be conducted that will require the efficient return of large payloads to low Earth orbit (LEO) from missions to the moon or planets such as Mars. To accomplish this task, the return vehicles will utilize aerocapture techniques that will involve re-entry and deceleration at high altitudes, and to design these vehicles, a thorough understanding of the physical phenomena will be required. Because of the high altitudes associated with aerocapture, the vehicle flowfields will be dominated by chemical, thermal, and radiative nonequilibrium phenomena, which in many cases have not been extensively studied since the Apollo era.[1] Recently, as a result of the Aeroassisted Flight Experiment (AFE) program, results have been presented for aerocapture flowfields in the range of 7.5–10 km/s (Refs. 2–7). These results have demonstrated the importance of nonequilibrium phenomena in this flight regime.

However, for a Martian return vehicle the minimum nominal Earth entry velocity is approximately 12 km/s and the vehicle might be required under certain conditions to be able to operate and survive at Earth entry speeds up to 16 km/s.[8] At these higher velocities, the nonequilibrium phenomena will be different from those associated with the AFE vehicle. In the stagnation region, for example, nonequilibrium should be dominated by electron impact ionization processes instead of dissociation reactions; extensive thermal nonequilibrium involving at least three temperatures (heavy particle, vibrational, and electron) will exist; and the radiative heat transfer may be significantly affected by local thermodynamic nonequilibrium or nonequilibrium radiation effects. In addition, the electron temperature and nonequilibrium chemistry will be strongly coupled, and this coupling will influence the radiative heat transfer to the vehicle. Furthermore, at the higher end of the velocity range (14–16 km/s), the radiative transfer and the flowfield gasdynamics will be coupled due to the significant energy losses associated with radiation cooling.

Currently, several different engineering models and reaction rates have been postulated for electron impact ionization chemistry, all of which depend on the accurate prediction of electron temperature. The purpose of the present effort is to examine these different electron impact ionization models using flowfield results obtained from both inviscid and viscous, nonequilibrium chemistry, multitemperature computational models. By comparing the results with each other, the consequences of using a specific model can be determined. Furthermore, by comparing these results with experimental data, a suitable ionization model for the stagnation region can be determined.

Problem Formulation

Flowfield Models

In this study both inviscid and viscous flowfield representations have been utilized. For the inviscid calculations an improved version of a previously developed[6] nonequilibrium chemistry axisymmetric inverse method based on the work of Grosse[9] has been utilized as the basic Euler equation flow solver. This method permits arbitrary chemistry, includes options for a variety of vibration dissociation coupling models, and, in the computation of radiative transfer, accounts for nongray gas spectral and local thermodynamic nonequilibrium phenomena. For the present effort it has been further modified to include an electron temperature model and both one- and two-step atomic ionization models.

Since at the high altitudes and low densities of interest in aerocapture both viscous phenomena and wall thermal boundary-layer effects will be important, calculations have also been obtained using a modified version of the NASA Langley nonequilibrium chemistry viscous shock-layer code VSL3DNQ, which is an axisymmetric version of the SHTNEQ code described in Ref. 10. Like the inviscid code, this viscous shock-layer (VSL) method has also been modified to include an electron temperature model and both one- and two-step atomic ionization formulations. In addition, it has been combined with a nongray emission-absorption radiation model to permit the computation of radiative heat transfer. However, the effects of radiation gasdynamic coupling due to radiation cooling have not yet been included in the VSL formulation.

Presented as Paper 89-1729 at the AIAA 24th Thermophysics Conference, Buffalo, NY, June 12–14, 1989; received July 13, 1989; revision received Dec. 18, 1989.

*Professor, Department of Aerospace Engineering. Associate Fellow AIAA.

†Research Assistant, Department of Aerospace Engineering. Student Member AIAA.

Electron Impact Ionization

At conditions of interest for Earth return from Mars, the nonequilibrium chemistry region behind the bow shock will be dominated by ionization chemistry. Initially, ions will be produced via reactions involving NO^+ and N_2^+ and precursor photoionization, but once significant dissociation has occurred and reasonable amounts of atomic nitrogen and oxygen are present, the atoms will directly ionize in collisional reactions. Of these the most important are the electron impact reactions:

$$N + e^- = N^+ + e^- + e^- \tag{1a}$$

$$O + e^- = O^+ + e^- + e^- \tag{1b}$$

since they can induce electron avalanche and, thus, strongly affect the length and character of the nonequilibrium zone.

The classical model for these reactions uses standard forms for the species production terms, reaction rates, and equilibrium constant. This approach essentially assumes that the ionization mechanism proceeds via a one-step process, and a widely used set of reaction rates for these reactions consists of the following:

For $N + e^- = N^+ + e^- + e^-$,

$$k_f = 1.1 \times 10^{32} T_e^{-3.14} \exp(-169{,}000/T_e) \tag{2}$$

$$k_b = 2.2 \times 10^{40} T_e^{-4.5} \tag{3}$$

where k_f and k_b are the forward and reverse rate coefficients based on the local electron temperature T_e.

For $O + e^- = O^+ + e^- + e^-$,

$$k_f = 3.6 \times 10^{31} T_e^{-2.91} \exp(-158{,}000/T_e) \tag{4}$$

$$k_b = 2.2 \times 10^{40} T_e^{-4.5} \tag{5}$$

Following normal practice, it is assumed that in these reactions the governing temperatures are the electron temperatures. These rates were presented by Kang et al.[11] as part of an extensive reaction chemistry set, and results using this set yielded good agreement with electron probe measurements on the flank region of the RAM-C flight vehicle experiment. Both recombination coefficients, Eqs. (3) and (5), have the form resulting from elementary[12] and variational theory three-body collision theory,[13] and the coefficient is near the upper bound determined by Makin and Keck.[13] In fact, several figures in Ref. 11 are labeled "Results are for upper-bound reaction rate coefficients for de-ionization reactions."

Similar recombination rates were also used in reflected shock-tunnel nozzle flow investigations of C^+ recombination and O_2^+ and N_2^+ dissociative recombination in which good results were obtained.[14-16] However, as noted by the investigators, these experiments may not have been sensitive to these reactions since in one case the leading coefficient in Eq. (3) was varied by plus and minus two orders of magnitude with no effect on the data.[16] Also, these laboratory and flight experiments were for flows dominated by recombination and at lower electron densities and temperatures (2500–8000 K) than those that are of interest in the current investigation. Thus, although not establishing the validity of these rates for the present conditions, these experiments do not indicate that they are incorrect.

However, Park[17,18] measured the nitrogen ionic recombination rate at a nominal temperature of 10,000 K using an arc plasma wind tunnel and obtained values that corresponded to a recombination rate of

$$k_b = 5.02 \times 10^{42} T_e^{-5.27} \tag{6}$$

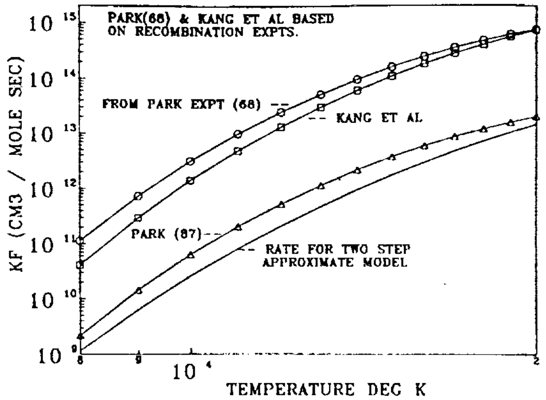

Fig. 1 Comparison of forward rate constants for $N + e^- = N^+ + e^- + e^-$.

which is in reasonable agreement with the value of Kang et al.[11] He also suggested that the forward rate be obtained from the equilibrium constant, K_{eq}, via

$$K_{eq} = k_f/k_b \tag{7}$$

Both the Park forward rate corresponding to Eq. (6) and the Kang et al. forward rate given in Eq. (2) are plotted in Fig. 1. As can be seen, the agreement between the two rates over the range of electron temperatures of interest in the present study is good.

Now it should be recognized that, for the high temperatures of interest in the present effort, three-body deionization recombination will include significant electron capture into low-lying levels and collisional de-excitation should be rapid.[12] In addition, although the atomic electronic excited state populations may be in a Boltzmann distribution during recombination [i.e., local thermodynamic equilibrium (LTE)], at T_e, experimental evidence[19] indicates that many of the excited state population densities may not be in equilibrium with the number density of free electrons. As will be discussed later, this nonequilibrium with the free electrons during recombination is in contrast with the behavior that can be assumed to occur behind a shock wave during ionization.

Recently, Park[4] used a two-temperature ionizing air model and obtained good agreement with shock-tube, shock-tunnel, and flight measurements of phenomena immediately behind a shock front and/or in the stagnation zone and forward face region of blunt bodies. For these studies several of the reaction rates were adjusted in order to yield good comparisons with experimental data, and the forward rates for the reactions in Eq. (1) are considerably different from those given by Eqs. (2–7). These rates consist of the following:

For $N + e^- = N^+ + e^- + e^-$,

$$k_f = 2.5 \times 10^{33} T_e^{-3.82} \exp(-168{,}600/T_e) \tag{8}$$

For $O + e^- = O^+ + e^- + e^-$,

$$k_f = 3.9 \times 10^{33} T_e^{-3.78} \exp(-158{,}500/T_e) \tag{9}$$

and the forward rate for atomic nitrogen electron impact ionization is plotted in Fig. 1. Note that it is almost two orders of magnitude smaller than the rates based on recombination.

The second model for atomic ionization is an engineering approximation based on various theories involving the ionization of argon[20-24] and the application of these theories to nitrogen and oxygen.[25,26] This approach assumes that atomic ionization is not a one-step process but proceeds via a two-step chain involving excitation to an excited state followed by rapid ionization controlled by the local charged particle concentrations and the electron temperature. This concept applies not only to electron impact ionization but also to heavy particle ionization involving atom-atom and atom-ion collisions.

Unfortunately, because of the two-step process, the usual mass production rate formulation is not completely adequate.

For example, assume that the atom-atom ionization process proceeds as follows:

$$N_g + M = N^* + M \tag{10}$$

$$N^* = N^+ + e^- \tag{11}$$

where N^* refers to atomic nitrogen in an excited state. By assuming that the first step is rate determining, that dN^*/dt is approximately zero, and that the ground state concentration approximately equals the atom concentration, kinetics yields the rate of species mass production per unit volume $\dot{\omega}_s$ to be

$$\dot{\omega}_{N^*,\,\mathrm{total}} = \mathfrak{M}_N \{ k_f [N_g][M] - k_b [N^*][M] \} + \dot{\omega}_{N^*,11} \tag{12}$$

where k_f and k_r are for Eq. (10), brackets denote concentration, $\mathfrak{M}_s$ is the molecular weight of species s, and the subscript 11 refers to Eq. (11). However, by assumption,

$$\dot{\omega}_{N^*,\mathrm{total}} = 0$$

so that

$$\dot{\omega}_{N^*,11} = -\mathfrak{M}_N \{ k_f [N_g][M] - k_b [N^*][M] \} \tag{13}$$

But k_f and k_r are related by the equilibrium constant for Eq. (10):

$$K_{eq} = \frac{g^* \exp(-E^*/kT)}{g_g} = \frac{k_f}{k_b}$$

where g is the degeneracy of the indicated energy level E, and k is the Boltzmann constant. Thus, Eq. (13) becomes

$$\dot{\omega}_{N^*,11} = -\mathfrak{M}_N k_f [N_g][M] \left\{ 1 - \frac{g_g \exp(E^*/kT)[N^*]}{g^*[N_g]} \right\} \tag{14}$$

At this point, a rate expression relating the excited state to the ions and free electrons could be introduced instead. However, based on experimental evidence for monoatomic gases,[19,24] it can be assumed as an approximation that the excited states of nitrogen are in equilibrium with the free electrons and ions at the electron temperature. Thus,

$$\frac{N_e N_{N+}}{N_{N^*}} = \frac{Q^{el}_{N+} Q_{e-} \exp(-X/kT_e)}{g^*} \tag{15}$$

where X is the ionization potential from the excited state, Q^{el}_s is the electronic partition function of species s, and Q_{e-} is the partition function for the electrons defined by

$$Q_{e-} = 2 \left(\frac{2\pi m_e k T_e}{h^2} \right)^{3/2}$$

where h is the Planck constant and m_e is the electron particle mass. Substituting Eq. (15) into Eq. (14) and noticing that

$$\dot{\omega}_{e,11} = (\mathfrak{M}_e / \mathfrak{M}_N) \dot{\omega}_{N^*,11}$$

yields, for $M = N$,

$$\dot{\omega}_{e,N} = \mathfrak{M}_e k_f [N]^2 \left[1 - \frac{g_g \exp\left(\frac{E^*}{kT} + \frac{X}{kT_e} \right) AV[e^-][N^+]}{Q_{e-} Q^{el}_{N+} [N]} \right] \tag{16}$$

where AV is Avogadro's constant, and the subscript 11 is replaced by the incident particle for the two-step reaction, M.

A similar analysis for $M = N^+$ ionization yields

$$\dot{\omega}_{e,N+} = \mathfrak{M}_e k_f [N][N^+] \times \left[1 - \frac{Q^{el}_N \exp\left(\frac{E^*}{kT} + \frac{X}{kT_e} \right) AV[e^-][N^+]}{Q_{e-} Q^{el}_{N+} [N]} \right] \tag{17}$$

whereas, for electron impact ionization, $M = e^-$, the result is

$$\dot{\omega}_{e,e} = \mathfrak{M}_e k_f [N][e^-] \left[1 - \frac{g_g \exp\left(\frac{I}{kT_e} \right) AV[e^-][N^+]}{Q_{e-} Q^{el}_{N+} [N]} \right] \tag{18}$$

Similar expressions could be obtained for atomic oxygen ionization.

Notice that the production rates involving heavy particles (atoms and ions) are governed by both the electron and the heavy particle temperature, whereas the production rate for the atom-electron reactions involves only the electron temperature but has the classical form. Furthermore, the forward rate coefficient is for the limiting step and only uses the energy of the assumed excited state and not the ionization energy. Wilson,[25] using the work of Petschek and Byron,[27] assumed that the rate-limiting step in the ionization process was the excitation of the atoms to the level involving the largest energy jump, i.e., to the $3s^4P$ for nitrogen and to the $3s^5S$ state for oxygen, and they proposed a form for the excitation rate. It should be noted that for oxygen and nitrogen this rate-limiting step is for the temperatures of interest here and differs from that used in Ref. 13, which was only 2.5 eV below the ionization level.

Using this theory, Wilson obtained good agreement with shock-tube data for ionization distances behind shock waves in air. Subsequently, these forms were used to deduce rates that were used to study nonequilibrium radiating phenomena behind reflected shock waves[26] and the AFE stagnation region.[6]

Thus, based on the theory and results presented in Refs. 24–26, reaction rates consistent with the two-step approximate model given by Eqs. (10–18) consist of the following:

For $N + e^- = N^+ + e^- + e^-$,

$$k_f = 4.16 \times 10^{13} T_e^{0.5} \exp(-120{,}000/T_e) \tag{19}$$

For $O + e^- = O^+ + e^- + e^-$,

$$k_f = 5.49 \times 10^{13} T_e^{0.5} \exp(-104{,}500/T_e) \tag{20}$$

For $N + N = N^+ + e^- + N$ and $N + N^+ = N^+ + e^- + N^+$,

$$k_f = 2.34 \times 10^{11} T^{0.5} \exp(-120{,}000/T) \tag{21}$$

The forward rate given by Eq. (19) is also shown in Fig. 1 and is in reasonable agreement with the ionization rate of Park.[4] As can be seen, both of the rates associated with ionization processes are considerably slower than those deduced from recombination experiments and theory. However, the difference might be due to fundamental differences in the processes involved. In the shock-tube case the process is dominated by forward ionization, and in the rate derivation it was assumed that the excited states were in equilibrium with the free electrons and ions. In the shock- and arc-tunnel experiments, the chemistry is dominated by recombination, and, as mentioned earlier, there is experimental evidence[19] that during recombination the excited states may not be in equilibrium with the free electrons.

Electron Temperature Model

Besides chemical nonequilibrium, it is possible for a partially ionized gas to have regions of thermal nonequilibrium between electrons and the other heavier species. Such thermal nonequilibrium occurs because the rate of energy exchange between electrons and heavy particles is very slow due to the large mass differences in the species, and it is characterized by different free electron and heavy particle temperatures. Since atomic ionization and radiative transfer are dependent on and strongly coupled to the electron temperature, accurate models for computing it are essential.

Over the years a variety of models for determining the electron temperature have been presented[4-6,20-23,26,28-33] that differ in detail, level of complexity, and ease of solution. All of these start from the equation representing conservation of electron energy, which can be written as

$$\frac{\mathrm{D}(\rho_e h_e)}{\mathrm{D}t} + \rho_e U_e \cdot \frac{\mathrm{D}(u)}{\mathrm{D}t} + \frac{\partial}{\partial r} \cdot q_e + \rho_e h_e \left(\frac{\partial}{\partial r} \cdot u \right)$$
$$- \frac{\mathrm{D}(p_e)}{\mathrm{D}t} + [\tau_e] : \left[\frac{\partial}{\partial r} ; u \right] - N_e X_e \cdot U_e$$
$$- \dot{\omega}_e \frac{u^2}{2} = \sum_{j=1}^{S} (\xi_{ej} + U_e \cdot P_{ej}) + Q_e \tag{22}$$

If Bremmstrahlung and viscous stress effects are ignored, this equation becomes, showing only one dimension for simplicity,

$$\rho_e u_e \frac{\partial h_e}{\partial x} - u \frac{\partial p_e}{\partial x} + \frac{\partial}{\partial x} \left(-\lambda_e \frac{\partial T_e}{\partial x} \right) + \frac{\partial}{\partial x} (\rho_e U_e h_e)$$
$$+ \dot{\omega}_e h_e - h_e \frac{\partial}{\partial x} (\rho_e U_e) - \dot{\omega}_e \frac{u^2}{2} = U_e \frac{\partial p_e}{\partial x}$$
$$+ \sum_{j=1}^{S} (\xi_{ej} + U_e P_{ej}) + Q_e \tag{23}$$

where the first term on the right side represents the effect of external forces and is obtained from the electron momentum equation; the second term accounts for the rate of energy gain by electrons due to elastic encounters because of thermal motion of the particles; the third term represents the energy gain resulting from elastic encounters because of the relative fluid motion of the electrons; and the last term represents energy change due to inelastic encounters. The velocity U_e is the electron diffusion velocity.

In the past, several investigators,[20-23,26] using the full electron energy equation, have obtained results which indicate that when significant ionization is present in the postshock nonequilibrium zone the electron temperature is essentially constant at a value 10-15% above the theoretical equilibrium temperature until the heavy particle temperature falls to that value. After that, the two temperatures are essentially the same. Obviously, the use of such a constant temperature would simplify the electron temperature calculations, and this approach has been used in approximate flowfield solutions[31,34] and was considered for the present study. However, preliminary calculations demonstrated the difficulty of selecting a priori an appropriate effective constant electron temperature, and this approach was abandoned.

Another approach successfully used in the past for AFE flowfields[4,6] is to assume that the nitrogen vibrational temperature and the electron temperature are equal and to combine the electron and vibrational energy equations. This method is based on experimental data[35] and theoretical calculations[4,5] which show that, near 7000 K, vibrational processes strongly influence the electron temperature. However, for the conditions of the present study, temperatures are normally above 10,000 K, dissociation occurs rapidly behind the shock front, and the concentration of N_2 is very low over most of the nonequilibrium zone. Thus, vibration electronic coupling should not be significant, and this approach was not utilized in the present study.

Another model that has been used in the past[32,33] is the "quasiequilibrium approximation," in which all derivative terms are neglected in the electron energy equation. If it is further assumed that the charge exchange cross section between atoms and ions is sufficient to ensure that they have the same diffusion velocity and, due to rapid dissociation, that the concentration of diatomic molecules is low over most of the shock layer, then diffusion terms can also be neglected. Thus, Eq. (23) becomes

$$\dot{\omega}_e h_e - \dot{\omega}_e \frac{u^2}{2} = \sum_{j=1}^{S} \xi_{ej} + Q_e \tag{24}$$

Since vibration electronic coupling has been neglected, the inelastic term Q_e is composed of effects due to chemical reactions involving electrons. When an electron is created by an electron-atom reaction, the electron that caused the ionization will lose energy equivalent to the ionization potential E_I plus the energy of the created electron, which on the average is, say, e_{av}. The original electrons will rapidly equilibrate by elastic collisions and will have collectively lost energy $E_I + e_{av}$. The equilibration between the original electrons and the newly created one will not affect the energy per unit volume since it only involves a transfer of energy from one particle to another. Thus, the net energy loss from an electron atom ionization process is E_I, and the total is $\dot{\omega}_{e,eA} E_I / m_e$.

Similarly, every time an atom-atom ionization occurs, an electron of average energy e_{AA} is created, and the total energy gain for these processes is $\dot{\omega}_{e,AA} e_{AA} / m_e$. This is also the case for atom-ion ionization. Thus,

$$Q_e = -\frac{\dot{\omega}_{e,eA} E_I}{m_e} + \frac{\dot{\omega}_{e,AA} e_{AA}}{m_e} + \frac{\dot{\omega}_{e,AI} e_{AI}}{m_e} \tag{25}$$

For the present conditions, however, the electron-atom process should be the dominant ionization mechanism and the last two terms should be negligible.[21,26] For the parts of the flowfield where the other reactions are important, the concentration of electrons should be low enough that any error resulting from neglecting them in Eq. (25) should be small. Thus, only the first term of Eq. (25) need be retained.

General forms for the elastic interaction terms have been derived using collision integral theory in Ref. 36. Since diffusion effects are ignored in the quasiequilibrium model, these interaction terms can be reduced to

$$\xi_{ej} = [(m_e T_e)^{1/2} / m_j] S_{ej} \mathrm{N}_e \mathrm{N}_j (1.03478 \times 10^{-23})(T - T_e) \tag{26}$$

where centimeter-gram-second units are assumed; terms involving m_e have been dropped relative to heavy particle masses; and S_{ej} is the collision cross section between electrons and species j.

By substituting Eqs. (25) and (26) into Eq. (24), dropping the small term involving u^2 and rearranging, an approximate equation for the free electron temperature is

$$T_e = T - \frac{1.23357 \times 10^{-10}}{T_e^{1/2} SX [\mathrm{e}^-] m_e}$$
$$\times \left(\dot{\omega}_{e,e\mathrm{N}} E_{I_\mathrm{N}} + \dot{\omega}_{e,e\mathrm{O}} E_{I_\mathrm{O}} + \dot{\omega}_e \frac{5}{2} k T_e \right) \tag{27}$$

where

$$SX = \mathrm{N}_\mathrm{N} S_{e\mathrm{N}} + \mathrm{N}_\mathrm{O} S_{e\mathrm{O}} + \mathrm{N}_{\mathrm{N}^+} S_{e\mathrm{N}^+} + \mathrm{N}_{e\mathrm{O}^+} S_{e\mathrm{O}^+}$$
$$+ 1/2 (\mathrm{N}_{\mathrm{N}_2} + \mathrm{N}_{\mathrm{O}_2}) S_{eM}$$

Note that this equation is nonlinear since the cross sections are functions of translational and electron temperature as well as concentrations and that the various production rates also depend on both temperatures. In the present study an iterative method for solving this equation has been developed and included in both the inviscid and viscous flowfield solvers.

Chemistry Models

Since the primary objective of the present effort is to use multitemperature flowfield models to investigate the effect of different impact ionization models, the reaction chemistry schemes have been kept as simple as possible. For air, the 10 species, 11 reaction model shown in Table 1 has been used. Although this scheme is not as complete as some others (Ref. 11, for example), it should be adequate for the present study. In addition, numerical experiments were conducted using for the nitrogen dissociation reaction a series of reaction rates that varied by several orders of magnitude. For the conditions investigated, no significant effects on the ionization processes were observed.

However, since the air model did not contain all possibilities, particularly with respect to dissociation and oxygen ionization, results have also been obtained assuming a pure nitrogen freestream. At the conditions of interest, nitrogen is a reasonable representation of nonequilibrium radiating air, and more details can be included using a smaller number of species and reactions. The nitrogen reaction chemistry set consisting of five species and eight reactions is shown in Table 2. Notice that charge exchange is included.

In general, with the exception of the atomic ionization reactions, the rates shown in Tables 1 and 2 are similar to those used by other investigators[3,6,26,33,35] and are in the form

$$k_{f,b} = AT^{B} \exp(-E/T)$$

As noted in the tables, computations involving the one-step ionization models and the rates in Eqs. (2-5) will be termed case 1, and those using the two-step ionization model and the rates in Eqs. (19) and (20) are case 2.

Table 1 Air reaction system

Reaction		A	B	E	Direction
$O_2 + M = 2O$	$+M$	1.19×10^{21}	-1.5	59,380	Forward
$NO + M = N$	$+O+M$	5.18×10^{21}	-1.5	75,490	Forward
$N_2 + M = 2N$	$+M$	2.27×10^{21}	-1.5	0	Backward
$N + O_2 = NO$	$+O$	1.00×10^{12}	0.5	3,120	Forward
$N_2 + O = NO$	$+N$	7.00×10^{13}	0.0	38,016	Forward
$N + O = NO^+$	$+e^-$	1.80×10^{21}	-1.5	0	Backward
$N + N = N_2{}^+$	$+e^-$	1.40×10^{13}	0.0	67,800	Forward
$N + N = N$	$+N^+ + e^-$	2.34×10^{11}	0.5	120,000	Forward
$N + N^+ = 2N^+$	$+e^-$	2.34×10^{11}	0.5	120,000	Forward
$N + e^- = N^+$	$+2e^-$	Eqs. (2) and (3) for case 1, (19) for case 2			
$O + e^- = O^+$	$+2e^-$	Eqs. (4) and (5) for case 1, (20) for case 2			

Table 2 Nitrogen reaction system

Reaction		A	B	E	Direction
$N_2 + N_2 = 2N$	$+N_2$	4.70×10^{17}	-0.5	113,000	Forward
$N_2 + N = 2N$	$+N$	4.085×10^{22}	-1.5	113,000	Forward
$N_2 + M = 2N$	$+M$	1.90×10^{17}	-0.5	113,000	Forward
$N_2 + N^+ = N_2{}^+$	$+N$	2.02×10^{11}	0.8	13,000	Forward
$N + N = N_2{}^+$	$+e^-$	1.40×10^{13}	0.0	67,800	Forward
$N + N = N$	$+N^+ + e^-$	2.34×10^{11}	0.5	120,000	Forward
$N + N^+ = 2N^+$	$+e^-$	2.34×10^{11}	0.5	120,000	Forward
$N + e^- = N^+$	$+2e^-$	Eqs. (2) and (3) for case 1, (19) for case 2			

Vibration Dissociation Coupling

It is well established that, in general, vibration dissociation coupling strongly influences the dissociation of diatomic molecules.[4-6] However, at the temperatures and velocities associated with the present study, dissociation occurs rapidly, and the influence of vibration dissociation coupling on the ionization processes is small. To confirm this, numerical experiments were conducted with the inviscid flowfield model using vibrational equilibrium, coupled vibration-dissociation-vibration (CVDV) coupling, and modified CVDV (MCVDV) coupling, and no significant differences between the results regarding the ionization processes were observed. Consequently, in the inviscid flow solver, the MCVDV model developed in Ref. 6 has been used. This coupling model includes corrections to the Landau-Teller relaxation time correlation to prevent unrealistically short relaxation times at high temperatures and accounts for the diffusive nature of vibrational relaxation at high temperatures.[4]

In its original form the viscous shock-layer code, VSL3DNQ, did not contain any vibration dissociation coupling model. Since the inviscid studies indicated that, for conditions associated with Earth entry return from Mars, vibrational coupling effects were small, the VSL code has not been modified, and all viscous calculations have assumed vibrational equilibrium.

Radiation Model

At the lower velocities associated with the Earth return from Mars of an aeroassisted orbital transfer vehicle (AOTV), i.e., 12 km/s, radiative heat transfer and associated self-absorption effects should be important, but the total radiative losses from the flowfield should be sufficiently small so that there is not any significant radiative gasdynamic coupling. Thus, once a flowfield solution has been obtained for a given reaction chemistry system, the flowfield solution can be used to compute the body radiative heat transfer. In the present study, the tangent slab approximation has been used, the wall surface is assumed to be nonemitting and nonablating, and precursor effects are assumed negligible. Also, an eight-step nongray absorption coefficient model based on the work of Olstad[37] and similar to that used in Ref. 6 has been used. However, it has been modified to yield, under equilibrium conditions, results with respect to both magnitude and spectral distribution that in general agree with RADICAL, the NASA Langley version of a detailed radiation program documented in Ref. 38. Based on a series of calculations, these modifications consisted of a reduction in the effective absorption cross sections in the frequency range of 6.89–10.98 eV, which is composed not only of continuum radiation but also several important lines. This step model has yielded reasonable engineering results for AFE flowfields[6] and, in conjunction with an approximate flow solver, has correlated well with the Fire 2 flight experiment.[34]

A spectral comparison between stagnation-point radiative heating predictions obtained using the present eight-step model and RADICAL is shown in Fig. 2. These results were obtained using the viscous flow solver with 99 points between the shock and the wall, case 1 rates, and assuming an adiabatic wall, and almost the entire shock layer for this case was in chemical and thermal equilibrium. The presence of line contributions is evident in the RADICAL results by the tall narrow peaks on top of the continuum curves in the infrared (0–3.1 eV) and ultraviolet (8–12 eV). Since the radiative heating to the wall is the area under these curves, it can be seen that, in general, the two models agree quite well, and, in fact, the results are within 15% overall. [Note that the vacuum ultraviolet (VUV) band in the eight-step model that starts at 14.56 eV actually extends to 31 eV.] However, the eight-step model still does appear to slightly overpredict the heating in the range of 6.89–10.98 eV, and further improvements can probably still be made. Nevertheless, particularly when computational efficiency is considered, the modified eight-step absorption coefficient model should be adequate for engineering and comparison studies.

In addition, the present radiation model contains a method for computing approximate correction factors that account for the effects of local thermodynamic nonequilibrium (LTNE). Such LTNE can exist in the chemical nonequilibrium

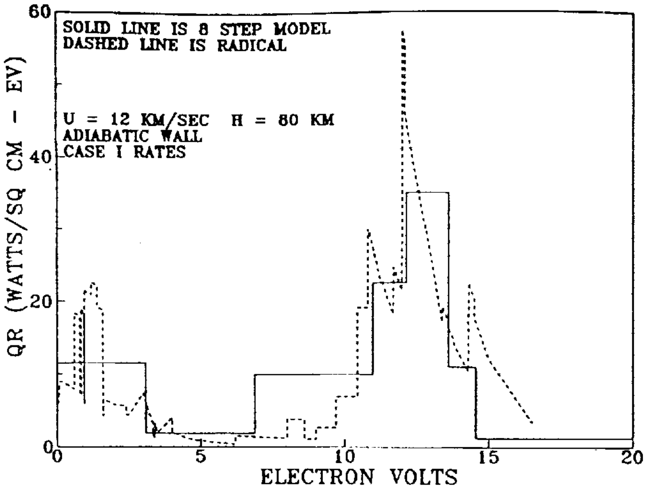

Fig. 2 Stagnation-point radiative heat transfer from RADICAL and eight-step model.

region immediately behind the shock front where, due to ionization via excited states, the populations of the electronic states may not be that predicted by an LTE assumption using the ground state. The rationale behind these factors and their derivation has been presented in Refs. 6 and 34, and similar factors have been used for monoatomic gases.[20-23] The inclusion of radiation nonequilibrium effects is essential for accurately predicting radiative heat transfer at high-altitude conditions.[4-6,34]

Originally, these LTNE factors were expressed in terms of the degree of dissociation and ionization,[6,34] which were often difficult to compute accurately. However, Greendyke[39] has pointed out that they can be more simply expressed in terms of the partition functions. Thus, the atomic nitrogen LTNE correction factor can be written as

$$\frac{N_{N} + N_{e} Q_{N}^{el} \exp(169{,}000/T_{e})}{N_{N} Q_{N}^{el} + Q_{e-}} \tag{28}$$

For radiation processes involving the ground state, this factor is multiplied by the blackbody function for that region to yield the effective source function, and the absorption coefficient is unchanged. On the other hand, for processes involving excited states, the factor is multiplied by the absorption cross section to yield the effective absorption coefficient, and the source function for that spectral region is unchanged. Additional details are presented in Ref. 6, and similar forms can be obtained for molecular radiation.

For cases where the reaction chemistry set is such that an opposite rate is obtained from a forward or reverse rate in conjunction with an equilibrium coefficient computed from partition functions, the correction factor form given in Eq. (28) is appropriate. This situation is the case with the two-step ionization model, whose rates have been designated case 2. In other words, in that case the factor predicted by Eq. (28) will go to one as the flow approaches ionization equilibrium.

However, when the one-step ionization rates of Kang et al.[11] are used, case 1, the ionization equilibrium coefficient is determined by the ratio of the forward-to-reverse rates [Eqs. (2-5)] and not by partition functions. In that case the atomic nitrogen LTNE correction factor should be computed using

$$(N_{N} + N_{e})/N_{N} A\, V K_{eq} \tag{29}$$

and the equilibrium coefficient is given by

$$K_{eq} = k_{f}/k_{b} = 5 \times 10^{-9} T_{e}^{1.36} \exp(-169{,}000/T_{e}) \tag{30}$$

If this approach is not taken, the factors will not approach one as chemical equilibrium is approached, and ridiculous answers may result.

For viscous cases in which a cool wall is considered, recombination processes will dominate in the wall thermal layer, and, as mentioned earlier, there is evidence that during recombination the excited states may not be in equilibrium with the free electrons and ions and the electronic states may all be populated according to a Boltzmann distribution, i.e., in LTE with the ground state. Consequently, in the wall thermal layer, the radiation should be computed using the local electron temperature and nonequilibrium species concentrations, and the LTNE factors should not be used (or set to unity).

Discussion of Results

Inviscid and viscous results have been obtained for the stagnation region of a 2.3-m nose radius axisymmetric blunt body for a freestream velocity of 12 km/s at an altitude of 80 km. This condition was selected because it is within the range of possible Martian return trajectories, and yet the velocity is low enough that radiation losses should be minor, at the most a few percent, compared to the total flow energy. Thus, radiation cooling and gasdynamic coupling effects should be small. Each inviscid solution covers the region between the shock and the body and from the centerline up to 10 cm above the axis and is typically composed of over 10,000 computational points. Inviscid solutions using both air and nitrogen freestreams have been obtained. Viscous solutions have been obtained along the stagnation streamline for nitrogen freestreams for adiabatic and cool wall situations. In both cases the wall was assumed to be nonemitting and noncatalytic, and in the cool wall case the wall temperature was assumed to be 1650 K, which is representative of nonablating heat shield materials.

Inviscid Results

Although flowfield properties along 21 different streamlines in the stagnation region were actually computed, details will only be presented for streamline C, which crossed the shock front 1.5 cm above the axis. This streamline is shown in Fig. 3 as a solid line, along with several other streamlines, the shock front, and the body. Depending on the reaction chemistry system, streamline C was typically composed of 700–2000 spatial grid points.

Figure 4 shows air results obtained using the one-step ionization model with case 1 rates, the quasiequilibrium electron temperature model, and MCVDV vibration dissociation coupling. Although individual vibrational temperatures were computed for N_2, O_2, NO, NO^+, and N_2^+, for clarity they are not included on the plots. Immediately behind the shock front, the heavy particle temperature T is almost 70,000 K, whereas the electron temperature T_e is at the freestream value, 180.65 K. Initially, T_e rapidly rises to about 10,000 K, whereas the heavy particle temperature falls sharply due to the rapid

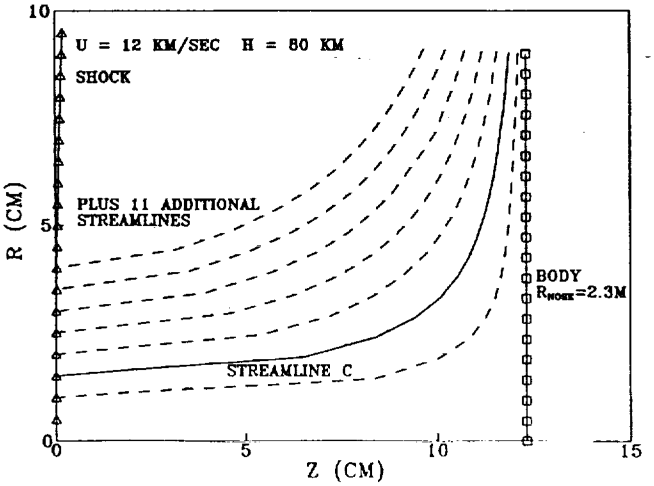

Fig. 3 Solution region for inviscid cases showing streamline C.

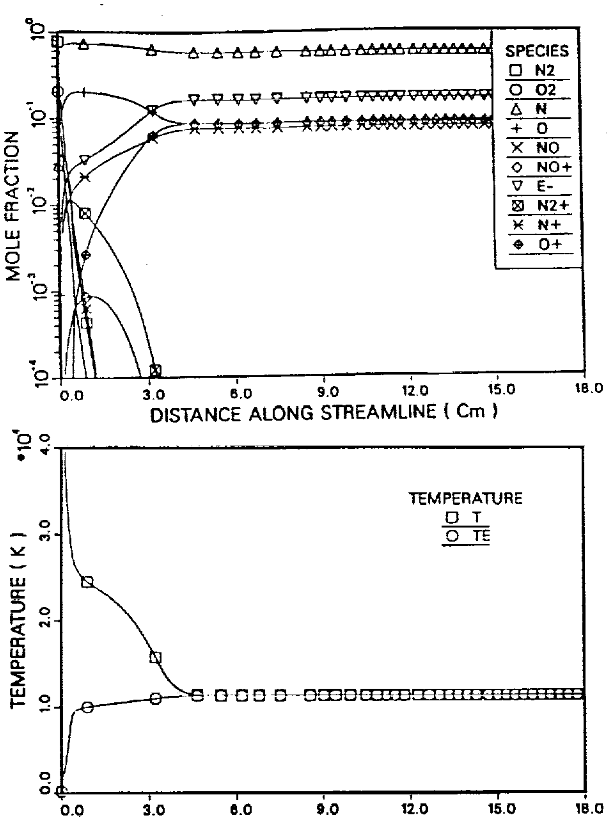

Fig. 4 Species and temperature profiles for air along streamline C, inviscid flow, case 1.

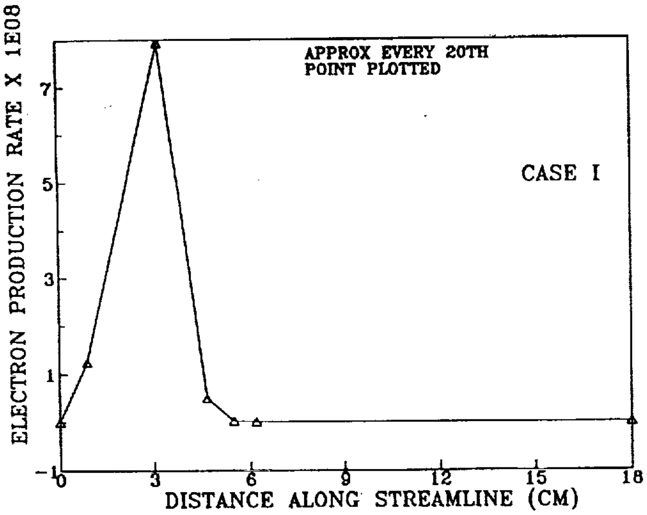

Fig. 5 Electron mass production rate along streamline C, inviscid case 1.

dissociation of N_2 and O_2. Subsequently, the electron temperature gradually increases until it equilibrates with the heavy particle temperature.

As can be seen on the concentration profiles, in the region immediately behind the shock front the concentration of atomic nitrogen and oxygen rises extremely rapidly, indicating that dissociation essentially occurs in the shock "front" as has been assumed in some approximate solutions.[25,34] Also N_2^+, NO, and NO^+ peak rapidly and essentially "disappear," and from a practical standpoint the entire nonequilibrium portion of the flowfield is dominated by atomic ionization. Interestingly, at the end of the equilibrium zone, the concentrations of N^+ and O^+ are similar. Furthermore, the heavy particle temperature and $[e^-]$ profiles exhibit a change in curvature around 2.5 cm, which is associated with the onset of electron avalanche from the electron impact ionization reactions.

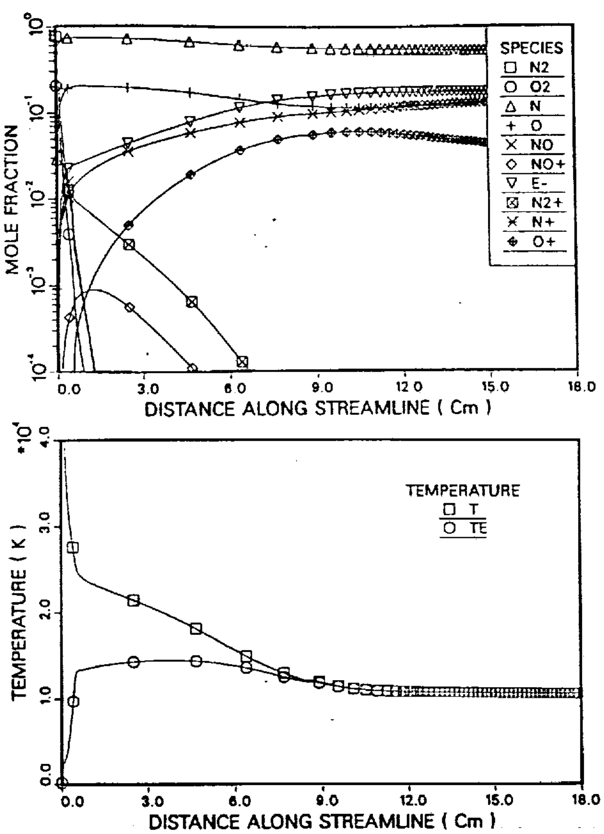

Fig. 6 Species and temperature profiles for air along streamline C, inviscid flow, case 2.

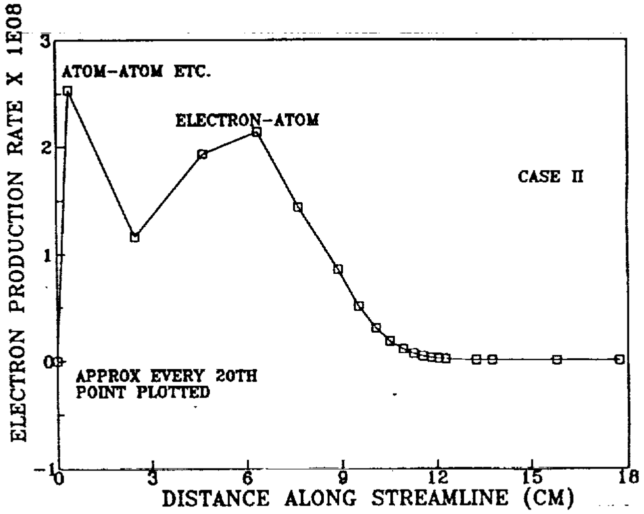

Fig. 7 Electron mass production rate along streamline C, inviscid case 2.

The magnitude of this phenomena is shown in Fig. 5, which portrays the total electron production rate [in g/(cm^3-s)] for this case. Although the plot is somewhat lacking in detail since only approximately every twentieth point is plotted, it can be seen that avalanche starts at about 1 cm along the streamline. Apparently, by this point other ionization reactions have produced sufficient electrons, and the electron temperature has risen sufficiently to permit electron impact ionization to dominate. Both Figs. 4 and 5 indicate that for the case 1 rates the flow equilibrates in about 4.5 cm. It should be noted that the high electron production rate associated with the case 1 impact ionization rates prevents the free electron temperature from peaking and instead leads to its gradual rise until equilibrium is attained.

Inviscid results obtained using the two-step approximate ionization model with case 2 rates are shown for air in Figs. 6

and 7. The [N] and [O] profiles indicate rapid dissociation and are similar to those with the one-step model shown in Fig. 4. Likewise, the peak values for [N_2^+] and [NO^+] are similar but occur slightly later. The electron temperature initially rises to about 14,000 K, after which it remains relatively constant until it equilibrates with the heavy particle temperature. As can be seen by comparing the values in Figs. 7 and 5, the electron production rate for this case is significantly lower than that for the case 1 situation, and as a result the electron temperature is higher over most of the nonequilibrium region.

The biggest difference, however, between the case 1 and case 2 air results is in the behavior and length of the atomic ionization region. After the initial dissociation, the decrease in heavy particle temperature and increase in electron concentration is, by comparison, slow, and equilibrium is not achieved until 11 cm along the streamline. In addition, the [N^+] concentration is significantly higher than the [O^+] value. This latter difference is due to the fact that in this case the equilibrium composition is determined from the equilibrium coefficient computed by partition functions, whereas for the one-step case 1 rates it is specified by the ratio of the forward and reverse rates in Eqs. (2-5). At the present equilibrium temperatures, these two approaches yield equilibrium constants that differ by an order of magnitude, with resultant differences in final composition and temperatures.

In addition, Fig. 7 shows that the electron production rate for the two-step ionization model is different from that for the one-step case. Initially, electrons are created due to NO^+, N_2^+, atom-atom, and atom-ion reactions, and the production from these reactions rapidly peaks and then decreases. However, once [e^-] becomes sufficiently high, electron-atom processes become important, the electron production rate increases, and electron avalanche occurs. However, since the two-step electron-atom ionization rate is less, the process is slower than in the one-step model and the time and distance to equilibrium is longer.

It is believed that these inviscid results demonstrate that predictions of ionization relaxation are strongly dependent on the atomic ionization model and the electron impact ionization rate.

Viscous Results

Using the nitrogen reaction chemistry set given in Table 2, viscous results have been obtained for the stagnation streamline with the modified VSL3DNQ code. In all cases, 99 points have been used between the shock front and the wall, and binary diffusion between molecular and atomic species has been included. Unlike the inviscid solver, which primarily used the partition function approach, the thermodynamic properties in the viscous solutions were computed using the curve fits presented by Gnoffo et al.[40]

Figure 8 shows temperature and concentration profiles for the cool wall case (T_w = 1650 K) for the case 1 electron impact ionization rate. Notice that computational points have been clustered in the region immediately behind the shock front where nonequilibrium effects should be important and in the region near the wall where thermal and concentration gradients could be large. In the outer portion of the shock layer, these results are almost identical to the equivalent inviscid case in that dissociation is rapid behind the shock front, the electron temperature "peaks" and then gradually rises to equilibrate with the heavy particle temperature, and about two-thirds of the shock layer is in chemical equilibrium. In addition, the results show that the cool wall thermal layer affects about 20% of the shock layer and that in this region ion and molecular recombination processes are dominant. For this case the shock standoff distance was 11.8 cm and the computed convective heating rate to the noncatalytic wall was 46.7 W/cm².

Stagnation profiles for the two-step ionization model and the case 2 electron impact ionization are presented in Fig. 9. For the nonequilibrium zone behind the shock front, the dissociation is rapid and N_2^+ rapidly peaks and disappears; two-thirds or more of the shock layer is affected by ionization nonequilibrium relaxation. In addition, the relaxing temperature profile never reaches a constant plateau but smoothly merges into the wall thermal layer. For this case the shock detachment length was 12.0 cm and the convective heating was 44.4 W/cm².

The electron production rate for this cool wall case is presented in Fig. 10. Although there are some differences between this profile and the inviscid curve shown in Fig. 7 due to

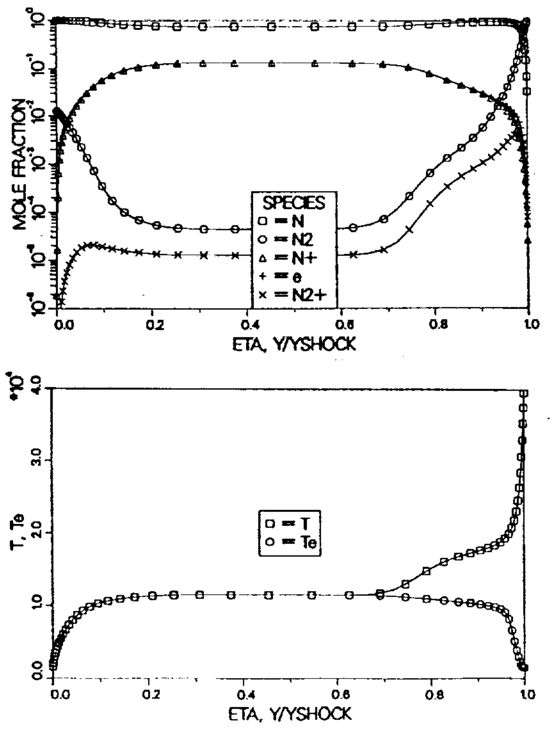

Fig. 8 Stagnation streamline species and temperature profiles, viscous case 1.

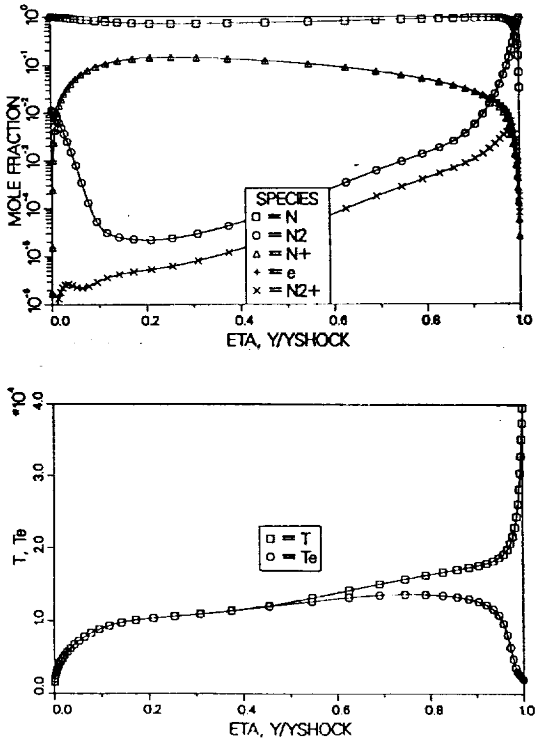

Fig. 9 Stagnation streamline species and temperature profiles, viscous case 2.

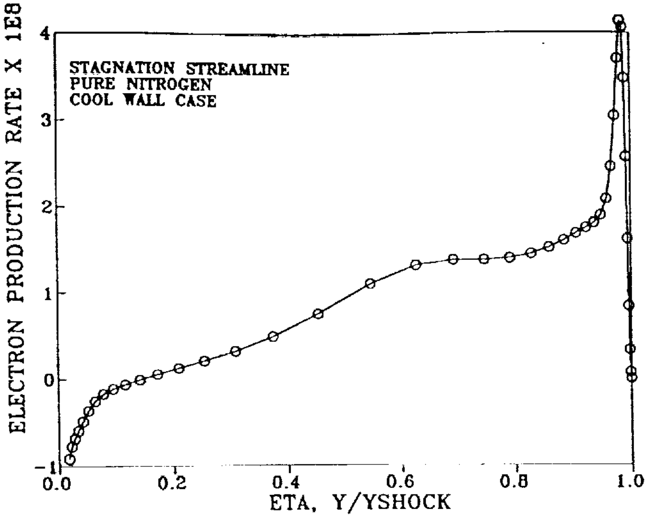

Fig. 10 Stagnation streamline electron mass production rate, viscous flow, case 2.

differences in velocity along and location of the streamlines, the overall pattern is similar. Initially, electron production is high due to N_2^+ ionization, atom-atom, and atom-ion reactions, and then it decreases. Subsequently, electron-atom ionization becomes important, as evidenced by the plateau around y/yshock of 0.8, followed by an approach toward equilibrium. Unlike Fig. 8, no second peak appears in the viscous profile, possibly due to diffusion effects and to the influence of the charge exchange reaction. Also, the electron production rate indicates that an equilibrium region is never achieved along the stagnation streamline, but that the flow simply transitions from an ionizing flow to one involving recombination (negative production rates) in the wall thermal layer.

Obviously, the different species concentration and temperature profiles between the case 1 and case 2 models and rates will greatly influence the predicted radiative heat transfer to the vehicle surface, since radiative heating depends on both electron temperature and species concentrations. However, it also depends on the extent of radiative nonequilibrium or the degree to which the excited state populations are depleted due to ionization. This nonequilibrium has previously been referred to as local thermodynamic nonequilibrium (LTNE) in the discussion concerning the radiation model, and it can be approximately accounted for via LTNE correction factors such as those in Eqs. (28) and (29).

Values for the correction factors for atomic nitrogen radiation are shown in Fig. 11 for both the case 1 and case 2 rates and models. For the one-step case 1 model, the correction factor is small in the chemical nonequilibrium zone, but then it rises rapidly and is essentially unity through the rest of the stagnation layer. Thus, for the one-step impact ionization model most of the shock layer is in local thermodynamic equilibrium radiatively. Similarly, the two-step case 2 factors are also very small in the chemical nonequilibrium zone, but they subsequently increase only slowly, and only very near the body in the wall thermal layer do they become one. Hence, for the case 2 flowfield, radiative nonequilibrium or LTNE effects are very important. Interestingly, when the approximate technique of Ref. 34 is applied to this case, it also predicts that most of the stagnation region is in LTNE.

In examining these results it should be realized that the two-step ionization chemistry and LTNE radiation models are approximate and are the most optimistic from the standpoint of reducing radiation and the rate of ionization, since they assume that the excited states are in equilibrium with the ions and free electrons. In actuality, the rate of ionization from the excited state, Eq. (11), may be finite, and the extent of LTNE indicated by the case 2 results on Fig. 11 may be less. Thus, the two sets of results in Fig. 11 could be viewed as bracketing the problem.

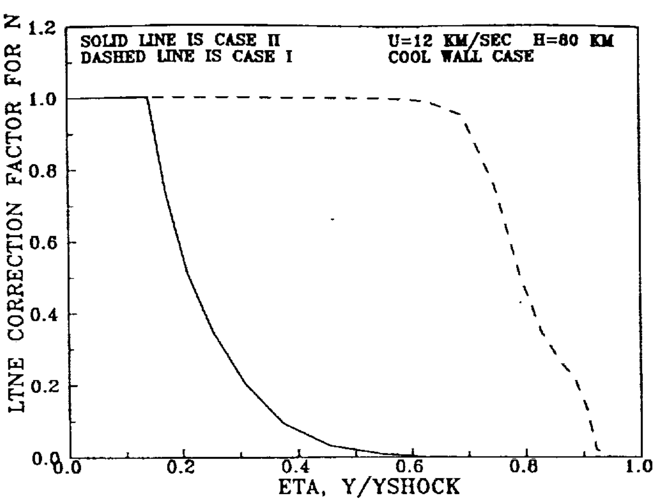

Fig. 11 Nonequilibrium radiation correction factors along stagnation streamline.

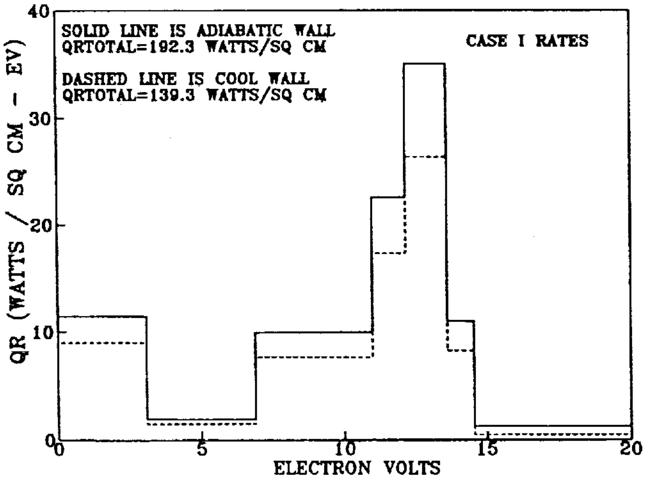

Fig. 12 Stagnation-point radiative heat transfer for case 1.

Stagnation-Point Radiative Heat Transfer

The viscous stagnation streamline nonequilibrium flowfields have been used to compute the radiative heat transfer to the wall. In all cases the wall has been assumed to be nonemitting and nonablating, and results have been obtained for both an adiabatic and the cool wall case. Considering the many factors involved in the current models, these radiative heating results should not be construed as definitive and should be used primarily for comparison purposes and model development until they have been verfied by more detailed models and/or experiments. Nevertheless, these results do include both the ultraviolet and the visible-infrared spectrum, emission and absorption phenomena, the variation of absorption coefficients with wavelength, chemical and thermal nonequilibrium, and radiative nonequilibrium. Thus, the present results include many effects not accounted for in other studies,[8] which assumed the gas cap to be in equilibrium and transparent and only included emission in the visible and infrared (IR) spectrum.

Figures 12 and 13 present stagnation-point radiative heat transfer for the present cases as a function of energy, and several significant points are evident. First, there is an order of magnitude difference in heat transfer both totally and in the individual spectral regions between the one-step case 1 flowfield and the two-step case 2 results. This difference is due to the larger chemical nonequilibrium region predicted by the case 2 rates and the subsequent greater extent of the radiative nonequilibrium zone. Second, for both ionization models most of the radiation reaching the wall for the region below 6.89 eV (above 1800 Å), which is often referred to as the visible region since it is optically visible through quartz and sapphire windows, is in the region below 3.1 eV and is due to IR continuum and lines.

Third, the absorption effects of the cool wall thermal layer may not be as great as previously hoped.[5,8,33] With the present data, the effect of the wall thermal layer can be determined by comparing the cool wall results with the adiabatic wall values. For the case 1 situation in Fig. 12, lowering the wall temperature to 1650 K reduces the overall radiative heating 28%, and in the separate spectral bands the reduction is 22–25%, except for the VUV band from 14.56–31 eV. For that band the reduction is 61%, indicating that the far vacuum ultraviolet is extensively absorbed in the cool wall layer. Likewise, for the case 2 rates, Fig. 13 shows a reduction due to wall cooling of 46% in the total radiative heating. In this case, since the total input is considerably less than that for the one-step model, the thermal boundary layer has more of an effect. In the individual bands the reduction ranges from 39 to 44%, but again in the 14.56–31-eV VUV band the reduction is large (72%). Obviously, for both cases, although a cool wall significantly attenuates the far VUV and somewhat reduces the heating from other regions of the spectrum, significant radiative heat transfer still reaches the wall. This trend is consistent with previous approximate calculations at similar conditions.[34]

Fourth, there is significant radiative heat input to the wall from the spectral region above 6.89 eV (below 1801 Å). In fact, for both ionization models approximately 75% of the total radiative heating is from this region. This result is consistent with what has been observed and predicted for the Fire 2 experiment,[1,33,41] and it is also consistent with the shock-tube experiments of Wood et al.[42] Wood and co-workers conducted measurements with and without a quartz window and determined that 50–75% of the total radiant intensity was from the ultraviolet region of the spectrum. Interestingly, they also concluded from their experiments that a cool boundary layer would not absorb appreciably.

Comparison with Experimental Data

Based on the temperature, species, and radiative heat transfer profiles discussed earlier, it is apparent that the choice of ionization model and electron impact ionization rate greatly affects the resultant predictions, and it would be desirable to determine which model is more appropriate for blunt-body calculations. Although there is almost no radiation experimental data at the present velocity and pressure conditions, Wilson[25] did make measurements of the ionization rate of air behind shock waves having velocities between 9 and 12.5 km/s. By making IR measurements at around 6.1 μ, he was able to determine variations in electron density and thus the ionization relaxation distances.

Consequently, the concentration and temperature profiles for the present inviscid air data along streamline C have been used to compute theoretical IR emission profiles similar to those measured by Wilson for both the case 1 and case 2 models. These profiles are shown in Fig. 14 and have the same general shape as the signals measured by Wilson. Following his procedure the intercept with the equilibrium value of a line drawn through the maximum slope of the rising signal has been used to determine an ionization distance, denoted by the vertical dashed line on the figure, for each ionization model. Then the shock-tube data of Wilson have been used, accounting for differences in freestream pressure and for particle velocity differences behind a normal shock and along streamline C, to determine an experimental ionization distance for the present case. These distances are shown by the square symbols on Fig. 14. The center symbol is the nominal value, whereas the endpoints correspond to the data scatter and error band limits indicated in Ref. 25. As can be seen, the agreement between the shock-tube data and the prediction obtained using the two-step ionization model and the case 2 electron impact ionization rates is very good. Thus, it appears that a two-step ionization model in conjunction with ionization reaction rates based on forward processes should be used for the computation of nonequilibrium blunt-body flowfields associated with Earth aerocapture from Mars.

However, this conclusion does not mean that the ion recombination rates used by Kang et al.[11] or measured by Park[17] are in error. Unfortunately, there are many possible explanations for the observed differences. First, there could be an error in the experimental data[25] or its interpretation to the present problem. Second, at the current electron densities and temperatures, the results of Hinnov and Hirschberg[19] and of Bates et al.[43] indicate that the effective recombination rate is not strictly a function of electron temperature and that radiative recombination is still significant. Thus, the flow may not be totally collision-dominated. In such a situation, if a measured or effective reverse rate were used via an equilibrium constant to determine a forward rate, the resulting forward rate would be too large. As pointed out by Park,[18,44,45] the effective forward and reverse rates are only related via the equilibrium constant if the flow is collision-dominated. Third, there is the possibility[18] that, in the region immediately behind the shock front and due to the time scales involved, the forward and reverse rates are not related by the equilibrium constant and reasonable chemistry can only be predicted using a proper forward rate. Fourth, there exists the possibility that the elec-

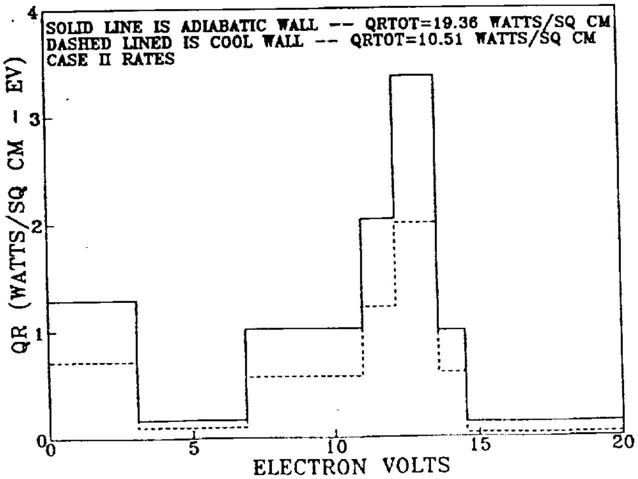

Fig. 13 Stagnation-point radiative heat transfer for case 2.

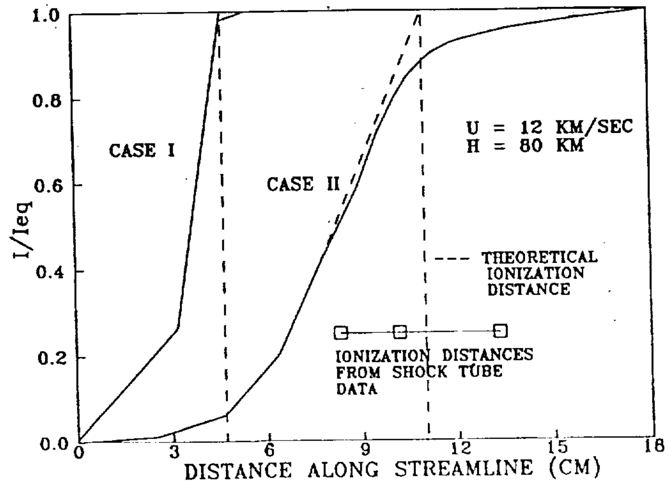

Fig. 14 Theoretical emission profiles and ionization distances for streamline C.

tronic temperatures are not in reality the same as the free electron temperature, and this fact requires the use of a different set of rates. A discussion of this situation and also of the details of atomic ionization are presented in Refs. 45 and 46. Finally, as mentioned previously, there exists the possibility that ionic recombination in a nozzle or arc tunnel is not the direct inverse of atomic ionization behind a shock wave. If anything, the present results indicate the difficulty of creating engineering models for these problems and the need for further analytical and experimental investigation. Nevertheless, based on the results presented here and the reaction rates discussed in Ref. 47, it is believed that the present two-step model with case 2 rates is appropriate for stagnation region computations.

Future Efforts

In the near future there are plans to continue these studies by developing a nonequilibrium radiation model based upon RADICAL. This new model will be incorporated into the VSL code along with radiation gasdynamic coupling. In addition, there exists a need to improve the ionization chemistry model and the LTNE correction factors by taking into account finite-rate processes between excited state atoms and ions. Also, there is a definite need for additional experimental data at velocities and pressures appropriate for a Mars return AOTV. This data should be for an ionizing, as opposed to a recombining, flow and probably could be obtained in a shock tube, although flight data would be desirable. Finally, the inclusion of preshock precursor, photoionization and recombination, and shock and wall slip effects would be desirable.

Conclusion

Based on the results presented, it appears that an approximate two-step ionization model in conjunction with quasiequilibrium electron temperature model is suitable for the computation of nonequilibrium blunt-body flowfields associated with Earth aerocapture from Mars. Also, nonequilibrium chemical and radiation effects are important at these conditions throughout the entire stagnation zone, and, compared to equilibrium predictions, these nonequilibrium phenomena can lead to a reduction in radiative heating. Furthermore, compared to an adiabatic wall, a cool wall results in a significant reduction in radiative heating due to absorption near the wall. However, the present results also indicate a need for further analytical and experimental investigations.

Acknowledgments

The authors gratefully acknowledge the assistance of the Associate Provost for Computing for providing a portion of the computational resources used in this effort. This work was initiated under a subportion of NASA Grant NAG 9-192 from the NASA Johnson Space Center (JSC). The authors thank the technical monitor, Carl Scott, Aerosciences Branch, JSC, for his suggestions, and Ken Sutton, Aerothermodynamics Branch, NASA Langley Research Center, for his comments and assistance in providing the RADICAL and VSL3DNQ programs. T. A. Gally is partially supported by a NASA Graduate Student Researchers Fellowship through the NASA Johnson Space Center.

References

[1] Sutton, K., "Air Radiation Revisited," *Progress in Astronautics and Aeronautics: Thermal Design of Aeroassisted Orbital Transfer Vehicles,* Vol. 96, edited by H. F. Nelson, AIAA, New York, 1985, pp. 419–441.

[2] Moss, J. N., Bird, G. A., and Dogra, V. K., "Nonequilibrium Thermal Radiation for an Aeroassist Flight Experiment Vehicle," AIAA Paper 88-0081, Jan. 1988.

[3] Gnoffo, P. A., and Green, F. A., "A Computational Study of the Flowfield Surrounding the Aeroassist Flight Experiment Vehicle," AIAA Paper 87-1575, June 1987.

[4] Park, C., "Assessment of Two Temperature Kinetic Model for Ionizing Air," AIAA Paper 87-1574, June 1987.

[5] Candler, G., and Park, C., "The Computation of Radiation from Nonequilibrium Hypersonic Flows," AIAA Paper 88-2678, June 1988.

[6] Carlson, L. A., Bobskill, G. J., and Greendyke, R. B., "Comparison of Vibration Dissociation Coupling and Radiative Heat Transfer Models for AOTV/AFE Flowfields," AIAA Paper 88-2673, June 1988.

[7] Li, C. P., and Wey, T.C., "Numerical Simulation of Hypersonic Flow Over an Aeroassist Flight Experiment Vehicle," AIAA Paper 88-2675, June 1988.

[8] Park, C., and Davies, C. B., "Aerothermodynamics of Manned Mars Mission," AIAA Paper 89-0313, Jan. 1989.

[9] Grosse, W. L., "A Thin Shock Layer Solution for Nonequilibrium, Inviscid Flows in Earth, Martian, and Venusian Atmospheres," NASA TN D-6529, Dec. 1971.

[10] Thompson, R. A., "Comparison of Nonequilibrium Viscous Shock Layer Solutions with Windward Surface Shuttle Heating Data," AIAA Paper 87-1473, June 1987.

[11] Kang, S. W., Jones, W. L., and Dunn, M. G., "Theoretical and Measured Electron Density Distributions at High Altitudes," *AIAA Journal,* Vol. 11, No. 2, 1973, pp. 141–149.

[12] Zeldovich, Y. B., and Raizer, Y. P., *Physics of Shock Waves and High Temperature Hydrodynamic Phenomena,* Academic, New York, 1966, pp. 407–413.

[13] Makin, B., and Keck, J. C., "Variational Theory of Three-Body Electron Ion Recombination Rates," *Physical Review Letters,* Vol. 11, No. 6, Sept. 15, 1963, pp. 281–283.

[14] Dunn, M. G., "Measurement of $C^+ + e^- + e^-$ and $CO^+ + e^-$ Recombination in Carbon Monoxide Flows," *AIAA Journal,* Vol. 9, No. 11, 1971, pp. 2184–2191.

[15] Dunn, M. G., and Lordi, J. A., "Measurement of $O_2^+ + e^-$ Dissociative Recombination in Expanding Oxygen Flows," *AIAA Journal,* Vol. 8, No. 4, 1970, pp. 614–618.

[16] Dunn, M. G., and Lordi, J. A., "Measurement of $N_2^+ + e^-$ Dissociative Recombination in Expanding Nitrogen Flows," *AIAA Journal,* Vol. 8, No. 2, 1970, pp. 339–345.

[17] Park, C., "Measurement of Ionic Recombination Rate of Nitrogen," *AIAA Journal,* Vol. 6, No. 11, 1968, pp. 2090–2094.

[18] Park, C., "Collisional Ionization and Recombination Rates of Atomic Nitrogen," *AIAA Journal,* Vol. 7, No. 8, 1969, pp. 1653–1654.

[19] Hinnov, E., and Hirschberg, J. G., "Electron-Ion Recombination in Dense Plasmas," *Physical Review,* Vol. 125, No. 3, 1962, pp. 795–801.

[20] Nelson, H. F., and Goulard, R., "Structure of Shock Waves with Nonequilibrium Radiation and Ionization," *Physics of Fluids,* Vol. 12, No. 8, 1969, pp. 1605–1617.

[21] Chapin, C. E., "Nonequilibrium Radiation and Ionization in Shock Waves," Purdue Univ., Lafayette, IN, AA&ES Rept., June 1967.

[22] Foley, W. H., and Clarke, J. H., "Shock Waves Structured by Nonequilibrium Ionizing and Thermal Phenomena," *Physics of Fluids,* Vol. 16, No. 3, 1973, pp. 373–383.

[23] Vinolo, A. R., and Clarke, J. H., "Interrelated Structures of the Transport Shock and Collision Relaxation Layer in a Multitemperature, Multilevel Ionized Gas," *Physics of Fluids,* Vol. 16, No. 10, 1973, pp. 1612–1620.

[24] Zeldovich, Y. B., and Raizer, Y. P., *Physics of Shock Waves and High Temperature Hydrodynamic Phenomena,* Academic, New York, 1966, pp. 382–396, 505–515.

[25] Wilson, J., "Ionization Rate of Air Behind High Speed Shock Waves," *Physics of Fluids,* Vol. 9, No. 10, 1966, pp. 1913–1921.

[26] Carlson, L. A., "Radiative Gasdynamic Coupling and Nonequilibrium Effects Behind Reflected Shock Waves," *AIAA Journal,* Vol. 9, No. 5, 1971, pp. 858–865.

[27] Petschek, H., and Byron, S., "Approach to Equilibrium Ionization Behind Strong Shock Waves in Argon," *Annals of Physics,* Vol. 1, No. 3, 1957, pp. 270–315.

[28] Dix, D. M., "Energy Transfer Processes in a Partially Ionized Two Temperature Gas," *AIAA Journal,* Vol. 2, No. 12, 1964, pp. 2081–2090.

[29] Dix, D. M., "The Governing Macroscopic Equations of Partially Ionized Gases," Aerospace Corporation Rept. TDR-69-2330-04 TN-2, July 1962.

[30] Lee, J. H., "Basic Governing Equations for the Flight Regimes of Aeroassisted Orbital Transfer Vehicles," *Progress in Astronautics and Aeronautics: Thermal Design of Aeroassisted Orbital Transfer Vehicles,* Vol. 96, edited H. F. Nelson, AIAA, New York, 1985, pp. 3–53.

[31]Carlson, L. A., "Radiative Cooling and Nonequilibrium Chemistry Coupling Behind Normal Shock Waves," *AIAA Journal*, Vol. 10, No. 2, 1972, pp. 230–232.

[32]Tiwari, S. N., and Szema, K. Y., "Effects of Precursor Heating on Radiative and Chemically Reacting Viscous Flow Around a Jovian Entry Body," NASA CR-3186, Oct. 1979.

[33]Gupta, R. N., "Navier Stokes and Viscous Shock Layer Solutions for Radiating Hypersonic Flows," AIAA Paper 87-1576, June 1987.

[34]Carlson, L. A., "Approximations for Hypervelocity Nonequilibrium Radiating, Reacting, and Conducting Stagnation Regions," AIAA Paper 88-2672, June 1988.

[35]Carlson, L. A., and Rieper, R. G., "Electron Temperature and Relaxation Phenomena Behind Shock Waves," *Journal of Chemical Physics*, Vol. 57, No. 2, 1972, pp. 760–766.

[36]Carlson, L. A., "Expressions for the Exchange of Energy and Momentum Between Gases at Different Temperatures and Velocities," *Physics of Fluids*, Vol. 13, No. 7, 1970, pp. 1869–1870.

[37]Olstad, W. B., "Nongray Radiating Flow about Smooth Symmetric Bodies," *AIAA Journal*, Vol. 9, No. 1, 1971, pp. 122–130.

[38]Nicolet, W., "User's Manual for the Generalized Radiation Transfer Code (RAD/EQUIL)," NASA CR-116353, Oct. 1969.

[39]Greendyke, R. B., Private Communication, Analytical Methods and Services Corp., Hampton, VA, 1989.

[40]Gnoffo, P. A., Gupta, R. N., and Shinn, J., "Governing Equations and Physical Models for Hypersonic Air Flows in Thermal and Chemical Nonequilibrium," NASA TP-2867, 1989.

[41]Bird, G. A., "Nonequilibrium Radiation During Reentry at 10 km/sec," AIAA Paper 87-1543, June 1987.

[42]Wood, A. D., Hoshizaki, H., Andrews, J. C., and Wilson, K. H., "Measurements of the Total Radiant Intensity of Air," *AIAA Journal*, Vol. 7, No. 1, 1969, pp. 130–139.

[43]Bates, D. R., Kingston, A. E., and McWhirter, R. W. P., "Recombination Between Electrons and Atomic Ions. I. Optically Thin Plasmas," *Proceedings of the Royal Society of London, Series A*, Vol. 267, No. 1330, 1962, pp. 297–312.

[44]Park, C., "Spectral Line Intensities in a Nonequilibrium Nitrogen Plasma," *Journal of Quantitative Spectroscopy and Radiative Transfer*, Vol. 8, No. 10, 1968, pp. 1633–1653.

[45]Park, C., "Comparison of Electron and Electronic Temperatures in Recombining Nozzle Flow of Ionized Nitrogen-Hydrogen Mixture. Part 1. Theory," *Journal of Plasma Physics*, Vol. 9, No. 2, 1973, pp. 187–215.

[46]Kunc, J. A., and Soon, W. H., "Nonequilibrium of High Temperature Nitrogen and Oxygen," AIAA Paper 88-2779, June 1988.

[47]Park, C., "A Review of Reaction Rates in High Temperature Air," AIAA Paper 89-1740, June 1989.

AIAA 91-1463

A Flowfield Coupled Excitation and Radiation Model for Nonequilibrium Reacting Flows

T. A. Gally, L. A. Carlson, and D. Green
Texas A&M University
College Station, Texas

AIAA 22nd Fluid Dynamics, Plasma Dynamics & Lasers Conference
June 24-26, 1991 / Honolulu, Hawaii

A Flowfield Coupled Excitation and Radiation Model for Nonequilibrium Reacting Flows

Thomas A. Gally*, Leland A. Carlson**
and
Derek Green†
Texas A&M University
College Station, Texas

Abstract

A second order method has been developed to correct a radiative transfer analysis for possible local thermodynamic nonequilibrium effects. This method uses a two species excitation model for nitrogen with chemical reaction rates obtained from the detailed atomic transition method of Kunc and Soon. Results obtained from this new method show more atomic line radiation that the authors' previous first order method. As improvements to the flowfield representation used in the computations, a full three temperature energy model has also been incorporated and a new multicomponent diffusional model developed.

Nomenclature

B_ν = black body function
c_p = specific heat at constant pressure
D = dissociation energy
$\mathcal{D}$ = binary diffusion coefficient
e = energy per unit mass
E = electronic state energy level
E_n = integro-exponential function of order n
$\mathcal{E}$ = electostatic field strength
F = external force per unit mass
g = degeneracy
h = enthalpy per unit mass
I = ionization energy
k = Boltzmann constant
K = absorption coefficient
m = particle mass
N = number density
p = pressure
q_r = radiative heat flux
Q = electronic partition function
Q_e = electron translational partition function
r = wall reflectivity
S = source function
T = temperature
u^j = mass averaged velocity components
U = diffusion velocity
x^j = coordinate axis
Z = Molecular charge
α = wall absorptivity
ϵ = wall emissivity
ε = magnitude of electron charge
η = heat conduction coefficient
ρ = density
σ = radiative cross section
τ = relaxation time
τ_ν = optical thickness
ν = frequency

subscripts

e = electron
f = forward rate (production)
pc = continuum process
pq = line process
r = reverse rate (depletion)
s, t = species
sh = value at shock
tr = translational
v = vibrational
w = value at wall
ν = frequency

Introduction

A great deal of interest has been placed recently on the design of aerobraking vehicles for use with both inter-orbit maneuvering and inter-planetary deceleration. In particular, a major goal of such experimental projects as the Aeroassist Flight Experiment (AFE) is the development of the computational tools for the accurate prediction of the aerodynamic environment which determines the heating and controllabilty of such vehicles. Both low speed inter-orbit and high speed inter-planetary missions will spend the aerobraking portion of their trajectories at very high, low density altititudes where previously developed space vehicles spent only short durations. Thus, the computational aerodynamic tools to be used must correctly handle the chemical, thermal and radiative nonequilibrium phenomena associated with low-density flows.

Previous work[1,2] concentrated on some aspects of the nonequilibrium nature of aerobraking flowfields. For example, the primary topic of discussion in Ref. 1 was electron-impact ionization rates. This chemical rate is important in both determining the amount of chemical nonequilibrium in the flow and in calculating the electron temperature, T_e. Existing rates in the literature varied over several orders of magnitude with accompanying differences in T_e profiles and wall radiative heating rates, which is a strong function of T_e. In Ref.2, the effects

---

* NASA Graduate Student Researcher, Student Member
** Professor Aerospace Engineering, Associate Fellow AIAA
† Graduate Research Assistant

of thermodynamic nonequilibrium on the magnitude and nature of the radiative environment was investigated. Comparisons were made with the FIRE II flight test measurements and a wide range of possible mission profile conditions were investigated.

A number of topics for future work were identified from the previous work. First, a two-temperature, T_{tr} and T_e, model had been used exclusively in Refs. 1 and 2, in which it was assumed that $T_v = T_{tr}$. This model is probably accurate for the higher speed conditions above 12 km/sec where the flow is ionization dominated and few diatomic particles exist. However, at the lower speeds and particularly for the speeds associated with the AFE vehicle, the flowfield is dissociation dominated; and a separate vibrational energy equation can be expected to affect the total results. In addition, electron-vibrational coupling will affect the predicted T_e profile and thus the radiative environment. Second, diffusional phenomena seemed to significantly affect chemical nonequilibrium and also the extent of atomic thermodynamic nonequilibrium. Since the diffusional model then being used was determined to be inadequate, a new model was developed as described later. Finally, a new atomic local second order thermodynamic nonequilbrium model was conceived, which is a compromise between the simple and fast method used previously and the complex methods used by other authors.

Problem Formulation

The computational model used in this report is an extension of the coupled viscous shock layer (VSL) and radiative transfer method described in detail in Refs. 1 and 2. The VSL portion of the code originated as the VSL3DNQ[3] code developed at NASA Langley. After modifications were made to the thermodynamic and transport coefficient calculations and multi-temperature effects, T_{tr} and T_e, were included, the flowfield was iteratively coupled with the radiative transfer model of Nicolet[4] in a manner which included chemical and local thermodynamic nonequilibrium (LTNE) phenomena.

Three additional modifications have been made for the present paper. First, a vibrational energy equation has been added for the calculation of a third temperature, T_v, which describes the average vibrational energy state of all the diatomic species. Second, a new diffusional model has been developed to improve the calculation of the diffusional fluxes of mass and energy. Finally, to improve LTNE predictions, second order radiative correction factors similar to those used in Refs. 1 and 2 have been devolped for a two-step excitation model for atomic nitrogen.

Vibrational Temperature Model

The vibrational energy equation added to the VSL calulations has the following form for simple Cartesian coordinates.

$$\rho u^j c_{p_v} \frac{\partial T_v}{\partial x^j} = \frac{\partial}{\partial x^j}\left(\eta_v \frac{\partial T_v}{\partial x^j}\right) + \sum_s \rho_s U_s \frac{\partial h_{v_s}}{\partial x^j} \qquad (1)$$

$$+ \sum_s \rho_s A \frac{(e_{v_s}(T_{tr}) - e_{v_s})}{\tau_s} + \sum_s \rho_s \frac{(e_{v_s}(T_e) - e_{v_s})}{\tau_{e,s}}$$

$$+ \sum_s (e_{v_s} - E_s)\left(\frac{\partial \rho_s}{\partial t}\right)_f - \sum_s (e_{v_s} - G_s)\left(\frac{\partial \rho_s}{\partial t}\right)_r$$

In this equation, c_{p_v} is the frozen vibrational specific heat at constant pressure calculated from the species specific heats by $\sum_s c_{p_{v,s}} \rho_s/\rho$; and the vibrational termperature, T_v, represents the average vibrational energy of all the diatomic species. While multiple vibrational temperatures are often used, one for each vibrating species, it can be argued[5] that the vibrational-vibrational energy exchange rates are not well modeled by available methods; and, thus, results with multiple vibrational termparatures may not be meaningful. In addition, for the results with a nitrogen only gas presented in this report, there is only one dominant vibrator, N_2, the vibrational contribution from $N^+{}_2$ being small.

The translational-vibrational energy exchange model used is a modification of the non-preferential CVDV model described in Refs. 6 and 7. The terms involved with the $T_{tr} - T_v$ coupling model are the third, fifth and sixth on the right hand side of Eq. 1. The differences from the CVDV model occur, first, in the calculation of the relaxation time, τ_s. This relaxation time is that proposed by Park[8] which sums the relaxation time of Millikan and White[9], τ_s^{MW}, with a high temperature correction factor such that

$$\tau_s = \tau_s^{MW} + \frac{1}{c_s \sigma_v N_s}$$

where c_s is the average species molecular speed and σ_v is a limiting cross section calculated by[10]:

$$\sigma_s = 10^{-17}(50,000^\circ K/T_{tr})^2 \mathrm{cm}^2.$$

The second modification, also suggested by Park[10], is the inclusion of the multiplier A on the third right hand side term of Eq. 1. This multiplier attempts to correct the original Landau and Teller relaxation rate for high temperature diffusive effects and has the form

$$A = \left|\frac{T_{tr,sh} - T_v}{T_{tr,sh} - T_{v,sh}}\right|^{(3.5\, exp(-5000^\circ K/T_v) - 1)}.$$

The electron-vibrational energy exchange is accounted for by the fourth right hand side term of Eq. 1 and is taken from the work of Lee[11] as curve fitted by Candler and Park[12]:

$$log(p_e \tau_e) = 7.50(log\, T_e)^2 - 57.0\, log\, T_e + 98.70$$

for $T_e < 7000^\circ K$, and

$$log(p_e \tau_e) = 2.36(log\, T_e)^2 - 17.9\, log\, T_e + 24.35$$

for $T_e \geq 7000^\circ K$.

Lee suggests a correcting factor for the electron-vibrational relaxation similar to the factor A used for translational-vibrational relaxation. As with the translation-vibrational relaxation factor, this term is intended to increase the relaxation time or decrease the amount of coupling between the electron energy and vibrational energy. Unfortunately the form of the correction, developed for the case were T_e and T_v are initially far apart, has the opposite effect for our conditions where T_e and T_v are initially close together in value behind the shock. For this reason, the suggested correction has not been included in the present model and the calculated results may tend to show too much electron-vibrational coupling.

The electron-vibrational coupling factor must also be included in the electron temperature equation, which for this paper is the full electron/electronic energy equation described in Ref. 2. The electron/electronic energy equation is similar in form to Eq. 1 and includes the effects of conduction, convection, diffusion, chemical energy depletion, heavy particle-electron translation coupling, and now electron-vibrational coupling.

Diffusional Model

In the stagnation region of a blunt entry vehicle, large gradients in species concentration occur in the nonequilibrium region behind the shock front and in the thermal boundary layer near the wall. As a result, diffusion effects in these regions are generally important and need to be considered in the evaluation of mass and energy flux. There are currently a number of diffusional models commonly used including the multi-component models used by Moss[13] and Gnoffo et al.[14], the binary model[15] based upon the work of Fay and Kemp[16,17], and the constant Lewis number multi-component approximation of Ref. 18. The latter is the method originally incorporated into our VSL code.

While diffusional effects play an important role in the level of chemical nonequilibruim which can occur behind a shock wave, they can be seen most easily in the near wall, thermal boundary layer of most reentry flows. Although the flow in this region is at low normal velocities and the density is much greater than the other portions of the shock layer, the flow is typically not in equilibrium in this region; and in fact a significant level of dissociation is present on the surface of non-catalytic walls no matter how cool the surface may be. For catalytic walls, the associated high heating rates are due the diffusive flux of energy to the wall as a result of the large concentration gradients. In addition, due to the chemical nonequilibrium induced by diffusional effects, the simple atomic LTNE model used in the radiative analysis is also strongly affected by the amount of diffusion. As a result, a more accurate diffusional model has been developed and incorporated into the flowfield model. The development of this model follows.

If the effects of presure and thermal diffusion are neglected, the general diffusion velocity equation for a multicomponent gas is[19] for each species

$$\sum_t \frac{x_s x_t}{\mathcal{D}_{st}}(U_t - U_s) = \nabla x_s - \frac{\rho_s F_s}{p} + \frac{\rho_s}{\rho p}\sum_t \rho_t F_t. \quad (2)$$

In these equations, $\mathcal{D}_{st}$ is, to a first approximation, the binary diffusion coefficient for species s into species t, and F_s represents external forces acting upon species s. Note that while the above equations were obtained by Chapman and Cowling[19] for a single temperature gas (primarily due to the fact that the first approximation of Enskog for the Bolzmann equation assumes equilibrium between particles), a simple extension for multi-temperatures can be made if the pressure and concentrations are calculated using multi-temperature methods and the diffusion coefficients are determined using the appropriate temperatures. For the present method, T_e is used to calculate $\mathcal{D}_{st}$ if either of the colliding partners is an electron and T is used for heavy particle encounters.

If the externally applied force term is set equal to the electrostatic force due to charge separation, then $F_s = e\mathcal{E}Z_s/m_s$ and if charge separation is not large, it is approximately true that $\sum_t \rho_t F_t = 0$. Eq. 2 then becomes

$$\sum_t \frac{x_s x_t}{\mathcal{D}_{st}}(U_t - U_s) = \nabla x_s \quad (3)$$

for neutral particles and

$$\sum_t \frac{x_s x_t}{\mathcal{D}_{st}}(U_t - U_s) = \nabla x_s - \frac{N_s e\mathcal{E}Z_s}{p} \quad (4)$$

for ions and electrons. For most conditions of interest, the flowfield can be adequately described by only including singly charged positive ions in the flowfield chemistry model. In this case, to each ion diffusion equation there can be added N_s/N_e times the electron diffusion equation in order to eliminate the electrostatic force terms. The resulting ion diffusion equations are

$$\sum_t \frac{x_s x_t}{\mathcal{D}_{st}}(U_t - U_s) + \sum_t \frac{x_s x_t}{\mathcal{D}_{et}}(U_t - U_e) = \nabla x_s + \frac{N_s}{N_e}\nabla x_e. \quad (5)$$

To avoid the difficulty of specifying the strength of the electrostatic field, $\mathcal{E}$, in the electron diffusion equation, the ambipolar assumption is made that

$$\sum_{t=ions} N_t U_t = N_e U_e. \quad (6)$$

Note that this is not an assumption that the electrostatic term is small or zero, but rather that the electrostatic force for small charge separations is sufficiently large enough to cause the electrons to diffuse with an ion.

The original set of diffusional equations (Eq. 2) can easily be shown to be linear dependent; and an additional condition that the total diffusional mass flux be zero must also be used, i.e.

$$\sum_t \rho_t U_t = 0 \quad (7)$$

which replaces one of the original set. After the ambipolar assumption is used, the new set of equations (Eq. 3 for neutrals, Eq. 5 for ions, and Eq. 6 for electrons) are not strictly linear dependent, but are very poorly conditioned. Eq. 7 should still be used to replace one of the neutral or ionic equations.

For this paper, an additional simplification is used based upon the observation that since $U_s \sim U_e$ and $\mathcal{D}_{es} \gg \mathcal{D}_{st}$ for $t \neq e$, the neutral and ionic equations can be approximated by, respectively,

$$\sum_{t \neq e} \frac{x_s x_t}{\mathcal{D}_{st}}(U_t - U_s) = \nabla x_s$$

$$\sum_{t \neq e} \frac{x_s x_t}{\mathcal{D}_{st}}(U_t - U_s) = \nabla x_s + \frac{N_s}{N_e}\nabla x_e.$$

The above set is linear dependent which, with the two additional conditions of ambipolar diffusion and zero total diffusional mass flux, Eqs. 6 and 7, can be solved for all of the diffusional velocities, U_s.

Second Order Atomic LTNE Model

The flowfield solution is coupled with the radiative transport package of RADICAL[4] developed by Nicolet. The methods used by Niclolet assume that the electronic states of the radiating species are in local thermodynamic equilibrium (LTE) with each other and that their populations can be described by a Bolzmann distribution. A technique was developed previously[1,2] for correcting the RADICAL calculations to account for LTNE in both the atomic and molecular state populations.

The molecular electronic states populations are calculated using a quasi-steady approach similar to that described in Ref. 10; and, from these, LTNE population correction factors for the principle molecular radiation bands are obtained. Specifically, correction factors are determined for the N_2 Birge-Hopfield, first positive, and second positive bands, and for the N_2^+ first negative band. Ref. 2 should be consulted for more detail.

Also discussed in Ref. 2 is a first order atomic LTNE radiation correction. This model is predicated on the observation that for many monatomic gases, including argon, nitrogen, and oxygen, there exist one or more low lying ground energy states separated from the lowest excited energy state by an energy jump which is a large fraction of the ionization energy from the ground state. The model assumes that the excitation jump from ground to first excited state controls the ionization process, and that the excited states, because of their proximity in energy to the ionized state, are in equilibrium with the free electrons and ions. With this approach, the atomic nitrogen LTNE correction factor[1,2,20], which represents the ratio of the actual population in an excited state to that which would exist for a Boltzmann distribution, can be written as

$$\frac{N_{N+} N_e Q_N \, exp(169000^\circ K/T_e)}{N_N Q_{N+} Q_e}.$$

The above assumptions and resulting approximation are extremely simple to calculate and implement. At the other end of the spectrum are the methods of Park[8] and Kunc and Soon[21] which handle possible LTNE effects by performing detailed state population calculations under the quasi-steady assumption. Park's and Kunc's methods differ in the treatment of the free electrons and ions; Kunc et al. allow the free ions and electron populations to be determined as part of the solution, allowing LTNE to occur only as a consequence of radiative state depletion, while Park uses the ion and electron population calculated from the flowfield solution, allowing nonequilibrium chemistry to affect bound state populations. Either way, the detailed methods are computationally intensive and are not suitable for a radiative coupled solution if computational usage is a consideration.

After extensively reviewing the work on argon of Foley and Clarke[22] and Nelson[23] and the air and nitrogen work of Park[8], Kunc and Soon[21], and others, it was decided to develop a second order LTNE model for high temperature nitrogen by subdividing atomic nitrogen into two species. The first, termed N_g, for N ground, represents the nitrogen atoms in the first three low lying electronic states of nitrogen. The second, termed N^* or N excited, represents those nitrogen atoms populating the remaining upper electronic states. The relative densities of these subspecies will then be determined by appropriate reaction rates between themselves, N^+, e^-, etc and the electronic states of each are assumed to be in local thermodynamic equilibrium (LTE). It is believed that this approach has the potential to be a significant improvement over the present model in that it will allow a finite rate of ionization from excited states while retaining the fundamental two step ionization process. In addition, by determining the excited state number densities directly from the flowfield computation, the appropriate atomic LTNE factors are directly obtainable and more accurate.

The thermodynamic state of the two species, N_g and N^*, are determined by the standard methods used for monoatomic gases:

$$Q_{N_g} = \sum_{p=1}^{3} g_p e^{-E_p/kT_e}$$

$$Q_{N^*} = \sum_{p=4}^{max} g_p e^{-(E_p - E_4)/kT_e}$$

$$Q_N = Q_{N_g} + Q_{N^*} e^{-E_4/kT_e}$$

$$h_{N_g} = \frac{5}{2}\frac{kT}{m_N} + \frac{1}{m_N Q_{N_g}} \sum_{p=1}^{3} g_p E_p e^{-E_p/kT_e} + h^\circ_{N_g}$$

$$h_{N^*} = \frac{5}{2}\frac{kT}{m_N} + \frac{1}{m_N Q_{N^*}} \sum_{p=4}^{max} g_p (E_p - E_4) e^{-(E_p - E_4)/kT_e} + h^\circ_{N^*}$$

where the zero point energies are, $h^\circ_{N_g} = h^\circ_N = 3.36 \times 10^{11}$ ergs/gm and $h^\circ_{N^*} = h^\circ_{N_g} + E_4/m_N = 1.05 \times 10^{12}$ ergs/gm. The collision cross sections for both species, needed to calculate viscous transport properties, are assumed to be the same as for the original gas, N.

As mentioned earlier, new reactions must be specified to relate the two new species, N_g and N^*. These reactions are:

$$N_g + e^- = N^* + e^-$$
$$N_g + e^- = N^+ + 2e^-$$
$$N^* + e^- = N^+ + 2e^-$$

It was decided to use the method for calculating detailed excitation rates given in Ref. 21. A computer program was written which calculated the individual rates for each allowed transition process and computed effective rates for the above reaction equations assuming local thermodynamic equilibrium exists between the excited states grouped into each species. Results were obtained for a number of electron temperatures and then curve fit as shown in Fig. 1. These rates are part of the complete chemical reaction set shown in Table 2.

The radiative transport model must also be modified to account for the LTNE populations of N_g and N^* relative to each other. Under the assumption of a radiating tangent slab, the heat flux to a surface can be calculated as, assuming a non-emitting precursor:

$$-q_{r_\nu}(x) = 2\pi \int_0^{\tau_{\nu,sh}} sgn(t_\nu - \tau_\nu) S_\nu E_2(|t_\nu - \tau_\nu|) dt_\nu$$
$$- 2E_3(\tau_\nu)\pi \left(\epsilon_w B_{\nu,w} - 2\tau_w \int_0^{\tau_{\nu,sh}} E_2(t_\nu) S_\nu dt_\nu \right)$$

where τ_ν is the optical thickness determined by

$$\tau_\nu = \int_0^x K_\nu dy.$$

The absorption and source functions used in these expressions are the sum of all radiative contributs at the frequency ν.

Absorption coefficients derived from either theory or experiment are normally expressed as the product of the absorbing state number density and a radiative cross section:

$$K_{\nu_{pc}} = N_p \sigma_{pc}(\nu)$$

or by assuming a Bolzmann distribution exists between the electronic states,

$$(K_{\nu_{pc}})_{LTE} = N_N \left(\frac{g_p e^{-E_p/kT_e}}{Q_N} \sigma_{pc}(\nu) \right) = N_N \sigma'_{pc}(\nu).$$

Thus, an absorption coefficient using the actual state number density, N_p, can be obtained from one calculated assuming LTE by

$$K_{\nu_{pc}} = \frac{N_p}{(N_p)_{LTE}} (K_{\nu_{pc}})_{LTE}$$

where

$$\frac{N_p}{(N_p)_{LTE}} = \frac{N_p}{N_N} \frac{Q_N}{g_p e^{-E_p/kT_e}}$$

It is desired to have the LTNE corrections in terms of the known number density populations, N_g and N^*. If state p is one of the low lying states and since we have assumed these states are in LTE each other,

$$N_p = N_g \frac{g_p e^{-E_p/kT_e}}{Q_{N_g}}$$

and

$$\frac{N_p}{(N_p)_{LTE}} = \frac{N_{N_g}}{N_N} \frac{Q_N}{Q_{N_g}} = \frac{N_{N_g}}{(N_{N_g})_{LTE}}$$

Similarly, if p is one of the excited states,

$$N_p = N^* \frac{g_p e^{-(E_p - E_*)/kT_B}}{Q_{N^*}}$$

and

$$\frac{N_p}{(N_p)_{LTE}} = \frac{N_{N^*}}{N_N} \frac{Q_N}{Q_{N^*} e^{-E_*/kT_e}} = \frac{N_{N^*}}{(N_{N^*})_{LTE}}$$

The absorption coefficient for atomic line radiation is similar in form to that for the continuum process, but uses a radiative cross section which is a function of both the absorbing, p, and the emitting state, q.

$$K_{\nu_{pq}} = N_p \sigma_{pq}(\nu)$$

However, since the number density dependence is only with the absorbing state, the LTNE corrections described above for continuum radiation also apply to the line radiation.

The source function at thermodynamic equilibrium is equal to the black body, B_ν.

$$(S_{\nu_{pc}})_{LTE} = (S_{\nu_{pq}})_{LTE} = B_\nu = \frac{2h\nu^3}{c^2} (e^{h\nu/kT_e} - 1)$$

The source function for atomic continuum processes under LTNE conditions is given by[24,25]:

$$S_{\nu_{pc}} = \frac{(N_p)_E}{N_p} \frac{2h\nu^3}{c^2} \left(e^{h\nu/kT_e} - \frac{(N_p)_E}{N_p} \right)^{-1}$$
$$= \frac{(N_p)_E}{N_p} \frac{e^{h\nu/kT_e} - 1}{e^{h\nu/kT_e} - \frac{(N_p)_E}{N_p}} (S_{\nu_{pc}})_{LTE}$$

where the subscript E indicates a number density for state p calculated by assuming that state is in thermodynamic equilibrium with the free electrons and ions. Thus, if I is the ionization energy,

$$(N_p)_E = N_{N^+} N_e \frac{g_p e^{-(E_p - I)/kT_e}}{Q_{N^+} Q_e}$$

It can further be observed that when p is a low lying state $e^{h\nu/kT_e} \gg (N_p)_E/N_p$ and $e^{h\nu/kT_e} \gg 1$ while for the highly excited states, $(N_p)_E/N_p \simeq 1$. Thus

$$S_{\nu_{pc}} \simeq \frac{(N_p)_E}{N_p}(S_{\nu_{pc}})_{LTE}$$

As before, the LTNE correction can be written in term of the known number densities so that if p is one of the ground states,

$$\frac{(N_p)_E}{N_p} = \frac{N_{N+}N_e}{N_{N_g}}\frac{Q_{N_g}e^{I/kT_e}}{Q_{N+}Q_e} = \frac{(N_{N_g})_E}{N_{N_g}}$$

while if p is an excited state,

$$\frac{(N_p)_E}{N_p} = \frac{N_{N+}N_e}{N_{N^*}}\frac{Q_{N^*}e^{(I-E_*)/kT_e}}{Q_{N+}Q_e} = \frac{(N_{N^*})_E}{N_{N^*}}$$

The source function for the radiative transition from state q to state p under LTNE conditions is[20,21]:

$$\begin{aligned} S_{\nu_{pq}} &= \frac{N_q}{N_p}\frac{(N_p)_{LTE}}{(N_q)_{LTE}}\frac{2h\nu^3}{c^2}\left(e^{h\nu/kT_e} - \frac{N_q}{N_p}\frac{(N_p)_{LTE}}{(N_q)_{LTE}}\right)^{-1} \\ &= \frac{N_q}{N_p}\frac{(N_p)_{LTE}}{(N_q)_{LTE}}\frac{e^{h\nu/kT_e} - 1}{e^{h\nu/kT_e} - \frac{N_q}{N_p}\frac{(N_p)_{LTE}}{(N_q)_{LTE}}}(S_{\nu_{pq}})_{LTE} \end{aligned}$$

If the transition is between two excited states, then, since it has been assumed that these states are in thermodynamic equilibrium, the LTNE source function becomes identical to that for LTE. If the transition is between an excited state and a ground state, it can be approximated that $e^{h\nu/kT_e} \gg 1$ and $e^{h\nu/kT_e} \gg N_q(N_p)_{LTE}/N_p(N_q)_{LTE}$ so that it is approximately true that

$$\begin{aligned} S_{\nu_{pq}} &= \frac{N_q}{N_p}\frac{(N_p)_{LTE}}{(N_q)_{LTE}}(S_{\nu_{pq}})_{LTE} \\ &= \frac{N_{N^*}}{N_{N_g}}\frac{(N_{N_g})_{LTE}}{(N_{N^*})_{LTE}}(S_{\nu_{pq}})_{LTE} \end{aligned}$$

Discussion of Results

Several sets of results have been obtained using the models presented in the previous sections. In all cases, these results are for the stagnation streamline on a vehicle having a 2.3 meter nose radius, utilize ninety-nine points between the wall and shock front, and use a nitrogen freestream. For those cases which assume that excited electronic states are in equilibrium with the free ions and electrons, the nonequilibrium chemistry is shown on Table 1. For those cases utiilizing the second order local thermodynamic nonequilibrium model for atoms, the corresponding nonequilibrium chemistry model is shown on Table 2. In addition, the wall has been assumed to be radiatively black, noncatalytic to atomic recombination, fully catalytic to ionic recombination and at a temperature of 1650°K. This wall temperature was selected to insure significant cool wall thermal effects and is representative of the maximum temperature of nonablating surfaces. However, it is recognized that for the higher speed case considered the cummulative head load associated with the mission profile dictates the use of ablative surfaces and higher wall temperatures. Finally, an approximate boundary condition representing the wall sheath effects on electrons has been utilized as discussed in Ref. 2. Since the VSL flowfield method uses shock fitting, shock slip boundary conditions have been used for all cases in order to properly conserve total energy.

To investigate the thermal, diffusion, and radiation models, two entry condition have been considered. The first, sometimes referred to as "AFE CFD Point 4", corresponds to a "max Q" point for an AFE vehicle at which the freestream conditions are 9.326 km/sec, 26.4 dynes/cm^2, and 200°K; while the second point is for the same vehicle but at 14 km/sec and 80 km altitiude. The latter is typical of a Mars return vehicle at an altitude where nonequilibrium phenomena could be significant. All of the 14 km/sec cases considered were calculated with radiative-gasdynamic coupling included. Since the AFE cases do not have significant radiative coupling, the radiation calculations have been made from the converged solutions. All radiation calculations have been made with LTNE effects accounted for using the molecular model and either the first or second order atomic models described previously.

Thermal Nonequilibrium Model

All the results presented in this section were calculated using the constant Lewis number (1.4) diffusional model from Miner and Lewis[18] and the chemical reaction set of Table 1 while radiative LTNE effects were calculated using the first order model. As a result, the results in this section are comparable to the results presented in Ref. 2 with the important distinction that the two temperature model used previously assumed $T_v = T_{tr}$ while the cases labeled as two termperature in this paper assume $T_v = T_e$.

The first results presented in Figs. 2 and 3 were obtained using a two temperature model wherein the electron/electronic and vibrational energies are assumed to be highly coupled and in equilibrium with each other[10]. This effect was acheived computationally by summing the two equations term by term and solving together. An alternate and, atleast theoretically, identical approach could have been achieved by solving the orignal equation set while forcing the electron-vibrational relaxation times, τ_e, to approach zero.

Fig. 2 shows that the AFE CFD 4 case is in chemical and thermal nonequilibrium for almost the entire shock layer and that the chemistry is dissociation dominated, the ionization level being very low. The thermal nonequilibrium is particularly interesting in the region of the wall where $T_v - T_e$ exceed the heavy particle translational temperature. In the wall region, both the ionic and atomic recombinations are dumping energy into the electron and vibrational energies respectively. It is assumed[1] that ionic recombinations occur primarily by the reverse of the electron-impact ionization reaction and that each recombination adds I to the electron translational energy while the CVDV model[6,7] assumes that each atomic recombination adds $G_s - e_{v,s} \simeq D_s/2 - e_{v,s}$ to the vibrational energy of species s. Since $T_v - T_e$ exceeds T_{tr} in the wall thermal layer it follows that either or both of the recombination reactions is adding energy faster that the translational-vibrational and translational-electron exchange processes can remove it. The maximum value reached by the $T_v - T_e$ temperature was 8515°K at y/yshock=0.83.

Unlike the AFE CFD 4 case, the 14 km/sec case shown in Fig 3. shows a pronounced peak in the $T_v - T_e$ profile of about 17000°K at .83. Both thermal and chemical equilibrium occur for this case at abount .70 although, due to radiative cooling, the temperature continues to drop after this point along with gradual changes in the chemical composition. While the AFE CFD 4 point was dominated by dissociation, at this speed dissociation occurs very rapidly behind the shock front and ionization processes dominate most of the flow, reaching a peak degree of ionization of about 35%.

Results with the full three temperature model without electron-vibrational coupling are shown in Fig. 4 and 5. These cases represent the other extreme relative to the two temperature cases since there is no direct energy exchange mechanism between the electrons and the vibrational states. Indirectly some energy exchange still occurs through the coupling of both T_e and T_v to T_{tr}.

Comparing the three temperature results of Fig. 4 with the two temperature results of Fig. 2 it is seen that except for a greatly different T_e profile, the profiles are very similar. The vibrational temperature does peak a little sooner and higher at the shock front for the three temperature model, 9100°K at 0.91, but has the same profile over the rest of the shock layer, including the overshoot in the thermal boundary layer. Without T_e coupling, this high T_v indicates that energy production due to atomic recombinations is significant in the wall region as has been seen by other investigators[14]. As a result of electron energy depletion through electron impact ionization, the electron temperature is much lower behind the shock front for this model than before, which results in a much lower radiative heat flux. Also the lower electron temperature and its effect on the electron impact ionization rate increases the amount of chemical nonequilibrium at the shock front and in turn slightly increases the shock standoff distance.

As can be seen from the T_e profile, a shock slip condition was not enforced for the electron/electronic equation. Numerical problems with the slip boundary condition, coupled with the small magnitude of electron number density have not yet been resolved. This omission, however, does not have a significant effect on the other flow properties since the electron heat conduction is very small at the shock and also does not have a strong effect on the T_e profile itself. The electron temperature solution appears to be uncoupled from the shock boundary condition. This result is consistent with the quasi-equilibrium electron formulation previously used by the authors[1,2] in which it was assumed that chemical energy production and collisional energy transfer dominate the other terms in the electron energy equation and that T_e is primarly determined by the balance of the two.

The 14 km/sec case shown in Fig. 5, when compared with Fig. 3, shows the exact opposite trends as were noticed for the AFE CFD 4 case. The T_e profile is very similar in shape to the $T_v - T_e$ profile while T_v is greatly different. The vibrational temperature peaks much higher, 23000°K at 0.86, and equilibrates sooner with T_{tr}, due to high translational coupling. T_e peaks only slightly lower at 16900°K and 0.82 and as a result there is a slightly lower radiative flux.

In the thermal layer, the three temperature T_v initially dips below T_{tr} before rising above near the wall as in the two temperature case. Without electron coupling, diffusive effects in the thermal layer are important in the vibrational energy equation, and the flux of cool N_2 particles away from the wall lowers the vibrational energy until the atomic recombination reactions occur rapidly enough to raise T_v. This diffusive cooling effect was not seen in the AFE CFD 4 case due to the lower concentration gradients in N_2 and thus lower diffusive flux. The electron temperature in the thermal layer shows the same trends as were noted for the two temperature case.

Fig. 6 and 7 show results for the AFE CFD 4 and 14 km/sec cases, respectively, where the three temperature model is used with electron-vibrational coupling, as described previously in the theory section. As might be expected these results are in between the two extreme cases of the two temperature model and the three temperature model without $T_v - T_e$ coupling. In the AFE CFD 4 case the electron temperature has been increased toward T_v in the shock front, equilibrates with it around 0.70 and stays in equilibrium throught the rest of the shock layer except for a slight divergence immediately off the wall. The higher T_e profile results in a factor of two larger radiative flux than the uncoupled $T_v - T_e$ case, but it is still lower that the two temperature case.

For the 14 km/sec case, $T_v - T_e$ coupling lowers the vibrational temperature in the shock front region (from a peak value of 23000°K to 22200°K) while slightly raising the T_e profile and reduces the amount of diffusional cooling of T_v in the wall thermal layer. Percentage wise, the two temperature assumption has a slightly greater effect on the radiative flux for the lower speed case than the higher, 30% compared to 20%. The percentage differences would be further apart for the two cases if it were not for the fact that LTNE corrections tend to reduce the amount of radiation from the thermal nonequilibrium regions.

Diffusion Model

The results presented in this section were calculated using the chemical reaction set of Table 1 and first order LTNE radiative corrections, but for these cases the full diffusional model described above has been used. Figs. 8 and 9 show the results for the AFE CFD 4 case and 14 km/sec case, respectively. These cases were calculated using the three temperature, $T_v - T_e$ coupled thermal model and can be compared with the results in Figs. 6 and 7 to see the effect of various diffusional models.

Surprisingly, the profile changes associated with the different diffusional models are very small with the effect on the 14 km/sec case being slightly more noticable than for the AFE CFD 4 case. The results may be explained by the fact that for the AFE CFD 4 case, the flow is dominated by the species N_2 and N and thus a binary diffusion model with Le=1.4 is probably sufficient to describe most of the flow details. At 14 km/sec and in the shock front region, the flow goes from being N_2-N dominated to N-N^+ dominated; but the collisional cross sections of N_2 and N^+ with respect to N differ by about an order of magnitude. Thus a single Lewis number in this region is not sufficient, although using a lower Lewis number to reflect the reduced diffusional effects in N-N^+ flow may have better represented the majority of the flow region. The above conclusions might not be applicable in an air mixture shock layer, however, since the additional species will generally result in regions where the flow is essentially not binary in nature.

Also, in flows where multiple ionic species coexist at the same concentrations, the new treatment of the ambipolar diffusional effects may be an important factor in the ionic species equations. A close evaluation of the species concentration profiles in Fig. 8 shows some unusual behavior at the shock front where the N^+ and N^+_2 profiles cross. However, these results need further study before firm conclusions can be stated.

Second Order Atomic LTNE Model

The results in this final section are cases which used the full diffusional model, the chemical reaction rates of Table 2, and the second order atomic LTNE model discussed in the theory section of this paper. The AFE CFD 4 results shown in Fig. 10 are very close to the previous results shown in Fig. 8. The only significant difference is in the N^+ and N_2^+ profiles at the shock front. The new rate for exitation of N is faster that the rate in Table 1 which leads to a faster total ionization rate even though the ionization from the excited states is not infinite. As a result of this faster ionization rate, there is a higher concentration of N^+ near the shock; and as a result of the charge exchange reaction and ambipolar diffusion effects, the higher N^+ concentration in turn slightly lowers the N^+_2 concentration. The calculated N^* population is very low and closely follows the T_e profile in detail as can partially be seen from the figure.

This case can also be compared to the similar case results presented in Ref. 2. The total radiation calculated in Ref. 2 is lower than the current results, due primarily to a lower T_e temperature calculated by the quasi-equilibrium electron/electronic energy equation used in Ref. 2. The radiative spectral differences between the previous case and this present case, however, should be due to the differences in the first and second order LTNE correction methods. The radiative spectral details of the radiation reaching the wall for the AFE CFD 4 case are shown in Fig. 11 in two forms; the first shows the atomic line radiation having been grouped into convenient blocks while the second shows the atomic lines in full detail. Having the lines grouped gives a better visual description of the magnitude of the relative radiative process whereas the detailed presentation bears more similarity to experimental results.

While the radiation shown in Fig. 11 is still dominated by the $N_2^+(1-)$ molecular band in the 2-4 eV range, these new results show a much larger contribution from atomic lines in both the infrared (IR) and ultra-violet (UV) regions, especially in the IR region. In fact, the first order LTNE results from Ref. 1 showed almost no atomic radiation at all due to the large region of LTNE predicted for this case. The second order LTNE model predicts less LTNE for line radiation since the excited atomic electronic energy states are not as depleted as before.

The 14 km/sec case shown in Fig. 12 exhibits significant differences from the results in Fig. 9. The higher nitrogen excitation rate in Table 2 has shortened the nonequilibrium region at the shock front and lowered the peak T_e from 16650°K to 14560°K. Since this case is dominated by ionization chemistry, it would be expected that the results are sensitive to the ionization/excitation rates. The group and detailed wall radiation spectral plots are given as Fig. 13. Atomic radiation dominates for this case and most of it comes from the continuum UV bands. Strongly emitting IR lines are still seen and the high UV lines, above 11 eV, are highly absorbed at the lines centers.

Rather than compare these results to the earlier results which are greatly different in the chemical and thermal profiles, it was decided to redo the results of Fig. 9 using the higher excitation rate for N in place of the electron impact rate in Table 1. In this manner, first order LTNE results could be obtained with a chemical model very similar to that for the second order LTNE method. The flowfield profiles for this case are shown in Fig. 14. As expected, these profiles are very similar to those of Fig. 12 except that the peak T_e is lower, 13860°K, and equilibrium occurs slightly sooner. The earlier equilibration is to be expected since the first order LTNE assumes instantaneous equilibration of the excited states with the ions and electrons while the second order has a finite rate.

The radiative spectral plots for this case are shown in Fig. 15. In comparing these result to those in Fig. 13, three important differences are noticed. First, the IR line radiation is enhanced in the second order model over the first order model. This greater amount of emission is due to the lower level of thermodynamic nonequilibrium predicted from the second order method. The first order method predicts a largely depleted excited state population in the peak T_e region which reduces the line radiation from this region. Also, because of the reduced line radiation, absorption of the UV lines in the wall boundary layer is more significant for the first order LTNE model than for the second order model. The difference in UV line center absorption is the second noticable difference between Figs. 15 and 13. Finally, the N^+_2 (1-) molecular band is larger for the second order LTNE model. This difference appears to be due to a number of subtle changes in the two flowfilds such as different radiative cooling effects and different N^+_2 number densities caused by the charge exchange chemical reaction.

Conclusions

The use of a three temperature model including electron-vibrational coupling can lead to significant differences in the thermal profiles from those obtained with a two temperature model. The effects on chemistry are not as noticable due to the fact that the combined $T_v - T_e$ model tends to predict a temperature closest to the dominant energy for the flow conditions, i.e. closer to T_v in dissociation dominated flows and closer to T_e in ionization dominated flows. The differences in the thermal profiles for the two models results in differences of 20% to 30% in the radiative heat flux to the wall for the cases considered. These radiative differences would be more significant except that

LTNE effects tend to inhibit emission from the regions of thermal nonequilibrium.

A higher order diffusion model was developed and compared to a simple constant Lewis number multi-component diffusional model. The use of more exact diffusional models, while desirable for completeness of a solution method, was not seen to have a significant effect on results with a nitrogen gas, which tends to exhibit binary diffusive effects. Differing diffusion models may result in more noticable flowfield differences in more complex gas mixtures due to higher order diffusional effects.

The second order LTNE model developed for this paper has shown difficiencies in the first order LTNE model. While both models predict similar total heat fluxes, the spectral content of the radiation is different. Radiation reaching the wall with the second order LTNE model shows a greater IR line contribution and less UV line center absorption. The electron impact excitation calculated for the second order LTNE model is faster by an order of magnitude than the previous current rate. Using this faster rate with the first order model can closely reproduce much of the chemical behavior of the second order model.

Acknowledgement

This work was primarily supported by NASA Grant NAG-1-1003 from the Langley Research Center, with Dr. Lin C. Hartung as technical monitor. Mr. Gally is partially supported by a NASA Graduate Student Researchers Fellowship through the NASA Johnson Space Center.

REFERENCES

[1] Carlson, L. A. and Gally, T. A., "The Effect of Electron Temperature and Impact Ionization on Martian Return AOTV Flowfields," AIAA Paper 89-1729, June 1989.

[2] Carlson, L. A. and Gally, T. A., "Nonequilibrium Chemical and Radiation Coupling Phenomena in AOTV Flowfields," AIAA Paper 91-0569, January 1991.

[3] Thompson, R. A., "Comparison of Nonequilibrium Viscous Shock Layer Solutions with Windward Surface Shuttle Heating Data," AIAA Paper 87-1473, June 1987.

[4] Nicolet, W. E., "User's Manual for the Generalized Radiation Transfer Code (RAD/EQUIL or RADICAL)," NASA CR 116353, October 1969.

[5] Park, C., ***Nonequilibrium Hypersonic Aerothermodynamics***, John Wiley & Sons, New York, 1990, pp. 166-167.

[6] Treanor, C. E. and Marrone, P. V., "Effect of DIssociation on the Rate of Vibration Relaxation," *Physics of Fluids*, vol. 5, No. 9, September 1962, pp. 1022-1026.

[7] Marrone, P. V., "Inviscid, Nonequilibirum Flow behind Bow and Normal Shock Waves, Part I. - General Analysis and Numerical Examples," Cornell Aeronautical Laboratory Report No. QM-1626-a-12(I), May 1963.

[8] Park, C., "Calculation of Nonequilibrium Radiation in the Flight Regimes of Aeroassisted Orbital Transfer Vehicles," in ***Thermal Design of Aeroassisted Orbital Transfer Vehicles***, Progress in Astronautics and Aeronautics, Vol. 96, Ed. H. F. Nelson, AIAA, 1985, pp. 395-418.

[9] Millikan, R. C. and White, D. R., "Systematics of Vibrational Relaxation," *Journal of Chemical Physics*, vol. 39, No. 12, December 1963, pp. 3209-3213.

[10] Park, C., "Assessment of Two Temperature Kinetic Model for Ionizing Air," AIAA Paper No. 87-1574, June 1987.

[11] Lee, J. H., "Electron-Impact Vibrational Excitation Rates in the Flowfield of Aeroassisted Orbital Transfer Vehicles," in ***Thermophysical Aspects of Re-entry Flows***, Progress in Astronautics and Aeronautics, Vol. 103, Eds. J. N. Moss and C. D. Scott, AIAA, 1986, pp. 197-224.

[12] Candler, G. and Park, C., "The Computation of Radiation from Nonequilibrium Hypersonic Flows," AIAA 88-2678, June 1988.

[13] Moss, J. N., "Reacting Viscous Shock Layer Solutions with Multicomponent Diffusion and Mass Injection," NASA TR-R-411, June 1974.

[14] Gnoffo, P. A., Gupta, R. N., and Shinn, J. L.,, "Conservation Equations and Physical Models for Hypersonic Air Flows in THermal and Chemical Nonequilibrium," NASA TP 2867, February 1987.

[15] Carlson, L. A., "Radiative Gasdynamic Coupling and Nonequilibrium Effects Behind Reflected Shock Waves," *AIAA Journal*, vol. 9, No. 5, May 1971, pp. 858-865.

[16] Fay, J. A. and Kemp, N. H., "Theory of Stagnation Point Heat Transfer in a Partially Ionized Diatonic Gas," *AIAA Journal*, vol. 1, No. 12, December 1963, pp. 2741-2751.

[17] Camac, M. and Kemp, N. H., "A Multi-temperature Boundary Layer," Avco Research Report 184, August 1964.

[18] Miner, E. W. and Lewis, C. H., "Hypersonic Ionizing Air Viscous Shock Layer Flows over Nonanalytic Blunt Bodies," NASA CR-2550, May 1975.

[19] Chapman, S. and Cowling, T. G., ***The Mathematical Theory of Non-Uniform Gases***, Cambridge, 1964,pp. 343-349.

[20] Carlson, L. A., Bobskill, G. J., and Greendyke, R. B., "Comparison of Vibration Dissociation and Radiative Transfer Models for AOTV/AFE Flowfields," *J. of Thermophysics and Heat Transfer*, vol. 4, No. 1, January 1990, pp. 16-26.

[21] Kunc, J. A. and Soon, W. H., "Collisional Radiative Nonequilibrium in Partially Ionized Atomic Nitrogen," *Physical Review A*, vol. 40, No. 10, November 15, 1989, pp. 5822 ff.

[22] Foley, W. H. and Clarke, J. H., "Shock Waves Structered by Nonequilibrium Ionizing and Thermal Phenomena," *Physics of Fluids*, vol. 16, No. 3, March 1973, pp. 1612-1620.

[23] Nelson, H. F., "Nonequilibrium Structure of Argon Shock Waves," *Physics of Fluids*, vol. 16, No. 12, December 1973, pp. 2132-2142.

[24] Chapin, C. E., "Nonequilibrium Radiation and Ionization in Shock Waves," AA&ES Report, June 1967, Purdue, Univ., Lafayette, Ind.

[25] Clarke, J. H. and Ferrari, C., "Gas Dynamics with Nonequilibrium Radiative and Collisional Ionization," *Physics of Fluids*, vol. 8, December 1965, pp. 2121-2139.

Reaction	A	B	E
N_2+N =2N +N	4.085×10^{22}	-1.5	113100
N_2+N_2 =2N +N_2	4.70×10^{17}	-0.5	113100
N_2+e^- =2N^++e^-	3.00×10^{24}	-1.6	113100
N_2+N^+=N_2^++N	1.00×10^{12}	0.5	12200
N +N =N_2^++e^-	1.40×10^{13}	0.0	67800
N +e^- =N^+ +2e^-	4.16×10^{13}	0.5	120000
N +N =N +N^++e^-	2.34×10^{11}	0.5	120000
N +N^+=2N^++e^-	2.34×10^{11}	0.5	120000

Rates in the form $k_f = A\ T^B \exp(-E/T)$.
$T = T_e$ in electron impact reactions.

Table 1. Reaction System for First Order LTNE Model

Reaction	A	B	E
N_2+N =2N_g +N	4.085×10^{22}	-1.5	113100
N_2+N_2 =2N_g +N_2	4.70×10^{17}	-0.5	113100
N_2+N^+=2N_g +N^+	1.90×10^{17}	-0.5	113100
N_2+e^- =2N^++e^-	3.00×10^{24}	-1.6	113100
N_2+N^+=N_2^++N_g	1.00×10^{12}	0.5	12200
N_g+N_g =N_2^++e^-	1.40×10^{13}	0.0	67800
N_g+N =N +N^++e^-	2.34×10^{11}	0.5	120000
N_g+N^+=2N^++e^-	2.34×10^{11}	0.5	120000
N_g+e^- =N^+ +2e^-	2.50×10^{16}	0.0	169000
N_g+e^- =N^* +e^-	5.56×10^{16}	0.0	121000
N^*+e^- =N^+ +2e^-	4.11×10^{17}	0.0	48900

Rates in the form $k_f = A\ T^B \exp(-E/T)$.
$T = T_e$ in electron impact reactions.
$N = N_g + N^*$.

Table 2. Reaction System for Second Order LTNE Model

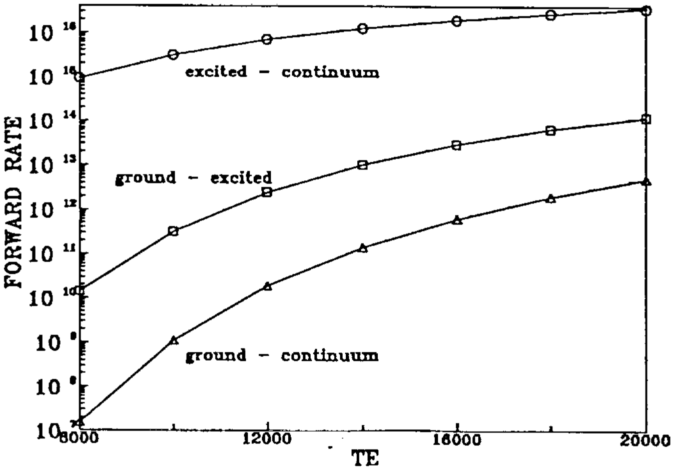

Fig. 1 Excitation and Ionization Rates for Nitrogen-Electron Collisions

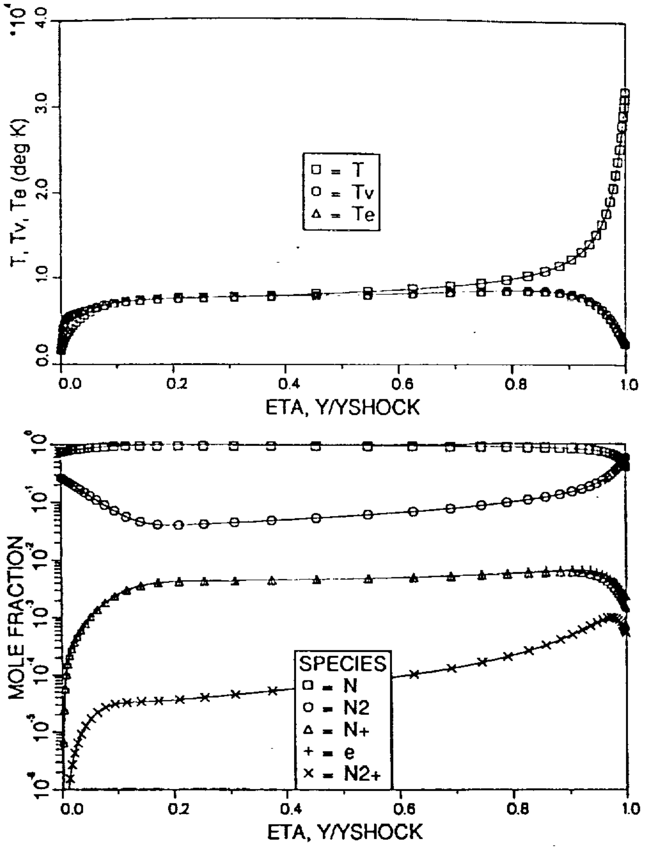

Fig. 2 Stagnation Profiles for AFE CFD Point 4 Two Temperature Model, QR=2.51 watts/cm², QC=27.6 watts/cm², YSHOCK=13.1 cm

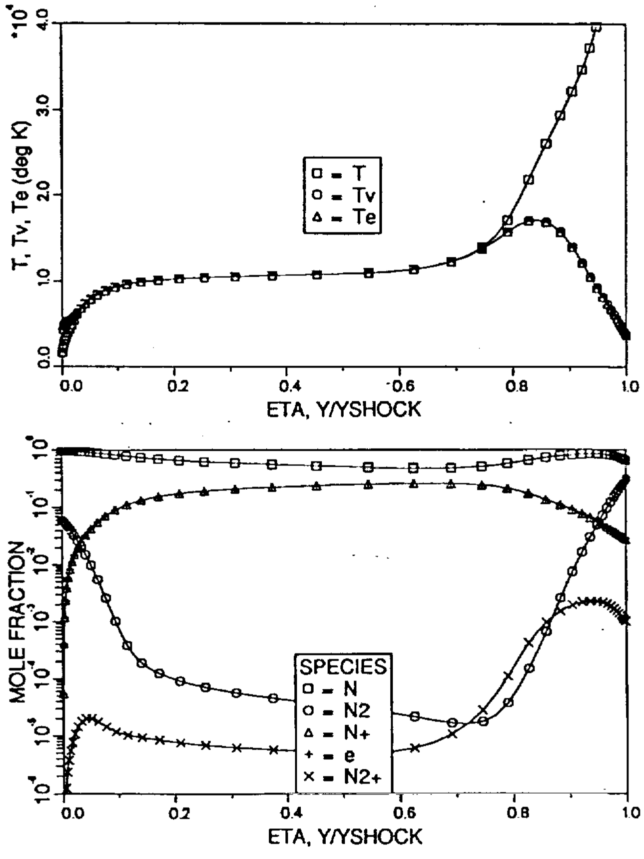

Fig. 3 Stagnation Profiles for 14 km/sec Case Two Temperature Model, QR=115.9 watts/cm², QC=66.2 watts/cm², YSHOCK=9.69 cm

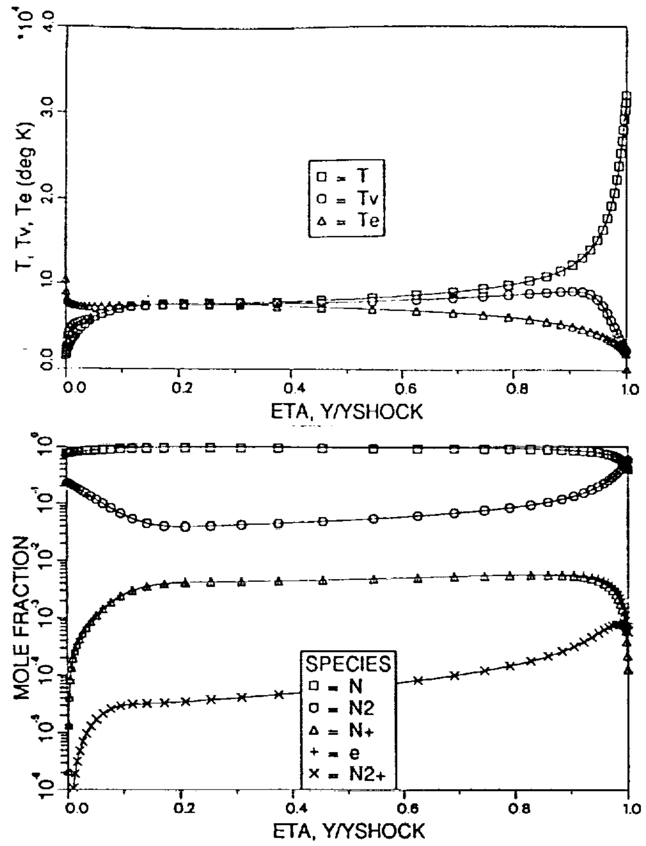

Fig. 4 Stagnation Profiles for AFE CFD Point 4
Three Temperature Model, without T_v-T_e Coupling
QR=1.02 watts/cm^2, QC=26.0 watts/cm^2,
YSHOCK=13.1 cm

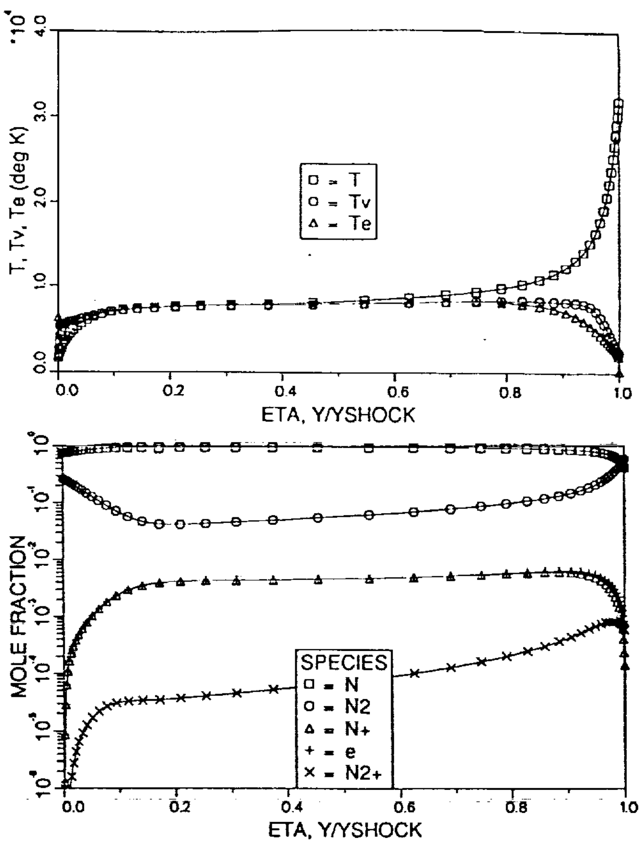

Fig. 6 Stagnation Profiles for AFE CFD Point 4
Three Temperature Model, with T_v-T_e Coupling
QR=1.93 watts/cm^2, QC=27.2 watts/cm^2,
YSHOCK=13.1 cm

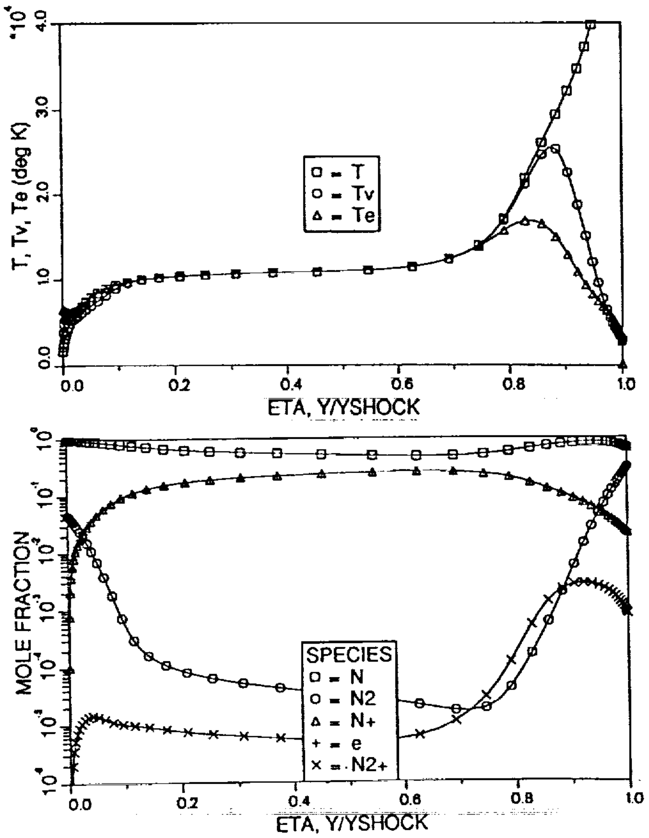

Fig. 5 Stagnation Profiles for 14 km/sec Case
Three Temperature Model, without T_v-T_e Coupling
QR=98.2 watts/cm^2, QC=61.2 watts/cm^2,
YSHOCK=9.77 cm

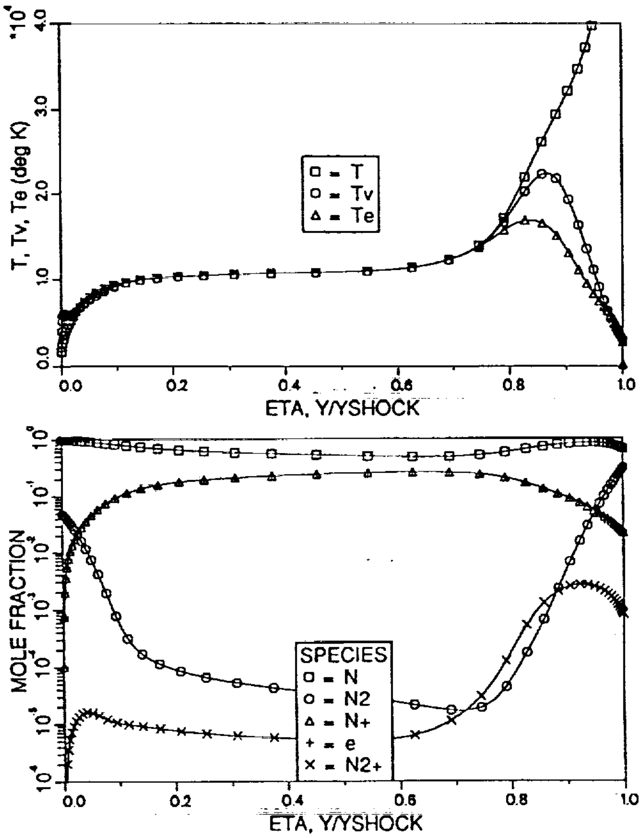

Fig. 7 Stagnation Profiles for 14 km/sec Case
Three Temperature Model, with T_v-T_e Coupling
QR=97.7 watts/cm^2, QC=59.9 watts/cm^2,
YSHOCK=9.77 cm

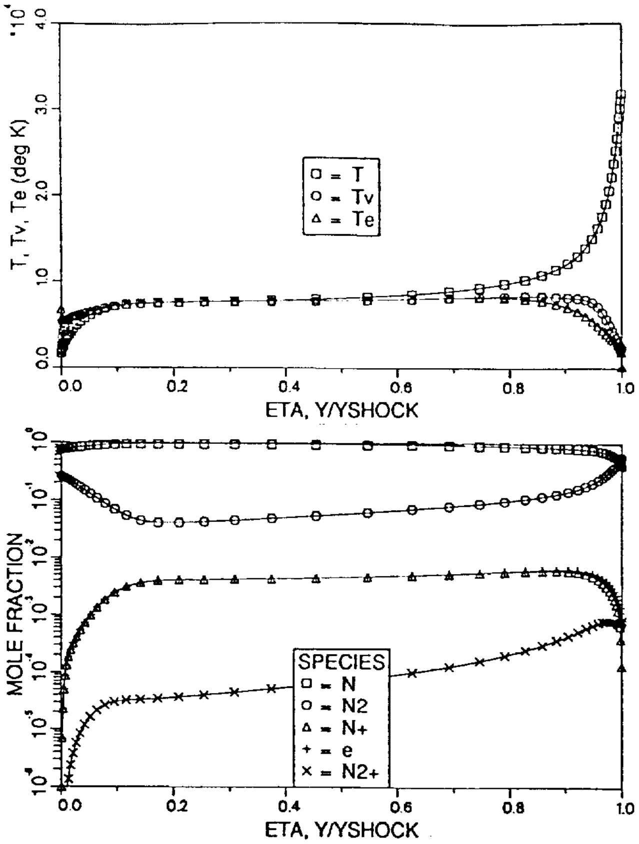

Fig. 8 Stagnation Profiles for AFE CFD Point 4
Full Multicomponent Diffusion Model, QR=1.95 watts/cm², QC=27.3 watts/cm², YSHOCK=13.1 cm

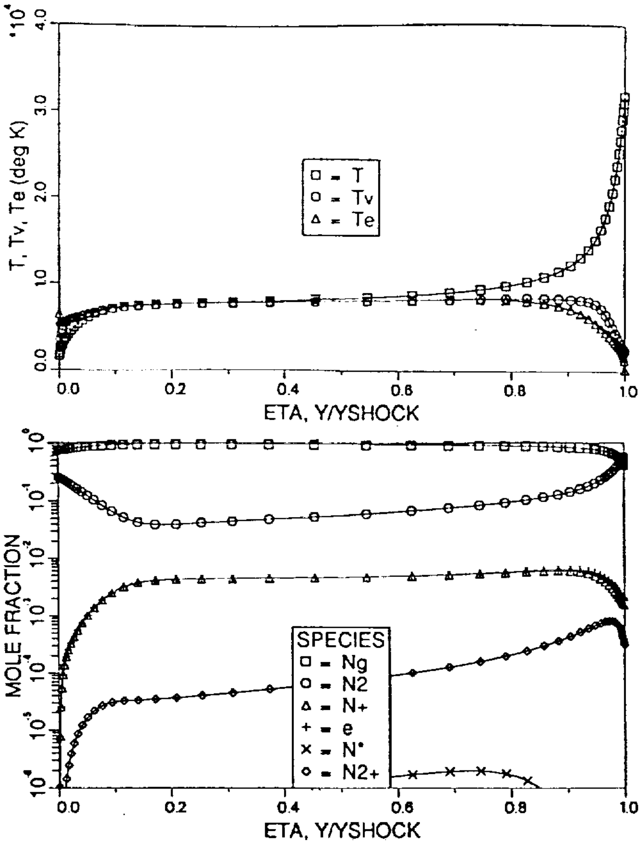

Fig. 10 Stagnation Profiles for AFE CFD Point 4
Second Order LTNE Model, QR=2.38 watts/cm², QC=27.8 watts/cm², YSHOCK=13.1 cm

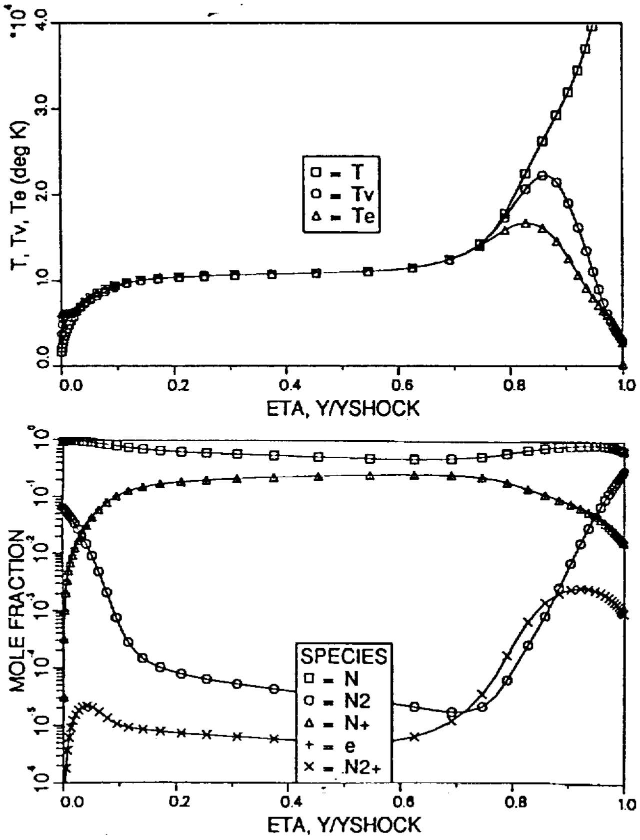

Fig. 9 Stagnation Profiles for 14 km/sec Case
Full Multicomponent Diffusion Model, QR=98.2 watts/cm², QC=53.8 watts/cm², YSHOCK=9.82 cm

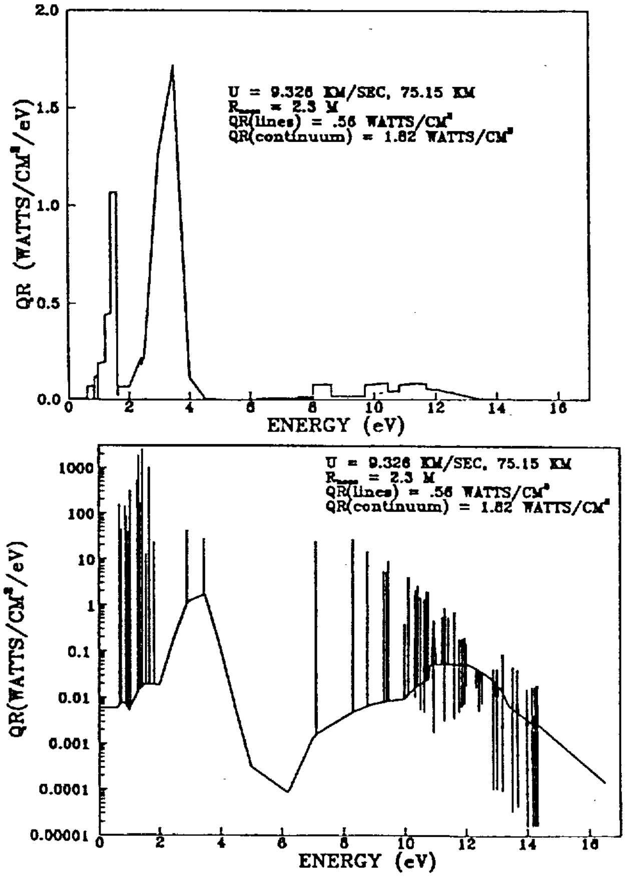

Fig. 11 Spectral Radiation Profiles for
AFE CFD Point 4, Second Order LTNE Model

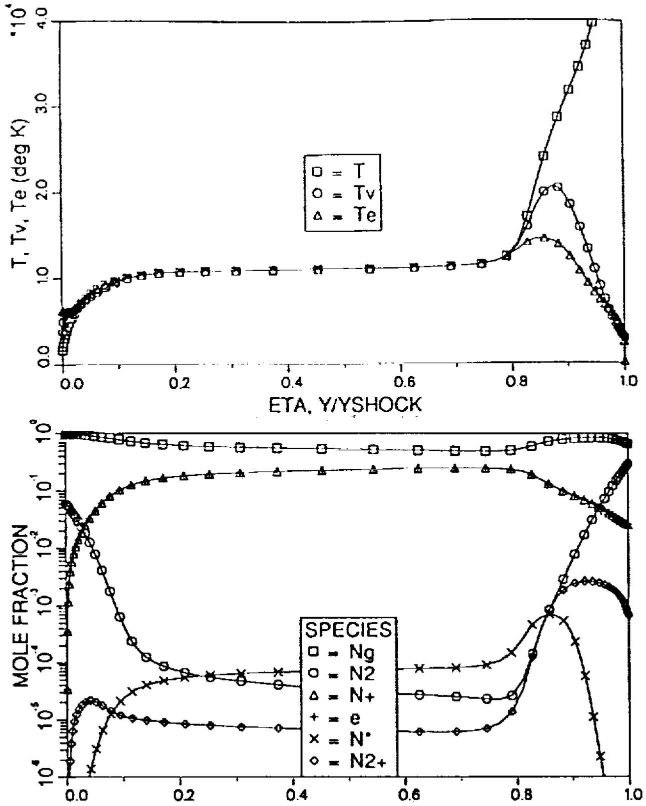

Fig. 12 Stagnation Profiles for 14 km/sec Case Second Order LTNE Model, QR=89.0 watts/cm², QC=55.1 watts/cm², YSHOCK=9.59 cm

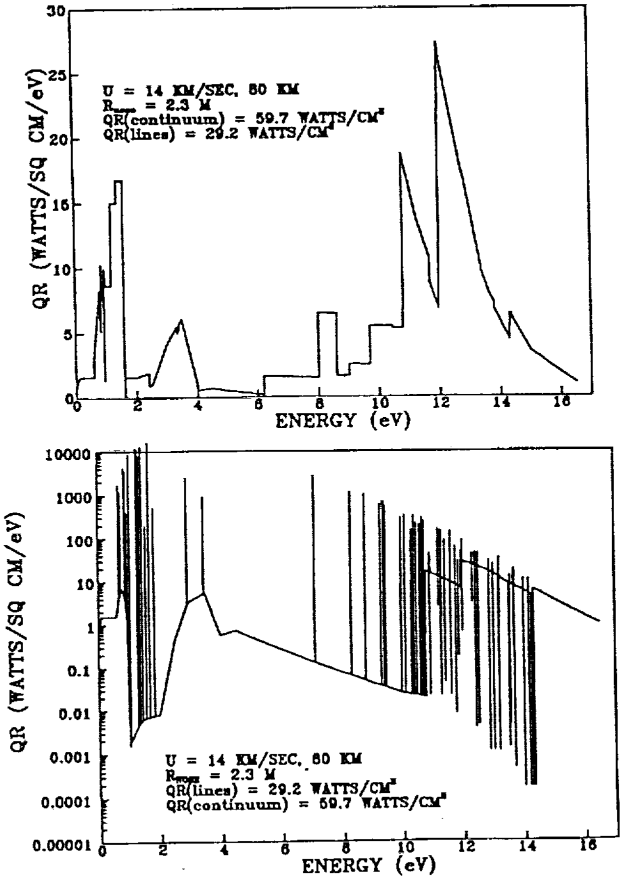

Fig. 13 Spectral Radiation Profiles for 14 km/sec Case, Second Order LTNE Model

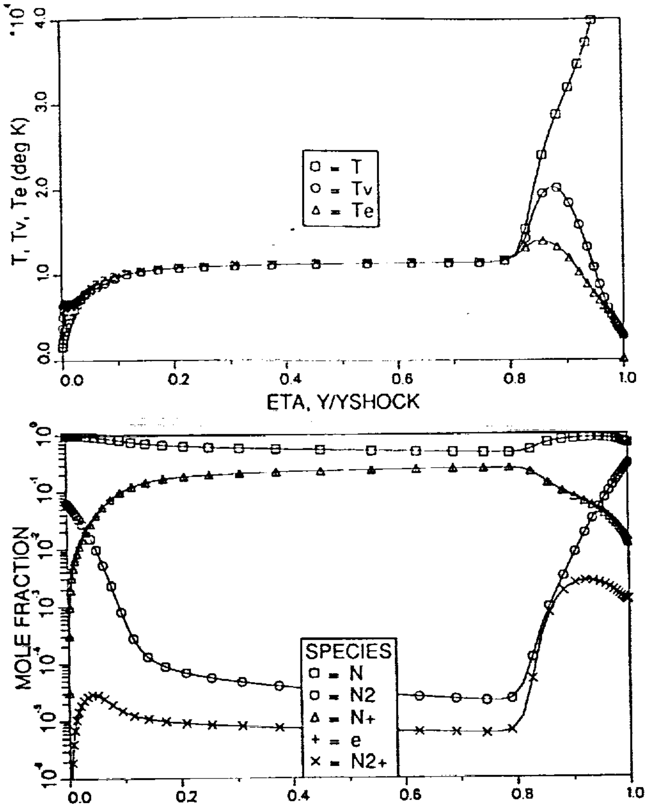

Fig. 14 Stagnation Profiles for 14 km/sec Case First Order LTNE Model with New Excitation Rate QR=82.2 watts/cm², QC=54.3 watts/cm², YSHOCK=9.58 cm

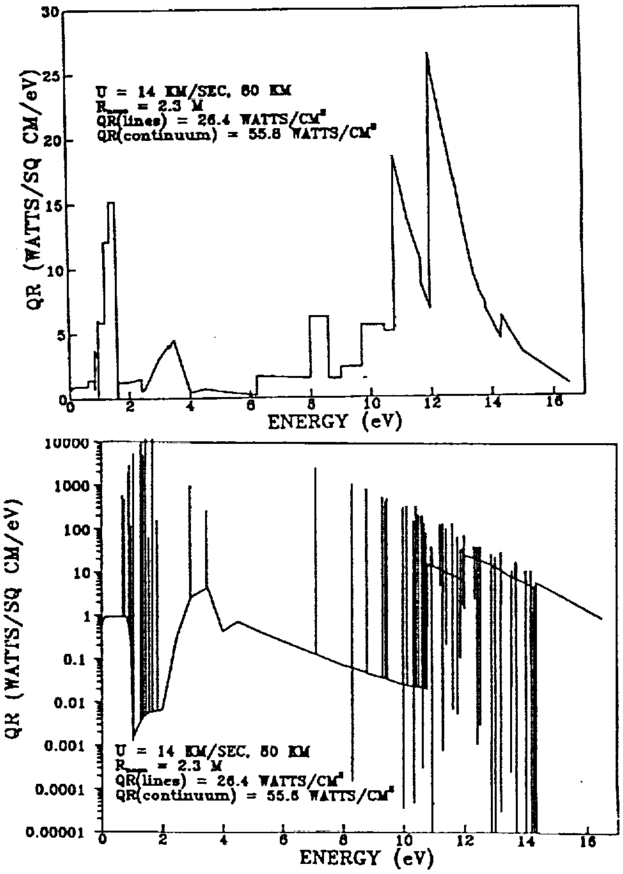

Fig. 15 Spectral Radiation Profiles for 14 km/sec Case First Order LTNE Model with New Excitation Rate

AIAA 91-1465
The Effects of Shock Wave Precursors Ahead of Hypersonic Entry Vehicles

S.A. Stanley and L.A. Carlson
Texas A&M University
College Station, TX

AIAA 22nd Fluid Dynamics, Plasma Dynamics & Lasers Conference
June 24-26, 1991 / Honolulu, Hawaii

The Effects of Shock Wave Precursors Ahead of Hypersonic Entry Vehicles

Scott A. Stanley*

and

Leland A. Carlson**
Texas A&M University
College Station, TX

Abstract

A model has been developed to predict the magnitude and characteristics of the shock wave precursor ahead of a hypervelocity vehicle. This model includes both chemical and thermal nonequilibrium, utilizes detailed mass production rates for the photodissociation and photoionization reactions, and accounts for the effects of radiative absorption and emission on the individual internal energy modes of both atomic and diatomic species. Comparison of the present results with shock tube data indicates that the model is reasonably accurate. A series of test cases representing earth aerocapture return from Mars indicate that there is significant production of atoms, ions and electrons ahead of the shock front due to radiative absorption and that the precursor is characterized by an enhanced electron/electronic temperature and molecular ionization. However, the precursor has a negligible effect on the shock layer flow field.

Nomenclature

AF - Radiation attenuation factor (-)
D_n - Dissociation energy for the nth species (eV)
e - Energy per unit mass (erg/g)
e''_e - Electron/electronic energy (erg/g)
E - Energy per particle (eV)
E_3 - Third exponential integral (-)
h - Static enthalpy (erg/g)
$h\nu$ - Photon energy (eV)
H - Total enthalpy (erg/g)
I_i - Ionization energy of the ith species (eV)
k - Boltzmann's constant (1.38×10^{-16} erg/°K)
k'_ν - Absorption coefficient (1/cm)
m_n - Mass per particle of the nth species (g)
M_n - Molecular weight of the nth species (g/Mole)
n_{diss} - Number of bound-free dissociation processes
n_{mb} - Number of molecular bands
n_s - Number of species
N_n - Number density of the nth species ($1/\text{cm}^3$)
p - Pressure (dyn/cm^2)
q - Radiative flux (W/cm^2)
$\hat{R}$ - Universal gas constant (8.317×10^7 erg/°K gram Mole)
T - Heavy particle temperature (°K)
T_e - Electron/electronic temperature (°K)
V - Velocity (cm/sec)
$\dot{w}$ - Mass production rate of the nth species (g/cm^3 sec)
x - Spatial variable in the precursor (cm)
Y - Absorption coefficient ratio (-)
β - One-half of the angle subtended by the body
ν - Frequency (1/sec)
ρ - Density (g/cm^3)
τ - Optical depth (-)

Subscripts
$elct$ - Electronic
i - for the ith process
j - for the jth electronic level
n - For the nth species
rot - Rotational
tr - Translational
vib - Vibrational
ν - At the frequency ν

Superscripts
TS - Tangent slab approximation
s - At the shock

Introduction

The recent emphasis placed on a mission to Mars and the subsequent return of samples has caused an increased interest in the development of accurate methods for predicting the fluid flow around hypersonic entry vehicles. This interest is a result of the plan to use an aerocapture technique to provide the reduction in velocity necessary to place the spacecraft in earth orbit. This technique uses aerodynamic drag, resulting from the interaction of the spacecraft with the earth's atmosphere, instead of propulsive braking to slow the vehicle to orbital speeds. Such an approach provides a reduction in the fuel necessary for the mission and an increase in the payload capabilities. A vehicle entering the earth's atmosphere upon return from Mars will experience velocities in the high hypersonic

---

* Member AIAA

** Professor Aerospace Engineering, Associate Fellow AIAA range, 11 Km/sec to 16 Km/sec.[1,2]

The majority of the recent work associated with hypersonic flow fields has involved the shock layer; but the shock wave precursor, on the other hand, has received little attention. The precursor is the region ahead of the shock wave in which radiation, primarily ultraviolet, emitted by the hot shock layer is reabsorbed by the gas. This absorption of radiation causes a heating of the gas in the precursor and the production of atoms as well as ions through the photoionization and photodissociation reactions. These changes might also in turn affect the gas behind the shock front. For example, the preheating of the gas in the precursor as well as the introduction of electrons and ions could potentially increase the rate at which the gas behind the shock approaches equilibrium. It has also been shown that for certain conditions the absorption of radiation ahead of the shock can cause significant increases in the radiative heating to the body.[3,4] Further, the presence of free electrons in the precursor can significantly affect communications with and identification of entry vehicles.[5,6]

Much of the previous work on shock wave precursors has been performed using shock tubes and shock tunnels[7,8,9] and a number of computational studies have also been performed.[10,11,12,13] The majority of this previous work, however, has involved monatomic gasses and is therefore not directly applicable to the earth's atmosphere.

The studies by Tiwari and Szema[13,14] as well as by Omura and Presley[15,16] involve diatomic gases and therefore are significant to a study of the earth's atmosphere. Tiwari and Szema calculated the effects of the precursor on the shock layer and the radiative heating of a body entering the hydrogen atmosphere of Jupiter, while Omura and Presley conducted a shock tube study of the electron densities ahead of strong shock waves in nitrogen as well as air.

The objective of this study was to develop a technique for predicting the character and magnitude of the chemical and thermal nonequilibrium shock wave precursor ahead of a hypervelocity entry vehicle that includes in detail the mass production due to photodissociation and photoionization of the various species and properly accounts for radiative absorption and emission effects on the internal energy modes of both atomic and diatomic species. A secondary objective was to ascertain the effect of this precursor on the vehicle flow field.

Radiative Transfer Formulation

In most of the previous work investigating shock wave precursors, several assumptions have been imposed on the radiative transfer calculations. A common assumption has been that the shock layer emits radiation as a black body at the equilibrium temperature behind the shock front.[10,12,17] Also, several of the previous works have utilized a multiple step absorption coefficient model[1,13,14] where at a given temperature, the species radiative properties have been assumed constant over specific frequency regions. However, since photochemical reactions are being considered, variations in the radiative transfer can cause significant changes in the gas. Likewise, the spectral details are very important in these calculations since the important radiative processes occur over different frequency ranges and the frequency of the photon absorbed as well as the process through which it is absorbed directly affects how the photon energy changes the energy of the gas. Without sufficient spectral detail, it is not possible to ascertain what portion of the radiation absorbed causes photoionization or photodissociation and what portion simply causes an increase in the internal energy of the gas.

Because of the necessity of accurate radiation predictions for the calculation of the photochemical reactions, it was decided that a complete spectrally detailed method of calculating the radiative flux was in order. Thus, an extensively modified version of the program RADICAL was utilized. This program, originally created by Nicolet[18], allows the user to select the frequency points used for the continuum radiation, so it was possible to obtain the spectral detail necessary for accuracy in the calculation of the photochemical reactions. RADICAL also performs detailed calculations of the atomic line radiation.

RADICAL, like many of the schemes currently used in the calculation of radiative transfer, uses the tangent slab approximation. This assumption is a one-dimensional approximation of the full equation of radiative transfer, which treats the radiation emitted at a point in the gas as if it were emitted by an infinite plane of gas positioned perpendicular to the direction of travel of the radiation. Since the thickness of the shock layer is much smaller than the body dimensions, each point in the shock layer is positioned close enough to the body that the rest of the gas in the radiating shock layer indeed appears to be of infinite extent; therefore, this is a reasonable assumption in the shock layer. The precursor, on the other hand, can extend to distances ahead of the shock which are of the same order of magnitude as the body diameter. Therefore, in the precursor, the radiating shock layer no longer appears to be of infinite extent but instead appears to be a slab of finite diameter.

In the one-dimensional problem, as in the shock layer, absorption is the only method by which the radiation is attenuated as it travels through the gas. Therefore, any decrease in the radiative intensity through the gas can be attributed to absorption, which in turn causes an increase in the energy of the gas equal to the decrease in the radiative energy. Since the shock layer does not appear to be of infinite extent at each point in the precursor, however, the radiation no longer behaves one-dimensionally. Consequently, in the precursor the radiative transfer is a three-dimensional problem in which a decrease in the radiative intensity can occur due to the geometry as well as due to absorption.

This geometric attenuation in the precursor occurs due to the fact that the radiative energy emitted by the finite diameter shock layer propagates radially outward into the forward 180 degree semisphere. Therefore, as the energy emitted progresses outward the area through which it passes increases, thus producing a decrease in the radiative flux. This decrease, however, is not due to absorption by the gas and therefore has no effect on the gas.

Thus to use RADICAL for the radiation calculations, it was necessary to correct for the geometric attenuation of the radiation. This was done by expressing the radiative flux in the precursor as

$$q_\nu = AF_\nu \, q_\nu^{TS} \tag{1}$$

where q_ν^{TS} is the radiative flux at the point of interest using the tangent slab approximation and AF_ν is the geometric attenuation factor defined by

$$AF_\nu = \left[1 - Cos^2(\beta) \frac{E_3\big((\tau_\nu - \tau_\nu^s) Sec(\beta)\big) - E_3\big(\tau_\nu Sec(\beta)\big)}{E_3(\tau_\nu - \tau_\nu^s) - E_3(\tau_\nu)}\right] \tag{2}$$

In this expression, β is half of the angle subtended by the body as viewed from the point of interest in the precursor. This expression is derived in detail by Stanley[19]

In the species continuity and energy equations, the terms involving the radiation appear as a divergence of the flux and are defined to account for the absorption and emission of radiation at a point. However, simple differentiation of equation (1) yields

$$\frac{\partial q_\nu}{\partial x} = AF_\nu \frac{\partial q_\nu^{TS}}{\partial x} + q_\nu^{TS} \frac{\partial AF_\nu}{\partial x} \tag{3}$$

In this expression, the first term on the right hand side is the change in the radiative flux due to the emission and absorption of radiation and the second term is the change due to the geometry of the problem and should not affect the gas. Therefore, the second term was neglected in the flow field calculations. Notice that if the second term was included in the species continuity and energy equations, an essentially transparent radiation would appear to be absorbed due to the spatial variation of the attenuation factor.

In order to properly account for the effects of absorption and emission of radiation on the energy of the gas, it is necessary to have an understanding of how each radiative process physically changes the particles involved. The effects of the absorption and emission of radiative energy on the internal energy modes depends on the type of radiative process as well as the frequency of the photon absorbed or emitted. Radiative processes can be separated into three categories: free-free, bound-bound and bound-free. While free-free and bound-bound processes cause a change in the energy of the gas with no chemical change, the bound-free processes are associated with chemical reactions in the gas, such as photoionization or photodissociation.

Photodissociation of the relatively cool nitrogen in the precursor occurs through a process called predissociation, a radiationless process in which a molecule transitions from a discreet electronic state to a dissociated state.[20] In cool nitrogen, this predissociation occurs primarily through the Lyman-Birge-Hopfield molecular band and the subsequent transfer out of the $a^1\Pi_g$ state into the repulsive $^5\Sigma_g^+$ state, Figure 1.

The radiative processes included in the calculation of the emission and absorption in the shock layer and precursor for this study are given in Table 1. The radiative processes included in the shock layer are those originally accounted for in the modified version of RADICAL. These processes include not only the continuum processes, but also the atomic lines associated with the nitrogen atom. Since only continuum processes were included in the precursor, the continuum mechanisms originally included in RADICAL were retained. Also, the photoionization of molecular nitrogen, the Lyman-Birge-Hopfield molecular band and the dissociation of molecular nitrogen through a continuum adjoining the Lyman-Birge-Hopfield band were added to the processes in RADICAL.

The absorption coefficients for photoionization of molecular nitrogen and the Lyman-Birge-Hopfield molecular band were determined using theoretical expressions derived according to Zel'dovich and Raizer[21]. For the photoionization process, the absorption coefficient was found to be given by the expression

$$k_\nu = 1.9986 x 10^{-14} \frac{N_{N_2}}{(h\nu)^3} \sum_{j=j^*}^{\infty} \frac{1}{j^3} e^{-(x_1 - x_j)}$$
$$x_j = \frac{\left(I_{N_2} - E_{elct_j}\right)}{kT} \tag{4}$$

where the photon energy, $h\nu$, is given in electron volts. The lower limit on the summation over the electronic states in this equation is governed by the requirement that the photon energy be greater than the binding energy for the state. Otherwise, the photon has insufficient energy to cause photoionization.

For this study, the summation in equation (4) was limited to the lowest four electronic states of the nitrogen molecule. However, in the cool precursor the populations of all except the ground electronic state were small. It should be noted that equation (4) provides values near the ionization threshold on the same order of magnitude as those predicted by Zel'dovich and Raizer[22] as well as those predicted by Marr[23].

The absorption coefficient for the Lyman-Birge-Hopfield molecular band was found to be given by

$$k_{\nu} = 9.1458x10^{16}\frac{N_{N_2}}{T}\, e^{-\frac{(113,314.97-11,610.14\,h\nu)}{T}} \tag{5}$$

This equation was obtained from expressions given by Zel'dovich and Raizer[21] using an absorption oscillator strength of $3.7x10^{-6}$ from Allen[24] and then correcting to match experimental predictions given by Watanabe[25]. The absorption coefficient for the dissociation continuum adjoining this molecular band was assumed to be given by the expression

$$k_{\nu} = 4.97x10^{-20}N_{N_2} \tag{6}$$

The constant in this equation was taken from the data presented by Watanabe for absorption through this process in cool air.

Precursor Formulation

For this study, the earth's atmosphere was modeled as pure nitrogen rather than a nitrogen oxygen mixture. This approach is a common simplifying assumption when performing nonequilibrium, hypervelocity flow field calculations since a nitrogen gas represents the properties of air quite well. In dealing with the precursor, however, the primary concern was whether or not the absorption processes of nitrogen sufficiently model those of air. After careful consideration it was decided that due to the predominance of nitrogen in the atmosphere it would be reasonable to represent the atmosphere as nitrogen in this initial study.

The effects of thermal nonequilibrium in the precursor were included in this study by permitting the free electrons and heavy particles to have different temperatures. Further, it was assumed that the free electrons and electronic states were in equilibrium at a common temperature, which as discussed by Nelson and Goulard[11], is one of the limiting cases for the precursor. For this region of the gas, the temperature governing the electronic states would normally be expected to be greater than the heavy particle temperature but less than the electron temperature. Thus, ideally a three temperature model should be used allowing a separate electronic temperature. Nevertheless, since the mechanisms and expressions for the transfer of energy between the electronic states and the free electrons are not well known or well understood, it was decided to use only a two temperature model. However, in order to correct for the local thermodynamic nonequilibrium between the electrons and the electronic states, a collision limiting correction[26] was applied to the populations of the molecular electronic states when computing the radiative emission and absorption phenomena.

For this study, the mass production rates in the precursor due to collisional reactions were neglected in comparison to those due to photochemical reactions. The photoreactions used in the precursor include the dissociation of molecular nitrogen and the ionization of both molecular and atomic nitrogen, i.e.

$$N_2 + h\nu \overset{k_{\nu 1}'}{\leftrightarrow} 2N$$

$$N_2 + h\nu \overset{k_{\nu 2}'}{\leftrightarrow} N_2^+ + e^-$$

$$N + h\nu \overset{k_{\nu 3}'}{\leftrightarrow} N^+ + e^-$$

The elastic collisional terms in the electron/electronic energy equation were evaluated using the collisional cross sections of Gnoffo, Gupta and Shinn[27].

The effects of the absorption of radiation through free-free and bound-bound processes were also included in this study. While these processes do not cause chemical reactions, they do cause an increase in the energy of the gas and their effects must be included in the electron/electronic energy equation. Absorption through atomic lines was neglected due to the expected low concentration of atomic species.

The equations governing the fluid properties on the stagnation streamline in the precursor are the steady, one-dimensional, nonequilibrium Euler equations.

Global Continuity

$$\frac{\partial}{\partial x}(\rho V) = 0 \tag{7}$$

Momentum

$$\rho V\frac{\partial V}{\partial x} \div \frac{\partial p}{\partial x} = 0 \tag{8}$$

Energy

$$\rho V\frac{\partial H}{\partial x} \div \frac{\partial q}{\partial x} = 0 \tag{9}$$

In equation (9), H is the total enthalpy of the gas defined in terms of the static enthalpy such that

$$H = h + \frac{1}{2}V^2 \tag{10}$$

where

$$h = \frac{p}{\rho} + \sum_{n=1}^{n_s}\left(e_{tr_n} + e_{rot_n} + e_{vib_n} + e_{elct_n} + e^o_n\right) \tag{11}$$

The second term in equation (9) is the gradient of the radiative flux. This term accounts for the increase or decrease in the energy of the gas due to absorption and emission of radiation. In addition to these equations, the equation of state for a two temperature gas is required,

$$p = \rho \hat{R} T \sum_{n=1}^{n_s}\left(\frac{\rho_n}{\rho}\frac{1}{M_n}\right) + \rho\frac{\hat{R}}{M_{e^-}}\frac{\rho_{e^-}}{\rho}(T_e - T) \tag{12}$$

To allow for the effects of thermal nonequilibrium, an electron/electronic energy equation was added to these equations,

$$\begin{aligned}\frac{d}{dx}(\rho V e''_e) = {} & -p_e\frac{\partial V}{\partial x} + \sum_{n=1}^{n_s}\xi_{e,n} + \dot{w}_e\frac{V^2}{2} - \frac{\partial q}{\partial x} \\ & + \sum_{i=1}^{n_{diss}}\int_0^\infty \frac{Y^p_{v_i}\left(hv - \Delta E_{elct_i} - D_i\right)}{hv}\frac{\partial q_v}{\partial x}\,dv \\ & + \sum_{i=1}^{n_{mb}}\int_0^\infty \frac{Y^p_{v_i}\left(hv - E^{upp}_{elct_i} + E^{low}_{elct_i}\right)}{hv}\frac{\partial q_v}{\partial x}\,dv\end{aligned} \tag{13}$$

where

$$e''_e = \frac{\rho_{e^-}}{\rho}e_{e^-} + \sum_{n=1}^{n_s}\left(e_{elct_n} + e^o_n\right) \tag{14}$$

In this equation, e_{e^-} is the kinetic energy of the free electrons, $3/2kT_e/m_{e^-}$, while $e_{elct\ n}$ and e_n^o are the electronic and zero point energies of the nth species. The last three terms on the right hand side of equation (13) allow for the effects of the absorption of radiation. This equation is derived in detail in Reference 19.

Chemical nonequilibrium was accounted for in the precursor through the addition of a species continuity equation for each of the five species in the problem. These equations are of the form

$$\rho V\frac{\partial\left(\frac{\rho_n}{\rho}\right)}{\partial x} = -m_n\int_0^\infty \frac{Y^s_{v_n}}{hv}\frac{\partial q_v}{\partial x}\,dv \tag{15}$$

where

$$\begin{aligned} Y^s_{v_{N_2}} &= -\frac{k'_{v_1} + k'_{v_2}}{k'_{v_{tot}}} & Y^s_{v_{N_2^+}} &= \frac{k'_{v_2}}{k'_{v_{tot}}} \\ Y^s_{v_N} &= \frac{2k'_{v_1} - k'_{v_3}}{k'_{v_{tot}}} & Y^s_{v_{N^+}} &= \frac{k'_{v_3}}{k'_{v_{tot}}} \\ Y^s_{v_{e^-}} &= \frac{k'_{v_2} + k'_{v_3}}{k'_{v_{tot}}} \end{aligned} \tag{16}$$

The term on the right hand side of equation (15) is the mass production rate of the nth species due to photoprocesses. The absorption coefficients, k'_{v1}, k'_{v2} and k'_{v3} are those for the absorption and emission processes associated with each of the three photochemical reactions discussed previously. Equation (15) is derived in detail in Reference 19.

In all of the above equations, the radiative terms, $\partial q/\partial x$, are the changes in the radiative flux due only to the absorption of radiation and not those due to the geometry of the problem as discussed in the previous section.

Shock Layer Formulation

In order to properly model the precursor ahead of a shock wave, it is necessary to know the spectral details of the radiation which passes from the shock layer and through the shock front to the precursor. In order to calculate these spectral details, the conditions of the gas in the shock layer must be known in detail. For the flight conditions of interest in this study, a number of important phenomena such as chemical and thermal nonequilibrium must be included to properly model the shock layer. Also, since the effects of radiation are of primary importance in the precursor, it is desirable that they be included in the shock layer model. The inclusion of these three phenomena can significantly affect the radiation and hence the precursor.

For this portion of the flow field, a viscous shock layer, VSL, scheme based on a version of the NASA code VSL3DNQ[28] was used. The version of VSL3DNQ used in this study was modified extensively by Carlson and Gally[29]. These modifications primarily involved the nonequilibrium chemistry and the effects of thermal nonequilibrium.

However, they also modified the code to allow the shock layer and radiation calculations to be coupled to the gas dynamics, thus incorporating the effects of the emission and absorption of radiation into the flow field solution.

Results and Discussion

Figure 2 compares of the electron mass fractions found by Omura and Presley[15,16] in the precursor ahead of a shock wave in a nitrogen gas to those calculated using the present method. Omura and Presley measured the electron densities in the precursor using a 12 inch shock tube. The shock velocity for their case was 11.89 Km/sec. Shown in this figure, along with Omura and Presley's results, are two curves showing the electron mass fractions calculated using the current method. The dashed curve was calculated using Omura and Presley's freestream conditions and shock velocity with a 12 inch diameter body. However, the solid curve was calculated using a lower freestream density and pressure than Omura and Presley along with a larger diameter body scaled so that the conditions match those of Omura and Presley's case using binary scaling.

As can be seen from this figure, the electron mass fractions calculated using this method match those found by Omura and Presley reasonably well near the shock front. However, far from the shock they deviate. It is believed that the differences in the electron mass fraction far from the shock are due to the reflection of the radiative flux off of the shock tube walls in the Omura and Presley case. This reflection should greatly increase the quantity of radiation present far ahead of the shock wave over that which would be present in a free field such as is being used for the calculations. This increased presence of radiation far from the shock would induce greater absorption and thus an increase in the production of electrons due to photoionization. It is also interesting to note how well the two sets of calculations match using binary scaling.

The results discussed in the remainder of this section are representative of "typical" conditions for an aerobrake vehicle entering the earth's atmosphere upon return from Mars. These results were calculated for the stagnation streamline of a 2.3 meter nose radius vehicle at three altitudes, 72 Km, 75 Km and 80 Km. The shock layer calculations were made using 52 points between the shock wave and the body and allowing for atomic local thermodynamic nonequilibrium as well as radiation/gasdynamic coupling. The radiation calculations were made using 74 continuum frequency points selected to provide good spectral detail in the ultraviolet absorption region of interest in the precursor. A wall temperature of 1650 °K was used in both the shock layer and the radiation calculations.

72 Km, 16 Km/sec

Figure 3 shows the heavy particle temperature, electron/electronic temperature, pressure and the five species mole fraction variations through the precursor for this case. The radiative flux through the shock front for this case was 1,385.0 W/cm^2 and the spectral details of this radiation are shown in Figure 4. The shock standoff distance for this case was 6.60 cm. The radiation emitted from the shock layer for this case was the greatest of all of those considered. Thus this case experienced the largest flow field perturbations in the precursor region.

From these figures, it can be seen that the heavy particle temperature and pressure increased steadily through the precursor region. However, even for this extreme case the changes in these values were small. The density and velocity of the gas were found to be essentially constant in the precursor. This behavior verifies what was shown by Tiwari and Szema[13,14] and assumed by many others[10,11,12,15].

The electron/electronic energy of the gas also increased from a value of essentially zero in the freestream to a value on the order of 10^9 immediately ahead of the shock front. It should be noted that 99 percent of the radiative energy absorbed in the precursor affected the electron/electronic energy of the gas and only 1 percent of the energy affected the heavy particle translational, rotational and vibrational energies of the gas. Likewise, of the increase in the electron/electronic energy, 96 percent was involved with an increase in the zero point energy of the gas. Therefore, the majority of the energy absorbed in the precursor was involved with the ionization and dissociation of the gas.

The electron/electronic temperature behaved differently in the precursor than the other gas properties. It increased steadily to a maximum value of approximately 6,300 °K at a distance of 40 shock standoff distances ahead of the body. It then decreased rapidly to a value of 4,290 °K immediately ahead of the shock front. This decrease in the electron/electronic temperature was a result of the production of "low" energy electrons through photoionization caused by photons of frequencies only slightly larger than the ionization threshold of N_2. The production of these "low" energy electrons caused a decrease in the average energy per electron, hence a decrease in the electron/electronic temperature. That this decrease was a result of the production of "low" energy electrons rather than due to a transfer of energy from the electrons through elastic collisions was evident since there was no decrease in the electron/electronic energy accompanying this decrease in the electron/electronic temperature. This decrease also coincided with a region of rapid increase in the electron concentration in the gas due to the photoionization of molecular nitrogen.

The photons with energy near the ionization threshold of molecular nitrogen were absorbed rapidly in front of the shock since the strongest absorption region for an ionization process is at frequencies near the threshold. The higher energy photons in the weaker absorption range, far from the threshold, escaped to distances further from the shock where they were absorbed causing the creation of high energy electrons. The production of these high energy electrons resulted in a high electron/electronic temperature far from the shock. However, although the electron/electronic temperature was high far from the shock the electron mass fraction in this region was extremely small. It should be noted that a similar decrease in the precursor electron temperature near the shock was also predicted by Foley and Clarke[12], although they attributed it to collisional electron impact ionization.

Considering the mole fractions of the five species, it can be seen that the dominant chemical reaction far from the shock was the photoionization of atomic nitrogen. However, near the shock photoionization of molecular nitrogen dominated. The mole fractions of the ionized nitrogen molecule immediately ahead of the shock were at least an order of magnitude greater than those for the nitrogen atom and ionized nitrogen atom; although, there were significant quantities of all three species.

Due to the fact that the dominant change in the precursor was due to the photoionization of molecular nitrogen, the thickness of the precursor was considered to be the distance through which this reaction had an effect. By this definition, for this case the shock precursor thickness was in the range of 75 shock standoff distances, or 495 cm. Although there was a slight heating of the gas as well as the production of nitrogen atoms through photodissociation at greater distances from the shock, their effects were small compared to the changes within 495 cm of the shock front.

As can be seen in Figure 4, the radiation propagating through the shock wave from the shock layer into the precursor was distributed over a wide range of frequencies. A large portion of this radiative energy was in the infrared frequency range ($h\nu \leq 5$ eV). Most of the radiation in this region was emitted by the entry body itself; although, embedded within the continuum radiation from the body were a number of atomic lines. Also, the peak of radiation near 3.5 eV was due to three molecular bands, the 1st negative band of $N_2{}^+$ and the 1st and 2nd positive bands of N_2. There was also a large quantity of radiative energy in the ultraviolet frequency range. That above 10 eV was due primarily to the Birge-Hopfield band of molecular nitrogen as well as the ionization continuum and lines of atomic nitrogen. Through the visible frequency ranges (5 eV $\leq h\nu \leq$ 8 eV) there was very little radiative energy.

The second curve on Figure 4 shows the radiative flux at a position 75 shock standoff distances ahead of the shock front uncorrected for the geometric attenuation. By comparing this uncorrected radiative flux to the radiative flux through the shock front, it is possible to ascertain in what portion of the frequency range the cool precursor absorbed. This figure shows that the precursor absorbed radiation strongly at frequencies above the ionization threshold of molecular nitrogen, 15.59 eV. Although there was energy absorbed at frequencies less than this threshold due to photodissociation of molecular nitrogen and photoionization of atomic nitrogen, the amount of energy absorbed in these processes was small compared to that absorbed in the photoionization of molecular nitrogen. This result agrees with the previous statements that the dominant reaction was molecular ionization.

Through the course of this study it was found that even though there was significant production of dissociated and ionized nitrogen in the precursor region, the precursor had very little effect on the gas in the shock layer. By including these perturbed preshock conditions in the viscous shock layer calculations, it was found that they had negligible effect on the shock layer solution and produced no measurable change in the radiative heat transfer to the body. The primary change due to the inclusion of the precursor was in the conditions of the gas immediately behind the shock wave. Neglecting the precursor, the mass fractions for the free electrons, ions and atoms were zero upon crossing the shock; however, including the effects of the precursor these mass fractions had nonzero values. Likewise, including the effects of the precursor resulted in a slight increase in the electron temperature in the region immediately behind the shock front. However, within two spatial points of the shock front the shock layer solutions with and without the precursor agreed.

Parametric Studies

Figure 5 shows the electron number densities and the electron/electronic temperature in the precursor for three cases. All three of these cases were at a velocity of 16 Km/sec; however, each case was at a different altitude, 72 Km, 75 Km and 80 Km. The shock standoff distance and radiative flux through the shock front for each of these cases are presented in Table 2.

From these figures, it can be seen that for a constant velocity the magnitude of the changes in the precursor increased with decreasing altitude. This inverse relationship corresponds with trends observed by Dobbins[17] and was a result of two factors. First and foremost, as shown in Table 2, with the decrease in altitude the radiative flux through the shock increased due to an increase in the extent of the equilibrium region in the shock layer. Second, with the increase in density at the lower altitudes, a larger percentage of the radiation passing through the shock was absorbed before being attenuated due to the geometry.

It should also be noted that as the altitude decreased, the length of the precursor region decreased. This change was a result of the increased density at the lower altitudes, which caused the radiative mean free paths to decrease. Hence, the radiation was absorbed in a shorter distance ahead of the shock. This trend was also predicted by previous studies.[11]

Figure 6 shows the electron number densities and electron/electronic temperature for four cases. All of these cases were at an altitude of 80 Km and the freestream velocities ranged from 10 to 16 Km/sec. The shock standoff distance and radiative flux through the shock front for each of these cases are presented in Table 2.

From these figures, it can be seen that at a constant altitude, as the freestream velocity increased the magnitude of the electron number densities in the precursor also increased. This trend was a result of the increase in the equilibrium temperature in the shock layer as the velocity increased and the accompanying rise in the radiative flux through the shock front; this trend is also in agreement with the results and predictions of previous researchers.[16,17] The precursor thickness also increased with velocity, again as a result of the increased radiative flux with velocity. As the radiative energy passing through the shock increased, a larger distance was required for this energy to be absorbed or attenuated ahead of the shock.

The increase in the velocity had varied effects on the electron/electronic temperature, however. The electron/electronic temperature at the shock decreased with velocity from 10 to 14 Km/sec. However, from 14 to 16 Km/sec it increased. This varied effect is due to differences in the quantity of "low" energy electrons created immediately ahead of the shock due to the ionization of molecular nitrogen. In fact, at 10 Km/sec there was insufficient ionization of molecular nitrogen ahead of the shock to cause a decrease in the electron/electronic temperature.

Conclusions

In this paper, a model for predicting the magnitude and characteristics of the shock wave precursor ahead of a hypervelocity vehicle has been presented. This method includes detailed mass production for photodissociation and photoionization and accounts for the effects of emission and absorption on the individual energy modes of the gas. This technique includes the effects of both chemical and thermal nonequilibrium as well as in the radiative flux calculations the consequences of local thermodynamic nonequilibrium for the molecular species.

This method has been used to determine the shock wave precursor ahead of vehicles entering the earth's atmosphere upon return from Mars. Comparison of the results to previous shock tube studies has shown that the method provides reasonably accurate results. The test cases have shown that there is significant production of atoms, ions, and electrons ahead of the shock front and that the precursor is characterized by molecular ionization and an enhanced electron/electronic temperature. However, the precursor has negligible effect on the subsequent shock layer flow field.

Acknowledgement

This work was primarily supported by NASA grant NAG-1-1003 from the NASA Langley Research Center, with Lin C. Hartung acting as technical monitor.

References

1 Smith, G.L., "Radiation-Induced Precursor Flow Field Ahead of a Reentering Body", PhD Thesis, Virginia Polytechnic Institute, Blacksburg, VA, March 1968.

2 Williams, S.D., "Pavlosky, J.E., and Curry, D.M., "A Preliminary TPS Design for MRSR-Aerobraking at Mars and at Earth", AIAA Paper 90-0052, Jan. 1990.

3 Lasher, L.E., and Wilson, K.H., "Effects of Shock Precursor Heating on Radiative Flux to Blunt Bodies", Lockheed Missiles and Space Co., Palo Alto, CA, NASA-CR-1265, 1969.

4 Tiwari, S.N., and Szema, K.Y., "Effects of Precursor Heating on Chemical and Radiative Nonequilibrium Viscous Flow Around a Jovian Entry Body", AIAA Paper 78-907, May 1978.

5 Wetzel, L., "Far-Flow Approximation for Precursor Ionization Profiles", *AIAA Journal*, Vol. 2, No. 7, July 1964, pp. 1208-1214.

6 Lederman, S., and Wilson, D.S., "Microwave Resonant Cavity Measurements of Shock Produced Electron Precursor", *AIAA Journal*, Vol. 5, No. 1, Jan. 1967, pp. 71-77.

7 Shreffler, R.G., and Christian, R.H., "Boundary Disturbances in High Explosive Shock Tube", *J. Appl. Phys.*, Vol. 25, No. 3, March 1954, pp. 324-331.

8 Voorhies, H.G., and Scott, F.R., "optical Measurements in a Helium Shock Tube", *Bull. Amer. Phys. Soc.*, Vol. 4, June 1959, p. 40.

9 Weymann, H.D., "Electron Diffusion Ahead of Shock Waves in Argon", *Phys. of Fluids*, Vol. 3, No. 4, July 1960, pp. 545-548.

10 Murty, S.S.R., "Effects of Line Radiation on Precursor Ionization", *J. Quant. Spect. Rad. Trans.*, Vol. 8, Sept. 1968, pp. 531-554.

11 Nelson, H.F., and Goulard, R., "Structure of Shock Waves with Nonequilibrium Radiation and Ionization", *Phys. of Fluids*, Vol. 12, No. 8, Aug. 1969, pp. 1605-1617.

12 Foley, W.H., and Clarke, J.H., "Shock Waves Structured by Nonequilibrium Ionizing and Thermal Phenomena", *Phys. of Fluids*, Vol. 16, No. 3, March 1973, pp. 373-383.

13 Tiwari, S.N., and Szema, K.Y., "Radiation Induced Precursor Flow Field Ahead of a Jovian Entry Body", AIAA Paper 77-768, June 1977.

14 Tiwari, S.N., and Szema, K.Y., "Influence on Precursor Heating on Viscous Flow Around a Jovian Entry Body", AIAA Paper 78-190, Jan. 1978.

15 Omura, M., and Presley, L.L., "Electron Density Measurements Ahead of Shock Waves in Air", *AIAA Journal*, Vol. 7, No. 12, Dec. 1969, pp. 2363-2365.

16 Omura, M., and Presley, L.L., "Further Studies of Precursor Electron Densities Ahead of Shock Waves", *Proceedings of the 4th Plasma Sheath Symposium*, NASA-SP-252, Oct. 1970, pp. 335-358.

17 Dobbins, R.A., "Photoexcitation and Photoionization of

Argon Ahead of a Strong Shock Wave", AIAA Paper 68-666, June 1968.

[18] Nicolet, W.E., "Advanced Methods for Calculating Radiation Transport in Ablation Product Contaminated Boundary Layers", Aerotherm Corp., Mountain View, CA, NASA-CR-1656, Sept. 1970.

[19] Stanley, S.A., "The Effects of Shock Wave Precursors Ahead of Hypersonic Entry Vehicles", Master's Thesis, Texas A&M University, College Station, TX, Dec. 1990.

[20] Herzberg, G., *Molecular Spectra and Molecular Structure, I. Spectra of Diatomic Molecules*, 2nd ed., Krieger, Malabar, FL, 1989.

[21] Zel'dovich, Y.B., and Raizer, Y.P., *Physics of Shock Waves and High-Temperature Phenomena*, Vol. 1, Academic Press, New York, NY, 1966.

[22] Zel'dovich, Y.B., and Raizer, Y.P., *Physics of Shock Waves and High-Temperature Hydrodynamic Phenomena*, Vol. 2, Academic Press, New York, NY, 1967.

[23] Marr, G.V., *Photoionization Processes in Gases*, Academic Press, New York, NY, 1967.

[24] Allen, R.A., "Air Radiation Graphs: Spectrally Integrated Fluxes Including Line Contributions and Self Absorption", Avco Corporation, Everett, MA, NASA-CR-556, 1965.

[25] Watanabe, K., "Ultraviolet Absorption Processes in the Upper Atmosphere", *Advances in Geophys.*, Vol. 5, 1958, pp. 153-221.

[26] Horton, T.E., "Radiative Coupled Nonequilibrium Flow Fields Associated with Aeroassisted Orbital Transfer", University of Mississippi, University, MS, NASA Contractor Rept. NAG-1-496, March 1986.

[27] Gnoffo, P.A., Gupta, R.N., and Shinn, J.L., "Conservation Equations and Physical Models for Hypersonic Air Flows in Thermal and Chemical Nonequilibrium", NASA Langley Research Center, Hampton, VA, NASA-TP-2867, Feb. 1989.

[28] Thompson, R.A., "Comparison of Nonequilibrium Viscous Shock Layer Solutions with Windward Surface Shuttle Heating Data", AIAA Paper 87-1473, June 1987.

[29] Carlson, L.A., "Nonequilibrium Radiation and Chemistry Models for Aerocapture Vehicle Flowfields", Texas A&M University, College Station, TX, TAMRF Rep. No. 6382-90-02, June 1990.

Table 1: Radiative Processes Included in the Shock Layer and Precursor

Radiative Process	Freq. Range
Shock Layer	
Free-Free, Bremsstrahlung	$0.0 < h\nu$
N - Low Frequency ionization (Highly excited states)	$0.0 < h\nu$
- High Frequency Ionization (Ground and first two excited states)	$10.9 < h\nu$
- Atomic Lines	–
N_2 - Birge-Hopfield Molecular Band	$6.50 < h\nu < 12.77$
- 1st Positive Molecular Band	$0.75 < h\nu < 4.5$
- 2nd Positive Molecular Band	$0.75 < h\nu < 4.5$
N_2^+- 1st Negative Molecular Band	$2.23 < h\nu < 4.46$
Precursor	
Free-Free, Bremsstrahlung	$0.0 < h\nu$
N - Low Frequency Ionization (Highly excited states)	$0.0 < h\nu$
- High Frequency Ionization (Ground and first two excited states)	$10.8 < h\nu$
N_2 - Ionization Continuum (Ground and first three excited states)	$8.24 < h\nu$
- Birge-Hopfield Molecular Band	$6.5 < h\nu < 12.77$
- 1st Positive Molecular Band	$0.75 < h\nu < 4.5$
- 2nd Positive Molecular Band	$0.75 < h\nu < 4.5$
- Lyman-Birge-Hopfield Molecular Band	$4.77 < h\nu < 9.78$
- Dissociation Continuum (Adjoining Lyman-Birge-Hopfield molecular band)	$9.78 < h\nu$
N_2^+- 1st Negative Molecular Band	$2.23 < h\nu < 4.46$

Table 2: Shock Standoff Distances and Radiative Fluxes

V (Km/sec)	Alt. (Km)	x_{shock} (cm)	q_{shock} (W/cm^2)
16	72	6.60	1,385.0
16	75	6.72	776.2
16	80	7.25	264.5
14	80	8.69	126.9
12	80	10.70	65.9
10	80	11.14	54.2

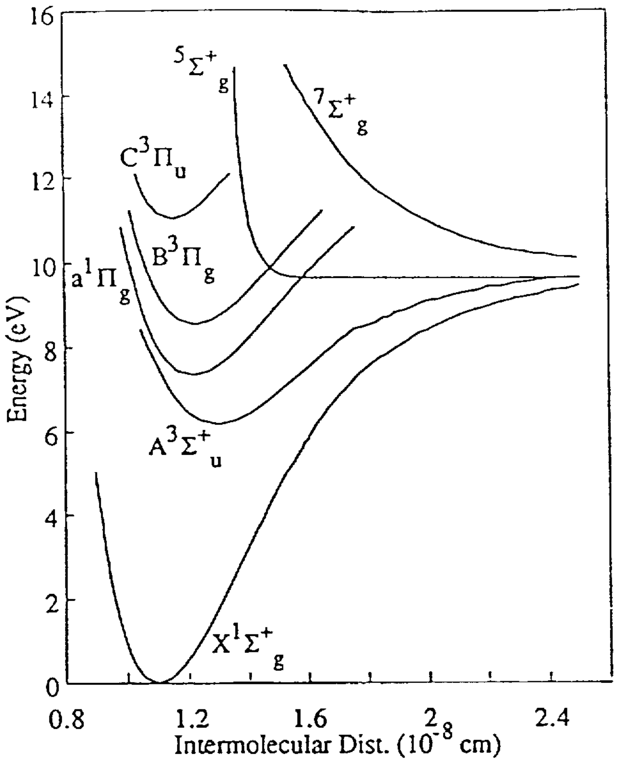

Fig. 1: Potential Energy Diagram of N_2

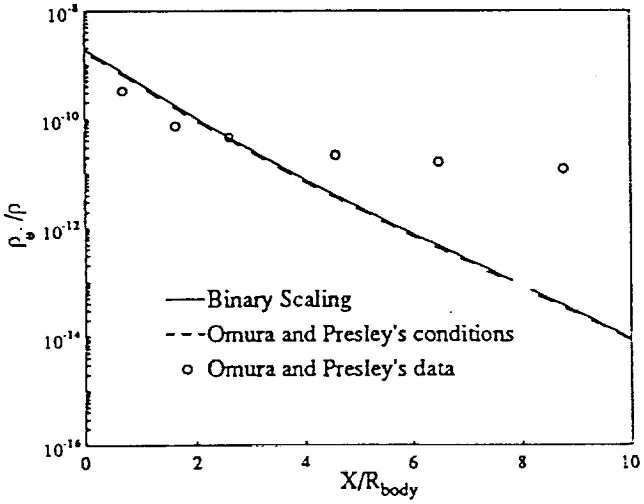

Fig. 2: Comparison Between Current Method and Shock Tube Data from Omura and Presley

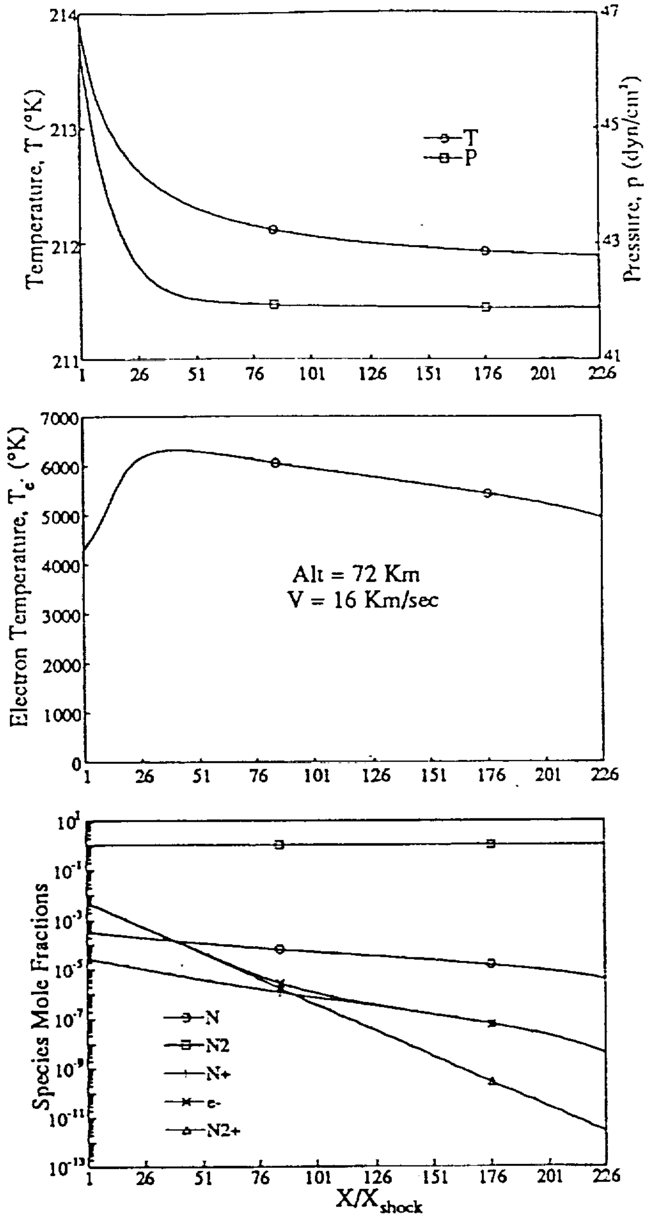

Fig. 3: Precursor Profiles for 16Km/sec Case at 72Km Alt.

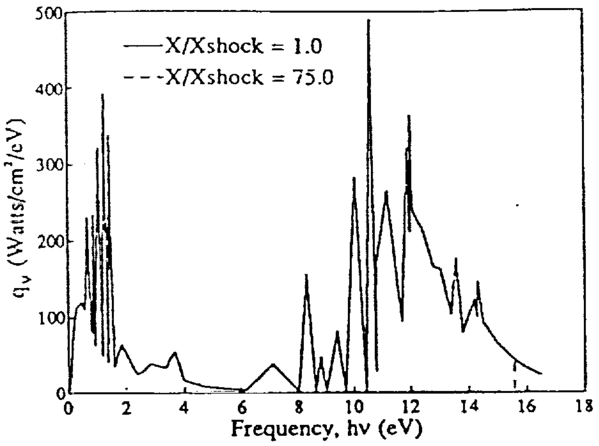

Fig. 4: Radiative Transfer for 16Km/sec Case at 72Km Alt.

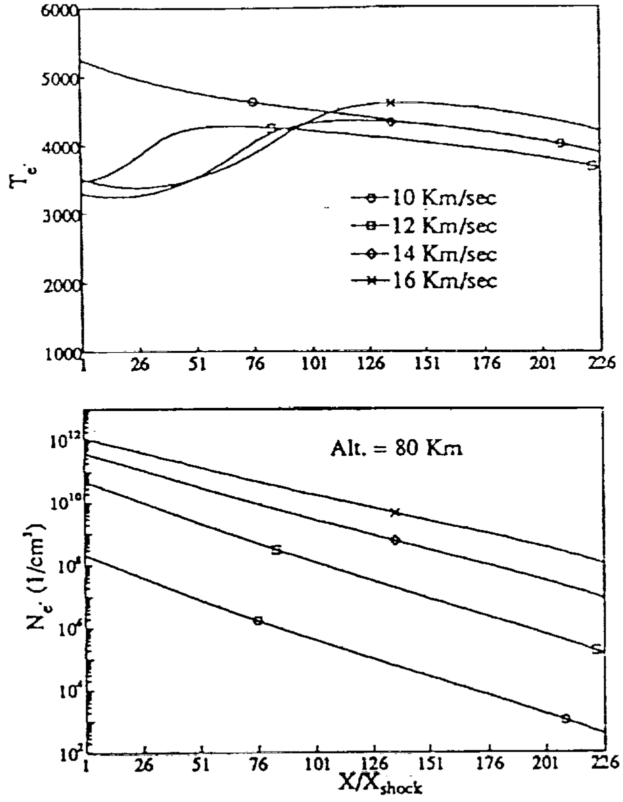

Fig. 6: Variation of the Precursor Flowfield with Changes in Freestream Velocity

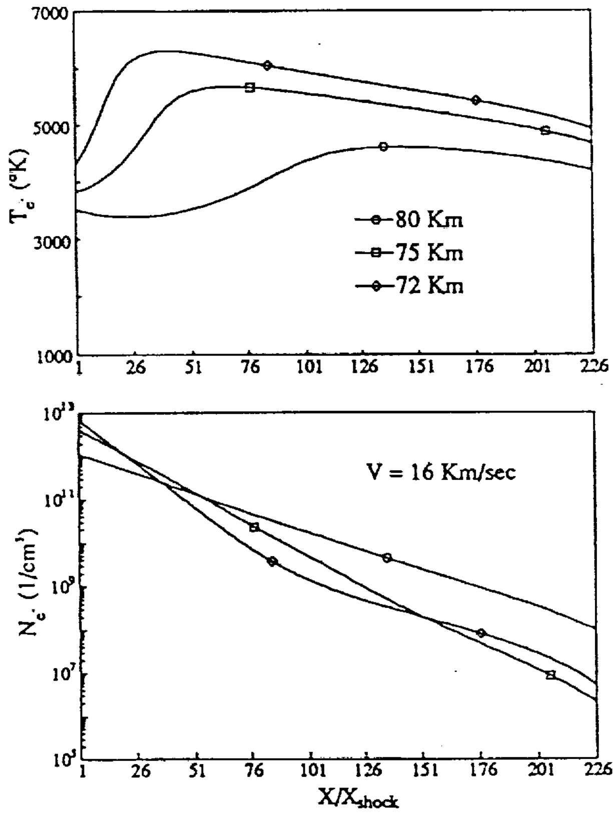

Fig. 5: Variation of the Precursor Flowfield with Changes in Altitude

Effects of Shock Wave Precursors Ahead of Hypersonic Entry Vehicles

S. A. Stanley and L. A. Carlson

Reprinted from

Journal of Spacecraft and Rockets

Volume 29, Number 2, March-April 1992, Pages 190-197

AIAA

A publication of the
American Institute of Aeronautics and Astronautics, Inc.
The Aerospace Center, 370 L'Enfant Promenade, SW
Washington, DC 20024-2518

JOURNAL OF SPACECRAFT AND ROCKETS
Vol. 29, No. 2, March-April 1992

Effects of Shock Wave Precursors Ahead of Hypersonic Entry Vehicles

Scott A. Stanley*
Lockheed Engineering and Sciences Company, Houston, Texas 77058
and
Leland A. Carlson†
Texas A&M University, College Station, Texas 77843

A model has been developed to predict the magnitude and characteristics of the shock wave precursor ahead of a hypervelocity vehicle entering the Earth's atmosphere. This model includes both chemical and thermal nonequilibrium, utilizes detailed mass production rates for the photodissociation and photoionization reactions, and accounts for the effects of radiative absorption and emission on the individual internal energy modes of both atomic and diatomic species. For this study, the Earth's atmosphere is modeled as pure nitrogen rather than as a nitrogen oxygen mixture. Comparison of the present results with shock tube data indicates that the model is reasonably accurate. A series of test cases representing Earth aerocapture return from Mars indicate that there is a significant production of atoms, ions, and electrons ahead of the shock front due to radiative absorption and that the precursor is characterized by an enhanced electron/electronic temperature and molecular ionization. However, the precursor has a negligible effect on the shock layer flowfield.

Nomenclature

AF = radiation attenuation factor
D_n = dissociation energy for the nth species, eV
E = energy per particle, eV
E_3 = third exponential integral
e = energy per unit mass, erg/g
e_e'' = electron/electronic energy, erg/g
H = total enthalpy, erg/g
h = static enthalpy, erg/g
$h\nu$ = photon energy, eV
I_i = ionization energy of the ith species, eV
k = Boltzmann's constant, 1.38×10^{-16} erg/K
k_ν' = absorption coefficient, 1/cm
M_n = molecular weight of the nth species, g/mole
m_n = mass per particle of the nth species, g
N_n = number density of the nth species, $1/\mathrm{cm}^3$
n_{diss} = number of bound-free dissociation processes
n_{mb} = number of molecular bands
n_s = number of species
p = pressure, $\mathrm{dyne/cm}^2$
q = radiative flux, $\mathrm{W/cm}^2$
$\hat{R}$ = universal gas constant, 8.317×10^7 erg/K g mole
T = heavy particle temperature, K
T_e = electron/electronic temperature, K
V = velocity, cm/s
$\dot{w}_n$ = mass production rate of the nth species, $\mathrm{g/cm}^3$ s
x = spatial variable in the precursor, cm
Y = absorption coefficient ratio
β = one-half of the angle subtended by the body
ν = frequency, 1/s
ξ = energy production due to inelastic collisions, $\mathrm{W/cm}^3$
ρ = density, $\mathrm{g/cm}^3$
τ = optical depth

Subscripts

elct = electronic
i = for the ith process
j = for the jth electronic level
n = for the nth species
rot = rotational
tr = translational
vib = vibrational
ν = at the frequency ν

Superscripts

TS = tangent slab approximation
s = at the shock

Introduction

THE recent emphasis placed on a mission to Mars and the subsequent return of samples has caused an increased interest in the development of accurate methods for predicting the fluid flow around hypersonic entry vehicles. This interest is a result of the plan to use an aerocapture technique to provide the reduction in velocity necessary to place the spacecraft in Earth orbit. This technique uses aerodynamic drag, resulting from the interaction of the spacecraft with the Earth's atmosphere, instead of propulsive braking to slow the vehicle to orbital speeds. Such an approach provides a reduction in the fuel necessary for the mission and an increase in the payload capabilities. A vehicle entering the Earth's atmosphere upon return from Mars will experience velocities in the high hypersonic range, 11-16 km/s.[1,2]

The majority of the recent work associated with hypersonic flowfields has involved the shock layer; the shock wave precursor, on the other hand, has received little attention. The precursor is the region ahead of the shock wave in which radiation, primarily ultraviolet, emitted by the hot shock layer is reabsorbed by the gas. This absorption of radiation causes a heating of the gas in the precursor and the production of atoms as well as ions through the photoionization and photodissociation reactions. These changes might also in turn affect the gas behind the shock front. For example, the preheating of the gas in the precursor as well as the introduction of electrons and ions could potentially increase the rate at which the gas behind the shock approaches equilibrium. It has also been shown that for certain conditions the absorption of radiation ahead of the shock can cause significant increases in the radia-

---

Presented as Paper 91-1465 at the AIAA 22nd Fluid Dynamics, Plasma Dynamics, and Lasers Conference, Honolulu, HI, June 24-26, 1991; received July 12, 1991; revision received Oct. 29, 1991; accepted for publication Oct. 29, 1991.

*Associate Engineer, Navigation, Control, and Aeronautics Department, 2400 NASA Road 1. Member AIAA.

†Professor, Aerospace Engineering Department. Associate Fellow AIAA.

tive heating to the body.[3,4] Further, the presence of free electrons in the precursor can significantly affect communications with and identification of entry vehicles.[5,6]

Much of the previous work on shock wave precursors has been performed using shock tubes and shock tunnels.[7-9] A number of computational studies have also been performed.[10-13] The majority of this previous work, however, has involved monatomic gases and is therefore not directly applicable to the Earth's atmosphere.

The studies by Tiwari and Szema[13,14] as well as by Omura and Presley[15,16] involve diatomic gases and therefore are significant to a study of the Earth's atmosphere. Tiwari and Szema calculated the effects of the precursor on the shock layer and the radiative heating of a body entering the hydrogen atmosphere of Jupiter, whereas Omura and Presley conducted a shock tube study of the electron densities ahead of strong shock waves in nitrogen as well as air.

The objective of this study was to develop a technique for predicting the character and magnitude of the chemical and thermal nonequilibrium shock wave precursor ahead of a hypervelocity entry vehicle that includes in detail the mass production due to photodissociation and photoionization of the various species and properly accounts for radiative absorption and emission effects on the internal energy modes of both atomic and diatomic species. A secondary objective was to ascertain the effect of this precursor on the vehicle flowfield.

Radiative Transfer Formulation

In most of the previous work investigating shock wave precursors, several assumptions have been imposed on the radiative transfer calculations. A common assumption has been that the shock layer emits radiation as a black body at the equilibrium temperature behind the shock front.[10,12,17] Also, several of the previous works have utilized a multiple step absorption coefficient model[1,13,14] where, at a given temperature, the species radiative properties have been assumed constant over specific frequency regions. However, since photochemical reactions are being considered, variations in the radiative transfer can cause significant changes in the gas. Likewise, the spectral details are very important in these calculations since the important radiative processes occur over different frequency ranges and the frequency of the photon absorbed as well as the process through which it is absorbed directly affects how the photon energy changes the energy of the gas. Without sufficient spectral detail, it is not possible to ascertain what portion of the radiation absorbed causes photoionization or photodissociation and what portion simply causes an increase in the internal energy of the gas.

Because of the necessity of accurate radiation predictions for the calculation of the photochemical reactions, it was decided that a complete spectrally detailed method of calculating the radiative flux was in order. Thus, an extensively modified version of the program RADICAL was utilized. This program, originally created by Nicolet,[18] allows the user to select the frequency points used for the continuum radiation, so it was possible to obtain the spectral detail necessary for accuracy in the calculation of the photochemical reactions. RADICAL also performs detailed calculations of the atomic line radiation.

RADICAL, like many of the schemes currently used in the calculation of radiative transfer, uses the tangent slab approximation. This assumption is a one-dimensional approximation of the full equation of radiative transfer, which treats the radiation emitted at a point in the gas as if it were emitted by an infinite plane of gas positioned perpendicular to the direction of travel of the radiation. Since the thickness of the shock layer is much smaller than the body dimensions, each point in the shock layer is positioned close enough to the body that the rest of the gas in the radiating shock layer indeed appears to be of infinite extent; therefore, this is a reasonable assumption in the shock layer. The precursor, on the other hand, can extend to distances ahead of the shock that are of the same order of magnitude as the body diameter. Therefore, in the precursor, the radiating shock layer no longer appears to be of infinite extent but instead appears to be a slab of finite diameter.

In the one-dimensional problem, as in the shock layer, absorption is the only method by which the radiation is attenuated as it travels through the gas. Therefore, any decrease in the radiative intensity through the gas can be attributed to absorption, which in turn causes an increase in the energy of the gas equal to the decrease in the radiative energy. Since the shock layer does not appear to be of infinite extent at each point in the precursor, however, the radiation no longer behaves one dimensionally. Consequently, in the precursor the radiative transfer is a three-dimensional problem in which a decrease in the radiative intensity can occur due to the geometry as well as the absorption.

This geometric attenuation in the precursor occurs because the radiative energy emitted by the finite diameter shock layer propagates radially outward into the forward 180 deg semisphere. Therefore, as the energy emitted progresses outward, the area through which it passes increases, thus producing a decrease in the radiative flux. This decrease, however, is not due to absorption by the gas and therefore has no effect on the gas.

Thus, to use RADICAL for the radiation calculations, it was necessary to correct for the geometric attenuation of the radiation. This was done by expressing the radiative flux in the precursor as

$$q_\nu = AF_\nu q_\nu^{TS} \tag{1}$$

where q_ν^{TS} is the radiative flux at the point of interest using the tangent slab approximation and AF_ν is the geometric attenuation factor defined by

$$AF_\nu = \left\{ 1 - \cos^2(\beta) \frac{E_3[(\tau_\nu - \tau_\nu^S)\sec(\beta)] - E_3[\tau_\nu \sec(\beta)]}{E_3(\tau_\nu - \tau_\nu^S) - E_3(\tau_\nu)} \right\} \tag{2}$$

In this expression, β is half of the angle subtended by the body as viewed from the point of interest in the precursor. This expression is derived in detail by Stanley.[19]

In the species continuity and energy equations, the terms involving the radiation appear as a divergence of the flux and are defined to account for the absorption and emission of radiation at a point. However, simple differentiation of Eq. (1) yields

$$\frac{\partial q_\nu}{\partial x} = AF_\nu \frac{\partial q_\nu^{TS}}{\partial x} + q_\nu^{TS} \frac{\partial AF_\nu}{\partial x} \tag{3}$$

In this expression, the first term on the right-hand side is the change in the radiative flux due to the emission and absorption of radiation, and the second term is the change due to the geometry of the problem and should not affect the gas. Therefore, the second term was neglected in the flowfield calculations. Notice that if the second term was included in the species continuity and energy equations, an essentially transparent radiation would appear to be absorbed due to the spatial variation of the attenuation factor.

To properly account for the effects of absorption and emission of radiation on the energy of the gas, it is necessary to have an understanding of how each radiative process physically changes the particles involved. The effects of the absorption and emission of radiative energy on the internal energy modes depend on the type of radiative process as well as the frequency of the photon absorbed or emitted. Radiative processes can be separated into three categories: free-free, bound-bound, and bound-free. While free-free and bound-bound processes cause a change in the energy of the gas with no chemical change, the bound-free processes are associated with chemical reactions in the gas, such as photoionization or photodissociation.

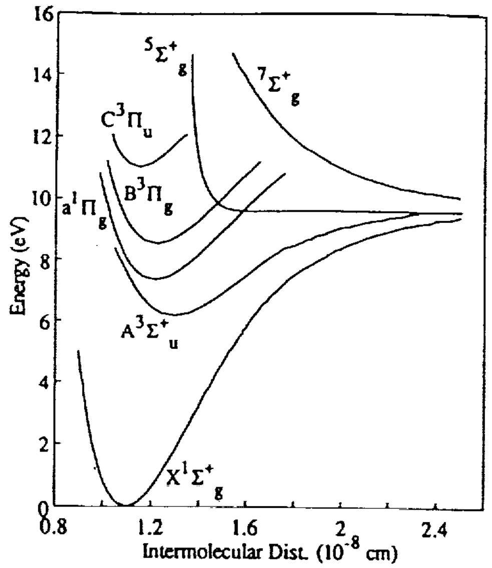

Fig. 1 Potential energy diagram of N_2.

Table 1 Radiative processes included in the shock layer and precursor

	Radiative process	Frequency range
Shock layer		
	Free-free, bremsstrahlung	$0.0<h\nu$
N	Low frequency ionization (highly excited states)	$0.0<h\nu$
	High frequency ionization (ground and first two excited states)	$10.9<h\nu$
	Atomic lines	—
N_2	Birge-Hopfield molecular band	$6.5<h\nu<12.77$
	First positive molecular band	$0.75<h\nu<4.5$
	Second positive molecular band	$0.75<h\nu<4.5$
N_2^+	First negative molecular band	$2.23<h\nu<4.46$
Precursor		
	Free-free, bremsstrahlung	$0.0<h\nu$
N	Low frequency ionization (highly excited states)	$0.0<h\nu$
	High frequency ionization (ground and first two excited states)	$10.8<h\nu$
N_2	Ionization continuum (ground and first three excited states)	$8.24<h\nu$
	Birge-Hopfield molecular band	$6.5<h\nu<12.77$
	First positive molecular band	$0.75<h\nu<4.5$
	Second positive molecular band	$0.75<h\nu<4.5$
	Lyman-Birge-Hopfield molecular band	$4.77<h\nu<9.78$
	Dissociation continuum (adjoining Lyman-Birge-Hopfield molecular band)	$9.78<h\nu$
N_2^+	First negative molecular band	$2.23<h\nu<4.46$

Photodissociation of the relatively cool nitrogen in the precursor occurs through a process called predissociation, a radiationless process in which a molecule makes a transition from a discreet electronic state to a dissociated state.[20] In cool nitrogen, this predissociation occurs primarily through the Lyman-Birge-Hopfield molecular band and the subsequent transfer out of the $a^1\Pi_g$ state into the repulsive $^5\Sigma_g^+$ + state (Fig. 1).

The radiative processes included in the calculation of the emission and absorption in the shock layer and precursor for this study are given in Table 1. The radiative processes included in the shock layer are those originally accounted for in the modified version of RADICAL. These processes include not only the continuum processes but also the atomic lines associated with the nitrogen atom. Since only continuum processes were included in the precursor, the continuum mechanisms originally included in RADICAL were retained. Also, the photoionization of molecular nitrogen, the Lyman-Birge-Hopfield molecular band, and the dissociation of molecular nitrogen through a continuum adjoining the Lyman-Birge-Hopfield band were added to the processes in RADICAL.

The absorption coefficients for photoionization of molecular nitrogen and the Lyman-Birge-Hopfield molecular band were determined using theoretical expressions derived according to Zel'dovich and Raizer.[21] For the photoionization process, the absorption coefficient was found to be given by the expression

$$k_\nu = 1.9986 \times 10^{-14} \frac{N_{N2}}{(h\nu)^3} \sum_{j=j^*}^{\infty} \frac{1}{j^3} e^{-(x_1 - x_j)} \tag{4a}$$

$$x_j = \frac{(I_{N2} - E_{\mathrm{elcl}_j})}{kT} \tag{4b}$$

where the photon energy $h\nu$ is given in electron volts. The lower limit on the summation over the electronic states in this equation is governed by the requirement that the photon energy be greater than the binding energy for the state. Otherwise, the photon has insufficient energy to cause photoionization.

For this study, the summation in Eqs. (4) was limited to the lowest four electronic states of the nitrogen molecule. However, in the cool precursor the populations of all except the ground electronic state were small. It should be noted that Eqs. (4) provide values near the ionization threshold on the same order of magnitude as those predicted by Zel'dovich and Raizer[22] as well as those predicted by Marr.[23]

The absorption coefficient for the Lyman-Birge-Hopfield molecular band was found to be given by

$$k_\nu = 9.1458 \times 10^{16} \frac{N_{N2}}{T} \exp\left[-\frac{(113{,}314.97 - 11{,}610.14h\nu)}{T}\right] \tag{5}$$

This equation was obtained from expressions given by Zel'dovich and Raizer[21] using an absorption oscillator strength of 3.7×10^{-6} from Allen[24] and then correcting to match experimental predictions given by Watanabe.[25] The absorption coefficient for the dissociation continuum adjoining this molecular band was assumed to be given by the expression

$$k_\nu = 4.97 \times 10^{-20} N_{N2} \tag{6}$$

The constant in this equation was taken from the data presented by Watanabe for absorption through this process in cool air.

Precursor Formulation

For this study, the Earth's atmosphere was modeled as pure nitrogen rather than a nitrogen oxygen mixture. This approach is a common simplifying assumption when performing nonequilibrium, hypervelocity flowfield calculations since a nitrogen gas represents the properties of air quite well. In dealing with the precursor, however, the primary concern was whether or not the absorption processes of nitrogen sufficiently model those of air. After careful consideration it was decided that due to the predominance of nitrogen in the atmosphere it would be reasonable to represent the atmosphere as nitrogen in this initial study.

The effects of thermal nonequilibrium in the precursor were included in this study by permitting the free electrons and heavy particles to have different temperatures. Further, it was assumed that the free electrons and electronic states were in equilibrium at a common temperature, which, as discussed by Nelson and Goulard,[11] is one of the limiting cases for the precursor. For this region of the gas, the temperature governing the electronic states would normally be expected to be greater than the heavy particle temperature but less than the electron temperature. Thus, ideally a three temperature model should be used allowing a separate electronic temperature.

Nevertheless, since the mechanisms and expressions for the transfer of energy between the electronic states and the free electrons are not well known or well understood, it was decided to use only a two temperature model. However, to correct for the local thermodynamic nonequilibrium between the electrons and the electronic states, a collision limiting correction[26] was applied to the populations of the molecular electronic states when computing the radiative emission and absorption phenomena.

For this study, the mass production rates in the precursor due to collisional reactions were neglected in comparison with those due to photochemical reactions. The photoreactions used in the precursor include the dissociation of molecular nitrogen and the ionization of both molecular and atomic nitrogen, i.e.,

$$N_2 + h\nu \xleftrightarrow{k_{\nu 1}} 2N$$

$$N_2 + h\nu \xleftrightarrow{k_{\nu 2}} N_2^+ + e^-$$

$$N + h\nu \xleftrightarrow{k_{\nu 3}} N^+ + e^-$$

The elastic collisional terms in the electron/electronic energy equation were evaluated using the collisional cross sections of Gnoffo et al.[27]

The effects of the absorption of radiation through free-free and bound-bound processes were also included in this study. Although these processes do not cause chemical reactions, they do cause an increase in the energy of the gas, and their effects must be included in the electron/electronic energy equation. Absorption through atomic lines was neglected due to the expected low concentration of atomic species.

The equations governing the fluid properties on the stagnation streamline in the precursor are the steady, one-dimensional, nonequilibrium Euler equations.

Global continuity:

$$\frac{\partial}{\partial x}(\rho V) = 0 \tag{7}$$

Momentum:

$$\rho V \frac{\partial V}{\partial x} + \frac{\partial p}{\partial x} = 0 \tag{8}$$

Energy:

$$\rho V \frac{\partial H}{\partial x} + \frac{\partial q}{\partial x} = 0 \tag{9}$$

In Eq. (9), H is the total enthalpy of the gas defined in terms of the static enthalpy such that

$$H = h + ½ V^2 \tag{10}$$

where

$$h = \frac{p}{\rho} + \sum_{n=1}^{n_s} (e_{\mathrm{tr}_n} + e_{\mathrm{rot}_n} + e_{\mathrm{vib}_n} + e_{\mathrm{elct}_n} + e_n^0) \tag{11}$$

The second term in Eq. (9) is the gradient of the radiative flux. This term accounts for the increase or decrease in the energy of the gas due to absorption and emission of radiation. In addition to these equations, the equation of state for a two temperature gas is required,

$$p = \rho \hat{R} T \sum_{n=1}^{n_s} \left(\frac{\rho_n}{\rho} \frac{1}{M_n} \right) + \rho \frac{\hat{R}}{M_{e^-}} \frac{\rho_{e^-}}{\rho} (T_e - T) \tag{12}$$

To allow for the effects of thermal nonequilibrium, an electron/electronic energy equation was added to these equations,

$$\frac{\partial}{\partial x}(\rho V e_e'') = -p_e \frac{\partial V}{\partial x} + \sum_{n=1}^{n_s} \xi_{e,n} + \dot{w}_e \frac{V^2}{2} - \frac{\partial q}{\partial x}$$
$$+ \sum_{i=1}^{n_{\mathrm{diss}}} \int_0^\infty \frac{Y_{\nu_i}^p (h\nu - \Delta E_{\mathrm{elct}_i} - D_i)}{h\nu} \frac{\partial q_\nu}{\partial x} \mathrm{d}\nu$$
$$+ \sum_{i=1}^{n_{mb}} \int_0^\infty \frac{Y_{\nu_i}^p (h\nu - E_{\mathrm{elct}_i}^{\mathrm{upp}} + E_{\mathrm{elct}_i}^{\mathrm{low}})}{h\nu} \frac{\partial q_\nu}{\partial x} \mathrm{d}\nu \tag{13}$$

where

$$e_e'' = \frac{\rho_{e^-}}{\rho} e_{e^-} + \sum_{n=1}^{n_s} (e_{\mathrm{elct}_n} + e_n^0) \tag{14}$$

In this equation, e_{e^-} is the kinetic energy of the free electrons, $3/2kT_e/m_{e^-}$, whereas e_{elct_n} and e_n^0 are the electronic and zero point energies of the nth species. The last three terms on the right-hand side of Eq. (13) allow for the effects of the absorption of radiation. This equation is derived in detail in Ref. 19.

Chemical nonequilibrium was accounted for in the precursor through the addition of a species continuity equation for each of the five species in the problem. These equations are of the form

$$\rho V \frac{\partial(\rho_n/\rho)}{\partial x} = -m_n \int_0^\infty \frac{Y_{\nu_n}^s}{h\nu} \frac{\partial q_\nu}{\partial x} \mathrm{d}\nu \tag{15}$$

where

$$Y_{\nu_{N_2}}^s = -\frac{k'_{\nu_1} + k'_{\nu_2}}{k'_{\nu_{\mathrm{tot}}}} \tag{16a}$$

$$Y_{\nu_{N_2^+}}^s = \frac{k'_{\nu_2}}{k'_{\nu_{\mathrm{tot}}}} \tag{16b}$$

$$Y_{\nu_N}^s = \frac{2k'_{\nu_1} - k'_{\nu_3}}{k'_{\nu_{\mathrm{tot}}}} \tag{16c}$$

$$Y_{\nu_{N^+}}^s = \frac{k'_{\nu_3}}{k'_{\nu_{\mathrm{tot}}}} \tag{16d}$$

$$Y_{\nu_{e^-}}^s = \frac{k'_{\nu_2} + k'_{\nu_3}}{k'_{\nu_{\mathrm{tot}}}} \tag{16e}$$

The term on the right-hand side of Eq. (15) is the mass production rate of the nth species due to photoprocesses. The absorption coefficients, k'_{ν_1}, k'_{ν_2}, and k'_{ν_3} are those for the absorption and emission processes associated with each of the three photochemical reactions discussed previously. Equation (15) is derived in detail in Ref. 19.

In all of the previous equations, the radiative terms $\partial q/\partial x$ are the changes in the radiative flux due only to the absorption of radiation and not those due to the geometry of the problem as discussed in the previous section.

The equations governing the flowfield properties in the precursor were solved using a space marching technique starting at a point far from the shock front and marching in toward the shock wave. The point furthest from the shock wave was assumed to be far enough from the radiating shock layer that the ultraviolet radiation was absorbed between this point and the shock; thus the gas properties at this point were forced to remain at the freestream conditions. The spacing between each spatial point was adjusted as the solution progressed to prevent the changes in the flowfield properties between each point from becoming too large. This procedure forced a large concentration of points in the regions of large gradients and allowed the distance between the points to increase in regions of small gradients. At each individual point in the precursor, the governing equations, Eqs. (7-16), were solved using an iterative procedure.

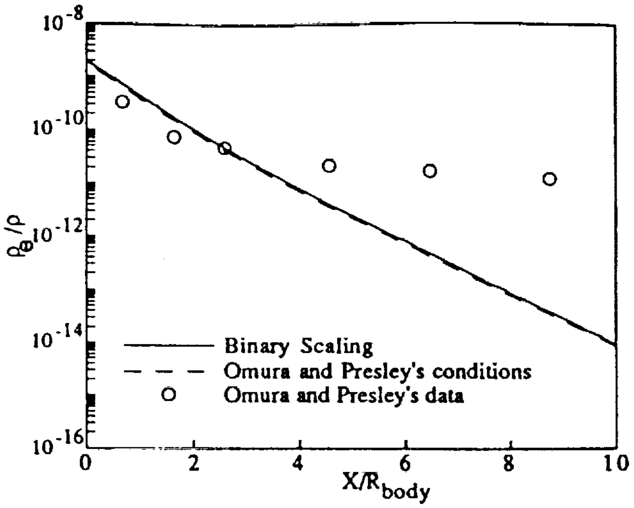

Fig. 2 Comparison between current method and shock tube data from Omura and Presley.[15,16]

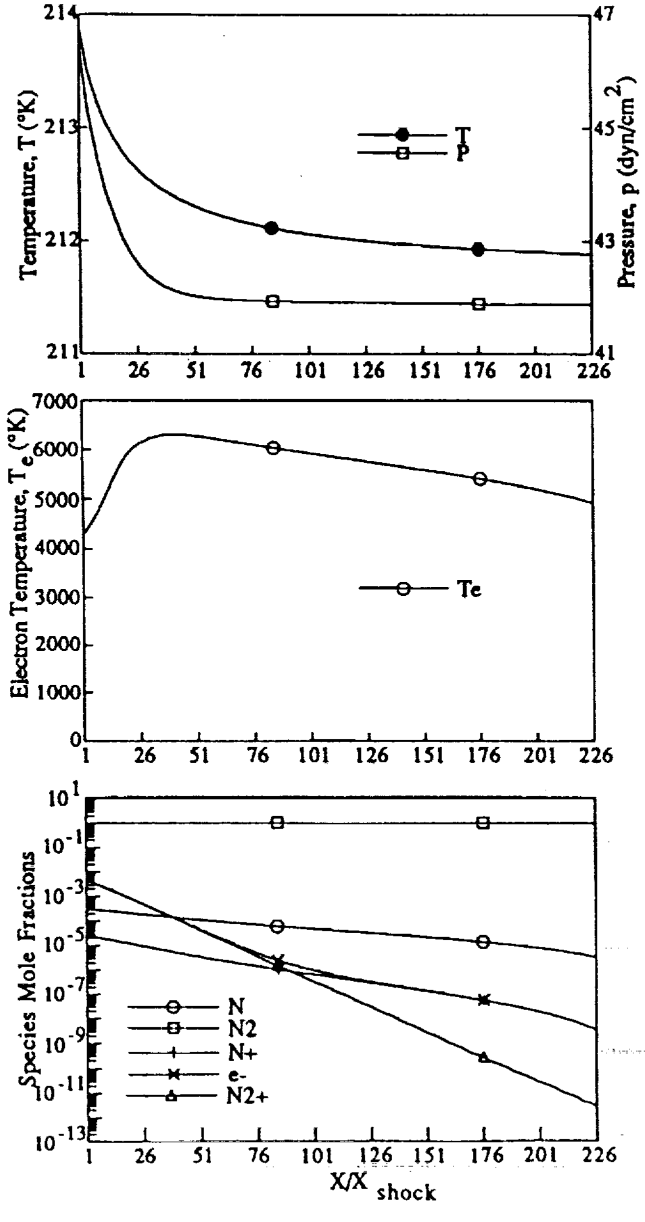

Fig. 3 Precursor profiles for 16 km/s case at 72 km altitude.

Shock Layer Formulation

To properly model the precursor ahead of a shock wave, it is necessary to know the spectral details of the radiation that passes from the shock layer and through the shock front to the precursor. To calculate these spectral details, the conditions of the gas in the shock layer must be known in detail. For the flight conditions of interest in this study, a number of important phenomena such as chemical and thermal nonequilibrium must be included to properly model the shock layer. Also, since the effects of radiation are of primary importance in the precursor, it is desirable that they be included in the shock layer model. The inclusion of these three phenomena can significantly affect the radiation and hence the precursor.

For this portion of the flowfield, a viscous shock layer (VSL) scheme based on a version of the NASA code VSL3DNQ[28] was used. The version of VSL3DNQ used in this study was modified extensively by Carlson.[29] These modifications primarily involved the nonequilibrium chemistry and the effects of thermal nonequilibrium. However, the code was also modified to allow the shock layer and radiation calculations to be coupled to the gas dynamics, thus incorporating the effects of the emission and absorption of radiation into the flowfield solution.

Results and Discussion

Figure 2 compares the electron mass fractions found by Omura and Presley[15,16] in the precursor ahead of a shock wave in a nitrogen gas with those calculated using the present method. Omura and Presley measured the electron densities in the precursor using a 12-in. shock tube. The shock velocity for their case was 11.89 km/s. Shown in this figure, along with Omura and Presley's results, are two curves showing the electron mass fractions calculated using the current method. The dashed curve was calculated using Omura and Presley's freestream conditions and shock velocity with a 12-in.-diam body. However, the solid curve was calculated using a lower freestream density and pressure than Omura and Presley along with a larger diameter body scaled so that the conditions match those of Omura and Presley's case using binary scaling.

As can be seen from this figure, the electron mass fractions calculated using this method match those found by Omura and Presley reasonably well near the shock front. However, far from the shock they deviate. It is believed that the differences in the electron mass fraction far from the shock are due to the reflection of the radiative flux off of the shock tube walls in the Omura and Presley case. This reflection should greatly increase the quantity of radiation present far ahead of the shock wave over that which would be present in a free field such as is being used for the calculations. This increased presence of radiation far from the shock would induce greater absorption and thus an increase in the production of electrons due to photoionization. It is also interesting to note how well the two sets of calculations match using binary scaling.

The results discussed in the remainder of this section are representative of "typical" conditions for an aerobrake vehicle entering the Earth's atmosphere upon return from Mars. These results were calculated for the stagnation streamline of a 2.3 m nose radius vehicle at three altitudes: 72, 75, and 80 km. The shock layer calculations were made using 52 points between the shock wave and the body and allowing for atomic local thermodynamic nonequilibrium as well as radiation/gasdynamic coupling. The radiation calculations were made using 74 continuum frequency points selected to provide good spectral detail in the ultraviolet absorption region of interest in the precursor. A wall temperature of 1650 K was used in both the shock layer and the radiation calculations.

72 km, 16 km/s

Figure 3 shows the heavy particle temperature, electron/electronic temperature, pressure, and the five species mole fraction variations through the precursor for this case. The

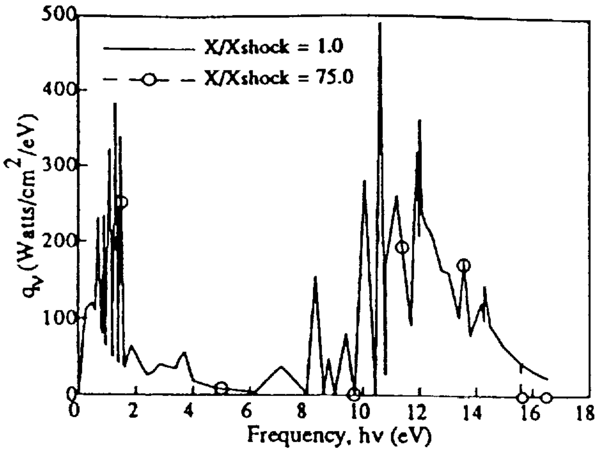

Fig. 4 Radiative transfer for 16 km/s case at 72 km altitude.

radiative flux through the shock front for this case was 1385.0 W/cm^2, and the spectral details of this radiation are shown in Fig. 4. The shock standoff distance for this case was 6.60 cm. The radiation emitted from the shock layer for this case was the greatest of all of those considered. Thus this case experienced the largest flowfield perturbations in the precursor region.

From these figures, it can be seen that the heavy particle temperature and pressure increased steadily through the precursor region. However, even for this extreme case the changes in these values were small. The density and velocity of the gas were found to be essentially constant in the precursor. This behavior verifies what was shown by Tiwari and Szema[13,14] and assumed by many others.[10-12,15]

The electron/electronic energy of the gas also increased from a value of essentially zero in the freestream to a value on the order of 10^9 immediately ahead of the shock front. It was observed from comparisons of the total energy increase in the precursor to the electron/electronic energy increase that 99% of the radiative energy absorbed affected the electron/electronic energy of the gas. Only 1% of the energy absorbed affected the heavy particle translational, rotational, and vibrational energies of the gas. Furthermore, by comparing the increase in the zero point energy of the gas with the increase in the electron/electronic energy, it was found that 96% of the increase in the electron/electronic energy was involved with an increase in the zero point energy. From this, it was found that the majority of the energy absorbed in the precursor was involved with the ionization and dissociation of the gas.

The electron/electronic temperature behaved differently in the precursor than the other gas properties. It increased steadily to a maximum value of approximately 6300 K at a distance of 40 shock standoff distances ahead of the body. It then decreased rapidly to a value of 4290 K immediately ahead of the shock front. This decrease in the electron/electronic temperature was a result of the production of "low" energy electrons through photoionization caused by photons of frequencies only slightly larger than the ionization threshold of N_2. The production of these low energy electrons caused a decrease in the average energy per electron, hence a decrease in the electron/electronic temperature. That this decrease was a result of the production of low energy electrons rather than due to a transfer of energy from the electrons through elastic collisions was evident since there was no decrease in the electron/electronic energy accompanying this decrease in the electron/electronic temperature. This decrease also coincided with a region of rapid increase in the electron concentration in the gas due to the photoionization of molecular nitrogen.

The photons with energy near the ionization threshold of molecular nitrogen were absorbed rapidly in front of the shock since the strongest absorption region for an ionization process is at frequencies near the threshold. The higher energy photons in the weaker absorption range, far from the threshold, escaped to distances further from the shock where they were absorbed, causing the creation of high energy electrons. The production of these high energy electrons resulted in a high electron/electronic temperature far from the shock. However, although the electron/electronic temperature was high far from the shock, the electron mass fraction in this region was extremely small. It should be noted that a similar decrease in the precursor electron temperature near the shock was also predicted by Foley and Clarke,[12] although they attributed it to collisional electron impact ionization.

Considering the mole fractions of the five species, it can be seen that the dominant chemical reaction far from the shock was the photoionization of atomic nitrogen. However, near the shock, photoionization of molecular nitrogen dominated. The mole fractions of the ionized nitrogen molecule immediately ahead of the shock were at least an order of magnitude greater than those for the nitrogen atom and ionized nitrogen atom, although there were significant quantities of all three species.

Because the dominant change in the precursor was due to the photoionization of molecular nitrogen, the thickness of the precursor was considered to be the distance through which this reaction had an effect. By this definition, for this case the shock precursor thickness was in the range of 75 shock standoff distances or 495 cm. Although there was a slight heating of the gas as well as the production of nitrogen atoms through photodissociation at greater distances from the shock, their effects were small compared with the changes within 495 cm of the shock front.

As can be seen in Fig. 4, the radiation propagating through the shock wave from the shock layer into the precursor was distributed over a wide range of frequencies. A large portion of this radiative energy was in the infrared frequency range ($h\nu \leq 5$ eV). Most of the radiation in this region was emitted by the entry body itself, although embedded within the continuum radiation from the body were a number of atomic lines. Also, the peak of radiation near 3.5 eV was due to three molecular bands, the first negative band of N_2^+ and the first and second positive bands of N_2. There was also a large quantity of radiative energy in the ultraviolet frequency range. That above 10 eV was due primarily to the Birge-Hopfield band of molecular nitrogen as well as the ionization continuum and lines of atomic nitrogen. Through the visible frequency ranges (5 eV $\leq h\nu \leq$ 8 eV) there was very little radiative energy.

The second curve in Fig. 4 shows the radiative flux at a position 75 shock standoff distances ahead of the shock front uncorrected for the geometric attenuation. By comparing this uncorrected radiative flux with the radiative flux through the shock front, it is possible to ascertain in what portion of the frequency range the cool precursor absorbed. This figure shows that the precursor absorbed radiation strongly at frequencies above the ionization threshold of molecular nitrogen, 15.59 eV. Although there was energy absorbed at frequencies less than this threshold due to photodissociation of molecular nitrogen and photoionization of atomic nitrogen, the amount of energy absorbed in these processes was small compared with that absorbed in the photoionization of molecular nitrogen. This result agrees with the previous statements that the dominant reaction was molecular ionization.

Through the course of this study it was found that even though there was significant production of dissociated and ionized nitrogen in the precursor region, the precursor had very little effect on the gas in the shock layer. By including these perturbed preshock conditions in the viscous shock layer calculations, it was found that they had negligible effect on the shock layer solution and produced no measurable change in the radiative heat transfer to the body. The primary change due to the inclusion of the precursor was in the conditions of the gas immediately behind the shock wave. Neglecting the

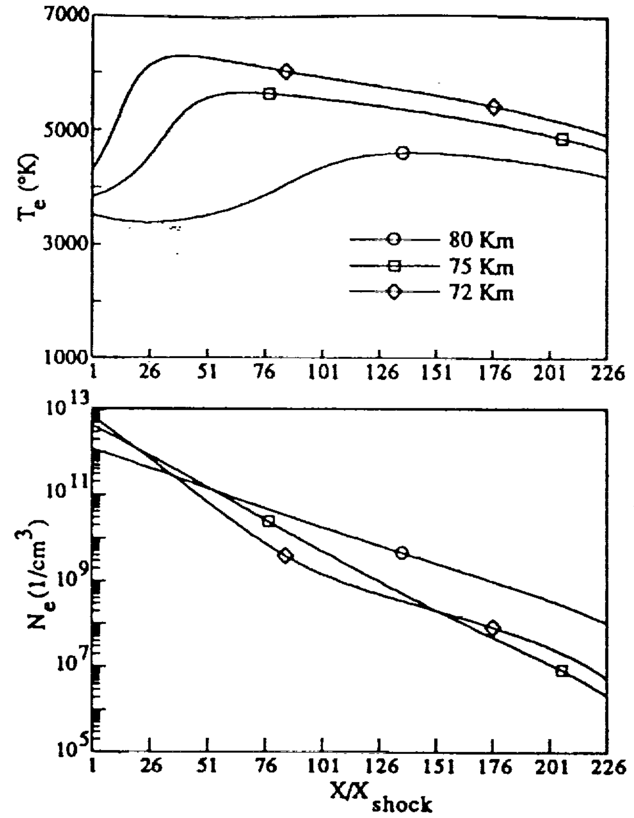

Fig. 5 Variation of the precursor flowfield with changes in altitude.

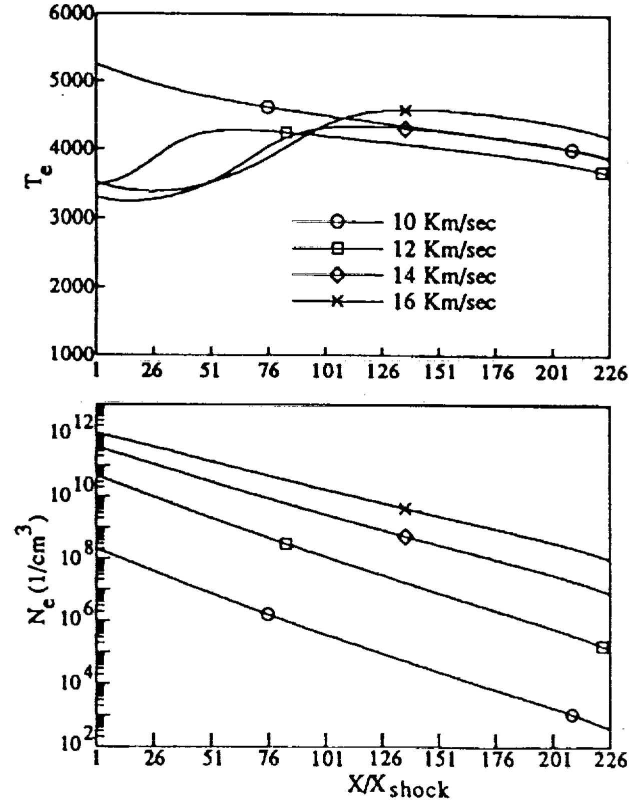

Fig. 6 Variation of the precursor flowfield with changes in freestream velocity.

Table 2 Shock standoff distances and radiative fluxes

V, km/s	Alt., km	X_{shock}, cm	q_{shock}, W/cm^2
16	72	6.60	1385.0
16	75	6.72	776.2
16	80	7.25	264.5
14	80	8.69	126.9
12	80	10.17	65.9
10	80	11.14	54.2

precursor, the mass fractions for the free electrons, ions, and atoms were zero upon crossing the shock; however, including the effects of the precursor, these mass fractions had nonzero values. Likewise, including the effects of the precursor resulted in a slight increase in the electron temperature in the region immediately behind the shock front. However, within two spatial points of the shock front the shock layer solutions with and without the precursor agreed.

Parametric Studies

Figure 5 shows the electron number densities and the electron/electronic temperature in the precursor for three cases. All three of these cases were at a velocity of 16 km/s; however, each case was at a different altitude: 72, 75, and 80 km. The shock standoff distance and radiative flux through the shock front for each of these cases are presented in Table 2.

From these figures, it can be seen that for a constant velocity the magnitude of the changes in the precursor increased with decreasing altitude. This inverse relationship corresponds with trends observed by Dobbins[17] and was a result of two factors. First and foremost, as shown in Table 2, with the decrease in altitude the radiative flux through the shock increased due to an increase in the extent of the equilibrium region in the shock layer. Second, with the increase in density at the lower altitudes, a larger percentage of the radiation passing through the shock was absorbed before being attenuated due to the geometry.

It should also be noted that as the altitude decreased, the length of the precursor region decreased. This change was a result of the increased density at the lower altitudes, which caused the radiative mean free paths to decrease. Hence, the radiation was absorbed in a shorter distance ahead of the shock. This trend was also predicted by previous studies.[11]

Figure 6 shows the electron number densities and electron/electronic temperature for four cases. All of these cases were at an altitude of 80 km, and the freestream velocities ranged from 10 to 16 km/s. The shock standoff distance and radiative flux through the shock front for each of these cases are presented in Table 2.

From these figures, it can be seen that, at a constant altitude, as the freestream velocity increased the magnitude of the electron number densities in the precursor also increased. This trend was a result of the increase in the equilibrium temperature in the shock layer as the velocity increased and the accompanying rise in the radiative flux through the shock front; this trend is also in agreement with the results and predictions of previous researchers.[16,17] The precursor thickness also increased with velocity, again as a result of the increased radiative flux with velocity. As the radiative energy passing through the shock increased, a larger distance was required for this energy to be absorbed or attenuated ahead of the shock.

The increase in the velocity had varied effects on the electron/electronic temperature, however. The electron/electronic temperature at the shock decreased with velocity from 10 to 14 km/s. However, from 14 to 16 km/s it increased. This varied effect is due to differences in the quantity of low energy electrons created immediately ahead of the shock due to the ionization of molecular nitrogen. In fact, at 10 km/s there was insufficient ionization of molecular nitrogen ahead of the shock to cause a decrease in the electron/electronic temperature.

Conclusions

In this paper, a model for predicting the magnitude and characteristics of the shock wave precursor ahead of a hypervelocity vehicle in the Earth's atmosphere has been presented. This model treats the Earth's atmosphere as a nitrogen gas. This method includes detailed mass production for photodissociation and photoionization and accounts for the effects of emission and absorption on the individual energy modes of the gas. This technique includes the effects of both chemical and thermal nonequilibrium in the flowfield as well as, in the radiative flux calculations, the consequences of local thermodynamic nonequilibrium for the molecular species.

This method has been used to determine the shock wave precursor ahead of vehicles entering the Earth's atmosphere upon return from Mars. Comparison of the results with previous shock tube studies has shown that the method provides reasonably accurate results. The test cases have shown that there is significant production of atoms, ions, and electrons ahead of the shock front and that the precursor is characterized by molecular ionization and an enhanced electron/electronic temperature. However, for the conditions considered in this study, the precursor has negligible effect on the subsequent shock layer flowfield. For flowfield calculations around entry vehicles at greater velocities or which penetrate deeper into the Earth's atmosphere at similar velocities to those studied here, the precursor could be significant. However, even at the conditions considered in this study, the free electrons present in the precursor could have significant impact on communication with the entry vehicle.

Acknowledgment

This work was primarily supported by NASA Grant-1-1003 from the NASA Langley Research Center, with Lin C. Hartung acting as technical monitor.

References

[1] Smith, G. L., "Radiation-Induced Precursor Flow Field Ahead of a Reentering Body," Ph.D. Dissertation, Virginia Polytechnic Inst. and State Univ., Blacksburg, VA, March 1968.

[2] Williams, S. D., Pavlosky, J. E., and Curry, D. M., "A Preliminary TPS Design for MRSR-Aerobraking at Mars and at Earth," AIAA Paper 90-0052, Jan. 1990.

[3] Lasher, L. E., and Wilson, K. H., "Effects of Shock Precursor Heating on Radiative Flux to Blunt Bodies," NASA-CR-1265, 1969.

[4] Tiwari, S. N., and Szema, K. Y., "Effects of Precursor Heating on Chemical and Radiative Nonequilibrium Viscous Flow Around a Jovian Entry Body," AIAA Paper 78-907, May 1978.

[5] Wetzel, L., "Far-Flow Approximation for Precursor Ionization Profiles," *AIAA Journal*, Vol. 2, No. 7, 1964, pp. 1208-1214.

[6] Lederman, S., and Wilson, D. S., "Microwave Resonant Cavity Measurements of Shock Produced Electron Precursor," *AIAA Journal*, Vol. 5, No. 1, 1967, pp. 71-77.

[7] Shreffler, R. G., and Christian, R. H., "Boundary Disturbances in High Explosive Shock Tube," *Journal of Applied Physics*, Vol. 25, No. 3, 1954, pp. 324-331.

[8] Voorhies, H. G., and Scott, F. R., "Optical Measurements in a Helium Shock Tube," *Bulletin of the American Physical Society*, Vol. 4, 1959, p. 40.

[9] Weymann, H. D., "Electron Diffusion Ahead of Shock Waves in Argon," *Physics of Fluids*, Vol. 3, No. 4, 1960, pp. 545-548.

[10] Murty, S. S. R., "Effects of Line Radiation on Precursor Ionization," *Journal of Quantitative Spectroscopy and Radiative Transfer*, Vol. 8, Sept. 1968, pp. 531-554.

[11] Nelson, H. F., and Goulard, R., "Structure of Shock Waves with Nonequilibrium Radiation and Ionization," *Physics of Fluids*, Vol. 12, No. 8, 1969, pp. 1605-1617.

[12] Foley, W. H., and Clarke, J. H., "Shock Waves Structured by Nonequilibrium Ionizing and Thermal Phenomena," *Physics of Fluids*, Vol. 16, No. 3, 1973, pp. 373-383.

[13] Tiwari, S. N., and Szema, K. Y., "Radiation Induced Precursor Flow Field Ahead of a Jovian Entry Body," AIAA Paper 77-768, June 1977.

[14] Tiwari, S. N., and Szema, K. Y., "Influence on Precursor Heating of Viscous Flow Around a Jovian Entry Body," AIAA Paper 78-190, Jan. 1978.

[15] Omura, M., and Presley, L. L., "Electron Density Measurements Ahead of Shock Waves in Air," *AIAA Journal*, Vol. 7, No. 12, 1969, pp. 2363-2365.

[16] Omura, M., and Presley, L. L., "Further Studies of Precursor Electron Densities Ahead of Shock Waves," *Proceedings of the 4th Plasma Sheath Symposium*, NASA-SP-252, Oct. 1970, pp. 335-358.

[17] Dobbins, R. A., "Photoexcitation and Photoionization of Argon Ahead of a Strong Shock Wave," AIAA Paper 68-666, June 1968.

[18] Nicolet, W. E., "Advanced Methods for Calculating Radiation Transport in Ablation Product Contaminated Boundary Layers," NASA-CR-1656, Sept. 1970.

[19] Stanley, S. A., "The Effects of Shock Wave Precursors Ahead of Hypersonic Entry Vehicles," M.S. Thesis, Texas A&M Univ., College Station, TX, Dec. 1990.

[20] Herzberg, G., *Molecular Spectra and Molecular Structure, I. Spectra of Diatomic Molecules*, 2nd ed., Krieger, Malabar, FL, 1989.

[21] Zel'dovich, Y. B., and Raizer, Y. P., *Physics of Shock Waves and High-Temperature Phenomena*, Vol. 1, Academic, New York, 1966.

[22] Zel'dovich, Y. B., and Raizer, Y. P., *Physics of Shock Waves and High-Temperature Hydrodynamic Phenomena*, Vol. 2, Academic, New York, 1967.

[23] Marr, G. V., *Photoionization Processes in Gases*, Academic, New York, 1967.

[24] Allen, R. A., "Air Radiation Graphs: Spectrally Integrated Fluxes Including Line Contributions and Self Absorption," NASA-CR-556, 1965.

[25] Watanabe, K., "Ultraviolet Absorption Processes in the Upper Atmosphere," *Advances in Geophysics*, Vol. 5, 1958, pp. 153-221.

[26] Horton, T. E., "Radiative Coupled Nonequilibrium Flow Fields Associated with Aeroassisted Orbital Transfer," Univ., of Mississippi, NASA CR NAG-1-496, University, MS, March 1986.

[27] Gnoffo, P. A., Gupta, R. N., and Shinn, J. L., "Conservation Equations and Physical Models for Hypersonic Air Flows in Thermal and Chemical Nonequilibrium," NASA-TP-2867, Feb. 1989.

[28] Thompson, R. A., "Comparison of Nonequilibrium Viscous Shock Layer Solutions with Windward Surface Shuttle Heating Data," AIAA Paper 87-1473, June 1987.

[29] Carlson, L. A., "Nonequilibrium Radiation and Chemistry Models for Aerocapture Vehicle Flowfields," Texas A&M Univ., TAMRF Rept. No. 6382-90-02, College Station, TX, June 1990.

Ernest V. Zoby
Associate Editor

AIAA 92-2972

An Approximate Local Thermodynamic Nonequilibrium Radiation Model for Air

T. A. Gally and L. A. Carlson
Texas A&M University
College Station, TX

AIAA 23nd
Plasmadynamics & Lasers Conference
July 6-8, 1992 / Nashville, TN

For permission to copy or republish, contact the American Institute of Aeronautics and Astronautics
370 L'Enfant Promenade, S.W., Washington, D.C. 20024

An Approximate Local Thermodynamic Nonequilibrium Radiation Model for Air

Thomas A. Gally*
and
Leland A. Carlson**
Texas A&M University
College Station, Texas

Abstract

A radiatively coupled viscous shock layer analysis program which includes chemical and thermal nonequilibrium is used to calculate stagnation point flow profiles for typical aeroassisted orbital transfer vehicle conditions. Two methods of predicting local thermodynamic nonequilibrium radiation effects are used as a first and second order approximation to this phenomena. Tabulated results for both nitrogen and air freestreams are given with temperature, species, and radiation profiles for some air conditions. Two body solution results are shown for 45 and 60 degree hyperboloid bodies at 12 km/sec and 80 km altitude. The presented results constitute an advancement in the engineering modeling of radiating nonequilibrium reentry flows.

Nomenclature

A_{cp}, B_{pc}, B_{cp} = continuum transition Einstein coefficients
A_{qp}, B_{pq}, B_{qp} = line transition Einstein coefficients
B_ν = black body function
E = electronic state energy level
$\mathcal{E}_n$ = integro-exponential function of order n
f_e = electron energy distribution function
g = degeneracy
h = enthalpy per unit mass
I_ν = radiative intensity
k = Boltzmann constant
K = absorption coefficient
m = particle mass
N = number density
$\dot{q}_r$ = radiative heat flux
Q = partition function
r = wall reflectivity
S = source function
T = temperature
α = wall absorptivity
ϵ = wall emissivity
ν = frequency
σ = radiative cross section
τ = optical thickness
χ = ionization potential
ω = steradian

subscripts

e = electron or electronic
g = ground state
tr = translational
v = vibrational
w = value at wall
ν = frequency

Introduction

In past work[1-3], the authors have developed a radiatively coupled viscous shock layer (VSL) flow solver. This program, derived from the VSL3DNQ program from NASA Langley[4] and the RADICAL radiation transport method of Nicholet[5,6], currently includes viscous effects, diffusion, conduction, chemical nonequilibrium, and thermal nonequilibrium. To account for local thermodynamic nonequilibrium (LTNE) effects on radiation emmission and absorption, a first order correction method was included in Ref. 2. More recently[3], a second order LTNE method was developed and used to calculate typical AOTV results for a nitrogen freestream gas. In this paper, both the first and second order LTNE correction methods have been extended to an air gas mixture. Also, downstream flow profiles for 45 and 60 degree hyperboloid bodies are presented.

Chemical Rate Model

Two different sets of chemical reactions and rates have been used for the calculations, depending upon whether the gas is nitrogen or air. For nitrogen only, the reaction set of Table I is used. The source of these reactions are Dung and Kang[7] for all except the electron impact reactions (reactions 3 and 6) and the heavy particle ionization (reactions 7 and 8). The electron impact ionization rate was deduced by Wilson[8] for conditions of thermodynamic nonequilibrium. The electron impact dissociation rate is that of Park[9] while the heavy particle ionization rates were deduced by Carlson[10]. The reactions set used for air, shown in Table II, were obtained primary from references by Park[9,11,12], except for the electron impact ionization rates (reactions 7 and 8), which are new rates whose derivation is discussed in a later section, and heavy particle ionization (reaction 26) of N, where Carlson's rate is used.

In the calculation of chemical rates in a multitemperature environment, some modifications to the basic theory are needed based upon both theory and qualitative observations. Consider for example the heavy particle dissociation reaction for nitrogen (reaction 1 and 2 in both Tables I and II). Most researchers[13,14]

---

* *Asst. Lecturer Aerospace Engineering, Member AIAA*

** *Professor Aerospace Engineering, Associate Fellow AIAA*

	Reaction	A	B	E
1	N_2+N =N +N +N	4.085×10^{22}	-1.5	113100
2	N_2+N_2 =N +N +N_2	4.70×10^{17}	-0.5	113100
3	N_2+e^- =N^+ +N^++e^-	3.00×10^{24}	-1.6	113100
4	N_2+N^+=N_2^++N	1.00×10^{12}	0.5	12200
5	N +N =N_2^++e^-	1.40×10^{13}	0.0	67800
6	N +e^- =N^+ +e^- +e^-	4.16×10^{13}	0.5	120000
7	N +N =N +N^++e^-	2.34×10^{11}	0.5	120000
8	N +N^+=N^+ +N^++e^-	2.34×10^{11}	0.5	120000

Rates in the form $k_f = A\ T^B \exp(-E/T)$.
$T = T_e$ in electron impact reactions.

Table I: Reaction System for Nitrogen

	Reaction	A	B	E
1	N_2+M1 =N +N +M1	3.00×10^{22}	-1.6	113200
2	N_2+M2 =N +N +M2	7.00×10^{21}	-1.6	113200
3	O_2+M1 =O +O +M1	1.00×10^{22}	-1.5	59500
4	O_2+M2 =O +O +M2	2.00×10^{21}	-1.5	59500
5	NO +M3 =N +O +M3	1.10×10^{17}	0.0	75500
6	NO +M4 =N +O +M4	5.00×10^{15}	0.0	75500
7	O +e^- =O^+ +e^- +e^-	6.35×10^{15}	0.0	106200
8	N +e^- =N^+ +e^- +e^-	5.08×10^{16}	0.0	121000
9	NO +O =N +O_2	8.40×10^{12}	0.0	19450
10	N_2+O =NO +N	6.40×10^{17}	-1.0	38400
11	N_2+e^- =N +N +e^-	3.00×10^{24}	-1.6	113100
12	N +O =NO^++e^-	5.30×10^{12}	0.0	31900
13	N +N =N_2^+ +e^-	2.00×10^{13}	0.0	67500
14	NO^++O =N^+ +O_2	1.00×10^{12}	0.5	77200
15	N^++N_2 =N_2^+ +N	1.00×10^{12}	0.5	12200
16	O^++NO =N^+ +O_2	1.40×10^{5}	1.9	26600
17	NO^++N =O^+ +N_2	3.40×10^{13}	-1.08	12800
18	O^++N_2 =N_2^+ +O	9.10×10^{11}	0.36	22800
19	NO^++N =N_2^+ +O	7.20×10^{13}	0.0	35500
20	O +O =O_2^+ +e^-	1.10×10^{13}	0.0	80600
21	O_2^++N =N^+ +O_2	8.70×10^{13}	0.14	28600
22	O_2^++N_2 =N_2^+ +O_2	9.90×10^{12}	0.0	40700
23	O_2^++O =O^+ +O_2	4.00×10^{12}	-0.09	18000
24	NO^++O_2 =O_2^+ +NO	2.30×10^{13}	0.41	32600
25	NO^++O =O_2^+ +N	7.20×10^{12}	0.29	48600
26	N +M5 =N^+ +e^- +M5	2.34×10^{11}	0.5	120000

Rates in the form $k_f = A\ T^B \exp(-E/T)$.
$T = T_e$ in electron impact reactions.
M1 = N,N^+,O,O^+
M2 = N_2,N_2^+,O_2,O_2^+,NO,NO^+
M3 = N,N^+,O,O^+,NO
M4 = N_2,N_2^+,O_2,O_2^+,NO^+
M5 = N,N^+

Table II: Reaction System for Air

agree that the forward rate is a function of both the amount of translational energy found in the colliding partner and in the vibrational energy state of the N_2 molecule. To account for this difference, Treanor and Marrone[14,15], in developing the CVDV model used in the vibrational energy equation, show that a correction factor based upon both T and T_v should be used to correct the forward rate based upon T alone. Alternately, Park[13] developed a theory which uses an average temperature, $T_a = T^n T^{n-1}$, to calculate the forward rate without any corrective multiplier. Originally, the value of n was 0.5 although later studies[16,17] suggest that values of n up to about 0.8 may be appropriate. For this study, the corrections from the CVDV theory were used for the dissociation reactions of N_2, O_2, and NO to be consistent with the vibrational-translational exchange theory and also to avoid the selection and evaluation of an appropriate value of n. Both theories agree that the reverse recombination rate is a function of the translational energy alone.

The other set of reactions which must be modified for thermal nonequilibrium are the electron impact reactions. These reactions are predominantly functions of the energy available in the translational energy of the free electrons which may be at a significantly different temperature than the heavy particles. The electron temperature, T_e, is thus used in the calculation of these forward rates. In the electron impact dissociation reaction it is also argueably true that the vibrational energy state of the N_2 molecule is important in the final rate. In a two temperature model where $T_v = T_e$ this is already accounted for, while for three temperatures Park[9,11] argues that electron energy alone is important, although a later source indicates the use of an averaged temperature[12]. The ionization reactions (reaction 6 of Table I and reactions 7 and 8 of Table II) may also be considered to be a function of the electronic energy; but since it is already assumed that free and bound electrons are in thermal equilbrium, this does not affect the rate. The reverse deionization rate is also considered to be a function of the electron temperature.

Rather than specify both a forward and reverse reaction rate for all chemical reactions, it is common practice to specify only one and calculate the other using the equilibrium constant from the relation $k_{eq} = k_f/k_r$. This method insures that at thermal and chemical equilibrium the proper species concentrations will exist as predicted from thermodynamic theory. Using this equilibrium constant approach assumes that the above relation is valid under nonequilibrium chemistry conditions (an assumption generally accepted as valid or at least necessary) and that the equilibrium constant can be suitably defined under conditions of thermal nonequilibrium.

For the purposes of this paper, the following procedures were used to calculate the forward and reverse rates under thermodynamic nonequilibrium. The forward, endothermic rate is calculated using the temperature of the energy mode associated with providing the absorbed energy. The exception is the dissociation reactions where only the heavy particle temperature is used in calculating k_f; this rate is later corrected for thermal nonequilibrium using a modified CVDV method[3] as noted above. Multitemperature partitions functions for each species are then used to calculate the equilibrium constant. In this calculation, an exponential term representing the heat of reaction appears; it is evaluated using the forward rate temperature since it is usually the equivalent to the exponential term occuring in the forward reaction rate. The reverse rate is then calculated from $k_r(T, T_v, T_e) = k_f(T_f)/k_{eq}(T, T_v, T_e)$. Since endothermic reactions dominate in the thermal nonequilibrium region behind the shock, this method gives the correct qualitative effect in this region. The exothermically dominated cool wall region, by constrast, is largely near thermal equilibrium.

An alternate approach for calculating non-thermal equilibrium reaction rates is suggested by Park (Ref. 12). As an example of this method, suppose that for some reaction the forward rate is determined by an averaged temperature, T_a, while the reverse rate is determined by the heavy particle temperature T (such as the Park dissociation model). Under this method, if the the forward rate is calculated as $k_f(T_a)$, the reverse rate would be calculated by $k_b(T) = k_f(T)/k_{eq}(T)$. This method is particularly suited for use with equilibrium constants which have been curve fit as functions of a single temperature.

Radiation Theory

The radiation model used in this research effort is the radiative transport portion of the equilibrium shock layer analysis program called RADICAL[5,6]. The radiation transport equation used by RADICAL is one-dimensional, normal to the body, and assumes that radiation transport tangent to the body has a net zero change in flux in the tangent direction due to the relatively smaller gradients in species concentrations and temperatures in the tangent direction. This assumption is called the tangent slab aproximation and can be justified by the fact that for the thin shock layers under consideration here, the ratio of shock layer thickness to the surface radius of curvature is on the order of 0.05. RADICAL also allows radiative properties to be specified at the wall to account for the frequency dependent reflectivity and transmissivity of differing surface materials. Radiation emitted into the freestream gas is assumed to be lost with no radiative precursor effects calculated. A recent study by Stanley and Carlson[18] shows that while precursor effects are not truely negligible, they do not have a significant effect on the shock layer regions.

Included in the RADICAL model are the phenomena of atomic line, atomic continuum, molecular band, and free-free Braumstruhlung radiation. The radiating species modeled include all the important species of a nitrogen/oxygen mixture plus argon, hydrogen, and a number of carbon compounds which may be present due to an ablating surface. The method of solution used by RADICAL consists of performing an initial sweep through the radiation spectrum accounting for only the continuum modeled processes. A second sweep is then made for only the frequency widths of the line processes. Since the transport equation for continuum and line radiation is not separable, an exact solution procedure for the lines would include the calculation of the continuum absorptivity at each frequency point within the line width. However, this process can easily double the time required to calculate each line contribution. To avoid this complication, Nicolet includes an approximate method in his analysis whereby a number of lines may be conviently grouped together if they are closely spaced or in a frequency range where the background continuum absorptivity may be assumed to be a constant. A single continuum absorptivity is then used in the calculation of each line group, and the difference between the calculation of this constant continuum alone and the line group calculation is the net "contribution" to the total flux of the line group.

Equilibrium Radiation

In atomic continuum radiation there are three contributions to the local change in radiative intensity at any frequency, ν: emission, absorption, and induced emission. These processes can be mathematically expressed by the following[19]:

$$\begin{aligned} \text{emission:} \quad & h\nu A_{cp} N_e N_i f_e(h\nu - \chi_p) h\, d\nu\, d\omega \\ \text{absorption:} \quad & h\nu B_{pc} I_\nu N_p\, d\nu\, d\omega \\ \text{induced emission:} \quad & h\nu B_{cp} I_\nu N_e N_i f_e(h\nu - \chi_p) h\, d\nu\, d\omega \end{aligned}$$

where N_e, N_i and N_p are the number density populations of the free electrons, ions and state p of the species involved in the process; and A_{cp}, B_{pc} and B_{cp} are the Einstein coefficients for the transition. The term $f_e(h\nu - \chi_p)$ is the energy distribution function of the free electrons having energy $h\nu - \chi_p$ above the ionization potential of state p. The spatial rate of change of intensity per unit angle and frequency at any point is the sum of the emission and induced emission minus the absorption at that point.

$$\begin{aligned} \frac{\partial I_\nu}{\partial n} = & (N_e N_i h f_e(h\nu - \chi_p) B_{cp} - N_p B_{pc}) h\nu I_\nu \\ & + h\nu N_e N_i h f_e(h\nu - \chi_p) A_{cp} \end{aligned}$$

Through detailed balancing at local thermodynamic equilibrium (LTE) conditions, the Einstein coefficients can be shown to be related by the formulas given below, which are assumed to be valid for both equilibrium and non-equilibrium conditions.

$$\begin{aligned} \frac{B_{pc}}{B_{cp}} &= \left(\frac{N_e N_i}{N_p}\right)_{LTE} h f_e(h\nu - \chi_p) e^{h\nu/kT_e} \\ \frac{A_{cp}}{B_{cp}} &= \frac{2h\nu^3}{c^2} \end{aligned}$$

Applying these relations and simplifying yields

$$\frac{\partial I_\nu}{\partial n} = -K_{\nu_{pc}}(I_\nu + S_{\nu_{pc}})$$

where $K_{\nu_{pc}}$ and $S_{\nu_{pc}}$ are the absorption coefficient and source function defined by:

$$\begin{aligned} K_{\nu_{pc}} &= h\nu N_p B_{pc} \left(1 - \frac{N_e N_i}{N_p} \left(\frac{N_p}{N_e N_i}\right)_{LTE} e^{-h\nu/kT_e}\right) \\ S_{\nu_{pc}} &= \frac{N_e N_i}{N_p} \left(\frac{N_p}{N_e N_i}\right)_{LTE} \frac{2h\nu^3}{c^2} \\ & \quad \left[e^{h\nu/kT_e} - \frac{N_e N_i}{N_p} \left(\frac{N_p}{N_e N_i}\right)_{LTE}\right]^{-1} \end{aligned} \tag{1}$$

Under equilibrium conditions these relations reduce to:

$$K_{\nu_{pc}} = h\nu(N_p)_{LTE} B_{pc}\left(1 - e^{-h\nu/kT_e}\right)$$

$$S_{\nu_{pc}} = \frac{2h\nu^3/c^2}{e^{h\nu/kT_e} - 1} = B_\nu \tag{2}$$

In addition, since the excited state population $(N_p)_{LTE}$ is not given explicitly as part of the flowfield solution, it must be calculated from the total population of the particles, N, assuming an equilibrium Boltzmann excitation profile. This relation is:

$$\frac{(N_p)_{LTE}}{N} = \frac{g_p e^{-E_p/kT_e}}{\sum_p g_p e^{-E_p/kT_e}} \tag{3}$$

The need for the excited state population is often avoided altogether by redefining the absorption coefficient in terms of the total number density of the species and a radiative cross section using the following:

$$K_{\nu_{pc}} = N\sigma_{\nu_{pc}}$$

where

$$\sigma_{\nu_{pc}} = h\nu B_{pc}\frac{g_p e^{-E_p/kT_e}}{\sum_p g_p e^{-E_p/kT_e}}\left(1 - e^{-h\nu/kT_e}\right)$$

For line radiation where N_q is the population of the bound emitting state, the important processes are

$$\begin{aligned} \text{emission}: &\quad h^2\nu A_{qp} N_q d\nu d\omega \\ \text{absorption}: &\quad h\nu B_{pq} I_\nu N_p d\nu d\omega \\ \text{induced emission}: &\quad h^2\nu B_{qp} I_\nu N_q d\nu d\omega \end{aligned}$$

The radiative transport equation is the same as that for continuum process but with the absorption coefficient and source function given by:

$$K_{\nu_{pq}} = h\nu N_p B_{pq}\left(1 - \left(\frac{N_p}{N_q}\right)_{LTE}\frac{N_q}{N_p}e^{-h\nu/kT_e}\right)$$

$$S_{\nu_{pq}} = \frac{N_q}{N_p}\left(\frac{N_p}{N_q}\right)_{LTE}\frac{2h\nu^3}{c^2}\left[e^{h\nu/kT_e} - \frac{N_q}{N_p}\left(\frac{N_p}{N_q}\right)_{LTE}\right]^{-1}$$

Also as before, under thermodynamic equilibrium, the above expression can be reduced. The result is exactly the same as for continuum processes.

$$K_{\nu_{pq}} = h\nu(N_p)_{LTE} B_{pq}\left(1 - e^{-h\nu/kT_e}\right)$$

$$S_{\nu_{pq}} = \frac{2h\nu^3/c^2}{e^{h\nu/kT_e} - 1} = B_\nu$$

$$\sigma_{\nu_{pq}} = h\nu B_{pq}\frac{g_p e^{-E_p/kT_e}}{\sum_p g_p e^{-E_p/kT_e}}\left(1 - e^{-h\nu/kT_e}\right)$$

At any given frequency, a number of processes are likely to be contributing to the local absorption and emission of radiation. Because radiation emitted by one process may be subsequently absorbed by another, all radiative processes at a particular frequency are coupled. To solve the transport equations, the total absorption coefficient and source function, K_ν and $S\nu$, are used, which are simply the sum of all the process specific values. With these definitions, the radiative transport equations may be integrated spatially between the shock front and the wall surface to obtain the radiative heat flux, $\dot{q}_\nu$, at any point. Under the tangent slab assumption this flux equation is:

$$-\dot{q}_\nu(x) = 2\pi\int_0^{\tau_{\nu,sh}} sgn(t_\nu - \tau_\nu)S_\nu \mathcal{E}_2(|t_\nu - \tau_\nu|)dt_\nu$$
$$- 2\mathcal{E}_3(\tau_\nu)\pi\left(\epsilon_w B_{\nu,w} - 2r_w\int_0^{\tau_{\nu,sh}} \mathcal{E}_2(t_\nu)S_\nu dt_\nu\right)$$

where τ_ν is the optical thickness determined by

$$\tau_\nu = \int_0^x K_\nu dy.$$

A subsequent integration over the entire frequency range yields the total heat flux which is used in the radiative loss term in the global energy equation.

First Order Atomic LTNE Model

A first order LTNE model developed by Carlson et al.[20] assumes that the excited states of nitrogen and oxygen are in local thermodynamic and chemical equilibrium with the free electrons and ions of each species. This assumption follows from that used by Petscheck and Byron[21] for argon and Wilson[8] for nitrogen which is that the excitation from ground to excited state proceeds much slower than the subsequent ionization of the excited state. Carlson's assumption goes further, however, by assuming that the excited to continuum rate is fast enough that the excited species involved may be considered in local chemical equilibrium throughout the flowfield.

Before this assumption can be applied to the radiative transport equations, a relationship between the number density populations of each involved excited state must be defined. Nitrogen will be specifically discussed below but all the equations and concepts apply equally well to oxygen with the appropriate substitutions. From equilibrium chemical kinetics, the total number density of neutral particles, ions, and electrons are related by:

$$\left(\frac{N_{N+}N_e}{N_N}\right)_{LTE} = \frac{Q_{N+}Q_e}{Q_N}e^{-169{,}000/kT_e}$$

where 169,000°K is the ionization potential of ground state nitrogen (158,900°K for oxygen). Using Eq. 3, any excited state population, N_p, may then also be related to that of the ions and electrons by:

$$\left(\frac{N_{N+}N_e}{N_p}\right)_{LTE} = \frac{Q_{N+}Q_e}{g_p}e^{-(169{,}000-E_p)/T_e} \qquad (4)$$
$$= \frac{Q_{N+}Q_e}{g_p}e^{-\chi_p/kT_e}$$

Under the above LTNE assumptions, the number density of the excited states can still be calculated from the above relation. However, rather than being in LTE, the excited state is in equilibrium with the free electrons and ions alone, which is indicated by the subscript E:

$$(N_p)_E = \frac{g_p N_{N+}N_e}{Q_{N+}Q_e}e^{\chi_p/kT_e}. \qquad (5)$$

To determine how to adapt RADICAL to use the newly defined state populations, consider the relation between the absorption coefficient and source function for continuum radiation given by Eq. 1 for any condition and Eq. 2 for equilibrium:

$$K_{\nu_{pc}} = \frac{N_p}{(N_p)_{LTE}}\Pi_{pc}(K_{\nu_{pc}})_{LTE} \qquad (6)$$
$$S_{\nu_{pc}} = \frac{N_{N+}N_e}{N_p}\left(\frac{N_p}{N_{N+}N_e}\right)_{LTE}\frac{1}{\Pi_{pc}}(S_{\nu_{pc}})_{LTE}$$

where to simplify the expression, Π_{pc} has been defined by:

$$\Pi_{pc} = \left(e^{h\nu/kT_e}-1\right)^{-1}$$
$$\left[e^{h\nu/kT_e} - \frac{N_{N+}N_e}{N_p}\left(\frac{N_p}{N_{N+}N_e}\right)_{LTE}\right]$$

If the state being considered is an excited state, the ratio of equilibrium to nonequilibrium populations used in evaluating Π_{pc} and in the source function reduce to unity by the LTNE assumption, giving $\Pi_{pc} = 1$; and the excited state source function is the same as for LTE. The excited state absorption coefficient, however, must still be corrected by the ratio $N_p/(N_p)_{LTE}$, which can be evaluated from known species populations by using Eqs. 3 and 5 to be:

$$\frac{N_p}{(N_p)_{LTE}} = \frac{(N_p)_E}{(N_p)_{LTE}} = \frac{N_{N+}N_e}{N_N}\frac{Q_N}{Q_{N+}Q_e}e^{169{,}000/T_e}. \qquad (7)$$

Alternately, if the state, p, is a ground state, then the exponential term for most temperatures is much larger ($exp(h\nu/kT_e) \sim 10^7$ for $T_e = 10{,}000°$) than the ratio of expected nonequilibrium to equilibrium populations and again $\Pi_{pc} = 1$. Also, since the ground states are in LTE with the total state population, the ratio $N_p/(N_p)_{LTE}$ is unity and the ground state absorption coefficient is unmodified. The ground state source function, however, must be corrected by the ratio

$$\frac{N_{N+}N_e}{N_p}\left(\frac{N_p}{N_{N+}N_e}\right)_{LTE} = \frac{(N_p)_E}{N_p} = \frac{(N_p)_E}{(N_p)_{LTE}} \qquad (8)$$

where Eqs. 4 and 5 have been used in the reduction. This ratio is the same given in Eq. 7.

For line processes, the relation between equilibrium and non-equilibrium absorption coefficients and source functions are:

$$K_{\nu_{pq}} = \frac{N_p}{(N_p)_{LTE}}\Pi_{pq}(K_{\nu_{pq}})_{LTE} \qquad (9)$$
$$S_{\nu_{pq}} = \frac{N_q}{N_p}\left(\frac{N_p}{N_q}\right)_{LTE}\frac{1}{\Pi_{pq}}(S_{\nu_{pq}})_{LTE}$$

where

$$\Pi_{pq} = \left(e^{h\nu/kT_e}-1\right)^{-1}\left[e^{h\nu/kT_e} - \frac{N_q}{N_p}\left(\frac{N_p}{N_q}\right)_{LTE}\right]$$

Using an argument parallel to that used for continuum processes, it can be shown that $\Pi_{pq} \sim 1$ under most conditions. The absorption coefficient is then exactly the same as for the continuum processes, depending only upon the population of the absorbing state. LTNE corrections for line radiation are then the same as those described above for continuum radiation.

To determine how to correctly evaluate the line source function, two possibilities must be considered. The first is that both states are excited states, and the second is that one is excited and the other is in one of the lowest three "ground" states. The case of radiative transition between two ground states is forbidden by the radiative selection rules and has not been observed to occur. If both are excited states, then each number density can be calculated from Eq. 5 and the ratio of the two is:

$$\frac{N_q}{N_p} = \left(\frac{N_q}{N_p}\right)_E = \frac{g_q}{g_p}e^{(E_p-E_q)/T_e} \qquad (10)$$

while the number densities at LTE can be calculated from Eq. 3 to get the ratio:

$$\left(\frac{N_p}{N_q}\right)_{LTE} = \frac{g_p}{g_q}e^{(E_q-E_p)/T_e} \qquad (11)$$

Since the ratios in Eqs. 10 and 11 are inverses of each other, the net correction to be applied to the excited to excited line source function is one.

If the lower state, p, is a ground state then the actual number density N_p is the same as that calculated at LTE. The remaining ratio of the actual number density of state p to that which it would be at LTE is the same ratio shown in Eq. 8. Thus, the correction to the excited to ground line source function is the same as that given in Eq. 7.

Second Order Atomic LTNE Model

After extensively reviewing the work on argon of Foley and Clarke[22] and Nelson[23] and the air and nitrogen work of Park[24], Kunc and Soon[25,26], and others, it was decided to develop a second order LTNE model for high temperature nitrogen and oxygen by subdividing each atomic species into two separate species. Since the formulation for both nitrogen and oxygen are the same except for the actual excitation energies used and the final rate coefficients, most of the follow discussion will concentrate on nitrogen but is directly applicable to oxygen.

The first nitrogen subspecies, termed N_g, for N ground, represents the nitrogen atoms in the first three low lying electronic states of nitrogen. The second, termed N^* or N excited, represents those nitrogen atoms populating the remaining upper electronic states. The relative densities of these subspecies will then be determined by appropriate reaction rates between themselves, N^+, e^-, etc.; and the electronic states of each are assumed to be in local thermodynamic equilibrium with themselves. This approach has the potential to be a significant improvement over the first order model in that it allows a finite rate of ionization from excited states while retaining the fundamental two step ionization process. In addition, by determining the excited state number densities directly from the flowfield computation, the appropriate atomic LTNE factors are directly obtainable and should be more accurate.

The thermodynamic state of the two species, N_g and N^*, are determined by the standard methods used for monoatomic gases:

$$Q_{N_g} = \sum_{p=1}^{3} g_p e^{-E_p/kT_e}$$

$$Q_{N^*} = \sum_{p=4}^{max} g_p e^{-(E_p - E_4)/kT_e}$$

$$Q_N = Q_{N_g} + Q_{N^*} e^{-E_4/kT_e}$$

$$h_{N_g} = \frac{5}{2}\frac{kT}{m_N} + \frac{1}{m_N Q_{N_g}} \sum_{p=1}^{3} g_p E_p e^{-E_p/kT_e} + h^\circ_{N_g}$$

$$h_{N^*} = \frac{5}{2}\frac{kT}{m_N} + \frac{1}{m_N Q_{N^*}} \sum_{p=4}^{max} g_p (E_p - E_4) e^{-(E_p - E_4)/kT_e} + h^\circ_{N^*}$$

where the zero point energies are, $h^\circ_{N_g} = h^\circ_N = 3.36 \times 10^{11}$ ergs/gm and $h^\circ_{N^*} = h^\circ_{N_g} + E_4/m_N = 1.05 \times 10^{12}$ ergs/gm. For oxygen the zero point energies are, $h^\circ_{O_g} = h^\circ_O = 1.56 \times 10^{11}$ ergs/gm and $h^\circ_{O^*} = h^\circ_{O_g} + E_4/m_O = 7.07 \times 10^{11}$ ergs/gm. The collision cross sections for both lower level and upper level subspecies are needed to calculate viscous transport properties and are assumed to be the same as for the original species, N or O.

The methods presented by Kunc and Soon in Refs. 25 and 26 have been used to calculate the electron impact excitation and ionization rates involving these new species. For the excitation of nitrogen from a ground states, i, to an excited states, j, the excitation rate is given by:

$$C_{pq} = 10^{-8} \left(\frac{\mathcal{R}\chi_q}{k(E_q - E_p)\chi_p} \right)^{3/2} \frac{Q_k}{2l_p + 1} exp\left(\frac{(E_p - E_q)}{T_e} \right) G_k$$

where the units on C_{pq} are cm^3/sec, $\mathcal{R}$ is the Rydberg constant, Q_k is an angular factor for the transition and G_k is a rate function determined by the electron temperature and two transition specific constants tabulated in Ref. 25. The excitation rate for one of the ground states at any given temperature can be calculated by summing the above rates over all the excitation states, q. The combined rate for all three ground states is found by multiplying each individual rate by the LTE number density ratio given below and summing.

$$\frac{N_p}{N_g} = \frac{g_p e^{-E_p/T_e}}{Q_{N_g}} \tag{12}$$

The rate of ionization from each ground state is similar to that for the excitation process and is given by:

$$C_{pc} = 10^{-8} \left(\frac{\mathcal{R}}{\chi_p} \right)^{3/2} \frac{Q_k}{2l_p + 1} exp\left(\frac{-\chi_p}{T_e} \right) G_k$$

The Q_k factors for the three transitions ground states p=1,2 and 3 are 4/3, 3 and 4, respectively. The G_k factors are again determined by other parameters given in Ref. 25. The individual gound state ionization rates are combined into a single rate in the same manner described for the excitation rate.

The method for obtaining the ionization rates are originally from the work of Gryzinski and Kunc[27], which calculates an analytic collision cross section from the expresion:

$$\sigma_{pc} = \frac{\pi e^4}{\chi_p^2} \frac{m}{[(\lambda^2 + k_g)^{1/2} + 1]^2} \left[1 + \frac{2}{(\lambda^2 + k_g)^{1/2}} + \frac{2}{3}\left(1 + \frac{1}{\lambda^2} \right) \right] \left(1 - \frac{1}{\lambda^2} \right)$$

where λ^2 is the ratio of energy of the colliding particle to the ionization potential and k_g is the ratio of the average binding energy of the electrons to the first ionization potential of the outer shell. This collision cross section must be integrated over the all possible colliding energies greater that the ionization potential to get the actual ionization rate.

	Reaction	A	B	E
1	$N_g + e^- = N^* + e^-$	5.08×10^{16}	0.0	121000
2	$N_g + e^- = N^+ + e^- + e^-$	2.96×10^{16}	0.0	169000
3	$N^* + e^- = N^+ + e^- + e^-$	8.95×10^{17}	0.0	48900
4	$O_g + e^- = O^* + e^-$	6.35×10^{15}	0.0	106200
5	$O_g + e^- = O^+ + e^- + e^-$	2.67×10^{16}	0.0	158900
6	$O^* + e^- = O^+ + e^- + e^-$	9.49×10^{17}	0.0	52700
	Rates in the form $k_f = A\, T_e^{\,B} \exp(-E/T_e)$.			

Table III: Added Reactions for Second Order LTNE

$$C_{pe} = \frac{8\pi}{m_e^2} \int_{\chi_p}^{\infty} e f_e(e) \sigma_{pe} de$$

The combined excitation rate from all excited states is calculated by multiplying each individual rate by the ratio of its population to the total excited population as given below and adding.

$$\frac{N_p}{N^*} = \frac{g_p e^{-E_p/T_e}}{Q_{N^*}} \tag{13}$$

The above procedures give the electron impact rates for only a single temperature. The final calculated rates given in Table III were determined by using these procedures for the range of electron temperatures between 4000° and 20,000°K and using a least squares curve fit of these discrete values.

Very similar procedures have been used for the electron impact rates of oxygen using the tabulated parameters in Ref. 26. As suggested by Kunc and Soon, however, the particular excitation rates of 1-4, 1-5, 1-6 and 1-7 were calculated using experimental results of the suggested authors. For each transition, the slope of the cross section at the excitation enegy cutoff, σ'_{1q}, was used with the excitation theory of Zeldovich and Raizer[28] to calculate the particular excitation rates.

$$C_{1q} = kT_e \sigma'_{1p} \left(\frac{8kT_e}{\pi m_e}\right)^{1/2} \left(\frac{\chi_1}{kT_e} + 2\right) e^{-\frac{\chi_1}{kT_e}}$$

The derivation of LTNE correction factors for equilbrium absorption and source functions is similar to that of the first order LTNE mode. Thus, the starting poing is Eqs. 6 for continuum processes and Eqs. 9 for line processes. Using the same arguments as for the first order model, it can be shown that the two factors Π_{pc} and Π_{pq} will be approximately equal to one. Thus for continuum processes, the LTNE absorption function can be calculated by:

$$K_{\nu_{pc}} = \frac{N_p}{(N_p)_{LTE}} (K_{\nu_{pc}})_{LTE}$$

where

$$\frac{N_p}{(N_p)_{LTE}} = \frac{N_p}{N_N} \frac{Q_N}{g_p e^{-E_p/kT_e}}$$

Since the actual number density of state p in not part of the gasdynamic solution, it is desired to recast this expression in terms of the parent state, N_g or N^*. If p is a ground state, Eq. 12 can be used to obtain:

$$\frac{N_p}{(N_p)_{LTE}} = \frac{N_{N_g}}{N_N} \frac{Q_N}{Q_{N_g}} = \frac{N_{N_g}}{(N_{N_g})_{LTE}}$$

Similarly, if p is one of the excited states, use of Eq. 13 yields

$$\frac{N_p}{(N_p)_{LTE}} = \frac{N_{N^*}}{N_N} \frac{Q_N}{Q_{N^*} e^{-E_4/kT_e}} = \frac{N_{N^*}}{(N_{N^*})_{LTE}}$$

The absorption coefficient for atomic line radiation is similar in form to that for the continuum process, but uses a radiative cross section which is a function of both the absorbing, p, and the emitting state, q. However, since the number density dependence is only with the absorbing state, the LTNE corrections described above for continuum radiation also apply to the line radiation.

The previously obtained form for the continuum source function in LTNE is:

$$S_{\nu_{pc}} = \frac{(N_p)_E}{N_p} (S_{\nu_{pc}})_{LTE}$$

As before, the LTNE correction can be written in terms of the known number densities so that if p is one of the ground states,

$$\frac{(N_p)_E}{N_p} = \frac{N_{N+} N_e}{N_{N_g}} \frac{Q_{N_g} e^{I/kT_e}}{Q_{N+} Q_e} = \frac{(N_{N_g})_E}{N_{N_g}}$$

while if p is an excited state,

$$\frac{(N_p)_E}{N_p} = \frac{N_{N+} N_e}{N_{N^*}} \frac{Q_{N^*} e^{(I-E_4)/kT_e}}{Q_{N+} Q_e} = \frac{(N_{N^*})_E}{N_{N^*}}$$

The source function for the radiative transition from state q to state p under LTNE conditions is:

$$S_{\nu_{pq}} = \frac{N_q}{N_p} \frac{(N_p)_{LTE}}{(N_q)_{LTE}} (S_{\nu_{pq}})_{LTE}$$

If the transition is between two excited states, then, just as for the first order LTNE model, the above number density ratios cancel and the LTE and LTNE source functions are seen to be equal. If the lower state is a ground state, Eq. 12 and Eq. 13 yield the result:

$$S_{\nu_{pq}} = \frac{N_{N^*}}{N_{N_g}} \frac{(N_{N_g})_{LTE}}{(N_{N^*})_{LTE}} (S_{\nu_{pq}})_{LTE}$$

Molecular NLTE

For the most part, radiation from molecules is in the form of line emision and absoption associated with transitions between electronic states. Unlike the simple line structure of atoms, however, molecular radiation appears in bands of lines due to the added probability of changes in vibrational or rotational energy during transition. Performing detailed analysis for each individual line in the bands is an enormous task requiring detailed knowledge of the population density of each molecular, vibrational, and rotational state; the transition probabilities for each individual line; and the difusiveness of each line due to quantum mechanical interference effects. In addition, each transtion band may end in a continuum structure associated with the possible photo-dissociation of the molecule during transition. As a result, it is common practice to model molecular bands as having only a continuum structure with a total continuum contribution equal to the sum of the individual lines.

The radiating molecular species included by Nicolet in the RADICAL package include the contributions from N_2,O_2,NO, and N_2^+, with the later two species being the largest radiators. While this research has mainly concentrated upon the development of methods for atomic LTNE, it was desired to have some reasonable means for also estimating the molecular LTNE effects for the above species. A simple model had been developed by Carlson et al.[20] using arguments similar to the first order atomic LTNE model. However, due to the more complex methods of vibrational and electronic excitation in molecules and since most molecules do not show a decisive split in the energy states of ground and excited states this method was subsequently considered to be too approximate. Instead, the quasi-steady state method (QSSM) of Park[24] has been used. The basic assumption of this method is that given the total species number densities of atoms and molecules from a gasdynamic solution, the excited state populations of the molecules can be calculated by balancing the rates of excitation and de-excitation through electron collisions, heavy particle collisions, and spontaneous radiative emisions (radiative absorption is not included). A similar method for atomic excitation was discussed earlier but not used due to the importance of atomic absorption and coupling between radiation and chemistry. However, the lack of any other theory for molecular excitation made the QSSM method a reasonable approach to include molecular LTNE effects.

One result of the QSSM method is the output of ratios of excited state populations to the populations calculated assuming LTE. Since RADICAL includes only molecular lines, although modeled as continuum, these population ratios can, based upon the lengthy discussion of atomic LTNE corrections, be directly applied to the LTE calculated absorption coefficient and source function using:

$$K_{\nu_{pq}} = \frac{N_p}{(N_p)_{LTE}}(K_{\nu_{pq}})_{LTE}$$

$$S_{\nu_{pq}} = \frac{N_q}{(N_q)_{LTE}}\frac{(N_p)_{LTE}}{N_p}(S_{\nu_{pq}})_{LTE}$$

where p is the absorbing state (lower) and q the emiting state. For N_2, the excited states calculated are the X, A, B, a, and C states. The N_2 radiation bands included in RADICAL and the corresponding upper and lower states are: 1st Positive between B-A, 2nd Positive between C-B and the Birge-Hopfield band between c-X. The upper state of the Birge-Hopfield band, c, is not specifically calculated but shares the same excitation behavior as state C in that it is a predissociated state. As such, the nonequilibrium population ratios of state C were used in calculating the LTNE factors for this band.

The bands of NO which RADICAL models are the γ (A-X), β (B-X), δ (C-X) and ϵ (?-X); it is not clear from references what precisely is the upper state of the ϵ band, but Herzberg[29] argues that this band is really just an extension of the γ band with slight frequency shifting caused by interference with other bands. The states calcuated in the QSSM method are the A, B, and C states. Thus, all of the above processes could be properly adjusted for LTNE. However, an additional complication exist in RADICAL due the modeling of both the ϵ and δ bands with a single term. Since it could not be determined how to split this term into the two components, it was decided to correct the entire term as though it were the ϵ band alone, on the assumption that this radiation dominates the δ radiation.

The calculation of N_2^+ was more straight forward since RADICAL only includes the 1st negative band, and both the upper and lower state of this band are explicitly calculated in the QSSM method. Similarly, O_2 radiation is modeled with only the Schumann-Runge band; but only the upper state of this transition is calculated and not the lower state, which is the ground state of O_2. However, results with all the other species show that the ground state of each is rarely out of LTE; so the lower state correction for O_2 was set to unity.

Radiation-Gasdynamic Coupling

To account for the loss or gain of energy from the flowfield due to radiative effects, additional terms must be added to the governing energy equations. For the global energy equation, this process is straight forward since it is obvious that any change in the local radiative energy flux must come from some form of gasdynamic energy. The total flux quantity, $\nabla \dot{q}_r$, is thus added as a scalar property into the global energy equation.

If all the processes of radiative emission and absorption are considered, it is seen that portions of the total flux are being absorbed or emitted as: chemical energy in the breaking of bonds (photo-ionization and photo-dissociation), electronic energy state transitions, excess ionization energy imparted to freed electrons, free-free electron energy, changes in vibrational energy states, and changes in rotational energy states. These effects are listed in order of magnitude for radiation associated with very high speed reentry such as lunar or martian return where atomic radiation dominates and radiative-gasdynamic coupling is very important. At lower velocities such as those for the AFE, molecular radiation dominates and the first source (chemical bonding energy) may be much less than the other sources. The magnitude of radiative-gasdynamic coupling is also much less important at the lower velocities. The last two sources potentially effect the vibrational and rotational energy although they are generally not included by investigators.

The fraction of the total energy flux not expended in breaking chemical bonds should be accounted for as a loss or gain of electron-electronic energy. To do this, however, requires a detailed accounting in the radiation transport model of each contributing process and the associated radiative energy flux. Such an effort was made by Stanley and Carlson[18] in their consideration of hypersonic precursor effects. A review of their work shows the great difficulty envolved in extracting photo-ionization rates out of the radiation calculation even when only considering a simplified radiative model. The extensive numerical considerations which would have to be made in order to include photo-ionizaton processes and to properly model the gain or loss of electron-electronic energy are beyond the scope of this work. Futher, the total effects of including these phenomena is not considered important at the conditions to be considered but may have some applicability to higher altitude, lower density flows.

Discussion of Results

A total of seven different flight conditions have been used to obtain stagnation point solutions (see Table IV). The first three match conditions from the flight results of the Fire 2[30] test for which total heat transfer and selective bands of radiative heat transfer were measured. The flight times of 1634, 1636, and 1637.5 seconds include conditions ranging from significant chemical non-equilbrium to equilibrium. The next case is the maximum dynamic pressure point for a proposed AFE flight profile and has been labeled as CFD solution point 4 as part of the CFD development-verification portion of that test program. This case may be typical of conditions for inter-orbit aeroassisted vehicles and is a low speed, large nose radius condition dominated by vibrational rate processes and molecular radiation. The last three conditions are at 80 km altitude and 12, 14, and 16 km/sec velocity, respectively. These conditions might be considered representative of inter-planetary aerocapture conditions with the low speed for lunar returns and the higher speeds for possible Mars return earth entries. Two additional cases were considered at 12 km/sec and 80 km for the downstream solutions of 60° and 45° hyperboloid body shapes with a 100 cm nose radius. These shapes were chosen to be close approximations to the nose region of a 60° sphere cone configuration without having the curvature discontinuity problems related to that geometric configuration.

For the Fire 2 cases, the freestream conditions and wall temperature are those measured during the flight test at the indicated times. The heat shield of the test vehicle was made of beryllium, which is considered to be fully catalytic to molecular recombinations; and the numerical results to be shown were made using a fully catalytic surface boundary condition. The spectral reflectivity properties of the radiative measuring device are also reported in Ref. 30 and have been used in determining the total radiative heat transfer to the surface.

For all the other cases, the wall temperature has been assumed to be at 1650°K. This value reflects the expected maximum temperature a non-ablating heat shield may withstand, although it is recognized that the cummulative heat loading expected for aerocapture at the higher velocity conditions will probably be much higher than that allowed for current non-ablating materials. The surface for these cases is also assumed to be catalytic to ionic recombinations but non-catalytic to atomic recombinations and to be radiatively black. This behavior is consistent with the properties of shuttle type reaction cured glass heat shield tiles.

Case	Altitude km	Speed km/sec	R_{nose} cm	Notes
1634	76.42	11.36	74.7	Fire 2, 1634 sec
1636	71.04	11.31	74.7	Fire 2, 1636 sec
1637.5	67.05	11.25	74.7	Fire 2, 1637.5 sec
AFE4	75.2	9.326	230	AFE CFD Point 4
12	80	12.0	230	Lunar AOTV
14	80	14.0	230	Martian AOTV
16	80	16.0	230	Martian AOTV
60	80	12.0	100	60° Hyperboloid
45	80	12.0	100	45° Hyperboloid

Table IV: Solution Cases and Conditions

A 99 point grid between the shock front and the vehicle surface has been used which resolves both the regions of non-equilibrium at the shock front and the cool wall. Shock slip conditions were used on all cases to properly conserve the species and energy flux in the shock jump relations. The three temperature thermal model and multicomponent diffusional model has also be used. While being a more complete description of the diffusive properties of the gas mixture, the results obtained with this diffusive method are very similar to results which may be obtained with a constant Lewis number approach (with Le = 1.4)[3,31].

First Order Atomic LTNE Model

Results were obtained using the first order LTNE model for all the above cases and three different species/reaction sets: nitrogen gas with Wilson derived electron impact excitation rate, nitrogen gas with the newly derived electron impact excitation rate (reaction 1, Table III), and air with the rates from Table II. The first set of results are summarized in Table V and are comparable to results shown in Ref. 2. The first tabulated value is the calculated stand off distances between shock and body, Δ. The next is the total convective heat transfer which is the the sum of the contributions from conduction and catalyticity. The total radiative heat transfer absorbed by the wall is also shown both before and after radiative cooling has been coupled with the gasdynamic solution. A breakdown of the coupled radiative heat transfer to the wall into line and continuum contributions is also given for the incident wall radiation. Since for the Fire 2 conditions the wall was not a black body, the absorbed amount is not the total of the two incident values. Also, since the mechanisms of continuum and lines are not separable, the line value is really the contribution of the lines above the background continuum value.

The ground to excited excitation rate shown in Table III should be analogous to the electron impact ionizaton rate of Wilson[7] shown in Table I, since Wilson deduced his rate based upon the assumption that the excitation process was a limiting step in the ionization of atoms. As such, a new set of results for nitrogen have been generated using this rate in place of Wilson's rate. A summary of these results is given in Table VI

			Coupled Q_r			Uncoupled Q_r
Case	Δ	Q_c	Cont.	Lines	Absorbed	Absorbed
1634	4.67	196.	4.92	1.12	3.94	4.07
1636	4.35	285.	15.7	14.1	22.5	23.8
1637.5	4.23	361.	32.0	39.3	54.5	59.3
AFE4	13.2	17.2	1.87	0.03	1.90	1.93
12	13.6	24.6	15.7	10.8	26.5	28.2
14	12.0	41.0	56.6	43.1	99.6	119.
16	11.0	64.7	127.	101.	228.	301.

Δ is shock standoff distance in cm.
Q_c is convective heat transfer to wall in watts/sq cm.
Q_r is radiative heat flux to wall in watts/sq cm.
Lines and Continuum values are incident upon wall.

Table V: Summary of Results for Nitrogen and Wilson Rates

			Coupled Q_r			Uncoupled Q_r
Case	Δ	Q_c	Cont.	Lines	Absorbed	Absorbed
1634	4.47	195.	4.80	3.36	5.92	-
1636	4.17	284.	16.0	18.2	26.3	-
1637.5	4.13	361.	31.3	42.5	56.5	-
AFE4	13.2	17.2	1.87	0.03	1.90	-
12	13.1	26.8	14.2	9.92	24.1	-
14	11.6	44.4	49.9	37.2	87.0	-
16	10.6	66.7	110.	85.0	195.	-

Δ is shock standoff distance in cm.
Q_c is convective heat transfer to wall in watts/sq cm.
Q_r is radiative heat flux to wall in watts/sq cm.
Lines and Continuum values are incident upon wall.

Table VI: Summary of Results for Nitrogen with New Rates

for the radiatively coupled solutions; uncoupled solutions were not generated.

The AFE4 results with the new rate are seen to be identical to those with the Wilson rate as might have been expected since atomic electron impact processes are not important at this condition. All the other results show a marked difference from those calculated using the Wilson rate. With the new, faster rate, the electron temperature peaks lower and equilibrium occurs sooner which in turn causes a shorter stand off distance. This combination of effects results in a lower radiative flux to the wall for the 80 km altitude cases than seen previously. The Fire 2 cases, however, have the same changes in profiles and stand off distances yet higher radiative heat transfers. For these cases with the smaller radius nose, the percentage of the total region in thermodynamic non-equilibrium behind the shock layer is greater than the 80 km cases, particularly for the 1634 second condition. The increased level of thermodynamic equilibrium and an associated higher radiative emission with the new electronic impact ionizaton rate results in greater atomic line radiation and an increased total flux.

			Coupled Q_r			Uncoupled Q_r
Case	Δ	Q_c	Cont.	Lines	Absorbed	Absorbed
1634	5.32	193.	11.5	7.16	13.6	14.6
1636	4.69	281.	29.6	31.4	46.9	54.4
1637.5	4.52	362.	52.6	70.1	93.0	115.
AFE4	14.8	14.9	3.78	0.10	3.88	3.99
12	14.5	28.5	21.9	14.0	35.9	42.6
14	12.8	47.9	61.6	45.6	107.	142.
16	11.6	71.0	125.	96.2	221.	327.

Δ is shock standoff distance in cm.
Q_c is convective heat transfer to wall in watts/sq cm.
Q_r is radiative heat flux to wall in watts/sq cm.
Lines and Continuum values are incident upon wall.

Table VII: Summary of Results for Air, 1st Order LTNE

Results using air as the freestream gas and the chemical reaction set of Table II are summarized in Table VII. A comparison of the tabulated radiative fluxes shows that the amount of radiation in air is greater than that for nitrogen alone. One reason for this difference is that the air results have a higher equilibrium temperature than the corresponding nitrogen results. For the 1634 second case the difference is almost 400°K at 30% of the shock layer away from the wall. Since the ionization potential of oxygen is lower than that of nitrogen, less heavy particle energy is expended in ionizing the air mixture than nitrogen alone. The equilibrium temperature is thus higher and the radiation correspondingly greater. The above argument does not apply for the AFE4 case which has no significant ionization. It is believed for this case the increase in radiation with air is due to the inclusion of NO which is a strong radiator even in small quantities. An additional factor causing the higher radiative fluxes is the larger stand off distances associated with air in all of the cases. This increase is attributed to a slower rate of thermal and chemical equilibrations due to a change in the dissociation rates between Table I and Table II.

The calculated heat transfer results in air and the flight data of the Fire 2 test are compared graphically in Fig. 1. A similar comparison for nitrogen using the first order LTNE model and the Wilson electron impact rate has been given in Ref. 1. The Fire 2 vehicle included three different heat transfer gauges. The first was a total calorimeter which measured the sum of the convective and absorbed radiative flux. The flight data and the numerical comparisons are indicated by the label "QC + ALPHA*QR" and the square symbols, respectively. The numerical results compare favorably, but are slightly higher, with the flight data at all three times. Since the bulk of this heat transfer is due to catalycity, the differences may be due to the modeling of the suface as fully catalytic as opposed to having a high but finite catalycity. This possibility may be supported by the results of Ref. 32, which obtained good correlation with Fire 2 data by not assuming fully catalytic walls.

Two other gauges measured the radiative heat transfer over the frequency ranges of 0.02 to 6.2 eV and 2 to 4 eV, respectively. The first range covers most the spectrum from the low infrared through the visible ranges and includes the radiative phenomena associated with the high line transitions and most of the molecular band radiation. The flight data from this gauge is shown as the dashed line on the figure. The second range is over a region of mostly molecular band radiation and in particular that of N_2^+

and NO. The flight data from this gauge showed a large amount of scatter[44], particularly in the early trajectory times, and is indicated on the figure by the region bounded by the limits of the scatter. The numerical solutions for this case are shown as the diamond and circular data points for the 0.02 to 6.2 eV and 2 to 4 eV ranges, respectively. The 0.02 to 6.2 eV numerical results are reasonably close to that of the flight data at all conditions, but do not appear to follow the trend of the flight data. The 2 to 4 eV numerical results on the other hand are consistently higher than the flight data, although they follow the trend of the upper boundary of scatter.

The 2 to 4 eV comparisons, which are primarily comparisons of molecular radiation, indicate that there may be a need to reevaluate the use of the quasi-steady state model in calculating molecular LTNE. If more LTNE was predicted theoretically, the numerical molecular radiation would be reduced; and in particular the amount of reduction would be greater. This effect would reduce the 2 to 4 eV radiation in the correct manner to move the numerical results into the measured flight data. In addition, if it is accepted that the molecular contributions are high and realize that the difference between the 0.02 to 6.2 eV and the 2 to 4 eV data is primarily due to atomic line processes, it can be deduced that the atomic line predictions for the Fire 2 results follow the correct trend but may be consistently low.

Second Order Atomic LTNE Model

All of the results shown for air in the previous section using the first order atomic LTNE model have been also computed using the second order model. The chemical reactions set of Table II with the electron impact reactions replaced by the two step processes given in Table III has been used in calculating the gasdynamic flowfield solution. The high rate of ionization from excited oxygen and nitrogen caused some stability problems in situations where there was a large amount of thermal equilibrium. To avoid this problem and obtain converged solutions, this rate needed to be reduced by one third for the 1636, 1637.5, 14 and 16 cases. A summary of all the results is given in Table VIII with the radiative coupled solution profiles given in Figs.2 through 15. In addition to the gasdynamic profiles of temperature and species concentration, two plots showing the spectral content of the wall radiation are given. In the lower presentation, a detailed representation of the spectral radiative content is given showing easily the location and form of the sharp line radiation against the smooth continuum background. Each line, while appearing to be nearly discontinuous, has actually been subdivided into 15 discrete points to give detail to the line center and the wings. Because of the logrithmic axis needed to present this data, it is very difficult to deduce anything but qualitative observations from this presentation format. On the other hand, the upper presentation uses convenient line groupings over widths of the spectrum to show the summed contributions. In this form, the total area under the curve represents the total radiative flux to the wall; and the individual contributions made due to specific processes and spectral regions are easily observed.

			Coupled Q_r			Uncoupled Q_r
Case	Δ	Q_c	Cont.	Lines	Absorbed	Absorbed
1634	5.33	193.	11.5	11.7	15.9	17.6
1636	4.75	282.	31.5	42.4	54.4	60.4
1637.5	4.55	361.	53.1	77.6	97.5	119.
AFE4	14.8	15.0	3.91	0.60	4.51	4.71
12	14.5	29.1	22.2	17.4	39.6	47.3
14	12.6	46.9	60.1	53.8	114.	159.
16	11.4	70.2	122.	105.	227.	344.

Δ is shock standoff distance in cm.
Q_c is convective heat transfer to wall in watts/sq cm.
Q_r is radiative heat flux to wall in watts/sq cm.
Lines and Continuum values are incident upon wall.

Table VIII: Summary of Results for Air, 2nd Order LTNE

The following observations can be made for the second order LTNE results which apply to all cases. The gasdynamic solutions are very similar to those calculated for the first order LTNE results. In both models the LTNE population correction factors are small in the thermal nonequilibrium region behind the shock front indicating a depopulation of the excited states by chemical reactions, and both show a region of over population of the atomic electronic states in the wall thermal layer where the reverse ionization reactions dominate. In addition, both models exhibit extensive thermal nonequilibrium over much of the shock layer, and in particular the vibrational and electron temperatures do not equilibrate until near chemical equilibrium. The only significant difference is the presence of the excited state populations in the species mole fraction profiles. Since the species profiles are not affected by using the multistep ionization rates as opposed to the single step rate, these results seem to validate Wilson's assumption that the ground to excitation process is indeed rate limiting. A comparson of the radiation from the two models shows that the continuum contribution has effectively remained the same. However, the line contribution has increased in all cases implying that the calculated excited state species are not fully in equilibrium with the free electrons and ions as assumed for the first order method since this equilibrium results in a depletion of the excited state population in regions of chemical nonequilibrium such as behind the shock front where the ionization level is increasing.

A comparison of the second order LTNE Fire 2 results with the flight data is made in Fig. 16. The 2 to 4 eV, which were high before, are even higher with the new model due to the increase in the few atomic lines in this range. The numerical results for the range of 0.02 to 6.2 eV are now much too high at both 1634 and 1636 seconds, while they are close at 1637.5 seconds. Since the increase in infrared line contribution places the current results above the measured 0.02 to 6.2 eV data, the possibility that the second order LTNE method is now underpredicting the level of LTNE must be considered. Results of Park[24] using the QSSM method for determining excited state populations indicate a continuously increasing divergence from LTE with increasing excitation levels as opposed to the two regions of LTE, ground and excited, assumed for this current method. The larger amount of LTNE at highly excited states as compared to the lower excited states would contribute to decreasing the amount of radiation from the high line transitions (infrared). One possible resolution of this difference may be to consider not only two levels of LTE for atomic nitrogen and oxygen, but also two electronic temperatures if energy exchange rates between the two levels could be determined.

At 1634 seconds, the relatively constant enthalpy profile and the small difference between coupled and uncoupled wall radiative absorption indicates that radiation cooling is insignificant. From the temperature and species profiles it is seen that at this condition, the shock layer is in extensive chemical and thermal nonequilibrium. Comparing these results to those previously reported for nitrogen alone, Ref. 2, shows some differences in the thermal realxation which may be attributed to the different dissociation rates in the Dung and Kang reaction set for nitrogen and the Park reaction set for air.

The solutions at 1636 seconds and 1637.5 seconds show progressively less nonequilibrium behind the shock layer. By 1637.5 seconds, the temperature profile (Fig. 6) indicates a post shock nonequilibrium region of only about 25% of the total thickness. The equilibrium temperature and amount of equilibrium ionization is roughly equivalent at all three times since the flight velocity and, thus, the total enthalpy are not significantly different. The total radiative flux increases with time, however, since the vehicle is decending into denser gas regions and the total number density of the radiating species is increasing. As can be seen from the change in the radiative flux when radiation/gasdynamic coupling is included, at both 1636 and 1637.5 seconds a noticable amount of radiative cooling is present.

The trend of shifting from molecular to atomic dominated radiation at later times in the trajectory can be seen by comparing the spectral radiative results at the different case conditions. At 1634 seconds, Fig. 3, the total radiative flux is nearly equally divided between the molecular radiation (mainly between 2 and 4 eV) and the atomic line and continuum radiation. For the region between 0 and 6 eV, the molecular contribution dominates the atomic contribution. At 1636 seconds, Fig. 5, both the total and 0 to 6 eV radiative flux is predominantly atomic although molecular is still significant. Finally at 1637.5 seconds, Fig. 7 the relative contribution of molecules is reduced further but is still significant in the lower band region.

The radiatively coupled result for the AFE4 conditions in air are presented in Figs. 8 through 9. The species mole fraction profiles also show the effect of the different dissociation rates used in Table II with the N_2 profile having a greater degree of nonequilibrium than previous nitrogen results. The spectral radiation plots of Fig. 9 indicate quite clearly that molecular species are the only significant contributor at these conditions. This result combined with the above observation that the current molecular LTNE method may not be totally accurate indicates that further research is needed in this area.

The 12 km/sec case, when originally considered with the Wilson electron impact ionization rate, Ref. 2, showed extensive chemical and thermal nonequilibrium through the shock layer; although, with the use of the new rate the nonequilibrium region was reduced to only 35 to 40% of the shock layers. The excited state populations, N^* and O^*, as seen in Fig. 10 closely follow the electron-electronic temperature profile. The radiation profiles in Fig. 11 indicate that the radiative wall flux at this condition is predominantly from atomic radiation. This observation could also have been made by considering the species profiles which show that almost total molecular dissociation has occured by the end of the nonequilibrium zone. The decrease in the enthalpy and percent ionization indicate that radiative cooling is significant for this case.

As the velocity is increased to 14 and 16 km/sec, the increase in total enthalpy of the freestream flow results in higher temperatures and percent ionizations in the shock layer. The extent of nonequlibrium is also progressively decreased due to an increasing density behind the shock and, thus, an increasing number of collisions. This increasing density is not a result of a stronger shock wave, since inviscid, frozen gas shock relations show that a maximum density jump of 6.0 can be expected for air, but is due to the larger decrease in heavy particle temperature between the shock and the equilibrium region. The pressure behind the shock is relatively constant which means that density must increase in an inverse relation with temperature. The 14 and 16 km/sec results also show progressively larger effects due to radiative cooling with the 16 km/sec have a coupled wall radiative flux one third lower than the uncoupled result.

Hyperbolic Body Solutions

As mentioned previously, two downstream solutions have also been obtained for 60° and 45° hyperboloid bodies with a nose radius of 100 cm. The calculations are radiatively coupled using the first order LTNE method; but due to the low total heat flux, there is no significant radiative energy loss from the shock layer. In calculating these results, two modifications were made to the existing code in an attempt to smooth out shock slope discontinuities occuring near the stagnation line of the axisymetric flow. First, the alternate approach for calculating shock standoff distance, Δ, given by Miner and Lewis[33] has been used. This method uses the exact mass flow through a cylindrical stream tube to calculate the necessary mass flux through the shock layer as opposed to a differential approximation previously used. Second, the stagnation streamline Δ has been calculated by extrapolating the downstream solutions with the condition that the first derivative of Δ with respect to surface length should be zero at the stagnation point. This change corrected an apparent underprediction of the stagnation point Δ. While this method can have stability problems due to the explicit determination of the stagnation Δ from previous global iteration information, convergence can be acheived with under-relaxation of the changes in shock shape between global iterations.

The converged shock shapes for both conditions are shown in Fig. 17 along with the specified body shapes and a comparison with the body shape of a 60° sphere cone. The 60° hyperboloid has a noticably thicker shock layer in the stagnation region even though visibly the surface slopes and curvature in this region are equivalent. This difference indicates that global iteration is properly providing an upstream influence from the blunter body. The 45° hyperboloid body is also seen to be a slightly better approximation to the sphere cone shape in the fore region although the surface slope is shallower than the cone angle on the afterbody.

The radiative and convective heating data for both hyperboloid bodies is presented in Fig. 18. Due to the increased standoff distance, the 60° hyperboloid shows a greater radiative heat flux than the 45° shape. Also, while the radiative flux to the 45° body decreases significantly downstream from the stagnation point, the 60 degree case remains relatively constant. This behavior is due to a combination of effects: Δ increases faster, the shock temperatures and percent ionization decrease less rapidly and the relative amount of equilibrium in the shock layer also increases downstream for the 60° case. The profiles shown in Figs. 19 and 21 help show this point. Note these results were made using a three temperature model but the results for T_v are left off on these plots to avoid confusion. On these plots, three solution profiles are shown for distances of S/R_{nose} of 0, .5, and 1.

The radiation frequency spectra for the two cases, Figs. 20 and 22, are similar at the stagnation point in both cases. Downstream at S/R of 1 the amount of radiation at all frequencies has decreased for the 45° case. However, for the 60° case, the molecular and infrared line radiation has increased over the stagnation levels while the ultraviolet radiation has decreased. This shift to the infrared is consistent with a lowering of the equilibrium temperature downstream and a higher concentrations of molecules and non-ionized atoms in this region.

The convective heat flux for the 60° case is lower as shown in Fig. 18 due to the thicker thermal boundary layer which follows from the thicker total shock layer. Both the 60° and 45° cases show an initial increase in the convective heat flux between the stagnation point and the first point downstream. Results from other authors working with sphere cones[34-36] show a small variance in Q_c in this region but not an actual increase. On the other hand Candler and Park[37] predict a very pronounced increase with a blunter, ellipsoidal nose shape. Otherwise, both the convective and radiative heat fluxes presented here are consistent with those shown in Refs. 34-37 considering the differences in body geometry and surface catalycity.

Conclusions

A survey of solutions using the complete gasdynamic model coupled with an LTNE corrected radiation model demonstrates the usefullness of the current method. Comparisons with Fire 2 flight data are encouraging; but some improvement are needed, particularly in the area of molecular LTNE methods.

A second order LTNE model for air has been evaluated in comparisons with an existing first order model. The results are similar; but the second order LTNE model consistently shows a higher level of atomic line radiation, indicating that the first order assumption of full equilibrium between the excited states with the ions and electrons may not be completely justified. Comparisons of the second order LTNE model with Fire 2 flight data on the other hand, show an apparent excessive amount of atomic line radiation attributed to transitions between the higher excited states. Thus, the new model may be underestimating the amount of LTNE in the very upper excited state regions.

A complete gasdynamic-radiative coupled flowfied solution method has been developed for the purpose of evaluating the effects of LTNE prediction methods and radiative cooling. In the development of this method, consideration has been given to the modeling of the following phenomena: multi-temperatures (thermal nonequilibrium), chemical nonequilibrium in a multi-temperature environment, multicomponent-multitemperature diffusion, and thermodynamic and viscous property calculation. The numerical robustness of the method has allowed the evaluation of the radiative heating environment over a wide range of flight and vehicle conditions. These results along with observations made concerning the effects on the radiative environment predicted with a second order LTNE method consistitute a significant advancement in the engineering modeling of nonequilibrium reentry flows.

Acknowledgement

This work was primarily supported by NASA Grant NAG-1-1003 from the Langley Research Center, with Dr. Lin C. Hartung as technical monitor.

REFERENCES

[1] Carlson, L. A. and Gally, T. A., "The Effect of Electron Temperature and Impact Ionization on Martian Return AOTV Flowfields," *Journal of Thermophysics and Heat Transfer*, vol. 5, No. 1, January 1991, pp. 9 20.

[2] Carlson, L. A. and Gally, T. A., "Nonequilibrium Chemical and Radiation Coupling Phenomena in AOTV Flowfields," AIAA Paper 91-0569, January 1991.

[3] Gally, T. A., Carlson, L. A. and Green, D., "A Flowfield Coupled Excitation and Radiation Model for Nonequilibrium Reacting Flows," AIAA Paper 91-1463, June 1991.

[4] Thompson, R. A., "Comparison of Nonequilibrium Viscous Shock Layer Solutions with Windward Surface Shuttle Heating Data," AIAA Paper 87-1473, June 1987.

[5] Nicolet, W. E., "Advanced Methods for Calculating Radiation Transport in Ablation-Product Contaminated Boundary Layers," NASA CR 1656, September 1970.

[6] Nicolet, W. E., "Rapid Methods for Calculating Radiation Transport in the Entry Environment," NASA CR 2528, April 1975.

[7] Kang, S. W., Jones, W. L., and Dunn, M. G., "Theoretical and Measured Electron Density Distributions at High Altitudes," *AIAA Journal*, vol. 11, No. 2, February 1973, pp. 141-149.

[8] Wilson, J., "Ionization Rate of Air Behind High Speed Shock Waves," *The Physics of Fluids*, vol. 9, No. 10, October 1966, pp. 1913-1921.

[9] Park, C., ***Nonequilibrium Hypersonic Aerothermodynamics***, John Wiley & Sons, New York, 1990, Pp. 166-167.

[10] Carlson, L. A., "Radiative Trasfer, Chemical Nonequilibrium, and Two-Temperature Effects Behind a Reflected Shock

Wave in Nitrogen," Ph.D. Dissertation, Ohio State Univerity, 1969

[11] Park, C., "A Review of Reaction Rates in High Temperature Air," AIAA Paper 89-1740, June 1989.

[12] Park, C., Howe, J. T., Jaffe, R. L., and Candler, G. V., "Chemical-Kinetic Problems of Future NASA Missions," AIAA Paper 91-0464, January 1991.

[13] Park, C., "Assessment of Two Temperature Kinetic Model for Ionizing Air," AIAA Paper 87-1574, June 1987.

[14] Treanor, C. E. and Marrone, P. V., "Effect of DIssociation on the Rate of Vibration Relaxation," *Physics of Fluids*, vol. 5, No. 9, September 1962, pp. 1022-1026.

[15] Marrone, P. V., "Inviscid, Nonequilibirum Flow behind Bow and Normal Shock Waves, Part I. - General Analysis and Numerical Examples," Cornell Aeronautical Laboratory Report No. QM-1626-a-12(I), May 1963.

[16] Sharma, S. P., Huo, W. M. and Park, C., "The Rate Parameters for Coupled Vibration-Dissociation in a Generalized SSH Approximation," AIAA Paper 88-2714, June 1988.

[17] Hartung, L., Mitcheltree, R. A. and Gnoffo, P.A., "Stagnation Point Nonequilibrium Radiative Heating and the Influence of Energy Exchange Models," AIAA Paper 91-0571, January 1991.

[18] Stanley, S. and Carlson, L. A., "The Effects of Shock Wave Precursors Ahead of Hypersonic Engry Vehicles," AIAA Paper 91-1465, June 1991.

[19] Chapin, C. E., "Nonquilibrium Radiation and Ionization in Shock Waves," AA&ES Report, June 1967, Purdue, Univ., Lafayette, Ind.

[20] Carlson, L. A., Bobskill, G. J., and Greendyke, R. B., "Comparison of Vibration Dissociation and Radiative Transfer Models for AOTV/AFE Flowfields," *J. of Thermophysics and Heat Transfer*, vol. 4, No. 1, January 1990, pp. 16-26.

[21] Petschek H. and Byron S., "Approach to Equilibrium Ionization behind Strong Shock Waves in Argon," *Annals of Physics*, vol. 1, 1957, pp. 270-315.

[22] Foley, W. H. and Clarke, J. H., "Shock Waves Structered by Nonequilibrium Ionizing and Thermal Phenomena," *Physics of Fluids*, vol. 16, No. 3, March 1973, pp. 1612-1620.

[23] Nelson, H. F., "Nonequilibrium Structure of Argon Shock Waves," *Physics of Fluids*, vol. 16, No. 12, December 1973, pp. 2132-2142.

[24] Park, C., "Calculation of Nonequilibrium Radiation in the Flight Regimes of Aeroassisted Orbital Transfer Vehicles," in ***Thermal Design of Aeroassisted Orbital Transfer Vehicles***, Progress in Astronautics and Aeronautics, Vol. 96, Ed. H. F. Nelson, AIAA, 1985, pp. 395-418.

[25] Kunc, J. A. and Soon, W. H., "Collisional Radiative Nonequilibrium in Partially Ionized Atomic Nitrogen," *Physical Review A*, vol. 40, No. 10, November 15, 1989, pp. 5822 ff.

[26] Kunc, J. A. and Soon, W. H., "Thermal Nonequilibrium in Partially Ionized Atomic Oxygen," *Physical Review A*, vol. 41, No. 2, January 15, 1990, pp. 825 ff.

[27] Gryzinski, M. and Kunc, J. A., "Collisional Inoisation [sic] and the Atomic Model," *Journal of Physics B: Atomic and Molecular Physics*, vol. 19, 1986, pp. 2479 ff.

[28] Zel'dovich, Y. B. and Raizer, Y. P.,***Physics of Shock Waves and High-Temperature Hydrodynamic Phenomena, Volume I***, Academic Press, New York 1966,pp. 390-391.

[29] Herzberg, G., ***Molecular Specta and Molecular Structure I. Spectra of Diatomic Molecules, 2nd Edition***, Krieger, Malabar, 1950,pp. 558-559.

[30] Cauchon, D. L., McKee, C. W., and Cornette, E. S., "Spectral Measurements of Gas-Cap Radiation During Project Fire Flight Experiments at Reentry Velocities Near 11.4 Kilometers per Second," NASA TM X-1389, October 1967.

[31] Gally, T. A., "Development of Engineering Methods for Nonequilibrium Radiative Phenomena about Aeroassisted Entry Vehicles," Ph.D. Dissertation, Texas A&M University, May 1992.

[32] Bird, G. A., "Nonequilibrim Radiation During Re-Entry at 10 km/sec," AIAA Paper 87-1543, June 1987.

[33] Miner, E. W. and Lewis, C. H., "Hypersonic Ionizing Air Viscous Shock-Layer Flows over Nonanalytic Blunt Bodies," NASA CR-2550, May 1975.

[34] Hartung, L. C., "Development of a Nonequilibrium Radiative Heating Prediction Method for Coupled Flowfield Solutions," AIAA Paper 91-1406, June 1991.

[35] Mitcheltree, R. A., "Parametric Study of Dissociation and Ionization Models at 12 Kilometers/Second," *Journal of Spacecraft and Rockets*, vol. 23, No. 6, November-December 1991, pp. 619-627.

[36] Hartung, L. C. and Hassan, H. A., "Radiation Transport around Axisymmetric Blunt Body Vehicles Using A Modified Differential Approximation," AIAA Paper 92-0119, January 1992.

[37] Candler, G. and Park, C., "The Computation of Radiation from Nonequilibrium Hypersonic Flows," AIAA Paper 88-2678, June 1988.

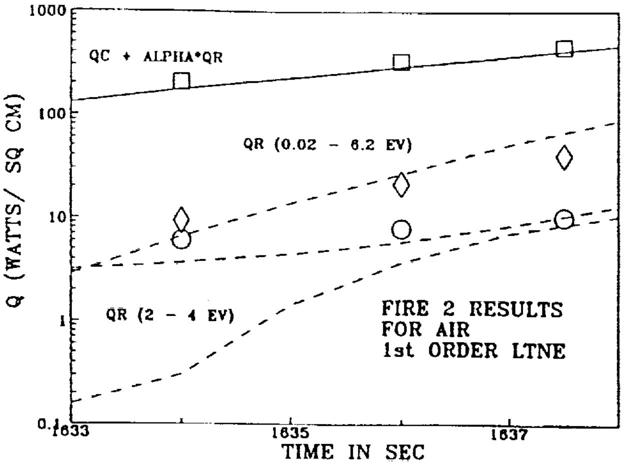

Fig.1: Comparison of First Order LTNE Methods With Fire 2 Flight Test Measurements

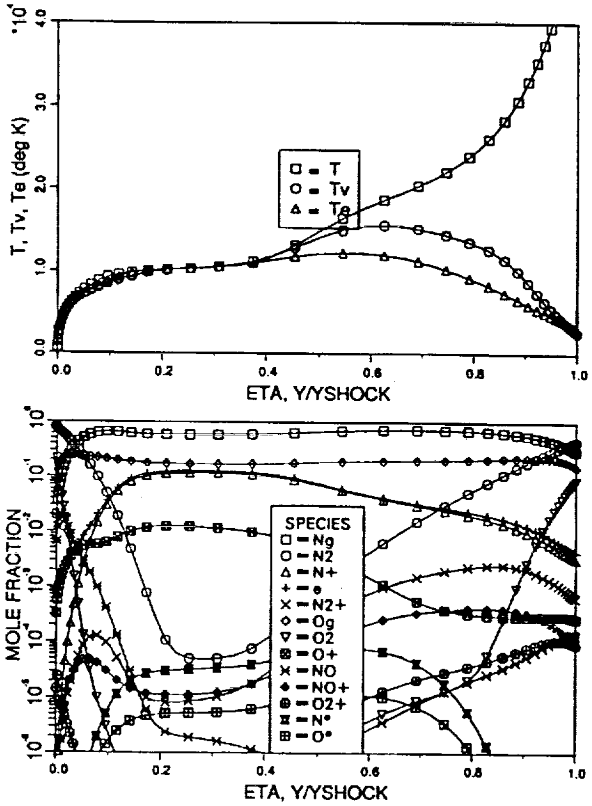

Fig.2: Case 1634 - Air Results with Second Order LTNE Model, Temperature and Mole Fractions

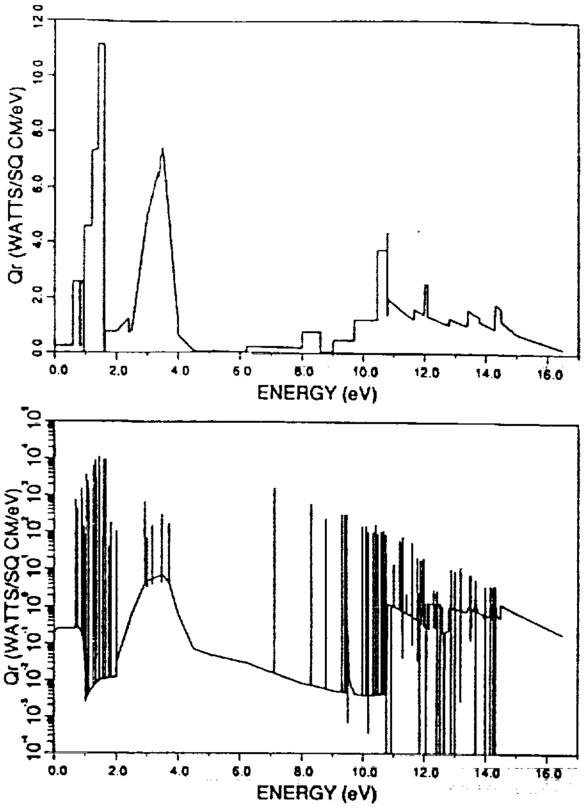

Fig.3: Case 1634 - Air Results with Second Order LTNE Model, Grouped and Detailed Radiation Spectra

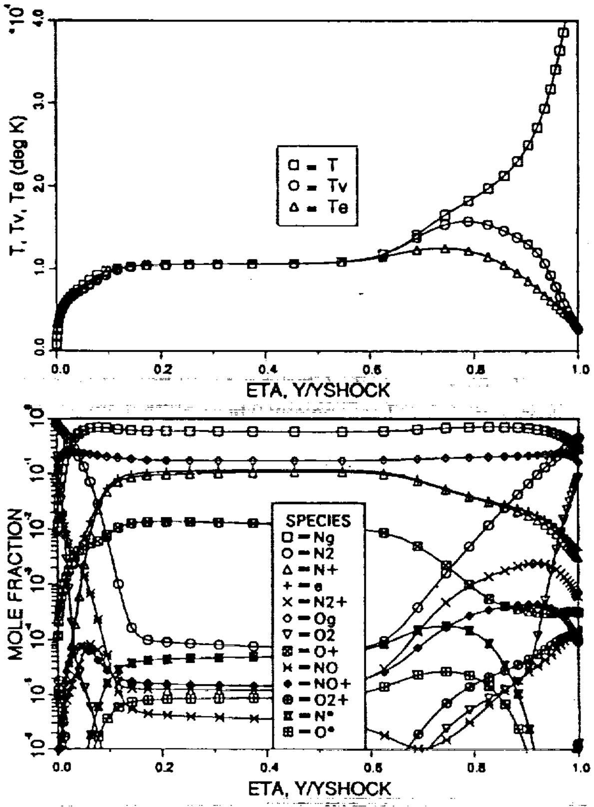

Fig.4: Case 1636 - Air Results with Second Order LTNE Model, Temperature and Mole Fractions

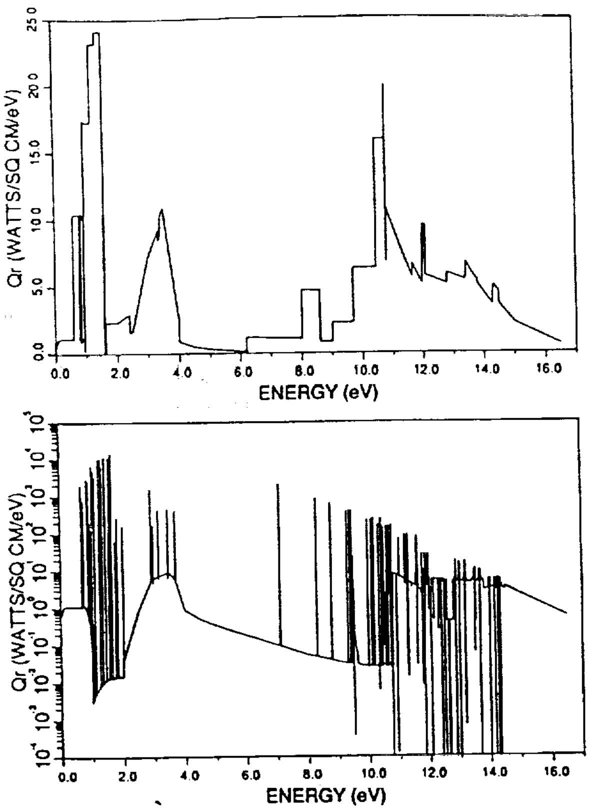

Fig.5: Case 1636 - Air Results with Second Order LTNE Model, Grouped and Detailed Radiation Spectra

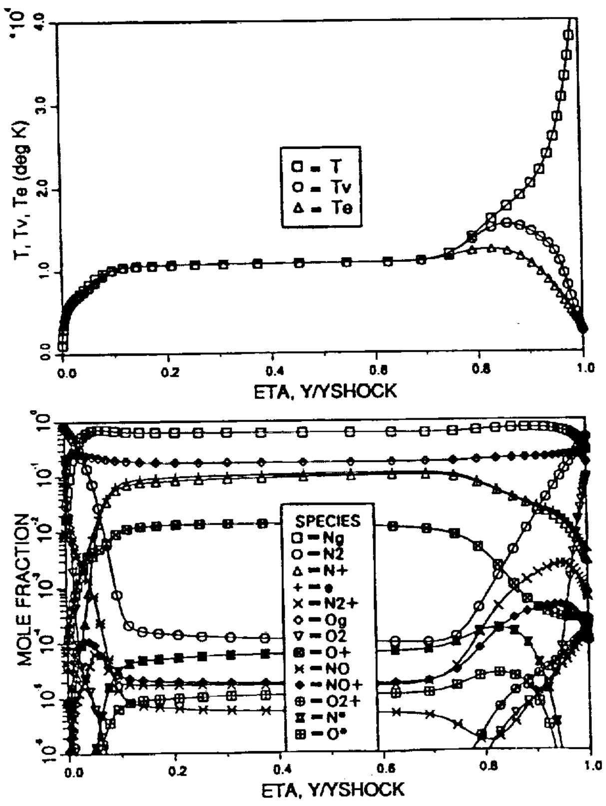

Fig.6: Case 1637.5 - Air Results with Second Order LTNE Model, Temperature and Mole Fractions

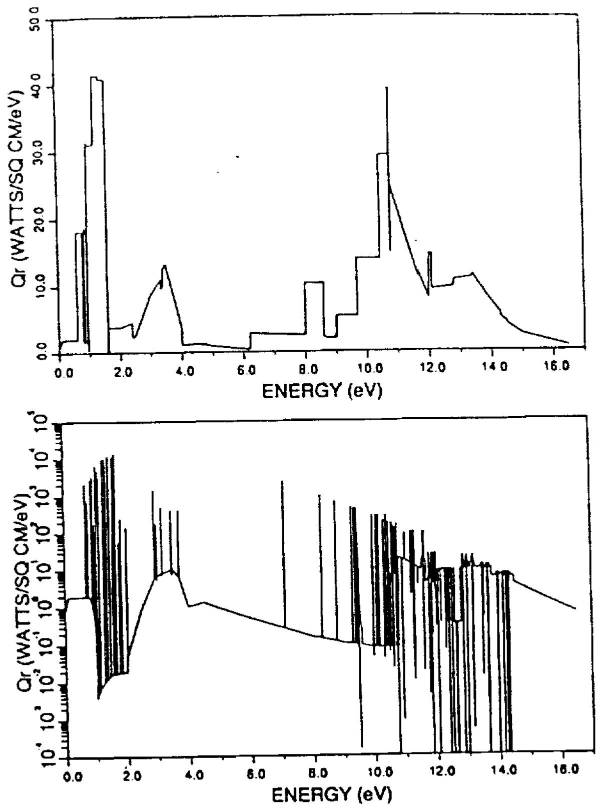

Fig.7: Case 1637.5 - Air Results with Second Order LTNE Model, Grouped and Detailed Radiation Spectra

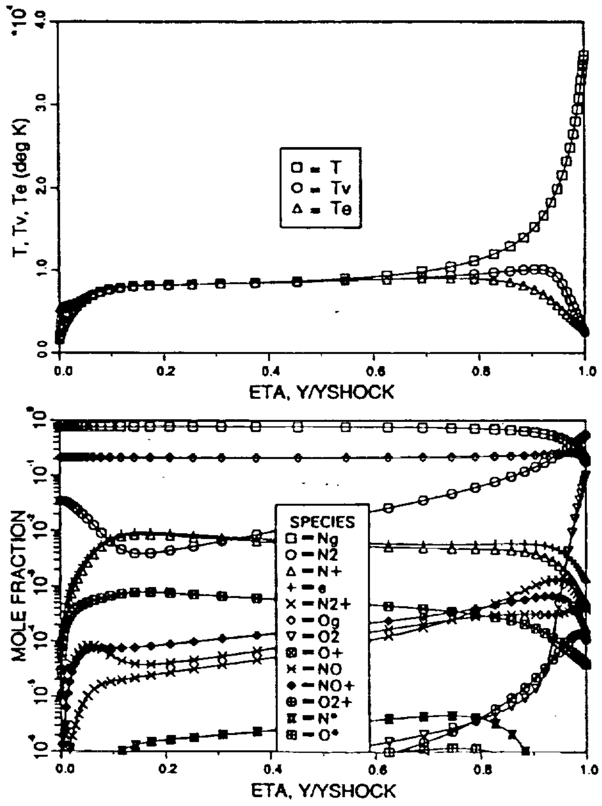

Fig.8: Case AFE4 - Air Results with Second Order LTNE Model, Temperature and Mole Fractions

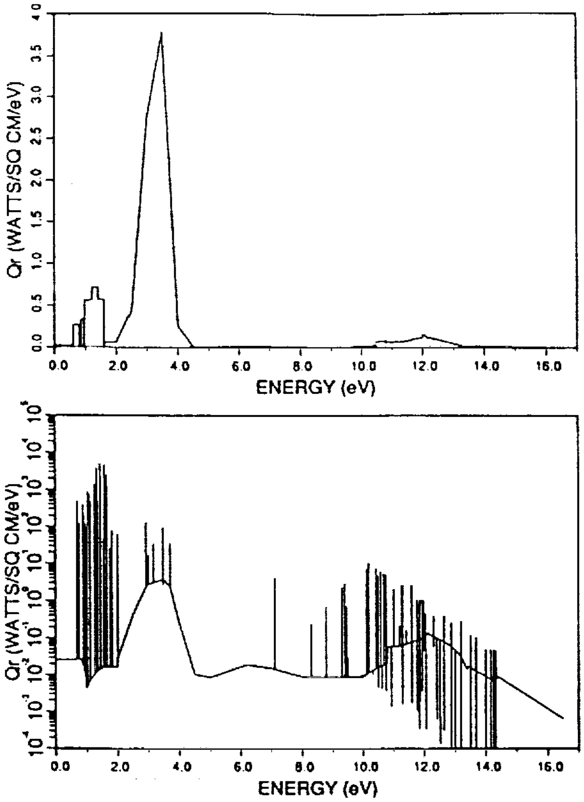

Fig.9: Case AFE4 - Air Results with Second Order LTNE Model, Grouped and Detailed Radiation Spectra

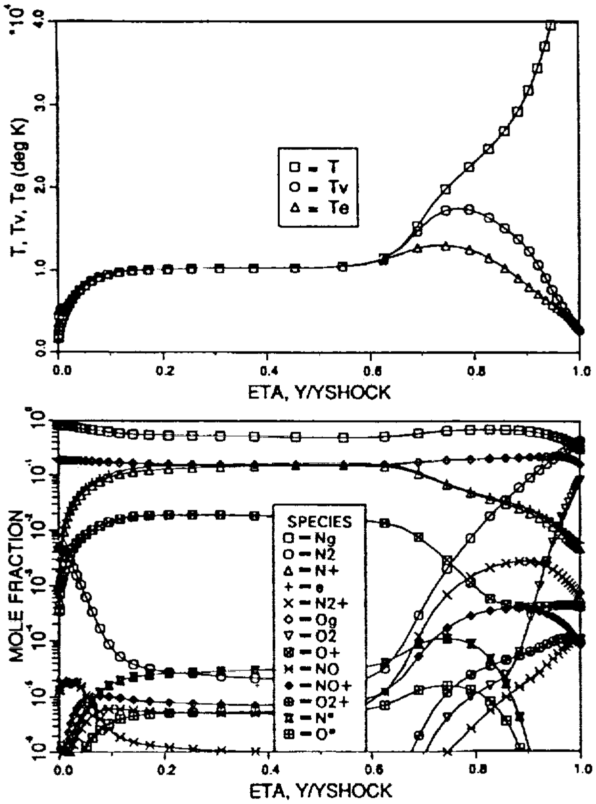

Fig.10: Case 12 - Air Results with Second Order LTNE Model, Temperature and Mole Fractions

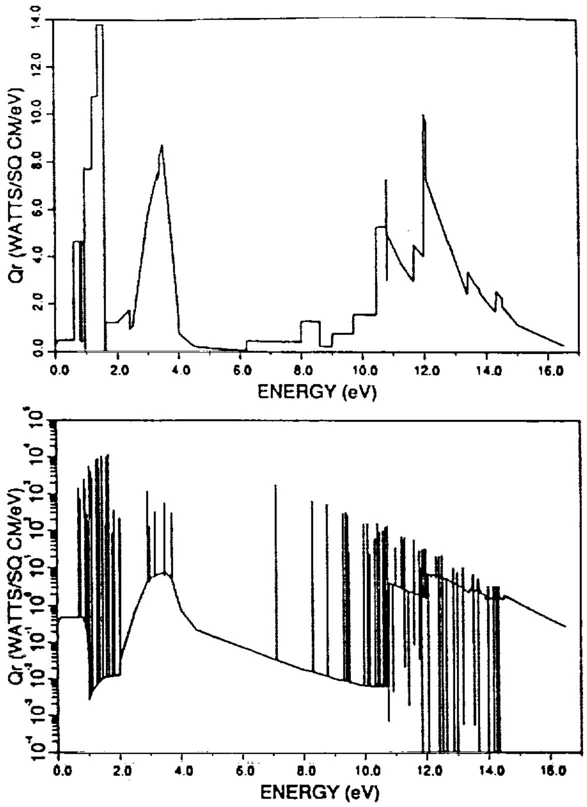

Fig.11: Case 12 - Air Results with Second Order LTNE Model, Grouped and Detailed Radiation Spectra

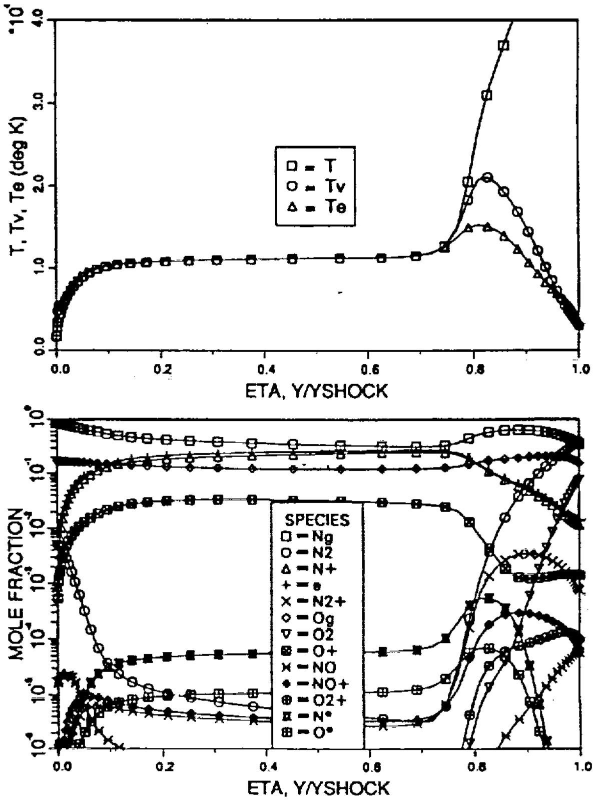

Fig.12: Case 14 - Air Results with Second Order LTNE Model, Temperature and Mole Fractions

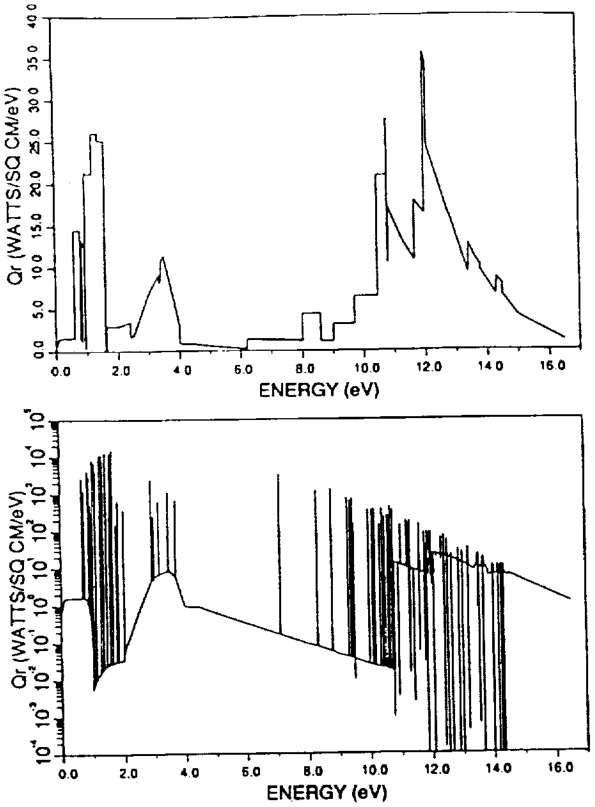

Fig.13: Case 14 - Air Results with Second Order LTNE Model, Grouped and Detailed Radiation Spectra

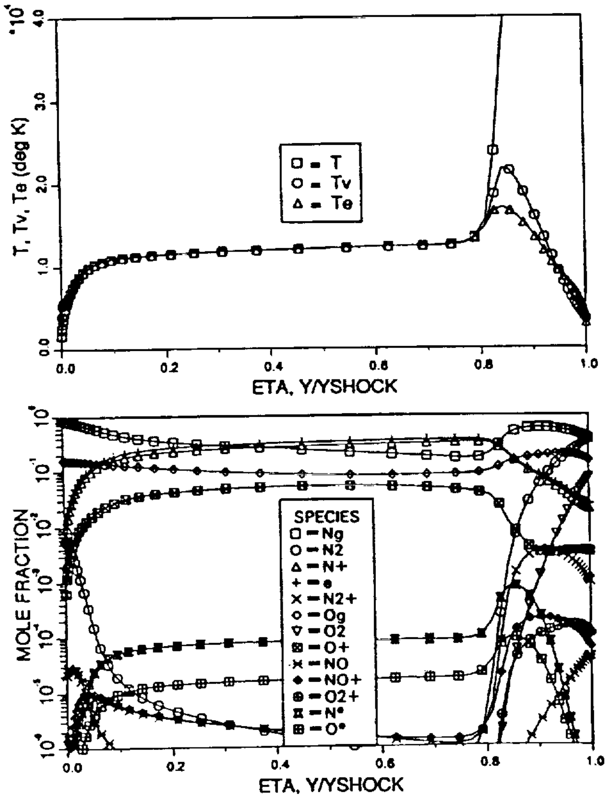

Fig.14: Case 16 - Air Results with Second Order LTNE Model, Temperature and Mole Fractions

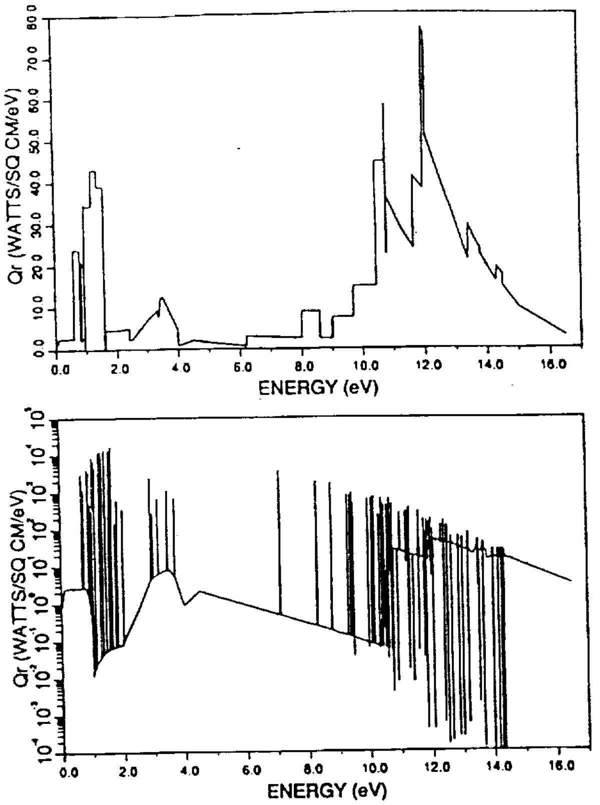

Fig.15: Case 16 - Air Results with Second Order LTNE Model, Grouped and Detailed Radiation Spectra

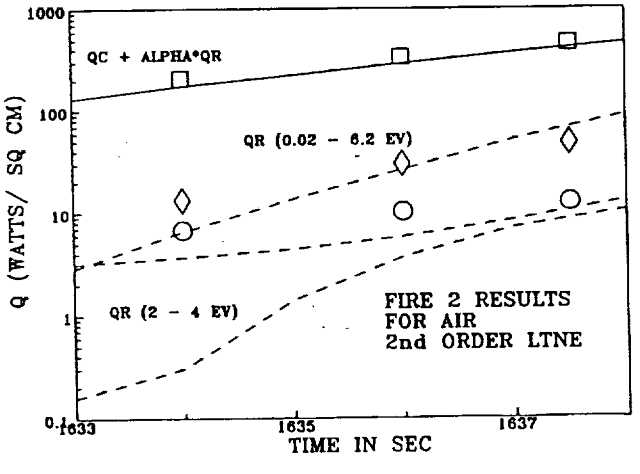

Fig.16: Comparison of Second Order LTNE Methods With Fire 2 Flight Test Measurements

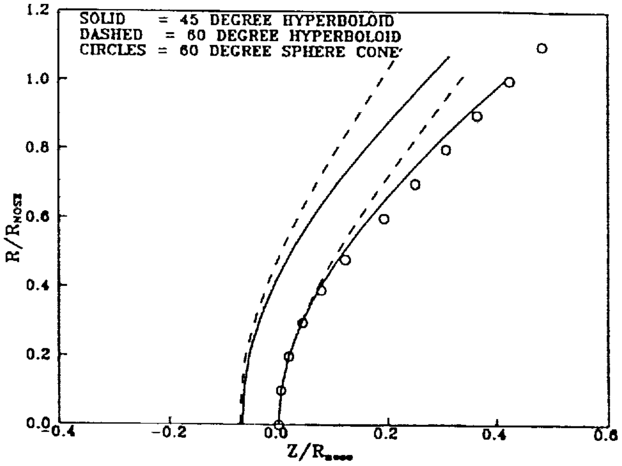

Fig.17: Shock Shapes

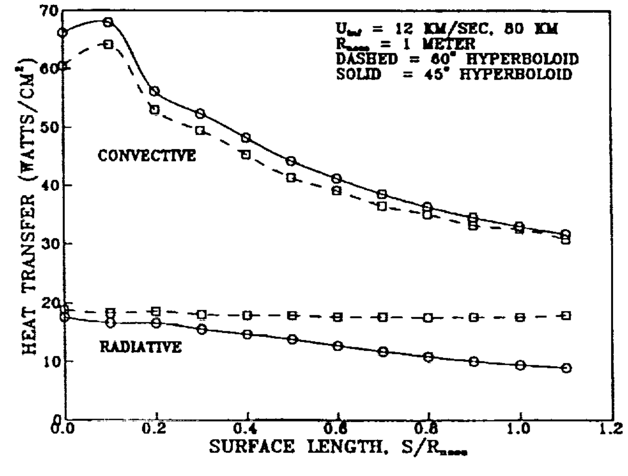

Fig.18: Convective and Radiative Heat Fluxes around Body

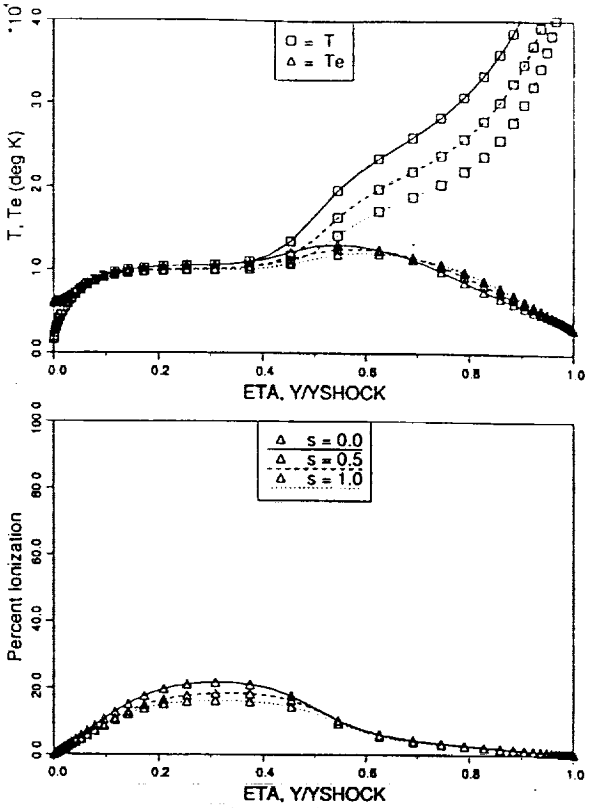

Fig.19: Downstream Flowfield Profiles for 60° Hyperboloid

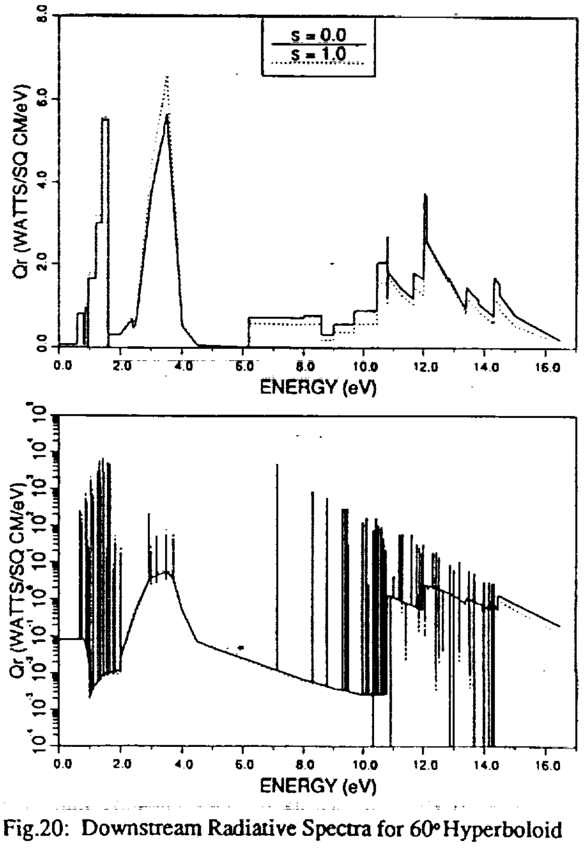

Fig.20: Downstream Radiative Spectra for 60° Hyperboloid

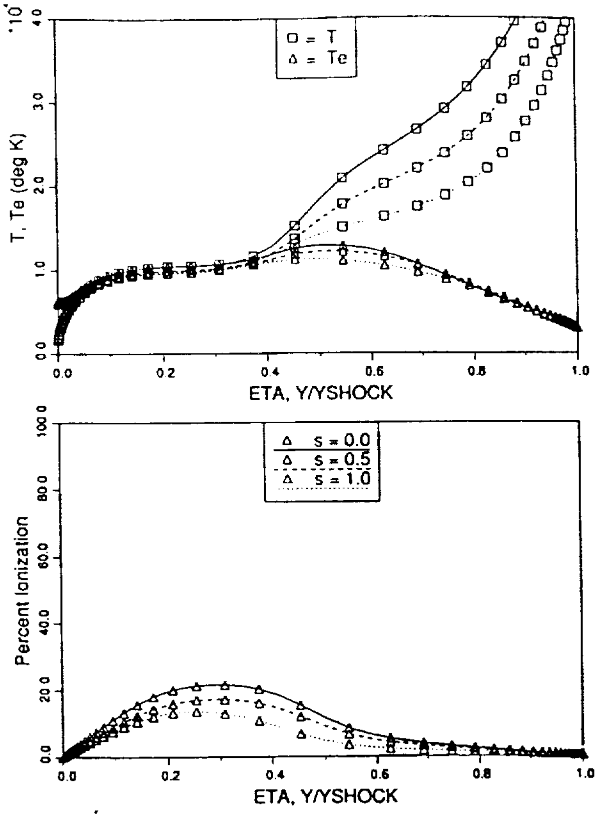

Fig.21: Downstream Flowfield Profiles for 45°Hyperboloid

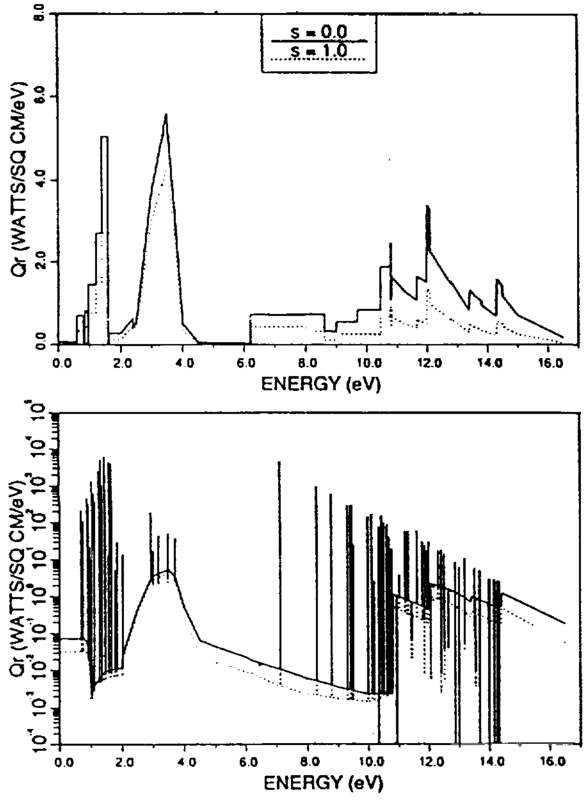

Fig.22: Downstream Radiative Spectra for 45°Hyperboloid

Nonequilibrium Chemical and Radiation Coupling, Part I: Theory and Models

L. A. Carlson and T. A. Gally

Reprinted from

Journal of Thermophysics and Heat Transfer

Volume 6, Number 3, July-September 1992, Pages 385-391

AIAA

A publication of the
American Institute of Aeronautics and Astronautics, Inc.
The Aerospace Center, 370 L'Enfant Promenade, SW
Washington, DC 20024-2518

JOURNAL OF THERMOPHYSICS AND HEAT TRANSFER
Vol. 6, No. 3, July–Sept. 1992

Nonequilibrium Chemical and Radiation Coupling, Part I: Theory and Models

Leland A. Carlson* and Thomas A. Gally†
Texas A&M University, College Station, Texas 77843

A flowfield model for the stagnation region of high-altitude entry vehicles which includes nonequilibrium chemistry, multitemperature, viscous, conduction, and diffusion effects is presented. The model contains coupled nongray nonequilibrium radiative transfer and accounts for local thermodynamic nonequilibrium phenomena for both atoms and molecules. Several approaches for modeling electron-electronic energy are presented ranging from a quasiequilibrium free electron model to a full electron-electronic equation. Comparison with Fire 2 flight data verifies that the model is reasonably accurate. Based on these results for Fire 2 radiation cooling/coupling is measurable and important, the wavelength character of the radiative heat transfer varies with time, and local thermodynamic nonequilibrium is important and should be included.

Nomenclature

B = black body function
C^f_{sum} = diffusive energy flux, Eq. (10)
c_e = mean thermal velocity of electrons
c^f_p = frozen specific heat at constant pressure, Eq. (7)
c_{p_r} = specific heat at constant pressure of species r
$\mathcal{D}$ = binary diffusion coefficient
E = ionization potential
E_2, E_3 = exponential integrals
h = enthalpy
h_1, h_3 = geometric factors
K = absorption coefficient
k = Boltzmann constant
m = mass
N = number density
n, s, ϕ = coordinate axis
p = pressure
Q = partition function
q_r = radiative heat flux
r_w = wall reflectivity
S = source function
T = temperature
U = diffusional velocity
u, v, w = mass averaged velocity components
$\dot{w}$ = chemical production rate
$YSHOCK$ = shock standoff distance
y_s = shock standoff distance
ϵ = Reynolds number parameter
ϵ_w = wall emissivity
ε = magnitude of electron charge
η = heat conduction coefficient
ξ_e = rate of elastic electron energy exchange
ρ = density
τ = optical thickness
Φ = wall sheath electric potential
Ω_e = rate of inelastic electron energy exchange

Subscripts
e = electron
el = electron impact reaction
r = species
s = value behind shock
ν = frequency

Superscripts
e = electronic
n, $n + 1$ = iteration step
tr = translational

Introduction

IN the future, space programs will be conducted which will require the efficient return of large payloads from missions to the moon or to the planets. To accomplish this task, the return vehicles will either utilize direct entry at very high velocities or aerocapture techniques. In either case, a significant portion of the entry will involve high velocities at high altitudes; and, during this part of the trajectory, the vehicle flowfields will be dominated by chemical, thermal, and radiative nonequilibrium phenomena. To design and operate such vehicles, it is essential to develop engineering flowfield models which appropriately and accurately describe these chemical, thermal, and radiative nonequilibrium processes and the coupling between them.

Previously,[1] the importance of properly predicting electron temperature and modeling electron impact ionization was investigated and a quasiequilibrium free electron energy model and a two-step ionization model formulated. In addition, an approximate method of handling nonequilibrium atomic radiation, which assumed that the excited states of atoms are in equilibrium with the local free electrons and ions, was developed[1-3] and applied to an eight-step nongray emission-absorption radiation model. While the results obtained with these models were informative, the lack of detail in the radiation model, particularly with respect to atomic lines and the molecular ion bands, indicated a need for improvement, and the approximate nature of the nonequilibrium molecular radiation portion of the model appeared to underestimate the molecular band radiation. Further, the quasiequilibrium free electron energy model assumed that the electronic temperature was determined solely by the free electron temperature. While this approximation should be good for many conditions of interest in aerocapture and entry, it was felt that additional models should be developed to improve the modeling of electron energy and temperature due to their importance in determining nonequilibrium ionization chemistry and radiative transfer.

Presented as Paper 91-0569 at the AIAA 29th Aerospace Sciences Meeting, Reno, NV, Jan. 7–10, 1991; received Jan. 22, 1991; revision received Aug. 5, 1991; accepted for publication Aug. 27, 1991.

*Professor, Aerospace Engineering Department. Associate Fellow AIAA.

†NASA Graduate Student Researcher, Aerospace Engineering Department. Student Member AIAA.

Thus, the objective of this paper is to present an improved engineering flowfield model for high-altitude AOTV flowfields having extensive chemical, thermal, and radiative nonequilibrium. In a companion paper,[4] this model is applied over a wide range of conditions to investigate the magnitude and extent of nonequilibrium chemical and radiation coupling phenomena in high altitude entry vehicle flowfields.

Problem Formulation

Flowfield Model

The flowfield model used in this investigation is a viscous shock layer analysis which includes the effects of chemical nonequilibrium, multitemperature thermal nonequilibrium (heavy particle and electron or electron-electronic temperature), viscosity, heat conduction, diffusion, and radiative gasdynamic coupling. The basic method, which is a significantly modified version of the NASA Langley code VSL3DNQ[5] is similar to the version used in Ref. 1, but a number of additional modifications have been incorporated since the earlier study. First, the viscous shock layer (VSL) code has been coupled with modified versions of the radiation routines of the NASA Langley program, RADICAL,[6] which is described below, giving the ability to calculate flowfield solutions with the effects of radiative cooling present. This coupling is achieved by adding to the global energy equation the divergence of the radiative flux, $\nabla \cdot q_r$. Second, the chemical reaction rate input data has been changed to allow the use of a single reaction rate, k_f or k_b, and the equilibrium constant, K_{eq}, rather than using both forward and backward rates. With this modification, species concentrations in the equilibrium regions of a flowfield are now in agreement with results from equilibrium analysis. Third, the effects of multitemperatures on the shock jump conditions and thermodynamic state variables have been improved.

One of the advantages of a VSL method is the ability to distribute many flowfield points in regions of large gradients, such as in the region immediately behind the shock front and in the highly nonequilibrium thermal layer near the wall. However, this approach requires proper shock front jump conditions since diffusion and thermal conduction phenomena can be significant in the region immediately behind the shock front. Thus, the present method includes multitemperature shock slip boundary conditions, and the importance of including and utilizing these conditions is shown in Ref. 4. In addition, the present method permits various wall catalytic properties and includes appropriate spectral variations in the treatment of the wall boundary conditions.

Radiative Transfer Model

The radiation analysis in RADICAL is a detailed method which includes atomic continuum radiation, molecular band radiation, and atomic line radiation for the standard CHON (carbon, hydrogen, oxygen, nitrogen) gas system. While the original method used individual species number densities and assumed a Boltzmann distribution to calculate the excited state number densities for each species, and, from this data, the individual radiative absorption coefficients associated with each radiative process, such an approach is not suitable for nonequilibrium conditions. Thus, the original model has been extensively expanded and modified to include nonequilibrium chemical and thermal effects and to account for excited state population distributions different from those predicted by a Boltzman distribution. Under the assumption of a radiating tangent slab, the radiative heat flux at a surface located at point x can be calculated as, assuming a nonemitting precursor

$$-q_{r,\nu}(x) = 2\pi \int_0^{\tau_{\nu,s}} \mathrm{sgn}(t_\nu - \tau_\nu) S_\nu E_2(|t_\nu - \tau_\nu|)\, \mathrm{d}t_\nu$$

$$-2E_3(\tau_\nu)\pi \left(\epsilon_w B_{\nu,w} - 2r_w \int_0^{\tau_{\nu,sh}} E_2(t_\nu) S_\nu\, \mathrm{d}t_\nu\right) \qquad (1)$$

where τ_ν is the optical thickness determined by

$$\tau_\nu = \int_0^x K_\nu\, \mathrm{d}y \qquad (2)$$

The absorption and source functions used in these expressions are the sum of all radiative contributions at the frequency ν. In the present engineering approach, this nonequilibrium radiation flux, its divergence, the absorption coefficients, and the source functions are computed by the modified RADICAL radiative analysis code using actual species concentrations, the appropriate electron-electronic temperature, and correction factors on the effective source function S_ν and absorption coefficients K_ν. This correction factor approach accounts for the existence of non-Boltzmann distribution state populations (i.e., local thermodynamic nonequilibrium, LTNE) and effectively determines the correct state populations. It should be noted that in solving the global energy equation, the $\nabla \cdot q_r$ term is coupled to the flowfield solution by updating it about every 10 iterative cycles.

Nonequilibrium Molecular Radiation Model

Previously, an approximate LTNE model for molecular radiation had been developed,[3] but it is now believed that this model overcorrected and underestimated the actual molecular radiation. This belief is reenforced by experimental measurements made in molecular radiation dominated shock flows which exhibit a radiation intensity peak behind the shock front in conjunction with the predicted electron temperature peak. Thus, significant depletion of all of the excited molecular states, as predicted by the theory of Ref. 3, is not expected. Consequently, an improved model for molecular nonequilibrium radiation has been developed.

After examining various approaches, a quasisteady approach similar to that of Ref. 7 has been developed which computes the electronic state populations associated with the radiating molecular bands. Specifically, for N_2, the populations of the $X^1\Sigma_g^+$, $A^3\Sigma_u^+$, $B^3\Pi_g$, $a^1\Pi_g$, and $C^3\Pi_u$ states are computed; while for N_2^+ the $X^2\Sigma_g^+$, $A^2\Pi_u$, $B^2\Sigma_u^+$, and $D^2\Pi_g$ are included. This approach has been incorporated into the flowfield and radiative transport code, and there is no assumption concerning the existence of equilibrium between excited molecular states and atoms as there was in Ref. 3. Thus, in this new molecular model, both source functions and absorption coefficients associated with molecular band radiation are corrected for nonequilibrium effects. However, in this quasisteady approach there is the inherent assumption that the rates used to determine the state populations are compatible with the overall rate chemistry. For the molecules, it is believed that the various rates are reasonably well known and that this inherent assumption is satisfied.

The upper state of the Birge-Hopfield band, $b^1\Pi_u$, is a highly excited state and its population is not one of those calculated in the quasi-steady solution from above. This state is similar to the $C^3\Pi_u$ state in that it lies entirely above the dissociation limit and, as shown in Ref. 8, is in close equilibrium with the atomic number density for collisionally dominated conditions. As a result, the state population correction calculated for the $C^3\Pi_u$ state is also used to calculate the LTNE $b^1\Pi_u$ population. In general, results indicate that for the N_2 Birge-Hopfield band, $b^1\Pi_u$ to $X^1\Sigma_g^+$ transition, the correction factor for the absorption coefficient is frequently near unity but that for the corresponding source function it is quite small in the nonequilibrium portion of the shock layer immediately behind the shock front. Since the absorption coefficient depends upon the number density of the absorbing state and the effective source function is proportional to the ratio of the populations of the emitting and the absorbing states, this behavior is what would "normally" be expected. For the $N_2(BH)$ band, emission is from high excited states, which should be depleted by nonequilibrium effects, and absorption is to the ground electronic state, whose population density should be closely predicted by a Boltzmann distribution. Likewise the $N_2(1+)$, $B^3\Pi_g$ to $A^3\Sigma_u^+$ transition, typically displays only a slight nonequilibrium correction for the source function, but its nonequilibrium absorption coefficient is significantly decreased from that predicted using Boltzmann distributions. This trend is also "expected" since $N_2(1+)$ involves two excited states, $B^3\Pi_g$ and $A^3\Sigma_u^+$. On the other hand, while the absorption coefficient factor for $N_2(2+)$, $C^3\Pi_u$ to $B^3\Pi_g$ transition, is similar to that for $N_2(1+)$, the source function for $N_2(2+)$ is typically significantly reduced in the chemical and thermal nonequilibrium region behind the shock front, indicating that predissociation is significantly depleting the population of the $C^3\Pi_u$ electronic state.

The most interesting result, however, is that the $N_2^+(1-)$ radiation, $B^2\Sigma_u^+$ to $X^2\Sigma_g^+$ transition, is usually only slightly affected by nonequilibrium phenomena. This result is in agreement with experiments which, at least at lower velocities, have indicated a strong $N_2^+(1-)$ contribution. However, since the number density of N_2^+ is often only significant in the region immediately behind the shock front, any $N_2^+(1-)$ radiation should originate from that region. This feature is discussed further in the results section and in Ref. 4.

Another phenomenon associated with the molecular nonequilibrium radiation is that often in the thermal boundary layer near the wall, several of the factors accounting for LTNE exceed unity and become large. This behavior indicates an overpopulation of excited states above values which would be predicted by a Boltzmann distribution, when intuitively an equilibrium distribution might be expected due to the increased density near the wall. However, the thermal boundary layer is often in significant nonequilibrium since the chemical reaction rates are finite and cannot keep up with the true local equilibrium; and these finite rates lead to atom and sometimes ion concentrations above local equilibrium. In addition, diffusion tends to perturb the species population densities and causes atom and ion densities above equilibrium values, which in turn creates enhanced molecular excited state populations. This enhancement, however, does not lead to increased radiative emission from the gas near the wall, and, probably due to the lower electron-electronic temperature in that region, it does not for the cases examined appear to affect the radiative heat transfer. Thus, in the present studies limitations on the molecular nonequilibrium correction factors have not been imposed.

Nonequilibrium Atomic Radiation Model

Local thermodynamic nonequilibrium effects on atomic radiation are also computed by applying modification or correction factors, which account for the deviations in state populations from Boltzmann distributions, to the absorption coefficient and source function values utilized in the radiative analysis. Such atomic LTNE definitely exists in the chemical nonequilibrium region immediately behind the shock front[1-3,7,9] where, due to ionization from excited states, the populations of the higher electronic states will be lower than predicted by a local thermodynamic equilibrium (LTE) assumption using the ground state. Likewise, in regions of recombination the reverse processes can lead to state populations above those obtained using LTE.

The current model, which should probably be termed a first order approximation, has been presented previously in Refs. 1–3 and similar models have been used for monatomic gases.[10-13] This model assumes that atomic ionization proceeds by excitation from the three low ground states (for nitrogen) to the high excited states, followed by rapid ionization. Further, the model assumes that excitation from the ground states to the higher states is a rate limiting step for the ionization process and that the excited states, because of their energy proximity to the ionized state, are in equilibrium with the free electrons and ions. With this approach,[1-3] the atomic nitrogen LTNE correction factor, which represents the ratio of the actual population in an excited state to that which would exist for a Boltzmann distribution, can be written as

$$\frac{N_{N^+} N_e Q_N^e \exp(169000/T_e)}{N_N Q_{N^+}^e Q_e} \tag{3}$$

This factor is usually less than one in ionization regions and can be greater than one in zones involving extensive deionization.

In contrast, Park[8] and Kunc et al.[14] handle atomic LTNE by using a quasisteady analysis in which, while rate processes between all the bound states and between the bound states and the ionized state are assumed finite, they are assumed to be fast relative to changes induced by the flowfield (quasisteady hypothesis). Thus, at any point in a flowfield an equilibrium between the states will exist which is perturbed from a Boltzmann distribution due to large radiative absorption/emission or chemical non-equilibrium. Kunc et al. have performed calculations in which they specify the electron temperature and the total number of charged particles (defined as two times the number of atoms plus the number of ions plus the number of electrons), leaving the actual number of ions and free electrons to be determined as part of the unknown populations.

Park, on the other hand, in the application of his method[7] assumes the number of ions and electrons to be given by a flowfield solution. Under this approach, a non-Boltzmann distribution can be achieved even in the absence of radiation, if the number of ions and electrons differs from equilibrium. To be totally correct, however, the excitation and ionization rates associated with each level must overall be consistent with the ionization rates used in the flowfield solution.

Obviously, the present first-order approach and those of Park and Kunc et al. represent the extremes of modeling LTNE atomic phenomena. While the present first order approach is simplified in its assumption that the rates between the excited states and the free ions and electrons are infinitely fast (i.e., local equilibrium), it does directly couple the predicted excited state populations to the flowfield and, unlike the detailed quasisteady approaches, it is not computationally intensive. In addition, the latter are sensitive to the choice of the individual rates; and it is difficult to know which rate to adjust when comparing with experimental results and attempting to improve the correlation. Finally, the present model when coupled with a compatible electron impact ionization rate has been shown to yield good agreement with experimental ionization distances.[1]

Electron-Electronic Energy Models

For the present studies, three different electron-electronic energy models have been developed and investigated. The first, termed the quasiequilibrium electron energy model (QEE), is essentially a free electron energy model in which all derivative terms in the electron energy equation are neglected; and it can be expressed as

$$\dot{w}_e h_e'' - \dot{w}_e \frac{u^2}{2} = \sum_r \xi_{er} + \Omega_e \tag{4}$$

where the ξ_{er} terms account for elastic collisional effects and Ω_e represents inelastic effects due to chemical reactions in which electrons contribute or receive energy (electron impact reactions). It should be noted that the term $\dot{w}_e u^2/2$ is usually very small and can be neglected. This model was previously presented in Ref. 1, which contains additional details. The second is termed the quasiequilibrium electron-electronic energy model (QEEE) and is similar to the first model in that it computes the electron temperature assuming quasiequilibrium. However, it explicitly accounts for the effect of elastic and inelastic collisions on the energy contained in electronic states of each species as well as the free electron energy; and, thus, the resulting temperature is truly representative of electron-electronic energy. The resulting equation is

$$\dot{w}_e h_e^{tr} + \sum_r \dot{w}_r h_r^e - \dot{w}_e \frac{u^2}{2} = \sum_r \xi_{er} + \Omega_e \tag{5}$$

where the term $\Sigma \dot{w}_r h_r^e$ accounts for the production and depletion of electronic energy due to chemical reactions.

The third model utilizes a full combined electron-electronic energy conservation equation which includes the effects of convection, conduction, and diffusion, in addition to the production and loss of electron energy through elastic and inelastic collisions. This full electron-electronic (FEE) energy equation for the stagnation line is

$$\rho u c_p^e \frac{\partial T_e}{\partial n} - \frac{\partial}{\partial n}\left(\eta_e \frac{\partial T_e}{\partial n}\right) - \left(\sum_r \rho \mathfrak{D}_r c_{p_r}^e \frac{\partial}{\partial n}\frac{\rho_r}{\rho}\right)\frac{\partial T_e}{\partial n}$$

$$-u\frac{\partial p_e}{\partial n} + \dot{w}_e h_e^{tr} + \sum_r \dot{w}_r h_r^e = \sum_r \xi_{er} + \Omega_e \tag{6}$$

where

$$c_p^e = c_{p_e}^{tr}\frac{\rho_e}{\rho} + \sum_r c_{p_r}^e \frac{\rho_r}{\rho} \tag{7}$$

In this equation, the viscous work terms have not been included due to the fact that they are of lower order. In addition, radiation effects on electron-electronic energy have been neglected as have diffusion effects[15] on the form of the collisional energy exchange factor, ξ_{er}. The latter are expected to be small in most cases due to the rapid dissociation of molecules and the existence of ambipolar diffusion. However, it might be important at some of the lower AFE velocities. It should be noted that Eq. (6) is equivalent to that presented in Refs. 16 and 17. However, it differs slightly from that presented in Refs. 1 and 15 in that these contain the additional terms

$$\dot{w}_e \frac{u^2}{2} + U_e \frac{\partial p_e}{\partial n}$$

which arise as a result of the differences in the derivation of the species energy and momentum equations. It is believed that these additional terms occur as a result of using the more detailed approach of Chapman and Cowling.[18] In any event, based upon order of magnitude estimates these two terms are expected to be small, and their neglect in the present studies should not affect the results.

When Eqs. (6) and (7) are expressed in three dimensions and transformed into the viscous shock-layer coordinate system they become

$$A_0 \frac{\partial^2 T_e}{\partial n^2} + A_1 \frac{\partial T_e}{\partial n} + A_2 T_e + A_3 + A_4 \frac{\partial T_e}{\partial s} + A_5 \frac{\partial T_e}{\partial \phi} = 0 \tag{8}$$

$$A_0 = -\epsilon^2 \frac{\eta_e \eta_s}{y_s{}^2}$$

$$A_1 = -\epsilon^2 \frac{\eta_s}{y_s{}^2}\left[\frac{\partial \eta_e}{\partial n} + \frac{\eta_e}{h_3}\frac{\partial h_3}{\partial n} + \frac{\eta_e}{h_1}\frac{\partial h_1}{\partial n}\right]$$

$$+ \frac{c_p^e \rho_s}{y_s}\left[\rho v - \frac{\rho u_s u n}{h_1}\frac{\partial y_s}{\partial s} - \frac{\rho w n}{h_3}\frac{\partial y_s}{\partial \phi}\right] - \frac{\epsilon^2}{y_s^2} C_{\text{sum}}^e$$

$$A_2 = \rho_s \rho \frac{\partial}{\partial T_e}(\dot{w}h)^e - \frac{\partial}{\partial T_e}\sum_r \xi_{er}$$

$$A_3 = -\frac{u_s u \rho_s}{h_1}\frac{\partial p_s}{\partial s} + \frac{\rho_s u_s u n}{h_1 y_s}\frac{\partial y_s}{\partial s}\frac{\partial p_e}{\partial n} - \frac{\rho_s v}{y_s}\frac{\partial p_e}{\partial n}$$

$$+ \frac{\rho_s w n}{h_3 y_s}\frac{\partial y_s}{\partial \phi}\frac{\partial p_e}{\partial n} + \rho_s \rho (\dot{w}h)^e - \rho_s \rho T_e \frac{\partial}{\partial T_e}(\dot{w}h)^e$$

$$- \sum_r \xi_{er} + T_e \frac{\partial}{\partial T_e}\sum_r \xi_{er}$$

$$A_4 = \frac{\rho_s u_s \rho u c_p^e}{h_1}$$

$$A_5 = \frac{\rho_s \rho w c_p^e}{h_3} \tag{9}$$

where

$$C_{\text{sum}}^e = C_{p_e}^{tr}\mathfrak{D}_e \frac{\partial}{\partial n}\frac{\rho_e}{\rho} + \sum_r C_{p_r}^e \mathfrak{D}_r \frac{\partial}{\partial n}\frac{\rho_r}{\rho}$$

$$\cdot(\dot{w}h)^e = \dot{w}_e h_e^{tr} + \sum_r \dot{w}_r h_r^e + \dot{w}_{el} E_{el} \tag{10}$$

and h_1 and h_3 are geometric factors for the axisymmetric coordinate system.

This full electron energy equation is integrated into the VSL code by setting up the terms in the same form as those for the global energy equation and then solving the equations using the existing routine for solving the global energy equation. In the cascade order of solving the governing conservation equations typical of VSL methods, the electron energy equation is included following the global energy equation, which is where the QEE or QEEE equation is normally included. Initially, the electron energy equation was not well behaved when solved in this manner primarily due to the large order of magnitude of the elastic exchange and chemical production terms, which, since they are nonlinear, were originally included explicitly in the calculations. Consequently, to provide iterative stability, these terms have been linearized as follows:

$$[(\dot{w}h)^e]^{n+1} = [(\dot{w}h)^e]^n + (T_e^{n+1} - T_e^n)\left(\frac{\partial}{\partial T_e}(\dot{w}h)^e\right)^n \tag{11}$$

$$\xi_{er}^{n+1} = \xi_{er}^n + (T_e^{n+1} - T_e^n)\left(\frac{\partial \xi_{er}}{\partial T_e}\right)^n \tag{12}$$

Another item which should be considered in modeling electron-electronic energy is the proper boundary condition on electron temperature at the wall. In most past analyses,[1,8] it has been assumed that at the wall the electron temperature is equal to the wall temperature. Since the heavy particle temperature is also assumed equal to the wall temperature at the wall, this approach effectively assumes that the electron temperature is equal to the heavy particle temperature. At first this approach seems reasonable and follows the philosophy that in the thermal boundary layer near the wall the flow should be near equilibrium and collision dominated. However, in the thermal boundary layer the chemical reaction rates are finite and often cannot keep up with local equilibrium. This lag combined with diffusion leads to atom, ion, and electron densities above equilibrium values and in turn enhanced excited state populations. In addition, in the electron-electronic energy equation ionic recombination yields an increase in electron energy and tends to force the electron temperature above the heavy particle temperature.

Further, since almost all walls are catalytic to ions and electrons, there exists a thin plasma sheath adjacent to the wall across which a potential develops in order to maintain zero charge flux at the sheath edge. Since the thickness of the plasma sheath is negligible in comparison to that of the wall thermal layer, the edge of the sheath can be construed as being physically at the wall. Thus, the proper wall boundary conditions on the continuum equations should be obtained by matching the particle description in the plasma sheath to the corresponding continuum description at the wall. Examination of appropriate sheath models shows that continuity of electron energy flux requires[19-21]

$$\left(\eta_e \frac{\partial T_e}{\partial n} - \rho_e U_e h_e\right)_{n=0}$$

$$= [2kT_e + |\varepsilon\Phi|] \frac{N_e c_e}{4} \exp\left(\frac{-|\varepsilon\Phi|}{kT_e}\right) \tag{13}$$

where the sheath potential is determined by enforcing charge neutrality at the sheath edge. If the wall is catalytic to ions and electrons, this free electron boundary condition can be approximated as $\partial T_e/\partial n = 0$. While this condition is not strictly applicable to the electronic temperature at the wall, its usage for the electronic temperature as well as the free electron temperature should not induce any significant error.[21] Thus, this approximate boundary condition has been incorporated as an option into the present full electron-electronic equation model. Finally, analysis indicates that the heavy particle species, being in good contact with the wall, should be at the wall temperature.

Since the present flowfield formulation does not include vibrational nonequilibrium, the above electron-electronic energy models do not include vibrational-electronic coupling. While this phenomena should not be important at higher entry velocities due to the rapid dissociation of diatomic species in and near the shock front, it could be important at lower velocities. Thus, efforts are in progress to include vibrational nonequilibrium and vibrational electronic coupling; and these have been reported in Ref. 22.

Discussion of Results

In order to ensure that the present method and models are reasonably correct and appropriate, results have been obtained for five trajectory points along the Fire 2 entry profile covering the time period from 1634 through 1637.5 s. These points were selected because they encompass a period of the flight involving extensive chemical and thermal nonequilibrium and changing radiative behavior. In all cases, the results are for the stagnation streamline, utilize 99 points between the shock front and the wall, and, for simplicity, assume a nitrogen freestream. The nonequilibrium chemistry model is similar to the case II set of Ref. 1 and is shown in Table 1, and it should be representative of high temperature radiating air. For diffusion, the approximate multicomponent model of Ref. 23 has been used. Since in a high-temperature ionized diatomic gas, charge exchange and ambipolar effects cause atoms, ions, and electrons to all have to a first approximation similar diffusion velocities, such a gas should be dominated by only two diffusion velocities, that of the molecules and that of the atoms, ions, and electrons. For such cases, previous studies[24,25] have shown that the differences between using a constant Lewis number of 1.0 or 1.4 or a variable Lewis number are small, and thus the commonly used value of 1.4 has been used.[26] Hence, the present model should adequately represent the diffusion phenomena present, including multi-component effects.

Table 1 Reaction rate system

Reaction	A	B	E
$N_2 + N = 3N$	4.085×10^{22}	−1.5	113100
$N_2 + N_2 = 2N + N_2$	4.70×10^{17}	−0.5	113100
$N_2 + N^+ = N_2^+ + N$	2.02×10^{11}	0.8	13000
$N + N = N_2^+ + e^-$	1.40×10^{13}	0.0	67800
$N + e^- = N^+ + 2e^-$	4.16×10^{13}	0.5	120000
$N + N = N + N^+ + e^-$	2.34×10^{11}	0.5	120000
$N + N^+ = 2N^+ + e^-$	2.34×10^{11}	0.5	120000
$N_2 + e^- = 2N^+ + e^-$	3.00×10^{24}	−1.6	113100

Rates in the form $k_f = AT^B \exp(-E/T)$.
$T = T_e$ in electron impact reactions.

These Fire 2 results have been computed assuming a fully catalytic wall at the wall temperature measured in flight, and the full electron-electronic energy model has been used in conjunction with the approximate wall sheath boundary condition on the electron temperature. Slip conditions have been enforced at the shock, and the correct wall absorptivity and reflection properties of the wall, as described in Refs. 27 and 28, have been included. Finally, coupled nongray radiative transfer has been included, and local thermodynamic nonequilibrium effects have been accounted for using the molecular and first-order atomic models described above.

Figures 1 and 2 show temperature and concentration pro-

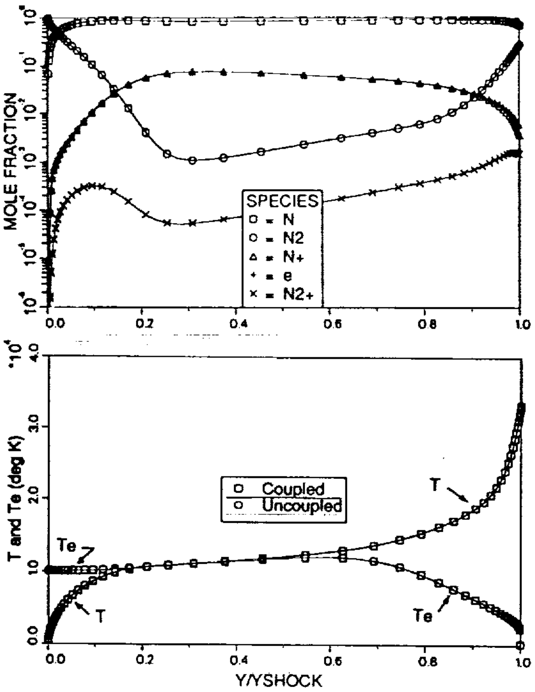

Fig. 1 Stagnation profiles for Fire 2 at 1634 s, *YSHOCK* = 4.12 cm.

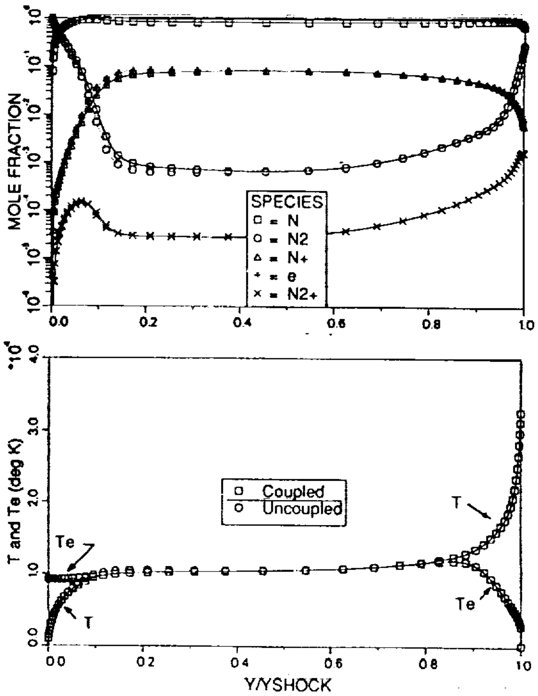

Fig. 2 Stagnation profiles for Fire 2 at 1637.5 s, *YSHOCK* = 3.72 cm.

files for two of these trajectory points. At 1634 s (Fig. 1), as evidenced by comparing the "Coupled" and "Uncoupled" temperature profiles, radiation cooling/coupling is insignificant, and the temperature and species profiles show that the flow never approaches a chemical equilibrium situation with extensive thermal nonequilibrium existing in the region behind the shock front and in the thermal boundary layer. The latter results from the sheath boundary condition on electron temperature and three body ion recombination which adds energy to both the free electrons and the excited electronic states. Interestingly, results obtained by forcing T_e to equal T_w at the wall yielded only slight differences in heating and the flowfield structure.

By 1637.5 s (Fig. 2), the temperature profile indicates that the postshock nonequilibrium region comprises only about 20% of the layer and that much of the flowfield is in equilibrium. However, while thermal equilibrium is achieved near *y/ySHOCK* of 0.75, careful examination reveals that ionization equilibrium is not reached until about *y/ySHOCK* of 0.55. Further, as indicated by the temperature decrease and changes in species concentrations, radiation coupling/cooling is evident throughout much of the shock layer. These phenomena can be seen more easily on Fig. 3 which portrays the enthalpy behavior along the stagnation streamline. The profiles show that in the coupled case the enthalpy decreases significantly due to radiative energy losses in the shock layer. While not shown, the degree of ionization in this region also decreases due to the loss of energy by radiation.

In Fig. 4, the present predictions for various heating rates are compared to the flight data. In flight, a total calorimeter measured the sum of the convective heating plus that portion of the radiative heating absorbed by the gauge, which is indicated by the *QC + ALPHA*QR* line on the figure. The present predictions, indicated by the open squares, are in reasonable agreement with the flight data; and, while not shown, the current predictions for convective heating are in excellent agreement with corresponding values of Refs. 29–31. The high value at 1634 s is typical of theoretical predictions, and, since this condition is dominated by convective heating, the difference may indicate that at this point the wall (or gauge) was not fully catalytic. This possibility is suggested by the results of Ref. 32 which obtained good correlation with Fire 2 data by not assuming fully catalytic walls.

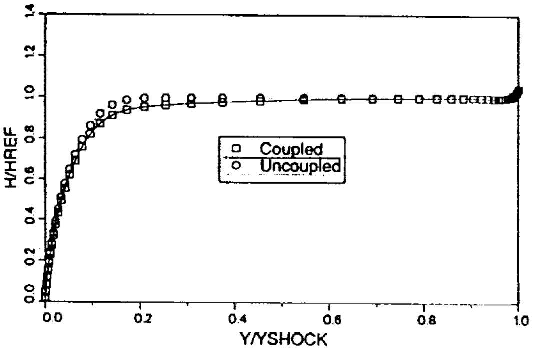

Fig. 3 Enthalpy profiles for Fire 2 at 1637.5 s.

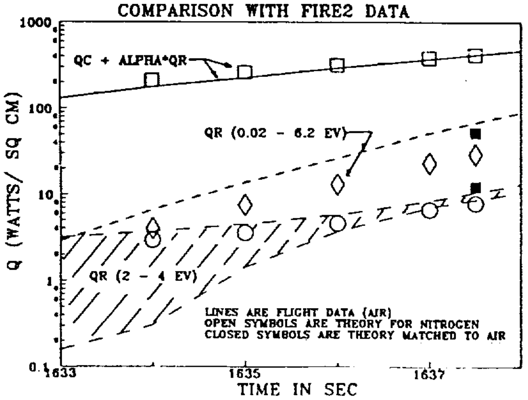

Fig. 4 Comparison of present Fire 2 predictions (nitrogen) with flight data (air).

Also shown on Fig. 4 are comparisons for radiative heating to the wall for two wavelength regions, 0.02–6.2 eV which is in the visible and infrared, and 2–4 eV which primarily should be due to $N_2^+(1-)$ emission. For the latter case, the flight data[27,28] exhibited extensive scatter, and this is indicated on the figure by the cross-hatching. The present predictions in the 2–4 eV range are within the data scatter at early times and slightly low at the later times, while the predictions for the visible and infrared regions are low throughout the times considered. However, the data do appear to have the correct trends.

At first glance the radiation predictions appearing on Fig. 4 are disturbing due to their underprediction. However, the Fire 2 data is a single experiment, and thus must be viewed with care, and the present results are for a nitrogen freestream and not air. While it is generally true that equilibrium nitrogen and equilibrium air will yield almost identical wall radiative heating rates if they are at the same temperature and pressure, identical freestream conditions will yield for the Fire 2 cases cooler equilibrium temperatures for nitrogen than for air. For example, for the 1637.5 s case, the equilibrium temperature for a nitrogen freestream would be 10555K, while for an air freestream it would be 11021K. This small 4.5% difference leads to a radiative heating rate for air 60% higher than that for nitrogen. Since the present results were obtained matching freestream conditions on velocity, temperature, and pressure and not postshock conditions, the present radiative heating predictions should be below the flight values, particularly at the later times where the flow is approaching equilibrium. As can be seen on Fig. 4, this situation is indeed the case.

To further test this conjecture, a case was run using a slightly different freestream velocity and pressure that were designed to match the 1637.5 case in air. While this test was not completely successful in that the resultant temperature was still slightly low, the radiative heating results from this case, shown as solid symbols on Fig. 4, are higher and closer to the flight data.

To further identify the characteristics of the radiative heating of Fire 2, the stagnation point radiative flux is presented on Fig. 5 as a function of energy (frequency) for two trajectory points. On this plot, the line and continuum contributions are plotted jointly. Also, for convenience, the line radiation is presented for lines that are close together as an average value over an appropriate width. It should be noted, however, that in the actual calculations the lines are treated individually using appropriate line shapes.

At 1634 s most of the radiative flux is in continuum radiation between 2 and 4 eV and in infrared lines, with about 20% of the total being from lines. In fact, for this condition 70% of

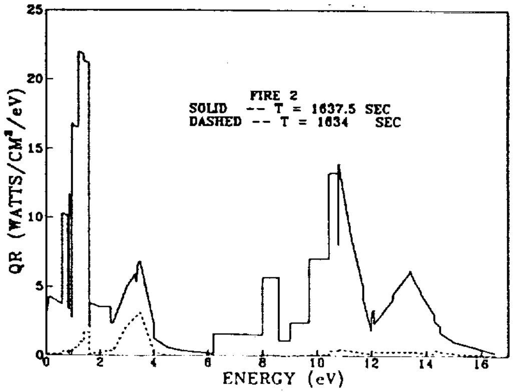

Fig. 5 Spectral variation of stagnation point radiative heat transfer for Fire 2.

the predicted stagnation point radiation is below 6.2 eV. In contrast, by 1637.5 s there is extensive line and VUV flux, and the character of the radiation has changed so that 53% is from lines and only 43% of the total is below 6.2 eV. However, at all trajectory points there is extensive radiation in the 2–4 eV range.

Based upon these comparisons with the Fire 2 flight data, it is believed that the present method and models are reasonable and appropriate. Thus, they should be useful in studying a wide variety of entry vehicle flowfield situations.

Conclusions

In this paper an engineering flowfield model suitable for analyzing the stagnation region of high altitude entry vehicles having extensive nonequilibrium has been presented. This model includes nonequilibrium chemistry, multitemperature, viscous, conduction, and diffusion effects. It also includes coupled nongray radiative transfer in a form that contains the effect of local thermodynamic nonequilibrium on the emission and absorption characteristics of atoms and molecules. The boundary conditions permit multitemperature shock slip and a partially or fully catalytic wall having frequency dependent radiative properties. Comparison with Fire 2 flight data indicates that the model has the correct behavior and is reasonably accurate. Based on the comparisons, the following conclusions can be stated:

1) Radiation cooling/coupling is important and is measurable even in the early portions of the Fire 2 trajectory.

2) Radiation heat transfer should be included and varies as to source. In the early stages of the Fire 2 entry, the radiative transfer is primarily molecular and infrared lines. Later, atomic VUV continuum and line radiation become very important.

3) Local thermodynamic nonequilibrium phenomena are important for many species, affects most radiative phenomena, and should be included in all models. While $N_2^+(1-)$ radiation is relatively unaffected by LTNE, LTNE depopulates the excited states of atoms and N_2 molecules, affects the radiation in the postshock nonequilibrium region, and can lead to an overpopulation of excited states in regions of radiative cooling and in the wall thermal layer.

Acknowledgments

This work was primarily supported by NASA Grant NAG-1-1003 from the Langley Research Center, with Lin C. Hartung as technical monitor. T. A. Gally is partially supported by a NASA Graduate Student Researchers Fellowship through the NASA Johnson Space Center.

References

[1] Carlson, L. A., and Gally, T. A., "The Effects of Electron Temperature and Impact Ionization on Martian Return AOTV Flowfields," *Journal of Thermophysics and Heat Transfer*, Vol. 5, No. 1, 1991, pp. 9–20.

[2] Carlson, L. A., "Approximations for Hypervelocity Nonequilibrium Radiating, Reacting, and Conducting Stagnation Regions," *Journal of Thermophysics and Heat Transfer*, Vol. 3, No. 4, 1989, pp. 380–388.

[3] Carlson, L. A., Bobskill, G. J., and Greendyke, R. B., "Comparison of Vibration Dissociation and Radiative Transfer Models for AOTV/AFE Flowfields," *Journal of Thermophysics and Heat Transfer*, Vol. 4, No. 1, 1990, pp. 16–26.

[4] Gally, T. A., and Carlson, L. A., "Nonequilibrium Chemical and Radiation Coupling, Part II: Results for AOTV Flowfields," *Journal of Thermophysics and Heat Transfer*, Vol. 6, No. 3, 1992, pp. 392–399.

[5] Thompson, R. A., "Comparison of Nonequilibrium Viscous Shock Layer Solutions with Shuttle Heating Measurements," *Journal of Thermophysics and Heat Transfer*, Vol. 4, No. 2, 1990, pp. 162–169.

[6] Nicolet, W. E., "User's Manual for the Generalized Radiation Transfer Code (RAD/EQUIL or RADICAL)," NASA CR 116353, Oct. 1969.

[7] Park, C., "Assessment of Two Temperature Kinetic Model for Ionizing Air," *Journal of Thermophysics and Heat Transfer*, Vol. 3, No. 3, 1989, pp. 233–244.

[8] Park, C., "Calculation of Nonequilibrium Radiation in the Flight Regimes of Aeroassisted Orbital Transfer Vehicles," *Thermal Design of Aeroassisted Orbital Transfer Vehicles*, Progress in Astronautics and Aeronautics, edited by H. F. Nelson, Vol. 96, AIAA, New York, 1985, pp. 395–418.

[9] Candler, G., and Park, C., "The Computation of Radiation from Nonequilibrium Hypersonic Flows," AIAA 88-2678, June 1988.

[10] Foley, W. H., and Clarke, J. H., "Shock Waves Structured by Nonequilibrium Ionizing and Thermal Phenomena," *Physics of Fluids*, Vol. 16, No. 3, 1973, pp. 1612–1620.

[11] Nelson, H. F., "Nonequilibrium Structure of Argon Shock Waves," *Physics of Fluids*, Vol. 16, No. 12, 1973, pp. 2132–2142.

[12] Nelson, H. F., and Goulard, R., "Structure of Shock Waves with Nonequilibrium Radiation and Ionization," *Physics of Fluids*, Vol. 12, No. 8, 1969, pp. 1605–1617.

[13] Chapin, C. E., "Nonequilibrium Radiation and Ionization in Shock Waves," Purdue Univ., AA&ES Rept., West Lafayette, IN, June 1967.

[14] Kunc, J. A., and Soon, W. H., "Collisional Radiative Nonequilibrium in Partially Ionized Atomic Nitrogen," *Physical Review A: General Physics*, Vol. 40, No. 10, 1989, pp. 5822 ff.

[15] Carlson, L. A., "Radiative Gasdynamic Coupling and Nonequilibrium Effects Behind Reflected Shock Waves," *AIAA Journal*, Vol. 9, No. 5, 1971, pp. 858–865.

[16] Gnoffo, P. A., Gupta, R. N., and Shinn, J. L., "Conservation Equations and Physical Models for Hypersonic Air Flows in Thermal and Chemical Nonequilibrium," NASA TP 2867, Feb. 1987.

[17] Lee, J. H., "Basic Governing Equations for the Flight Regimes of Aeroassisted Orbital Transfer Vehicles," *Thermal Design of Aeroassisted Orbital Transfer Vehicles*, Progress in Astronautics and Aeronautics, edited by H. F. Nelson, Vol. 96, AIAA, New York, 1985, pp. 3–53.

[18] Chapman, S. and Cowling, T. G., *The Mathematical Theory of Non-Uniform Gases*, Cambridge University Press, New York, 1964.

[19] Camac, M., and Kemp, N. H., "A Multitemperature Boundary Layer," Avco-Everett Research Lab., AVCO Research Rept. 184, Everett, MA, Aug. 1964.

[20] Dix, D. M., "Energy Transfer Processes in a Partially Ionized, Two-Temperature Gas," *AIAA Journal*, Vol. 2, No. 12, 1964, pp. 2081–2090.

[21] Park, C., *Nonequilibrium Hypersonic Aerothermodynamics*, Wiley, New York, 1990, pp. 139–141.

[22] Gally, T. A., Carlson, L. A., and Green, D., "A Flowfield Coupled Excitation and Radiation Model for Nonequilibrium Flows," AIAA Paper 91-1463, June 1991.

[23] Miner, E. W., and Lewis, C. H., "Hypersonic Ionizing Air Viscous Shock Layer Flows over Nonanalytic Blunt Bodies," NASA CR-2550, May 1975.

[24] Carlson, L. A., and Nerem, R. M., "Equilibrium Air Stagnation Point Boundary-Layer Calculations Using a Variable Heat of Dissociation Model," *Journal of Heat and Mass Transfer*, Vol. 11, 1968, pp. 699–707.

[25] Moss, J. N., "Reacting Viscous Shock Layer Solutions with Multicomponent Diffusion and Mass Injection," NASA Technical Rept. TR-R-411, June 1974.

[26] Rose, P. H., and Stark, W. I., "Stagnation Point Heat-Transfer Measurements in Dissociated Air," *Journal of Aerospace Sciences*, Vol. 25, Feb. 1958, pp. 86–97.

[27] Cauchon, D. L., "Radiative Heating Results from the Fire II Flight Experiments at a Reentry Velocity of 11.4 Kilometers Per Second," NASA TM X-1402, 1966.

[28] Cauchon, D. L., McKee, C. W., and Cornette, E. S., "Spectral Measurements of Gas-Cap Radiation During Project Fire Flight Experiments at Reentry Velocities Near 11.4 Kilometers Per Second," NASA TM X-1389, Oct. 1967.

[29] Gupta, R. N., "Navier Stokes and Viscous Shock Layer Solutions for Radiating Hypersonic Flows," AIAA Paper 87-1576, June 1987.

[30] Balakrishnan, A., Park, C., and Green, J. M., "Radiative Viscous Shock Layer Analysis of Fire, Apollo, and PAET Flight Data," *Thermophysical Aspects of Re-Entry Flows*, Progress in Astronautics and Aeronautics, edited by J. N. Moss and C. D. Scott, Vol. 103, AIAA, New York, 1986, pp. 514–540.

[31] Sutton, K., "Air Radiation Revisited," *Thermal Design of Aeroassisted Orbital Transfer Vehicles*, Progress in Astronautics and Aeronautics, Vol. 96, AIAA, 1985, pp. 419–442.

[32] Bird, G. A., "Nonequilibrium Radiation During Re-Entry at 10 km/sec," AIAA Paper 87-1543, June 1987.

Nonequilibrium Chemical and Radiation Coupling, Part II: Results for AOTV Flowfields

T. A. Gally and L. A. Carlson

Reprinted from

Journal of Thermophysics and Heat Transfer

Volume 6, Number 3, July-September 1992, Pages 392-399

AIAA

A publication of the
American Institute of Aeronautics and Astronautics, Inc.
The Aerospace Center, 370 L'Enfant Promenade, SW
Washington, DC 20024-2518

JOURNAL OF THERMOPHYSICS AND HEAT TRANSFER
Vol. 6, No. 3, July–Sept. 1992

Nonequilibrium Chemical and Radiation Coupling, Part II: Results for AOTV Flowfields

Thomas A. Gally* and Leland A. Carlson†
Texas A&M University, College Station, Texas 77843

A flowfield model for the stagnation region of high altitude entry vehicles which includes nonequilibrium chemistry, multitemperature, viscous, conduction, diffusion, coupled nongray nonequilibrium radiative transfer for atoms, and molecules, and local thermodynamic nonequilibrium phenomena has been applied to two Aeroassisted Flight Experiment (AFE) trajectory points, a high-speed return from Mars, a series of points at 80 km for 12–16 km/s, and three altitudes at 16 km/s. Based on these results shock slip is significant, radiation cooling/coupling is minor at AFE conditions but important by 14 km/s and dominant at 16 km/s, radiation for the AFE is small but important and primarily molecular, above 12 km/s atomic radiation is a significant or dominant portion of the total heating, and local thermodynamic nonequilibrium is important and should be included in all cases.

Nomenclature

c_p^f = frozen specific heat at constant pressure, Eq. (4)
c_{p_r} = specific heat at constant pressure of species r
$\mathcal{D}$ = binary diffusion coefficient
H = total enthalpy
$HREF$ = reference (freestream) total enthalpy
h = enthalpy
n = surface normal coordinate axis
p = pressure
Q_e = rate of inelastic electron energy exchange
$QR+$ = radiative flux to wall
q_r = radiative heat flux
T = temperature
u = mass averaged velocity
$\dot{w}$ = chemical production rate
$YSHOCK$ = shock standoff distance
y_s = shock standoff distance
η = heat conduction coefficient
ξ_e = rate of elastic electron energy exchange
ρ = density

Subscripts

e = electron
r = species

Superscripts

e = electronic
tr = translational

Introduction

In the future, space programs will be conducted which will require the efficient return of large payloads from missions to the moon or the planets. To accomplish this task, the return vehicles will utilize either direct entry at very high velocities or aerocapture techniques. In either case, a significant portion of the entry will involve high velocities at high altitudes, and during this part of the trajectory, the vehicle flowfields will be dominated by chemical, thermal, and radiative nonequilibrium phenomena. To design and operate such vehicles, it is essential to understand these chemical, thermal, and radiative nonequilibrium processes and the coupling between them at various flight conditions.

In a companion paper,[1] a viscous shock layer flowfield model for the stagnation region of high-altitude entry vehicles has been developed which includes nonequilibrium chemistry, multitemperature, coupled nongray nonequilibrium radiative transfer for atoms and molecules, and local thermodynamic nonequilibrium (LTNE) phenomena. The objective of this paper is to use this model over a wide range of conditions to investigate the magnitude and extent of nonequilibrium chemical and radiation coupling phenomena in high-altitude entry vehicle flowfields.

Description of Flowfield Model

The flowfield model used in this investigation is a viscous shock-layer analysis which includes the effects of chemical nonequilibrium, multitemperature thermal nonequilibrium (heavy particle and electron or electron-electronic temperature), and radiative transfer. Radiative gasdynamic coupling is achieved by including in the global energy equation the divergence of the radiative flux, $\nabla \cdot q_r$, and obtaining solutions iteratively. Details concerning the development of this model are in Refs. 1–4.

The radiation analysis is a modified version of RADICAL,[5] which is a detailed method that includes atomic continuum radiation, molecular band radiation, and atomic line radiation for the standard CHON (carbon, hydrogen, oxygen, nitrogen) gas system. To properly model nonequilibrium phenomena, this new radiative model uses actual species concentrations, the appropriate electron-electronic temperature, and modified forms for the source functions and absorption coefficients. These modifications account for the existence of excited state population distributions different from those predicted by a Boltzmann distribution (i.e., local thermodynamic nonequilibrium, LTNE), since non-Boltzmann distributions can significantly affect radiative emission and absorption.

The model also has the option of three different electron-electronic energy models. The first, termed the quasiequilibrium electron model (QEE), is a free electron energy model

---

Presented as Paper 91-0569 at the AIAA 29th Aerospace Sciences Meeting, Reno, NV, Jan. 7–10, 1991; received Jan. 22, 1991; revision received Aug. 5, 1991; accepted for publication Aug. 27, 1991.

*NASA Graduate Student Researcher, Aerospace Engineering Department. Student Member AIAA.

†Professor, Aerospace Engineering Department. Associate Fellow AIAA.

in which all derivative terms in the electron energy equation are neglected; and it can be expressed as

$$\dot{w}_e h_e^{tr} - \dot{w}_e \frac{u^2}{2} = \sum_r \xi_{er} + Q_e \tag{1}$$

where the ξ_{er} term account for elastic collisional effects and Q_e represents inelastic effects due to chemical reactions involving electrons. In this model the electronic temperatures are assumed to be equal to the free electron value.

The second is termed the quasiequilibrium electron-electronic energy model (QEEE) and is similar to the first model in that it computes the electron temperature assuming quasi-equilibrium. However, it also accounts for the effects of elastic and inelastic collisions on the energy contained in electronic states of each species as well as the free electron energy, and thus the resulting temperature is representative of electron-electronic energy. The resulting equation is

$$\dot{w}_e h_e^{tr} + \sum_r \dot{w}_r h_r^e - \dot{w}_e \frac{u^2}{2} = \sum_r \xi_{er} + Q_e \tag{2}$$

where the term $\Sigma_r \, \dot{w}_r h_r^e$ accounts for the production and depletion of electronic energy due to chemical reactions.

The third model utilizes a full combined electron-electronic energy conservation equation which includes the effects of convection, conduction, and diffusion, in addition to the production and loss of electron energy through elastic and inelastic collsions. This full electron-electronic energy equation (FEE) for the stagnation line is

$$\rho u c_p^e \frac{\partial T_e}{\partial n} - \frac{\partial}{\partial n}\left(\eta_e \frac{\partial T_e}{\partial n}\right) - \left(\sum_r \rho \mathfrak{D}_r c_{p_r}^e \frac{\partial}{\partial n} \frac{\rho_r}{\rho}\right) \frac{\partial T_e}{\partial n}$$

$$- u \frac{\partial p_e}{\partial n} + \dot{w}_e h_e^{tr} + \sum_r \dot{w}_r h_r^e = \sum_r \xi_{er} + Q_e \tag{3}$$

where

$$c_p^e = c_{p_e}^{tr} \frac{\rho_e}{\rho} + \sum_r c_{p_r}^e \frac{\rho_r}{\rho} \tag{4}$$

For more details concerning the electron-electronic energy models see Refs. 1–2.

Since the present flowfield formulation does not include vibrational nonequilibrium, the above electron-electronic energy models do not include vibrational-electronic coupling. While this phenomena should not be important at higher entry velocities due to the rapid dissociation of diatomic species in and near the shock front, it could be important at lower velocities. Thus, efforts are in progress to include vibrational nonequilibrium and vibrational electronic coupling, and these has been reported in Ref. 6.

Discussion of Results

Several sets of results obtained using the above methods and models are presented in this section. In all cases, results are for the stagnation streamline, utilize 99 points between the shock front and the wall, and, for simplicity, assume a nitrogen freestream. The nonequilibrium chemistry model is similar to the case II set of Ref. 2 and is shown in Table 1; and it should be representative of high-temperature radiating air. For diffusion, the approximate multicomponent model of Ref. 7 has been used. Since in a high-temperature ionized diatomic gas, charge exchange and ambipolar effects cause atoms, ions, and electrons to all have to a first approximation similar diffusion velocities, such a gas should be dominated by only two diffusion velocities, that of the molecules and that of the atoms, ions, and electrons. For such cases, previous studies[8,9] have shown that the differences between using a constant Lewis number of 1.0 or 1.4 or a variable Lewis number are small, and thus the commonly applied[10] value of 1.4 has been used. Hence, the present model should adequately represent the diffusion phenomena present, including multicomponent effects. In addition, the wall has been assumed to be radiatively black, noncatalytic to atomic recombination, fully catalytic to ionic recombination, and at 1650 K. This value, which corresponds approximately to the maximum possible for a nonablating surface, has been used for convenience and to illuminate cool wall phenomena. However, it is recognized that for many cases of interest the heat transfer load will be more than adequate to induce ablation and to raise the wall temperature to significantly higher values. Finally, in all cases, unless stated otherwise, shock slip is assumed, coupled nongray radiative transfer has been included, and local thermodynamic nonequilibrium effects have been accounted for using the molecular and first order atomic models described in Refs. 1 and 2.

Table 1 Reaction rate system

Reaction	A	B	E
$N_2 + N = 3N$	4.085×10^{22}	-1.5	113100
$N_2 + N_2 = 2N + N_2$	4.70×10^{17}	-0.5	113100
$N_2 + N^+ = N_2^+ + N$	2.02×10^{11}	0.8	13000
$N + N = N_2^+ + e^-$	1.40×10^{13}	0.0	67800
$N + e^- = N^+ + 2e^-$	4.16×10^{13}	0.5	120000
$N + N = N + N^+ + e^-$	2.34×10^{11}	0.5	120000
$N + N^+ = 2N^+ + e-$	2.34×10^{11}	0.5	120000
$N_2 + e^- = 2N^+ + e-$	3.00×10^{24}	-1.6	113100

Rates in the form $k_f = AT^B \exp(-E/T)$.
$T = T_e$ in electron impact reactions.

AFE CFD Point 2

This computational fluid dynamics (CFD) condition corresponds to what is often referred to as the "max Q" computational point for one of the initial AFE trajectories at which the freestream velocity, pressure, and temperature are 8.915 km/s, 15.715 dynes/cm², and 197.101K, respectively. For this case the nose radius has been assumed to be 2.3 m, and the electron temperature was required to equal the heavy particle temperature at the wall.

The results, presented on Figs. 1a and 1b, were obtained using the QEE model without the electron impact molecular dissociation reaction, and profiles obtained with both fixed and slip shock jump conditions using a Lewis number of 1.4 are portrayed. As shown, the electron temperature rapidly rises behind the shock front and equilibrates with the heavy particle temperature. However, as evidenced by the continual decrease in temperature and the variations in composition across the shock layer, the stagnation flow for this case is always in chemical nonequilibrium. Also, the wall thermal layer comprises approximately 20% of the 12.2-cm-thick shock layer. For this case, the convective heating was 13.55 W/cm², the total radiative heat flux to the wall was 1.56 W/cm², and radiative cooling effects were insignificant.

With respect to temperature, the effects of sip vs fixed shock jump conditions seem to be confined to a small region immediately behind the shock front. However, the impact on concentration and particularly on total enthalpy are significant. In fact, the total enthalpy profiles clearly show that the fixed shock boundary condition results in an incorrect value for enthalpy in the interior of the shock layer, leading to incorrect species concentration values. Interestingly, when a Lewis number of 1 is used with the fixed shock boundary conditions the enthalpy profile appears to be correct and when a value less than unity is used, the enthalpy is high in the flow interior. However, for the shock slip condition, the enthalpy profiles are unaffected by Lewis number. Since a Lewis number of 1.4 is more appropriate for describing atom-molecule diffusion, which is the dominant diffusion mechanism in this flow, and since the enthalpy ratio in the flow interior in the absence of significant radiative cooling should be unity, these

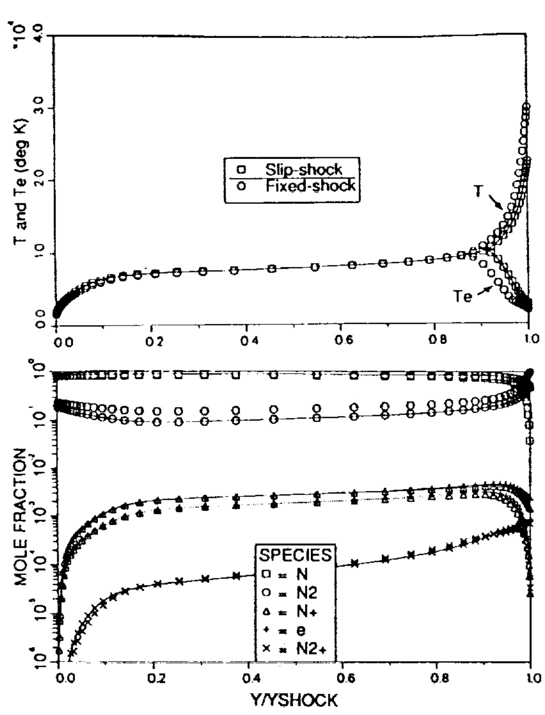

Fig. 1a Stagnation profiles for AFE CFD point 2 using QEE model, $U = 8.915$ km/s, $H = 77.9$ km, $QR = 1.56$ W/cm², $QC = 13.6$ W/cm², $YSHOCK = 12.2$ cm.

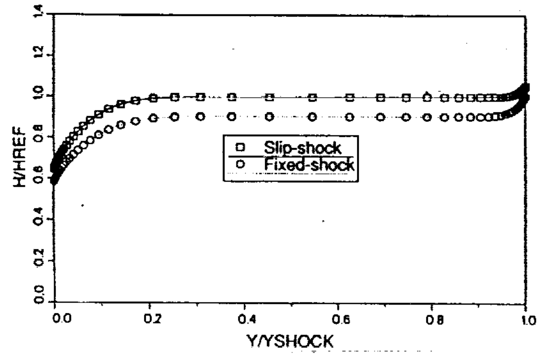

Fig. 1b Enthalpy profiles for AFE CFD point 2 using QEE model.

results demonstrate the importance of using slip shock boundary conditions at these conditions. Also, it should be noted that since the results shown on Fig. 1 are for a nitrogen freestream, the radiative heating values in air, based upon comparison with the Fire 2 data,[1] will probably be slightly higher.

AFE CFD Point 4

This condition corresponds to a "max Q" point for a heavier AFE vehicle at which the freestream conditions are 9.326 km/s, 26.4 dynes/cm², and 200 K. Stagnation line temperature and concentration profiles are presented on Fig. 2, which compares results obtained using the QEEE model including the electron impact dissociation reaction with those using the QEE energy model only. The primary effect of using the QEEE model is more extensive thermal nonequilibrium and a lower electron temperature through much of the shock layer. Also, the combined effect of electron impact dissociation and the QEEE model leads to a more dissociated flow having slightly different N_2 and N_2^+ profiles.

However, the most significant difference in the two models is the radiative heat transfer. For the QEEE case, the lower electron temperature yields a total radiative flux of 1.18 W/cm², a shock standoff distance of 11.96 cm, and a convective heating of 25.8 W/cm². For the QEE model it is 2.91 W/cm², 11.89 cm, and 25.7 W/cm², respectively.

Figure 3a shows the stagnation point continuum and line radiation distributions predicted with the QEEE model. In the actual radiative transfer analysis, lines are considered and integrated individually, but they are presented on Fig. 3a as average values for various line groups for convenience. While there are many infrared line groups and some in the ultraviolet, the line contributions are negligible compared to the continuum. Also, most of the continuum radiation (about 90%) is in the visible and infrared below 6.2 eV; and most of that is between 2 and 4 eV. At these conditions, this radiation is due to the $N_2^+(1-)$ band. In addition, there is some continuum contribution in the ultraviolet, probably due to nitrogen free-bound processes and N_2 Birge-Hopfield bands.

Figure 3b shows the same information as Fig. 3a except each line is shown individually. Many of the vacuum ultra-

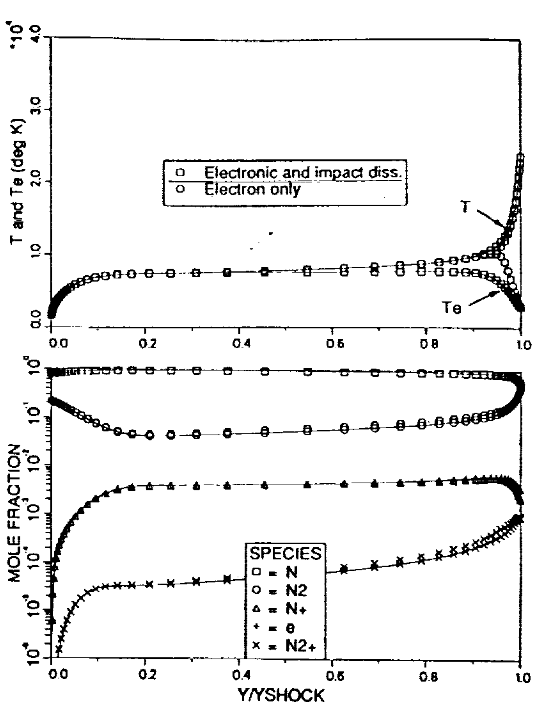

Fig. 2 Stagnation profiles for AFE CFD point 4 $U = 9.326$ km/s, $H = 75.2$ km. For QEEE Case: $QR = 1.18$ W/cm², $QC = 25.8$ W/cm², $YSHOCK = 12.0$ cm. For QEE Case: $QR = 2.91$ W/cm², $QC = 25.7$ W/cm², $YSHOCK = 11.9$ cm.

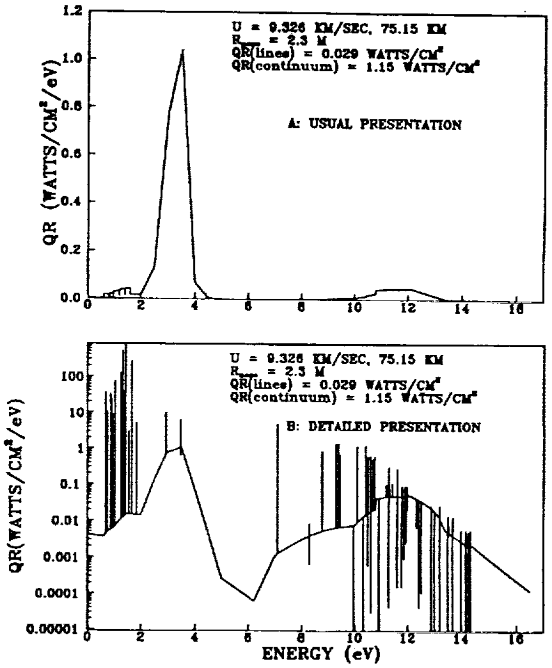

Fig. 3 Spectral variation of stagnation radiative heat transfer, AFE CFD point 4, QEEE model.

violet (VUV) lines above 10 eV are absorbing in their line centers, but the infrared (IR) lines are essentially transparent and appear to be strongly emitting. However, line radiation at this condition is insignificant compared to the continuum contribution.

As part of this study computations were also conducted using the QEE model without including molecular LTNE effects; and the resulting radiative heat transfer result was 8.90 W/cm². Obviously, molecular LTNE is important at AFE conditions and leads to lower radiative heating. Examination of the results indicate that the LTNE induced by chemical and thermal nonequilibrium drastically reduces radiation from the $N_2(1+)$ and $N_2(2+)$ bands and significantly decreases that due to N_2 Birge-Hopfield. However, $N_2^+(1-)$ is virtually unaffected by chemical and thermal nonequilibrium phenomena. Thus, on Fig. 3, the primary stagnation point radiation is in the continuum between 2 and 4 eV and is from the $N_2^+(1-)$ band.

At shock speeds below 10 km/s, shock tube radiative intensity photomultiplier measurements indicate a sharp rise to a peak immediately behind the shock front followed by a decrease until equilibrium is achieved.[11] Similar results have been obtained computationally for nonequilibrium flows for the visible region of the spectrum assuming the gas to be transparent.[12] Figure 4 shows for the present QEEE model the variation along the stagnation line of radiative flux towards the stagnation point, $QR+$, and its negative derivative, $-D(QR+)/DY$. The latter is essentially what Candler[12] and others have termed radiation intensity. As can be seen, $-D(QR+)/DY$ is similar to observed photomultiplier traces in having a peak near the shock front followed by a steady decrease towards the wall. For this case, no equilibrium plateau is achieved since the flow never reaches chemical equilibrium prior to the wall thermal boundary layer. (The oscillations near the wall are an artifact due to significant digit error resulting from providing the plot routine formatted data. The actual curve is smooth.) Comparison with the temperature plots indicates that the "intensity" peak corresponds to the maximum value in electron temperature, and near the wall the "intensity" is negative, indicating absorption. However, as shown by only the slight decrease in $QR+$, the amount of absorption near the wall is negligible at these conditions.

High-Speed Mars Return Case

In a recent paper,[13] results have been presented for the stagnation line of a one meter nose radius body at a trajectory point of 14.5 km/s at 65 km, which is representative of a high-speed Earth entry return from Mars. These results include chemical nonequilibrium, thermal nonequilibrium assuming that the vibrational, electronic, and electron temperatures can be represented by a single temperature and uncoupled nonequilibrium radiation. The investigators obtained for this trajectory point an uncoupled radiative heating rate of 1700 W/cm², a shock standoff distance of 5.7 cm, and a postshock chemical nonequilibrium zone 1.1 cm thick in which the electron-electronic vibrational temperature never significantly exceeded the equilibrium temperature. They also stated that most of the radiative heating was from the ultraviolet below 2000 A, that it originated from the nonequilibrium region behind the shock wave, and that very little was absorbed in the wall thermal layer. The latter is different from previous beliefs by some researchers[14] but is in agreement with approximate studies.[3] In addition, separate results were obtained for the same case with an equilibrium viscous shock-layer method[15] that used a coupled radiation model similar to RADICAL, and these predicted a standoff distance of 3.5 cm and a radiative heating rate of 970 W/cm².

To investigate these differences, the present model using the full electron-electronic energy model with LTNE effects and a partially catalytic wall has been applied to this case; and temperature and ionization profiles are presented on Fig. 5. Here, the predicted shock standoff distances are 3.92 cm and 3.67 cm for the radiatively uncoupled and coupled cases respectively, and most of the shock layer is in chemical equilibrium. The difference in the standoff lengths between the present results and the nonequilibrium result of Ref. 13 is believed to be primarily due to the electron temperature profile and its subsequent effect on chemistry. In Ref. 13 T_e is low in the region behind the shock front, possibly due to the combining of electron-electronic with vibrational phenomena. However, the present results show significant dissociation at the shock front with diatomic species being insignificant over most of the shock layer and ionization dominating the chemistry. Thus, in the present case the FEE energy model is strongly influenced by collisional and ionization phenomena, and T_e significantly exceeds the equilibrium temperature in the nonequilibrium zone. Since the dominant ionization mechanism behind the shock front is electron impact[2] which is governed by free electron temperature, this enhancement of T_e accelerates ionization, shortens the chemical nonequilibrium zone to about 0.3 cm, and decreases the overall shock-layer thickness. However, as expected, the present thickness prediction is greater than that for the equilibrium case discussed above. It should also be noted that the difference

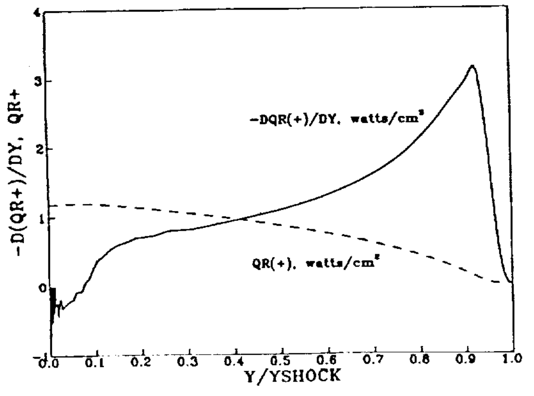

Fig. 4 Intensity and radiative flux towards stagnation point, AFE CFD point 4, QEEE model.

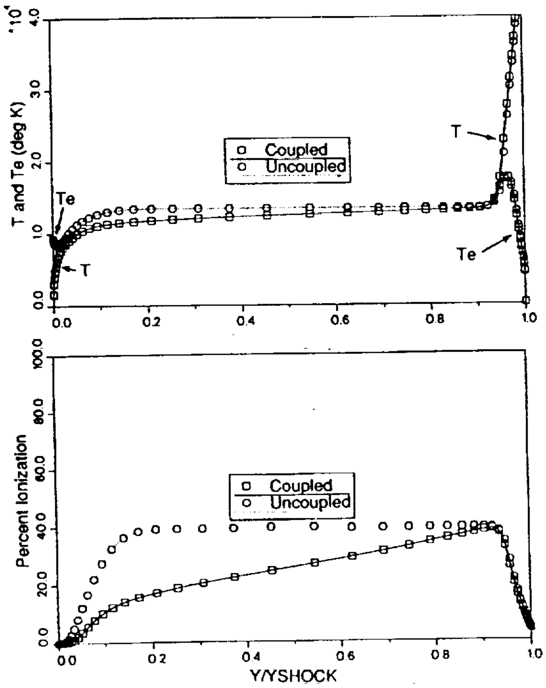

Fig. 5 Stagnation profiles at 14.5 km/s, 65 km, Rnose = 1 m. Uncoupled: QR = 2831 W/cm², QC = 426 W/cm², $YSHOCK$ = 3.92 cm. Coupled: QR = 1347 W/cm², QC = 430 W/cm², $YSHOCK$ = 3.67 cm.

between the present results and those of Ref. 13 show the strong sensitivity of solutions to electron temperature models at such trajectory points.

Results obtained with the present model predict the stagnation point radiative heat transfer for the case without any radiation gasdynamic coupling to be 2831 W/cm^2, which is higher than that of Ref. 13. Comparison of the spectral variation of the stagnation point radiative flux indicates that the present results have significant radiation above 11 eV, primarily due to free-bound continuum processes, while those of Ref. 13 have little or no flux in this region. Since both methods treat lines in detail, and since both have previously been shown to be in reasonable agreement in the visible and infrared, it appears that the differences are primarily due to the treatment of atomic continuum radiation in the vacuum ultraviolet. It should be noted that the present radiation model has for equilibrium conditions shown good agreement with experimental data over the total spectrum.[16] Further, the present results indicate that most of the radiation originates from the high-temperature equilibrium portion of the shock layer in the range $0.4 < y/YSHOCK < 0.9$ and not from the postshock nonequilibrium zone. In the latter, chemical nonequilibrium induces extensive local thermodynamic nonequilibrium and depopulates the excited states rapidly via ionization with the result that very little radiation originates in the nonequilibrium region.

Moreover, the radiation coupled results for this case indicate significant radiation cooling, as evidenced by the decrease in radiative heating to 1347 W/cm^2 and by the steady decrease in temperature and ionization throughout the equilibrium zone. Further, while the equilibrium coupled prediction for this case was only 970 W/cm^2, it is probable that the difference between it and the present prediction is due to the influence of reaction chemistry, differences in assumed wall catalycity, and the amount of absorption in the wall thermal layer. Basically, equilibrium chemistry should predict more molecules and, hence, more absorption. This possibility is supported by the equilibrium results which indicate that the wall thermal layer absorbs about 32% of the wall directed flux while in the present model only about 20% is absorbed. Thus, while most of the shock layer is in chemical equilibrium, nonequilibrium effects may still be important and affect the radiative heatings, and, obviously, radiation cooling is important for this case and needs to be included in an analysis model.

Velocity Effects at 80 km

Results have been obtained using the FEE model for a 2.3-m nose radius vehicle for three different velocities, 12, 14, and 16 km/s, at an altitude of 80 km. These velocities are, depending upon the trajectory chosen, within the possible range of entry speeds associated with certain Martian and Lunar return vehicles.

The temperature and composition profiles for the 12 km/s case are shown on Fig. 6; and, as shown by the continually decreasing temperature and the variation in the N$^+$ concentration, the entire shock layer at this flight condition is in chemical nonequilibrium. Immediately behind the shock front, which is 11.5 cm from the wall, the electron-electronic temperature slowly rises to a peak value and then gradually equilibrates with the heavy particle temperature. In the wall thermal layer, which comprises about 20% of the shock layer, deionization and recombination processes are important. For this case, when radiative coupling and LTNE effects are included, the radiative heat transfer is 24.3 W/cm^2 and the convective rate is 33 W/cm^2.

The temperature and composition profiles for the 14 km/s case are shown on Fig. 7. Since the freestream velocity is higher, the postshock nonequilibrium zone is shorter than at 12 km/s, occupying only the outer 30–40% of the 9.1-cm shock layer. The electron-electronic temperature rises rapidly and peaks at a value several thousand degrees above the equilibrium temperature, and the wall sheath representation only affects the electron temperature in a small zone near the wall. For this case the convective heating is 56.4 W/cm^2 and the radiative flux is 110.7 W/cm^2. Interestingly, especially when compared to the AFE cases, only about 10% of this radiative heating is due to molecular processes.

As part of this study, several cases were also conducted at this condition using the QEEE and QEE energy models; and the only difference between the models was that the peak in electron temperature was slightly higher and slightly farther from the shock front with the exact model than with the quasiequilibrium models. This behavior has been observed at freestream velocities of 12 km/s and higher and is in sharp

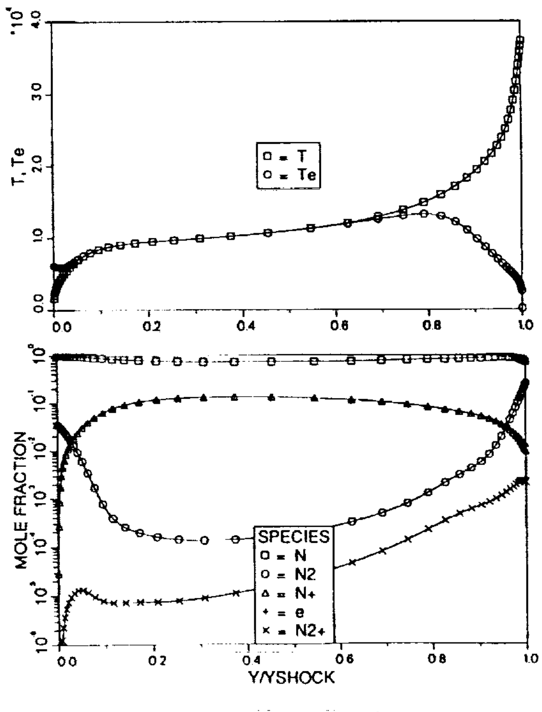

Fig. 6 Coupled stagnation profiles at 12 km/s, 80 km, Rnose = 2.3 m. QR = 24.3 W/cm^2, QC = 33 W/cm^2, $YSHOCK$ = 11.5 cm.

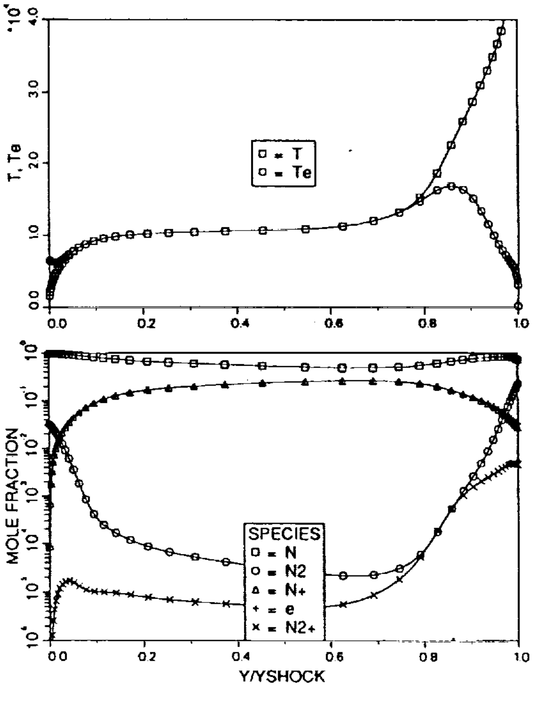

Fig. 7 Coupled stagnation profiles at 14 km/s, 80 km, Rnose = 2.3 m. QR = 111 W/cm^2, QC = 56.4 W/cm^2, $YSHOCK$ = 9.1 cm.

contrast to the trends displayed at the AFE velocities. At the higher velocities there are more electrons, and the flow is dominated by ionization processes. Consequently, the electron-electronic energy is dominated by the free electrons. At the lower AFE speeds, there is very little ionization and the electronic energy portion dominates the combination. Thus, the shape and character of the electron temperature profiles appears to be significantly different at the higher velocities than at AFE speeds.

The spectral variation in radiative heat flux to the wall at 14 km/s is shown on Fig. 8a, where the contributions due to line and continuum processes have been combined and the convenient representation of lines as group averages has been utilized. Here, the heating due to continuum and lines is similar in magnitude with extensive infrared and ultraviolet (UV) lines as well as significant VUV bound-free processes. In fact, only about 28% of the wall flux is from the visible and infrared below 6.2 eV. Notice that a measurable portion of the visible radiation is between 2 and 4 eV and is due to $N_2^+(1-)$ molecular radiation.

As mentioned previously, the actual radiative transfer analysis treats lines individually, and Fig. 8b displays the same information as Fig. 8a but with each line shown separately. From this representation, it is evident that in the visible and infrared the line radiation is primarily transparent. However, in the VUV, many of the line centers are highly absorbing, and careful examination of the spectral distribution shows that most of the line emission reaching the wall originates from the line wings.

In contrast to results below 10 km/s, shock tube photomultiplier results at higher speeds show that the radiative intensity peak behind a shock front changes from a single peak to a double hump peak system.[11] Experimental spectral data indicates that the first is due to molecular radiation near the shock front, while the second is atomic radiation coupled to the ionization process. Figure 9 shows for the 14 km/s condition theoretical predictions of the radiative flux towards the wall, $QR+$, and the negative of its derivative, $-DQR(+),DY$. As discussed previously, the latter is closely related to radiative intensity.

The present profile clearly exhibits this double hump behavior. The first peak corresponds to the maximum value of the electron temperature, while the second occurs at the onset of thermal equilibrium and the establishment of near Boltzmann distributions in the excited states. Subsequently, radiative cooling occurs and the "intensity" rapidly decreases. During this period, examination of the species concentrations and of LTNE phenomena indicates nonequilibrium recombination is induced with resultant overpopulation, compared to a Boltzmann distribution, of the excited states. Around $y/YSHOCK$ of 0.3 the flow begins to absorb more than it emits and $QR+$ begins to decrease. However, as shown by the $QR+$ profile, which only decreases slightly between 0.3 and the wall, the absorption in the wall thermal layer only results in a mild decrease in $QR+$ at this condition.

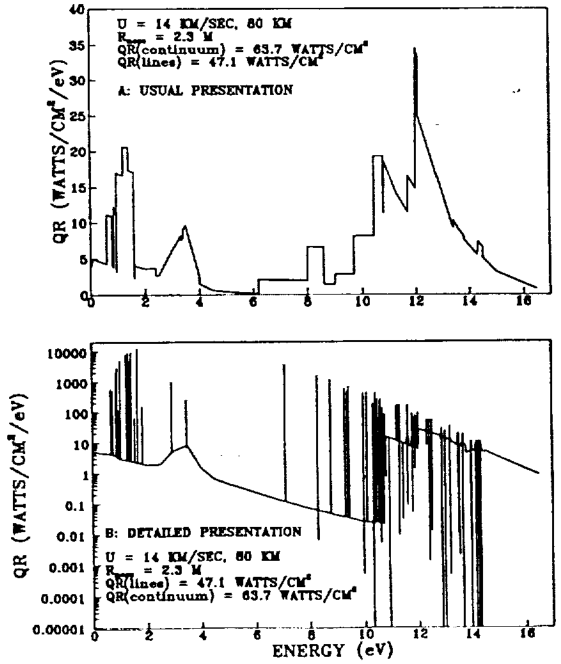

Fig. 8 Spectral variation of stagnation radiative heat transfer, 14 km/s, 80 km.

The temperature and composition profiles at 16 km/s are shown on Fig. 10, and the corresponding predicted radiative and convective heating rates are 272.6 and 87.3 W/cm², respectively. Here, the electron temperature rises very rapidly and peaks near 20,000 K, confirming the trend that as speed increases, the peak electron-electronic temperature increases in magnitude and occurs nearer to the shock front. Likewise, again due to the increase in velocity, the nonequilibrium zone is shorter at about 20–25% of the 7.5-cm shock layer. Finally, on Fig. 10 notice that radiation cooling effects induce both atomic and ionic recombination starting near the end of the postshock nonequilibrium zone and continuing all the way to the wall.

The effect on the temperature and ionization profiles of

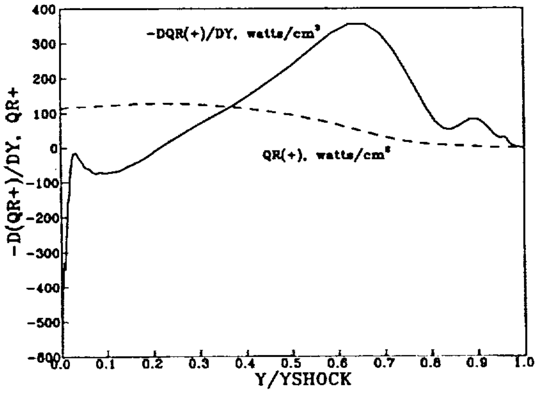

Fig. 9 Intensity and radiative flux towards stagnation point, 14 km/s, 80 km.

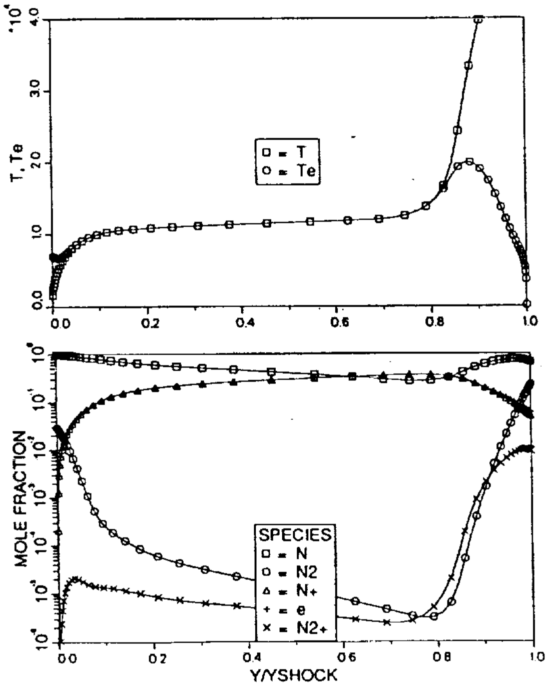

Fig. 10 Coupled stagnation profiles at 16 km/s, 80 km, Rnose = 2.3. QR = 273 W/cm², QC = 87.3 W/cm², $YSHOCK$ = 7.5 cm.

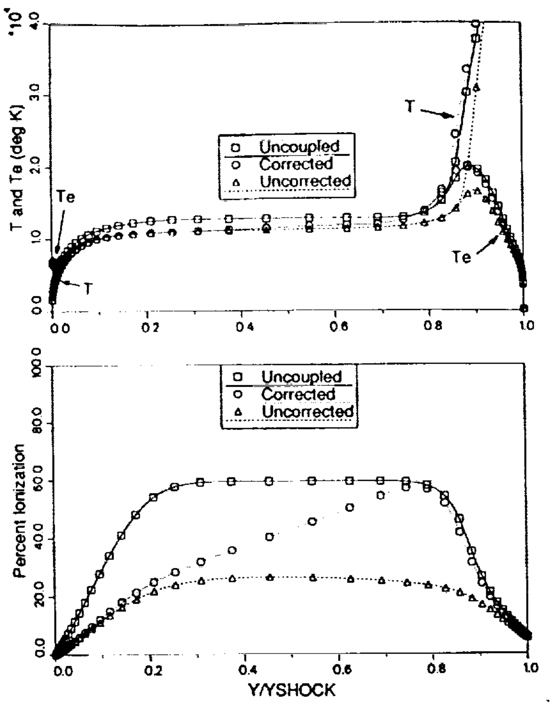

Fig. 11 LTNE and coupling effects at 16 km/s and 80 km.

including radiative gasdynamic coupling in the flowfield and local thermodynamic nonequilibrium effects in the radiation is shown for the 16 km/s case on Fig. 11. The curves denoted "Uncoupled" do not include either radiation cooling or LTNE phenomena and indicate for this case that nominally the nonequilibrium post-shock zone and the wall thermal layer each affect about 20% of the shock layer. For this case, the shock standoff distance is 8.16 cm. However, when radiation coupling is included but LTNE is excluded, the shock-layer thickness is reduced to 7.15 cm due to the lower temperature and increased density. The resultant profiles, designated as "Uncorrected," show that without LTNE effects significant cooling occurs in the nonequilibrium region with corresponding decreases in the electron and heavy particle temperatures and in the apparent length of the relaxation zone. Further, radiative losses through the shock front from the high-temperature nonequilibrium zone reduce the total enthalpy 40%, which leads to a cooler equilibrium zone having less than half the ionization of the uncoupled case.

Fortunately, when both radiation coupling and LTNE effects are included, the radiative losses are much less. As shown on the curves denoted as "Corrected," the corresponding temperature and ionization variations in the nonequilibrium post-shock region are only slightly affected since in that region the radiative losses are low due to LTNE effects. However, once equilibrium is nearly established around 0.8, radiative cooling becomes the dominant feature, the temperature steadily decreases, and the degree of ionization rapidly decreases. Obviously, at these conditions both LTNE phenomena and radiation coupling are important and need to be included.

A graphical summary of the 80-km radiative heating results is presented as Fig. 12, and several interesting features are evident. First, the inclusion of LTNE significantly affects the predicted radiative heat transfer at all three flight velocities, independent of whether or not radiative coupling is included. Second, the amount of radiative cooling is lower in the LTNE corrected predictions as compared to the local thermodynamic equilibrium (LTE) uncorrected flows; and, third, when both phenomena are properly included, radiative cooling ranges from relatively minor at 12 km/s to significant at 16 km/s.

Finally, for all three flight velocities, the predicted radiative heating is significant compared to the convective heating, and in the 16 km/s case the radiative heating is about three times the convective value. Since it is anticipated that advanced heat shield materials can withstand 70 W/cm^2 without ablating, these results indicate that at 80 km nonablative heat shields possibly could be used up to about 12.5 km/s.

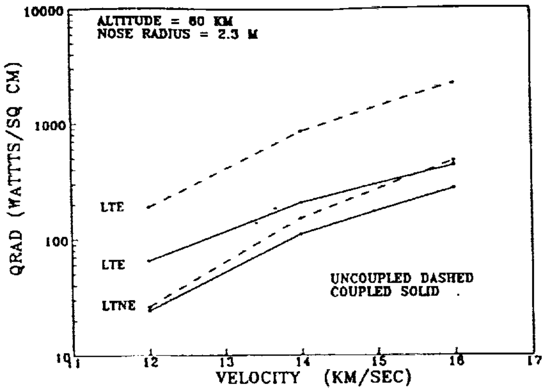

Fig. 12 LTNE and coupling effects on radiative heat transfer.

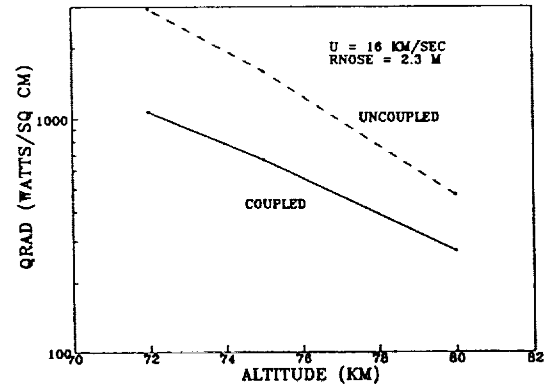

Fig. 13 Radiative gasdynamic coupling effects on radiative heat transfer.

Altitude Effects at 16 km/s

In order to investigate altitude effects and to use the model under a situation on a vehicle where most of the shock layer is in equilibrium, results have been obtained for the 2.3-m body at 16 km/s at 75 and 72 km as well as at 80 km. Since the resultant profiles do not exhibit any new phenomena, they are not shown. However, as the pressure increases with decreasing altitude, the postshock nonequilibrium chemical relaxation zone decreases significantly so that by 72 km it only encompasses about 5% of the shock layer. At that condition, the present model predicts a shock layer thickness of 7.05 cm, and radiative and convective heating rates of 1064 and 209 W/cm^2. Also, since the extent of nonequilibrium decreases with altitude, LTNE phenomena decrease and have a minor effect on the coupled radiative heat transfer predictions by 72 km. However, as shown on Fig. 13, radiative coupling/cooling is important at all three altitudes and increases as altitude decreases. Interestingly, the coupled results at 72 and 75 km, which have nearly equilibrium shock layers, are in excellent agreement with the equilibrium radiative heating predictions of Ref. 17. However, the present nonequilibrium radiative predictions at 80 km are higher than the equilibrium values of Ref. 17 at both 14 and 16 km/s.

Conclusions

In this paper a viscous shock layer engineering flowfield model suitable for analyzing the stagnation region of high-altitude entry vehicles having extensive chemical and radiative nonequilibrium has been applied to a variety of cases including two AFE trajectory points, a condition representative of the high-speed return from Mars of a small vehicle, a series of points at 80 km for velocities 12 to 16 km/s, and a study of the effects of altitude at 16 km/s. Based on these results the following conclusions can be stated:

1) Shock slip phenomena are important at all conditions investigated.

2) Radiation cooling/coupling is important for many cases. Specifically, a) it is a minor effect for the AFE conditions investigated; b) at 80 km, it is small at 12 km/s, important by 14 km/s, and very significant at 16 km/s at all altitudes; and c) it is very important for the high-speed Mars return case.

3) Radiation heat transfer should be included and varies as to spectral origin. Specifically, a) for the AFE, radiation, while small, is important and primarily molecular, $[N_2^+(1-)]$. b) At 12 km/s and above radiation is a significant portion of the total heating and is primarily due to atomic processes. By 14 km/s it is the dominant heating mechanism.

4) Local thermodynamic nonequilibrium is important and should be included in all models. In addition, a) LTNE depopulates the excited states of atoms and N_2 molecules in the postshock nonequilibrium region. b) LTNE can lead to an overpopulation of excited states in regions of radiative cooling and in the wall thermal layer. c) $N_2^+(1-)$ is relatively unaffected by LTNE. d) The importance of LTNE is independent of radiative coupling. e) The inclusion of LTNE reduces the magnitude of radiation cooling effects.

Acknowledgments

This work was primarily supported by NASA Grant NAG-1-1003 from the Langley Research Center, with Lin C. Hartung as technical monitor. T. A. Gally is partially supported by a NASA Graduate Student Researchers Fellowship through the NASA Johnson Space Center.

References

[1] Gally, T. A., and Carlson, L. A., "Nonequilibrium Chemical and Radiation Coupling, Part I: Theory and Models," *Journal of Thermophysics and Heat Transfer*, Vol. 6, No. 3, 1992, pp. 385–391.

[2] Carlson, L. A., and Gally, T. A., "The Effect of Electron Temperature and Impact Ionization on Martian Return AOTV Flowfields," *Journal of Thermophysics and Heat Transfer*, Vol. 5, No. 1, 1991, pp. 9–20.

[3] Carlson, L. A., "Approximations for Hypervelocity Nonequilibrium Radiating, Reacting, and Conducting Stagnation Regions," *Journal of Thermophysics and Heat Transfer*, Vol. 3, No. 4, 1989, pp. 380–388.

[4] Carlson, L. A., Bobskill, G. J., and Greendyke, R. B., "Comparison of Vibration Dissociation and Radiative Transfer Models for AOTV/AFE Flowfields," *Journal of Thermophysics and Heat Transfer*, Vol. 4, No. 1, 1990, pp. 16–26.

[5] Nicolet, W. E., "User's Manual for the Generalized Radiation Transfer Code (RAD/EQUIL or RADICAL)," NASA CR 116353, Oct. 1969.

[6] Gally, T. A., Carlson, L. A., and Green, D., "A Flowfield Coupled Excitation and Radiation Model for Nonequilibrium Flows," AIAA Paper 91-1463, June 1991.

[7] Miner, E. W., and Lewis, C. H., "Hypersonic Ionizing Air Viscous Shock Layer Flows over Nonanalytic Blunt Bodies," NASA CR-2550, May 1975.

[8] Carlson, L. A., and Nerem, R. M., "Equilibrium Air Stagnation Point Boundary-Layer Calculations Using a Variable Heat of Dissociation Model," *Journal of Heat and Mass Transfer*, Vol. 11, 1968, pp. 699–707.

[9] Moss, J. N., "Reacting Viscous Shock Layer Solutions with Multicomponent Diffusion and Mass Injection," NASA Technical Report TR-R-411, June 1974.

[10] Rose, P. H., and Stark, W. I., "Stagnation Point Heat-Transfer Measurements in Dissociated Air," *Journal of Aerospace Sciences*, Vol. 25, Feb. 1958, pp. 86–97.

[11] Wilson, J., "Ionization Rate of Air Behind High Speed Shock Waves," *The Physics of Fluids*, Vol. 9, No. 10, 1966, pp. 1913–1921.

[12] Candler, G., and Park, C., "The Computation of Radiation from Nonequilibrium Hypersonic Flows," AIAA 88-2678, June 1988.

[13] Park, C., and Milos, F. S., "Computational Equations for Radiating and Ablating Shock Layers," AIAA Paper 90-0356, Jan. 1990.

[14] Park, C., "Assessment of Two Temperature Kinetic Model for Ionizing Air," *Journal of Thermophysics and Heat Transfer*, Vol. 3, No. 3, 1989, pp. 233–244.

[15] Nicolet, W. E., Waterland, L. R., and Kendall, R. M., "Methods for Predicting Radiation Coupled Flowfields about Planetary Entry Probes," *Aerodynamic Heating and Thermal Protections Systems*, edited by L. S. Fletcher, Vol. 59, Progress in Astronautics and Aeronautics, AIAA, New York, 1978, pp. 120–136.

[16] Sutton, K., "Air Radiation Revisited," *Thermal Design of Aeroassisted Orbital Transfer Vehicles*, edited by H. F. Nelson, Vol. 96, Progress in Astronautics and Aeronautics, AIAA, New York, 1985, pp. 419–442.

[17] Sutton, K., and Hartung, L. C., "Equilibrium Radiative Heating Tables for Earth Entry," NASA TM 102652, May 1990.

Flowfield Coupled Excitation and Radiation Model for Nonequilibrium Reacting Flows

T. A. Gally, L. A. Carlson, D. Green

Reprinted from

Journal of Thermophysics and Heat Transfer

Volume 7, Number 2, April-June 1993, Pages 285–293

A publication of the
American Institute of Aeronautics and Astronautics, Inc.
The Aerospace Center, 370 L'Enfant Promenade, SW
Washington, DC 20024-2518

JOURNAL OF THERMOPHYSICS AND HEAT TRANSFER
Vol. 7, No. 2, April–June 1993

Flowfield Coupled Excitation and Radiation Model for Nonequilibrium Reacting Flows

Thomas A. Gally,* Leland A. Carlson,† and Derek Green‡
Texas A&M University, College Station, Texas 77843

A second-order method has been developed to correct a radiative transfer analysis for possible local thermodynamic nonequilibrium effects. This method uses a two-species excitation model for nitrogen with chemical reaction rates obtained from the detailed atomic transition method of Kunc and Soon. Results obtained from this new method show more atomic line radiation than the authors' previous first-order method. As improvements to the flowfield representation used in the computations, a full three-temperature energy model and a recently developed multicomponent diffusional model have also been incorporated.

Nomenclature

B_ν = blackbody function
c = speed of light
c_p = specific heat at constant pressure
E = electronic state energy level
E_n = integro-exponential function of order n
e = energy per unit mass
g = degeneracy
h = enthalpy per unit mass
I = ionization energy
K = absorption coefficient
k = Boltzmann constant
m = particle mass
N = number density
p = pressure
Q = electronic partition function
Q_e = electron translational partition function
q_r = radiative heat flux
r = wall reflectivity
S = source function
T = temperature
t = time
U = diffusion velocity
u^j = mass-averaged velocity components
x^j = coordinate axis
ε = wall emissivity
η = heat conduction coefficient
ν = frequency
ρ = density
σ = radiative cross section
τ = relaxation time
τ_ν = optical thickness

Subscripts

e = electron-electronic
f = forward rate (production)
pc = continuum process
pq = line process
r = reverse rate (depletion)
s = species
sh = value at shock
tr = translational
v = vibrational
w = value at wall
ν = frequency

Introduction

A GREAT deal of interest has been placed recently on the design of aerobraking vehicles for use with both interorbit maneuvering and interplanetary deceleration. In particular, a major goal of such experimental projects as the aeroassist flight experiment (AFE) is the development of the computational tools for the accurate prediction of the aerodynamic environment which determines the heating and controllability of such vehicles. Both low-speed interorbit and high-speed interplanetary missions will spend the aerobraking portion of their trajectories at very high, low-density altitudes where previously developed space vehicles spent only short durations. Thus, the computational aerodynamic tools to be used must correctly handle the chemical, thermal, and radiative nonequilibrium phenomena associated with low-density flows.

Previous work[1,2] concentrated on some aspects of the nonequilibrium nature of aerobraking flowfields. For example, the primary topic of discussion in Ref. 1 was electron-impact ionization rates. This chemical rate is important in both determining the amount of chemical nonequilibrium in the flow and in calculating the electron temperature T_e. Existing rates in the literature varied over several orders of magnitude with accompanying differences in T_e profiles and wall radiative heating rates, which is a strong function of T_e. In Ref. 2, the effects of thermodynamic nonequilibrium on the magnitude and nature of the radiative environment was investigated. Comparisons were made with the FIRE II flight test measurements, and a wide range of possible mission profile conditions were investigated.

A number of topics for future work were identified from the previous work. First, a two-temperature, T_{tr} and T_e, model had been used exclusively in Refs. 1 and 2, in which it was assumed that $T_v = T_{tr}$. This model is probably accurate for the higher speed conditions above 12 km/s where the flow is ionization-dominated and few diatomic particles exist. However, at the lower speeds and particularly for the speeds associated with the AFE vehicle, the flowfield is dissociation-dominated; and the inclusion of a separate vibrational energy equation can be expected to affect the total results. In addition, electron-vibrational coupling will affect the predicted T_e profile and, therefore, the radiative environment. Second, diffusional phenomena seemed to significantly affect chemical nonequilibrium and also the extent of atomic thermodynamic nonequilibrium. Since the diffusional model that was then

---

Presented as Paper 91-1463 at the AIAA 22nd Fluid Dynamics, Plasma Dynamics, and Lasers Conference, Honolulu, HI, June 24–26, 1991; received Aug. 12, 1991; revision received May 14, 1992; accepted for publication June 24, 1992.

*NASA Graduate Student Researcher. Student Member AIAA.

†Professor Aerospace Engineering. Associate Fellow AIAA.

‡Graduate Research Assistant.

being used was felt to be inadequate, a more complete model[3] has recently been incorporated into the flowfield solution. Finally, a new atomic local second-order thermodynamic nonequilibrium model was conceived, which is a compromise between the simple and fast method used previously and the complex methods used by other authors.

Problem Formulation

The computational model used in this report is an extension of the coupled viscous shock layer (VSL) and radiative transfer method described in detail in Refs. 1 and 2. The VSL portion of the code originated as the VSL3DNQ code[4] developed at NASA Langley. After modifications were made to the thermodynamic and transport coefficient calculations and multitemperature effects, T_{tr} and T_e, were included, the flowfield was iteratively coupled with the radiative transfer model of Nicolet[5] in a manner which included chemical and local thermodynamic nonequilibrium (LTNE) phenomena.

Three additional modifications have been made for this article. First, a vibrational energy equation has been added for the calculation of a third temperature, T_v, which describes the average vibrational energy state of all the diatomic species. Second, a new diffusional model has been developed to improve the calculation of the diffusional fluxes of mass and energy. Finally, to improve LTNE predictions, second-order radiative correction factors similar to those used in Refs. 1 and 2 have been developed for a two-step excitation model for atomic nitrogen.

Vibrational Temperature Model

The vibrational energy equation added to the VSL calculations has the following form for simple Cartesian coordinates:

$$\rho u^j c_{p_v} \frac{\partial T_v}{\partial x^j} = \frac{\partial}{\partial x^j}\left(\eta_v \frac{\partial T_v}{\partial x^j}\right) + \sum_s \rho_s U_s \frac{\partial h_{v_s}}{\partial x^j}$$
$$+ \sum_s \rho_s A \frac{[e_{v_s}(T_{tr}) - e_{v_s}]}{\tau_s} + \sum_s \rho_s \frac{[e_{v_s}(T_e) - e_{v_s}]}{\tau_{e,s}}$$
$$+ \sum_s (e_{v_s} - E_s)\left(\frac{\partial \rho_s}{\partial t}\right)_f - \sum_s (e_{v_s} - G_s)\left(\frac{\partial \rho_s}{\partial t}\right)_r \qquad (1)$$

In this equation, c_{p_v} is the frozen vibrational specific heat at constant pressure calculated from the species specific heats by $\Sigma_s\, c_{p_{v,s}}\rho_s/\rho$; and the vibrational temperature T_v represents the average vibrational energy of all the diatomic species. While multiple vibrational temperatures are often used, one for each vibrating species, it can be argued[6] that the vibrational-vibrational energy exchange rates are not well modeled by available methods; and, thus, results with multiple vibrational temperatures may not be meaningful. In addition, for the results with a nitrogen-only gas presented in this report, there is only one dominant vibrator, N_2, the vibrational contribution from N_2^+ being small.

The translational-vibrational energy exchange model used is a modification of the nonpreferential CVDV model described in Refs. 7 and 8. The terms involved with the $T_{tr} - T_v$ coupling model are the third, fifth, and sixth on the right side of Eq. (1). The differences from the CVDV model first occur, in the calculation of the relaxation time τ_s. This relaxation time is that proposed by Park[9] which sums the relaxation time of Millikan and White,[10] τ_s^{MW}, with a high temperature correction factor such that

$$\tau_s = \tau_s^{MW} + (1/c_s \sigma_v N_s)$$

where c_s is the average species molecular speed and σ_v is a limiting cross section calculated by[11]

$$\sigma_v = 10^{-17}(50{,}000\ \mathrm{K}/T_{tr})^2 \mathrm{cm}^2$$

The second modification, also suggested by Park,[11] is the inclusion of the multiplier A on the third right-side term of Eq. (1). This multiplier attempts to correct the original Landau and Teller relaxation rate for high temperature diffusive effects and has the form

$$A = \left|\frac{T_{tr,sh} - T_v}{T_{tr,sh} - T_{v,sh}}\right|^{[3.5\exp(-5000\ \mathrm{K}/T_v) - 1]}$$

The electron-vibrational energy exchange is accounted for by the fourth right-side term of Eq. (1) and is taken from the work of Lee[12] as curve-fitted by Candler and Park[13]

$$\log(p_e \tau_e) = 7.50(\log T_e)^2 - 57.0 \log T_e + 98.70$$

for $T_e < 7000$ K, and

$$\log(p_e \tau_e) = 2.36(\log T_e)^2 - 17.9 \log T_e + 24.35$$

for $T_e \geq 7000$ K.

Lee suggests a correcting factor for the electron-vibrational relaxation similar to the factor A used for translational-vibrational relaxation. As with the translation-vibrational relaxation factor, this term is intended to increase the relaxation time or decrease the amount of coupling between the electron energy and vibrational energy. Unfortunately, the form of the correction developed for the case was T_e and T_v, and being far apart initially has the opposite effect for our conditions where T_e and T_v are initially close together in value behind the shock. For this reason, the suggested correction has not been included in the present model and the calculated results may tend to show too much electron-vibrational coupling.

The electron-vibrational coupling factor must also be included in the electron temperature equation, which for this article is the full electron/electronic energy equation described in Ref. 2. The electron/electronic energy equation is similar in form to Eq. (1) and includes the effects of conduction, convection, diffusion, chemical energy depletion, heavy particle-electron translation coupling, and now electron-vibrational coupling.

Second-Order Atomic LTNE Model

The flowfield solution is coupled with the radiative transport package of RADICAL[5] developed by Nicolet. The methods used by Niclolet assume that the electronic states of the radiating species are in local thermodynamic equilibrium (LTE) with each other and that their populations can be described by a Boltzmann distribution. A technique was previously developed[1,2] for correcting the RADICAL calculations to account for LTNE in both the atomic and molecular state populations.

The molecular electronic states populations are calculated using a quasisteady approach similar to that described in Ref. 11; and from these, LTNE population correction factors for the principle molecular radiation bands are obtained. Specifically, correction factors are determined for the N_2 Birge-Hopfield, first-positive, and second-positive bands, and for the N_2^+ first-negative band. Reference 2 should be consulted for more detail.

Also discussed in Ref. 2 is a first-order atomic LTNE radiation correction. This model is predicated on the observation that for many monatomic gases, including argon, nitrogen, and oxygen, there exist one or more low-lying ground energy states separated from the lowest excited energy state by an energy jump which is a large fraction of the ionization energy from the ground state. The model assumes that the excitation jump from ground to first excited state controls the ionization process, and that the excited states, because of their proximity in energy to the ionized state, are in equilibrium with the free electrons and ions. With this approach, the atomic nitrogen LTNE correction factor,[1,2,14] which represents the ratio of the actual population in an excited state to that which would exist for a Boltzmann distribution, can be written as

$$\frac{N_{N^+} N_e Q_N \exp(169{,}000\ \mathrm{K}/T_e)}{N_N Q_{N^+} Q_e}$$

The above assumptions and resulting approximation are extremely simple to calculate and implement. At the other end of the spectrum are the methods of Park[9] and Kunc and Soon[15] which handle possible LTNE effects by performing detailed state population calculations under the quasisteady assumption. Park's and Kunc's methods differ in the treatment of the free electrons and ions; Kunc and Soon allow the free ions and electron populations to be determined as part of the solution, allowing LTNE to occur only as a consequence of radiative state depletion, while Park uses the ion and electron population calculated from the flowfield solution, allowing nonequilibrium chemistry to affect bound state populations. Either way, the detailed methods are computationally intensive and are not suitable for a radiative coupled solution if computational usage is a consideration.

After extensively reviewing the work on argon of Foley and Clarke[16] and Nelson,[17] and the air and nitrogen work of Park,[9] Kunc and Soon,[15] and others, it was decided to develop a second-order LTNE model for high-temperature nitrogen by subdividing atomic nitrogen into two species. The first, termed N_g, for N ground, represents the nitrogen atoms in the first three low-lying electronic states of nitrogen. The second, termed N^* or N-excited, represents those nitrogen atoms populating the remaining upper electronic states. The relative densities of these subspecies will then be determined by appropriate reaction rates between themselves, N^+, e^-, etc., and the electronic states of each are assumed to be in LTE. It is believed that this approach has the potential to be a significant improvement over the present model in that it will allow a finite rate of ionization from excited states while retaining the fundamental two-step ionization process. In addition, by determining the excited state number densities directly from the flowfield computation, the appropriate atomic LTNE factors are directly obtainable and more accurate.

The thermodynamic state of the two species, N_g and N^*, are determined by the standard methods used for monoatomic gases

$$Q_{N_g} = \sum_{p=1}^{3} g_p \exp(-E_p/kT_e)$$

$$Q_{N^*} = \sum_{p=4}^{\max} g_p \exp[-(E_p - E_4)/kT_e]$$

$$Q_N = Q_{N_g} + Q_{N^*} \exp(-E_4/kT_e)$$

$$h_{N_g} = \frac{5}{2}\frac{kT}{m_N} + \frac{1}{m_N Q_{N_g}} \sum_{p=1}^{3} g_p E_p \exp(-E_p/kT_e) + h^\circ_{N_g}$$

$$h_{N^*} = \frac{5}{2}\frac{kT}{m_N} + \frac{1}{m_N Q_{N^*}} \sum_{p=4}^{\max} g_p (E_p - E_4)$$

$$\cdot \exp[-(E_p - E_4)/kT_e] + h^\circ_{N^*}$$

where the zero point energies are, $h^\circ_{N_g} = h^\circ_N = 3.36 \times 10^{11}$ erg/g and $h^\circ_{N^*} = h^\circ_{N_g} + E_4/m_N = 1.05 \times 10^{12}$ erg/g. The collision cross sections for both species, needed to calculate viscous transport properties, are assumed to be the same as for the original gas, N.

As mentioned earlier, new reactions must be specified to relate the two new species, N_g and N^*. These reactions are

$$N_g + e^- = N^* + e^-$$

$$N_g + e^- = N^+ + 2e^-$$

$$N^* + e^- = N^+ + 2e^-$$

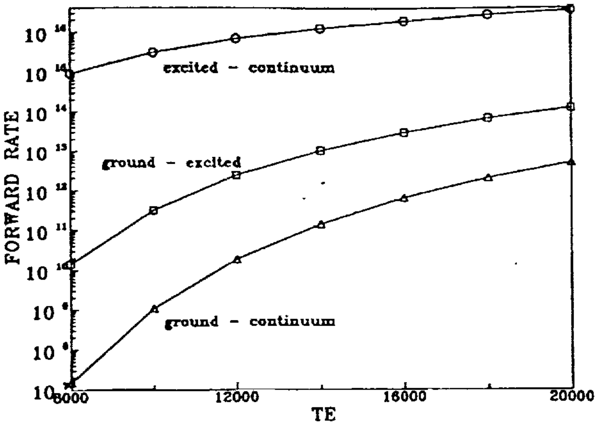

Fig. 1 Excitation and ionization rates for nitrogen-electron collisions.

It was decided to use the method for calculating detailed excitation rates given in Ref. 15. A computer program was written which calculated the individual rates for each allowed transition process and computed effective rates for the above reaction equations, assuming local thermodynamic equilibrium exists between the excited states grouped into each species. Results were obtained for a number of electron temperatures and then curve-fit as shown in Fig. 1. These rates are part of the complete chemical reaction set shown in Table 2.

The radiative transport model must also be modified to account for the LTNE populations of N_g and N^* relative to each other. Under the assumption of a radiating tangent slab, the heat flux to a surface can be calculated as, assuming a nonemitting precursor

$$-q_{r_\nu}(x) = 2\pi \int_0^{\tau_{\nu,sh}} \mathrm{sgn}(t_\nu - \tau_\nu) S_\nu E_2(|t_\nu - \tau_\nu|)\, dt_\nu$$

$$- 2E_3(\tau_\nu)\pi \left[\varepsilon_w B_{\nu,w} - 2r_w \int_0^{\tau_{\nu,sh}} E_2(t_\nu) S_\nu\, dt_\nu \right]$$

where τ_ν is determined by

$$\tau_\nu = \int_0^x K_\nu\, dy$$

The absorption and source functions used in these expressions are the sum of all radiative contributions at ν.

Absorption coefficients derived from either theory or experiment are normally expressed as the product of the absorbing state number density and a radiative cross section

$$K_{\nu_{pc}} = N_p \sigma_{pc}(\nu)$$

or by assuming a Boltzmann distribution exists between the electronic states

$$(K_{\nu_{pc}})_{\mathrm{LTE}} = N_N \left[\frac{g_p e^{-E_p/kT_e}}{Q_N} \sigma_{pc}(\nu) \right] = N_N \sigma'_{pc}(\nu)$$

Thus, an absorption coefficient using the actual state number density N_p can be obtained from one calculated assuming LTE by

$$K_{\nu_{pc}} = \frac{N_p}{(N_p)_{\mathrm{LTE}}} (K_{\nu_{pc}})_{\mathrm{LTE}}$$

where

$$\frac{N_p}{(N_p)_{\mathrm{LTE}}} = \frac{N_p}{N_N} \frac{Q_N}{g_p e^{-E_p/kT_e}}$$

It is desired to have the LTNE corrections in terms of the known number density populations, N_g and N^*. If state p is one of the low-lying states, and since we have assumed these states are in LTE with each other

$$N_p = N_g \frac{g_p e^{-E_p/kT_e}}{Q_{\mathrm{N}_g}}$$

$$\frac{N_p}{(N_p)_{\mathrm{LTE}}} = \frac{N_{\mathrm{N}_g}}{N_{\mathrm{N}}} \frac{Q_{\mathrm{N}}}{Q_{\mathrm{N}_g}} = \frac{N_{\mathrm{N}_g}}{(N_{\mathrm{N}_g})_{\mathrm{LTE}}}$$

Similarly, if p is one of the excited states

$$N_p = \mathrm{N}^*\{g_p \exp[-(E_p - E_*)/kT_E]/Q_{\mathrm{N}^*}\}$$

$$\frac{N_p}{(N_p)_{\mathrm{LTE}}} = \frac{N_{\mathrm{N}^*}}{N_{\mathrm{N}}} \frac{Q_{\mathrm{N}}}{Q_{\mathrm{N}^*} e^{-E_*/kT_e}} = \frac{N_{\mathrm{N}^*}}{(N_{\mathrm{N}^*})_{\mathrm{LTE}}}$$

The absorption coefficient for atomic line radiation is similar in form to that for the continuum process, but uses a radiative cross section which is a function of both the absorbing, p, and the emitting state, q

$$K_{\nu_{pq}} = N_p \sigma_{pq}(\nu)$$

However, since the number density dependence is only with the absorbing state, the LTNE corrections described above for continuum radiation also apply to the line radiation.

The source function at thermodynamic equilibrium is equal to B_ν

$$(S_{\nu_{pc}})_{\mathrm{LTE}} = (S_{\nu_{pq}})_{\mathrm{LTE}} = B_\nu = \frac{2h\nu^3}{c^2}(e^{h\nu/kT_e} - 1)$$

The source function for atomic continuum processes under LTNE conditions is given by[18,19]

$$S_{\nu_{pc}} = \frac{(N_p)_E}{N_p} \frac{2h\nu^3}{c^2} \left[e^{h\nu/kT_e} - \frac{(N_p)_E}{N_p} \right]^{-1}$$

$$= \frac{(N_p)_E}{N_p} \frac{e^{h\nu/kT_e} - 1}{e^{h\nu/kT_e} - [(N_p)_E/N_p]} (S_{\nu_{pc}})_{\mathrm{LTE}}$$

where the subscript E indicates a number density for state p calculated by assuming that state is in thermodynamic equilibrium with the free electrons and ions. Thus, if I is the ionization energy

$$(N_p)_E = N_{\mathrm{N}^+} N_e \{g_p \exp[-(E_p - I)/kT_e]/Q_{\mathrm{N}^+} Q_e\}$$

It can further be observed that when p is a low-lying state $e^{h\nu/kT_e} >> (N_p)_E/N_p$ and $e^{h\nu/kT_e} >> 1$ while for the highly excited states, $(N_p)_E/N_p \simeq 1$. Thus

$$S_{\nu_{pc}} \simeq [(N_p)_E/N_p](S_{\nu_{pc}})_{\mathrm{LTE}}$$

As before, the LTNE correction can be written in terms of the known number densities so that if p is one of the ground states

$$\frac{(N_p)_E}{N_p} = \frac{N_{\mathrm{N}^+} N_e}{N_{\mathrm{N}_g}} \frac{Q_{\mathrm{N}_g} e^{I/kT_e}}{Q_{\mathrm{N}^+} Q_e} = \frac{(N_{\mathrm{N}_g})_E}{N_{\mathrm{N}_g}}$$

while if p is an excited state

$$\frac{(N_p)_E}{N_p} = \frac{N_{\mathrm{N}^+} N_e}{N_{\mathrm{N}^*}} \frac{Q_{\mathrm{N}^*} \exp[(I - E_*)/kT_e]}{Q_{\mathrm{N}^+} Q_e} = \frac{(N_{\mathrm{N}^*})_E}{N_{\mathrm{N}^*}}$$

The source function for the radiative transition from state q to state p under LTNE conditions is[18,19]

$$S_{\nu_{pq}} = \frac{N_q}{N_p} \frac{(N_p)_{\mathrm{LTE}}}{(N_q)_{\mathrm{LTE}}} \frac{2h\nu^3}{c^2} \left(e^{h\nu/kT_e} - \frac{N_q}{N_p} \frac{(N_p)_{\mathrm{LTE}}}{(N_q)_{\mathrm{LTE}}} \right)^{-1}$$

$$= \frac{N_q}{N_p} \frac{(N_p)_{\mathrm{LTE}}}{(N_q)_{\mathrm{LTE}}} \frac{e^{h\nu/kT_e} - 1}{e^{h\nu/kT_e} - (N_q/N_p)[(N_p)_{\mathrm{LTE}}/(N_q)_{\mathrm{LTE}}]} (S_{\nu_{pq}})_{\mathrm{LTE}}$$

If the transition is between two excited states, since it has been assumed that these states are in thermodynamic equilibrium, the LTNE source function becomes identical to that for LTE. If the transition is between an excited state and a ground state, it can be approximated that $e^{h\nu/kT_e} >> 1$ and $e^{h\nu/kT_e} >> N_q(N_p)_{\mathrm{LTE}}/N_p(N_q)_{\mathrm{LTE}}$ so that it is approximately true that

$$S_{\nu_{pq}} = \frac{N_q}{N_p} \frac{(N_p)_{\mathrm{LTE}}}{(N_q)_{\mathrm{LTE}}} (S_{\nu_{pq}})_{\mathrm{LTE}}$$

$$= \frac{N_{\mathrm{N}^*}}{N_{\mathrm{N}_g}} \frac{(N_{\mathrm{N}_g})_{\mathrm{LTE}}}{(N_{\mathrm{N}^*})_{\mathrm{LTE}}} (S_{\nu_{pq}})_{\mathrm{LTE}}$$

Discussion of Results

Several sets of results have been obtained using the models presented in the previous sections. In all cases, these results are for the stagnation streamline on a vehicle having a 2.3-m nose radius, utilize 99 points between the wall and shock front, and use a nitrogen freestream. For those cases which assume that excited electronic states are in equilibrium with the free ions and electrons, the nonequilibrium chemistry is shown on Table 1. For those cases utilizing the second-order local thermodynamic nonequilibrium model for atoms, the corresponding nonequilibrium chemistry model is shown on Table 2. In addition, the wall has been assumed to be radiatively black, noncatalytic to atomic recombination, fully catalytic to ionic recombination, and at a temperature of 1650 K. This wall temperature was selected to insure significant cool wall thermal effects and is representative of the maximum temperature of nonablating surfaces. However, it is recognized that for the higher speed case considered, the cumulative head load associated with the mission profile dictates the use of ablative

Table 1 Reaction system for first-order LTNE model

Reaction	A	B	E
$\mathrm{N_2 + N = 2N + N}$	4.085×10^{22}	−1.5	113,100
$\mathrm{N_2 + N_2 = 2N + N_2}$	4.70×10^{17}	−0.5	113,100
$\mathrm{N_2} + e^- = 2\mathrm{N}^+ + e^-$	3.00×10^{24}	−1.6	113,100
$\mathrm{N_2 + N^+ = N_2^+ + N}$	1.00×10^{12}	0.5	12,200
$\mathrm{N + N = N_2^+} + e^-$	1.40×10^{13}	0.0	67,800
$\mathrm{N} + e^- = \mathrm{N}^+ + 2e^-$	4.16×10^{13}	0.5	120,000
$\mathrm{N + N = N + N^+} + e^-$	2.34×10^{11}	0.5	120,000
$\mathrm{N + N^+ = 2N^+} + e^-$	2.34×10^{11}	0.5	120,000

Rates in the form $k_f = AT^B \exp(-E/T)$. $T = T_e$ in electron impact reactions.

Table 2 Reaction system for second-order LTNE model

Reaction	A	B	E
$\mathrm{N_2 + N = 2N_g + N}$	4.085×10^{22}	−1.5	113,100
$\mathrm{N_2 + N_2 = 2N_g + N_2}$	4.70×10^{17}	−0.5	113,100
$\mathrm{N_2 + N^+ = 2N_g + N^+}$	1.90×10^{17}	−0.5	113,100
$\mathrm{N_2} + e^- = 2\mathrm{N}^+ + e^-$	3.00×10^{24}	−1.6	113,100
$\mathrm{N_2 + N^+ = N_2^+ + N_g}$	1.00×10^{12}	0.5	12,200
$\mathrm{N_g + N_g = N_2^+} + e^-$	1.40×10^{13}	0.0	67,800
$\mathrm{N_g + N = N + N^+} + e^-$	2.34×10^{11}	0.5	120,000
$\mathrm{N_g + N^+ = 2N^+} + e^-$	2.34×10^{11}	0.5	120,000
$\mathrm{N_g} + e^- = \mathrm{N}^+ + 2e^-$	2.50×10^{16}	0.0	169,000
$\mathrm{N_g} + e^- = \mathrm{N}^* + e^-$	5.56×10^{16}	0.0	121,000
$\mathrm{N}^* + e^- = \mathrm{N}^+ + 2e^-$	4.11×10^{17}	0.0	48,900

Rates in the form $k_f = AT^B \exp(-E/T)$. $T = T_e$ in electron impact reactions. $\mathrm{N = N_g + N^*}$.

surfaces and higher wall temperatures. Finally, an approximate boundary condition representing the wall sheath effects on electrons has been utilized as discussed in Ref. 2. Since the VSL flowfield method uses shock fitting, shock slip boundary conditions have been used for all cases in order to properly conserve total energy.

To investigate the thermal, diffusion, and radiation models, two entry conditions have been considered. The first, sometimes referred to as "AFE CFD Point 4," corresponds to a "max Q" point for an AFE vehicle at which the freestream conditions are 9.326 km/s, 26.4 dyne/cm², and 200 K; while the second point is for the same vehicle but at 14 km/s and 80-km altitude. The latter is typical of a Mars return vehicle at an altitude where nonequilibrium phenomena could be significant. All of the 14 km/s cases considered were calculated with radiative-gasdynamic coupling included. Since the AFE cases do not have significant radiative coupling, the radiation calculations have been made from the converged solutions. All radiation calculations have been made with LTNE effects accounted for using the molecular model, and either the first- or second-order atomic models described previously.

Thermal Nonequilibrium Model

All the results presented in this section were calculated using the constant Lewis number (1.4) diffusional model from Miner and Lewis[20] and the chemical reaction set of Table 1, while radiative LTNE effects were calculated using the first-order model. As a result, the results in this section are comparable to the results presented in Ref. 2, with the important distinction that the two-temperature model used previously assumed $T_v = T_{tr}$, while the cases labeled as two-temperature in this article assume $T_v = T_e$.

The first results presented in Figs. 2 and 3 were obtained using a two-temperature model wherein the electron/electronic and vibrational energies are assumed to be highly coupled and in equilibrium with each other.[11] This effect was achieved computationally by summing the two equations term-by-term and solving together. An alternate and, at least theoretically, identical approach could have been achieved by solving the original equation set, while forcing the electron-vibrational relaxation times τ_e to approach zero.

Figure 2 shows that the AFE CFD 4 case is in chemical and thermal nonequilibrium for almost the entire shock layer and that the chemistry is dissociation dominated, the ionization level being very low. The thermal nonequilibrium is particularly interesting in the region of the wall where $T_v - T_e$ exceed the heavy particle translational temperature. In the wall region, both the ionic and atomic recombinations are dumping energy into the electron and vibrational energies, respectively. It is assumed[1] that ionic recombinations occur primarily by the reverse of the electron-impact ionization reaction and that each recombination adds I to the electron translational energy, while the CVDV model[7,8] assumes that each atomic recombination adds $G_s - e_{v,s} \simeq D_s/2 - e_{v,s}$ to the vibrational energy of species s. Since $T_v - T_e$ exceeds T_{tr} in the wall thermal layer, it follows that either or both of the recombination reactions is adding energy faster that the translational-vibrational and translational-electron exchange processes can remove it. The maximum value reached by the $T_v - T_e$ temperature was 8515 K at y/yshock = 0.83.

Unlike the AFE CFD 4 case, the 14 km/s case shown in Fig 3. shows a pronounced peak in the $T_v - T_e$ profile of about 17,000 K at 0.83. Both thermal and chemical equilibrium occur for this case at about 0.70, although, due to radiative cooling, the temperature continues to drop after this point along with gradual changes in the chemical composition. While the AFE CFD 4 point was dominated by dissociation, at this speed dissociation occurs very rapidly behind the shock front and ionization processes dominate most of the flow, reaching a peak degree of ionization of about 35%.

Results with the full three-temperature model without electron-vibrational coupling are shown in Figs. 4 and 5. These cases represent the other extreme relative to the two-temperature cases since there is no direct energy exchange mechanism between the electrons and the vibrational states. Indirectly, some energy exchange still occurs through the coupling of both T_e and T_v to T_{tr}.

Comparing the three-temperature results of Fig. 4 with the two-temperature results of Fig. 2, it is seen that except for a greatly different T_e profile, the profiles are very similar. The vibrational temperature does peak a little sooner and higher at the shock front for the three-temperature model, 9100 K

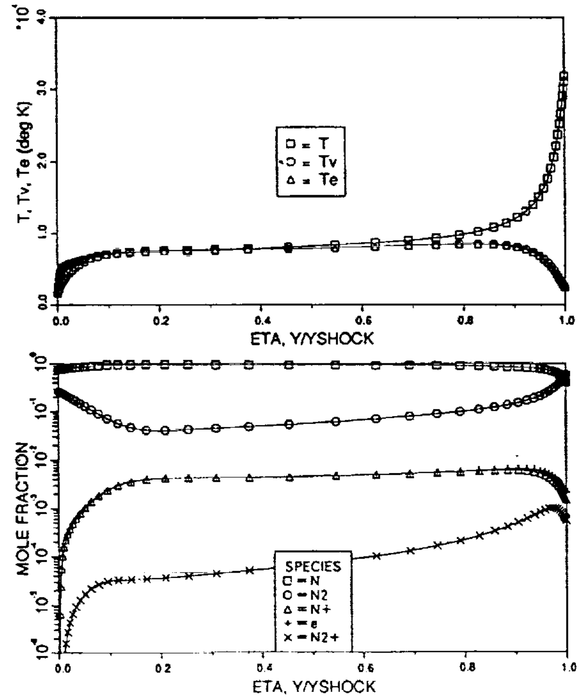

Fig. 2 Stagnation profiles for AFE CFD point 4 two-temperature model, QR = 2.51 W/cm², QC = 27.6 W/cm², YSHOCK = 13.1 cm.

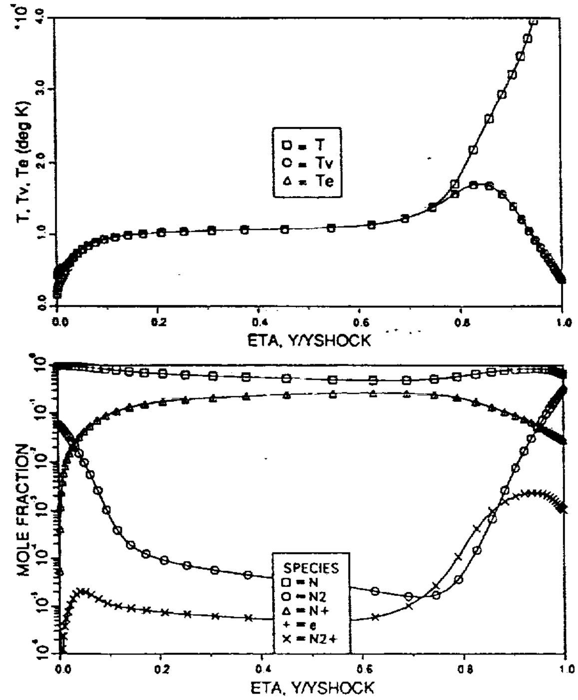

Fig. 3 Stagnation profiles for 14 km/s case two-temperature model, QR = 115.9 W/cm², QC = 66.2 W/cm², YSHOCK = 9.69 cm.

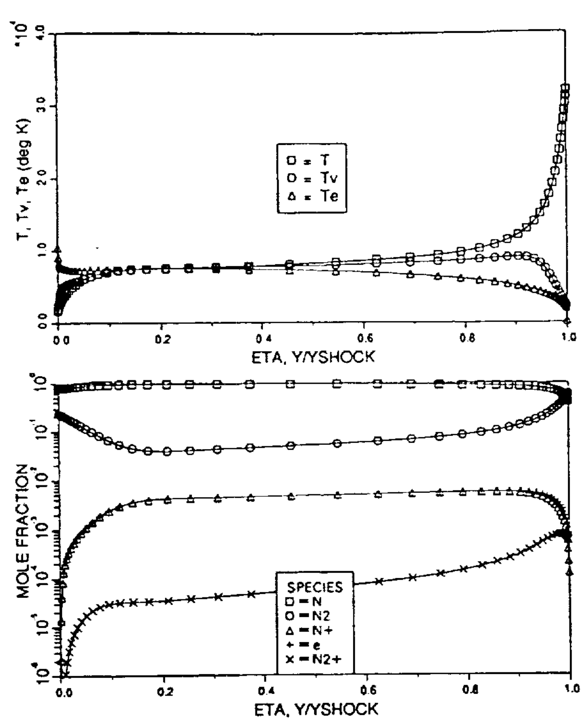

Fig. 4 Stagnation profiles for AFE CFD point 4 three-temperature model, without $T_v - T_e$ coupling, QR = 1.02 W/cm², QC = 26.0 W/cm², YSHOCK = 13.1 cm.

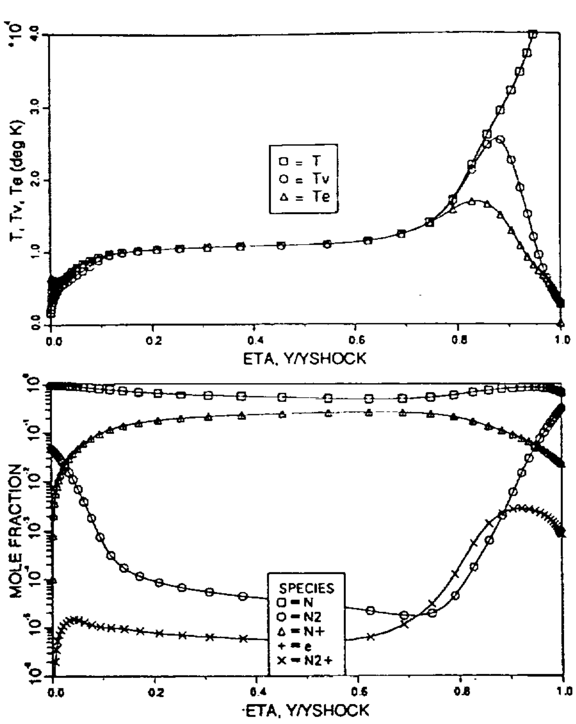

Fig. 5 Stagnation profiles for 14 km/s case three-temperature model, without $T_v - T_e$ coupling, QR = 98.2 W/cm², QC = 61.2 W/cm², YSHOCK = 9.77 cm.

at 0.91, but has the same profile over the rest of the shock layer, including the overshoot in the thermal boundary layer. Without T_e coupling, this high T_v indicates that energy production due to atomic recombinations is significant in the wall region, as has been seen by other investigators.[21] As a result of electron energy depletion through electron impact ionization, the electron temperature is much lower behind the shock front for this model than before, which results in a much lower radiative heat flux. Also, the lower electron temperature and its effect on the electron impact ionization rate increases the amount of chemical nonequilibrium at the shock front, and in turn, slightly increases the shock standoff distance.

As can be seen from the T_e profile, a shock slip condition was not enforced for the electron/electronic equation. Numerical problems with the slip boundary condition, coupled with the small magnitude of electron number density, have not yet been resolved. This omission, however, does not have a significant effect on the other flow properties since the electron heat conduction is very small at the shock and also does not have a strong effect on the T_e profile itself. The electron temperature solution appears to be uncoupled from the shock boundary condition. This result is consistent with the quasi-equilibrium electron formulation previously used by the authors[1,2] in which it was assumed that chemical energy production and collisional energy transfer dominate the other terms in the electron energy equation, and that T_e is primarily determined by the balance of the two.

The 14 km/s case shown in Fig. 5, when compared with Fig. 3, shows the exact opposite trends as were noticed for the AFE CFD 4 case. The T_e profile is very similar in shape to the $T_v - T_e$ profile, while T_v is greatly different. The vibrational temperature peaks much higher, 23,000 K at 0.86, and equilibrates sooner with T_{tr}, due to high translational coupling. T_e peaks only slightly lower at 16,900 K and 0.82, and as a result there is a slightly lower radiative flux.

In the thermal layer, the three-temperature T_v initially dips below T_{tr} before rising above near the wall as in the two-temperature case. Without electron coupling, diffusive effects in the thermal layer are important in the vibrational energy equation, and the flux of cool N_2 particles away from the wall lowers the vibrational energy until the atomic recombination reactions occur rapidly enough to raise T_v. This diffusive cooling effect was not seen in the AFE CFD 4 case due to the lower concentration gradients in N_2 and thus lower diffusive flux. The electron temperature in the thermal layer shows the same trends as were noted for the two-temperature case.

Figures 6 and 7 show results for the AFE CFD 4 and 14 km/s cases, respectively, where the three-temperature model is used with electron-vibrational coupling, as described previously in the theory section. As might be expected, these results are in-between the two extreme cases of the two-temperature model and the three-temperature model without $T_v - T_e$ coupling. In the AFE CFD 4 case, the electron temperature has been increased toward T_v in the shock front, equilibrates with it around 0.70, and stays in equilibrium through the rest of the shock layer except for a slight divergence immediately off the wall. The higher T_e profile results in a factor of two larger radiative flux than the uncoupled $T_v - T_e$ case, but it is still lower than the two-temperature case.

For the 14 km/s case, $T_v - T_e$ coupling lowers the vibrational temperature in the shock front region (from a peak value of 23,000 K to 22,200 K) while slightly raising the T_e profile, and reduces the amount of diffusional cooling of T_v in the wall thermal layer. Percentage-wise, the two-temperature assumption has a slightly greater effect on the radiative flux for the lower speed case than the higher, 30% compared to 20%. The percentage differences would be further apart for the two cases if it were not for the fact that LTNE corrections tend to reduce the amount of radiation from the thermal nonequilibrium regions.

Second-Order Atomic LTNE Model

The results in this final section are cases which used the full diffusional model of Ref. 3, the chemical reaction rates of Table 2, and the second-order atomic LTNE model discussed in the theory section of this article. Results obtained using full diffusional model do not differ significantly from those from the binary model in a nitrogen freestream[3] and should not effect the following observations. The AFE CFD 4 results shown in Fig. 8 are very close to the previous results shown in Fig. 6. The only significant difference is in the N^+

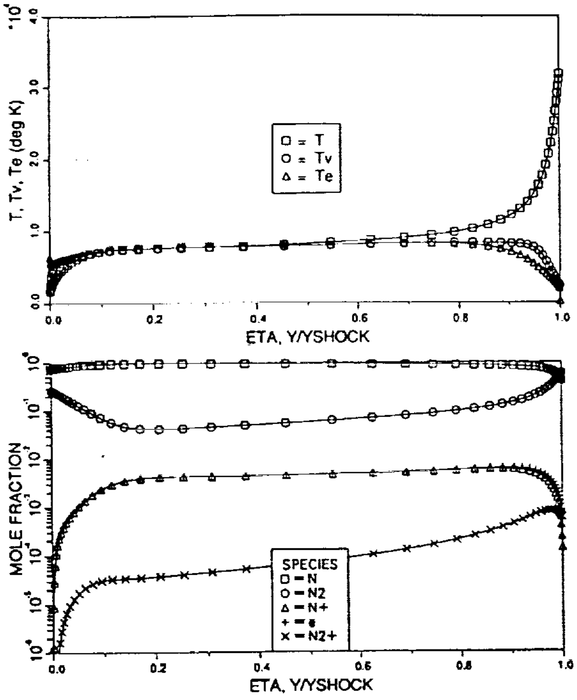

Fig. 6 Stagnation profiles for AFE CFD point 4 three-temperature model, with $T_v - T_e$ coupling, QR = 1.93 W/cm², QC = 27.2 W/cm², YSHOCK = 13.1 cm.

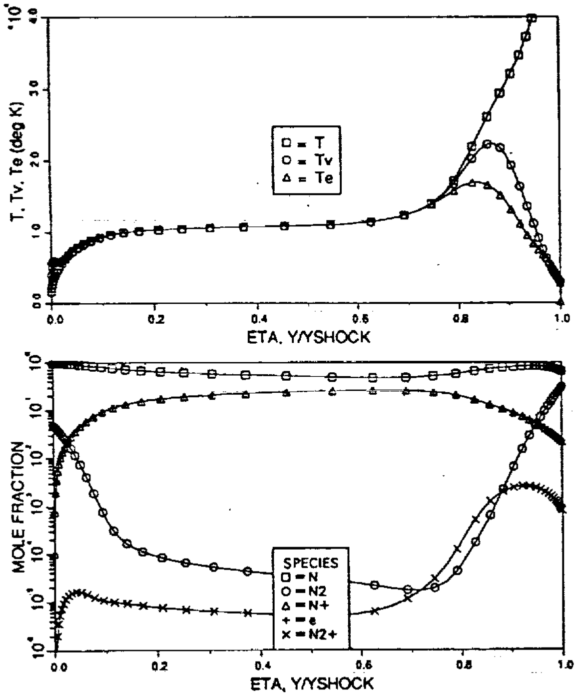

Fig. 7 Stagnation profiles for 14 km/s case three-temperature model, with $T_v - T_e$ coupling, QR = 97.7 W/cm², QC = 59.9 W/cm², YSHOCK = 9.77 cm.

and N_2^+ profiles at the shock front. The new rate for excitation of N is faster than the rate in Table 1 which leads to a faster total ionization rate even though the ionization from the excited states is not infinite. As a result of this faster ionization rate, there is a higher concentration of N^+ near the shock; and as a result of the charge exchange reaction and ambipolar diffusion effects, the higher N^+ concentration in turn slightly lowers the N_2^+ concentration. The calculated N^* population is very low and closely follows the T_e profile in detail as can partially be seen from the figure.

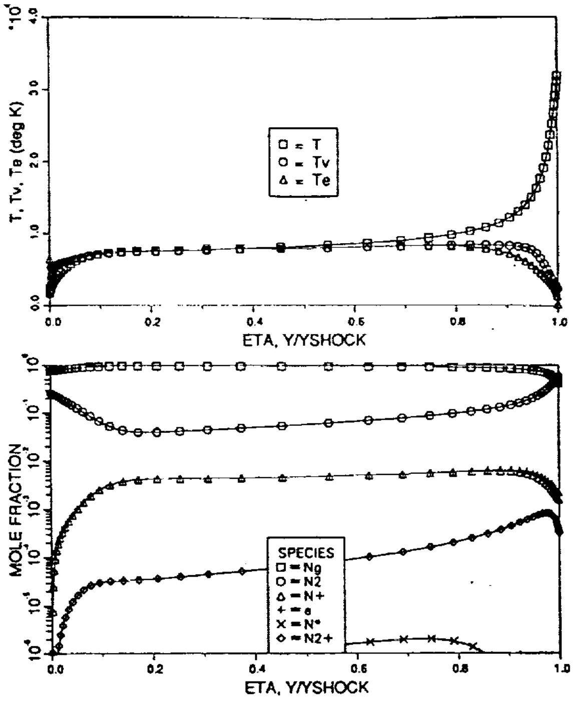

Fig. 8 Stagnation profiles for AFE CFD point 4 second-order LTNE model, QR = 2.38 W/cm², QC = 27.8 W/cm², YSHOCK = 13.1 cm.

This case can also be compared to the similar case results presented in Ref. 2. The total radiation calculated in Ref. 2 is lower than the current results, due primarily to a lower T_e temperature calculated by the quasiequilibrium electron/electronic energy equation used in Ref. 2. The radiative spectral differences between the previous case and this present case, however, should be due to the differences in the first- and second-order LTNE correction methods. The radiative spectral details of the radiation reaching the wall for the AFE CFD 4 case are shown in Fig. 9 in two forms; the first shows the atomic line radiation having been grouped into convenient blocks while the second shows the atomic lines in full detail. Having the lines grouped gives a better visual description of the magnitude of the relative radiative process, whereas the detailed presentation bears more similarity to experimental results.

While the radiation shown in Fig. 9 is still dominated by the $N_2^+(1-)$ molecular band in the 2–4 eV range, these new results show a much larger contribution from atomic lines in both the infrared (IR) and ultraviolet (UV) regions, especially in the IR region. In fact, the first-order LTNE results from Ref. 1 showed almost no atomic radiation at all due to the large region of LTNE predicted for this case. The second-order LTNE model predicts less LTNE for line radiation since the excited atomic electronic energy states are not as depleted as before.

The 14 km/s case shown in Fig. 10 exhibits significant differences from the results in Fig. 7. The higher nitrogen excitation rate in Table 2 has shortened the nonequilibrium region at the shock front and lowered the peak T_e from 16,650 K to 14,560 K. Since this case is dominated by ionization chemistry, it would be expected that the results are sensitive to the ionization/excitation rates. The group and detailed wall radiation spectral plots are given as Fig. 11. Atomic radiation dominates for this case and most of it comes from the continuum UV bands. Strongly emitting IR lines are still seen, and the high UV lines above 11 eV are highly absorbed at the lines' centers.

Rather than compare these results to the earlier results which are greatly different in the chemical and thermal profiles, it was decided to recalculate the results of Fig. 7 using

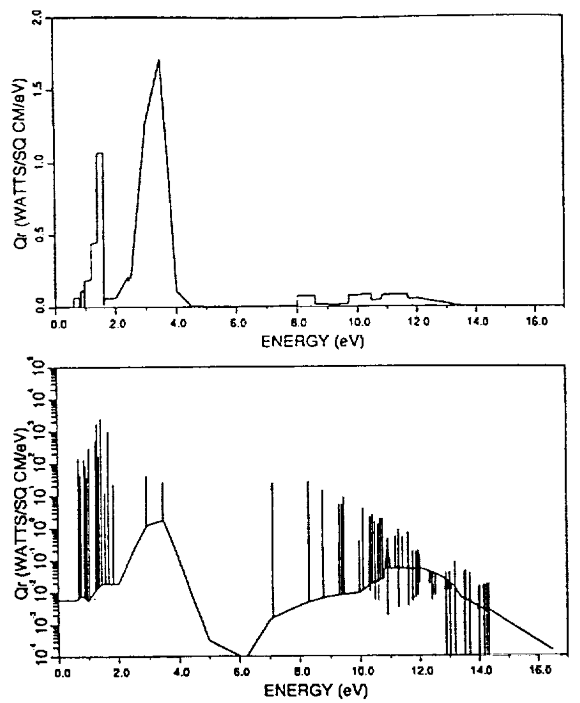

Fig. 9 Spectral radiation profiles for AFE CFD point 4, second-order LTNE model.

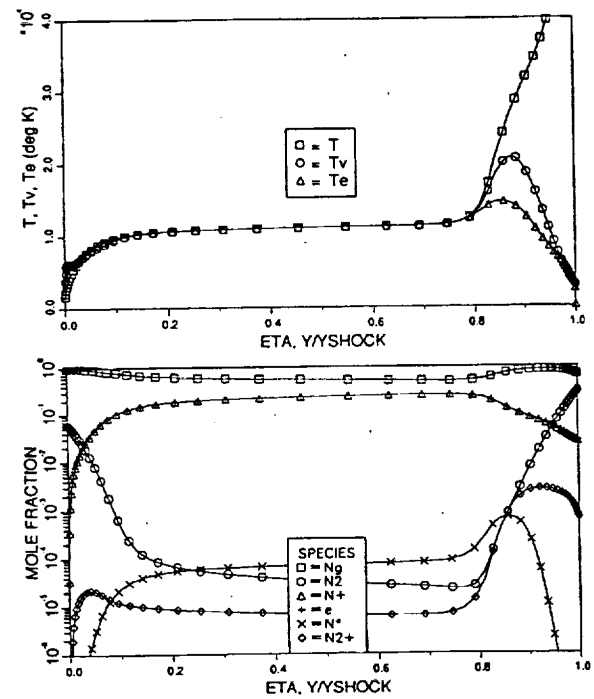

Fig. 10 Stagnation profiles for 14 km/s case second-order LTNE model, QR = 89.0 W/cm², QC = 55.1 W/cm², YSHOCK = 9.59 cm.

the higher excitation rate for N in place of the electron impact rate in Table 1. In this manner, first-order LTNE results could be obtained with a chemical model very similar to that for the second-order LTNE method. The flowfield profiles for this case are shown in Fig. 12. As expected, these profiles are very similar to those of Fig. 10 except that the peak T_e is lower, 13,860 K, and equilibrium occurs slightly sooner. The earlier equilibration is to be expected since the first-order LTNE assumes instantaneous equilibration of the excited states with the ions and electrons, while the second-order has a finite rate.

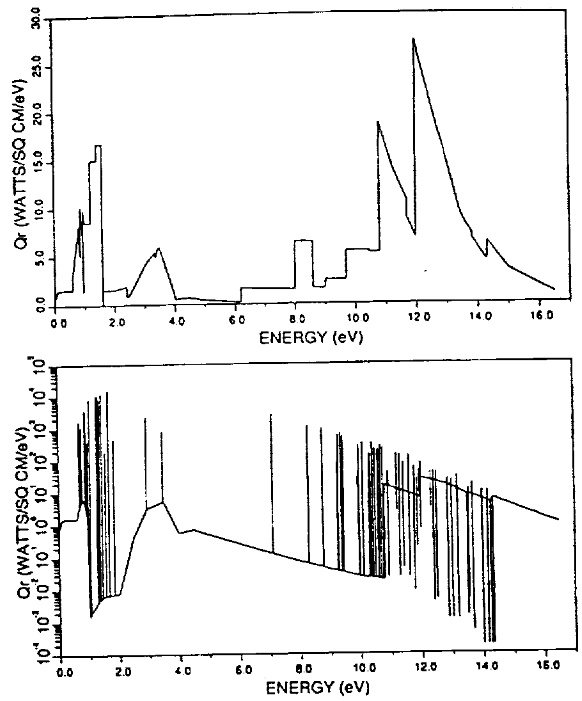

Fig. 11 Spectral radiation profiles for 14 km/s case, second-order LTNE model.

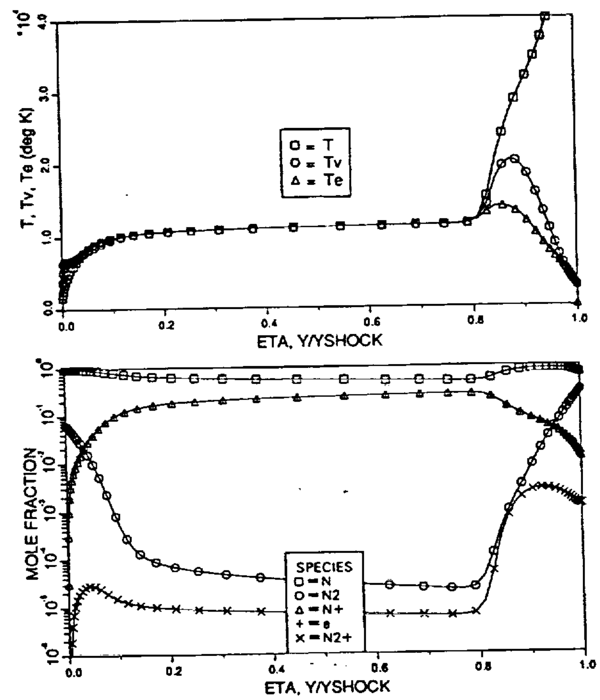

Fig. 12 Stagnation profiles for 14 km/s case first-order LTNE model with new excitation rate, QR = 82.2 W/cm², QC = 54.3 W/cm², YSHOCK = 9.58 cm.

The radiative spectral plots for this case are shown in Fig. 13. In comparing these results to those in Fig. 11, three important differences are noticed. First, the IR line radiation is enhanced in the second-order model over the first-order model. This greater amount of emission is due to the lower level of thermodynamic nonequilibrium predicted from the second-order method. The first-order method predicts a largely depleted excited state population in the peak T_e region, which reduces the line radiation from this region. Also, because of the reduced line radiation, absorption of the UV lines in the

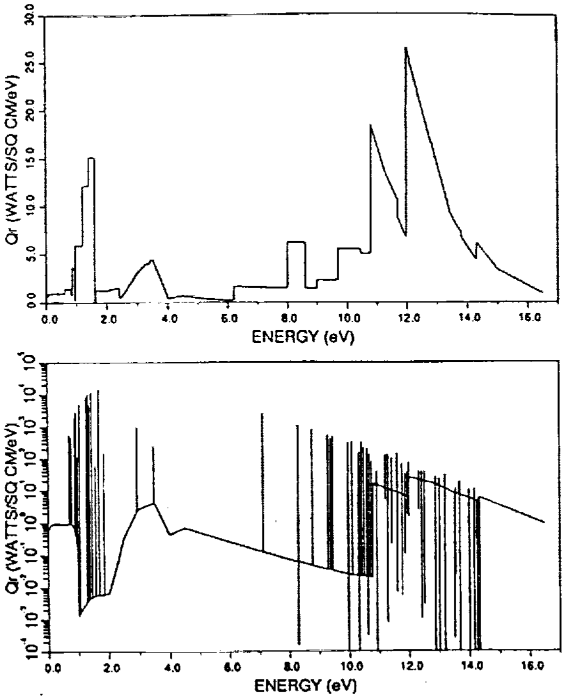

Fig. 13 Spectral radiation profiles for 14 km/s case first-order LTNE model with new excitation rate.

wall-boundary layer is more significant for the first-order LTNE model than for the second-order model. The difference in UV line center absorption is the second noticeable difference between Figs. 13 and 11. Finally, the N_2^+ (1-) molecular band is larger for the second-order LTNE model. This difference appears to be due to a number of subtle changes in the two flowfields such as different radiative cooling effects and different N_2^+ number densities caused by the charge exchange chemical reaction.

Conclusions

The use of a three-temperature model including electron-vibrational coupling can lead to significant differences in the thermal profiles from those obtained with a two-temperature model. The effects on chemistry are not as noticeable due to the fact that the combined $T_v - T_e$ model tends to predict a temperature closest to the dominant energy for the flow conditions, i.e., closer to T_v in dissociation dominated flows, and closer to T_e in ionization dominated flows. The differences in the thermal profiles for the two models results in differences of 20–30% in the radiative heat flux to the wall for the cases considered. These radiative differences would be more significant except that LTNE effects tend to inhibit emission from the regions of thermal nonequilibrium.

The second-order LTNE model developed for this article has shown deficiencies in the first-order LTNE model. While both models predict similar total heat fluxes, the spectral content of the radiation is different. Radiation reaching the wall with the second-order LTNE model shows a greater IR line contribution and less UV line center absorption. The electron impact excitation calculated for the second-order LTNE model is faster by an order of magnitude than the previous current rate. Using this faster rate with the first-order model can closely reproduce much of the chemical behavior of the second-order model.

Acknowledgments

This work was primarily supported by NASA Grant NAG-1-1003 from the Langley Research Center, with Lin C. Hartung as technical monitor. T. A. Gally is partially supported by a NASA Graduate Student Researchers Fellowship through the NASA Johnson Space Center.

References

[1] Carlson, L. A., and Gally, T. A., "The Effect of Electron Temperature and Impact Ionization on Martian Return AOTV Flowfields," AIAA Paper 89-1729, June 1989.

[2] Carlson, L. A., and Gally, T. A., "Nonequilibrium Chemical and Radiation Coupling Phenomena in AOTV Flowfields," AIAA Paper 91-0569, Jan. 1991.

[3] Gally, T. A., Carlson, L. A., and Green, D., "A Flowfield Coupled Excitation and Radiation Model for Nonequilibrium Reacting Flows," AIAA Paper 91-1463, June 1991.

[4] Thompson, R. A., "Comparison of Nonequilibrium Viscous Shock Layer Solutions with Windward Surface Shuttle Heating Data," AIAA Paper 87-1473, June 1987.

[5] Nicolet, W. E., "User's Manual for the Generalized Radiation Transfer Code (RAD/EQUIL or RADICAL)," NASA CR 116353, Oct. 1969.

[6] Park, C., *Nonequilibrium Hypersonic Aerothermodynamics*, Wiley, New York, 1990, pp. 166, 167.

[7] Treanor, C. E., and Marrone, P. V., "Effect of Dissociation on the Rate of Vibration Relaxation," *Physics of Fluids*, Vol. 5, No. 9, 1962, pp. 1022–1026.

[8] Marrone, P. V., "Inviscid, Nonequilibirum Flow Behind Bow and Normal Shock Waves, Part I.—General Analysis and Numerical Examples," Cornell Aeronautical Lab. Rept. QM-1626-a-12(I), Buffalo, NY, May 1963.

[9] Park, C., "Calculation of Nonequilibrium Radiation in the Flight Regimes of Aeroassisted Orbital Transfer Vehicles," *Thermal Design of Aeroassisted Orbital Transfer Vehicles*, edited by H. F. Nelson, Vol. 96, Progress in Astronautics and Aeronautics, AIAA, New York, 1985, pp. 395–418.

[10] Millikan, R. C., and White, D. R., "Systematics of Vibrational Relaxation," *Journal of Chemical Physics*, Vol. 39, No. 12, 1963, pp. 3209–3213.

[11] Park, C., "Assessment of Two Temperature Kinetic Model for Ionizing Air," AIAA Paper 87-1574, June 1987.

[12] Lee, J. H., "Electron-Impact Vibrational Excitation Rates in the Flowfield of Aeroassisted Orbital Transfer Vehicles," *Thermophysical Aspects of Re-entry Flows*, edited by J. N. Moss and C. D. Scott, Vol. 103, Progress in Astronautics and Aeronautics, AIAA, New York, 1986, pp. 197–224.

[13] Candler, G. and Park, C., "The Computation of Radiation from Nonequilibrium Hypersonic Flows," AIAA Paper 88-2678, June 1988.

[14] Carlson, L. A., Bobskill, G. J., and Greendyke, R. B., "Comparison of Vibration Dissociation and Radiative Transfer Models for AOTV/AFE Flowfields," *Journal of Thermophysics and Heat Transfer*, Vol. 4, No. 1, 1990, pp. 16–26.

[15] Kunc, J. A., and Soon, W. H., "Collisional Radiative Nonequilibrium in Partially Ionized Atomic Nitrogen," *Physical Review A*, Vol. 40, No. 10, 1989, pp. 5822 ff.

[16] Foley, W. H., and Clarke, J. H., "Shock Waves Structured by Nonequilibrium Ionizing and Thermal Phenomena," *Physics of Fluids*, Vol. 16, No. 3, 1973, pp. 1612–1620.

[17] Nelson, H. F., "Nonequilibrium Structure of Argon Shock Waves," *Physics of Fluids*, Vol. 16, No. 12, 1973, pp. 2132–2142.

[18] Chapin, C. E., "Nonequilibrium Radiation and Ionization in Shock Waves," AA&ES Rept., Purdue Univ., Lafayette, IN, June 1967.

[19] Clarke, J. H., and Ferrari, C., "Gas Dynamics with Nonequilibrium Radiative and Collisional Ionization," *Physics of Fluids*, Vol. 8, No. 12, 1965, pp. 2121–2139.

[20] Miner, E. W., and Lewis, C. H., "Hypersonic Ionizing Air Viscous Shock Layer Flows over Nonanalytic Blunt Bodies," NASA CR-2550, May 1975.

[21] Gnoffo, P. A., Gupta, R. N., and Shinn, J. L.," Conservation Equations and Physical Models for Hypersonic Air Flows in Thermal and Chemical Nonequilibrium," NASA TP 2867, Feb. 1987.

AIAA 93-3197

A Preferential Vibration Dissociation Coupling Model for Nonequilibrium Flowfields

D. E. McGough, L. A. Carlson, and T. A. Gally
Texas A&M University
College Station, TX

AIAA 24th Plasmadynamics & Lasers Conference

July 6-9, 1993 / Orlando, FL

A Preferential Vibration Dissociation Coupling Model for Nonequilibrium Flowfields

David E. McGough[*], Leland A. Carlson[**]
and
Thomas A. Gally[***]
Texas A&M University

Abstract

A preferential vibration-dissociation coupling model is incorporated into a radiatively coupled viscous shock layer code that also includes chemical, radiative, and thermal nonequilibrium. Stagnation point flow profiles are obtained for various Fire 2 flight conditions and for a typical 14 km/sec AOTV case, and comparisons are made with Fire 2 experimental data. Adjustments in molecular absorption coefficients are also made for several diatomic species. Based on comparisons with experimental data, very little preferential dissociation behavior is present in the Fire 2 flight conditions.

Nomenclature

c_p = constant pressure specific heat
D = dissociation energy
e = energy per unit mass
E_s = energy removed per dissociation
G_s = energy gained per recombination
h = enthalpy per unit mass
k = Boltzmann constant
k_f = forward reaction rate constant
k_{eq} = equilibrium rate constant
m = particle mass
N = cut off level in simple harmonic oscillator
N_ρ, N_j = number density
p = pressure
Q = vibrational partition function
Q_c = convective heat transfer
Q_r = radiative heat transfer
T = temperature
u^j = mass averaged velocity components
U_s = diffusion velocity
U = preferential temperature
x^j = coordinate axis
η = heat conduction coefficient
θ_v = characteristic vibrational temperature
ρ = density
σ = radiative cross section
τ = relaxation time

subscripts
e = electronic
f = forward rate (production)
r = reverse rate (depletion)
s = species
sh = value at shock
tr = translational
v = vibrational

Introduction

Chemical and radiative nonequilibrium effects dominate the flow around many hypersonic vehicles, such as those proposed for aerobraking maneuvers. In previous work[1-4], a radiatively coupled viscous shock layer (VSL) flow solver was developed from the VSL3DNQ program from NASA Langley[5] and the RADICAL radiation transport method of Nicolet.[6, 7] This program currently includes viscous effects, diffusion, conduction, chemical nonequilibrium, and thermal nonequilibrium. The program also includes a method to account for local thermodynamic nonequilibrium (LTNE) effects on radiation emission and absorption.

The coupling between the processes of dissociation and vibrational relaxation have a great effect on nonequilibrium flowfields. Methods have been developed which account for the effect of vibrational nonequilibrium on the molecular dissociation rates, and for the effect of dissociation on vibrational relaxation.[8, 9] One important difference between some of these methods is whether they

---

[*] *Graduate Research Assistant*
[**] *Professor Aerospace Engineering, Associate Fellow AIAA*
[***] *Visiting Assistant Professor, Member AIAA*

assume that dissociation occurs with equal probability from all vibrational energy levels, or with a higher probability from higher energy levels. A nonpreferential model assumes that dissociation will occur with an equal probability from all vibrational energy levels, given a sufficiently energetic collision. On the other hand, a preferential model assumes that, given a sufficiently energetic collision, dissociation will occur with a higher probability from higher energy levels. Previous work[3] developed a modified nonpreferential model after Treanor and Marrone.[8] This model is referred to as the MCVDV model. However, some authors[10, 11] suggest that the preferential model should be more physically correct. In this paper, a preferential model is included in the flow solver following the preferential model developed by Marrone and Treanor.[9] This model will be referred to as the preferential MCVDV model.

Flowfield Model

The VSL program developed previously[1-4] is used to solve for flowfield properties along the stagnation line between the shock and the body. All solutions presented are in an air mixture with eleven species and twenty-three reactions, as described in Ref. 4. The only changes made for this paper are to the vibration-dissociation coupling model, and to the absorption coefficients of some molecular band systems. These changes are described in more detail below.

Vibration-Dissociation Coupling

The vibrational energy equation used in the VSL equations has the following form in Cartesian coordinates.

$$\rho u^j c_{p_v}\frac{\partial T_v}{\partial x^j} = \frac{\partial}{\partial x^j}\left(\eta_v\frac{\partial T_v}{\partial x^j}\right) + \sum_s \rho_s U_s \frac{\partial h_{v_s}}{\partial x^j}$$
$$+\sum_s \rho_s A\frac{e_{v_s}(T_{tr})-e_{v_s}}{\tau_s} + \sum_s \rho_s \frac{e_{v_s}(T_e)-e_{v_s}}{\tau_e} \qquad (1)$$
$$+\sum_s (e_{v_s}-E_s)\left(\frac{\partial\rho_s}{\partial t}\right)_f - \sum_s (e_{v_s}-G_s)\left(\frac{\partial\rho_s}{\partial t}\right)_b$$

Vibration-vibration energy exchange rates between different vibrating molecules (N_2, O_2, NO, etc.) are not well known.[12] Therefore, only a single vibrational temperature has been used in the current model. An additional reason only one vibrational temperature has been used is the increased computational time associated with using different vibrational temperatures for each vibrating species.

The relaxation time, τ_s, used in the current model is that proposed by Park[13] which sums the relaxation time used by Millikan and White[14], τ_s^{MW}, with a high temperature correction factor as follows

$$\tau_s = \tau_s^{MW} + \frac{1}{c_s\sigma_s N_s}$$

where c_s is the average species molecular speed and σ_s is a limiting cross section calculated by[15]

$$\sigma_s = 10^{-17}\left(\frac{50{,}000K}{T_{tr}}\right)^2 cm^2$$

The second relaxation time in Eq. 1, which only affects the N_2 relaxation, is τ_e and is taken from the work of Lee[16] as curve fitted by Candler and Park[17] as

$$\log(p_c\tau_c) = 7.50(\log T_c)^2 - 57.0\log T_c + 98.70$$

for $T_c < 7000K$, and

$$\log(p_e\tau_e) = 2.36(\log T_e)^2 - 17.9\log T_e + 24.35$$

for $T_c >= 7000K$.

In the third term on the right side of Eq. (1), the factor A attempts to correct the relaxation rate for high temperature diffusion effects and is given by[15]

$$A = \left|\frac{T_{tr,sh}-T_v}{T_{tr,sh}-T_{v,sh}}\right|^{\left(3.5\exp\left(\frac{-5000K}{T_v}\right)-1\right)}$$

The changes made in the MCVDV model described earlier affect only the last two terms in Eq. 1. The first of these terms represents the vibrational energy lost in dissociation, and the second term represents the vibrational energy gained in recombination. The derivation of these terms is shown below.

Preferential MCVDV Model

In the nonpreferential model, a molecule involved in a collision with sufficient energy to cause dissociation will dissociate with equal probability from all vibrational energy levels. Of course, more dissociations will occur from the higher levels because less energy is required to reach the dissociation energy.

In the preferential model, molecules involved in collisions with sufficient energy to cause dissociation will have a greater probability of dissociating from higher vibrational energy levels. The probability of a molecule in the jth energy level dissociating is given by[9]

$$p_j = CF(j)N_j M(D-E_j) \qquad (2)$$

where N_j is the fractional number of molecules with vibrational energy E_j, $M(D - E_j)$ represents the number of collisions with sufficient energy to cause dissociation, F(j) is proportional to the probability that a molecule in the jth vibrational energy level will dissociate given a sufficiently energetic collision, and C is a constant such that $\Sigma p_j = 1$. F(j) is assumed to be[9]

$$F(j) = \exp\left(\frac{-(D-E_j)}{kU}\right) \qquad (3)$$

where U has dimensions of temperature and describes how quickly the probability of dissociation falls for low j. A value of U = ∞ forces F(j) = 1 and therefore corresponds to the nonpreferential model. Assuming a Boltzmann distribution in both the vibrational and translational modes, N_j and $M(D - E_j)$ can be expressed as

$$N_j = \frac{\exp\left(\frac{-E_j}{kT_v}\right)}{Q(T_v)} \qquad (4)$$

$$M(D-E_j)=\exp\left(\frac{-(D-E_j)}{kT_{tr}}\right) \quad (5)$$

Substituting Eq. 3 - 5 into Eq. 2 then gives for the probability of a dissociation from level j

$$p_j=\frac{C}{Q(T_v)}\exp\left(\frac{-E_j}{kT_F}\right)\exp\left[\frac{-D}{k}\left(\frac{1}{U}+\frac{1}{T_{tr}}\right)\right] \quad (6)$$

with

$$\frac{1}{T_F}=\frac{1}{T_v}-\frac{1}{T_{tr}}-\frac{1}{U}$$

The requirement that $\Sigma p_j = 1$ and the definition of the partition function then yields

$$C=\frac{Q(T_v)}{Q(T_F)}\exp\left[\frac{D}{k}\left(\frac{1}{U}+\frac{1}{T_{tr}}\right)\right]$$

Substituting this expression for C into Eq. 6 yields finally

$$p_j=\frac{\exp\left(\frac{-E_j}{kT_F}\right)}{Q(T_F)}$$

In Eq. 1, E_s, the amount of vibrational energy removed per dissociation, is then given by

$$E_s=\sum_j E_j p_j=\frac{\sum_j E_j \exp\left(\frac{-E_j}{kT_F}\right)}{Q(T_F)}$$
$$=kT_F^2\frac{\partial}{\partial T_F}[\ln Q(T_F)]$$

The amount of vibrational energy gained per recombination is simply equal to E_s with T_v in equilibrium with T_{tr}. With $T_v = T_{tr}$, $T_F = -U$. Therefore, G_s is given by

$$G_s=E_s(T_F=-U)$$

To obtain expressions for E_s and G_s, it is assumed that a simple harmonic oscillator models the vibrational energy. This is in contrast to Ref. 9, which used an anharmonic oscillator modeled by a Morse potential function. A simple harmonic oscillator is used here for computational simplicity. The differences between the simple harmonic oscillator and the anharmonic oscillator are also believed to have only a small effect for the flight conditions being investigated. The partition function for the simple harmonic oscillator is given by

$$Q(T_i)=\frac{1-\exp\left(\frac{-N\theta_v}{T_i}\right)}{1-\exp\left(\frac{-\theta_v}{T_i}\right)}$$

Then, the expressions for E_s and G_s simplify to

$$E_s=\frac{\theta_v}{\exp\left(\frac{\theta_v}{T_F}\right)-1}-\frac{N\theta_v}{\exp\left(\frac{N\theta_v}{T_F}\right)-1}$$
$$G_s=\frac{\theta_v}{\exp\left(\frac{-\theta_v}{U}\right)-1}-\frac{N\theta_v}{\exp\left(\frac{-N\theta_v}{U}\right)-1}$$

The last term that is different for the preferential model is the vibrational coupling factor, V, which adjusts the dissociation rate constant, k_f, to account for the effect of vibrational nonequilibrium. This factor is derived in Ref. 9, and has the form

$$V=\frac{k_f}{k_{eq}}=\frac{Q(T_{tr})Q(T_F)}{Q(T_v)Q(-U)}$$

Table I. Summary of Test Cases

Case	R_{nose} (cm)	V (km/s)	Altitude (km)	T_{wall} (K)
1634	74.7	11.36	76.42	615
1636	74.7	11.31	71.04	810
1637.5	74.7	11.25	67.05	1030
1639	74.7	11.14	63.11	1325
1640.5	74.7	10.97	59.26	1560
14	230	14	80	1650

In all the above equations, setting U = ∞ reduces the model to the nonpreferential model.

Radiation Model

The first order LTNE radiation model presented in Ref. 4 is used to calculate the radiative flux in the shock layer. However, experimental and theoretical studies by Laux and Kruger[18] and by Laux, Moreau, and Kruger[19] indicate that the normally accepted radiative transition probabilities for certain molecular bands are incorrect and need adjusting. Thus, as suggested in Ref. 18, the local thermodynamic equilibrium (LTE) absorption coefficients have been reduced in some of these studies by 10% for the N_2^+ first negative system and the N_2 second positive system, and by 15% for the N_2 first positive system from the values in Ref. 4. Although Ref. 18 also suggests changes for the NO beta, gamma, and O_2 Schumann-Runge bands, current studies of several flight conditions indicate that these changes have very little effect on the solution.

Discussion of Results

Table I gives a summary of the flight conditions investigated. The first five cases represent flight conditions at various times of the Fire 2 flight experiment. The first two flight times have significant amounts of nonequilibrium, while the last three contain progressively more equilibrium flow. The sixth case represents aerocapture conditions for a possible Martian return earth entry.

The freestream conditions and wall temperatures shown for the Fire 2 cases are those measured during the flight test at the times listed. The numerical solutions assume a fully catalytic wall boundary condition for the Fire 2 cases to be consistent with the beryllium heat shield used in the test vehicle and also include the radiative reflectance and absorption properties of the heat shield as a function of wavelength.

The last test case assumes the wall to be at 1650°K, which is the expected maximum temperature for a non-ablating heat shield. The solution assumes the surface for this case to be catalytic to ionic recombinations but

Table II. Summary of Results with U = D/3k

			Coupled Q_r		
Case	Δ	Q_c	Cont.	Lines	Absorbed
1634	5.77	188	13.4	4.97	12.4
1636	4.95	276	33.1	29.3	46.9
1637.5	4.68	356	56.2	67.1	93.3
1639	4.59	449	91.3	137	171
1640.5	4.53	538	120	220	248
14	13.8	57.9	61.5	44.3	106

Δ is shock standoff distance in cm.
Q_c is convective heat transfer in watts/cm^2.
Q_r is radiative heat flux to wall in watts/cm^2.
Lines and Continuum values are incident upon wall.

Table III. Summary of Results with U = 6D/k

			Coupled Q_r		
Case	Δ	Q_c	Cont.	Lines	Absorbed
1634	5.32	193	11.5	7.16	13.6
1636	4.69	281	29.6	31.4	46.9
1637.5	4.52	362	52.6	70.1	93
1639	4.47	444	82	133	161
1640.5	4.47	541	114	218	242
14	12.5	57	57.3	43.6	101

Δ is shock standoff distance in cm.
Q_c is convective heat transfer in watts/cm^2.
Q_r is radiative heat flux to wall in watts/cm^2.
Lines and Continuum values are incident upon wall.

non-catalytic to atomic recombinations and to be radiatively black.

The grid between the shock front and the body contains 99 points, which sufficiently resolves both nonequilibrium regions near the shock front and near the body. All cases assume shock slip conditions to conserve species and energy flux in the shock jump relations. A three temperature thermal model and a constant Lewis number diffusional model (with Le = 1.4) have also been used.

For all flight conditions, varying degrees of preferentiality were studied. Values of U of D/6k, D/3k, D/k, and 6D/k were used, with U=D/6k being the most preferential, and U=6D/k being practically nonpreferential. Solutions with U=6D/k and true nonpreferential solutions were only negligibly different. Therefore, this paper will assume that cases with U=6D/k are nonpreferential solutions. Also, all cases were run with both the reduced absorption coefficients and the nonreduced coefficients.

Preferential MCVDV Model

Table II summarizes results for the six cases with U=D/3k, which represents the amount of preferentiality recommended by Ref. 9. The first value in the table is the distance between the shock and the body, Δ. The second value is the total convective heat transfer, consisting of the contributions from conduction, diffusion, and catalycity. Also listed is the total radiative heat transfer absorbed by the wall. The radiative heat transfer has been coupled with the gasdynamic solution. The table also includes a breakdown of the coupled radiative heat transfer into line and continuum contributions. The absorbed value is less than the sum of the line and continuum contributions for the Fire 2 cases because the surface is not a black body.

Table III contains the same information as Table II, but with U=6D/k. Tables II and III therefore compare preferential and nonpreferential solutions. For all cases, the shock standoff distance is increased for the preferential solution, while for most cases the convective heat transfer is reduced or about the same. The continuum radiation is also higher for the preferential solutions, while the line contribution is lower for the earlier Fire 2 cases and slightly higher for the later times and for the 14 km/s case. The source of the decrease in the line contribution is currently being studied. The radiative flux absorbed is lower for the preferential case only for the earliest Fire 2 case. For the other cases, it is either unchanged or slightly higher. The probable reason for the slightly different behavior at different times of the Fire 2 cases is the amount of nonequilibrium in the flowfields of these cases. Since the earlier times contain significant amounts of nonequilibrium, the amount of preferentiality used has a significant effect on the solution. However, there is very little nonequilibrium present at the later times. Therefore, the amount of preferentiality used has only a mild effect on those solutions.

The differences in the flowfields for the preferential and nonpreferential solutions can be seen quite clearly in Fig. 1 and 2. Fig. 1 shows temperature and species concentration profiles for Fire 2 case 1634 with U=D/3k. Fig. 2 shows the same information with U=6D/k, a nonpreferential solution. Comparing the temperature profiles for the two cases, it is clear that the preferential solution increases the size of the nonequilibrium region behind the shock front. This behavior is expected for a preferential solution. Immediately behind the shock, the diatomic gases become vibrationally excited, and the molecules in the upper vibrational energy levels quickly dissociate due to the preferentiality, which leaves very few molecules in the upper vibrational energy levels. The molecules in the lower levels are much less likely to dissociate, reducing the dissociation rates. The lower dissociation rates in turn lengthen the vibrational relaxation times. Thus, the overall nonequilibrium region is lengthened.

The species concentration profiles in Fig. 1 and 2 also reflect the increased nonequilibrium region in the preferential case behind the shock front, particularly in the

N_2 and O_2 profiles. The concentration of N_2^+ is also especially important, since it is a very strong radiator. The peak concentration of N_2^+ occurs farther away from the shock front for the preferential solution than for the nonpreferential solution. This movement is caused by the lower dissociation rates and increased relaxation times of the preferential solution. Although the magnitude of the peak concentration of N_2^+ is nearly the same for both the preferential and the nonpreferential solutions, a high concentration of N_2^+ exists over a larger spatial region of the shock layer for the preferential case. Thus, the total concentration of N_2^+ in the shock layer is greater for the preferential solution. The effect of this increased concentration can be seen in Fig. 3 and 4, which show the spectral content of the wall radiation for the preferential and nonpreferential solutions of the 1634 case. The lower of the two plots in these figures is a detailed representation of the spectral radiative content. The upper plot uses line groupings over widths of the spectrum to show the summed contributions. The most obvious difference in these two plots in the increased radiation in the 2-4 eV range for the preferential case. The primary radiators in this range are N_2^+, N_2, and NO. Since the strongest of these radiators is N_2^+, its increased concentration is the main cause of the increased radiation in the 2-4 eV range and the increased continuum contribution seen in Tables II and III.

Fig. 5-8 present solutions of case 1634 with U=D/6k and U=D/k to show the effect of differing amounts of preferentiality. Fig. 5 and 6 show that increasing the preferentiality further increases the nonequilibrium region and the continuum contribution in the 2-4 eV range. Fig. 7 and 8 show that decreasing the amount of preferentiality decreases the nonequilibrium region and the continuum contribution in the 2-4 eV range, though they are still greater than the nonpreferential solution.

Fig. 9 compares the Fire 2 solutions with U=D/3k with the experimental data. The Fire 2 experiment contained three different heat transfer measurements. A total calorimeter measured the sum of the convective heat transfer and the absorbed radiative flux, which is shown on the figure as a solid line. Experimental values for the total calorimeter were not available above 1639 sec. as this is when the first heat shield began to melt. The corresponding numerical results are shown as squares. The other two gauges measured radiative intensity in the frequency ranges of 0.02 to 6.2 eV and 2 to 4 eV, respectively, from which the radiative heating can be computed assuming the gas to be optically thin. The first range covers most of the spectrum from low infrared through the visible range and is shown on the figure as a dashed line labeled Q_r (0.02 - 6.2 eV). The corresponding numerical results are shown as diamonds. The second range is a region consisting primarily of molecular band radiation of N_2^+ and NO. The experimental data in the 2 - 4 eV range was scattered over a large area, and is bounded by two dashed lines on the figure labeled Q_r (2 - 4 eV). The numerical results in this range are represented by circles. Also, all Fire 2 experimental values presented have been adjusted by the effective view factor of 0.84.

Fig. 10 shows the same information as Fig. 9 for a nonpreferential solution. Comparing Fig. 9 and 10, both the preferential and the nonpreferential solutions match the Fire 2 data reasonably well for the total heat transfer. For the preferential solution, percent errors range from 14 % at 1634 to 6.9 % at 1639. In the 0.02 - 6.2 and 2 - 4 eV ranges, however, the agreement with the flight data is not as good. At the early flight times, all the numerical results appear high. However, the preferential solution is significantly higher in the 2 - 4 eV range, with percent errors ranging from 165 % at 1634 sec. to 1.7 % at 1640.5 sec. The percent error of the nonpreferential solution is 64 % at 1634 sec., with the last three data points within the range of the experimental scatter. This behavior is due, once again, to the higher concentration of N_2^+ for the preferential solution. In the 0.02 -6.2 eV range, both solutions are about 42 % below the experimental values at the higher times. However, at the earlier flight times, the preferential solution is higher than the nonpreferential solution. Thus, the nonpreferential solution is more consistently low compared with the experimental results.

Returning for a moment to Tables II and III, there appears to be some inconsistency in the results at the higher flight times. At 1640.5, there is an increase in the continuum and line contributions and in the absorption for the preferential case, where at the lower times there was a decrease in the line contribution and in the absorption. This apparent inconsistency can be somewhat explained by viewing Fig. 11, which shows the temperature profiles and radiation spectrum for the preferential solution of Fire 2 case 1640.5. First of all, the temperature profile shows that the nonequilibrium region is very small, indicating that preferentiality has very little effect on equilibrium solutions. Tables II and III also illustrate this point, as the largest difference between the values in these tables at 1640.5 is a 5 % increase in the continuum contribution for the preferential case. A possible reason for some of the inconsistency at the higher times can be seen in the lower half of Fig. 11, which has a much different scale than the other radiation spectra shown. At this time, the contribution from the 2 -4 eV range is a small percentage of the overall radiation. Therefore, changes in the radiation from the ultraviolet range could be having a greater effect on the solution than the changes in the 2 - 4 eV range. However, the exact nature of the changes in the ultraviolet range is not yet known, but is under investigation.

While the Fire 2 cases sufficiently illustrate the effects of preferentiality, a few comments can also be made about the AOTV 14 km/s case. Comparing the values listed

Table IV. Summary of Results with U = D/3k and Reduced Absorption Coefficients

			Coupled Q_r		
Case	Δ	Q_c	Cont.	Lines	Absorbed
1634	5.78	188	13.6	6.21	12
1636	4.94	275	34.3	32.2	45.3
1637.5	4.68	355	55.1	69.3	92.9
1639	4.59	449	89.9	137	171
1640.5	4.54	539	119	221	248
14	13.8	59	61.3	44.9	106

Δ is shock standoff distance in cm.
Q_c is convective heat transfer in watts/cm^2.
Q_r is radiative heat flux to wall in watts/cm^2.
Lines and Continuum values are incident upon wall.

Table V. Summary of Results with U = 6D/k and Reduced Absorption Coefficients

			Coupled Q_r		
Case	Δ	Q_c	Cont.	Lines	Absorbed
1634	5.17	187	8.92	5.19	9.87
1636	4.69	279	28	30.1	46.5
1637.5	4.52	360	50.6	68.4	92.1
1639	4.48	446	82.2	134	162
1640.5	4.49	534	116	225	249
14	12.4	56.4	54.5	42.1	96.5

Δ is shock standoff distance in cm.
Q_c is convective heat transfer in watts/cm^2.
Q_r is radiative heat flux to wall in watts/cm^2.
Lines and Continuum values are incident upon wall.

in Tables II and III for this case, similarities to the later Fire 2 times can be seen. There is an increase in the continuum and line contributions and in the absorption for the preferential case, similar to the later Fire 2 times. However, Fig. 12 - 15 show that there is a significant amount of nonequilibrium for the 14 km/s case. Fig. 12 and 13 are a preferential solution while Fig. 14 and 15 are a nonpreferential solution. Once again, an increased nonequilibrium region behind the shock front can be seen for the preferential case, particularly in the N_2 and O_2 profiles. Also, notice that the radiation spectra are plotted on a different scale than the Fire 2 radiation spectra. The same increase in the contribution from the 2 - 4 eV range can be observed for the preferential case, and again is most likely due to an increase in the N_2^+ concentration. However, the source of the increased line contribution is unclear.

The comparisons of the numerical solutions with the Fire 2 data and the apparent inconsistencies among various cases illustrate that the amount of preferentiality has a complex effect on the solution. The reasons for this complex behavior is not currently well understood and needs further study.

Reduced Absorption Coefficients

The same cases described above were also run with the absorption coefficients of the N_2^+ first negative, N_2 first positive, and N_2 second positive systems reduced as described earlier. A summary of these results is shown in Tables IV and V. Table IV lists results for preferential solutions while Table V lists results for nonpreferential solutions. The comparisons between the preferential and nonpreferential solutions without the reduced absorption coefficients also apply for the solutions with the reduced absorption coefficients. The only difference appears to be that the line contribution is slightly higher for the preferential solution even at the earlier Fire 2 times, whereas for the nonreduced absorption coefficient cases the line contribution at the earlier times was slightly lower for the preferential cases. In general, though, the effect of preferentiality is the same for these cases.

The effect of reducing the absorption coefficients is not very clearly seen by comparing Tables IV and V with Tables II and III. There appear to be several inconsistencies between the nonreduced and the reduced solutions. For the preferential cases, the continuum contribution of the reduced coefficient cases is slightly higher for the earlier times, but slightly lower for the later times. The line contributions of the reduced coefficient cases are slightly higher or unchanged for all times, while the absorbed wall radiation is slightly lower for the earlier times and unchanged for the later times.

The trends are significantly different for the nonpreferential solutions. Here, the continuum contribution of the reduced coefficient cases is significantly lower at the earlier times, but slightly higher at the later times. This behavior is exactly the opposite from the preferential solutions. The line contribution and the absorbed heat transfer in the reduced coefficient cases are lower at the earlier times, but slightly higher at the later times. Any reductions in the continuum contributions should be primarily due to the reduced N_2^+ first negative absorption coefficient. Obviously, the preferentiality has a very complex effect on any solution, and this effect is made even more complex by changes in absorption coefficients.

Fig. 16 and 17 show temperature and species profiles and radiation spectrums for nonpreferential Fire 2 case 1634 with the reduced absorption coefficients. Comparing these figures with Fig. 2 and 4, it is clear that reducing the absorption coefficients has very little effect on the gasdynamic solution. On the other hand, the effect on the radiation spectra is obvious. The magnitude of the radiation in the 2 - 4 eV range is considerably lower for the reduced absorption coefficient case, further proof that the reduction in the continuum contribution is primarily due to the reduced N_2^+ first negative absorption coefficient.

Fig. 18 and 19 show the same information for a preferential solution with U=D/3k. Comparing these figures with Fig. 1 and 3, the same comments made for the nonpreferential solution also apply here. However, the magnitude of the effect of reducing the absorption coefficients appears to be smaller, indicating that the preferentiality has a stronger effect on the solution than reducing the absorption coefficients.

Fig. 20 compares the nonpreferential solution with the reduced absorption coefficients with the Fire 2 flight measurements. Comparing this figure with Fig. 9 and 10, the agreement with the experiment seems better with the reduced absorption coefficients. While the contribution in the 2 - 4 eV range is still high at the early flight time, it is not as high as before, with percent errors ranging from 40 % to 27 % at the earliest flight times. At the later flight times, the numerical data is within the range of the experimental scatter. Once again, the numerical results in the 0.02 - 6.2 eV range appear to be consistently low, with percent errors at the higher flight times around 45 %. However, at the earlier flight times, the reduced absorption coefficient results match the experimental results more closely than the nonreduced solutions. There does not appear to be much difference in the total heat transfer calculations. Since most of the total is convective heating, reducing the absorption coefficients does not have a large effect on the total heating.

For the AOTV 14 km/s case, the differences between the reduced and nonreduced coefficient cases also show some interesting behavior. For the preferential case, the convective heating increases slightly with the reduced coefficients. However, the convective heating decreases slightly with the reduced coefficients for the nonpreferential case. Other changes are also apparent in other values from Tables II - V for the 14 km/s case, further illustrating that more investigating needs to be conducted on the effects of preferentiality.

Conclusions

A preferential MCVDV model has been developed and evaluated by comparisons with a nonpreferential MCVDV model. The preferential solutions exhibit the proper behavior compared with the nonpreferential solutions. However, comparisons with Fire 2 flight measurements indicate better agreement with the nonpreferential model. A preferential temperature of U=D/3k also appears to introduce too large an amount of preferentiality into the solution for Fire 2 cases. A slightly larger value such as U=D/k may be more appropriate.

Solutions were also obtained using reduced absorption coefficients for the first negative band of N_2^+ and for the first and second positive bands of N_2. Comparisons with Fire 2 flight measurements for these solutions are encouraging, indicating that better calculations of radiative transition probabilities need to be included. However, the nonpreferential model still matches the flight measurements better than the preferential model. More investigations in the modeling of the N_2^+ first negative band may be needed. In all computations, this band is always very near LTE. If this is not true, the continuum contribution in the 2 - 4 eV range would be lowered at the earlier Fire 2 flight times, which have significant nonequilibrium.

Although the preferential model should be more physically correct than the nonpreferential model, current results indicate that little if any preferentiality is present in the Fire 2 flight conditions. Therefore, some modifications to the preferential model may be in order. Also, there are likely still questions concerning the modeling of some molecular LTNE and other radiative phenomena and research in these areas is continuing. It would appear that more theoretical and numerical studies in high temperature, nonequilibrium radiative phenomena are needed.

Acknowledgment

This work was primarily supported by NASA Grant NAG-1-1003 from the Langley Research Center, with Dr. Lin C. Hartung as technical monitor.

References

[1] Carlson, L. A. and Gally, T. A., "The Effect of Electron Temperature and Impact Ionization on Martian Return AOTV Flowfields," *Journal of Thermophysics and Heat Transfer*, vol.5, No. 1, January 1991, pp. 9-20.

[2] Carlson, L. A. and Gally, T. A., "Nonequilibrium Chemical and Radiation Coupling Phenomena in AOTV Flowfields," AIAA Paper 91-0569, January 1991.

[3] Gally, T. A., Carlson, L. A. and Green, D., "A Flowfield Coupled Excitation and Radiation Model for Nonequilibrium Reacting Flows," AIAA Paper 91-1463, June 1991.

[4] Gally, T. A. and Carlson, L. A., "An Approximate Local Thermodynamic Nonequilibrium Radiation Model for Air," AIAA Paper 92-2972, July 1992.

[5] Thompson, R. A., "Comparison of Nonequilibrium Viscous Shock Layer Solutions with Windward Shuttle Heating Data," AIAA Paper 87-1473, June 1987.

[6] Nicolet, W. E., "Advanced Methods for Calculating Radiation Transport in Ablation-Product Contaminated Boundary Layers," NASA CR 1656, September, 1970.

[7] Nicolet, W. E., "Rapid Methods for Calculating Radiation Transport in the Entry Environment," NASA CR 2528, April 1975.

[8] Treanor, C.E. and Marrone, P.V., "Effect of Dissociation on the Rate of Vibrational Relaxation," *Physics of Fluids*, vol. 5, No. 9, September, 1962, pp.1022-1026.

[9] Marrone, P.V. and Treanor, C.E., "Chemical Relaxation with Preferential Dissociation from Excited Vibrational Levels," *Physics of Fluids*, vol. 6, No. 9, September, 1963, pp.1215- 1221.

[10] Treanor, C. E. and Marrone, P. V., "Vibration and Dissociation Coupling Behind Strong Shock Waves," ***Dynamics of Manned Lifting Planetary Entry***, edited by S. M. Scala, John Wiley and Sons, New York, 1963, pp. 160-171.

[11] Gnoffo, P. A., Gupta, R. M. and Shinn, J. L. "Conservation Equations and Physical Models for Hypersonic Air Flows in Thermal and Chemical Nonequilibrium", NASA TP 2867, February 1989.

[12] Park, C., ***Nonequilibrium Hypersonic Aerothermodynamics***, John Wiley & Sons, New York, 1990, pp.166-167.

[13] Park, C., "Calculation of Nonequilibrium Radiation in the Flight Regimes of Aeroassisted-Orbital Transfer Vehicles," ***Thermal Design of Aeroassisted Orbital Transfer Vehicles***, Progress in Astronautics and Aeronautics, vol. 96, Ed. H.F. Nelson, AIAA 1985, pp.395-418.

[14] Millikan, R.C. and White, D.R., "Systematics of Vibrational Relaxation," *Journal of Chemical Physics*, vol. 39, No. 12, December, 1963, pp.3209-3213.

[15] Park, C., "Assessment of Two Temperature Kinetic Model for Ionizing Air," AIAA Paper 87-1574, June 1987.

[16] Lee, J.H., "Electron-Impact Vibrational Excitation Rates in the Flowfield of Aeroassisted Orbital Transfer Vehicles," ***Thermal Design of Aeroassisted Orbital Transfer Vehicles***, Progress in Astronautics and Aeronautics, vol. 96, Ed. H.F. Nelson, AIAA 1985, pp.197-224.

[17] Candler, G. and Park, C., "The Computation of Radiation from Nonequilibrium Hypersonic Flows," AIAA Paper 88-2678, June 1988.

[18] Laux, C. and Kruger, C., "Arrays of Radiative Transition Probabilities for the N_2 First and Second Positive, NO Beta and Gamma, N_2^+ First Negative, and O_2 Schumann-Runge Band Systems," *J. Quant. Spectrosc. Radiat. Transfer*, vol. 48, No. 1, pp.9-24, 1992.

[19] Laux, C., Moreau, S. and Kruger, C., "Experimental Study and Improved Modeling of High-Temperature Air Radiation," AIAA Paper 92-2969, July 1992.

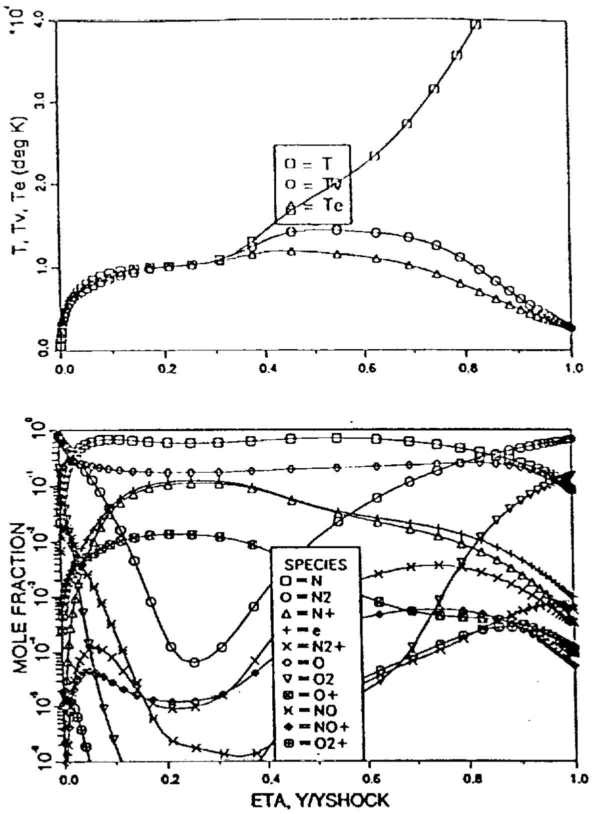

Fig. 1: Case 1634 - Air Results with U = D/3k, Temperature and Mole Fractions

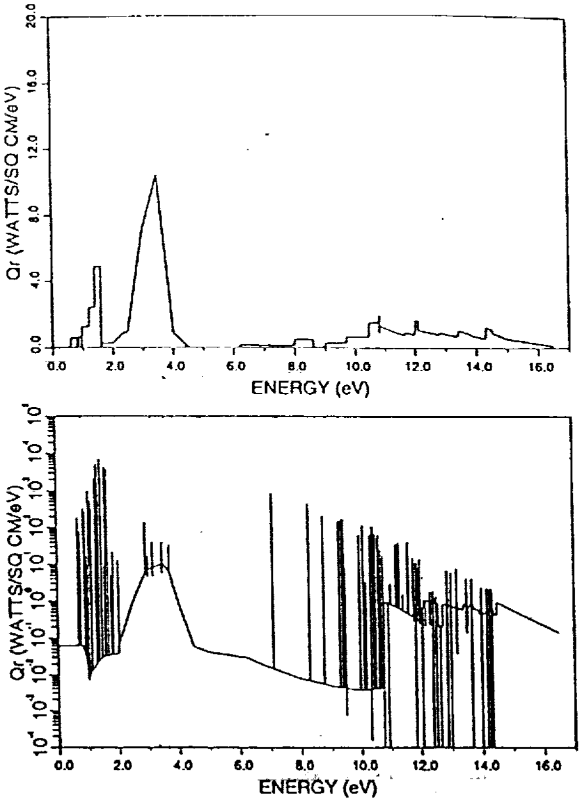

Fig. 3: Case 1634 - Air Results with U = D/3k, Grouped and Detailed Radiation Spectra

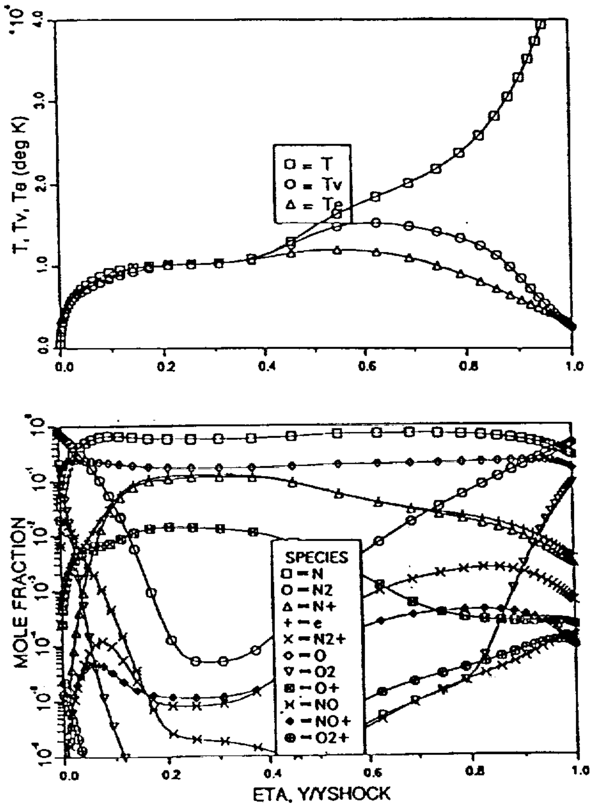

Fig. 2: Case 1634 - Air Results with U = 6D/k, Temperature and Mole Fractions

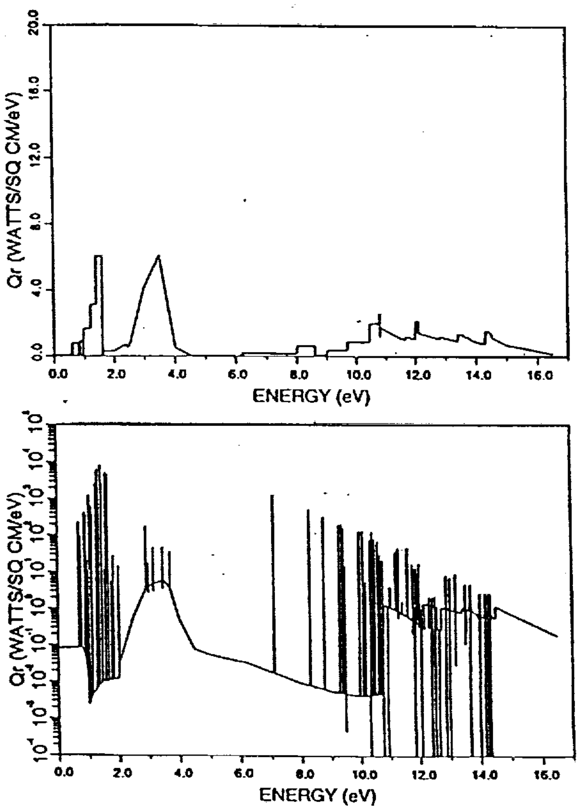

Fig. 4: Case 1634 - Air Results with U = 6D/k, Grouped and Detailed Radiation Spectra

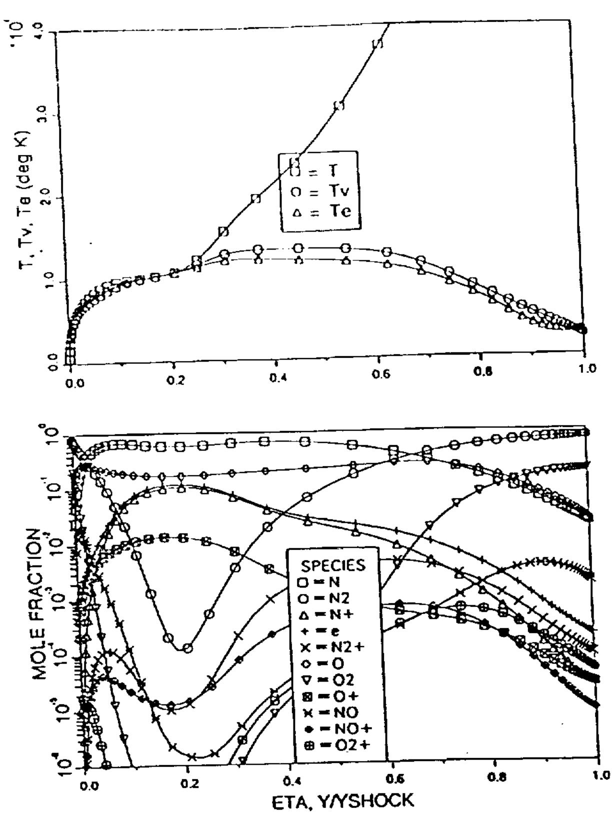

Fig. 5: Case 1634 - Air Results with U = D/6k, Temperature and Mole Fractions

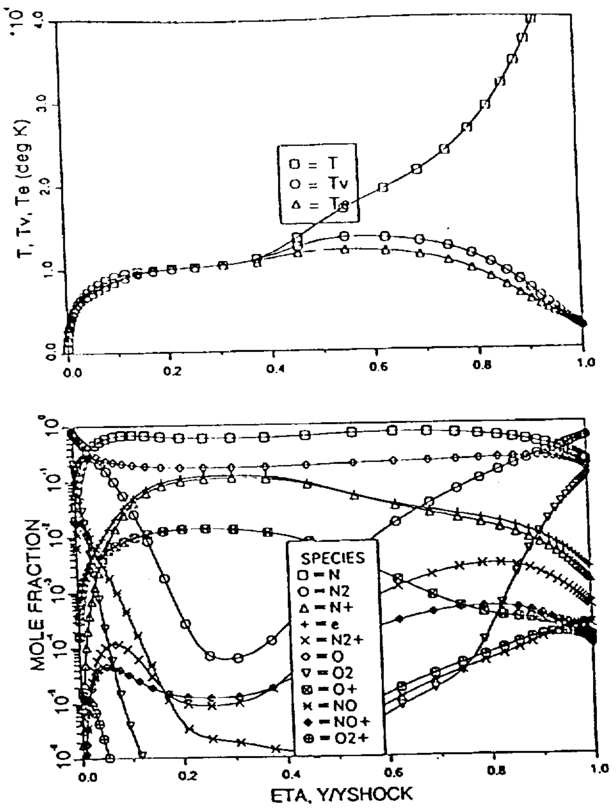

Fig. 7: Case 1634 - Air Results with U = D/k, Temperature and Mole Fractions

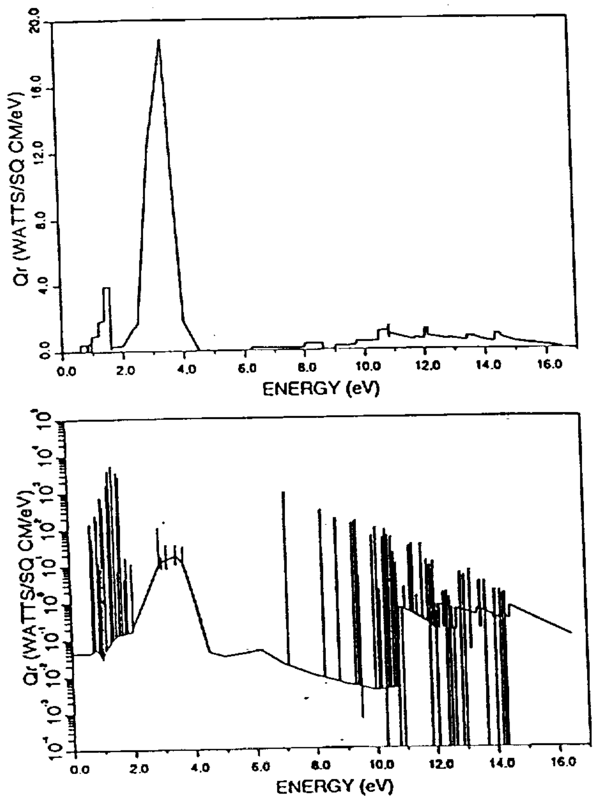

Fig. 6: Case 1634 - Air Results with U = D/6k, Grouped and Detailed Radiation Spectra

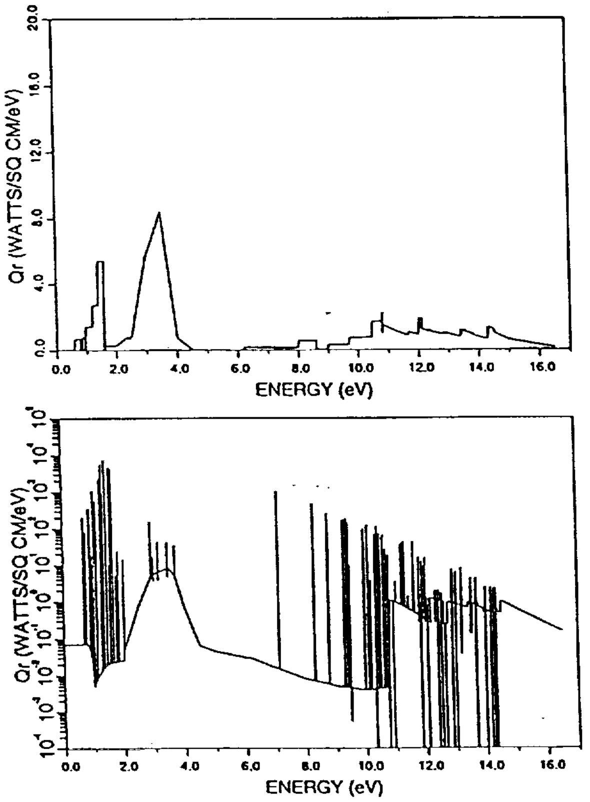

Fig. 8: Case 1634 - Air Results with U = D/k, Grouped and Detailed Radiation Spectra

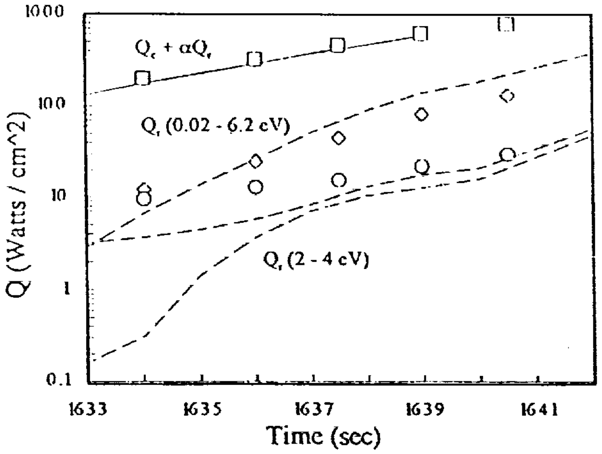

Fig.9: Comparison of Preferential Model (U=D/3k) With Fire 2 Flight Test Measurements

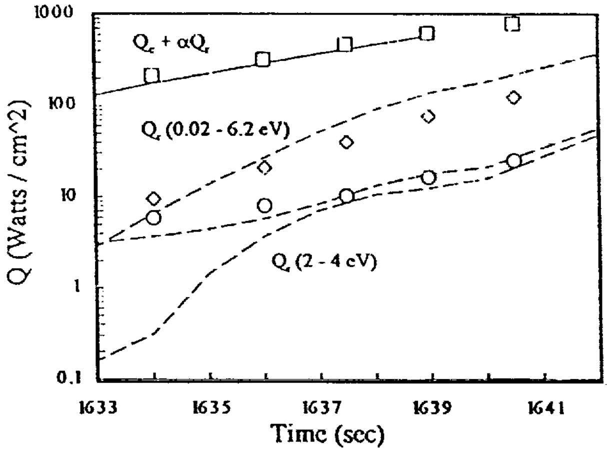

Fig.10: Comparison of Nonpreferential Model With Fire 2 Flight Test Measurements

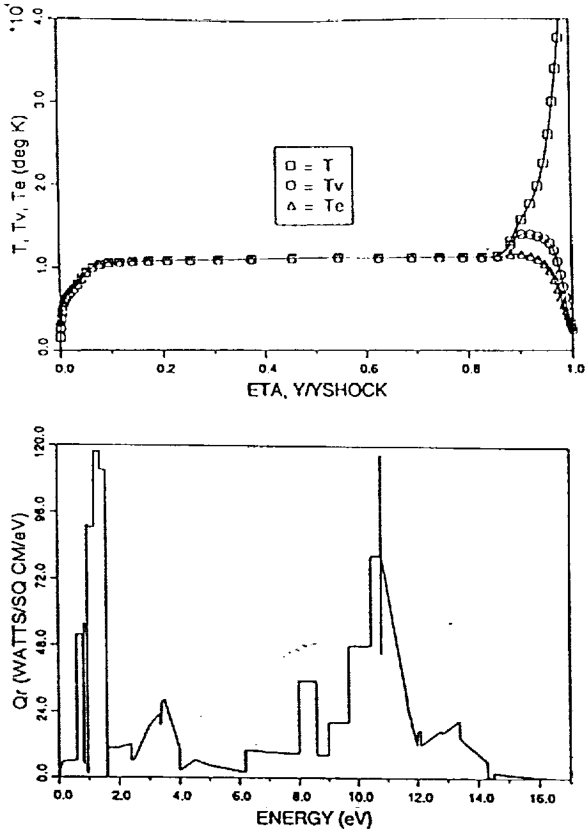

Fig. 11: Case 1640.5 - Air Results with U = D/3k, Temperature and Grouped Radiation Spectra

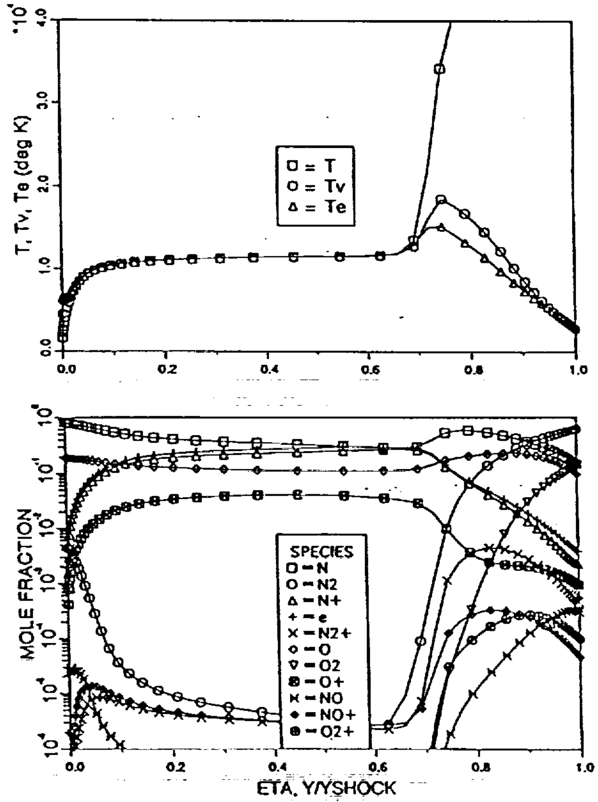

Fig. 12: Case 14 - Air Results with U = D/3k, Temperature and Mole Fractions

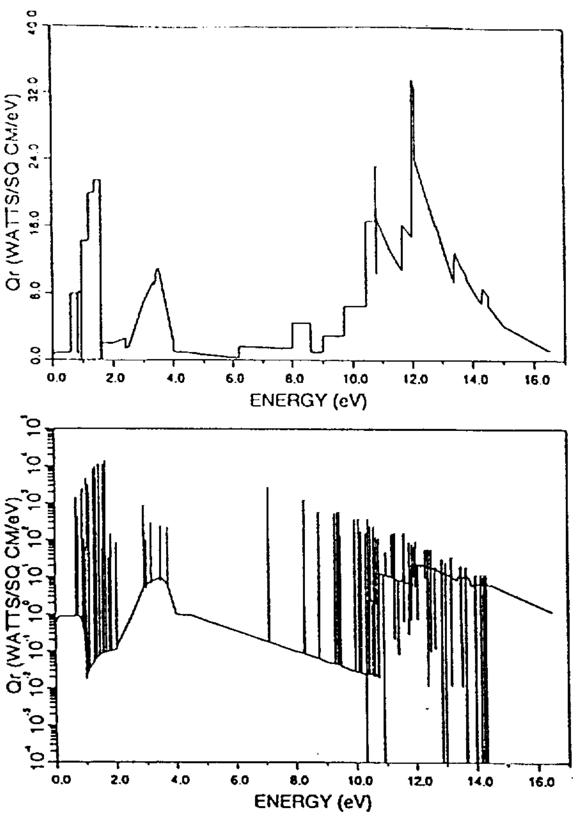

Fig. 13: Case 14 - Air Results with U = D/3k, Grouped and Detailed Radiation Spectra

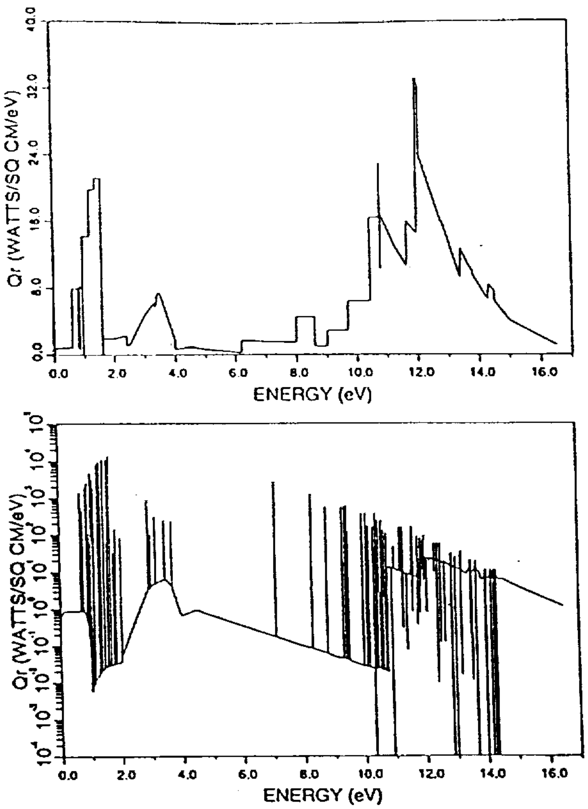

Fig. 15: Case 14 - Air Results with U = 6D/k, Grouped and Detailed Radiation Spectra

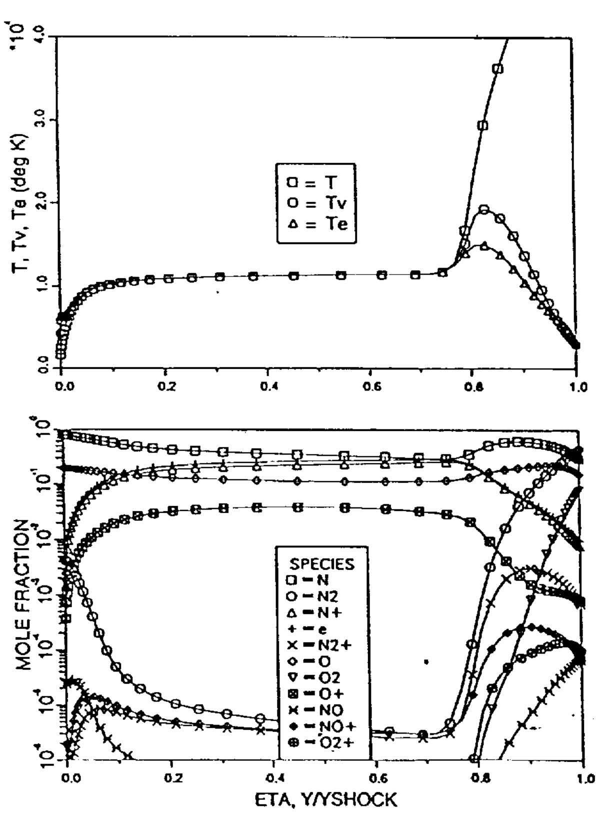

Fig. 14: Case 14 - Air Results with U = 6D/k, Temperature and Mole Fractions

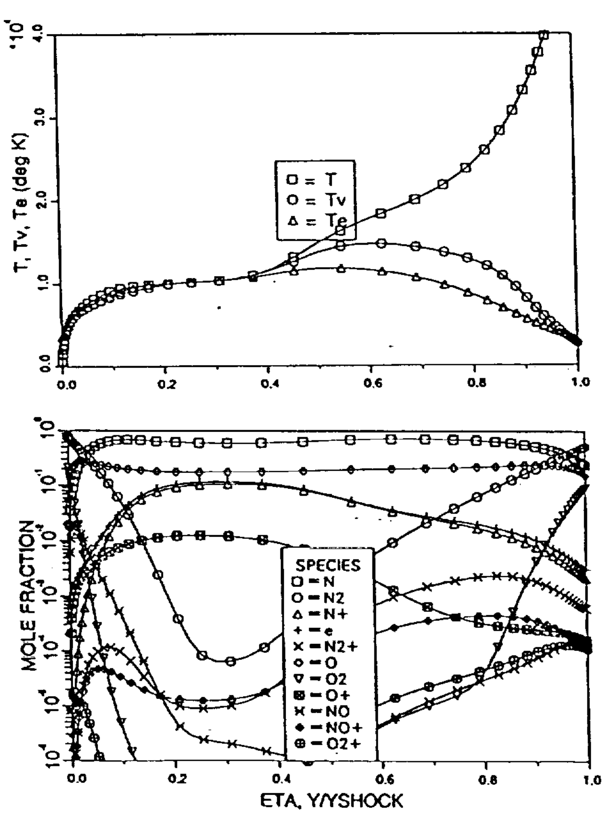

Fig. 16: Case 1634 - Air Results with U = 6D/k, Reduced Absorption Coefficients, Temperature and Mole Fractions

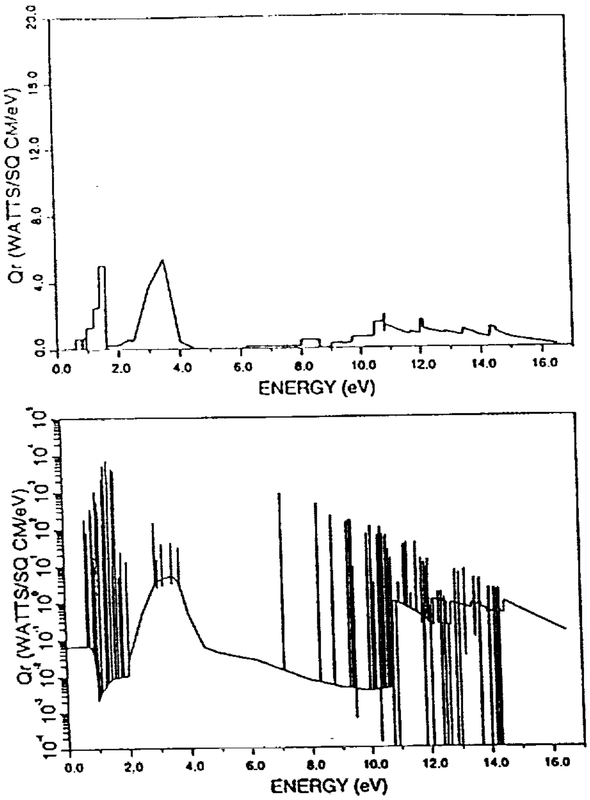

Fig. 17: Case 1634 - Air Results with U = 6D/k, Reduced Absorption Coefficients, Grouped and Detailed Radiation Spectra

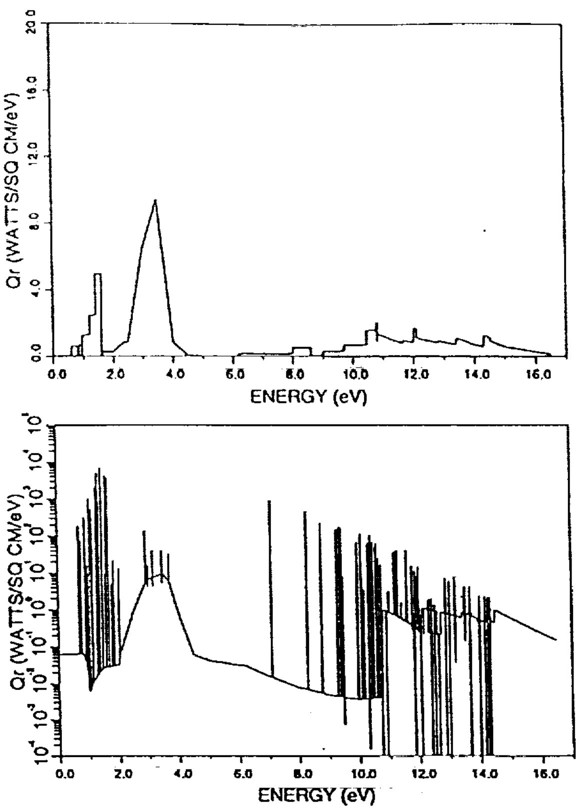

Fig. 19: Case 1634 - Air Results with U = D3/k, Reduced Absorption Coefficients, Grouped and Detailed Radiation Spectra

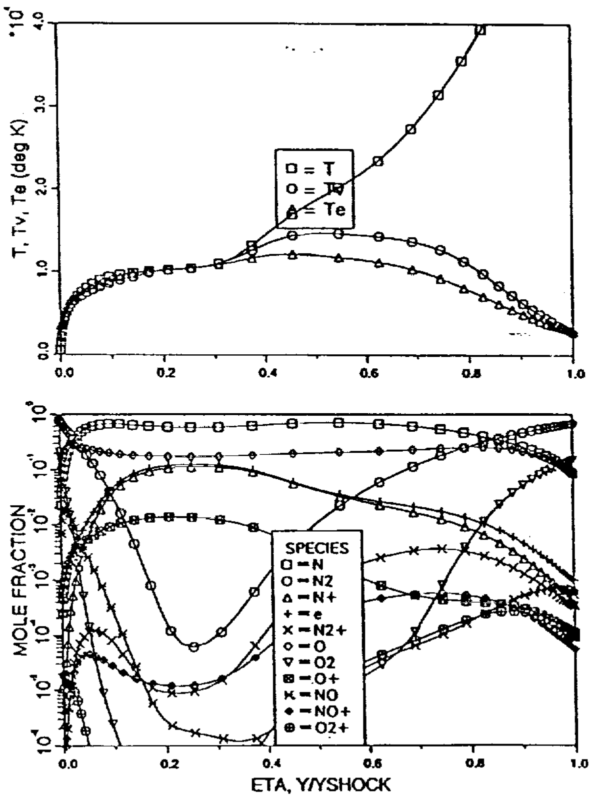

Fig. 18: Case 1634 - Air Results with U = D/3k, Reduced Absorption Coefficients, Temperature and Mole Fractions

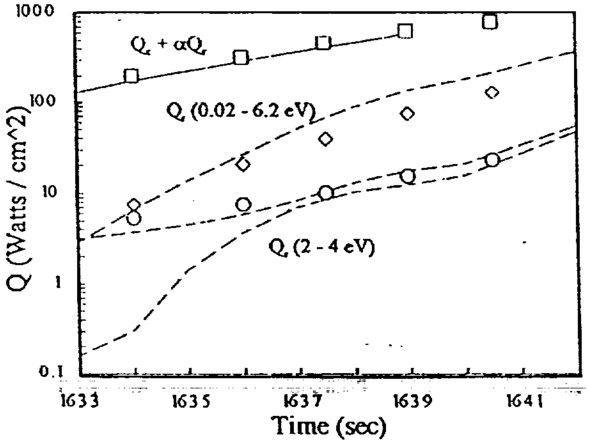

Fig.20: Comparison of Nonpreferential Model With Reduced Absorption Coefficients With Fire 2 Flight Test Measurements

AIAA 93-3230

Survey of Nonequilibrium Re-Entry Heating for Entry Flight Conditions

T. A. Gally and L. A. Carlson
Texas A&M University
College Station, TX

AIAA 24th Plasmadynamics & Lasers Conference

July 6-9, 1993 / Orlando, FL

Survey of Nonequilibrium Re-entry Heating for Entry Flight Conditions

Thomas A. Gally*
and
Leland A. Carlson**
Texas A&M University
College Station, Texas

Abstract

A viscous shock layer method has been developed which includes the effects of chemical and thermal nonequilibrium and is coupled with a radiation analysis which includes thermodynamic nonequilibrium effects. This code has been used to obtain solutions for a wide variety of nonequilibrium re-entry conditions in air. The results are tabulated and displayed graphically. Comparisons are made to similar results obtained for radiatively coupled equilibrium flow and conclusions drawn on the effect of nonequilibrium and in particular thermodynamic nonequilibrium on the radiative environment about re-entry vehicles.

Nomenclature

c_p = specific heat at constant pressure
$\dot{q}$ = heat flux
Q = heat flux
Rnose = nose radius
S = distance along body
T = Temperature
W = curvature smoothing factor
Δ = shock standoff distance
κ = curvature

subscripts

c = convective
e = electron or electronic
j = sphere-cone junction
r = radiative
v = vibrational
w = wall value
∞ = freestream value

Introduction

The proposal of a new class of re-entry vehicles in the recent past spurred the research into computational tools and theory for the calculation of nonequilibrium gas flows. The new vehicles, grouped under the general title of aero-assisted vehicles, are designed to use the upper levels of planetary atmospheres to achieve orbital/trajectory changes with a minimum expenditure of fuel. The application of such vehicles is for both interplanetary or lunar return missions and for inter-orbital runs such as between geosynchronous and low-earth orbits. The particular interest in nonequilibrium phenomena resulted from the long duration of time these new vehicles would spend in the upper atmosphere which previous re-entry vehicles rapidly passed through on their return to the planet surface. The now defunct Aeroassisted Flight Experiment (AFE) was partially designed with the goal of providing experimental evidence for the development, calibration, and verification of the physical and numerical models involved.

In support of the research push into nonequilibrium flows, the authors pursued the development of numerical tools for the rapid and accurate calculation of nonequilibrium effects (see Refs. 1-5). Attempts were made to use existing theories and methods in an integrated package which could be used for routine engineering analysis of re-entry flight conditions. The effects of chemical, thermal, and thermodynamic nonequilibrium along with radiative-gasdynamic coupling have been modeled in the single resulting program.

This paper provides a summary of this research effort with cited references for the interested reader to pursue. A survey of results for a diverse series of flight conditions and body sizes is also presented. These results may be used for interpolation or for comparison with other computation tools which may be developed.

Problem Formulation

Flow Field Model

The basis for the flowfield analysis is the VSL3DNQ program the authors obtained from NASA/Langley Research Center[6]. This code solves a viscous shock layer approximation to the Navier Stolkes equations for flow over axisymmetric bodies, possibly at angle-of-attack. Intended for use with nonequilibrium flows below 9 km/sec, the program included the effects of chemical nonequilibrium using a five species model (N, N_2, O, O_2, NO). Complete body solutions are obtained using a global shock shape iteration procedure. In this process an initial shock shape is either assumed or obtained from another analysis method. Using this shape, a new shock shape is calculated through the VSL solution over the body which may be used as input for subsequent calculations. Such "global" iterations are repeated, usually with shock shape relaxation and/or smoothing, until a converged shape is obtained.

Much of the authors' previous work has concentrated upon the solution of the stagnation streamline of spherical nose bodies. This solution is relatively insensitive to the full shock shape, and accurate solutions can be obtained by using an initial shock

---

* *Visiting Assistant Professor, Member AIAA*

** *Professor Aerospace Engineering, Associate Fellow AIAA* shape corresponding to another spherical nose body and scaling the stand-off distances to the calculated values. In this paper, the authors have considered the entire nose region of 60 degree sphere cones at zero angle-of-attack. For these cases, global flow solutions up to a surface distance 1.1 times the nose radius were calculated. This distance is well beyond the sphere-cone junction and is a region where the streamwise flow is supersonic everywhere except in the inner surface boundary layer. The latter is necessary to avoid shock shape convergence problems posed by an improper downstream boundary condition.

The original VSL3DNQ code has been extensively modified to extend its nonequilibrium capabilities. The chemistry package has been expanded to include up to 13 reacting species which are specified at run time by the user. Up to 50 chemical reactions may be input by providing both forward and reverse rates, or simply a forward rate with the reverse rate calculated internally via an equilibrium constant. The method of determining the equilibrium constants will be discussed in detail in a following section.

The program now includes thermal nonequilibrium effects through either a 2 temperature, T-T_v, or 3 temperature, T-T_v-T_e, model[4]. In the 2 temperature model, the rotational and heavy particle translational energies are assumed to be in equilibrium at the temperature T, while the vibrational, electronic, and free electron translational energies are assumed to be in equilibrium with each other at the temperature T_v which may be different from T. In the three temperature model, nonequilibrium may exist between the vibrational energy, T_v, and the electron and electronic energy, T_e.

For both models, energy exchange between the translational and vibrational modes is modeled using a modified Coupled Vibration-Dissociation-Vibration (CVDV) method[7,8]. The modifications consist of the relaxation time limiting and total rate adjustment suggested by Park[9,10]. Energy is exchanged between free electrons and heavy particles using an elastic collision model, and a free electron energy loss due to electron impact ionization and dissociation is included. For the three temperature model, an additional exchange of energy between electron and vibrational modes is modeled using the rates from J. H. Lee[11]. Also, two forms of the electron energy equation are available: a complete differential equation including all terms and an approximate algebraic equation obtained by dropping all terms but the exchange terms (translational to electron, vibrational to electron, and electron impact depletion). The latter equation is called the quasi-electron-electronic equation and is useful when starting solutions from an assumed initial profile or when low electron concentrations yield numerical difficulties with the differential equation.

The effect of multi-temperatures on chemical reactions rates has also been modeled. For the forward dissociation rates of O_2, N_2, and NO, the CVDV method includes a rate correction based upon the difference between T and T_v. This correction is applied to the forward rate calculated from T alone. The electron impact reactions forward rates are calculated using the electron temperature, T_e. For all other reactions the forward rates are calculated based upon the heavy particle translational temperature.

While reverse rates may be input directly, the authors generally use the reaction equilibrium constants to calculate the reverse rate. This method guarantees an equilibrium species concentration independent of the input rates. The equilibrium constants in turn are calculated from the species partition functions. Currently, the partition functions are obtained assuming fully excited rotational and vibrational modes without coupling between them, and assuming a harmonic oscillator[5]. The partition functions are always calculated using the three characteristic temperatures, thus yielding equilibrium constants which are also functions of all three temperatures.

This method for calculating the equilibrium constant influences the dependence of the reverse reaction rate. For the electron impact reactions, the reverse rates are strong functions of the electron temperature and weak functions of the heavy particle translational and/or vibrational temperature. The reverse rates for the dissociation reactions are obtained from the uncorrected forward rate (i.e. based upon T only) and the equilibrium constant. The reverse rates are thus strong functions of T and weaker functions of T_v and T_e. For the remaining reactions, the dependency can be complex and each requires an individual study.

Park[12] suggests an alternate method for calculating reverse rates using equilibrium constants and forward rates calculated using appropriate temperatures to obtain the expected reverse rate dependency. An attempt by the authors to use similar methods had the tendency to severly slow down some reactions like dissociation while greatly speeding up others like the ion exchange rates. In particular, in the shock front region where translation temperatures are high, the high rates for ion exchange were driving the chemical model to a quasi-equilibrium well before there was thermal equilibrium. Since the whole concept of using equilibrium constants in strong chemical and thermal nonequilibrium regions is in question, the authors opted for the previously described method which for their analysis yielded more reasonable results and had the expected physical consequence that chemical equilibrium was delayed until thermal equilibrium occurred.

The thermodynamic variables c_p and H are calculated using characteristic temperatures of rotation and vibration with the same basic assumptions as for the partition functions. The electronic contribution to both terms are modeled by including up to eight electronic energy levels.

The coefficients of conduction and viscosity are currently calculated using the collision cross section method of Gnoffo et al.[13] and includes multi-temperature effects. A full multicomponent diffusional model was developed[4] as part of this research program, but results obtained using this model are not significantly different from those obtained using a simple constant Lewis number, binary gas diffusion method[14]. Thus, all the results in this paper were obtained using the constant Lewis number model.

Radiation Model

The radiation method being used has been derived from the RADICAL (or RAD/EQUIL) code of Nicolet[15,16]. The radiation portion of RADICAL performs an equilibrium radiation analysis of a heated gas between a shock front and wall. The method includes the effects or self-absorption and variable wall optical properties. The radiating gas system includes all the primary radiating species of oxygen, nitrogen, argon, hydrogen and many common carbon molecules which appear around ablating surfaces.

Since the RADICAL code was developed with the goal of performing the radiation analysis efficiently and to good accuracy, the following approximations have been made. First, a tangent slab approximation is used. Under this assumption, the properties of the gas are assumed constant in the surface tangent directions. For blunt bodies where the shock standoff distance is typically on the order of 6 percent of the nose radius or less, this approximation should be valid. Second, to speed up calculation of the absorption function, the program uses line groupings internally for which the underlying continuum absorption may be assumed nearly constant. The frequency width of these line groupings is selectable by the user and have been chosen to reduce the error introduced by this assumption. Third, the molecular radiation contribution, while being a line phenomena, is calculated using a band model approximation. These models have been curve fit to experimental results and generally yield accurate results for the total radiative contribution but lack the detailed information more recent methods yield. However, due to the enormous computational savings obtained with the band model, their use is still desirable for many applications. Lastly, while most of the atomic bound-bound transitions are handled as discrete lines, the transitions between the very upper states of oxygen and nitrogen have been curve fit with band approximations. These transitions occur in the far infrared and do not contribute greatly to the total radiative flux; but again, the band modeling trades off some detailed information for the sake of computational efficiency.

The authors have developed two methods for including atomic local thermodynamic nonequilibrium (LTNE) effects, termed the first and second order models (Refs. 17,1,4,5). The first order model is based upon the observation by Wilson[18] that the lower three electronic states of nitrogen (and also oxygen) and all the upper states have relatively small energy differences between adjacent states when compared to the energy difference between the third and forth states. Thus a limiting step in the excitation to ionization of nitrogen and oxygen is the excitation between low lying states to the upper states across the 3-4 energy jump. Wilson used this observation to deduce a electron impact ionization rate for nitrogen which correlated well with the observed experimental ionization rates in nonequilibrium flow. The first order LTNE model extends this concept to a radiation model by adding the assumptions that the lower three states of both nitrogen and oxygen will be in near thermodynamic equilibrium with each other while the upper states will be in near equilibrium with each other and with the ionized state and free electrons. Since the relative populations of the ground state and ionized state are calculated using the chemical rate equation, this assumption ties the existence of thermodynamic equilibrium in nitrogen and oxygen to the formation of chemical equilibrium of the electron impact ionization reaction. These assumptions inhibit a burst of radiation which would otherwise be predicted near the electron temperature peak behind the shock front and yield results in good agreement with flight and shock tube measurements[4,5].

To test the validity of the assumption of equilibrium between the upper level states and the ionized states, the second order LTNE method was developed. In this method, thermodynamic equilibrium is still assumed between the low lying states and between the upper states, but excitation rates between the lower and upper levels as well as ionization rates from both the lower and upper levels are calculated using chemical rates deduced from the transition studies of Kunc and Soon[19,20]. The model is implemented by introducing the upper level states of both oxygen and nitrogen as two new species in the thermodynamic and chemical modeling of the flow, and allowing the relative nonequilibrium between all three species (ground, excited, and ionized) to be calculated as part of the flow field. Results from this method[4,5] indicate that while the second order method predicts less upper state deviation from equilibrium than the first order method, the two methods predict total radiation fluxes in close agreement and similar in spectral variance. Since the second order method suffers from being numerically stiff due to the fast chemical rates for ionization of the excited states, the first order method is more suitable for everyday calculations.

As in most equilibrium radiation analysis, the absorption coefficients used by RADICAL are calculated using radiative cross sections which have been evaluated in terms of the total species population density as opposed to the population of the particular states involved. Thus, a Boltzmann electronic state population is explicitly assumed. Also for equilibrium, the radiative source function reduces to simply the black body function. From the true nonequilibrium absorption and source functions[21] it can be shown[5] that the equilibrium values can be corrected for LTNE by factors determined from the ratio of actual state populations to state populations predicted by Boltzmann equilibrium. These LTNE correction factors are easily determined from the flow field solution and applied to the internal radiation calculations of RADICAL. This method of LTNE correction is common to both of the radiative nonequilibrium models described above.

The radiating molecular bands modeled by Nicolet in the RADICAL package include the contributions from N_2,O_2,NO, and N_2^+, with the later two species being the largest radiators. While this research has mainly concentrated upon the development of methods for atomic LTNE, it was desired to have some reasonable means for also estimating the molecular LTNE effects for the above species. A simple model had been developed by Carlson et al.[17] using arguments similar to the first order atomic LTNE model. However, due to the more complex methods of vibrational and electronic excitation in molecules and since most molecules do not show a decisive split in the energy states of ground and excited states this method was subsequently considered to be too approximate. Instead, the quasi-steady state method (QSSM) of Park[9] has been used. The basic assumption of this method is that given the total species number densities of atoms and molecules from a gasdynamic solution, the excited state populations of the molecules can be calculated by balancing the rates of excitation and de-excitation through electron collisions, heavy particle collisions, and spontaneous radiative emissions (radiative absorption is not included). This method typically predicts that the N_2^+ molecule is never far from being in Boltzmann equilibrium and thus may overpredict the amount of molecular radiation at lower flight speeds[5]. However, the level of molecular radiation is also very strongly influenced by the chemical dissociation model and the QSSM method suffices until there is more experimental verification of the currently available models.

Radiation-Gasdynamic Coupling

To account for the loss or gain of energy from the flowfield due to radiative effects, additional terms must be added to the governing energy equations. For the global energy equation, this process is straight forward since it is obvious that any change in the local radiative energy flux must come from some form of gasdynamic energy. The total flux quantity, $\nabla \vec{q}_r$, is thus added as a scalar property into the global energy equation.

If all the processes of radiative emission and absorption are considered, it is seen that portions of the total flux are being absorbed or emitted as: chemical energy in the breaking of bonds (photo-ionization and photo-dissociation), electronic energy state transitions, excess ionization energy imparted to freed electrons, free-free electron energy, changes in vibrational energy states, and changes in rotational energy states. These effects are listed in order of magnitude for radiation associated with very high speed reentry such as lunar or Martian return where atomic radiation dominates and radiative-gasdynamic coupling is very important. At lower velocities such as those for the AFE, molecular radiation dominates and the first source (chemical bonding energy) may be much less than the other sources. The magnitude of radiative-gasdynamic coupling is also much less important at the lower velocities. The last two sources potentially affect the vibrational and rotational energy although they are generally not included by investigators.

The fraction of the total energy flux not expended in breaking chemical bonds should be accounted for as a loss or gain of electron-electronic energy. To do this, however, requires a detailed accounting in the radiation transport model of each contributing process and the associated radiative energy flux. Such an effort was made by Stanley and Carlson[22] in their consideration of hypersonic precursor effects. A review of their work shows the great difficulty involved in extracting photo-ionization rates out of the radiation calculation even when only considering a simplified radiative model. The extensive numerical considerations which would have to be made in order to include photo-ionization processes and to properly model the gain or loss of electron-electronic energy are beyond the scope of this work. Further, the total effects of including these phenomena is not considered important at the conditions to be considered but may have some applicability to higher altitude, lower density flows.

Discussion of Results

Results have been obtained using the above analysis method for a wide range of nonequilibrium flight conditions as shown in Table I. The altitudes selected for analysis were 70, 75, and 80 km for which the corresponding freestream densities are 8.753E-5, 4.335E-5, and 1.995E-5 kg/m^3, respectively. Over this range, the flowfields vary from being predominately in chemical and thermal equilibrium to having large regions of nonequilibrium. This variance is shown by the temperature and mole fraction profiles in Figs. 1 and 2 for a flight velocity of 16 km/sec and altitudes of 70 and 80 km, respectively. At 70 km, the profiles indicate that equilibrium exists for approximately 85 percent of the shock layer although a slight gradient in both temperature and species concentration exist due to radiative cooling. By contrast, at 80 km only 65 percent of the shock layer is in equilibrium, and the nonequilibrium region near the shock front has almost tripled in size to one quarter of the standoff distance. The lower altitude represents a practical limit to the applicability of nonequilibrium analysis methods due to the numerical stiffness of most chemical nonequilibrium models. In fact, the solution at 16 km/sec and 70 km without radiative cooling could not be obtained due to numerical oscillations in the equilibrium region. Similarly, the altitude of 80 km may represent a practical limit for the applicability of continuum methods or at least shock fitted methods such as VSL due to the thickening of the shock itself as density decreases further.

Alt. (km)	*R*nose (m)	Vel. (km/sec)	Δ (cm)	Q_c (W/cm^2)	Q_r (W/cm^2)
80	2.3	9	13.51	8.75	1.55
80	2.3	10	13.95	16.0	4.12
80	2.3	12	12.31	36.0	27.8
80	2.3	14	10.70	64.1	90.1
80	2.3	16	9.66	97.8	197.
75	2.3	9	12.03	13.5	2.30
75	2.3	10	12.54	24.7	8.83
75	2.3	12	11.17	55.0	83.4
75	2.3	14	9.74	97.3	265.
75	2.3	16	8.73	151.	560.
70	2.3	9	11.27	26.4	3.60
70	2.3	10	11.83	43.0	21.2
70	2.3	12	10.70	88.8	216.
70	2.3	14	9.42	153.	644.
70	2.3	16	8.52	227.	1296.
75	1.0	9	6.09	21.5	1.80
75	1.0	10	6.28	39.3	5.10
75	1.0	12	5.52	85.1	45.1
75	1.0	14	4.82	150.	169.
75	1.0	16	4.34	226.	368.
75	0.5	9	3.46	34.0	1.08
75	0.5	10	3.49	52.6	2.72
75	0.5	12	3.23	128.	25.4
75	0.5	14	2.79	223.	98.0
75	0.5	16	2.54	340.	237.

Table I: Summary of Cases and Stagnation Results

The velocities selected for study ranged from 9 to 16 km/sec. The higher speed, 16 km/sec, is near the maximum reentry velocity of missions and configurations currently being considered. As seen in both Figs. 1 and 2, equilibrium ionization is almost 50 percent at this speed and almost no molecular species exist outside the shock front nonequilibrium layer. The radiative spectra at this speed is correspondingly dominated by atomic radiation processes as shown in Fig. 3. The lower part of this figure shows the actual detailed spectral content of the radiation incident upon the wall. The upper plot makes use of the internal line groupings in RADICAL to combine the total contributions of closely grouped lines and, due to the linear axis, is more indicative of the actual contribution of various spectral regions. Almost all of the radiation from molecules lies in the range of 2-4 eV and is obviously a small contribution to the total at this speed. By contast, at 9 km/sec the flow is ionized by less that 0.5 percent and the molecular nitrogen population is significant throughout the shock layer as seen in Fig. 4. The corresponding radiative spectra at 9 km/sec (shown in Fig. 5) consists almost solely of molecular radiation. Thus, this speed represents a lower limit for the need of an atomic nonequilibrium radiation model which is the main thrust of the author's work.

All the the bodies considered were 60°sphere cones with nose radii ranging between 0.5 and 2.3 m. The upper value corresponds to the well reported AFE configuration while the lower was selected as a reasonable minimum radius for a nonablating surface, although, as the results show, convective heating at most of the higher velocities would probably dictate the use of ablating materials. The flowfield model does not currently have a ablating surface capability, nor have the authors made any attempt to include typical ablation products in the radiation analysis, although the original RADICAL analysis does include many.

All the results which will be shown were calculated assuming a nonablating, radiative black wall surface at a fixed temperature of 1650°K. This temperature is a reasonable maximum temperature for the next generation, reusable, heat shield material. The gas mixture modeled was an eleven component air mixture using the chemical reaction set shown in Table II. The wall is assumed to be noncatalytic with respect to molecular recombinations, but catalytic to ionic recombinations. This is consistant with the properties of reactive cured glass (RCG) type surface materials. The diffusion model used is a constant Lewis model approach which yields results in good agreement with a full multi-component diffusional model developed by the authors as mentioned earlier.

The computational grid included 99 points between the fitted shock and the wall with clustering of grid points to both the shock front and wall thermal boundary layer. Downstream marching was performed using a step of ΔS=0.1 of the nose radius and was continued to a value of S/Rnose=1.1. Note that the sphere-cone junction occurs at S/Rnose=0.524 and at the last point, only the inner viscous boundary layer region was subsonic. To avoid numerical difficulties associated with the surface curvature discontinuity at the sphere-cone junction, a joining function was included which smooths the curvature jump out over the adjacent streamwise step locations. The function used is:

$$\kappa = \frac{1}{2} + \frac{1}{\pi} atan \left[\frac{(S_j - S)}{S_j} W \right]$$

The factor W controls the extent of smoothing; a value of 12 was used in the calculations.

	Reaction	A	B	E
1	$N_2 + M1 = N + N + M1$	3.00×10^{22}	-1.6	113200
2	$N_2 + M2 = N + N + M2$	7.00×10^{21}	-1.6	113200
3	$O_2 + M1 = O + O + M1$	1.00×10^{22}	-1.5	59500
4	$O_2 + M2 = O + O + M2$	2.00×10^{21}	-1.5	59500
5	$NO + M3 = N + O + M3$	1.10×10^{17}	0.0	75500
6	$NO + M4 = N + O + M4$	5.00×10^{15}	0.0	75500
7	$O + e^- = O^+ + e^- + e^-$	6.35×10^{15}	0.0	106200
8	$N + e^- = N^+ + e^- + e^-$	5.08×10^{16}	0.0	121000
9	$NO + O = N + O_2$	8.40×10^{12}	0.0	19450
10	$N_2 + O = NO + N$	6.40×10^{17}	-1.0	38400
11	$N_2 + e^- = N + N + e^-$	3.00×10^{24}	-1.6	113100
12	$N + O = NO^+ + e^-$	5.30×10^{12}	0.0	31900
13	$N + N = N_2{}^+ + e^-$	2.00×10^{13}	0.0	67500
14	$NO^+ + O = N^+ + O_2$	1.00×10^{12}	0.5	77200
15	$N^+ + N_2 = N_2{}^+ + N$	1.00×10^{12}	0.5	12200
16	$O^+ + NO = N^+ + O_2$	1.40×10^{5}	1.9	26600
17	$NO^+ + N = O^+ + N_2$	3.40×10^{13}	-1.08	12800
18	$O^+ + N_2 = N_2{}^+ + O$	9.10×10^{11}	0.36	22800
19	$NO^+ + N = N_2{}^+ + O$	7.20×10^{13}	0.0	35500
20	$O + O = O_2{}^+ + e^-$	1.10×10^{13}	0.0	80600
21	$O_2{}^+ + N = N^+ + O_2$	8.70×10^{13}	0.14	28600
22	$O_2{}^+ + N_2 = N_2{}^+ + O_2$	9.90×10^{12}	0.0	40700
23	$O_2{}^+ + O = O^+ + O_2$	4.00×10^{12}	-0.09	18000
24	$NO^+ + O_2 = O_2{}^+ + NO$	2.30×10^{13}	0.41	32600
25	$NO^+ + O = O_2{}^+ + N$	7.20×10^{12}	0.29	48600
26	$N + M5 = N^+ + e^- + M5$	2.34×10^{11}	0.5	120000

Rates in the form $k_f = A\,T^B \exp(-E/T)$.
$T = T_e$ in electron impact reactions.
$M1 = N, N^+, O, O^+$
$M2 = N_2, N_2{}^+, O_2, O_2{}^+, NO, NO^+$
$M3 = N, N^+, O, O^+, NO$
$M4 = N_2, N_2{}^+, O_2, O_2{}^+, NO^+$
$M5 = N, N^+$

Table II: Reaction System for Air

Stagnation Point Results

The stagnation point solutions for shock standoff distance, convective heat flux and radiative heat flux to the wall are included in Table I and shown graphically in Figs. 6-8. Results obtained by Sutton and Hartung[23] for equilibrium radiatively coupled shock layers are presented in Table III for comparison. The equilibrium results were linearly interpolated by density from the altitudes considered in Ref. 23. The stagnation standoff distances (Fig. 6) show a local maximum near 10 km/sec as has been seen in the equilibrium results. This maximum roughly divides the flight regimes for which molecular dissociation dominates the flow field (below 10 km/sec) from that for which ionization processes dominate (above 10 km/sec). The standoff distances themselves compare well with the equilibrium results but are consistantly higher as would be expected. The smallest difference is approximately 10 percent for the lowest altitude and largest nose radius. The difference increases with both increasing altitude and decreasing nose radius due to the larger extents of nonequilibrium in the shock layer with both changes.

Alt. (km)	*R*nose (m)	Vel. (km/sec)	Δ (cm)	Q_r (W/cm^2)
80	2.3	9	9.74	0.11
80	2.3	10	10.24	3.71
80	2.3	12	9.39	36.0
80	2.3	14	8.56	110.
80	2.3	16	7.93	242.
75	2.3	9	9.90	0.43
75	2.3	10	10.45	11.45
75	2.3	12	9.53	106.
75	2.3	14	8.59	314.
75	2.3	16	7.83	649.
70	2.3	9	10.08	1.37
70	2.3	10	10.65	28.7
70	2.3	12	9.67	258.
70	2.3	14	8.61	734.
70	2.3	16	7.75	1454.
75	1.0	9	4.30	0.20
75	1.0	10	4.56	6.86
75	1.0	12	4.23	71.8
75	1.0	14	3.88	227.
75	1.0	16	3.63	489.
75	0.5	9	2.15	0.11
75	0.5	10	2.29	4.30
75	0.5	12	2.14	49.0
75	0.5	14	1.99	162.
75	0.5	16	1.89	358.

Table III: Equilibrium Results from Ref. 23

It is of note that while the shock standoff distance is proportional to nose radius in equilibrium flows, the current nonequilibrium results do not show this simple dependancy. At 75 km/sec altitude, a good approximation to the relation between Δ and *R*nose at a constant velocity is given by:

$$\left(\frac{\Delta_1}{\Delta_2}\right) = 0.87\left(\frac{Rnose_1}{Rnose_2}\right)$$

However, insufficient data was generated to detemine if this relationship is valid for a wider range of nose radii or how this functionality varies with freestream density.

In Fig. 7 the calculated conductive heat transfer to the wall at the stagnation point are presented. The convective heat transfer shown is the sum of the heat fluxes due to conduction and due to catalysis of the ionic species at the surface. As expected, as density or velocity are increased, total energy flux in the shock layer increases and the wall heating rate rises, although not in direct proportion. Also, as the nose radius of the body is decreased, the convective heat rate increases due to the thinning of the thermal and viscous boundary layers on the body.

An attempt was made to curve fit the entire convective heat transfer results as a single power function of density, velocity and nose radius using a least squares technique. Examination of the curve fit results showed that a better fit for the upper velocities could be obtained by leaving the 9 km/sec data out of the process. The variation of heating with velocity apparently experiences a functional change at around the 9 - 10 km/sec range, much like what was seen for the standoff distance. This change could be due to the additional effect of ionic catalytic heating which accompanies significant ionization of the shock layer flow, i.e. above 10 km/sec. The final suggested fit is:

$$Q_c = 115.3\rho^{0.553}V^{2.36}R_{nose}^{-0.540}(1 - h_w/h_\infty)$$

The calculated convective heating values are shown reduced by this function in Fig. 9. The curve fit is seen to reproduce the original data to within 6 percent at all speeds, and within 3 percent for the velocities above 10 km/sec.

The calculated stagnation point radiative heat fluxes to the body surface are shown in Fig. 8. As with convective heating, the radiative heating is seen to increase with both increasing density and velocity. The reasons for increase are more complex, however, and are closely tied to the equilibrium temperature, density, and composition of the gas mixture behind the shock front. Also, since the total radiative flux depends upon the thickness of the radiating gas layer, the wall radiative flux decreases with decreasing nose radius since the shock standoff distances also decrease. Because of the complex dependancy of the factors influencing the radiative heating, all attempts to curve fit the calculated results with simple functions of density, velocity and nose radius resulted in approximations with unacceptable errors.

The comparison of nonequilibrium and equilibrium radiative heating rates in Tables I and III shows that the nonequilibrium results are mostly below that predicted by equilibrium. This would not be the case if the atomic LTNE corrections were not being used to reduce the radiation from the thermal nonequilibrium region where the electron temperature reaches its maximum. The exceptions to this trend are all the 9 km/sec cases and the 10 km/sec case at 80 km; these are the cases which are most dominated by molecular radiation. The conclusion from this is that the current method does predict an added molecular radiative contribution from the thermal nonequilibrium regions. However, a conclusion reached in Ref. 5 from the comparison of predicted to measured Fire 2[24] results was that the current QSSM method for molecular LTNE prediction may in fact be over estimating the amount of molecular species equilibrium and thus the amount of molecular nonequilibrium radiation. Thus, the enhanced nonequilibrium radiation at lower speeds may be in error.

It is of interest to note the impact of radiative cooling on the results. To show this, the radiative heating data in Table I which were obtained with radiative cooling are plotted againt the similar results without radiative cooling in Fig. 10. The dashed line in this figure has a slope of one. Thus, all the data points would lie on this line if radiative cooling did not affect the solution. The gradual departure of the data from this line indicates the increasing impact of radiative cooling on the final results. Table IV provides a tabulation of the radiatively uncoupled results for stagnation standoff distance, convective heating and radiative heating. The last column of this table are equilibrium data obtained by linear interpolation by freestream density of the results in Ref. 23. In

Alt. (km)	Rnose (m)	Vel. (km/sec)	Δ (cm)	Q_c (W/cm^2)	Q_r (W/cm^2)
80	2.3	9	13.59	8.79	1.53
80	2.3	10	14.15	17.5	4.75
80	2.3	12	12.66	41.7	31.4
80	2.3	14	11.33	76.8	114.
80	2.3	16	10.68	118.	275.
75	2.3	9	12.14	14.0	2.56
75	2.3	10	12.72	27.4	11.2
75	2.3	12	11.79	65.4	114.
75	2.3	14	10.76	123.	405.
75	2.3	16	10.38	185.	1008.
70	2.3	9	11.32	26.2	3.41
70	2.3	10	12.00	45.5	27.2
70	2.3	12	11.32	98.8	319.
70	2.3	14	10.82	171.	1165.
70	2.3	16	–	–	–
75	1.0	9	6.08	21.0	1.64
75	1.0	10	6.26	38.6	4.69
75	1.0	12	5.57	93.4	50.9
75	1.0	14	5.13	175.	217.
75	1.0	16	4.81	267.	514.
75	0.5	9	3.47	34.0	1.03
75	0.5	10	3.53	53.3	2.77
75	0.5	12	3.29	137.	26.8
75	0.5	14	2.83	245.	112.
75	0.5	16	2.68	387.	291.

Table IV: Summary of Radiatively Uncoupled Results

general, the effect of radiative cooling is to reduce all three of these variables. The results in Table IV were not converged to the same shock shape criteria as the radiative coupled data and thus there appear to be some discrepencies between Tables I and IV; in particular, some of the lower speed cases falsely indicate that the standoff distance and/or the heating rates increased with the addition of radiative cooling.

Nose Region Solutions

The variations of shock standoff distance, convective heat flux and radiative heat flux with distance along the body are shown in Figs. 11 through 13. The data in this figures have been nondimensionalized by the values at the stagnation point for each case in order to reduce all the data to a comparable scale. The data have also been grouped by flight velocity which provides the best comparison of related data. From the plots of shock standoff distance it is seen that the shock shape in the nose region is relatively unaffected by nose radius or altitude effects while a variation with velocity is noticable, but not dramatic. Interestingly, the greatest relative rate of growth of the standoff distance occurs for the 12 km/sec cases. Since the component of velocity normal to the conical body at 12 km/sec is 10.39 km/sec, the maximum growth at this speed may be related to the maximum in stagnation point standoff distance which was seen to occur near 10 km/sec. Also, the greatest scatter in data occurs for the 10 km/sec cases, but the reason for this behaviour is unclear. This scatter does however have an impact on the radiative heat fluxes as will be seen below.

With the exception of the 9 km/sec cases, the convective heating data shown in Figs. 12 all reduce to a narrow distribution range, although there is a slight trend for the smallest nose radius results to show a greater value in the aft regions. This trend is probably due to the merging of the shock front nonequilibrium layer with the thermal boundary layer as the standoff distance decreases. The data for the 9 km/sec are all noticably higher in the aft regions then that seen for the other velocities. This higher relative heating may be due to either a lack of significant catalytic heating or to a consistant merging of the shock and thermal layers at this speed. The oscilations in the profiles around S/Rnose = 0.6 in all cases is due to both the smoothing of the surface curvature near the sphere-cone junction and numerical problems with the solution when the curvature varies too greatly.

Finally, the downstream variations of radiative flux are shown in Fig. 13. Forward of the sphere-cone junction, the trends for each velocity are relatively consistant but the amount of radiation decrease between the stagnation point and juncture decreases with increasing velocity. A noticable exception to this is the highest radiation flux case (16 km/sec at 70 km) which has a trend significantly different from the other cases at the same velocity. The altered variation for this condition is most likely due to the large amount of radiation cooling which also occurs. Aft of the junction, the radiation flux increases in almost all the cases due to the growth of the shock standoff distance and thus the thickness of the heated gas layer. Also, in the aft region a much larger difference exists between the data for each velocity. Here, the general trend is for the relative amount of aft radiation to be higher for lower densities and smaller nose radii. The greatest difference between cases is seen for the 10 km/sec case which as noted above also had the greatest difference in shock standoff distance variations. As may be expected, the thicker shock layers correspond to the higher heat fluxes, but why this wide difference occurs at this velocity is unknown.

Conclusion

An analysis method which includes such phenomena as viscous effects, chemical nonequilibrium, thermal nonequilibrium, thermodynamic nonequilibrium and radiation-gasdynamic coupling has been developed for the analysis of flow over re-entry and aeroassisted flight vehicles. This analysis method has been used to generate results over the nose region of a 60° sphere-cone body at a number of nonequilibrium flight conditions. Comparison of these results with other equilibrium analsis indicates that the net effect of nonequilibrium and in particular atomic LTNE in the shock layer is to reduce the total radiative heat load to the vehicle surface. There is an indication that at low speeds molecular LTNE may enhance the nonequilibrium radiation, but these results are currently in question.

Acknowledgement

This work was primarily supported by NASA Grant NAG-1-

1003 from the Langley Research Center, with Dr. Lin C. Hartung as technical monitor.

References

[1] Carlson, L. A. and Gally, T. A., "Effect of Electron Temperature and Impact Ionization on Martian Return AOTV Flowfields," *Journal of Thermophysics and Heat Transfer*, vol. 5, No. 1, January 1991, pp. 9-20.

[2] Carlson, L. A. and Gally, T. A., "Nonequilibrium Chemical and Radiation Coupling, Part I: Theory and Models," *Journal of Thermophysics and Heat Transfer*, vol. 6, No. 3, July-September 1992, pp. 385-391.

[3] Carlson, L. A. and Gally, T. A., "Nonequilibrium Chemical and Radiation Coupling, Part II: Results for AOTV Flowfields," *Journal of Thermophysics and Heat Transfer*, vol. 6, No. 3, July-September 1992, pp. 392-399.

[4] Gally, T. A., Carlson, L. A. and Green, D., "A Flowfield Coupled Excitation and Radiation Model for Nonequilibrium Reacting Flows," *Journal of Thermophysics and Heat Transfer*, vol. 7, No. 2, April 1993, pp. 285-293.

[5] Gally, T. A. and Carlson, L. A., "An Approximate Local Thermodynamic Nonequilibrium Radiation Model for Air," AIAA Paper 92-2972, July 1992.

[6] Thompson, R. A., "Comparison of Nonequilibrium Viscous Shock Layer Solutions with Windward Surface Shuttle Heating Data," AIAA Paper 87-1473, June 1987.

[7] Treanor, C. E. and Marrone, P. V., "Effect of Dissociation on the Rate of Vibration Relaxation," *Physics of Fluids*, vol. 5, No. 9, September 1962, pp. 1022-1026.

[8] Marrone, P. V., "Inviscid, Nonequilibrium Flow behind Bow and Normal Shock Waves, Part I. - General Analysis and Numerical Examples," Cornell Aeronautical Laboratory Report No. QM-1626-a-12(I), May 1963.

[9] Park, C., "Calculation of Nonequilibrium Radiation in the Flight Regimes of Aeroassisted Orbital Transfer Vehicles," in ***Thermal Design of Aeroassisted Orbital Transfer Vehicles***, Progress in Astronautics and Aeronautics, Vol. 96, Ed. H. F. Nelson, AIAA, 1985, pp. 395-418.

[10] Park, C., "Assessment of Two Temperature Kinetic Model for Ionizing Air," AIAA Paper No. 87-1574, June 1987.

[11] Lee, J. H., "Electron-Impact Vibrational Excitation Rates in the Flowfield of Aeroassisted Orbital Transfer Vehicles," in ***Thermophysical Aspects of Re-entry Flows***, Progress in Astronautics and Aeronautics, Vol. 103, Eds. J. N. Moss and C. D. Scott, AIAA, 1986, pp. 197-224.

[12] Park, C., Howe, J. T., Jaffe, R. L., and Candler, G. V., "Chemical-Kinetic Problems of Future NASA Missions," AIAA Paper 91-0464, January 1991.

[13] Gnoffo, P. A., Gupta, R. N., and Shinn, J. L.,, "Conservation Equations and Physical Models for Hypersonic Air Flows in Thermal and Chemical Nonequilibrium," NASA TP 2867, February 1987.

[14] Miner, E. W. and Lewis, C. H., "Hypersonic Ionizing Air Viscous Shock Layer Flows over Nonanalytic Blunt Bodies," NASA CR-2550, May 1975.

[15] Nicolet, W. E., "Advanced Methods for Calculating Radiation Transport in Ablation-Product Contaminated Boundary Layers," NASA CR 1656, September 1970.

[16] Nicolet, W. E., "Rapid Methods for Calculating Radiation Transport in the Entry Environment," NASA CR 2528, April 1975.

[17] Carlson, L. A., Bobskill, G. J., and Greendyke, R. B., "Comparison of Vibration Dissociation and Radiative Transfer Models for AOTV/AFE Flowfields," *J. of Thermophysics and Heat Transfer*, vol. 4, No. 1, January 1990, pp. 16-26.

[18] Wilson, J., "Ionization Rate of Air Behind High Speed Shock Waves," *The Physics of Fluids*, vol. 9, No. 10, October 1966, pp. 1913-1921.

[19] Kunc, J. A. and Soon, W. H., "Collisional Radiative Nonequilibrium in Partially Ionized Atomic Nitrogen," *Physical Review A*, vol. 40, No. 10, November 15, 1989, pp. 5822 ff.

[20] Kunc, J. A. and Soon, W. H., "Thermal Nonequilibrium in Partially Ionized Atomic Oxygen," *Physical Review A*, vol. 41, No. 2, January 15, 1990, pp. 825 ff.

[21] Chapin, C. E., "Nonequilibrium Radiation and Ionization in Shock Waves," AA&ES Report, June 1967, Purdue, Univ., Lafayette, Ind.

[22] Stanley, S. and Carlson, L. A., "The Effects of Shock Wave Precursors Ahead of Hypersonic Entry Vehicles," AIAA Paper 91-1465, June 1991.

[23] Sutton, K. and Hartung, L. C., "Equilibrium Radiative Heating Tables for Earth Entry," NASA TM 102652, May 1990.

[24] Cauchon, D. L., McKee, C. W., and Cornette, E. S., "Spectral Measurements of Gas-Cap Radiation During Project Fire Flight Experiments at Reentry Velocities Near 11.4 Kilometers per Second," NASA TM X-1389, October 1967.

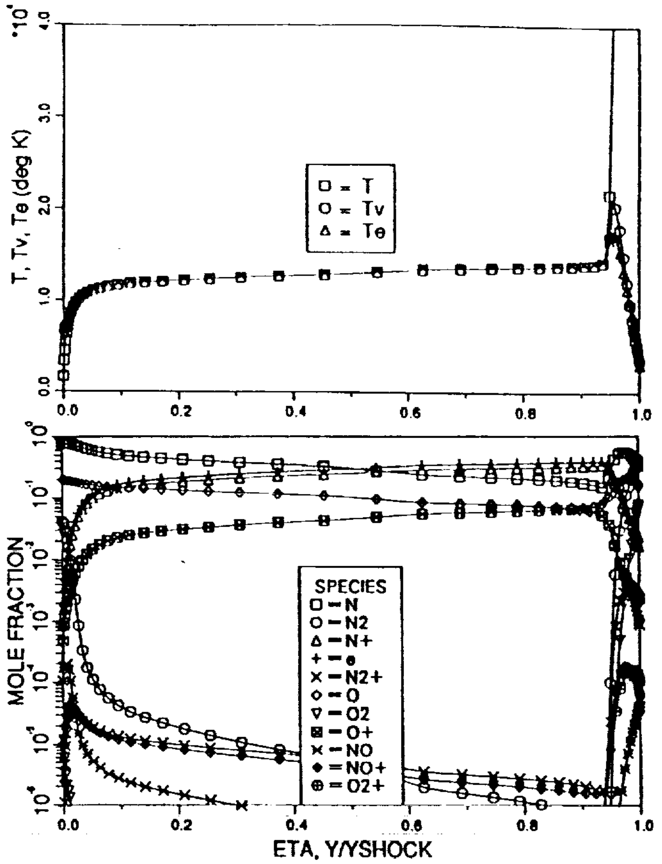

Figure 1: Stagnation Temperature and Mole Fraction Profile

*R*nose = 2.3 m, V = 16 km/sec, H = 70 km

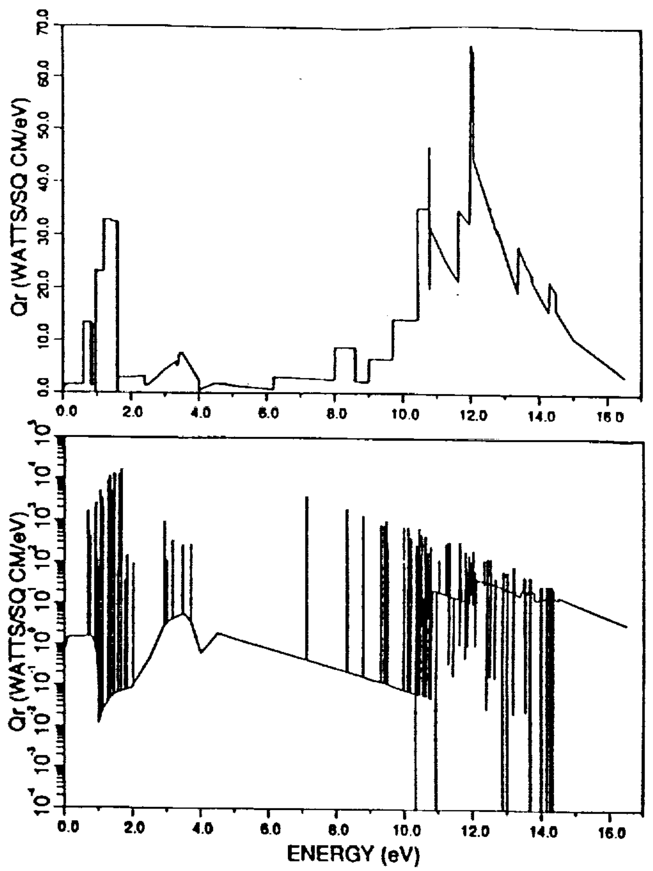

Figure 3: Radiative Heat Flux, Grouped and Detailed Spectra

*R*nose = 2.3 m, V = 16 km/sec, H = 80 km

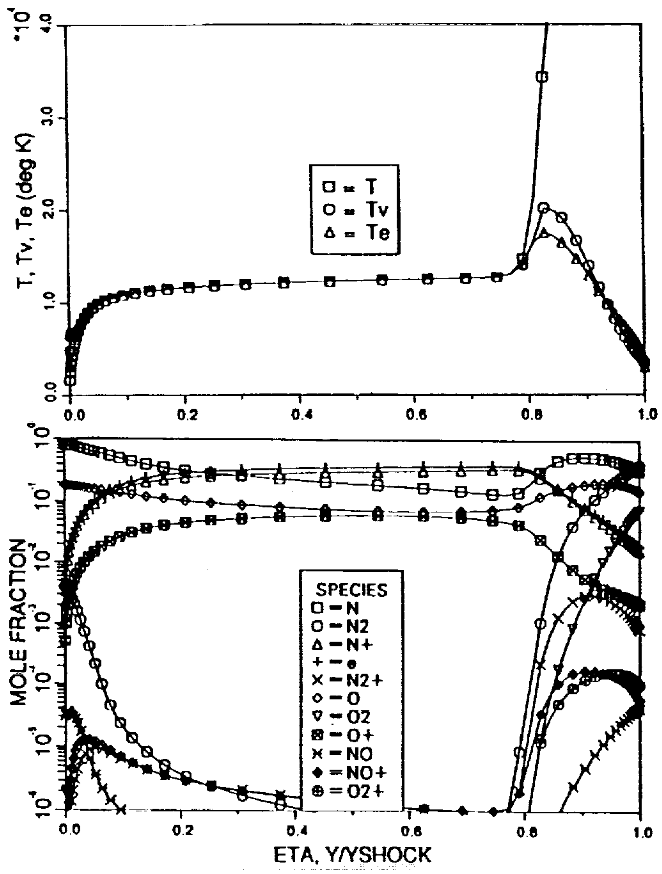

Figure 2: Stagnation Temperature and Mole Fraction Profile

*R*nose = 2.3 m, V = 16 km/sec, H = 80 km

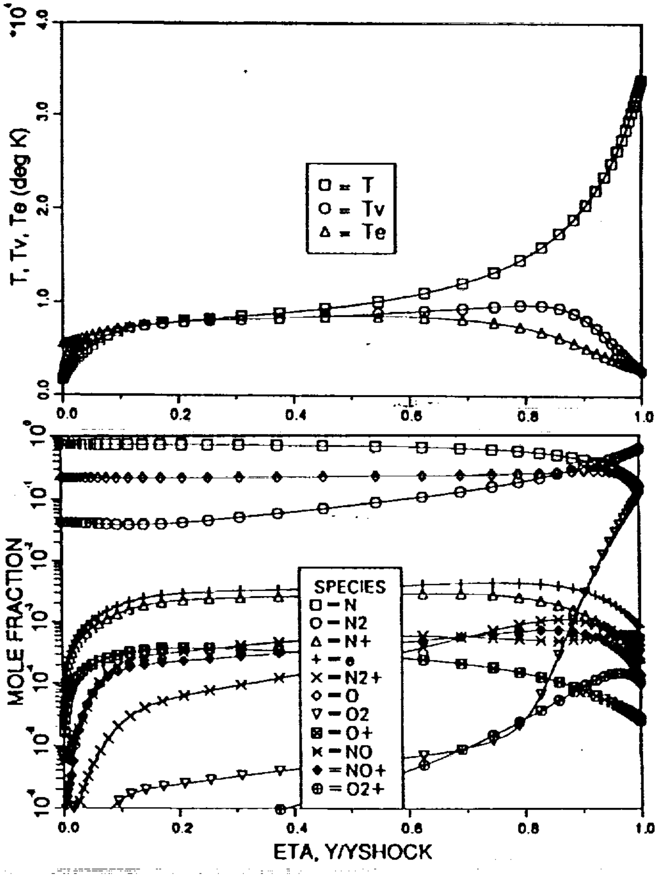

Figure 4: Stagnation Temperature and Mole Fraction Profile

*R*nose = 2.3 m, V = 9 km/sec, H = 80 km

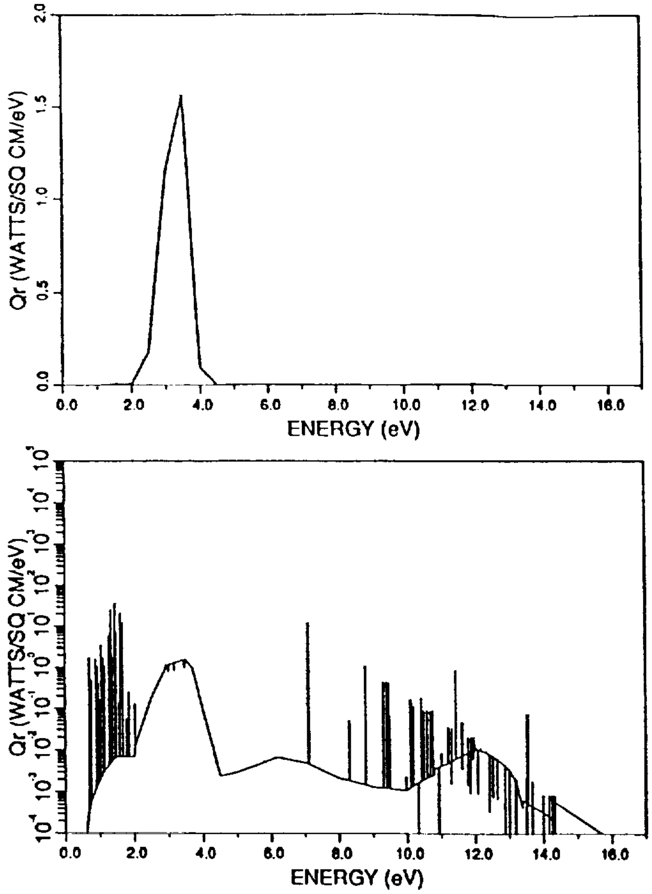

Figure 5: Radiative Heat Flux, Grouped and Detailed Spectra

*R*nose = 2.3 m, V = 9 km/sec, H = 80 km

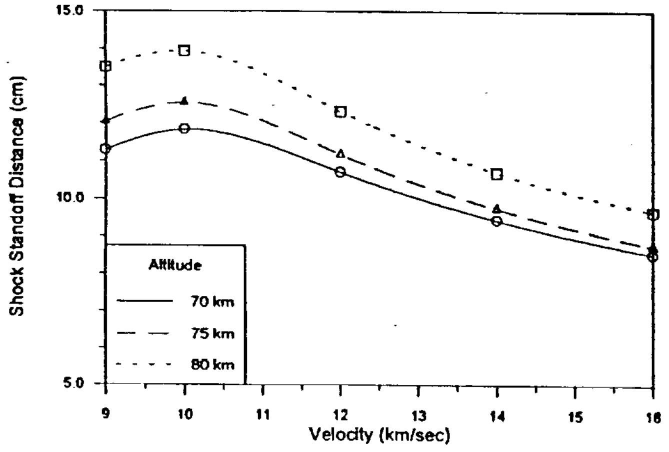

Figure 6: Stagnation Shock Standoff Distances

(a) versus altitude

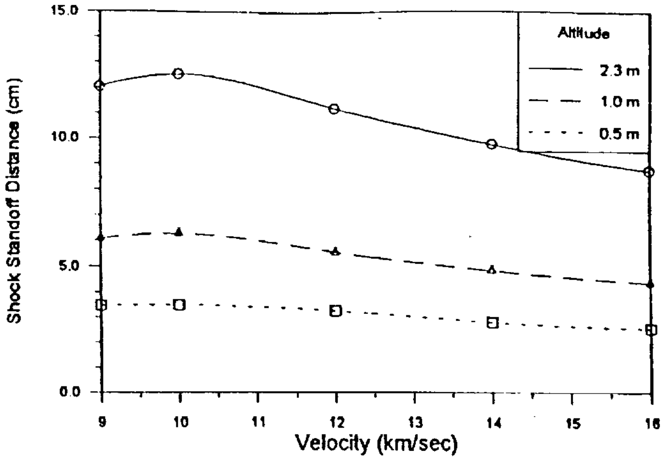

Figure 6: (b) versus nose radius

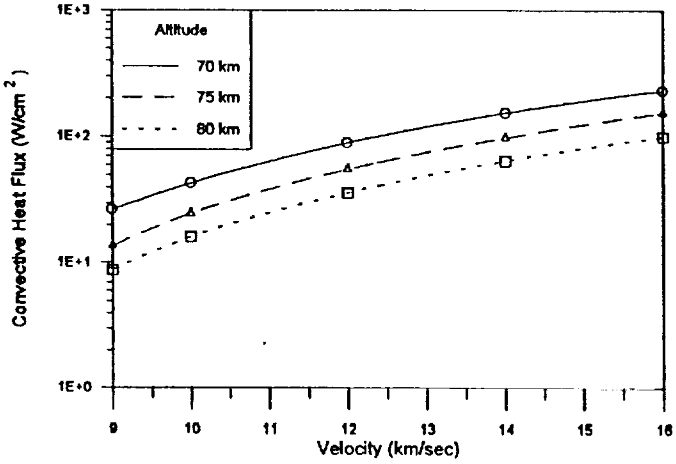

Figure 7: Stagnation Convective Heating Rates

(a) versus altitude

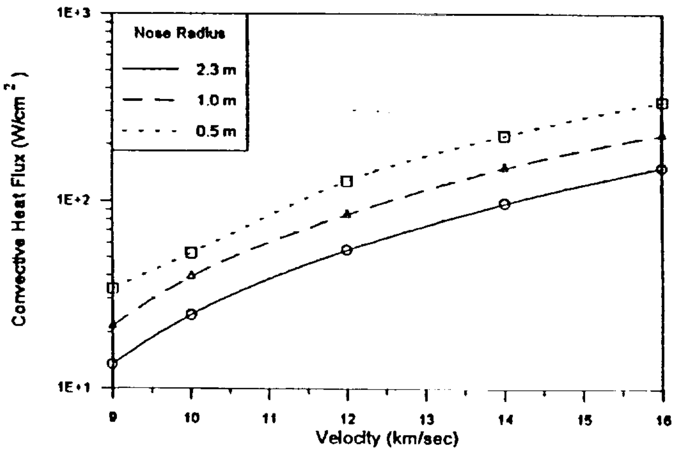

Figure 7: (b) versus nose radius

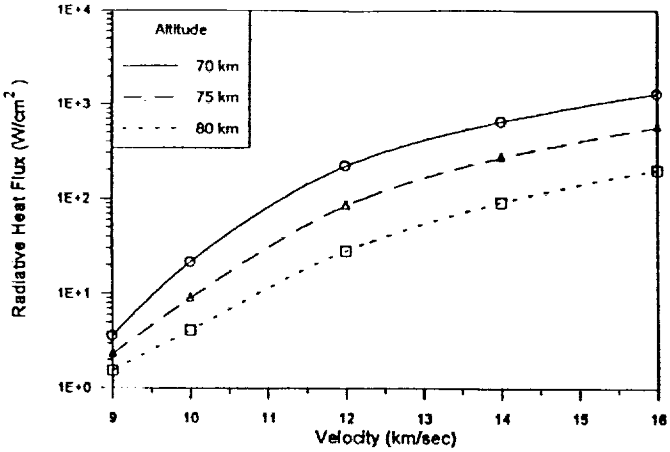

Figure 8: Stagnation Radiative Heating Rates
(a) versus altitude

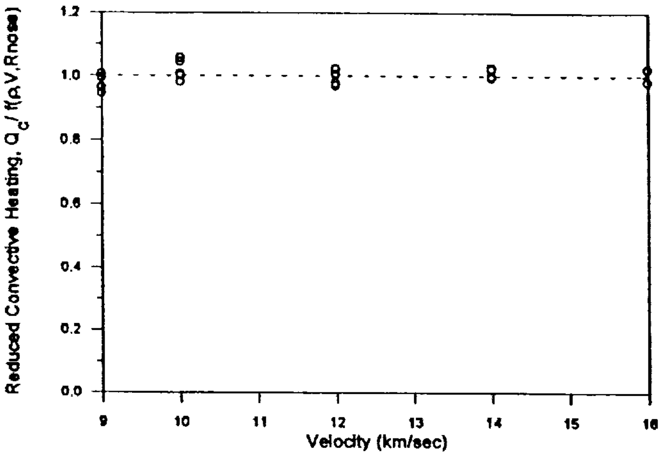

Figure 9: Convective Heat Transfer Correlation

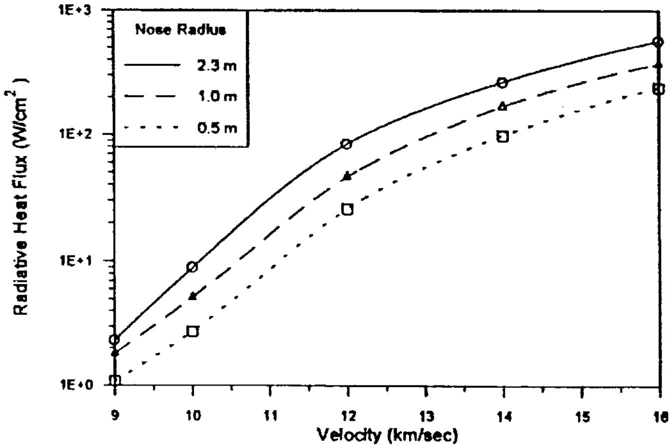

Figure 8: (b) versus nose radius

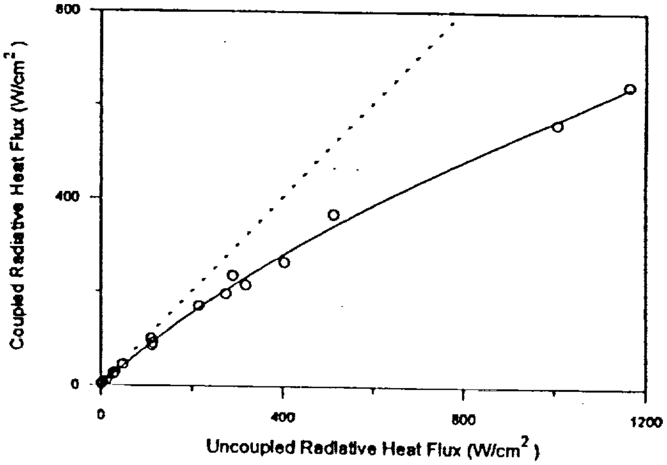

Figure 10: Radiative Cooling Effect of Heat Transfer

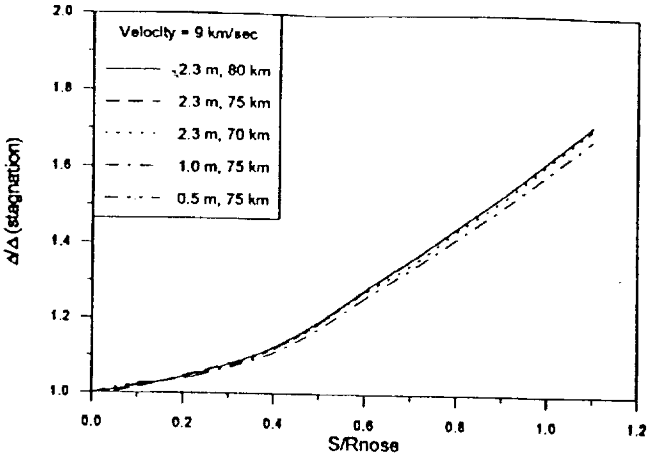

Figure 11: Streamwise Shock Standoff Distance Variations

(a) V = 9 km/sec

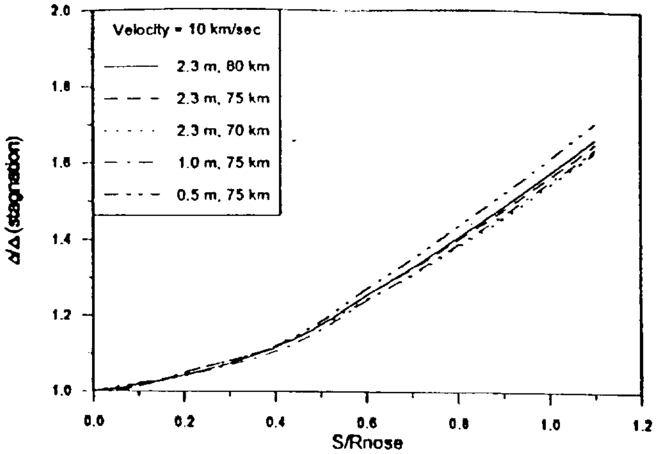

Figure 11: (b) V = 10 km/sec

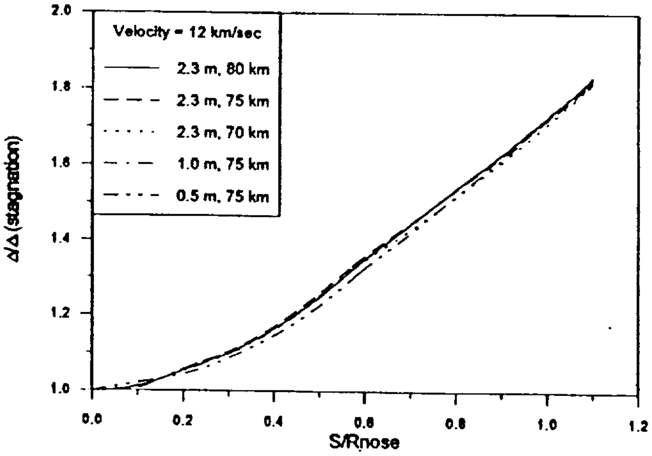

Figure 11: (c) V = 12 km/sec

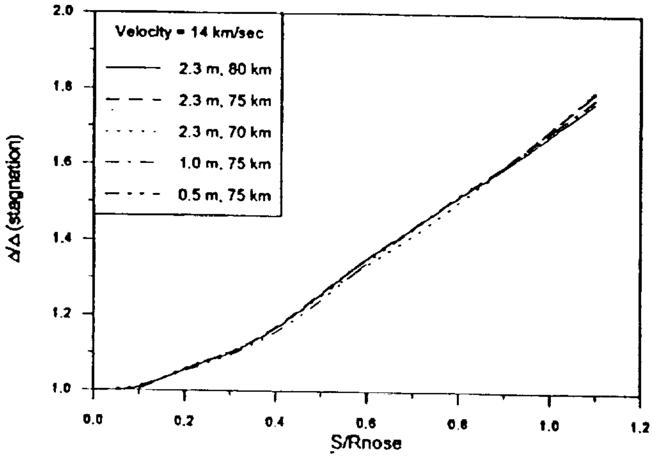

Figure 11: (d) V = 14 km/sec

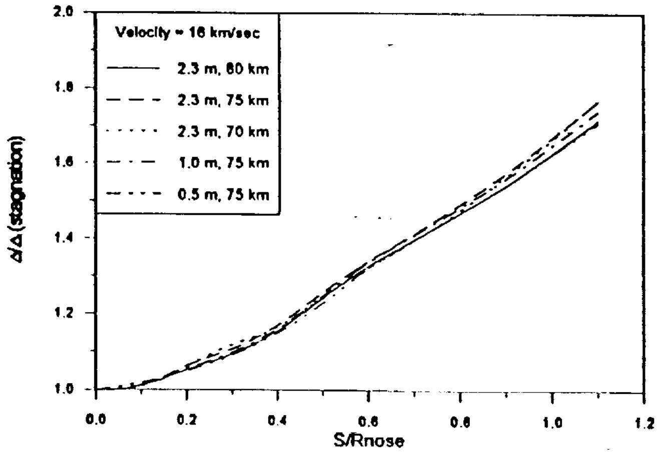

Figure 11: (e) V = 16 km/sec

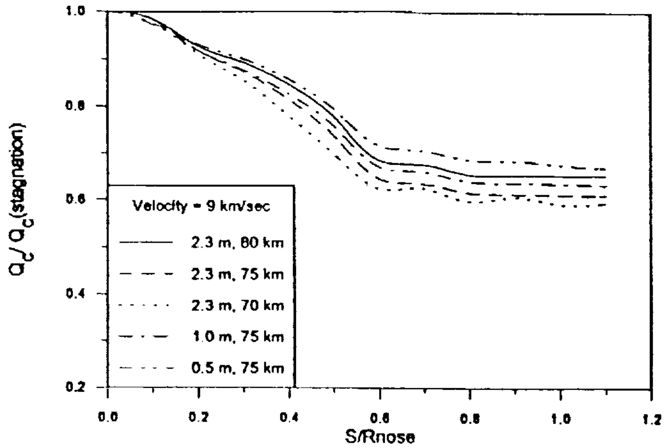

Figure 12: Streamwise Convective Heat Flux Variations
(a) V = 9 km/sec

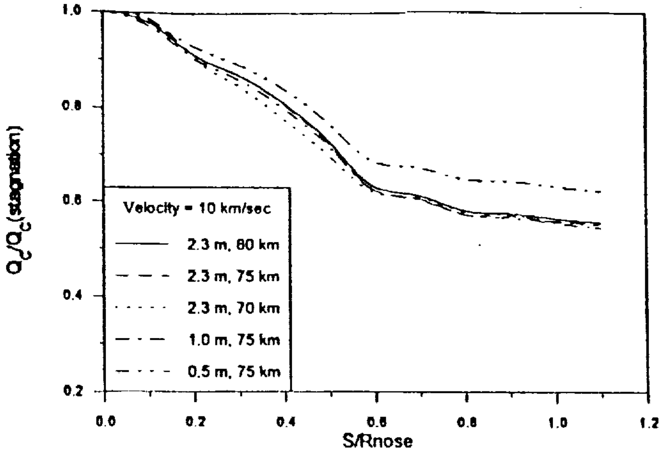

Figure 12: (b) V = 10 km/sec

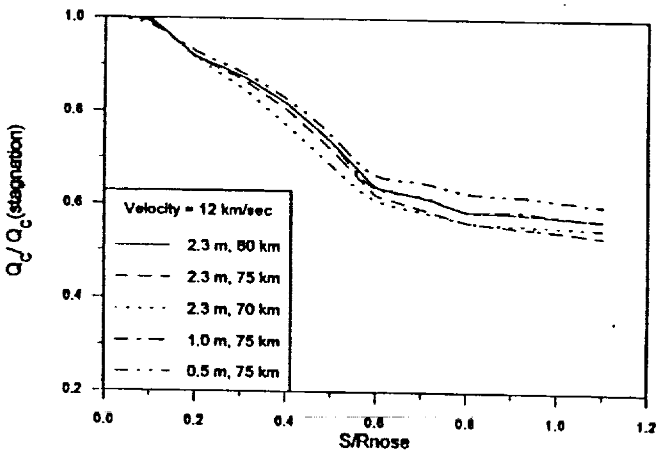

Figure 12: (c) V = 12 km/sec

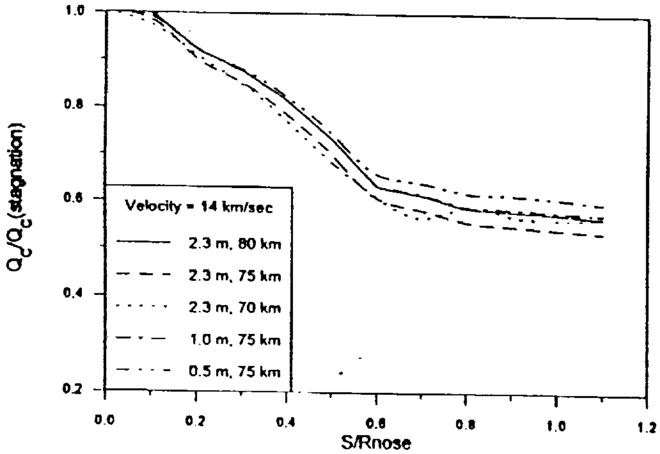

Figure 12: (d) V = 14 km/sec

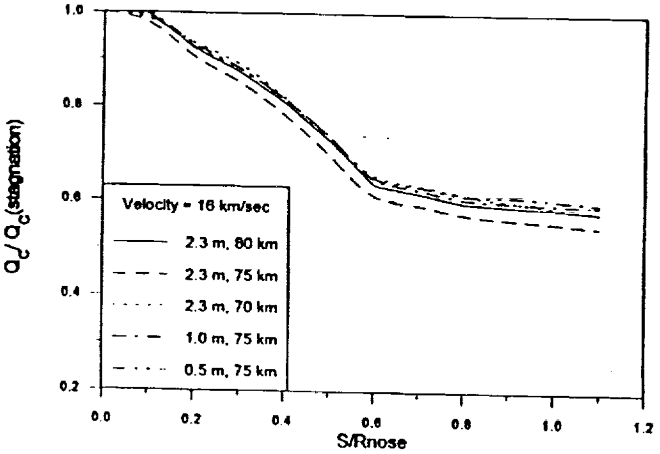

Figure 12: (e) V = 16 km/sec

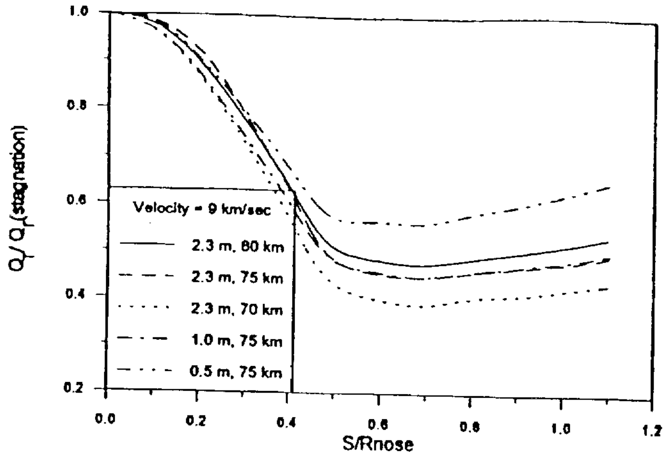

Figure 13: Streamwise Radiative Heat Flux Variations

(a) V = 9 km/sec

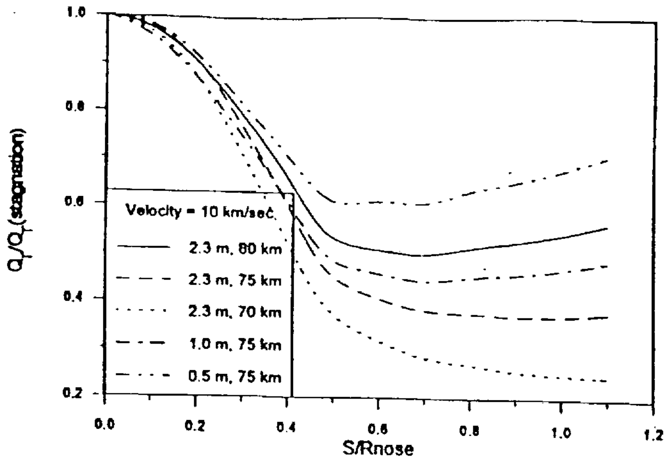

Figure 13: (b) V = 10 km/sec

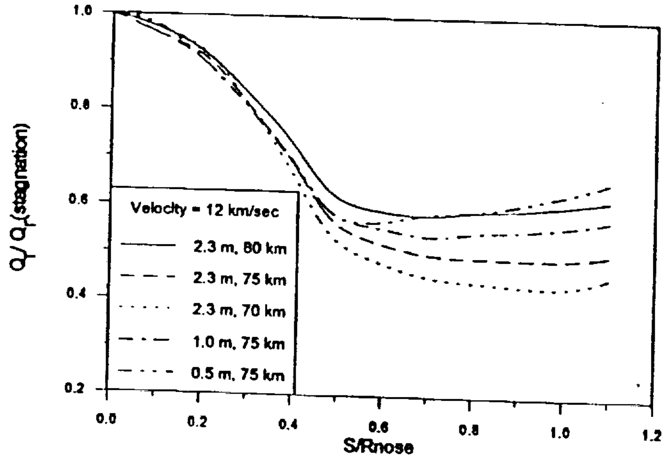

Figure 13: (c) V = 12 km/sec

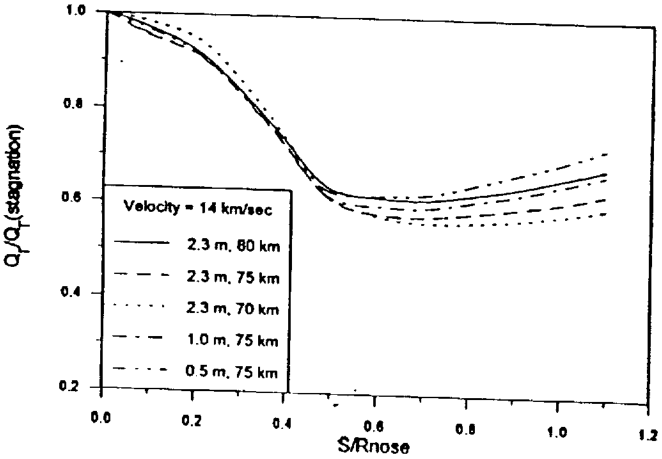

Figure 13: (d) V = 14 km/sec

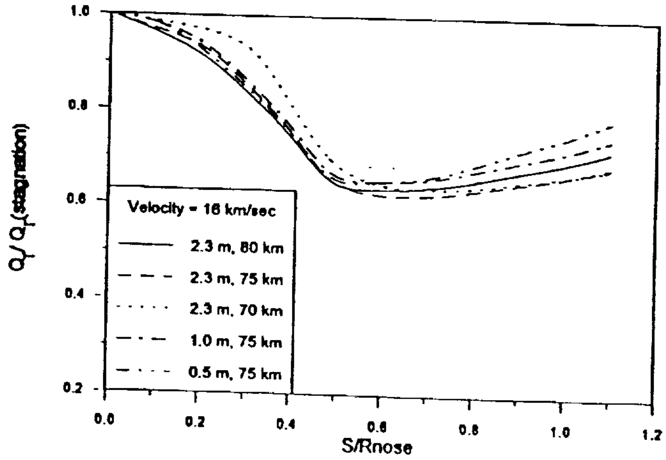

Figure 13: (e) V = 16 km/sec